European Commission
FP7, Grant Agreement 211743

Einstein gravitational wave Telescope conceptual design study

ET-0106A-10

F Acernese[21ac], S Aoudia[1], P Amaro-Seoane[10], F Barone[5ac], L Bosi[14], S Braccini[2], C Bradaschia[2,5], J van den Brand[3], C Van Den Broeck[4], G Cella[2], J Colas[5], K Danzmann[1], T Dent[6], R De Rosa[21ab], V Fafone[8ab], P Falferi[20], R Flaminio[7], J Franc[7], F Frasconi[2], A Freise[9], D Friedrich[1], G Gemme[22], E Genin[5], C Gräf[1], S Hild[13], K Kokeyama[9], B Krishnan[10], M Lorenzini[11], H Lück[1], E Majorana[15a], M Mantovani[2], B Mours[12], H Müller-Ebhardt[1], R Nawrodt[13], G Parguezt[5], A Pasqualetti[5], M Punturo[14,5], P Puppo[15a], D Rabeling[3], T Regimbau[16], S Reid[17], F Ricci[15ab], A Rocchi[8a], S Rowan[17], L Santamaría[18] B Sathyaprakash[6], L Storchi[14], S Tarabrin[1], A Thüring[1], P Weßels[19]
on behalf of the ET science team

Issue: 3

Date: February 18, 2011

[1]Max-Planck-Institut für Gravitationsphysik (Albert-Einstein-Institut) and Leibniz Universität Hannover, Callinstr. 38, 30167 Hannover, Germany
[2]INFN, Sezione di Pisa, I-56127 Pisa, Italy
[3]VU University Amsterdam, De Boelelaan 1081, 1081 HV, Amsterdam, The Netherlands
[4]Nikhef – National Institute for Subatomic Physics, Science Park 105, 1098 XG Amsterdam, The Netherlands
[5]European Gravitational Observatory (EGO), I-56021 Cascina (Pi), Italy
[6]Cardiff University, Cardiff, CF24 3AA, United Kingdom
[7]Laboratoire des Matériaux Avancés (LMA), IN2P3/CNRS, F-69622 Villeurbanne, Lyon, France
[8]INFN, Sezione di Roma Tor Vergata[a], Universitá di Roma Tor Vergata[b], I-00133, Roma, Italy
[9]University of Birmingham, Birmingham, B15 2TT, United Kingdom
[10]Max Planck Institute for Gravitational Physics (Albert Einstein Institute) Am Mühlenberg 1, D-14476 Potsdam, Germany
[11]INFN, Sezione di Firenze, I-50019 Sesto Fiorentino[a]; Università degli Studi di Firenze, I-50121[b], Firenze; Università degli Studi di Urbino 'Carlo Bo', I-61029 Urbino[c], Italy
[12]LAPP–IN2P3/CNRS, Université de Savoie, F-74941 Annecy-le-Vieux, France
[13]Friedrich-Schiller-Universität Jena PF 07737 Jena
[14]INFN, Sezione di Perugia, I-6123 Perugia,Italy
[15]INFN, Sezione di Roma[a]; Università 'La Sapienza'[b], I-00185 Roma, Italy
[16]Université Nice-Sophia-Antipolis, CNRS, Observatoire de la Côte d'Azur, F-06304 Nice
[17]Department of Physics and Astronomy, The University of Glasgow, Glasgow, G12 8QQ, UK
[18]LIGO, California Institute of Technology, Pasadena, CA 91125, USA
[19]Laser Zentrum Hannover e.V., Hollerithallee 8, D-30419 Hannover, Germany
[20]INFN, Gruppo collegato di Trento, Sez. di Padova and Istituto di Fotonica e Nanotecnologie CNR-ITC, I-38050 Povo (Trento), Italy
[21]INFN, Sezione di Napoli [a]; Università di Napoli 'Federico II'[b] Complesso Universitario di Monte S.Angelo, I-80126 Napoli; Università di Salerno[c], Fisciano, I-84084 Salerno, Italy
[22]INFN, Sezione di Genova; I-16146 Genova, Italy

Abstract

This document describes the Conceptual Design of a third generation gravitational wave observatory named Einstein Telescope ("ET"). The design of this new research infrastructure has been realised with the support of the European Community's Seventh Framework Programme (FP7/2007-2013) under grant agreement n 211743. In this document are described the fundamental design options, the site requirements, the main technological solutions, a rough evaluation of the costs and a schematic time plan.

This is a working and evolving copy. In the current version this document is still incomplete and could contain wrong or contradictory statements.

Contents

1 Introduction

The first generation of interferometric gravitational wave (GW) detectors (GEO600 [1], LIGO [2], TAMA [3], Virgo [4]) have reached or approached their design sensitivities, and thus demonstrated the effectiveness of the working principle. The major detectors currently operative are enhanced versions of the first generation (Virgo+ and E-LIGO), with higher laser power and some technological improvements.

Advanced detectors (like "Advanced LIGO" and "Advanced Virgo") will show a sensitivity improved roughly by a factor of ten with respect to the initial interferometers. They are based on technologies currently available, sometimes tested in reduced scale prototypes, but still to be implemented in full scale. According to the current models of GW sources, sensitivity of the advanced interferometers is expected to guarantee the detection of the signals generated by astro-physical sources within months to a year at most. For example, at the nominal sensitivity of the advanced detectors, the expected detection rate of the GW signal generated by a binary system of coalescing neutron stars is about a few tens per year. But apart from extremely rare events, the expected signal-to-noise ratio (SNR) of these detections obtained with the advanced detectors is too low for precise astronomical studies of the GW sources and for complementing optical and X–ray observations in the study of fundamental systems and processes in the Universe.

These considerations led the GW community (see Table 1) to start investigating a new (third) generation of detectors. With a considerably improved sensitivity these new machines will open the era of routine GW astronomy and with the ET project Europe will lead this scientific revolution. Since the first detection of a GW signal is expected to occur in the advanced interferometers, the evaluation of the scientific impact of ET it is especially focused on the observational aspects rather than on the detection capabilities.

To realise a third generation GW observatory with a significantly enhanced sensitivity (we defined a target of a factor of ten improvement in sensitivity for ET with respect to the advanced detectors in a wide frequency range), several limitations of the technologies adopted in the advanced interferometers must be overcome and new solutions to be developed are proposed in this document to reduce the fundamental and technical noises that will limit the next generation machines.

However, the first and main target of this document is the definition of the requirements and of the main characteristics of the site hosting ET, the design of the key elements of the research infrastructure, the rough evaluation of the costs and of the timeline of its implementation. To understand the importance and the need of the site and infrastructures in the ET design it is worth to recall the history of the current GW detector infrastructures, shown in Fig. 1; current and advanced detectors are using the same infrastructure that will be about 20 years old when the second generation will be online. Any further improvement of the sensitivity will be limited by the constraints of the site and infrastructure (arm length, local seismic noise, absence of cryogenic apparatus, vacuum pipe size, . . .). On the contrary, in order to realise a third-generation GW observatory like ET, an infrastructure hosting several detectors evolving for many decades is crucial.

Table 1: Institutions participating ("Beneficiaries") to the ET design study

Institute	Country
European Gravitational Observatory	Italy–France
Istituto Nazionale di Fisica Nucleare	Italy
Max-Planck-Gesellschaft zur Förderung der Wissenschaften e.V., acting through Max- Planck-Institüt für Gravitationsphysik	Germany
Centre National de la Recherche Scientifique	France
University of Birmingham	United Kingdom
Glasgow University	United Kingdom
Nikhef	The Netherlands
Cardiff University	United Kingdom

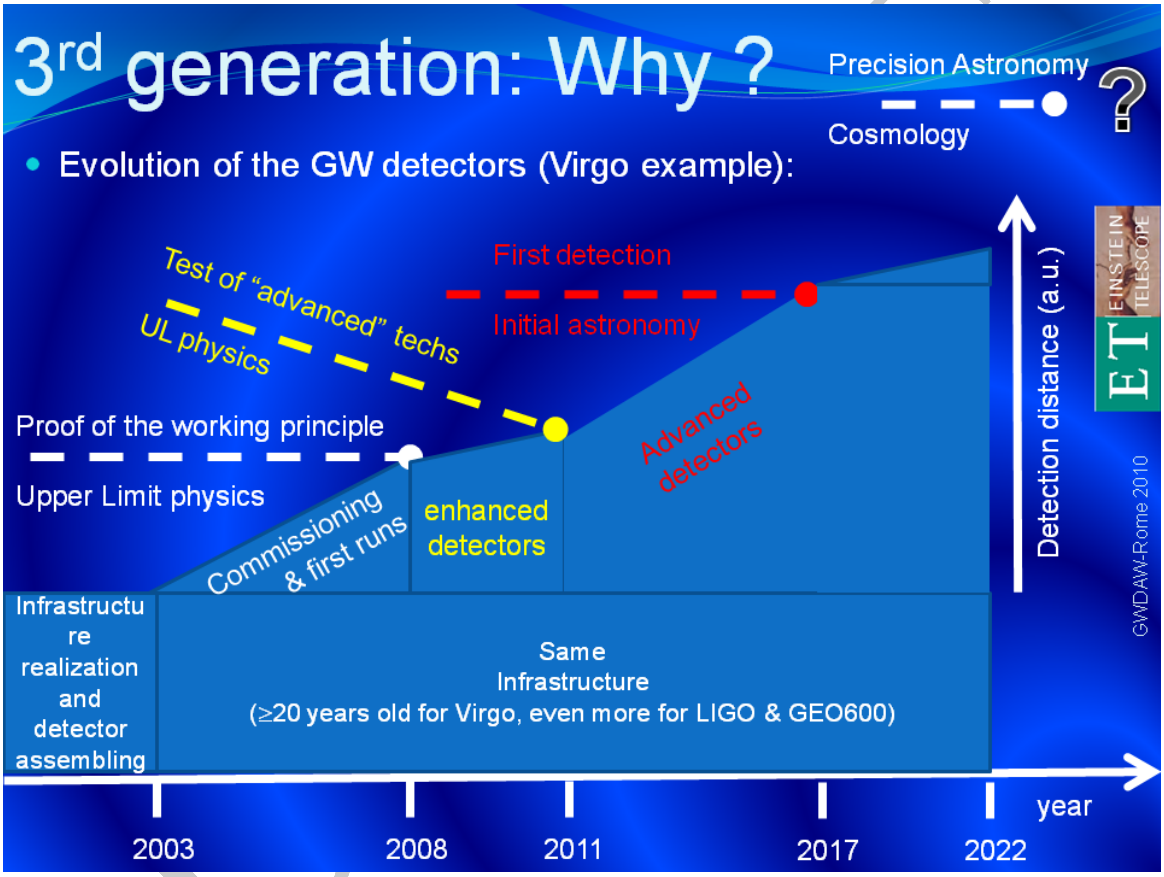

Figure 1: Evolution of the first and second generation GW detectors. Time is on the horizontal axis, detector performances in the vertical one. When the advanced detectors will be operative the hosting infrastructures will be more than 20 years old and any further improvement of the performances (sensitivity) will be suppressed by the limitation imposed by the infrastructures. (slide presented by M. Punturo at the GWDAW meeting, Rome Jan. 2010)

1.1 Overview of the ET observatory project

Authors: M.Punturo, H. Lueck

1.1.1 Observatory layout

In the following paragraph we will shortly describe the overall layout of the Einstein Telescope, easing the understanding of the Design Study document and providing a mental picture of the observatory while reading through the descriptions of the individual subsystems. An artists impression of the Einstein Telescope is given in figure 2

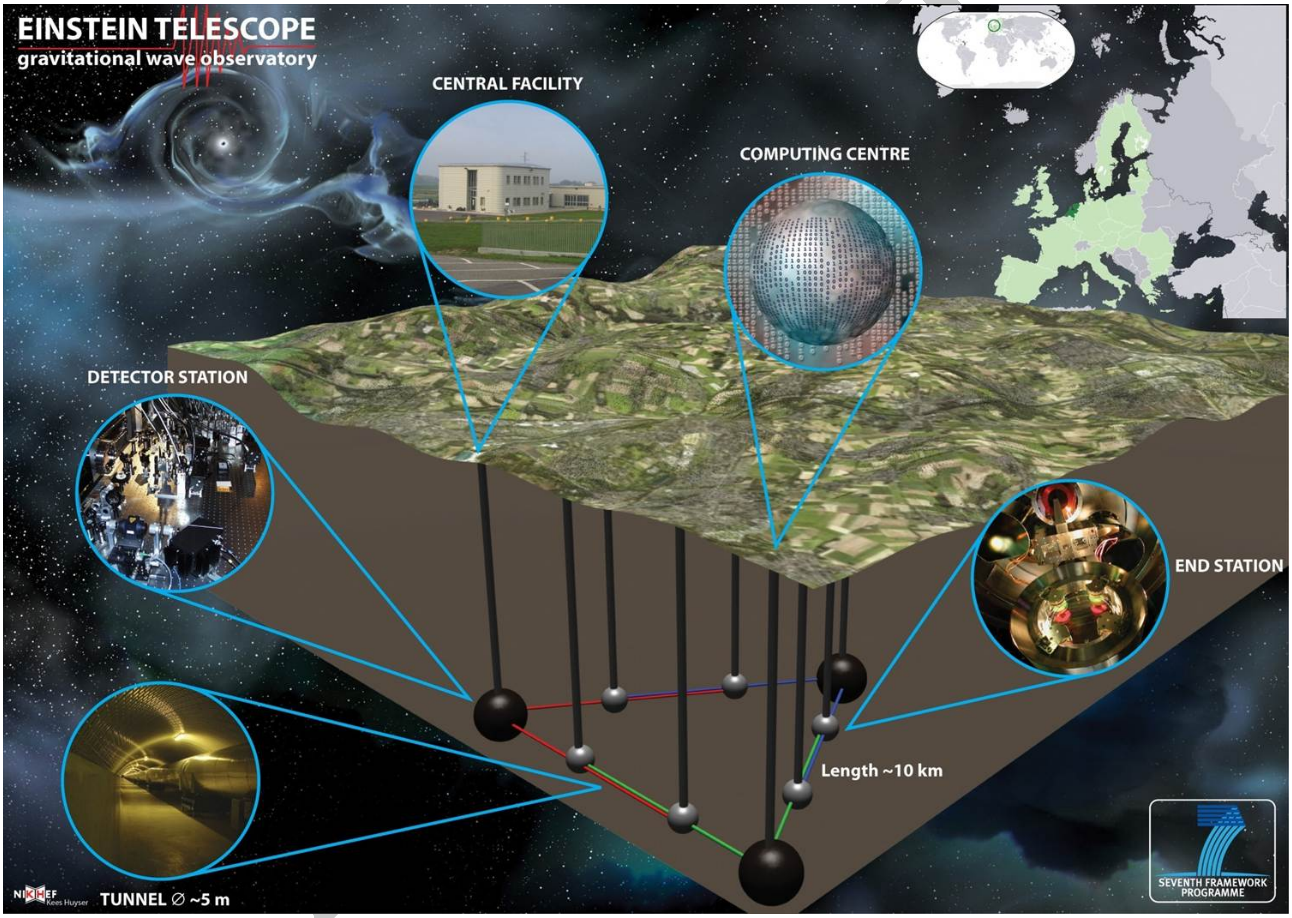

Figure 2: Artists view of the Einstein Telescope

The Einstein Telescope will be located underground at a depth of about 100 m to 200 m and, in the complete configuration, will consist of three nested detectors each in turn composed of two interferometers. The topology of each interferometer will be the dual recycled Michelson layout with Fabry-Perot arm cavities.

The sensitivity goal for the Einstein telescope evolved in the course of the design study. The initial goal of improving the sensitivity with respect to the 'advanced' detector generation by a factor of ten was driven by the need to get frequent high Signal-to-Noise-Ratio (SNR) events for doing efficient gravitational wave astronomy. The high frequency sensitivity was given by the maximum power feasible, the mid frequency range was governed by thermal noises and the low frequency range by either thermal or seismic noises. The initial estimates have been refined throughout the design study and finally resulted in the sensitivity shown in figure 4.

The conceptual design of a project of this financial scale has to be based on well proven and experimentally tested techniques. The sensitivity, which the Einstein Telescope project aims for, on the other hand, needs to exploit all state of the art technologies and drive them to the limit. This sensitivity can only be reached by significantly increasing the size of the detector beyond the size of currently available instruments and going to an underground location where the seismic noise is lower. By increasing the arm length to 10 km the influence of unavoidable displacement noises can be lowered to a sufficiently low level. In order to achieve a sufficient sensitivity at high frequency the light power in the interferometer arms needs to be increased to the Megawatt range, conflicting with the requirements of low radiation pressure noise and cryogenic temperature operation for a good sensitivity in the low frequency range. To fulfil both these requirements in a single detector is beyond the current state of the art. The Einstein telescope will therefore be realised in what we call a Xylophone arrangement shown in figure 196: a low frequency interferometer will be operated at low laser power and cryogenic temperatures around 20 K whereas the high frequency interferometer will be operated at high laser power and room temperature. Three of these hybrids detectors will be arranged in an equi lateral triangle with a baseline of 10 km. The optics for the interferometers will be suspended as multiple pendulums reaching an overall suspension length of about 20 m. Concerning the main mirrors we have to distinguish between the cryogenic interferometers and the room temperature operated ones. The room temperature optics will be of ultra low absorption fused silica, have a diameter of about 60 cm and a thickness of about 40 cm, giving a weight of about 250 kg. The cryogenic optics will either be made of sapphire or, more likely, of silicon. The dimensions will partly be determined by the maximum availabe bulk material size and otherwise comparable to the room temperature ones. A summary of the main parameters for the high and low temperature interferometers is given in table 16.
The sensitivity curve shown in figure 4 gives the sensitivity for a single detector with 10 km arm length and an angle of 90 ° between the arms. This is done for better comparison with the existing detectors and their 'advanced' versions. ET will in fact have three 10 km detectors and the angles between the arms will be 60 °. The resulting sensitivity in comparison with a single 90 ° detector depends on the source looked at, as the angular antenna pattern (see figure 171) and the polarization dependence (independent in the triangular case) influence the signal strength differently for different detector layouts. On average the sensitivity of the triple 60 ° detector is comparable to a single 90 ° one.
As the understanding of the achievable sensitivity of the Einstein Telescope evolved throughout the Design Study, different sensitivity curves are used in this document, named from ET-B to ET-D (see figure 3. The very first, preliminary sensitivity curve ET-A was a very rough, early estimate based on crude, obsolete estimates and will hence not be used int his document. ET-B is the sensitivity curve where each detector is build from a single interferometer, where the high power needed to achieve good high frequency performace compromises the low frequency performance. The next evolutionary step is the sensitivity curve ET-C, where each detector is split into two interferometers, each dedicated to a distinct frequency range (the Xylophone configuration). The latest sensitivity curve is given by ET-D, where imperfections like optical losses in cavities are included in the computations. As the later sensitivity curves only became available during the Design Study, some of the subsection results are still based on earlier versions, which will be indicated by the sensitivity curve acronym.

1.1.2 Observatory timeline

Authors: M.Punturo, H. Lueck
The realization of the ET observatory will be the final step of a long path and the initial act of a new scientific adventure. Several steps have been necessary (see Sec.6) to allow the realization of this conceptual design study document and few other important achievements are needed to reach the readiness condition for the observatory realization. The design of the new detector must evolve from the current conceptual phase to the technical design phase, successful R&D activities must confirm the feasibility of the solutions proposed in this document, but, first of all, it is crucial that advanced detectors confirm the effectiveness of their new technologies and that the gravitational wave signal is detected in these interferometers. For this reason the effective excavation of the ET site cannot start before the 2017 and 2018 is here taken as initial time (t_0) for the ET observatory realization. Being ET an observatory that will be *on air* for decades, the priority in the construction will be attributed to the site and infrastructures realization, selecting a modular philosophy for the detectors that will allow to

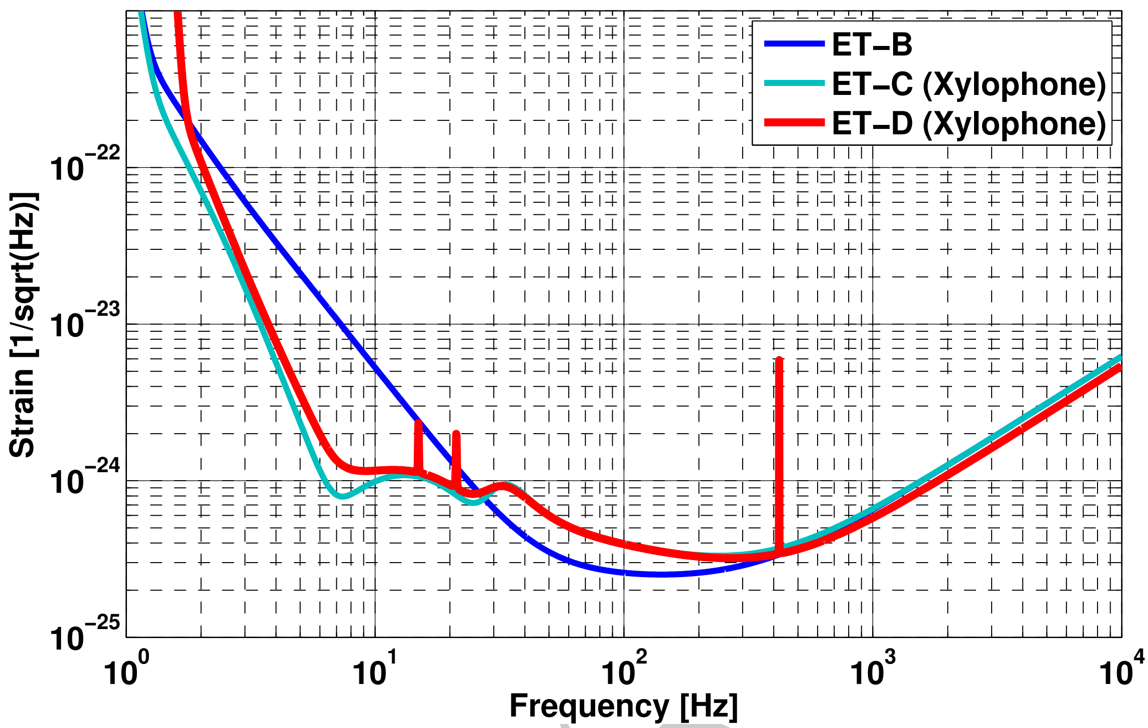

Figure 3: Sensitivity curves for ET used in this document. For details see text.

implement the different interferometers composing each detector with a schedule diluted in time. In this way, after about 6 years of construction, installation and commissioning, the first detector of the ET observatory could be operative at the end of the first half of the next decade.

1.1.3 Observatory costs

Authors: M.Punturo, H. Lueck
...

1.1.4 Document layout

Following this introductory section we will describe the scientific goals for the Einstein Telescope, outlining the scientific results that can be obtained and moreover the new science that can only be done with a third-generation observatory. The types of sources detectable with the Einstein telescope will be listed and event rates as well as signal-to-noise ratios will be estimated. Data analysis and computational challenges are described in subsections 2.6 to 2.8.
As the costs of the Einstein telescope are dominated by the construction of the tunnels, caverns, and vacuum system a full section will be dedicated to this topic. In this document we will concentrate on the scientific aspects of the site selection and we will leave the discussion of political and funding factors of influence to a later time. From the scientific point of view the seismic noise level and the homogeneity of the surrounding soil are of the biggest influence. Seismic noise levels have been measured at many locations in Europe and are compared to other sites that have been selected for gravitational wave detectors or are possible candidates for other high sensitivity experiments. The need of cooling the test masters for the observatory to cryogenic temperatures puts some constraints on the infrastructure and needs to be taken into account when discussing

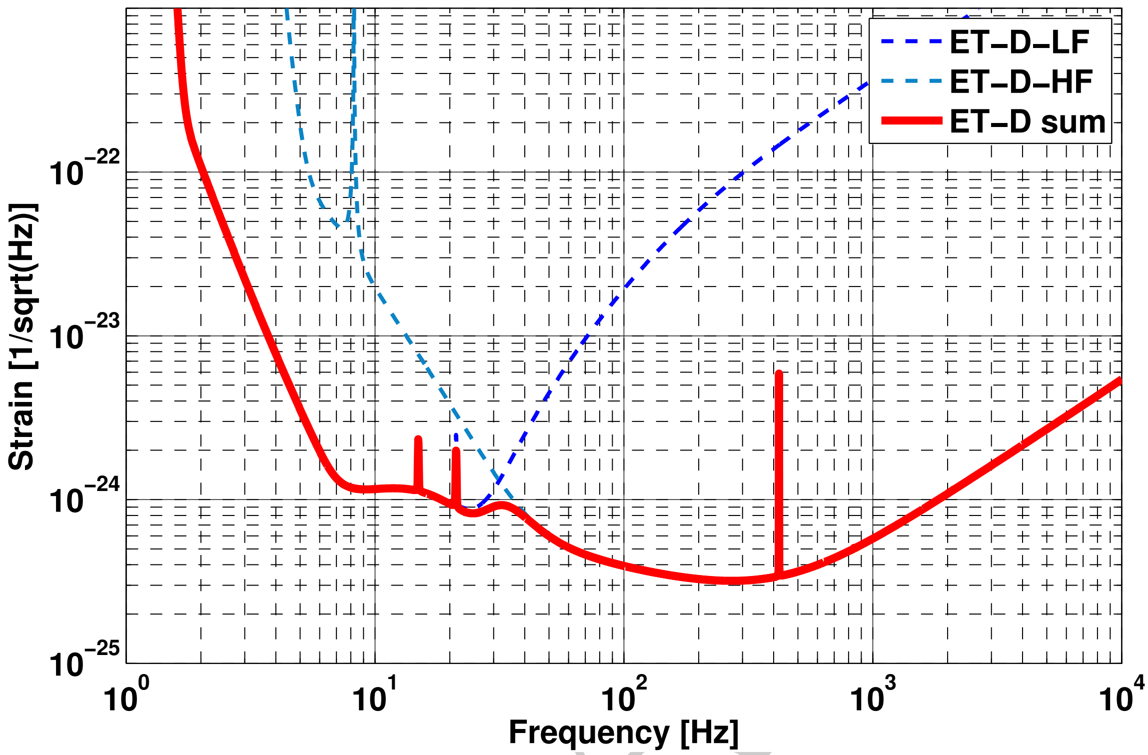

Figure 4: Sensitivity of the Einstein Telescope in the 'Xylophone' configuration. The sensitivity of the low frequency cryogenic interferometer is shown in the dashed dark blue curve and the one of the high frequency room temperature one in a dashed blue-green tone. The sum of both is given by the solid bright red curve.

safety issues.
As in the first generation of gravitational wave detectors and also in the advanced generation, the optics for the Einstein telescope need to be carefully suspended to keep them isolated from the seismic motion of the surrounding ground. A conceptual suspension design fulfilling these requirements and also allowing to cool the test masses is described in the next section.
The optical design of the observatory influences the sensitivity, the directionality, the redundancy of data streams, and the requirements to be put on the various subsystem.

2 Science case

Underline what is beyond the 2nd generation and what are the targets of ET

2.1 Einstein Telescope Science Goals

Some three hundred years after Galileo observed the Jovian satellites, the twentieth century heralded a new era in observational astronomy with radio and microwave antennas, gamma- and X-ray detectors, which revolutionized astronomy and opened the entire electromagnetic window for observing and understanding the Universe. A remarkable revelation coming from these observations is that about 96 percent of our Universe is invisible and that gravitational interaction powers the most luminous and spectacular objects and phenomena such as quasars, gamma-ray bursts, ultra luminous X-ray sources, pulsars, and the evolution of the early Universe.

Einstein's theory of gravity predicted that dynamical systems in strong gravitational fields will release vast amounts of energy in the form of gravitational radiation. This radiation has the potential to open a new window on the Universe, complementing the electromagnetic window. Russell Hulse and Joe Taylor were awarded the 1993 Nobel Prize in Physics for the discovery of a binary consisting of two neutron stars in close orbit in which indirect evidence for the emission of gravitational waves was found.

Interferometric gravitational wave (GW) detectors that are currently taking data and advanced detectors that will be built over the next ten years will be the first steps in establishing the field of gravitational astronomy through their detection of the most luminous sources such as the merger of binary neutron stars and black holes. Einstein Telescope will make it possible to observe a greater variety of phenomena, and provide a new tool for expanding our knowledge of fundamental physics, cosmology and relativistic astrophysics. Is the nature of gravitational radiation as predicted by Einstein's theory? Are black hole spacetimes uniquely given by the Kerr geometry? Do event horizons always form around gravitationally collapsing matter? How did the black holes at galactic nuclei form? What were the physical conditions in the very early Universe? What is the nature of quantum gravity and what is the origin of space and time? Are there really ten spatial dimensions? These are some key questions at the forefront of physics that future GW observations might shed some light on.

2.1.1 Fundamental physics

Astronomical sources of gravitational waves are essentially systems where gravity is extremely strong and often characterized by relativistic bulk motion of massive objects. The emitted radiation carries an uncorrupted signature of the nature of the space-time geometry and is therefore an invaluable tool to understand the behaviour of matter and geometry in extreme conditions of density, temperature, magnetic fields and relativistic motion. Here are some examples of how GW observations can impact fundamental physics.

In Einstein's theory, gravitational radiation travels at the speed of light and has two polarization states. In alternative theories of gravity one or both of these properties might not hold, owing to the presence of massive gravitons, or a scalar field mediating gravity in addition to the tensor field. Experimental tests of gravity, as well those afforded by the data from the Hulse-Taylor binary, are consistent with both Einstein's theory and one of its alternatives called the Brans-Dicke theory. Gravitational wave detectors will bring these theories vis-a-vis observations that could decisively rule out one or the other.

According to Einstein's gravity the space-time in the vicinity of black holes is described by a unique geometry called the Kerr solution. Observation of the radiation from the in-fall of stellar-mass black holes into intermediate-mass black holes will make it possible to test such uniqueness theorems. X-ray astronomy has provided firm indirect evidence that intense sources of x-rays may well host a black hole. An unambiguous signature of the black hole geometry, however, could eventually be provided by the detection of black hole quasi-normal modes: gravitational radiation with characteristic frequencies and decay times. Failure to detect such radiation from, for example, a newly formed black hole would mean that gravity is more exotic than what we currently believe, and might reveal new phases of matter at extremely high densities.

The most attractive versions of string theory require a ten- or eleven-dimensional space-time, far larger than what we perceive. In certain phenomenological models at the interface of string theory and cosmology, what we perceive as a four-dimensional Universe could be one part, or "brane", within a higher dimensional "bulk" Universe. The extra spatial dimensions may be compact and sub-millimetre-scale, or even macroscopically large, if their geometry has properties known as "warping". The key feature of brane-world theories is that gravitational interactions, and in particular gravitational waves, propagate in the bulk, while other interactions are restricted to the brane, which partly explains why gravity is so weak.

2.1.2 Relativistic Astrophysics

Astronomy has revealed a Universe full of diverse and exotic phenomena which remain enigmas decades after their discovery. Supernovae are the end-states of stellar evolution, resulting in gravitational collapse followed by a huge explosion of in-falling matter. Gamma-ray bursts are intense sources of gamma radiation that last only a few seconds to minutes yet emit more energy than a star does in its entire lifetime. Radio pulsars are compact objects as massive as the Sun but only about 10 km in size, and the regularity of their radio pulses rivals the best atomic clocks in the world. Transient radio sources thousands of light years away are associated with magnetic fields so strong that the emitted radiation could breakdown terrestrial radio stations. For each of these objects the source is believed to be couched in dense environs and strong gravitational fields and, therefore, is a potential source of gravitational radiation. For example, gamma-ray bursts could be produced by colliding neutron stars which are electromagnetically invisible for most of their lives but are very powerful emitters of GW. Transient radio sources could be the result of quakes in neutron stars with concomitant emission of GW. Observing such 'multi-messengers' (sources that are strong emitters of both EM and GW radiation) will help understand phenomena that have remained puzzles for decades.

The centre of every galaxy is believed to host a compact object a million to a billion times as massive as our Sun, a powerful emitter of optical, radio and other radiation. What is the nature of this object? How and when it form? Did it form from small 100 solar mass seeds and then grow by accreting gas and other compact objects? What is its relation to the size of the galaxy as a whole? These are some of the questions which a model of the formation of structure in the Universe must answer. While electromagnetic observations have provided valuable data, GW observations can help address some of the key questions on the formation and nature of these objects.

Future gravitational wave detectors will also be sensitive to a population of sources at very high red-shifts, helping us study cosmological evolution of sources, the history of star formation and its dependence on the matter content of the Universe, and development of large-scale structure in the Universe.

2.1.3 Cosmology

The twentieth century was the golden age of cosmology. With the advent of radio and microwave astronomy it was possible to finally address key questions about the origin of the Universe. The cosmic microwave background (CMB) is a relic radiation from the hot "Big Bang" that is believed to have been the initial condition for primordial nucleosynthesis. Since the early Universe was very dense, this radiation was in thermal equilibrium with matter for about 380,000 years after the Big Bang and cannot directly reveal the conditions in the very early phases of the Universe's history. The most direct way of observing the primaeval Universe is via the gravitational window with a network of two or more detectors. From fairly general assumptions one can predict the production of a stochastic background of GW in the early Universe, which travel to us unscathed as a consequence of their weak coupling to matter.

The most amazing aspect of the Universe is that only about 4% of its energy density appears in the form of visible matter, the rest being dark matter and dark energy. In order to understand the behaviour of these 'dark' contents it is necessary to have a standard candle – a population of sources whose distance from Earth can be inferred from their luminosity. Compact binaries are an astronomer's ideal standard candle: By measuring the signature of the gravitational radiation they emit, it is possible to infer their intrinsic parameters (e.g. the masses and spins of the component objects) and accurately deduce their luminosity distance. In fact, compact binaries eliminate the need to build a cosmic distance ladder – the process by which standard candles at different distances are calibrated in astronomy since there is no source that is suitable at all distances.

The synergy of multi-messenger astronomy is nowhere more apparent than in the use of standard sirens of gravity to test the concordance model of cosmology. ET might detect several hundred compact binary coalescence events each year in coincidence with short-hard gamma-ray bursts, provided, of course, the two are related. While gravitational observations would provide an unambiguous measure of the luminosity distance, the host galaxy of the GRB could be used to measure the redshift. By fitting the observed population to a cosmological model, it will be possible to measure the Hubble parameter, dark matter and dark energy densities, as well as the dark energy equation-of-state parameter.

The early history of the Universe may have witnessed several phase transitions as the temperature decreased through the energy scales of a Grand Unified Theory (GUT) and electroweak symmetry-breaking, and eventually to the current state in which we see four different fundamental interactions. During some phase transitions, cosmic strings form as one-dimensional topological defects at the boundaries of different phases. Vibrations of these strings at the speed of light can sometimes form a kink which emits a burst of gravitational radiation. The spectrum of such radiation has a unique signature which can help us detect cosmic strings and measure their properties, and thus provide a glimpse of the Universe as it underwent phase transitions.

Perhaps the most exciting discovery of the new window will be none of the above. If the astronomical legacy is any example, gravitational astronomy should unveil phenomena and sources never imagined in the wildest theories – a possibility of any new observational tool.

2.2 Sources of gravitational waves in ET

The goal of this Section is to give an overview of the sources expected to be observed by ET and problems to be addressed in the context of the Design Study. We will begin with a very brief introduction to gravitational waves and then go on to describe the sources, their properties and the problems that need to be addressed over the next two years.

Gravitational waves are described by a second rank tensor $h_{\alpha\beta}$, which, in a suitable coordinate system and gauge, has only two independent components h_+ and $h_\times$, $h_{xx} = -h_{yy} = h_+$, $h_{xy} = h_{yx} = h_\times$, all other components being zero. A detector measures only a certain linear combination of the two components, called the *response* $h(t)$, given by

$$h(t) = F_+(\theta, \varphi, \psi)h_+(t) + F_\times(\theta, \varphi, \psi)h_\times(t), \tag{1}$$

where F_+ and $F_\times$ are the detector antenna pattern functions, ψ is the polarization angle, and (θ, φ) are angles describing the location of the source on the sky. The angles are all assumed to be constant for a transient source but time-dependent for sources that last long enough so that the Doppler modulation of the signal due to the relative motion of the source and detector cannot be neglected.

2.2.1 Compact binary coalescences

A compact binary, consisting of neutron stars (NS) and/or black holes (BH), evolves by emitting gravitational radiation which extracts the rotational energy and angular momentum from the system, thereby leading to an inspiral of the two bodies towards each other. The dynamics of a compact binary consists of three phases: (i) The *early inspiral phase* in which the system spends 100's of millions of years and the luminosity in GW is rather low and the dynamics can be solved using approximation methods - the most popular being the post-Newtonian (PN) approximation. The inspiral signal has a characteristic shape, with slowly increasing amplitude and frequency and is called a *chirp* waveform. A binary signal that chirps (i.e. its frequency changes perceptibly during the course of observation) is an astronomer's *standard candle* [5] (see below) and by observing the radiation from a *chirping* binary we can measure the luminosity distance to the source. (ii) The *plunge* phase when the two stars are moving at a third of the speed of light and experiencing strong gravitational fields with the gravitational potential being $\varphi = GM/Rc^2 \sim 0.1$. This phase requires the full non-linear structure of Einstein's equations as the problem involves strong relativistic gravity, tidal deformation (in the case of BH-BH or BH-NS) and disruption (in the case of BH-NS and NS-NS) and has only recently been solved by numerical relativists (see below). Analytical solutions based on resummation of the PN series have been very successful in describing the merger phase. (iii) The *merger,* or *ringdown,* phase when the two systems have merged to form either a NS or BH, settling down to a quiescent state by radiating the deformations inherited during the merger. The emitted radiation can be computed using perturbation theory and gives the quasi-normal modes (QNM) of BH and NS. The QNM carry a unique signature that depends only on the mass and spin angular momentum in the case of BH, but depends also on the equation-of-state (EOS) of the material in the case of NS.

Post-Newtonian description of the inspiral signal The adiabatic evolution of a compact binary, during which the emission of gravitational waves causes the component stars of the system to *slowly* spiral-in towards each other, can be computed very accurately using the post-Newtonian (PN) expansion of the Einstein equations. Currently, the dissipative dynamics is known [6] to order $O(v^7/c^7)$, where v is the characteristic velocity in the system.

For a binary consisting of two stars of masses m_1 and m_2 (total mass $M \equiv m_1 + m_2$ and symmetric mass ratio $\nu \equiv m_1 m_2/M^2$) and located at a distance $D_{\rm L}$, the dominant gravitational wave amplitudes are

$$h_+(t) = \frac{2\nu M}{D_{\rm L}}(1+\cos^2\iota)\,[M\omega(t;t_0,M,\nu)]^{\frac{2}{3}}\cos[2\Phi(t;t_0,M,\nu)+\Phi_0]\,, \tag{2}$$

$$h_\times(t) = \frac{2\nu M}{D_{\rm L}}2\cos\iota\,[M\omega(t;t_0,M,\nu)]^{\frac{2}{3}}\sin[2\Phi(t;t_0,M,\nu)+\Phi_0]\,, \tag{3}$$

where ι is the angle of inclination of the binary's orbital angular momentum with the line-of-sight, $\omega(t)$ is the angular velocity of the equivalent one-body system around the binary's centre-of-mass and $\Phi(t;\,t_0, M, \nu)$ is the corresponding orbital phase. Parameters t_0 and Φ_0 are constants giving the epoch of merger and the orbital phase of the binary at that epoch, respectively.

The above expressions for h_+ and $h_\times$ are the dominant terms in what is essentially a PN perturbative series, an approximation technique that is used in solving the Einstein equations as applied to a compact binary. This dominant amplitude consists of only twice the orbital frequency. Higher order amplitude corrections contain other harmonics (i.e., phase terms consisting of $k\,\Phi(t)$, $k = 1, 3, 4, \ldots$). Also, the above expressions are written down for a system consisting of non-spinning components on a quasi-circular orbit. In reality, we can assume neither to be true. Waveforms for binaries on an eccentric inspiral orbit are known as are those with spin effects but we shall not discuss them here.

The adiabatic inspiral, during which the signal is approximated by (3), is followed by the merger of the compact objects, leading to the formation of a single black hole. This black hole then undergoes a rapid 'ringdown' as it settles down to a quiescent state. Following breakthroughs in 2005 [7–9], it is now possible to numerically solve the full Einstein equations for the last orbits, merger and ringdown of comparable mass black-hole-binary systems, and to calculate the emitted GW signal. Subsequent dramatic progress has lead both to simulations of rapidly increasing numerical accuracy and physical fidelity, and to the inclusion of larger numbers of GW cycles before merger, allowing full GR waveforms to be in principle useful for searches of black-hole binaries of ever lower mass; see Fig. 3 in [10]. The inclusion of merger and ringdown dramatically increases the signal-to-noise ratio, leading to a much larger distance reach than one would have with the inspiral signal alone. As we shall see below, having observational access to these later stages of the coalescence process will lead to key insights into the structure of neutron stars; in the case of black holes it will open up the genuinely strong-field dynamics of spacetime.

Standard Sirens of Gravity Cosmologists have long sought for standard candles that can work on large distance scales without being dependent on the lower rungs of cosmic distance ladder. In 1986, Schutz [5] pointed out that gravitational astronomy can provide such a candle, or, more appropriately, a *standard siren*, in the form of a chirping signal from the coalescence of compact stars in a binary. The basic reason for this is that the gravitational-wave amplitude depends only on the ratio of a certain combination of the binary masses and the luminosity distance. For chirping signals observations can measure both the amplitude of the signal and the masses very accurately and hence infer the luminosity distance.

The detector response depends only on a small number of signal parameters, which can all be measured either directly or indirectly. The signal is insensitive to the composition of the component stars and there is no complicated modelling that involves the structure of the stars or their environments. Consequently, the measurement of the luminosity distance is precise, except for statistical errors, whose magnitude depends on the signal-to-noise ratio (SNR), and systematic errors due to weak gravitational lensing. We will discuss the relative magnitude of these errors later on.

Substituting the expressions given in Eq. (3) for h_+ and $h_\times$ in Eq. (1), we get

$$h(t) = \frac{2\nu M}{D_{\rm eff}}\,[M\omega(t)]^{\frac{2}{3}}\cos[2\Phi(t) + \Phi_0'] . \tag{4}$$

Here $D_{\rm eff}$ is the effective distance to the binary, which is a combination of the true luminosity distance and the antenna pattern functions, and Φ_0' is a constant phase involving the various angles,

$$D_{\rm eff} \equiv \frac{D_{\rm L}}{\left[F_+^2(1+\cos^2\iota)^2 + 4F_\times^2\cos^2\iota\right]^{1/2}}, \quad \Phi_0' \equiv \Phi_0 + \arctan\left[-\frac{2F_\times\cos\iota}{F_+(1+\cos^2\iota)}\right]. \tag{5}$$

Note that $D_{\rm eff} \geq D_{\rm L}$. In the case of non-spinning binaries on a quasi-circular orbit, therefore, the signal is characterized by nine parameters in all, $(M, \nu, t_0, \Phi_0, \theta, \varphi, \psi, \iota, D_{\rm L})$.

Since the phase $\Phi(t)$ of the signal is known to a high order in PN theory, one employs matched filtering to extract the signal and in the process measures the two mass parameters $(M,\,\nu)$ (parameters that completely determine the phase evolution) and the two fiducial parameters $(t_0,\,\Phi_0)$. In general, the response of a single interferometer will not be sufficient to disentangle the luminosity distance from the angular parameters. However, EM identification (i.e., electromagnetic, especially optical, identification) of the source will determine the direction to the source, still leaving three unknown parameters $(\psi,\,\iota,\,D_{\rm L})$. If the signal is a transient, as would be the case in ground-based detectors, a network of three interferometers will be required to measure all the unknown parameters and extract the luminosity distance.

Although the inspiral signal from a compact binary is a standard siren, there is no way of inferring from it the red-shift to a source. The mappings $M \to (1+z)M$, $\omega \to \omega/(1+z)$, and $D_{\rm L} \to (1+z)D_{\rm L}$, in Eq. (3), leave the signal invariant. Note that a source with an intrinsic (i.e., physical) total mass $M_{\rm phys.}$ at a red-shift z will appear to an observer to be a binary of total mass $M_{\rm obs.} = (1+z)M_{\rm phys.}$. One must optically identify the host galaxy to measure its red-shift. Thus, there is synergy in GW and EM observations which can make precision cosmography possible, without the need to build a cosmic distance ladder. Later in this document we will see how to exploit compact binaries for fundamental physics and cosmography.

Cosmological evolution of compact object populations The calculation of the coalescence rate as a function of the redshift must take into account the following factors: the star formation rate history $SFR(z)$, the binary fraction $f_b(z)$, the formation efficiency of a given type of binary, i.e. the fraction of number of binaries that lead to formation of coalescing compact object binary, and their distribution of merger times. These quantities may depend on redshift since the stellar populations evolve with cosmic time. Let us examine the effects of evolution of each of these factors.

The star formation rate is known to increase strongly to the redshift $z = 2$, and there is a debate about its behavior for higher redshifts. At redshift $z = 2$, the star formation is estimated to be a factor of 10 larger than the present value at $z = 0$.

The distribution of merger times can be estimated either by analyzing the present population of compact objects binaries or by involving the population synthesis. The first approach is limited to deal with the double neutron star binaries, and suffers from small number statistics. The second involves several uncertainties due to parametrization of binary evolution. However the two approaches yield similar results. The distribution of merger times for the double neutron star binaries can be well approximated by a distribution $\propto t^{-1}$. The lower cutoff for the DNS systems lies somewhere between 10 and 100 Myrs. The population synthesis leads to similar conclusions about the distribution of merger times for BHNS and BBH systems, however the low time cutoff may probably lie higher.

The evolution of the properties of binaries with cosmic time. The main factor that may affect the evolution of the binaries as a function of redshift are the changes in the distribution of metallicity. Metallicity affects strongly the mass loss rate in stars, and hence has a strong influence on the masses spectrum of compact objects. The lower the metallicity the higher the maximum mass of a black hole that may be formed in the course of stellar evolution. This leads to to stabilization of mass transfers and therefore to increase in the formation rate of compact object binaries.

Taking together the above factors we see that there are several reasons why the coalescence rate should increase strongly as we go to redshifts of $z = 1$–2. First the local star formation rate increases and the overall number of binary formation is larger. Second, the typical delay times for the DNS systems are low therefore their merger rate density will roughly follow that of the SFR. In the case of BHNS or BBH systems he typical delay times between formation and coalescence may be as large as 1–3 Gyrs. This delays the peak of coalescence rate density with respect to the star formation rate. Thus the delays are significant but not crucial. Third, the metallicity evolution may lead to higher compact object formation rate for high redshifts, and formation of larger number of massive BBH binaries.

This consideration can be put into detailed numerical codes to yield predictions about the rates. However even without such strong numerical support one can readily estimate with the back of the envelope calculation that the ratio of the coalescence rate (per unit volume per unti time) to the local one should be at least a few. The local coalescence rate can only be estimated with observations since neither the observational not the indirect approach mentioned earlier can yield the estimate of the rate with the accuracy better that plus minus an order of magnitude.

The Einstein telescope will provide a large sample of coalescences with the precise measurement of their masses and redshifts. This will be an extremely valuable tool for analysis of the cosmic compact object formation history. The measurement of their masses will yield information on the metallicity evolution as well as evolution of most massive stars. The Einstein telescope will yield a cosmic compact object census up to redshift $z = 2$, and will yield information about black holes and neutron star formed even at earlier epochs because of the delays between formation and coalescence.

There are two distinct routes to form BH binary. The first, conventional way, is to start with binary system of two main sequence stars and trace their evolution. There are several big uncertainties in this process. The first one is the initial mass ratio function: what is the distribution of the mass ratio in the binary of two main sequence stars, how it depends on the metallicity and spectral type. The second, and probably the biggest uncertainty, is related to the "common envelope" evolution, where the NS (or BH) and Helium core are emerged and evolve in the gaseous environment of the star. In this stage the NS/BH could merge with Helium core and binary is not formed. The third uncertainty is related to the direction and magnitude of the kick exerted on the newly born BH from the assymetric supernova explosion. All the above is reflected in the uncertainties on the rate of such binaries [11, 12].

The BH binaries could also be formed in the dense environment such as galactic nuclei. In the galaxies with SMBH ($M < 10^7\,M_\odot$), the relaxation time is less than a Hubble time, and a steep cusp of stars and stellar mass BHs can be formed. BHs as more massive and compact objects will segregate into central ≈ 1 pc region. Other two dense regions are massive globular clusters and nuclear star clusters in the centers of low-mass galaxies which may not have SMBH. The densities in those regions are high enough to have multiple encounters with formation and/or hardening of the BH binaries.

Expected coalescence rates Black holes or neutron stars are expected to form after Type II supernovae, which occur roughly once a century in galaxies like our own. Most stars seem to form in binaries binaries; a fraction of compact binary progenitors will survive the kicks that supernovae impart; and roughly half of the

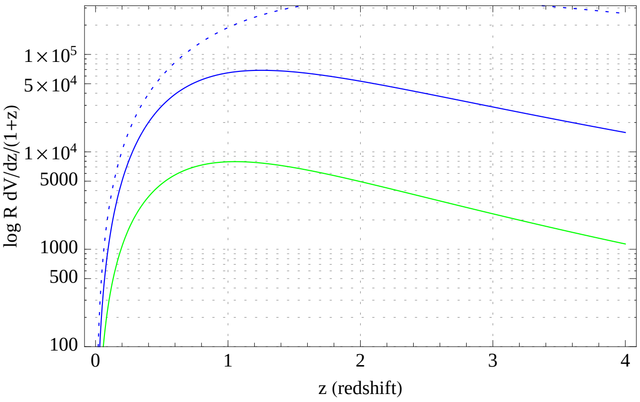

Figure 5: The merger rate dR/dz on our past light cone versus redshift. A thin dotted blue line extrapolates the Milky Way double neutron star merger rate to the universe using Eq. 6, which assumes that merger rates trace the star formation history [13] and that the Milky Way forms stars at a rate $dM/dt_{MW} \simeq \dot\rho_{MW}/n_{mw} = 3M_\odot$ yr^{-1}. More detailed calculations that account for the finite delay between binary birth and merger are shown in the two sold lines for NS-NS (blue) and BH-NS (green) binaries. These delays insure ET will probe the redshift region where most binaries merge.

remaining low-mass binaries (BH-NS; NS-NS) will inspiral and eventually merge through the gradual emission of radiation. With roughly $n_{mw} = 0.01$ Milky Way-like galaxy per Mpc^3, we anticipate a rate per comoving volume ρ_c large enough to permit many detections even for advanced-LIGO scale detectors (Table 2). For example, the binary pulsar population in the Milky Way implies a local NS-NS merger rate $\rho_c^{(NS-NS)} \simeq 0.2-6$ Myr^{-1} Mpc^{-3} [14–16].

With its vastly greater sensitivity, the Einstein Telescope will reach deep back into the universe. Due to an enhanced the star formation rate between $z \simeq 1-3$ [13], ET will probe a regime of possibly significantly enhanced compact object merger rates [17–19]. By way of illustration, because double neutron stars have a relatively short delay time, their formation rate roughly traces the star formation rate of the universe [17]. For example, assuming all gas forms stars similar to the present day Milky Way, the current Milky Way compact object merger rate ($R_{MW} = \rho_c n_{MW}$) and star formation rate per volume ($\dot\rho_{MW}$) allow us rescale the *total* star formation rate of the universe ($\dot\rho_{SFR}$) into an instantaneous merger rate per unit volume ($R_{mw} n_{MW} \dot\rho_{SFR}/\dot\rho_{MW}$). The total merger rate follows by adding up all contributions on the past light cone out to ET's sensitivity limit, via an estimate for the star formation rate $\dot\rho_{SFR}$ [13, 18] (cf. Figure 5, which adopts a more realistic model):

$$\frac{dR}{dz} = \frac{dV_c}{dz}\frac{\mathcal{R}(t)}{1+z} \simeq \frac{dV_c}{dz}\rho_c^{(NS-NS)}\frac{\dot\rho_{SFR}/\dot\rho_{MW}}{1+z}. \tag{6}$$

Depending on the target sensitivity and beampattern of the ET network, the expected detection rate is roughly proportional to the integral of this rate up to some peak redshift. For most target ET sensitivities this limiting redshift z_{max} is greater than 1 for double neutron stars, suggesting $O(10^6)$ detections per year. The enormous collections of events that ET-scale instruments will provide permit high-precision modeling inaccessible with the sparse statistics available to smaller detectors.

Lacking direct observational input, predictions for BH-BH and BH-NS binaries rely entirely on theory. Studies of isolated binary evolution in the Milky Way [20–23] and local universe [18] produce event rates roughly in the ranges shown in Table 2, depending on the assumptions adopted in the model. As with the NS-NS rate, the BH-NS merger rate is roughly proportional to the star formation rate [19] and therefore also increases substantially with redshift [Figure 5]; many detections are expected.

The BH-BH merger rate is much less certain. First, long expected delays between BH-BH birth and merger imply black holes born in the early universe could merge now [18]. Second, BH masses depend strongly on the metallicity of the gas from which the progenitor star forms, as stellar winds operate much less efficiently

Table 2: This Table gives the expected coalescence rates per Mpc^3 Myr in the local universe ($z \simeq 0$). Also shown are predicted event rates in Advanced LIGO (AL) and Einstein Telescope (ET).

Rate/Events	BNS	NS-BH	BBH
Rate (Mpc^{-1} Myr^{-1})	0.1-6	0.01-0.3	$2 \times 10^{-3} - 0.04$
Event Rate (yr^{-1} in AL)	0.4-400	0.2-300	2-4000
Event Rate (yr^{-1} in ET)	$O(10^3\text{-}10^7)$	$O(10^3)\text{-}10^7$	$O(10^4\text{-}10^8)$

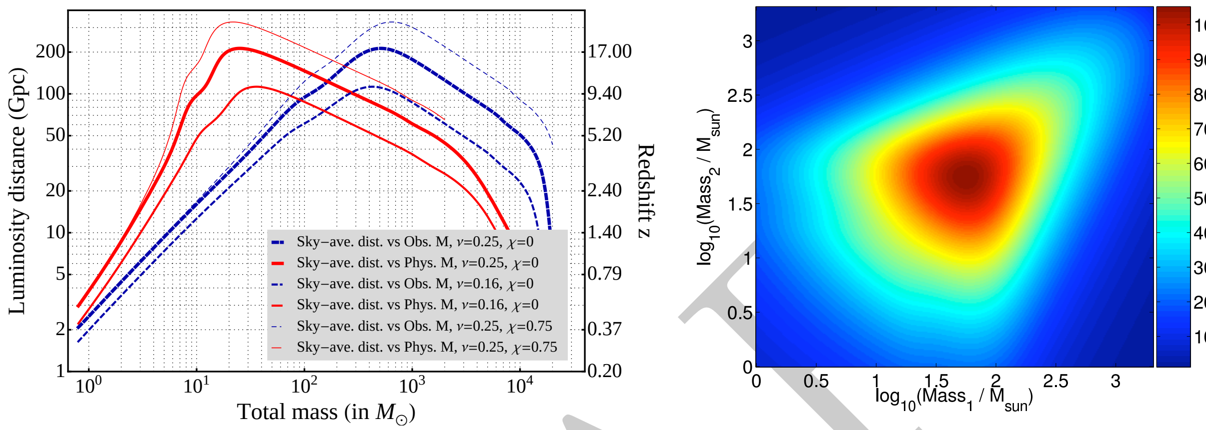

Figure 6: The left panel shows the range of the Einstein Telescope for inspiral signals from binaries as a function of the *intrinsic* (red solid line) and *observed* (blue dashed line) total mass. We assume that a source is visible if it produces an SNR of at least 8 in ET. The right panel shows in the plane of component masses the SNR for binaries at a distance of 3 Gpc.

[24]; so does the BH-BH binary formation rate [25]. In other words, low metallicity environments form both more binaries and binaries that can be detected farther away. Even restricting attention to the local universe, low-metallicity environments should be significantly over-represented in the present-day detection rate [26]. For example, the nearby BH-BH progenitor binary IC 10 X-1 both lies in a low metallicity environment and suggests a high BH-BH detection rate for initial LIGO ($O(0.5)$yr, strongly dependent on survey selection effects; see [27]). Further, in the early universe, where fewer generations of stars have produced metals, very massive binaries could form very frequently [25]. Third, being the most massive compact objects, black holes can *mass segregate* in interacting protoclusters. If enough protoclusters persist long enough for this process to occur, the BH-BH binary merger rate could be vastly enhanced [28–30]. As a practical matter, theory provides no useful upper bound; for example, the local BH-BH rate per mass bin is constrained only by existing gravitational wave measurements.

Expected distance reach and mass range A standard measure of the reach of a detector is the horizon distance D_h, defined as the distance at which a detector measures an SNR = 8 for an optimally-oriented and optimally-located binary, i.e. an overhead, face-on orbit. Suboptimally located and oriented sources are detected with SNR = 8 at closer distances. The sky-position averaged distance up to which a 3-detector ET network might detect inspiral signals from coalescing binaries with an SNR of 8 is shown in left panel of Fig. 6. We plot the range both as a function of the intrinsic (red solid lines) and observed (blue dashed lines) total mass. Those are related by the redshift function $z(d)$, which we compute according to the standard ΛCDM universe with parameters given by the first five years of the WMAP sky survey [31]. The binary systems are modeled by the phenomenological waveforms of [32] which comprise the inspiral, merger and ringdown stages of the coalescence. In left panel of Fig. 6 we show the reach associated to three physical configurations of the binary: equal-mass, non-spinning; non-spinning with mass ratio 1 : 4; and equal-mass, spin-aligned configuration with spins $\chi_1 = \chi_2 = \chi = 0.75$. Right panel displays the SNR for binaries located at 3 Gpc versus the component masses of the system. Our results show that a binary comprising two $1.4\,M_\odot$-neutron stars (BNS) can be

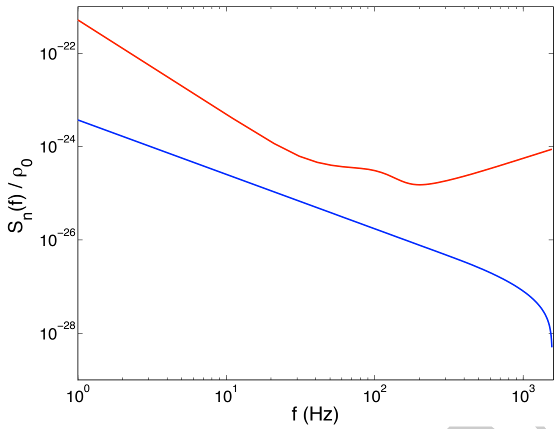

Figure 7: Spectral energy density of the background produced by the coalescence of double neutron stars, compared to the planned sensitivity of Einstein Telescope.

observed by ET from a red-shift of $z \simeq 2$, and that comprising a $1.4\,M_\odot$-neutron star and a $10\,M_\odot$-black hole (NS-BH) from $z \simeq 4$. Binaries formed by stellar-mass black holes will be visible at much larger distances, allowing the ET to explore cosmological distances of $z \simeq 10$ and further.

Contribution of intermediate-mass black holes Globular clusters may host intermediate-mass black holes (IMBHs) with masses in the $\sim 100 - 1000\ M_\odot$ range (see [33, 34] for reviews on IMBHs, and [35] for an announcement of a recently discovered ultra-luminous X-ray source that represents a possible IMBH detection). These may contribute to binary merger rates observable by the ET in two ways.

Since an IMBH will be the most massive object in the cluster, it will readily sink to the center and substitute into a binary with a compact-object companion. The binary will then harden through three-body interactions and eventually merge via an intermediate-mass-ratio inspiral (IMRI) on timescales of less than one billion years [36]. The number of detectable mergers depends on the unknown distribution of IMBH masses and their typical companions. According to [37], 300 events could be detected to $z = 1.5$ for 100-solar-mass (redshifted) primaries and 10-solar-mass (redshifted) secondaries, but the range and rates drop for higher-mass primaries and lower-mass secondaries.

If the stellar binary fraction in a globular cluster is sufficiently high, two or more IMBHs can form [38]. These IMBHs then sink to the center in a few million years, where they form a binary and merge via three-body interactions with cluster stars followed by gravitational radiation reaction (see [38, 39] for more details). Then the ET could detect $2000 \left(\frac{g}{0.1}\right) \left(\frac{g_{\rm cl}}{0.1}\right)$ mergers per year, where g is the fraction of all globular clusters hosting pairs of IMBHs, and $g_{\rm cl}$ is the fraction of star formation occurring in clusters. Mergers between pairs of globular clusters containing IMBHs can increase this rate by up to a factor of ~ 2 [40].

2.2.2 Continuous wave sources

The kinds of sources we consider in this section are ones which last for at least a few weeks or years, whose amplitude is constant (or at least roughly constant), and whose frequency varies relatively slowly over the observation time. These signals are expected to be produced by rapidly rotating non-axisymmetric neutron stars which are either isolated or in binary systems.

The waveforms for the two polarizations are taken to be

$$h_+(t) = A_+ \cos\Phi(t)\,, \qquad h_\times(t) = A_\times \sin\Phi(t) \tag{7}$$

where t is the time in the frame of the moving, accelerating detector, $\Phi(t)$ is the phase of the gravitational wave and $A_{+,\times}$ are the amplitudes; $A_{+,\times}$ are constant in time and depend on the other pulsar parameters such as its rotational frequency, moments of inertia, the orientation of its rotation axis, its distance from Earth etc. The phase $\Phi(t)$ takes its simplest form when the time coordinate used is τ, the proper time in the rest frame of the neutron star:

$$\Phi(\tau) = \phi_0 + 2\pi \sum_{n=0}^{s} \frac{f_{(n)}}{(n+1)!} \tau^{n+1} \tag{8}$$

where ϕ_0, $f_{(0)}$ and $f_{(n)}$ $(n \geq 1)$ are respectively the phase, instantaneous frequency and the spin-down parameters in the rest frame of the star at the fiducial start time $\tau = 0$, and s is the number of spin-down parameters included in our search. If ι is the angle between the line of sight to the star and its axis, then it is useful to write the amplitudes $A_{+,\times}$ in terms of a single number h_0

$$A_+ = \frac{1}{2} h_0 (1 + \cos^2 \iota)\,, \qquad A_\times = h_0 \cos \iota\,. \tag{9}$$

There are a number of mechanisms which may cause the star to be emitting gravitational waves. These include deformations of the neutron star crust, precession, magnetic fields, internal oscillation modes of the neutron star fluid etc.

Isolated neutron stars There are at present hundreds of pulsars known from either radio or X-ray observations. The parameters of many of these systems, i.e. the sky location and frequency evolution, have been accurately measured. We assume the GW phase evolution to be tightly correlated with the rotational phase as inferred from electromagnetic observations. For gravitational wave emission due to a non-negligible ellipticity, the GW emission occurs at twice the rotational frequency of the star. These two assumptions constrain the expected gravitational waveform upto an unknown initial phase ϕ_0, amplitudes $A_{+,times}$ and polarization angle ψ. It is then easy to search over these unknown parameters [41] and to either measure the amplitude h_0, or in the case that no signals are detected, to set upper limits on it.

The benchmark for these searches is the indirect upper bound on h_0 set by assuming that all of the kinetic energy of the star lost in the spindown is channeled into gravitational radiation. A straightforward calculation leads to the so-called spindown limit h_0^{sd}:

$$h_0^{sd} = 8.06 \times 10^{-19} \frac{I_{38}}{d_{kpc}} \sqrt{\frac{|\dot{\nu}|}{\nu}} \tag{10}$$

where $I_{38} = I/10^{38}\text{kg-m}^2$, d_{kpc} is the distance to the star in kpc, $\dot{\nu}$ is the spindown rate and ν is the spin frequency. This assumption is not expected to hold for any of the known pulsars where electromagnetic braking explains most of the spindown. Nevertheless, the spindown limit still a very useful benchmark for quantifying the astrophysical relevance potential targets and search results.

This procedure has been carried out for a number of known pulsars using data from the LIGO, GEO and Virgo detectors [42–44]. One highlight from these results is beating the spindown limit for the Crab pulsar [44] where the gravitational wave luminosity os constrained to be less than 6% of the spindown luminosity.

Let us now consider design noise curves for various detectors, including ET, and compare detectable values of h_0 with the spindown limits for a number of known pulsars. A useful benchmark for the detectability is given by

$$h_0 = 11.4 \sqrt{\frac{S_n(f)}{DT_{obs}}} \tag{11}$$

where $S_n(f)$ is the detector noise power-spectral density at a frequency f, T_{obs} is the observation time, and D is the number of detectors. The factor of 11.4 corresponds to a false alarm rate of 1% and a false dismissal rate of 10%. Figure 8 shows (left panel) the detectable amplitude for Initial and Advanced LIGO, Virgo and ET, and spindown limits for various known pulsars.

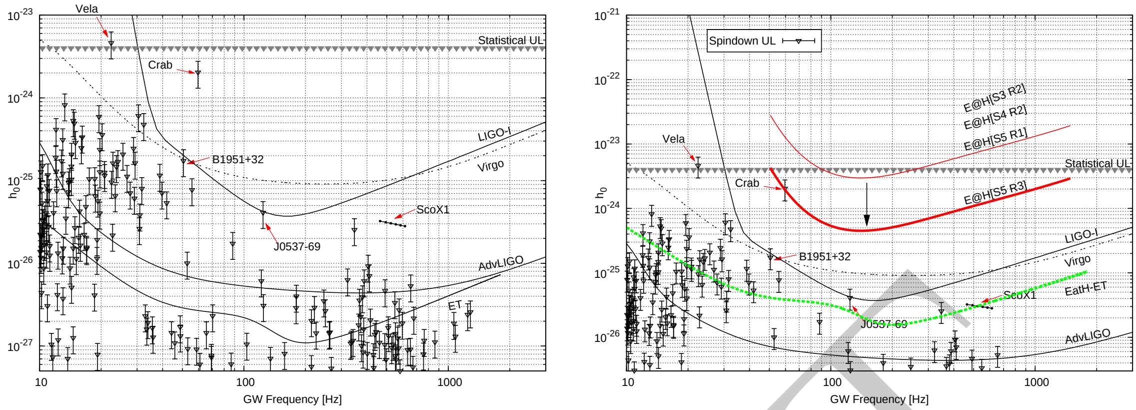

Figure 8: The left hand plot shows upper limits and the spindown limits for the known pulsars. Adapted from R.Prix, 2006. The right hand plot shows expected sensitivity for blind searches.

Let us turn now to the wide parameter space searches. Here we don't target a known pulsar but rather, as an example, one whose radio pulse is not beamed towards; such a neutron star might still be visible in the GW sky. These searches are computationally limited because the number of templates increases much faster than linearly with the observation time T_{obs}. The large number of templates affects the search sensitivity in three basic ways. The first and most obvious one is simply the discreteness of the template grid. Secondly, it also leads to a large number of statistical trials which increases the false alarm rate and thus leads to a larger effective threshold. Finally, and most importantly, it limits the largest observation time that we can consider; even given the increases in computer power following Moore's law, this will most likely still be true in the ET era.

The problem of computational cost is addressed by the so-called *semi-coherent* methods. These rely on breaking up the full data set into shorter segments, analyzing the segments coherently and combining the power from the different segments incoherently; there are a number of different techniques available for performing the incoherent combination. For these searches, the sensitivity, incorporating all the effects mentioned above is typically given by

$$h_0 \approx \frac{25}{N^{1/4}} \sqrt{\frac{S_n(f)}{DT_{coh}}} . \qquad (12)$$

This has been found to be a fairly good estimate (within $\sim 20\%$) of previous semi-coherent searches (see e.g. [45]).

Two sensitivity curves of ET have been proposed by S. Hild (the "pink" and "green" curves in his presentation at the Cardiff WP4 Meeting:
https://workarea.et-gw.eu/et/WG4-Astrophysics/meetings/cardiff-090325/
ET Sensitivity News, slide 10). One is the *ET-B* curve and the other, that we call it ET-B2, has a much worse sensitivity below $\sim$ 3 Hz but better around 10 Hz. Let us see what changes in the two cases for the search of GW from both known and unknown neutron stars. In Fig. (9) the top plot shows the minimum detectable amplitude, assuming *ET-B* sensitivity, an observation time $T_{obs} = 5\,$yr, a false alarm probability of 1% and a false dismissal probability of 10%, see Eq. (11), versus the spin-down limit of the known pulsars (taken from the ATNF Catalogue: http://www.atnf.csiro.au/research/pulsar/psrcat/). The bottom plot is done using (an approximate fit of) the *ET-B2* sensitivity curve. The important point is that no known pulsar (up to now) could emit a detectable signal with frequency below $\sim 2.5\,$Hz. This means that there is no gain in having a good sensitivity at extremely low frequencies. On the other hand, having a better sensitivity around 10 Hz impacts positively on the possibility of detection.

This can be seen also in Fig. (10) where the ellipticity corresponding to the minimum detectable amplitude is plotted, only for the sources for which the spin-down limit can be beaten in the given observation time T_{obs}.

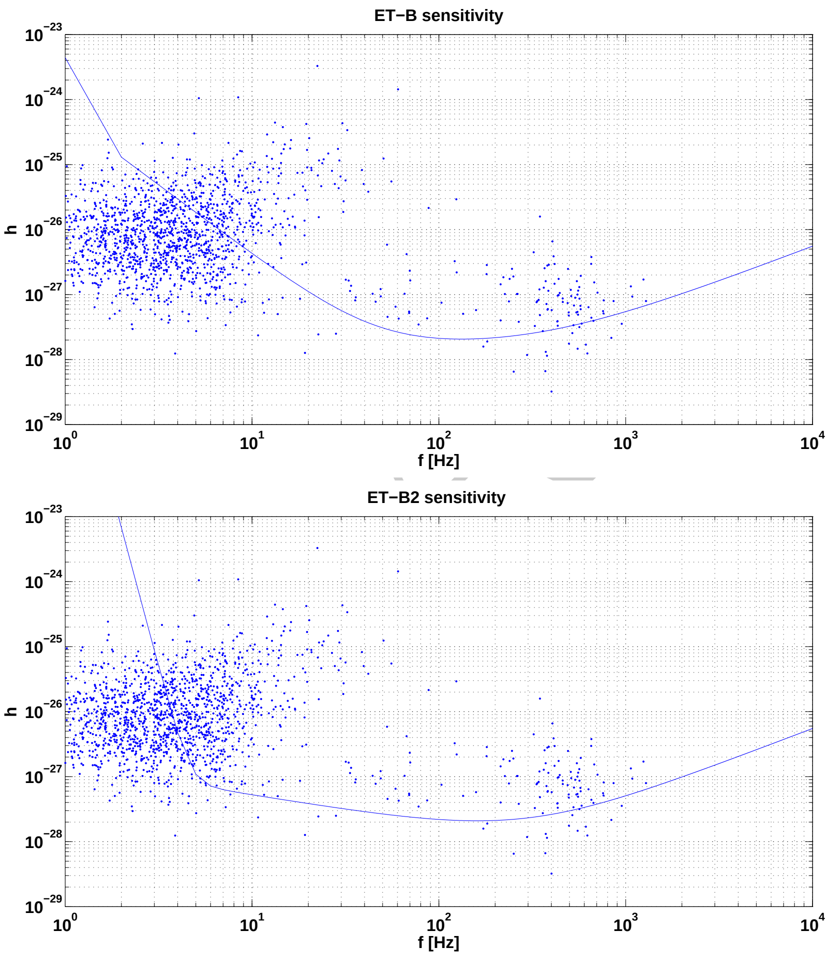

Figure 9: Minimum detectable amplitude with *ET-B* sensitivity (top) and *ET-B2* (bottom). An observation time $T_{obs} = 5\,\text{yr}$, a false alarm probability of 1% and a false dismissal probability of 10% are assumed.

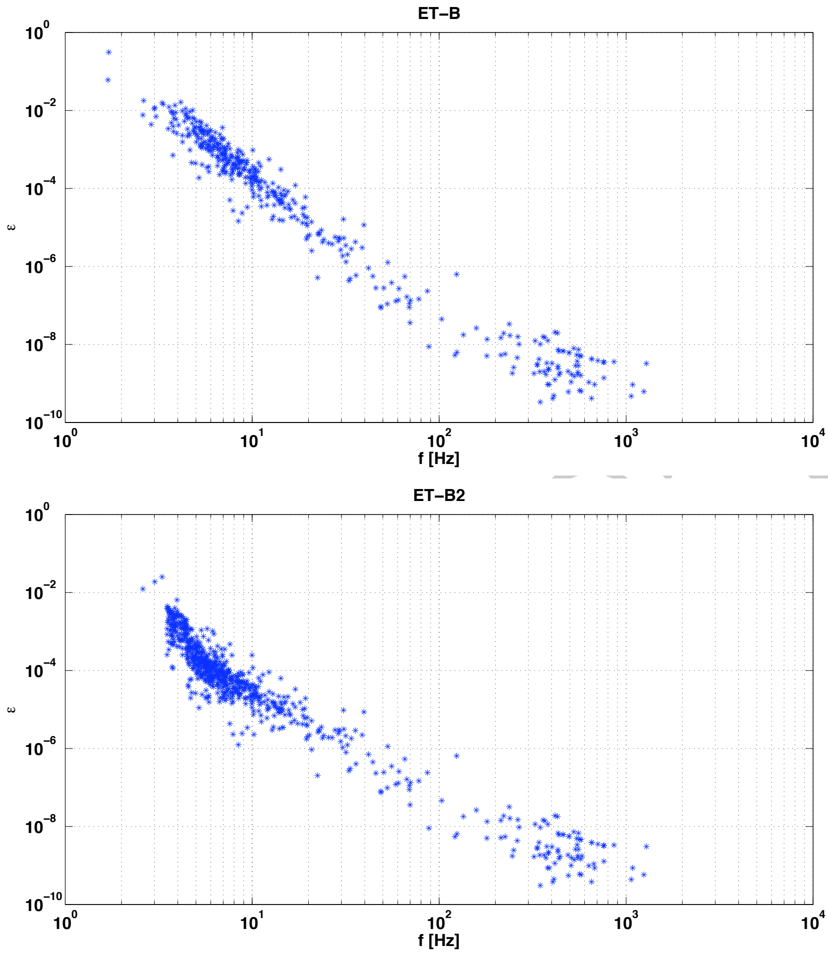

Figure 10: Minimum detectable ellipticity for known pulsars assuming *ET-B* sensitivity (top) and *ET-B2* sensitivity (bottom). The search parameters are the same as for Fig. (9).

Not only the number of pulsars for which the spin-down limit can be beaten is larger for the *ET-B2* curve (774 vs. 444) but, more important, the minimum ellipticy needed to produce a detectable signal is ~ 1 order of magnitude lower in the 10 Hz range. For instance, with *ET-B* we typically need ϵ in the range $0.1 - 5 \cdot 10^{-4}$ range for pulsars emitting around 10 Hz, while $\epsilon \sim 0.1 - 1 \cdot 10^{-5}$ is enough with *ET-B2*. The very few pulsars at frequencies below ~ 3 Hz for which the spin-down limit could be beaten with *ET-B*, but not with *ET-B2*, correspond to ellipticity in the 10^{-2} range, a value difficult to reach also assuming an exotic equation of state for neutron star matter. We must however keep in mind that the number of pulsars increases with decreasing frequency, and so also the probability that an extremely deformed, EM-dim, neutron star exists, provided such large deformations are really attainable in Nature.

Let us now consider the *blind* search for unknown neutron stars. For this case we plot in Fig. (11) the maximum distance of a source to be selected among the candidates of an all-sky incoherent or semi-coherent search, for different values of the neutron star ellipticity. An observation time $T_{obs} = 5\ yr$ and an FFT duration $T_{FFT} \simeq \frac{1.1 \cdot 10^5}{\sqrt{f}}\ s$, such that the Doppler effect does not spread the signal power outside a frequency bin, are assumed. Moreover, the threshold for the selection of candidates is chosen in order to have 10^9 candidates.

In practice, we do not expect detections for signal frequencies below ~ 10 Hz for $\epsilon < 10^{-5}$ (the corresponding r_{max} becomes unrealistically small). And also considering extremely deformed neutron star ($\epsilon > 10^{-5}$) signal frequencies below ~ 3 Hz are basically excluded. Then, having a better sensitivity at very low frequencies

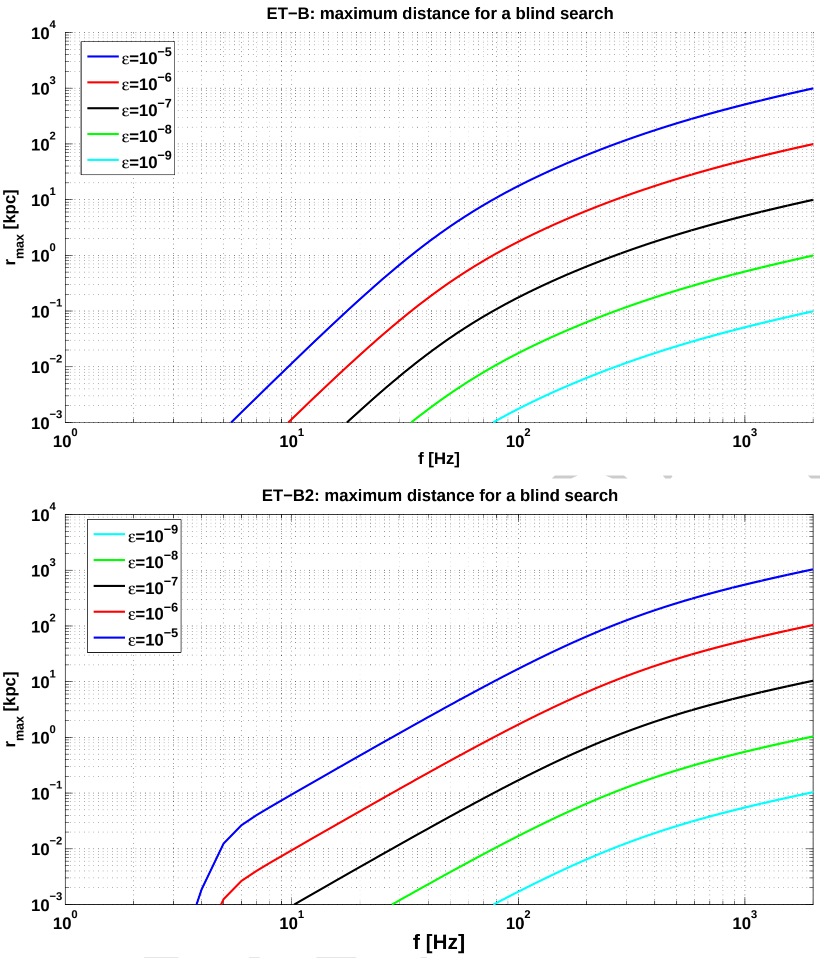

Figure 11: Maximum distance of an unknown source in order to be selected among the candidates of an all-sky search with *ET-B* sensitivity (top) and *ET-B2* sensitivity (bottom). Search parameters are given in the text.

gives basically no gain. On the other hand, having a better sensitivity around 10 Hz somewhat increases the possibility of detection: for instance, assuming $\epsilon = 10^{-5}$, the maximum distance that a search can reach goes from ~ 10 pc with *ET-B* to ~ 100 pc with *ET-B2* at 10 Hz, while it goes from ~ 150 pc to ~ 500 pc at 20 Hz.

This conclusion does not change even assuming a long coherent step (compatible with the computing power we can think will be available in the ET era), because the sensitivity increases only as $T_{coh}^{1/4}$, see Eq. (12).

Low-mass X-ray binaries Observations of accreting neutron stars lead to perhaps the most important reason why, irrespective of the mechanism at work, at least some neutron stars might be actally emitting detectable gravitational waves. This is the observation that even the fastest accreting neutron stars spin at rates much lower than the expected break-up frequency. The current record is 716 Hz, while the theoretically expected upper limit is more than 1 kHz. Following a suggestion by Bildsten [46], it is possible that this limit occurs because of the balance between the spin-up torque due to the accreting matter, and the spindown torque due to gravitational wave emission. A short calculation assuming a link between the observed X-ray luminosity with the accretion rate, and taking the mountain scenario for the emission mechanism leads to the following estimate

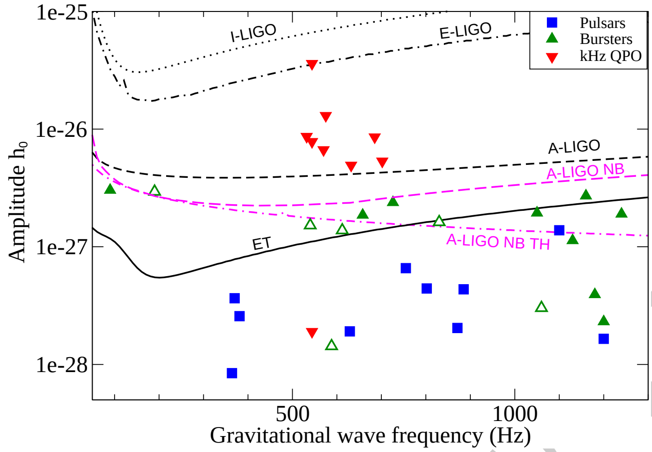

Figure 12: Sensitivity and the spin-balance limit for the accreting neutron stars.

of the GW amplitude:

$$h_0 = 3 \times 10^{-27} F_{-8}^{1/2} \left(\frac{R}{10\text{km}}\right)^{3/4} \left(\frac{1.4M_\odot}{M}\right)^{1/4} \left(\frac{1\text{ kHz}}{\nu_s}\right)^{1/2} . \tag{13}$$

This is seen to be depend on frequency: $h_0 \propto \nu_s^{-1/2}$.

2.2.3 Stochastic background

The superposition of a large number of unresolved sources of gravitational waves produces a stochastic background, which could be detected by cross-correlating two (or more) detectors [47]. We can distinguish between two contributions: a background of cosmological origin, a memory of the early stages of the Universe (see Section 2.5.5), and a background of astrophysical origin, a memory of the evolution of the galaxies and star formation.

The astrophysical contribution is important for at least two reasons. On the one hand, it may mask the cosmological background in some frequency windows; on the other hand, its detection would put strong constraints on the physical properties of compact objects and their evolution with redshift, such as the mass of neutron stars or black holes, the ellipticity and the magnetic field of neutron stars or the rate of compact binaries. What is particularly interesting is that using stochastic searches, we are able to put constraints on the mean values and not on the properties of the brightest sources, more likely in the tail of the distributions.

The spectrum of the gravitational stochastic background is usually characterized by the dimensionless energy parameter [47]:

$$\Omega_{gw}(\nu_o) = \frac{1}{\rho_c} \frac{d\rho_{gw}}{d\ln \nu_o} \tag{14}$$

where ρ_{gw} is the gravitational energy density, ν_o the frequency in the observer frame and $\rho_c = 3H_0^2/(8\pi G)$ the critical energy of the Universe. For a stochastic background of astrophysical origin:

$$\Omega_{gw}(\nu_o) = 5.7 \times 10^{-56} \nu_o \int_{z_{\min}}^{z_{\max}} \frac{\dot{\rho}^o(z)}{(1+z)E(z)} \frac{dE_{gw}}{d\nu}(\nu_o) dz \tag{15}$$

where $\dot{\rho}^o(z)$ is the number of events in an element of comoving volume and interval of time in the observer frame, $\frac{dE_{gw}}{d\nu}$ the typical spectral energy density of a single source and $E(z)$ a function that depends on the cosmology. We assume $h_0 = 0.7$ for the Hubble parameter and a flat Universe with 70% of dark energy.

Binary Neutron Stars Double neutron star coalescences, which may radiate about 10^{53} erg in the last seconds of their inspiral trajectory, up to $1.4 - 1.6$ kHz, may be the most important contribution in the ET frequency range [48–51]. In the quadrupolar approximation, the GW energy spectrum emitted by a binary system, which inspirals in a circular orbit is given by:

$$dE_{gw}/d\nu = \frac{(G\pi)^{2/3}}{3} \frac{m_1 m_2}{(m_1 + m_2)^{1/3}} \nu^{-1/3} \tag{16}$$

Assuming $m_1 = m_2 = 1.4$ M$_\odot$ for the star masses, the energy density increases as $\nu_o^{2/3}$ before it reaches a maximum of $\Omega_{gw} \sim 2 \times 10^{-9} \dot{\rho}_0$ at around 600 Hz, where $\dot{\rho}_0$ is the local rate in My^{-3} Mpc^{-3} (about 0.01 times the galactic rate). This means that ET should be able to detect the background from binaries even for the most pessimistic predictions of the coalescence rate, down to $\dot{\rho}_0 \sim 0.035$ (roughly equivalent to a galactic rate of 3 My^{-1}), for a signal-to-noise ratio of 3, after one year of observation.

Rotating neutron stars: tri-axial emission Rotating neutron stars with a triaxial shape may have a time varying quadrupole moment and hence radiate GWs at twice the rotational frequency. The total spectral gravitational energy emitted by a NS born with a rotational period P_0, and which decelerates through magnetic dipole torques and GW emission, is given by:

$$\frac{dE_{gw}}{d\nu} = K\nu^3 \left(1 + \frac{K}{\pi^2 I_{zz}} \nu^2\right)^{-1} \quad \text{with} \;\; \nu \in [0 - 2/\mathrm{P}_0], \tag{17}$$

where

$$K = \frac{192\pi^4 G I_{zz}^3}{5c^5 R^6} \frac{\varepsilon^2}{B^2 \sin^2\alpha}. \tag{18}$$

Here R is the radius of the star, $\varepsilon = (I_{xx} - I_{yy})/I_{zz}$ the ellipticity, I_{ij} the principal moment of inertia, B the magnetic field and α the angle between the rotation and the dipole axis.

The majority of neutron stars are born with magnetic fields of the order of $10^{12} - 10^{13}$ G and rotational periods of the order of tens or hundreds of millisecond [52–54], and very likely don't contribute very much to the stochastic background. But the population of newborn magnetars in which super-strong crustal magnetic fields ($B \sim 10^{14} - 10^{16}$ G) may have been formed by dynamo action in a proto-neutron star with very small rotational period (of the order of 1 ms) [55, 56], may produce a stochastic background detectable by ET [57].

For these highly magnetized neutron stars, the distortion induced by the magnetic torque becomes significant, overwhelming the deformation due to the fast rotation. When the deformation of the star is small ($K >> \pi^2 I \nu^{-2}$), the spindown is dominated by the magnetic torque but as the ellipticity increases GW emission may become the most important process. Taking $R = 10$ km for the radius, $I_{zz} = 10^{45}$ g cm^2 for the moment of inertia, and assuming that magnetars represent 10% of the population of NSs, we find that the stochastic signal is detectable with ET after an observation time $T = 1$ yr and with a signal to noise ratio of 3 when $\frac{\varepsilon}{B} > 1.5 \times 10^{-18}$. In the saturation regime where the spindown is purely gravitational, the energy density increases as ν_o^2 at low frequencies and reaches a maximum of $\Omega_{gw} \sim 1.3 \times 10^{-8}$ around 1600 Hz, giving a signal detectable by ET with a signal-to-noise ratio of 45.

Rotating neutron stars: initial instabilities The gravitational wave background signal from core collapse supernovae could be enhanced by a number of proposed post-collapse emission mechanisms. One intriguing mechanism is the bar-mode dynamical instability associated with neutron star formation. These instabilities derive their name from the 'bar-like' deformation they induce, transforming a disk-like body into an elongated bar that tumbles end-over-end. The resulting highly non-axisymmetric structure resulting from a compact astrophysical object encountering this instability makes such an object a potentially strong source of gravitational radiation and have been the subject of a number of numerical studies [58–62]. Howell et al. have calculated the background signal from this emission process using simulated energy spectra data, $dE_{gw}/d\nu$, from [63], who performed the first three dimensional hydrodynamic simulations for stellar core collapse in full general relativity.

Assuming a 20% occurrence of this instability, the authors find that the resulting background reaches a maximum of $\Omega_{gw} \sim 4 \times 10^{-10}$ around 2000 Hz would be detectable with a SNR of 3 after one year of integration. The optimistic event rate considered here is supported by suggestions that post collapse neutrino emission by the proto-neutron stars can induce contraction through cooling. This leads to increased spins though conservation of angular momentum [63]. The implication here is that the instability can set in tens of milliseconds post collapse, increasing the rate of occurrence.

The stochastic background from r-modes was first investigated by [64] and then reviewed by [65]. These estimates are based on the initial model of [66], which does not account for dissipation mechanisms such as the effect of the solid crust or the magnetic field, which may significantly reduce the gravitational instability. The spectral energy density of a single source is given by:

$$\frac{dE_{gw}}{d\nu} = \frac{2E_o}{\nu_{\rm sup}^2}\nu \;\text{ with }\; \nu \in [0 - \nu_{\rm sup}], \tag{19}$$

where $\nu_{\rm sup}$ is 4/3 of the initial rotational frequency and E_0 is the rotational energy lost within the instability window. For neutron stars with radius $R = 10$ km and mass $M = 1.4$ M$_\odot$ the spectrum evolves as $\Omega_{gw} \sim 10^{-12}\xi\nu_o^3$ where ξ is the fraction of NS stars born near the keplerian velocity and which enter the instability window, until it reaches a maximum at 900 Hz. ET may be able to detect this signal with a SNR > 3 and $T = 1$ yr if $\xi > 0.23\%$. We obtain similar constraints with the secular bar mode instability at the transition between Maclaurin and Dedekind configurations [67].

Core collapse The GW background from core collapse supernovas that result in the formation of black holes was first calculated in [70] using the relativistic numerical simulations of [71] and later by [72] who found similar results assuming that all the energy goes into the ringdown of the $l = m = 2$ dominant quasi normal mode. The frequency ν_* of this mode is given by [73]:

$$\nu_* \approx \frac{c^3}{2\pi G}(1 - 0.63(1-a)^{0.3})\frac{1}{M({\rm M}_\odot)} \tag{20}$$

where the mass of the BH is a fraction α of the mass of the progenitor and where a is the dimensionless spin factor ranging from 0 for a Schwarzschild BH to 1 in the extreme Kerr limit. The spectral energy distribution can be written as:

$$\frac{dE_{gw}}{d\nu} = \varepsilon M_{\rm bh}c^2\delta(\nu - \nu_*(M)) \tag{21}$$

where ε is the efficiency coefficient. Previous numerical simulations of [71] gave an upper limit of $\varepsilon \sim 7 \times 10^{-4}$ for an axisymmetric collapse, but accounting for more realistic scenarios, in particular the pressure reduction that triggers the collapse, [**?**] obtained an efficiency of the order of $10^{-7} - 10^{-6}$ so $2-3$ orders of magnitude smaller. Assuming that stars in the range $30 - 100$ M$_\odot$ can produce a BH, taking $\alpha = 10\%$, and $a = 0.6$ we find that the energy density ranges between $0.25 - 5.6$ kHz, with a maximum of $\Omega_{gw} \sim \varepsilon \times 10^{-8}$ around 1650 Hz, which means that an efficiency $> 2 \times 10^{-3}$ would give a signal detectable with a signal to noise ratio of 3 after one year of observation. Taking $\alpha = 20\%$, we find that the signal is detectable for efficiencies as small as 0.01%.

New estimates of the GW backgrounds generated by Pop III and Pop II sources have been recently published by [74]. These authors use the results of a numerical simulation by Tornatore et al.(2007) which follows the evolution, metal enrichment and energy deposition of both Population III and Population II stars. They predict the redshift dependence of the formation rate of black hole remnants of Population III stars with masses $100 - 500M_\odot$ and of neutron stars (black holes) remnants of Population II stars with masses $8 - 20M_\odot$ ($20 - 40M_\odot$). In order to characterize the single source emission, the most appropriate signals available in the literature have been adopted, namely:

- For Pop III stellar collapse, the waveform recently obtained by [75] using a 2D numerical simulation which follows the entire evolution of a zero metallicity $300M_\odot$ star, taking the effects of General Relativity. and neutrino transport into account

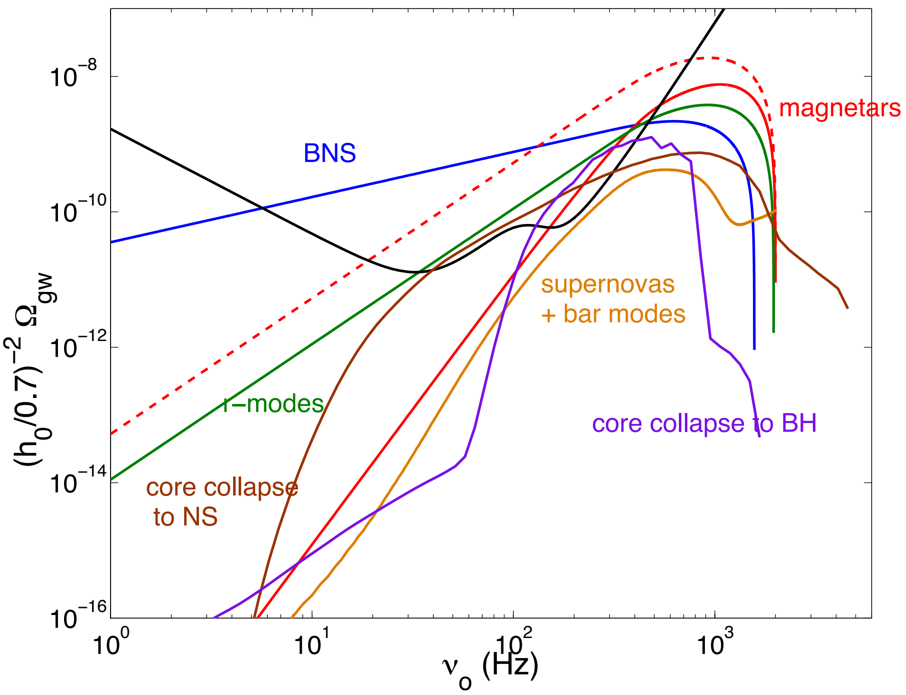

Figure 13: Energy density of the different contributions to the astrophysical background discussed in the text: magnetars (minimal detectable prediction in continuous red and model when the spindown is purely gravitational in dashed red), binary neutron stars in blue, dynamical bar modes in proto NS in yellow, r-modes assuming that 1% of newborn neutron stars cross the instability window in green, core collapse to black holes assuming an efficiency of 1% , a mass fraction of the progenitor of 10% and an angular parameter of 0.6 in purple, Pop II core collapse to NS (model of [68]) in brown and to BH (model D5a of [69]) in brown.

- For Pop II progenitors with masses in the range $8 - 20 M_{\odot}$ the emission spectrum corresponding to the model labelled as s15r in [76]; as an extreme and promising possibility, the gravitational wave emission produced by the excitation of the g-modes has also been considered using the template spectrum of [68].
- For Pop II progenitors with masses in the range $20 - 100 M_{\odot}$, the gravitational wave spectra from a set of models (D5a,D5d,A5b) obtained by [69] using numerical simulations in full General Relativity.

The background is out of reach for Pop III stellar collapse, but could be be detected for Pop II progenitors. The authors found that the energy density reaches a maximum of $\Omega_{gw} \sim 10^{-9}$ around 1000 Hz for the collapse to NS model of Ott (2005), giving a signal to noise ratio of 8.2, and of $\Omega_{gw} \sim 4 - 7 \times 10^{-10}$ around 500 Hz for the collapse to BH model of [69], giving a signal to noise ratio of between $1.6 - 7.1$.

The sources discussed in this section are summarized in Figure 13: here the ET sensitivity curve is estimated for two co-located or minimally separated interferometers with opening angle 60° and relative rotation angle 120°, an integration time of 1 year and a detection SNR of 2.56 [47]. However, a search for stochastic background with co-located detectors could encounter difficulty in separating signal from correlated noise sources: different ET topologies and detection strategies are under consideration.

2.2.4 Probing Core-Collapse Supernova Physics

Stellar collapse is the most energetic event in the Universe, releasing $\sim 10^{53}$ erg of gravitational energy in the compression of a massive star's iron core to a neutron star. Most of this energy ($\sim 99\%$) is emitted in neutrinos and only about 10^{51} erg go into energy of the core-collapse supernova (CC-SN) explosion. CC-SNe (SN types II, Ib, Ic) are $\sim$10 times more frequent than thermonuclear type-Ia SNe. A SN explosion pollutes the interstellar medium with the nucleosynthetic products of stellar evolution (CC-SNe are the Universe's primary source of oxygen) and enriches via the r-process the universe with rare heavy isotopes. The perturbation caused by an SN in its vicinity can trigger the formation of stellar systems and stellar collapse and CC-SNe are the birth sites of neutron stars (NSs) and stellar-mass black holes (BHs).

The Supernova Problem and GW observations The precise mechanism of explosion operating in CC-SNe is unknown [77–79]. When the inner part of the collapsing iron core reaches densities close to those in atomic nuclei, the strong force leads to a stiffening of the nuclear equation of state (EOS), resulting in *core bounce* of the inner core into the still infalling outer core. A shock wave is formed that propagates outward in mass and radius, but quickly loses energy due to the breakup of heavy nuclei and neutrinos that carry away energy from the postshock layer. The shock stalls, turns into an accretion shock and must be *revived* to drive a CC-SN explosion. If this does not happen, a BH will form on an accretion timescale of ~ 2 s. *What is the mechanism of shock revival?* This is the fundamental question and primary unsolved problem of CC-SN theory. Indications are strong that the CC-SN mechanism involves a multitude of multi-dimensional processes, including rotation, convection/turbulence, and various hydrodynamic instabilities of the stalled shock and in the proto-NS. This opens up the possibility of probing the supernova mechanism with gravitational waves (GWs). GWs, even more so than neutrinos, carry direct dynamical information from the supernova engine deep inside a dying massive star, a region generally inaccessible by the traditional means of observational astronomy. GWs form a core-collapse event have the potential of putting very strong constraints on the CC-SN mechanism [79, 80]. With initial and certainly second-generation interferometric GW detectors, this should be possible for an event in the Milky Way ($D \sim 10 - 15$ kpc) and the Magellanic Clouds [79] ($D \sim 50 - 70$ kpc), but even optimistic estimates of the CC-SN rate in this region do not predict more than $\sim 1 - 2$ events per century. This number roughly doubles if one includes the entire local group ($D \sim 1$ Mpc). In the region from $3 - 5$ Mpc a number of starburst galaxies increase the predicted and observed integrate SN rate to $\sim 0.5\,\mathrm{yr}^{-1}$. At $D \sim 10$ Mpc it is $\gtrsim 1\,\mathrm{yr}^{-1}$.

Supernova Science with ET The GW emission processes in a CC event emit GW strains h in the range $10^{-24} - 10^{-22}\,(D/1\,\mathrm{Mpc})$ and most of the emission takes place at frequencies of $\sim 200 - 1000$ Hz, but the various explosion scenarios exhibit unique spectral distributions and vary in total emitted energies [79, 80]. In addition, there is likely to be a low-frequency GW-memory-type component with large h up to $10^{-22}\,(D/1\,\mathrm{Mpc})$ at $0 - 20$ Hz. ET as currently envisioned [82] is sufficiently sensitive to detect GWs from various CC-SN scenarios out to $2 - 4$ Mpc. If the high-f sensitivity was increased by a factor of $\sim 2 - 3$, detection out to ~ 10 Mpc may

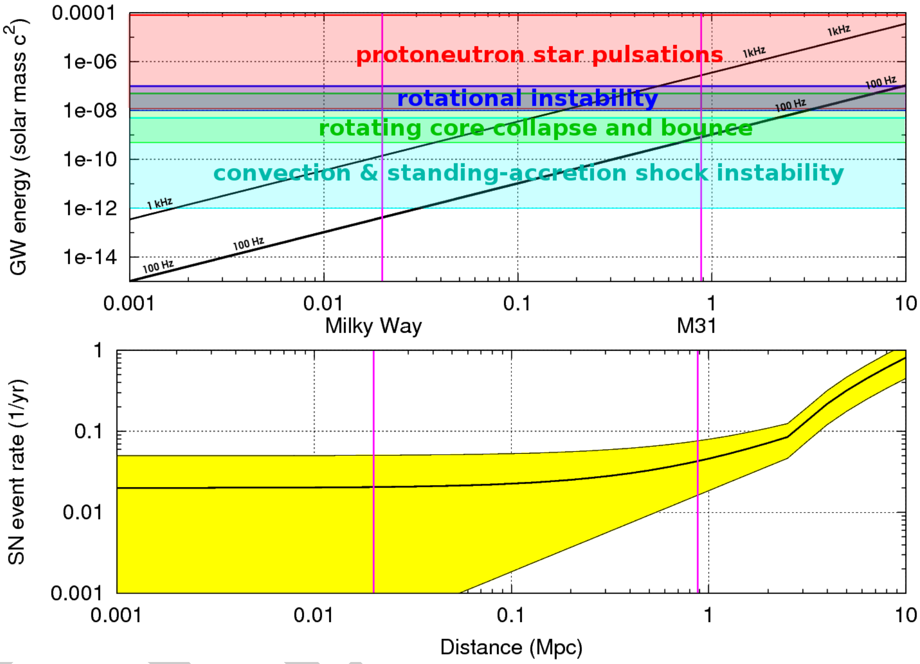

Figure 14: The upper plot displays the minimum GW energy that a supernova core collapse is required to radiate in order to be detectable by the Einstein telescope. We give two estimates assuming that the GW signature is described by a sine-Gaussian burst waveform. We consider two cases with a low-frequency $f = 100\,\mathrm{Hz}$ and with high-frequency $f = 1\,\mathrm{kHz}$ content. The minimum GW energy is given as a function of the source distance. We also indicate the expected range of radiated GW energy for several processes [79]. The lower plot shows an estimate of the cumulative event rate (with error bars) obtained from the star formation rate computed over a catalog of nearby galaxies [81].

be possible. Figure 14 summarizes the ET observational capabilities and examines each of the main generation processes of gravitational waves.

Even without this improvement, ET may see multiple CC-SNe during its lifetime and would have the power to provide strong hints for a particular SN mechanism and/or smoking-gun evidence against another – crucial astrophysics information that is unlikely to be attainable in other ways. At ET's implementation, megaton-class neutrino detectors will be operative and, having range similar to ET, will be able to provide coincident observations, narrowing down the time of the GW emission to $\sim 1\,\mathrm{ms}$. In addition, deep high-cadence optical transient surveys will be operative and targeting near-universe transients, providing additional coincident data as well as additional astrophysics output (progenitor type/mass, explosion morphology/energy etc.).

Impact Constraining the CC-SN mechanism will mean a breakthrough in our understanding of the large range of phenomena associated with stellar collapse, CC-SNe, BH and NS formation, and gamma-ray bursts (GRBs). However, the astrophysics and physics information provided by GWs observed from a CC event with ET goes beyond this: These GWs carry also information on the high-density nuclear EOS, explosion asymmetries and pulsar kicks, the formation of a BH in a failing CC-SN, and can help uncover rare events such as the accretion-induced collapse of a white dwarf to a NS or weak or failing CC-SNe that have very weak or absent EM signatures.

2.3 Strong field tests of GR and fundamental physics

The rich variety of sources and phenomena observed by gravitational wave detectors can be potentially used to address outstanding questions in fundamental physics. The sources in question will be in dense environs of ultra-strong gravity and thereby provide a cosmic laboratory for understanding phenomena and matter in extreme conditions of density, temperature, magnetic field, etc. Moreover, black hole binaries are fundamentally geometric objects whose interaction close to merger will provide insights into the nature of black hole space times and of gravity in ultra-strong fields. In this Section we will discuss what fundamental physics questions and strong-field tests of gravity could be addressed by 3G detectors.

2.3.1 Speed of gravitational waves and mass of the graviton

In Einstein's theory gravitational waves travel with the speed of light. This means that gravitons, particle analogs of gravitational waves, are massless particles. Although there is currently no strong motivation to consider massive graviton theories from an experimental point of view, they are natural extensions of Einstein's theory. In a massive graviton theory, gravitational waves would not travel at the speed of light and this can be tested by observation of gravitational-wave sources at very great distances. To do so we would need a source which emits at the same time both gravitational waves and electromagnetic radiation. By measuring the difference in their arrival times we could measure or constrain the speed of gravitational waves.

Supernovae in the local Universe and double neutron star and neutron star-black hole binaries are sources that are expected to exhibit after glows in electro-magnetic radiation soon after they emit a burst of of gravitational waves. If the source is near enough (a few Mpc in the case of supernovae and red-shifts of a few in the case of coalescing binaries) and the event is well-localized on the sky (fraction of a degree depending on the distance to the source), then it could be observed in coincidence as a transient EM and a GW event.

Current theories of supernovae and coalescing binaries cannot accurately predict how promptly after the collapse (in the case of SN) or merger (in the case of binaries) EM radiation will follow. However, the expected delay is no more than one second. If gravitational waves arrive a time Δt after EM waves, then the fractional difference in their speeds is given by

$$\frac{|\Delta v|}{c} = 3.2 \times 10^{-18} \left(\frac{|\Delta t|}{1\,\mathrm{s}}\right) \left(\frac{3\,\mathrm{Gpc}}{D}\right) \tag{22}$$

where we have assumed that the source is at a distance of $D = 3\,\mathrm{Gpc}$.

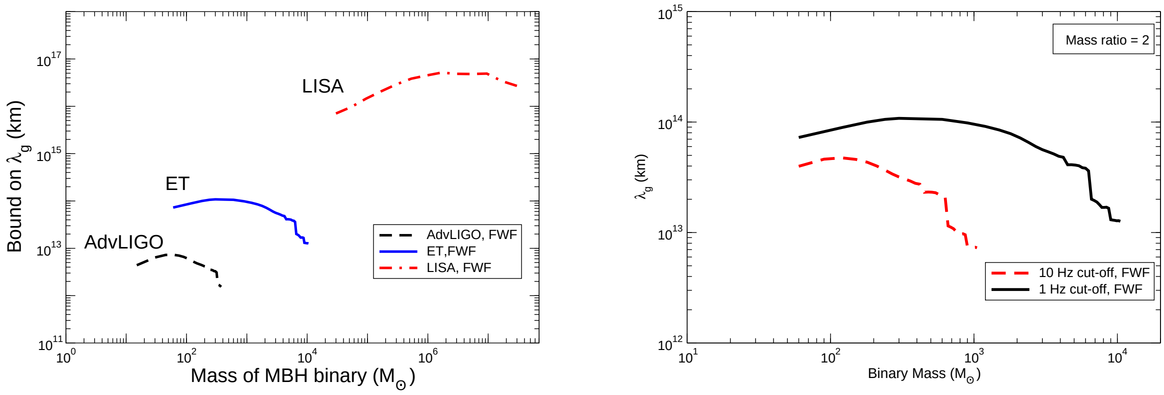

Figure 15: Left panel: Bounds on the graviton Compton wavelength that can be deduced from AdvLIGO, Einstein Telescope and LISA. The mass ratio is 2. The distance to the source is assumed to be 100 Mpc for AdvLIGO and ET, and 3 Gpc for LISA. Right panel: Possible bounds from ET when 1 Hz and 10 Hz are used as seismic cut-offs.

2.3.2 Limiting the mass of the graviton

Observations of inspiralling compact binaries (neutron stars or black holes) can be used to put bounds on the mass of the graviton, or equivalently the compton wavelength of the graviton [83]. These bounds do *not* require the detection of an electromagnetic counterpart associated with the GW signal.

The basic idea is simple: if there is a mass associated with the propagation of gravitational waves ("a massive graviton"), then the speed of propagation will depend on wavelength in the form $v_g \approx 1 - (\lambda/\lambda_g)^2$, where λ_g is the Compton wavelength of the graviton, in the limit where $\lambda \ll \lambda_g$. Irrespective of the nature of the alternative theory that predicts a massive graviton , it is reasonable to expect the differences between such a hypothetical theory and general relativity in the predictions for the evolution of massive compact binaries to be of order $(\lambda/\lambda_g)^2$, and therefore to be very small, given that $\lambda \sim 10^3$ km for stellar mass inspirals and $\sim 10^8$ km for massive black hole inspirals.

As a result, the gravitational waveform seen by an observer close to the source will be very close to that predicted by general relativity. However, as seen by a detector at a distance D, hundreds to thousands of Mpc away, the phasing of the signal will be distorted because of the shifted times of arrival, $\Delta t \sim D(\lambda/\lambda_g)^2$ of waves emitted with different wavelengths during the inspiral. In addition to measuring the astrophysical parameters of the system, such as masses and spins, the matched filtering technique permits one to estimate or bound such effects.

Here we examine the bounds possible from the observations of binary black holes by ET [84]. As our waveform model we begin with amplitude-corrected, general relativistic waveforms which are 3PN accurate in amplitude [85–88] and 3.5PN accurate in phasing [89–94]. We ignore the spins of the bodies in the binary system. Previous calculations used waveforms which are of Newtonian order in amplitude and 2PN order in phase. As opposed to the Newtonian waveforms, the 3PN amplitude-corrected waveforms contain all harmonics from Ψ up to $8\,\Psi$, where Ψ is the orbital phase (the leading quadrupole component is at 2Ψ).

The effect of a massive graviton is included in the expression for the orbital phase following Ref. [83]. The wavelength-dependent propagation speed changes the arrival time t_a of a wave of a given emitted frequency f_e relative to that for a signal that propagates at the speed of light; that time is given, modulo constants,by

$$t_a = (1+Z)\left[t_e + \frac{D}{2\lambda_g^2 f_e^2}\right], \tag{23}$$

where f_e and t_e are the wave frequency and time of emission as measured at the emitter, respectively, Z is the cosmological redshift, and

$$D \equiv \frac{(1+Z)}{a_0} \int_{t_e}^{t_a} a(t)dt\,, \tag{24}$$

where $a_0 = a(t_a)$ is the present value of the scale factor (note that D is not exactly the luminosity distance [1]). This affects the phase of the wave accordingly. In the frequency domain, this adds a term to the phase $\psi(f)$ of the Fourier transform of the waveform given by $\Delta\psi(f) = -\pi D/f_e\lambda_g^2$. Then, for each harmonic of the waveform with index k, one adds the term

$$\Delta\psi_k(f) = \frac{k}{2}\Delta\psi(2f/k) = -\frac{k^2}{4}\pi D/f_e\lambda_g^2\,. \tag{25}$$

Here $k = 2$ denotes the dominant quadrupole term, with phase 2Ψ, $k = 1$ denotes the term with phase Ψ, $k = 3$ denotes the term with phase 3Ψ, and so on.

This is an adhoc procedure because a massive graviton theory will undoubtedly deviate from GR not just in the propagation effect, but also in the way gravitational wave damping affects the phase, as well as in in the amplitudes of the gravitational waveform. If, for example, such a theory introduces a leading correction to the quadrupole phasing $\psi_{\rm quad} \sim (\pi\mathcal{M}f_e)^{-5/3}$ of order $(\lambda/\lambda_g)^2 \times (\pi\mathcal{M}f_e)^{-5/3}$, where $\mathcal{M}$ is the chirp mass, then the propagation induced phasing term (25) will be larger than this correction term by a factor of order $k^2(D/\mathcal{M})(\pi\mathcal{M}f_e)^{8/3} \sim (D/\mathcal{M})v^8$. Since $v \sim 0.1$ for the important part of the binary inspiral, and $D \sim$ hundreds to thousands of Mpc, it is clear that the propagation term will dominate. In any case, given the fact that there is no generic theory of a massive graviton, we have no choice but to omit these unknown contributions.

Our estimate of the bounds on the massive graviton parameter is based on the Fisher matrix formalism. We construct the Fisher matrix for the different detector noise PSDs using the amplitude corrected PN waveform model described earlier, converted to the Fourier domain using the stationary phase approximation. We use a six-dimensional parameter space consisting of the time and phase (t_c, ϕ_c) of coalescence, the chirp mass $\mathcal{M}$, the mass asymmetry parameter $\delta = |m_1 - m_2|/(m_1 + m_2)$, the massive graviton parameter $\beta_g = \pi^2 D\mathcal{M}/\lambda_g^2(1+Z)$, and the luminosity distance D_L. We fix the three angles, θ, ϕ and ψ which appear in the antenna pattern functions to be $\pi/3$, $\pi/6$ and $\pi/4$ respectively and the inclination angle of the binary to be $\iota = \pi/3$. Details of the Fisher matrix approach as applied to the compact binary coalescence signals can be found in Refs. [95–97], and more recently in Ref. [98] ,which critically reexamines the caveats involved in using the Fisher matrix formalism to deduce error bounds for various gravitational wave detector configurations.

The square root of each of the diagonal entries in the inverse of the Fisher matrix gives a lower bound on the error covariance of any unbiased estimator. Our focus here is solely on the diagonal element corresponding to the massive graviton parameter. The $1-\sigma$ error bar on β_g can be translated into a bound on the Compton wavelength using $\Delta\beta_g = \beta_g$, and this is the quantity that we use in the plots as well as in the discussions.

The results are shown in Figure 15. On the left panel, the bounds on the compton wavelength of the graviton achievable with the second generation detector AdvLIGO and the space based LISA are compared against those possible from ET. The typical bounds from ET could be an order of magnitude better than from AdvLIGO, but worse than LISA. The observable mass range is also much larger for ET in comparison with AdvLIGO and extends up to about $10^4 M_\odot$. In the right panel, we compare the effect of the seismic cut-off on the massive graviton bounds by considering 1 Hz and 10 Hz cut-offs. As one might expect, there is improvement in the accessible mass range by almost an order of magnitude when 1 Hz cut-off is used as cut-off as opposed to 10 Hz.

Note that though we have considered the sources for ET to be at 100 Mpc, the bounds in principle are more or less independent of the distance because in the definition of λ_g, there is a distance scale present. However, for very large distances the SNR may not be high enough and Fisher matrix estimate may not be reliable.

[1] For $Z \ll 1$, D is roughly equal to luminosity distance D_L. Hence we have assumed $D \simeq D_L$ in the case of ground based detectors for which we consider sources at 100 Mpc. For LISA, we have carefully accounted for this difference.

2.3.3 Bounds on Brans-Dicke parameter using ET

The Brans-Dicke (BD) theory of gravity [99] is an alternative theory of gravity which has an additional scalar field, which couples to matter, apart from the tensor field of general relativity. The coupling of the scalar field is described by a constant parameter ω_{BD}; in the limit of GR, $\omega_{BD} \to \infty$. Since scalar-tensor field theories predict dipolar gravitational radiation, this parameter is also a measure of the dipolar GW content.

The best bound on this parameter so far has come from the solar system experiment *Cassini*, by measuring the frequency shift of radio signas to and from the spacecraft as it orbited near the sun [100]. The resulting lower limit on ωBD is about 4×10^4.

Gravitational wave observations can also put interesting bounds on ω_{BD} [101, 102]. This is possible because the GW phasing formula for the BD case is same as that of GR except for an additional dipolar term proportional to ω_{BD}^{-1}. Hence it is possible to measure or bound this quantity from GW observations.

The dipolar GW content also depends on the internal structure of the compact body via a quantity called "sensitivity" s_A (see Sec. 3.3 of [103]).

$$\left(\frac{dE}{dt}\right)_{\rm dipole} \propto \frac{\mathcal{S}^2}{\omega_{BD}}, \qquad \mathcal{S} = s_1 - s_2 \tag{26}$$

where s_1 and s_2 are the sensitivities of the binary constituents. For binary neutron stars $\mathcal{S} \sim 0.05 - 0.1$, for NS-BH binaries $\mathcal{S} \sim 0.3$ and for a binary BH $\mathcal{S} = 0$. Therefore, for bounding BD theories one of the components of the binary should be a NS. The bound is also very sensitive to the asymmetry of the binary: the more asymmetric the binary, the worse is the bound. Due to these factors, GW bounds on the ω_{BD} are very weak (~ 5000 at best [101]). However, we point out that if ET has very good low frequency sensitivity (seismic

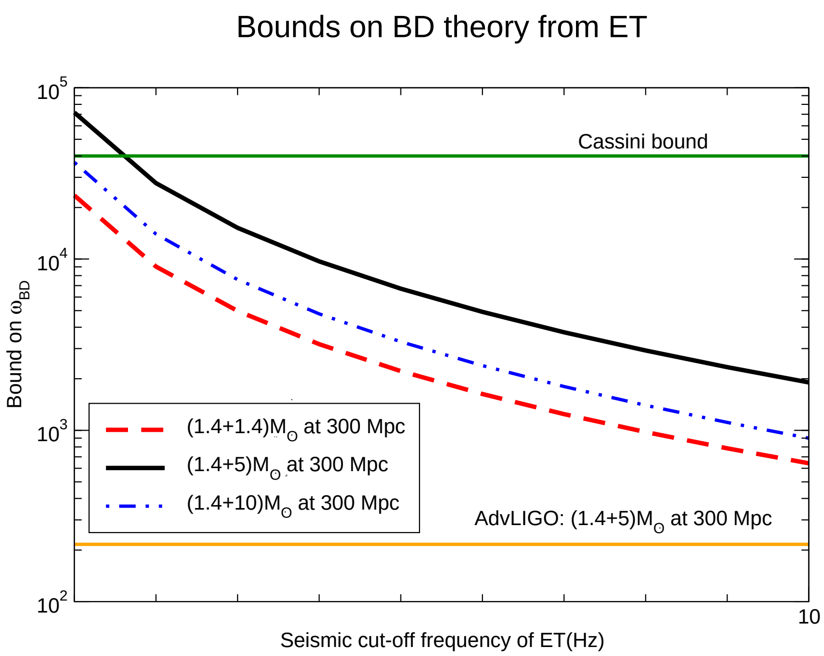

Figure 16: Bounds on Brans-Dicke parameter (ω_{BD}) from ET as a function of seismic cut-off frequency of ET. The existing bound from the Cassini experiment and the possible bounds from AdvLIGO are also shown.

cut-off frequency between $1 - 10$ Hz), the bounds from ET can beat the solar system bounds. Figure 16 shows the bound on ω_{BD} for different types of sources as a function of the seismic cut-off frequency of ET. The NS mass is assumed to be $1.4M_\odot$ and that of the BH to be either $5M_\odot$ or $10M_\odot$. The factor $\mathcal{S}$ of NS is assumed to be 0.1 and that of the BH is assumed to be 0.3. The best bounds would come from the observations of NS-BH binaries with the BH mass between $4 - 10M_\odot$ at 300 Mpc. If ET has a low frequency cut-off of 1Hz, then the bounds on ω_{BD} could be as high as $\sim 10^5$.

These bounds are likely to be the best possible by GW observations because estimates for LISA (a proposed space mission sensitive to low frequency GWs) for NS-BH binaries of total mass $\sim 10^3$ can beat the solar system bounds only if it observes a binary within 20-50 Mpc during its mission lifetime [104–106].

2.3.4 A more general test of GR and the effect of low frequency sensitivity

It is also possible to test for violations of GR without assuming a particular alternative model. One such a test was proposed by Arun et al. [107–109] and was based on the post-Newtonian expansion for the phase of an inspiral signal in the frequency domain:

$$\Psi(f) = -\phi_c + \sum_{j=0}^{7} \left[\psi_j + \psi_{jl} \ln(f)\right] f^{(j-5)/3}, \tag{27}$$

where the expressions for the coefficients ψ_j and ψ_{jl}, $j = 0, \ldots, 7$ can be found in [109]. Under the simplifying assumption that spins are zero, all these coefficients only depend on the two component masses m_1, m_2. Hence only two of the ψ_j, ψ_{jl} are independent, and a possible test of post-Newtonian theory (and hence of GR) is to check for consistency between any three of them. Particular attention has been given to ψ_3 and ψ_{5l}:

- ψ_3 is the lowest-order coefficient which gets contributions from scattering of gravitational waves off the spacetime near the binary: the so-called tail terms; hence it encapsulates the non-linear character of GR.
- ψ_{5l} is the lowest-order coefficient of a logarithmic term in (27). General relativity is not consistent with a simple Taylor expansion.

Fig. 17 illustrates the proposed test of GR for the triplets of coefficients (ψ_0, ψ_2, ψ_3) and $(\psi_0, \psi_2, \psi_{5l})$.

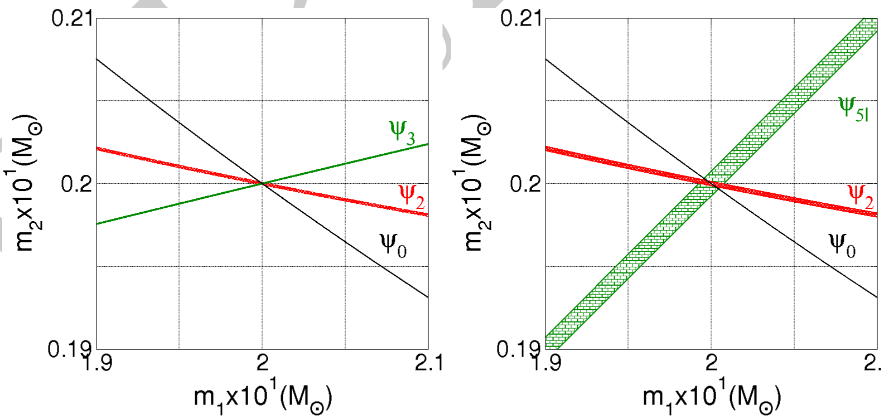

Figure 17: Plots showing the regions in the (m_1, m_2) plane corresponding to $1 - \sigma$ uncertainties in (ψ_0, ψ_2, ψ_3) (left) and $(\psi_0, \psi_2, \psi_{5l})$ (right), for a $(2, 20)\, M_\odot$ binary black hole at 300 Mpc observed by ET. The lower cut-off frequency was assumed to be 1 Hz.

The sensitivity at low frequency can have a dramatic effect on the ability to test GR, as shown in Fig. 18.

2.3.5 Measuring the dark energy equation of state and its variation with z

Over the past decade, evidence has emerged suggesting that the expansion of the Universe is accelerating. Possible explanations include a failure of general relativity at large length scales, a cosmological constant in the

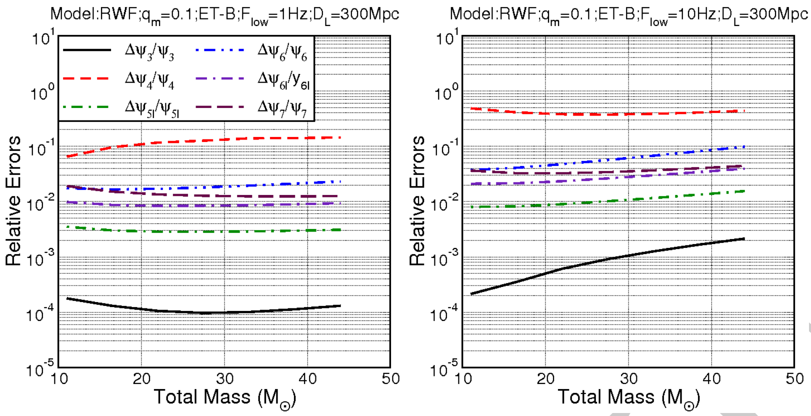

Figure 18: Varying the lower frequency cut-off can affect the accuracy in measuring phase coefficients by factors of several to an order of magnitude. On the left are relative errors with a 1 Hz cut-off, on the right with a 10 Hz cut-off.

Einstein equations, or a new contributor to the mass/energy content of the Universe called dark energy (see [110] for a review). Assuming a homogeneous and isotropic Universe, dark energy can be characterized by an equation of state of the form $p_{\rm DE} = w(z)\rho_{\rm DE}$, where $p_{\rm DE} < 0$ and $\rho_{\rm DE} > 0$ are the pressure and density, respectively. If the equation of state parameter $w(z)$ is constant and equal to -1 then this corresponds to having a positive cosmological constant in the gravitational field equations. Current constraints allow for this possibility, but other possibilities are not ruled out. The five year WMAP data combined with supernovae measurements and baryon acoustic oscillations in the galaxy distribution lead to the constraint $-1.11 < w < -0.86$ at the 95% confidence level [31].

The gravitational wave signal from inspiraling compact binaries (neutron stars and black holes) is particularly "clean" and well-understood. Consequently, as suggested by Schutz, one can think of using inspiral events as "standard sirens", much in the way Type Ia supernovae have been used as standard candles [5]. From the gravitational wave signal itself the luminosity distance $D_{\rm L}$ can be inferred, but not the redshift. However, if a particular compact binary coalescence event is accompanied by a sufficiently distinct electromagnetic counterpart, then it will be possible to find its position in the sky, identify the host galaxy, and obtain the redshift z. The relationship $D_{\rm L}(z)$ depends sensitively on cosmological parameters such as the Hubble constant at the current epoch H_0, the normalized matter and dark energy densities $\Omega_{\rm M}$ and $\Omega_{\rm DE}$, and the dark energy equation of state parameter w. For example, in a spatially flat FLRW Universe and assuming a constant w,

$$D_{\rm L}(H_0, \Omega_{\rm M}, \Omega_{\rm DE}, w; z) = (1+z) \int_0^z \frac{dz'}{H_0 \left[\Omega_{\rm M}(1+z')^3 + \Omega_{\rm DE}(1+z')^{3(1+w)}\right]^{1/2}}. \tag{28}$$

The intrinsic luminosity, and hence the luminosity distance, of an inspiral gravitational wave event can be inferred directly from their amplitude and from the component masses, which govern the structure of the signal. Thus, unlike Type Ia supernovae, their calibration does not depend on the brightness of other sources. Thus gravitational wave astronomy opens up the possibility of cosmography *without having to rely on the lower rungs of the cosmic distance ladder.*

Compact binary coalescences that involve a neutron star are assumed to have strong electromagnetic counterparts, mostly in the form of strongly beamed gamma radiation directed perpendicularly to the plane of the inspiral. Such events are believed to be the progenitors of short, hard Gamma Ray Bursts (GRBs): if the beam roughly points towards Earth then a flash of gamma radiation is seen, followed by an afterglow in the lower-frequency electromagnetic spectrum. This would then allow us to identify the host galaxy and obtain a redshift.

The gravitational wave signal from a NS-BH coalescence will be visible out to $z = 3.5$. Within the corresponding volume, it is reasonable to expect $\sim 10^4$ or more such coalescences per year, but depending on the opening angle of the gamma ray beam only a few percent of these will be visible as a GRB. Hence we should have a few hundred sources at our disposal for which the redshift can be measured. The uncertainty on z will be negligibly small, while $D_{\rm L}$ will be measurable with $\sim 3\%$ inaccuracy at $z = 1$, rising to $\sim 10\%$ at $z = 3.5$. Fitting the measured values of $D_{\rm L}$ against redshift by varying H_0, $\Omega_{\rm M}$, $\Omega_{\rm DE}$, and w in the relationship (28) should then allow for the determination of these cosmological parameters with uncertainties of 5% or better, as discussed further in Section 2.5.4.

2.3.6 Testing the uniqueness theorem of black hole spacetimes

It is generally accepted that the massive compact objects observed in the centres of most galaxies are massive, rotating black holes described by the Kerr metric of General Relativity. This belief comes in part from the uniqueness theorem, which is the result that the Kerr metric is the unique endstate of gravitational collapse [111]. However, this theorem is based on several assumptions – the spacetime is vacuum, axisymmetric and stationary; there is a horizon in the spacetime; and there are no closed timelike curves. If one of these assumptions were violated, then objects that deviate from the Kerr metric could exist.

In black hole binary systems where the mass of one object is much bigger than the other, many gravitational wave cycles are emitted while the smaller object is in the strong field region close to the larger object. These gravitational waves encode a map of the spacetime structure in the vicinity of the large black hole, which can be used to measure properties of the central object [112]. Using such observations to measure spacetime structure has been explored extensively in the context of extreme-mass-ratio inspirals (binaries of $\sim 10M_\odot$ objects with $\sim 10^6 M_\odot$ objects) for LISA (see [39] and references therein). There is an analogous source for ground based detectors, namely the inspiral of a $\sim 1M_\odot$ object into a $\sim 100M_\odot$ black hole. We refer to these as intermediate-mass-ratio inspirals (IMRIs) [113].

Explicit calculations have not yet been done for ET, but they do exist for Advanced LIGO [36, 113]. Extrapolating from those results, ET could see IMRI events out to a redshift $z \sim 3$ and could detect as many as several hundred events per year, although a few to a few tens is more likely. ET will observe these events for more cycles than Advanced LIGO, due to its better low-frequency performance, which is very important for the precision of spacetime mapping measurements.

Testing the black hole no-hair theorem The uniqueness of Kerr black holes as the endstate of collapse is sometimes referred to as the "no-hair theorem". A Kerr black hole has "no-hair" since the entire spacetime structure, characterised by "multipole moments", is determined by just two parameters, the black hole mass, M, and spin, S. It has been demonstrated that gravitational wave observations can measure the multipole moments independently of one another [112]. We can therefore directly verify that they satisfy the Kerr relationship

$$M_l + {\rm i}S_l = M({\rm i}S/M)^l \tag{29}$$

We need only to measure three multipole moments to rule out an object as a Kerr black hole.

It has been shown that IMRI observations with Advanced LIGO could detect an $O(1)$ deviation in the quadrupole moment of an object [113]. The precision achievable with ET should be at least a factor of 10 better than this due to the improved low-frequency performance. To put this in perspective, one alternative to black holes, boson stars, have quadrupole moments two orders of magnitude bigger than black holes of the same mass and spin [114].

Any deviations from the no-hair theorem that are detected will have profound implications for our understanding of relativity and of black holes. Persistent deviations from the theory may lead to important insights in the search for a fundamental theory that unifies all four forces of nature.

Are there naked singularities? One of the assumptions of the uniqueness theorem is that a horizon exists in the spacetime. This arises from a belief embodied by the "Cosmic Censorship Hypothesis" [115] (CCH), which states that any singularity will be enclosed by a horizon. The CCH arises from a desire for predictability in the

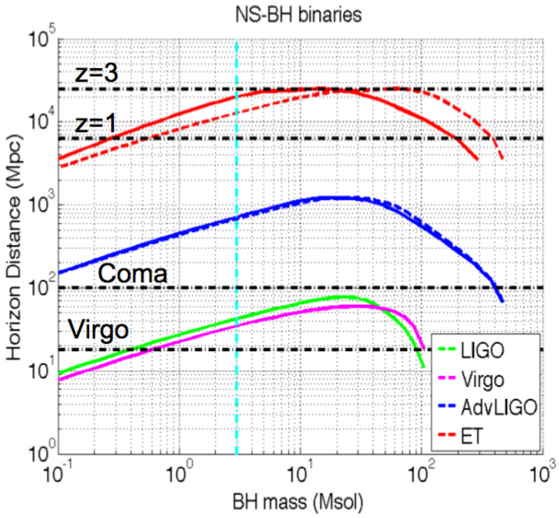

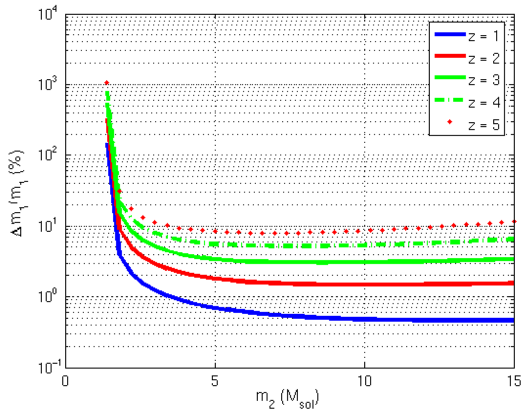

Figure 19: The plot on the left shows the horizon distance for neutron star-black hole binaries against black hole mass for initial and advanced LIGO, Virgo and ET. The solid coloured curves show the horizon distance against the *instrinsic* (non-redshifted) mass of the source. The dashed coloured curves show the horizon distance against the *observed* (redshifted by a factor of $1 + z$) mass of the source. The plot on the right shows the accuracy with which the mass of a neutron star can be determined from the inspiral signal, as a function of the mass of the companion object.

Universe — when Physics breaks down at a singularity, we do not want information from that to propagate into the rest of the Universe. However, the CCH is unproven and therefore "naked" singularities not enclosed within a horizon may still exist. Gravitational wave observations provide a unique way to look for these exotic objects. Observations may be indirect, via detection of a violation to the "no-hair" theorem. However, they may also be direct — if a horizon is not present in the spacetime, the gravitational waves will not cut-off when the object crosses the horizon [116], which will be a clear smoking gun signature for the absence of a clothing horizon in the system.

The Einstein Telescope will provide much more stringent constraints on potential violations of the CCH than are possible with Advanced LIGO. ET observations will therefore play an important role in answering the question as to whether naked singularities exist, which could have profound implications for our understanding of various aspects of the theory of relativity.

2.3.7 Limit on the maximum mass of "neutron stars"

It is generally believed that neutron stars have masses between $\sim 1.3\,M_\odot$ and $\sim 2\,M_\odot$, but such statements rely on guesses regarding the equation of state of dense nuclear matter. Above $2\,M_\odot$ a quark star might be created, or some other exotic object. Apart from the existence of such objects and their properties, an interesting question is how massive a star can be while still being stable. The left panel of Fig. 19 shows the maximum distance to which NS-BH binary inspirals can be seen in initial and advanced LIGO and Virgo, and in ET. The latter would have access to sources out to genuinely cosmological distances, up to redshifts of several, with an expected detection rate in the order of $10^6\,\mathrm{yr}^{-1}$. The right panel shows how accurately one would be able to measure the mass of a neutron star in an NS-BH inspiral process, as a function of the mass of the black hole as well as redshift. For a black hole mass $\gtrsim 5\,M_\odot$, the neutron star's mass can be inferred to a fraction of a percent out to $z = 1$, and up to a few percent out to a redshift of 2 or 3. This would enable us not only to establish the mass distribution of neutron stars and dense exotic objects, but also the evolution of this distribution over cosmological timescales.

2.4 Astrophysics

2.4.1 Equation-of-state of neutron stars from binary coalescence

Binary neutron stars are known to exist and for some of the systems in the Galaxy general-relativistic effects in the binary orbit have been measured to high precision. The inspiral and merger of two neutron stars in binary orbit is the inevitable fate of close-binary evolution, whose main dissipation mechanism is the emission of gravitational waves. The detection of gravitational waves from neutron stars binaries will provide a wide variety of physical information on the component stars, including their mass, spin, radius and equation of state (EOS). The central densities of isolated neutron stars, in fact, can range up to ten times nuclear saturation density, and during the merger and coalescence of two neutron stars the maximum density will rise even further before the remnant object collapses to a black hole. The behaviour of bulk matter at these densities is not well understood, and measurements of gravitational wave signals from neutron star sources can usefully constrain the EOS at the these densities.

Quantum chromodynamics is expected to be a complete description of matter at these energies; the uncertainty in theoretical understanding comes from the many-body problem with strong interactions. The description of bulk neutral matter in terms of hadrons such as protons and neutrons may need to be expanded to accomodate new particles that are formed at these energies, such as hyperons, pions, and kaons. In fact the appropriate degrees of freedom describing cold matter at very high density may no longer be hadrons but the quarks and gluons themselves, in some form of quark matter.

While isolated or inspiralling neutron stars are well described by the ground state of matter, i.e. with a "cold" EOS, the temperatures reached in the coalescence as a result of the strong shocks, will be significant and of the order of $\sim 10^{10} - 10^{12}$ K. Yet, just as measurements of the hot out-of-equilibrium ion collisons in RHIC constrain the ground state of dense nuclear matter, characteristics of the collisions neutron stars may be able to constrain the ground state of dense neutral matter.

Reviews of the current range of candidate equations of state and their constraint using astrophysical and heavy ion collision experiments can be found in [117–119].

The signature of the neutron star EOS can be found in almost any neutron-star sourced gravitational wave; in the peak frequencies of supernova waveforms [120, 121], in the possibility of accretion-induced crust mountains [122, 123], and in the astroseismology of glitches and other oscillation mode excitations. Studies which have specifically explored the effect of varying EOS (or varying compactness for a given mass, which implies EOS variation) on gravitational wave spectra include [124–128] for binary neutron star inspiral, [129–136] for binary neutron star coalescence, and [117, 137–139] for mixed binaries. The gravitational waves from binary inspiral and merger are expected to be frequantly measured, and the predicted signals have several interesting EOS-dependent features.

This is illustrated as a representative example in Figure 20 and which reports the simulations of [135]. In particular, the left panel on the top row shows the comparison in retarded-time evolution of the real part of the $\ell = m = 2$ component of the gravitational-wave signal $r\Psi_4$ for a high-mass binary (i.e. with a total mass of $3.2\,M_\odot$) when evolved with the a "cold" EOS (i.e. a polytropic one) or with a "hot" EOS (i.e. the ideal-fluid one). Similarly, the right panel on the top row shows the same comparison but for a low-mass binary (i.e. with a total mass of $2.9\,M_\odot$). Finally, the bottom row offers a representation of the same data but in frequency space. While none of the two EOSs considered here is realistic, they span in some sense the extrems of the range of possibilities. Most importantly they show that the gravitational-wave signal will be very sensitive on the mass of the stars and on the EOS.

While this is especially true in the post-merger phase, also the inspiral phase will provide important information on the EOS. Indeed, although for most of the inspiral of a binary neutron star system the stars are well-modeled as point particles, as they approach each other, an EOS dependent tidal deformation modifies their orbits, changing the late inspiral waveform. The measurability of this effect in gravitational wave detectors can be estimated using both post-Newtonian tidal deformation calculations and full numerical simulations of binary neutron stars with varying EOS.

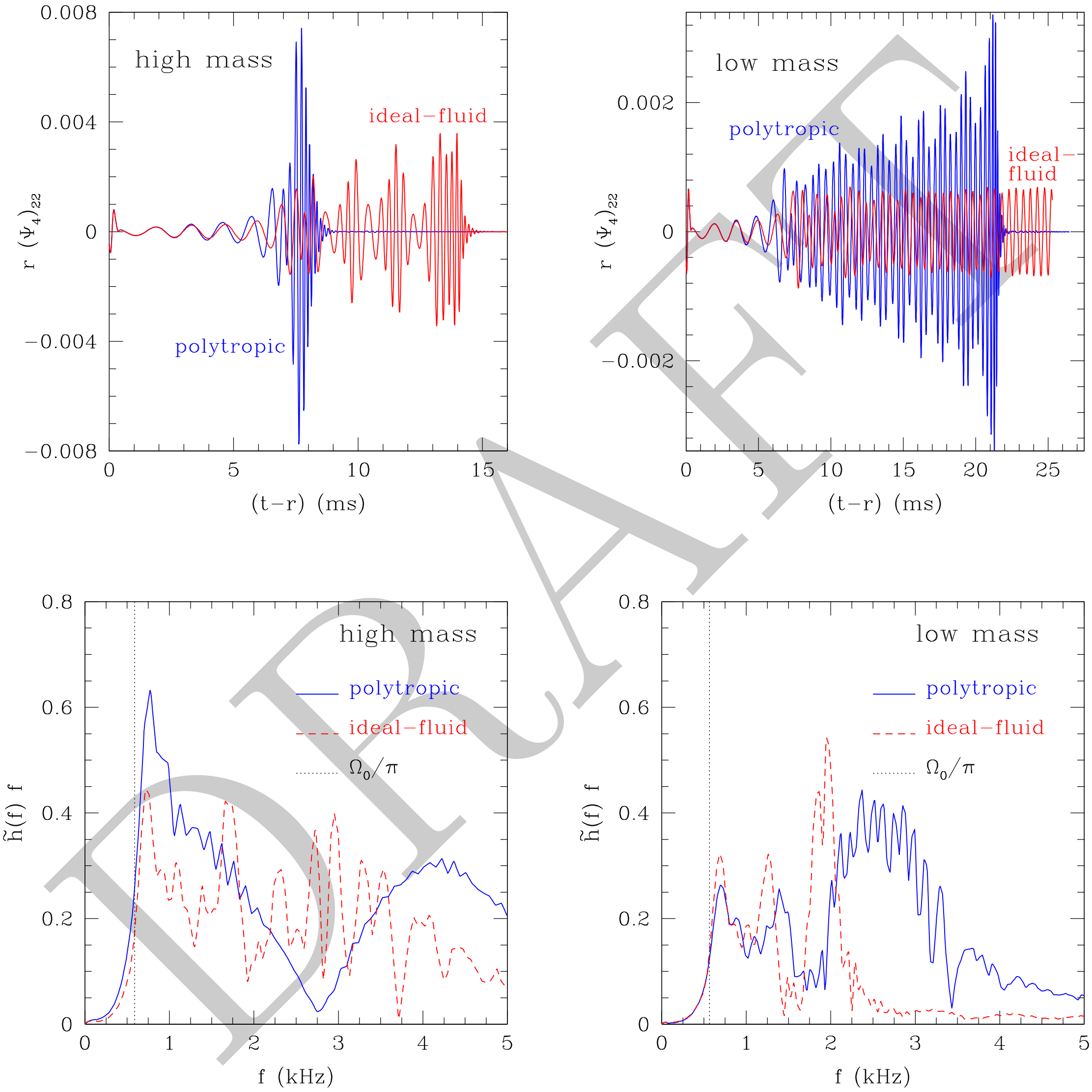

Figure 20: *Top row, left panel:* Comparison in retarded-time evolution of the real part of the $\ell = m = 2$ component of $r\Psi_4$ for a high-mass binary (i.e. with a total mass of $3.2\,M_\odot$) when evolved with the a "cold" EOS (i.e. a polytropic one) or with a "hot" EOS (i.e. the ideal-fluid one). *Top row, right panel:* The same as in the left panel but for a low-mass binary (i.e. with a total mass of $2.9\,M_\odot$). *Bottom row:* The same as in the top row but with the comparison being made in frequency space. Indicated with a vertical long-dashed line is twice the initial orbital frequency.

The set of numerical simulations of [128] using an ET proposed noise curve give, for a $1.35 M_\odot$–$1.35 M_\odot$ double neutron star binary at 100 Mpc in ET, estimates of the measurement uncertainty δR of isolated neutron star are of the order ± 0.5–1.0 km. This compares favorably to the range in predicted radius of roughly 9–16 km. Parameterizing the variation by the pressure at $5 \times 10^{14}\,\mathrm{g\,cm^{-3}}$, as in [127], gives estimates of δp_1, where p_1 is $\log(p/c^2)$, of order ± 0.05–0.10, compared to a range of roughly 13.0–13.8 for realistic EOS.

Estimates of a post-Newtonian tidal deformation following [126] give for a binary at 50 Mpc

- $\Delta\tilde{\lambda} \sim 1.22 \times 10^{36}$ for $1.35 - 1.35 M_\odot$
- $\Delta\tilde{\lambda} \sim 1.6 \times 10^{36}$ for $1.45 - 1.45 M_\odot$
- $\Delta\tilde{\lambda} \sim 1.85 \times 10^{36}$ for $1.35 - 1.7 M_\odot$

for inspiral *below 400 Hz*, where $\tilde{\lambda}(m_1, m_2)$ is a measure of tidal deformability in a given binary which ranges between 0.5×10^{36} g^2 cm^2 and 10×10^{36} g^2 cm^2 for realistic EOS.

The advantage of ET from the perspective of EOS understanding is not necessarily the larger number of detections possible with increased sensitivity, although information about mass distribuition of neutron star populations can also be useful for EOS constraint. Instead, ET will provide very strong signals at reasonable rates; for example two $1.4\,M_\odot$ neutron stars inspiralling towards each other within an effective distance of 100 Mpc, which is expected roughly once a year, would give a SNR in ET of over 900. This makes possible for the precise measurement of masses in early inspiral, the detection of small departures from point particle behaviour at moderate frequencies, and discrimination between merger and post-merger signals from different models at high frequencies.

An interesting feature that has emerged from studies of binary neutron star coalescences is the post-merger formation, in some cases, of a hyper-massive remnant object which oscillates and emits gravitational waveforms on fairly long timescales. The presence or absence of such post merger oscillations, as well as their characteristic frequency and duration, varies with the cold EOS. However, they are additionally sensitive to many physical effects from thermal properties, magnetic fields, and particle production, and so forth. The precise details of the signal, similarly to those from supernovae, are not easy to predict. However, the signal from such a post-merger oscillation is potentially visible with advanced detectors [131], and analysis of the signal following a measured inspiral may provide useful constraints on the underlying astrophysics.

It has recently become possible to compute the first complete and accurate simulations of the merger of a neutron stars binary through to the delayed formation of a BH and to its ringdown [135, 136]. By computing the complete gravitational wave signal produced in the process it was possible to show that the gravitational waves are strongly correlated to the properties of the sources emitting them. Differences in the EOS or in the initial mass of the system produced different signals with different power spectra and different durations.

Furthermore, magnetic fields (MFs) are commonly present in neutron stars and their possible impact on the dynamics of binary neutron stars has only begun to be examined. The `Whisky` code has been recently used to investigate the effect that MFs have on the gravitational wave emission produced during the inspiral and merger of magnetized neutron stars [140]. In particular it has been shown that MFs do have an impact after the merger (for initial MFs $B_0 \gtrsim 10^{12}$ G), but also during the inspiral (for sufficiently strong initial MFs with $B_0 \gtrsim 10^{16}$ G). These results, are quantified by computing the overlap between the waveforms produced during the inspiral by magnetized and unmagnetized binaries. Moreover, through the inclusion of more realistic equations of state and of a radiation transport scheme, it will be possible to increase considerably our level of understanding of these objects.

2.4.2 Equation-of-state of neutron stars from pulsar glitches

Many radio pulsars exhibit glitches, sudden spin-up events followed by a relaxation period towards stable secular spin-down. Pulsar glitches have a long observational history (beginning shortly after the discovery of the first pulsar) and so far over a hundred pulsars are known to have glitched at least once. Glitches have also been observed in magnetars. The archetypal glitching pulsar is Vela, which exhibits regular large glitches with an amplitude corresponding to a fractional spin frequency jump of the order of 10^{-6}.

Despite the wealth of observational data, the phenomenon of glitches remains an enigma from the theoretical point of view. It is widely believed that glitches are related with the existence of supefluids in the interior of mature neutron stars and that they involve a transfer of angular momentum from a superfluid component to the rest of the star, which includes the crust (to which the pulsar mechanism is presumed to be rigidly attached) and the charged matter in the core. A superfluid rotates by forming an array of quantised vortices and it can spin down provided the vortices can move outwards. If the vortex migration is impeded by 'pinning' to the other component then the superfluid cannot keep up with the spin-down due to electromagnetic braking. As a result a rotational lag develops between the two components until some critical level is reached at which the vortices unpin and transfer angular momentum to the rest of the star, and the two components are driven to corotation.

The nature of the instability causing vortex unpinning and the subsequent stage of relaxation of the system is poorly understood. One might hope that gravitational radiation detected by a glitch event could help unveil the key physics associated with this enigmatic phenomenon. It is likely that a glitch event involves the excitation of some of the inertial modes of the two-component system and the post-glitch relaxation is governed by the coupling of the two components through the vortex-mediated mutual friction force and the magnetic field. In fact, as recent work suggests, the glitch trigger-mechanism may be the result of a superfluid 'two-stream' instability setting in through the inertial modes of the system.

An instrument like ET would be the ideal tool for detecting a gravitational wave signal in the 10-100 Hz band which is the relevant one for the inertial modes of a Vela-like pulsar. The detection of gravitational wave signals from glitching pulsars would provide a tool for probing the interior matter of neutron stars and supplement the existing and future electromagnetic observations. The realisation of this exciting prospect will require (as in the case of other potential sources of gravitational radiation) the input of theoretical waveform templates. These waveforms should be computed using detailed multifluid hydrodynamical models for superfluid neutron stars, accounting for effects like vortex mutual friction and pinning.

2.4.3 Understanding relativistic instabilities in neutron stars via observation of r-modes

Just after the catastrophic implosion of a core-collapse supernova, gravitational waves could be emitted by the newborn, hot, rapidly rotating neutron star. In particular, this may occur due to the excitation of *r-modes* [64], non-radial pulsation modes of rotating stars for which the Coriolis force acts as the restoring force. The characteristic frequency of the GW is comparable to the rotation speed of the star. r-modes have an instability driven by gravitational radiation [141], inducing differential rotation at second order in the amplitude of the modes. The second order perturbation plays an important role in the nonlinear evolution of the r-mode instability, which makes detection of gravitational waves more difficult.

GW detection and measurement depends strongly on the r-mode saturation amplitude, which is estimated as much lower than unity by recent simulations and theory. Thus detection of such gravitational waves is more difficult than initially supposed. In this section we consider both the r-modes and another nonlinear effect, the differential rotation induced by r-modes [142]. The amount of such differential rotation is described by a parameter K, which may varying in the range $[-5/4, 10^{13}]$ depending on the model and initial conditions.

Such signals are an important opportunity for ET science, as they could provide a deep probe of aspects of neutron star formation and nuclear physics.

The strength of gravitational waves from r-modes The detectability of GW produced by r-modes depends on the amount of angular momentum that they carry away. As described in [143], for $K = 0$, the total angular momentum of the star decreases to 65% of its initial value, and part of the initial angular momentum of the star, about 58%, is transferred to the r-mode as a consequence of the rapid increase of the average differential rotation. Therefore the initial angular momentum carried away by gravitational waves is about

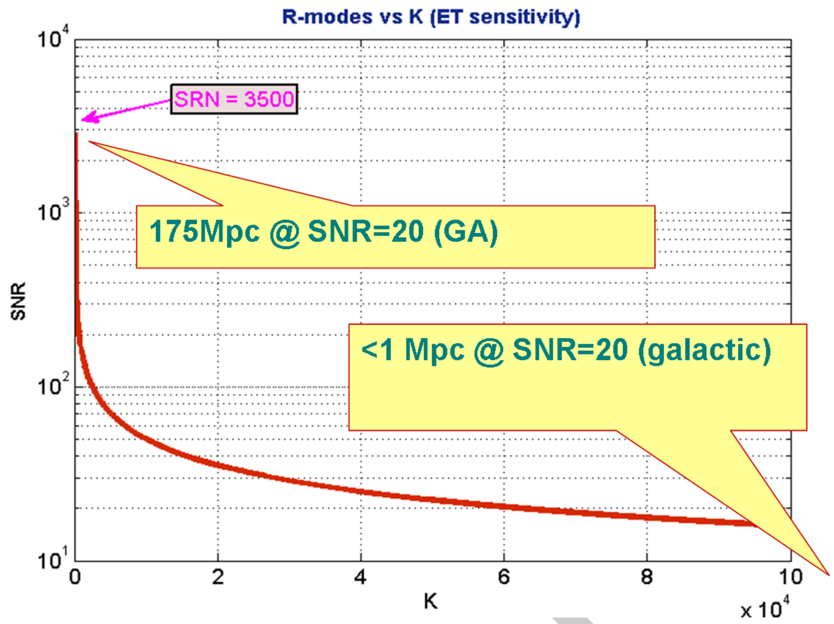

Figure 21: R-modes expected in Einstein Telescope.

35%. This result is strongly dependent on the value of K: for higher K the amount of angular momentum carried away by gravitational waves may even fall below 1%.

From the model in [143] the frequency f of the gravitational wave depends on the star angular velocity Ω by $f = 2\Omega/(3\pi)$. The frequency range is estimated as follows:

- $f_{min} \simeq [77 - 80]$ Hz, depending on the final value of the angular velocity $\Omega(t_f)$ and K;
- $f_{max} \simeq 1200$ Hz, depending on the initial value of the angular velocity Ω_0.

The amplitude in the frequency domain is given by:

$$H(f) = \frac{4.6 \times 10^{-25}}{\sqrt{2+K}} \sqrt{\frac{f_{max}}{f}} \frac{20\,\mathrm{Mpc}}{D}\,\mathrm{Hz}^{-1}$$

where D is the source distance, f the GW signal frequency and $f_{max} = 1191$ Hz is its maximum frequency.

We may estimate the signal to noise ratio (SNR) at ET by adapting a calculation made for Advanced LIGO in [143].[2] The optimal SNR is given by

$$\frac{S}{N} = \frac{250}{\sqrt{(2+K)}} \frac{20\,\mathrm{Mpc}}{D}.$$

The strong dependence on the unknown parameter K is clear, as shown in Figure 21 where we consider an SNR of 20, arbitrarily chosen for a confident observation of the signal. It is possible to conclude that the range of distances on which gravitational signal could be visible is really large. Considering the optimistic case when $K = 0$, we obtain a sight distance for an optimally oriented source of 175 Mpc; while considering the pessimistic case when $K = [10^5 - 10^6]$, the sight distance falls down to less than 1 Mpc (galactic sources).

R-modes and ET science goals A significant motivation for studying gravitational waves from the r-mode instability at ET is the opportunity to obtain a unique correlation with the nuclear physics and formation

[2]The sensitivity curve used for our estimation is ET-B.

processes of neutron stars. Such a signal could yield a fundamental probe of neutron star dynamics. Some possible implications are given below:

- In principle from gravitational wave signals and signal models it is possible to trace and quantify the initial conditions of the new born star such as initial frequency, initial temperature and others. This could lead to confirm or exclude a set of supernova models, star formation processes and NS models that agree with these experimental data.
- Another implication concerns neutron star nuclear physics models and the equation of state (EOS), potentially opening a window on the core and crust physics, especially superfluid aspects.
- The phenomenon of neutron star cooling due to neutron emission also interacts with the r-mode instability. In this case gravitational waves could provide information about the cooling rate and cooling model, which at the moment is assumed to follow the modified URCA process.

Hence, a possible observation of this signal by Einstein Telescope can put constraints on a set of theories concerning neutron star formation processes, nuclear physics models and the EOS.

Gravitational waves generated by the r-mode instability are a subject of considerable recent interest. We use here the results of considering the r-mode with $l = 2$ [143] , but more generally there are efforts to better understand the full dynamics of the newborn star considering higher numbers and different types of modes [144]. It is important to investigate fully such models and simulations as a science opportunity for ET.

2.4.4 Solving the enigma of GRB progenitors

Gamma-ray bursts (GRBs) are the most luminous explosions in the EM spectrum occurring in the universe. Through observations made by satellite-based gamma-ray observatories it was found that the the duration of the GRBs follows a bimodal distribution [145]. We classify GRBs either as *short-hard* or *long-soft* bursts depending on their duration and spectra. Through follow-up observations of the x-ray, optical and radio afterglow emission of GRBs it is possible to determine their sky-location, redshift and host galaxy.

Long GRBs are always associated with late-type star-forming host galaxies [146]. A handful of long GRBs have also been associated with supernovae [147–150]. It is therefore thought that core-collapse supernovae are the progenitor of long GRBs [151, 152].

Short GRBs are observed at lower redshifts than long GRBs are associated with a variety of galaxy types including early-type elliptical and lenticular galaxies without active star forming regions [153]. Currently, it is widely thought that merger of neutron star binaries or neutron star-black hole binaries (NS-BH) are the progenitors of most short-hard GRBs [154]. Some small fraction of short GRBs (less than 15% of known short GRBs) may be caused by soft gamma repeater flares (SGRs) [155, 156]. SGRs are described further in Section 2.4.4. Accurate predictions for the gravitational wave emission of the inspiral, merger and ringdown of compact binaries are possible through post-Newtonian approximations to Einstein's equations or through numerical relativity simulations. Searches for gravitational waves from inspiralling binaries using matched-filtering on data from initial interferometers (LIGO, Virgo, GEO) are underway. A search for the emission of GRB 070201 whose sky-locatiion error box overlaps the spiral arms of M31 was carried out in Ref. [157]. The matched-filter analysis excluded an inspiral progenitor for GRB 070201 if it was indeed located in M31 with a confidences of 99%.

It is typical to characterise the sensitivity of a gravitational wave observatory to inspiral distances by the horizon distance. The horizon distance is the distance at which we would measure a matched-filter signal-to-noise ratio of 8 for an optimally oriented (i.e., face-on) and overhead source. Figure 19, left plot, shows the horizon distance achieved by initial and advanced LIGO, Virgo and ET for NS-BH binaries with $m_{\rm NS} = 1.4 M_{\odot}$ and a range of BH masses.

Predicting the gravitational wave emission of core-collapse supernovae associated with long GRBs is more difficult and involves modelling the complicated internal dynamics of the collapsing star, see e.g., [79]. Searches

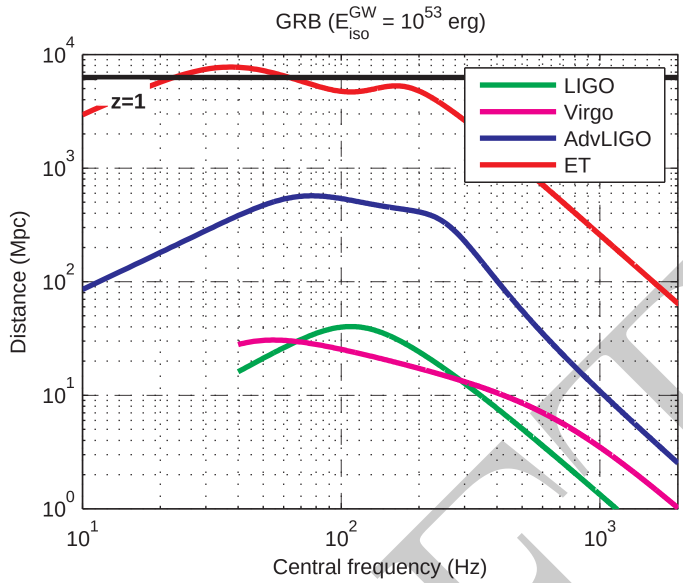

Figure 22: 90%-confidence lower limit on distance for GRB burst sources assuming a GRB energy emission of $E_{\rm GW}^{\rm iso} = 0.05 M_\odot c^2 \sim 9 \times 10^{52}$ergs. The solid horizontal black line near the top of the figure shows a redshift $z = 1$.

for unmodelled gravitational emission from GRBs on data from initial interferometers (LIGO, Virgo, GEO) are underway [157, 158].

From gravitational wave searches using coherent analysis techniques [158] we find that in general the 90%-confidence upper limit on $h_{\rm rss}$ gravitational wave amplitude is around an order of magnitude above the amplitude spectrum of the interferometer, i.e., $\sim 10 \times S_h(f)^{0.5}$. For narrow-band burst signals we can use the following approximation

$$E_{\rm GW}^{\rm iso} \simeq \frac{\pi^2 c^3}{G} D^2 f_0^2 h_{rss}^2 \tag{30}$$

where $E_{\rm GW}^{\rm iso}$ is the isotropic energy emission in gravitational waves, D is the distance of the source, f_0 is the central frequency, and h_{rss} is the root-sum-square amplitude of the gravitational wave:

$$h_{\rm rss} = \sqrt{\int (|h_+(t)|^2 + |h_\times(t)|^2)\ dt}\ . \tag{31}$$

From Eqn. 31 we can calculate a lower limit on source distance from our amplitude upper limit for a given assumption of $E_{\rm GW}^{\rm iso}$. For long GRBs the energy of emission in gravitational waves is not well known but has been estimated to be as high as $0.2 M_\odot c^2$ in the LIGO-Virgo frequency band of good sensitivity [159]. In Fig. 22 we estimate the distance to which various detectors are sensitive to a narrow-band burst of gravitational waves assuming $E_{\rm GW}^{\rm iso} = 0.05 M_\odot c^2$.

Soft Gamma Repeater Flares As described in section 2.4.4, a significant fraction, up to 15%, of short, hard γ-ray bursts may be associated with flaring activity in soft γ-repeaters (SGRs). These sources often undergo sporadic periods of activity which last from days to months where they emit short bursts of hard X-rays and soft γ-rays with luminosities $L \sim 10^{41}\,{\rm erg\,s^{-1}}$ and photon energies in the range 10-30 keV. Much more occassionally, they exhibit enormous, giant flares with luminosities as large as $10^{47}\,{\rm erg\,s^{-1}}$. There exist 4 known soft γ-repeaters, 3 in the milky way and 1 in the Large Magellanic cloud. It is generally believed that SGRs belong to a class of neutron star, magnetars, with extraordinarily large magnetic fields in the the range 10^{14}-10^{15} G where the flaring activity is due to sudden, violent reconfigurations of complex magnetic field topologies.

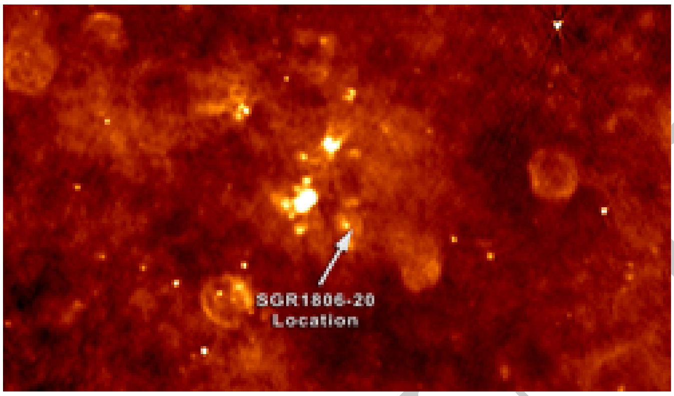

Figure 23: A high resolution, wide-field image of the area around SGR1806-20 as seen in radio wavelength. SGR1806-20 can not be seen in this image generated from earlier radio data taken when SGR1806-20 was ˇ201cradio quietˇ201d. The arrow locates the position of SGR1806-20 within the image. Credit: University of Hawaii.

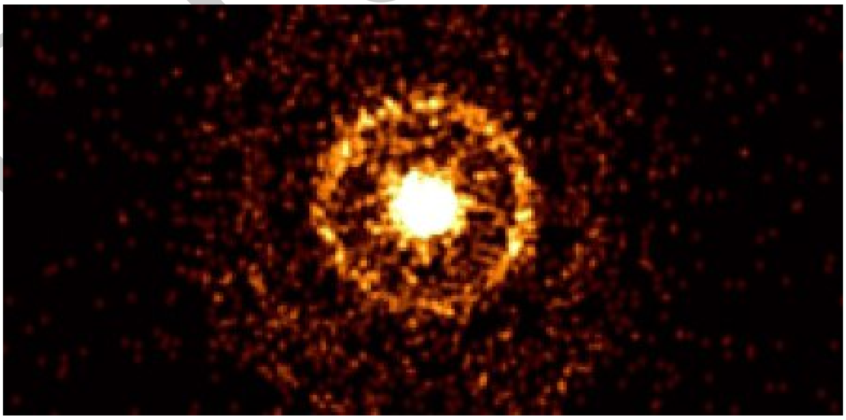

Figure 24: Swift's X-Ray Telescope (XRT) captured an apparent expanding halo around the flaring neutron star SGR J1550-5418. The halo formed as X-rays from the brightest flares scattered off of intervening dust clouds. Credit: NASA/Swift/Jules Halpern, Columbia University

The hardness of their spectra and the enormous luminosities involved mean that giant flares from nearby SGRs, such as that of SGR 1806-20 [160], represent an intriguing candidate progenitor scenario for some short duration γ-ray bursts. Indeed, in [161], the authors report a correlation between the positions of some short GRBs with those of low redshift galaxies, suggesting that $10-25\%$ of short GRBs occur in the local universe and, therefore, are likely to be associated with giant SGR flares. Furthermore, evidence for the existence of two classes of progenitors for short GRBs is provided in [156]. Here, it is found that a bimodal luminosity function, representing a dual-population of short GRB progenitors with low and high luminosities, is required to reproduce the observed distributions of short GRB luminosities. As well as statistical evidence, there have been observations of at least three individual short GRBs which present candidates for extragalactic SGR flares. Optical and infrared observations [162] of GRB 050906 suggest a tentative association with the local, fairly massive ($M \sim 10^{11} M_\odot$) starburst galaxy IC328 which lies at a redshift of $z = 0.031$. If GRB 050906 had indeed originated in IC328, the isotropic equivalent energy would be $E_{\rm ISO} \sim 1.5 \times 10^{46}$ erg in the 15-150 keV range. The giant flare from SGR 1806-20, by comparision, emitted $E_{\rm ISO} \sim 4 \times 10^{46}$ erg with photon energies > 30 keV. As well as the potential similarity in the energetics of this burst, the association with a starburst galaxy, where young, shortly lived magnetars are believed to be most prevalent, corroborates the SGR progenitor scenario. Two other short GRB-SGR flare candidates, GRB 051103 and GRB 070201, were detected by the Konus-Wind GRB spectrometer [163, 164]. The localisation area of GRB 051103 was found to lie near M81 (D=3.6 Mpc), suggesting an isotropic equivalent energy $E_{\rm ISO} = 7 \times 10^{46}$ erg. As remarked in [163], if GRB 051103 was *not* related to an SGR flare, we would expect an optical and/or transient in the localisation area, which has not been observed. Finally, the localisation area of GRB 070201 was found to overlap with the spiral arms of M31 (D=0.78 Mpc), leading to an estimate of $E_{\rm ISO} \sim 1.5 \times 10^{45}$ erg under the SGR flare scenario and, again, comparable to the giant flare from SGR 1806-20.

In addition to these types of arguments related to the energetics of the electromagnetic emission, gravitational wave observations can provide an extremely powerful tool to identify SGRs as sGRB progenitors. First, we note that the failure to detect the signature of a compact binary coalescence from sGRBs at distances where such a signal is expected can provide compelling evidence for the SGR progenitor scenario alone. Indeed, observations by the initial LIGO instruements recently excluded the coalescence of a binary neutron star system within M31 at more than 99% confidence as the progenitor for GRB 070201 [157]. Furthermore, a binary neutron star merger is excluded at distances less than 3.5 Mpc with 90% confidence. If, however, the progenitor had been an SGR flare, the LIGO observations imply an upper bound on the isotropic energy released as an unmodeled gravitational wave burst of $E^{\rm GW}_{\rm ISO} < 7.5 \times 10^{50}$ erg, within the bounds permitted by existing models.

The non-detection of an expected inspiral gravitational wave signature, however, is not the only way that an instrument like the Einstein telescope can provide evidence for the SGR progenitor scenario. In section **??**, we discuss giant SGR flares as a source of quasi-periodic oscillations, with quadrupolar components in the $\sim 10-40$ Hz range. Observations of these shear mode oscillations in gravitational waves, with no accompanying inspiral signal, would only be explicable under the SGR scenario. It is also possible that non-radial oscillatory modes would become excited by tectonic activity associated with a giant SGR flare [165]. These modes will then be damped by gravitational wave emission, resulting in a characteristic ring-down signal [166]. Various families of oscillatory modes, such as fluid (f), pressure (p) and purely space-time (w) modes may be excited and simultaneous gravitational wave observations of all three of these families can be used to place tight constraints on the neutron star equation of state [167]. The p and w modes, however, tend to have frequencies well above 4 kHz making the f-mode, with frequencies expected in the range $1-3$ kHz [168], the most accessible to currently planned gravitational wave observations. Again, gravitational wave observations of f-mode ring-downs associated with sGRBs, where there is no accompanying inspiral signal, would point directly to an SGR giant flare as the progenitor.

Current models for SGRs [122, 165, 169] indicate that they will emit less than 10^{46}ergs in gravitational waves. In the left panel of Fig. 25 we show 90%-confidence lower limits on the distances to which various gravitational wave detectors will be sensitive to gravitational wave bursts with this energy and we see that, in their most sensitive frequencies, the current generation of interferometers are just able to probe our own galaxy. While advanced LIGO improves this reach substantially, it is really only with the Einstein telescope that observations of gravitational waves associated with extra-galactic SGR flares become possible. Figure 25 shows the complementary plot of 90% energy upper limits obtainable by the various instruments for a galactic SGR. We typically

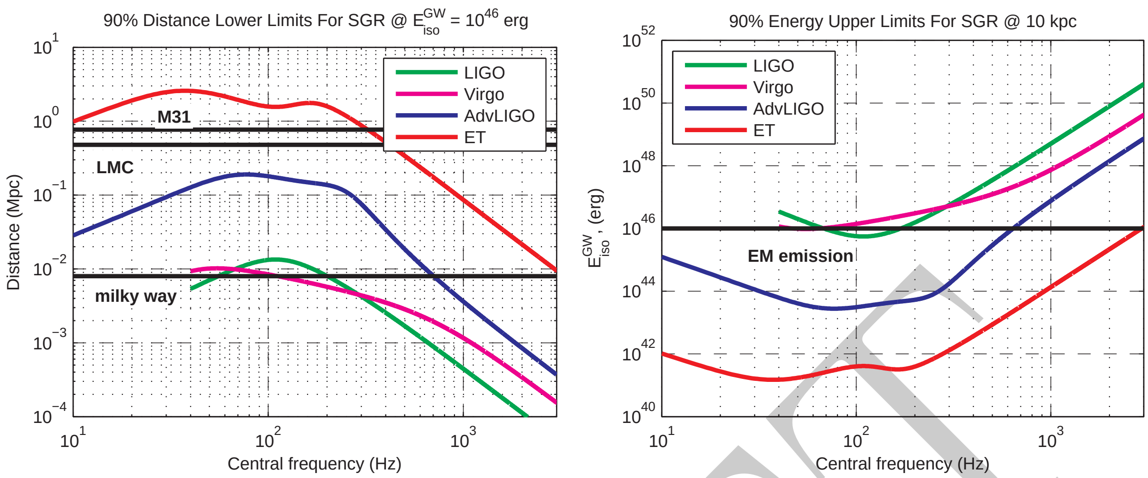

Figure 25: *Left panel*: 90%-confidence lower limit on distance for burst sources assuming $E_{\rm GW}^{\rm iso} = 10^{46}$ergs for an SGR progenitor scenario. Starting from the lower edge of the figure, the solid horizontal black lines show the distances to center of our galaxy, the distance to the large Magellanic cloud and the distance to M31 in Andromeda. *Right panel*: predicted 90% upper limits on isotropically emitted gravitational wave energy from a galactic SGR flare (i.e., distance of 10 kpc). The solid black horizontal line shows the expected upper limit of 10^{46} erg from energetic arguments alone.

take this to mean a distance of $\sim$ 10 kpc. Again, it is only with an instrument like the Einstein telescope that we are able to probe interesting energy regimes across the entire frequency spectrum one might reasonably expect for gravitational wave emission associated with SGR flares.

2.4.5 Understanding supernova cores

Stellar collapse is the most energetic event in the Universe, releasing $\sim 10^{53}$ erg of gravitational energy in the compression of a massive star's iron core to a neutron star. Most of this energy ($\sim$ 99%) is emitted in neutrinos and only about 10^{51} erg go into energy of the core-collapse supernova (CC-SN) explosion. CC-SNe (SN types II, Ib, Ic) are $\sim$10 times more frequent than thermonuclear type-Ia SNe. A SN explosion pollutes the interstellar medium with the nucleosynthetic products of stellar evolution (CC-SNe are the Universe's primary source of oxygen) and enriches via the *r*-process the universe with rare heavy isotopes. The perturbation caused by an SN in its vicinity can trigger the formation of stellar systems and stellar collapse and CC-SNe are the birth sites of neutron stars (NSs) and stellar-mass black holes (BHs).

The Supernova Problem and GW observations The precise mechanism of explosion operating in CC-SNe is unknown [77–79]. When the inner part of the collapsing iron core reaches densities close to those in atomic nuclei, the strong force leads to a stiffening of the nuclear equation of state (EOS), resulting in *core bounce* of the inner core into the still infalling outer core. A shock wave is formed that propagates outward in mass and radius, but quickly loses energy due to the breakup of heavy nuclei and neutrinos that carry away energy from the postshock layer. The shock stalls, turns into an accretion shock and must be *revived* to drive a CC-SN explosion. If this does not happen, a BH will form on an accretion timescale of $\sim$ 2 s. *What is the mechanism of shock revival?* This is the fundamental question and primary unsolved problem of CC-SN theory. Indications are strong that the CC-SN mechanism involves a multitude of multi-dimensional processes, including rotation, convection/turbulence, and various hydrodynamic instabilities of the stalled shock and in the proto-NS. This opens up the possibility of probing the supernova mechanism with gravitational waves (GWs). GWs, even more so than neutrinos, carry direct dynamical information from the supernova engine deep inside a dying massive star, a region generally inaccessible by the traditional means of observational astronomy. GWs form a core-collapse event have the potential of putting very strong constraints on the CC-SN mechanism [79, 80]. With initial and certainly second-generation interferometric GW detectors, this should be possible for an event in the

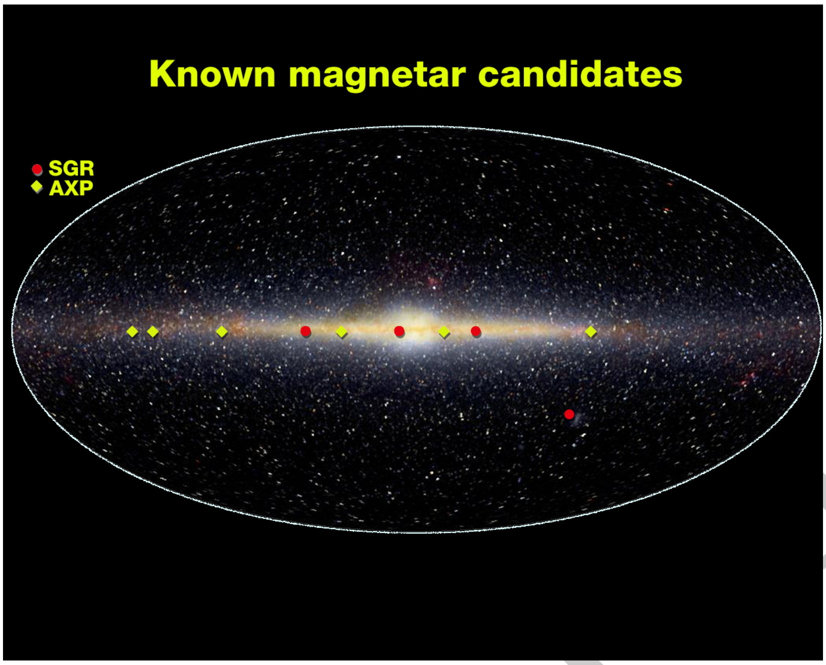

Figure 26: The locations of known magnetar candidates (Soft Gamma-ray Repeaters and Anomalous X-ray Pulsars) in the Milky Way. Credit: NASA/Marshall Space Flight Center

Milky Way ($D \sim 10 - 15\,\mathrm{kpc}$) and the Magellanic Clouds [79] ($D \sim 50 - 70\,\mathrm{kpc}$), but even optimistic estimates of the CC-SN rate in this region do not predict more than $\sim 1 - 2$ events per century. This number roughly doubles if one includes the entire local group ($D \sim 1\,\mathrm{Mpc}$). In the region from $3 - 5\,\mathrm{Mpc}$ a number of starburst galaxies increase the predicted and observed integrate SN rate to $\sim 0.5\,\mathrm{yr}^{-1}$. At $D \sim 10\,\mathrm{Mpc}$ it is $\gtrsim 1\,\mathrm{yr}^{-1}$.

Supernova Science with ET The GW emission processes in a CC event emit GW strains h in the range $10^{-24} - 10^{-22}\,(D/1\,\mathrm{Mpc})$ and most of the emission takes place at frequencies of $\sim 200 - 1000\,\mathrm{Hz}$, but the various explosion scenarios exhibit unique spectral distributions and vary in total emitted energies [79, 80]. In addition, there is likely to be a low-frequency GW-memory-type component with large h up to $10^{-22}\,(D/1\,\mathrm{Mpc})$ at $0-20\,\mathrm{Hz}$. ET as currently envisioned [82] is sufficiently sensitive to detect GWs from various CC-SN scenarios out to $2 - 4\,\mathrm{Mpc}$. If the high-f sensitivity was increased by a factor of $\sim 2 - 3$, detection out to $\sim 10\,\mathrm{Mpc}$ may be possible. Figure 14 summarizes the ET observational capabilities and examines each of the main generation processes of gravitational waves.

Even without this improvement, ET may see multiple CC-SNe during its lifetime and would have the power to provide strong hints for a particular SN mechanism and/or smoking-gun evidence against another – crucial astrophysics information that is unlikely to be attainable in other ways. At ET's implementation, megaton-class neutrino detectors will be operative and, having range similar to ET, will be able to provide coincident observations, narrowing down the time of the GW emission to $\sim 1\,\mathrm{ms}$. In addition, deep high-cadence optical transient surveys will be operative and targeting near-universe transients, providing additional coincident data as well as additional astrophysics output (progenitor type/mass, explosion morphology/energy etc.).

Impact Constraining the CC-SN mechanism will mean a breakthrough in our understanding of the large range of phenomena associated with stellar collapse, CC-SNe, BH and NS formation, and gamma-ray bursts (GRBs). However, the astrophysics and physics information provided by GWs observed from a CC event with ET goes beyond this: These GWs carry also information on the high-density nuclear EOS, explosion asymmetries and pulsar kicks, the formation of a BH in a failing CC-SN, and can help uncover rare events such as the accretion-induced collapse of a white dwarf to a NS or weak or failing CC-SNe that have very weak or absent EM signatures.

2.4.6 Explaining neutron star spin frequencies in low-mass X-ray binaries

Observations of accreting neutron stars lead to perhaps the most important reason why, irrespective of the mechanism at work, at least some neutron stars might be actally emitting detectable gravitational waves. This is the observation that even the fastest accreting neutron stars spin at rates much lower than the expected break-up frequency. The current record is 716 Hz, while the theoretically expected upper limit is more than 1 kHz. Following a suggestion by Bildsten [46], it is possible that this limit occurs because of the balance between the spin-up torque due to the accreting matter, and the spindown torque due to gravitational wave emission. A short calculation assuming a link between the observed X-ray luminosity with the accretion rate, and taking the mountain scenario for the emission mechanism leads to the following estimate of the GW amplitude:

$$h_0 = 3 \times 10^{-27} F_{-8}^{1/2} \left(\frac{R}{10\text{km}}\right)^{3/4} \left(\frac{1.4 M_\odot}{M}\right)^{1/4} \left(\frac{1\text{ kHz}}{\nu_s}\right)^{1/2}. \tag{32}$$

This is seen to be dependent on frequency: $h_0 \propto \nu_s^{-1/2}$.

2.4.7 Intermediate mass black holes

The existence of intermediate mass black holes (IMBHs) with masses in the range $10^2 - 10^4\, M_\odot$ has not yet been corroborated observationally, but these objects are of high interest for astrophysics. Our understanding of the formation and evolution of supermassive black holes, as well as galaxy evolution modeling and cosmography would dramatically change if an IMBH were to be observed. From the point of view of traditional electromagnetic astronomy, which relies on the monitoring of stellar kinematics, the direct detection of an IMBH seems to be rather far in the future. However, the prospect of the detection and characterization of an IMBH has good chances in lower-frequency GW astrophysics, in particular with ET. The detection and characterization of a binary containing an IMBH would corroborate the existence of such systems and provide a robust test of general relativity through tests of the black hole uniqueness theorem (see subsection 2.3.6).

Signals from IMBH binaries can start in the band of LISA, and sweep through to the ET band, allowing us to observe different aspects of the coalescence event, as illustrated in Fig. 27. For ET, a lower cut-off frequency of 1 Hz was assumed.

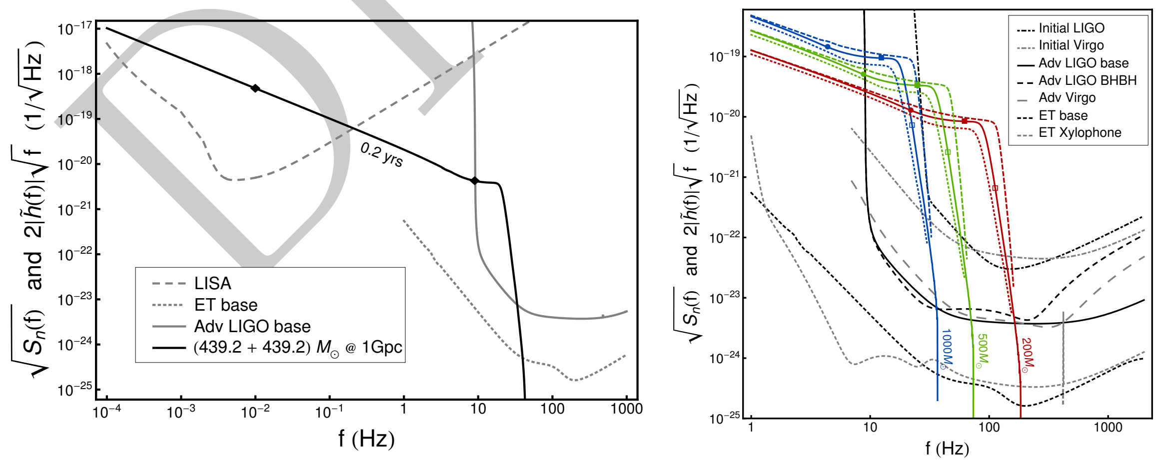

Figure 27: Left: different aspects of the inspiral, merger and ringdown signal from an intermediate mass black hole binary with masses $(439.2, 439.2)\, M_\odot$ at 1 Gpc can be studied as it passes from the LISA band into the ET band. The later, more interesting part of the evolution is seen in ET. Right: signals from IMBH binaries with different total masses. The solid lines are for equal mass, non-spinning binaries; the dashed lines for binaries with equal masses and dimensionless spins $\chi = 0.75$; and the dotted lines for zero-spin binaries with $m_2/m_1 = 3$.

2.5 Cosmology and Cosmography

2.5.1 Reconstruction of the evolution of compact binary coalescence rates by ET

The rate at which neutron stars and black holes coalesce at different redshifts can provide indirect but extremely valuable insights into star formation rate (SFR). We now consider how accurately ET would be able to distinguish between coalescence rate predictions from different SFR models. Considering that BNS coalescences are expected to be the most abundant, they are the best "trackers" of SFR , and these are the events we will focus on.

The rate per unit of time and per unit of comoving volume at which BNS systems are observed to coalesce at redshift z can be written as

$$\dot{\rho}_c^0(z) = \dot{\rho}_c^0(0)\frac{\dot{\rho}_{*,c}(z)}{\dot{\rho}_{*,c}(0)}. \tag{33}$$

Here $\dot{\rho}_c^0(0)$ is the coalescence rate at the current epoch, and $\dot{\rho}_{*,c}$ relates the past star formation rate to the rate of coalescence. One has

$$\dot{\rho}_{*,c}(z) = \int \frac{\dot{\rho}_*(z_f)}{(1+z_f)} P(t_d) dt_d, \tag{34}$$

where $\dot{\rho}_*$ is the SFR itself, z is the redshift at which the binary coalesces, z_f is the redshift at which the progenitor binary formed, and $P(t_d)$ is the probability distribution of the delay time t_d between the formation of the progenitor and coalescence. $P(t_d)$ has been estimated as

$$P(t_d) \propto \frac{1}{t_d} \quad \text{for } t_d > \tau_0, \tag{35}$$

where τ_0 is some minimum delay time. For more details we refer to [17] and references therein. As in that paper, for BNS coalescence we will assume $\tau_0 \sim 20$ Myr. The coalescence rate per unit redshift as observed in our local Universe is found by multiplying $\dot{\rho}_c^0$ by the gradient of comoving volume:

$$\frac{dR_c^0}{dz} = \dot{\rho}_c^0(z)\frac{dV_c}{dz}(z). \tag{36}$$

We may now ask how well ET will be able to discriminate between different SFR models $\dot{\rho}_*(z)$ through differences in the resulting observed BNS coalescence rates $\dot{\rho}_c^0(z)$. To this end we consider four different models:

- Hopkins and Beacom [13]: An update of an observational compilation by Hopkins [**?**], placing lower bounds using the evolution of stellar mass density, metal mass density, and supernova rate density, and an upper bound using Super-Kamiokande results for the electron antineutrino flux from core-collapse supernovae;
- Nagamine et al. [170]: An approach comparing and combining results from direct observations, a model using local fossil evidence at $z \sim 0$, and theoretical *ab initio* models;
- Fardal et al. [171]: A model involving a new proposal for the initial mass function with a view on reconciling SFR predictions with the total extragalactic background radiation;
- Wilkins et al. [172]: Based on stellar mass density measurements together with a new ansatz for the initial mass function.

We place simulated BNS sources according to the coalescence rates $\dot{\rho}_c^0(z)$ inferred from these four models using their proposed $\dot{\rho}_*(z)$, with a minimum delay time $\tau_0 = 20$ Myr. Sources are positioned uniformly in the sky; an SNR cut is imposed such that a source is disregarded unless $\rho > 8$. We (very) conservatively set the coalescence rate at the current epoch to $\dot{\rho}_c^0 = 0.03\,\mathrm{Mpc}^{-3}\mathrm{Myr}^{-1}$, in which case between $\sim 150,000$ and $\sim 275,000$ sources survive the SNR cut, depending on the SFR model. Note that this local coalescence rate will most likely already be measured by Advanced LIGO and Virgo, so that we may consider it a known quantity in the context of ET.

Given a fiducial cosmological model, one can associate a luminosity distance $D_{\rm L}(z)$ with each simulated source. In a spatially flat Friedman-Robertson-Walker universe, this relationship takes the form

$$D_{\rm L}(H_0, \Omega_{\rm M}, \Omega_\Lambda, w; z) = \frac{1+z}{H_0} \int_0^z \frac{dz'}{\left[\Omega_{\rm M}(1+z')^3 + \Omega_\Lambda(1+z)^{3(1+w)}\right]^{1/2}}, \tag{37}$$

where H_0 is the Hubble parameter at the current era, $\Omega_{\rm M}$ is the density of matter normalized by the critical density, Ω_Λ the density of dark energy (similarly normalized), and w is the equation-of-state parameter of dark energy. For definiteness, we choose our fiducial cosmological model such that $H_0 = 70\,{\rm kms^{-1}Mpc^{-1}}$, $\Omega_{\rm M} = 0.27$, $\Omega_\Lambda = 0.73$, and $w = -1$.

The distance measured from the gravitational wave signal, $\hat{D}_{\rm L}$, will be different from the true distance due to (i) the noise in the detector, and (ii) (de)magnification as a result of weak lensing. Thus, with each source we associate a "measured" luminosity distance

$$\hat{D}_{\rm L}(z) = D_{\rm L}(z) + \delta D_{\rm L}(z), \tag{38}$$

where $\delta D_{\rm L}(z)$ is drawn at random from a Gaussian distribution with a spread given by

$$\Delta D_{\rm L} = (\sigma_{\rm ET}^2 + \sigma_{\rm WL}^2)^{1/2}, \tag{39}$$

The contribution $\sigma_{\rm ET}$ is due to detector noise while $\sigma_{\rm WL}$ results from weak lensing. Note that $\Delta D_{\rm L}$ will depend not only on redshift but also on sky position and the orientation of the orbital plane. As a rule of thumb, one can take $\sigma_{\rm ET}/D_{\rm L} \simeq 1/\rho$, and for the weak lensing error we assume $\sigma_{\rm WL}/D_{\rm L} = 0.05z$.

Having distributed sources as described above and associated measured luminosity distances to them, we have a simulated "catalog" of detected inspiral events. Using the fiducial cosmological model, the measured luminosity distances $\hat{D}_{\rm L}(z)$ of Eq. (38) can be inverted to obtain measured redshifts $\hat{z}$. These recovered redshifts are then binned to obtain a recovered rate distribution $d\hat{R}_c^0/dz$. The measured luminosity distances and recovered redshift for one such catalog are shown in Fig. 28. By doing this for a large number of different simulated catalogs (say, 1000 catalogs), one can compute at an average and a 1-sigma spread for the number of sources in each recovered redshift bin.

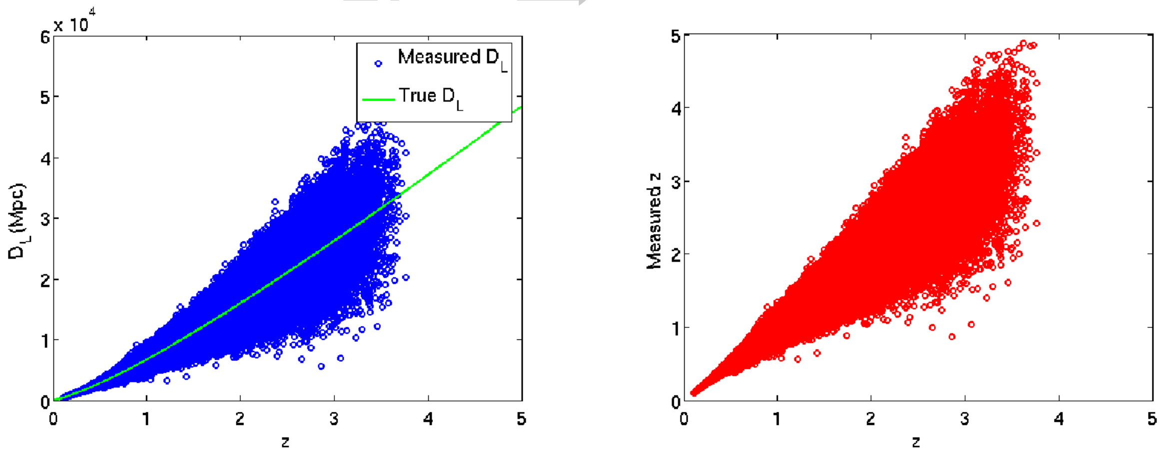

Figure 28: "Measured" luminosity distances (left) and inferred redshifts (right) for sources in a simulated catalog of BNS inspiral events.

To check how well ET will be able to distinguish between different coalescence rate predictions, we can fold in the anticipated efficiency $\epsilon(z)$, i.e., the fraction of coalescences at a given redshift that survive the SNR cut $\rho > 8$. The left panel of Fig. 29 shows efficiency as a function of redshift; it is essentially 1 up to $z \simeq 0.7$, after which it starts to drop rather quickly. Beyond $z \simeq 3.5$ no signals can be seen even when optimally positioned and oriented. The efficiency can be folded into the recovered rate distribution:

$$\left[\frac{dR_c^0(z)}{dz}\right]_{\text{recovered}} = \epsilon(z)^{-1}\frac{dR_c'(z)}{dz}, \tag{40}$$

where dR_c'/dz is the distribution inferred from binning the measured redshifts.

The right hand panel of Fig. 29 shows both the underlying rates $dR_c^0(z)/dz$ and the recovered rates, with 1-sigma spreads, for the four SFR models we are considering. First we note some systematic effects due to uncertainties in the redshift measurements:

- At small reshifts ($z \lesssim 1.5$), the recovered rate distribution is shifted very slightly to the left with respect to the underlying distribution. This is because of higher-redshift events ending up in lower redshift bins due to measurement errors. The effect is not compensated by lower redshift events ending up in higher redshift bins, because at lower redshifts the spread in measured redshift is smaller;
- At intermediate redshifts ($1.5 \lesssim 3$) the true coalescence rate is being underestimated (despite having folded in efficiency loss) because of events ending up in both higher and lower measured redshift bins;
- Beyond $z \simeq 3.5$ the recovered rate diverges, because there are still *measured* redshift values there, but the efficiency $\epsilon(z) \to 0$.

We see that ET can easily distinguish between the four models we took from recent literature. Generally, two models for BNS coalescence rates can be distinguished from each other if over at least one $\Delta z = 0.1$ redshift bin at $z \lesssim 1.5$, the number of sources in the bin differs by more than a few percent.

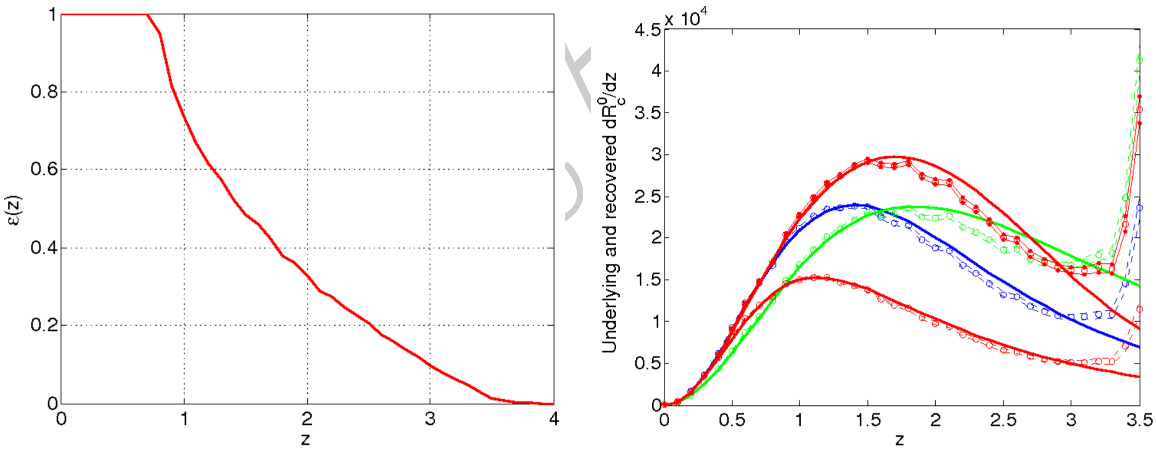

Figure 29: Left: the fraction of found versus missed signals as a function of redshift. Right: underlying and recovered coalescence rates (taking into account detection efficiency) for the models of Hopkins and Beacom [13] (top, red), Fardal et al. [171] (blue), Wilkins et al. [172] (bottom, red), and Nagamine et al. [170] (green). The solid lines are the true rates, the circles give the number of measured coalescences in a redshift bin, and the dashed lines give a 1-sigma spread in recovered redshifts.

2.5.2 Cosmological evolution of compact object populations

The calculation of the coalescence rate as a function of the redshift must take into account the following factors: the star formation rate history $SFR(z)$, the binary fraction $f_b(z)$, the formation efficiency of a given type of binary, i.e. the fraction of number of binaries that lead to formation of coalescing compact object binary, and their distribution of merger times. These quantities may depend on redshift since the stellar populations evolve with cosmic time. Let us examine the effects of evolution of each of these factors.

The star formation rate is known to increase strongly to the redshift $z = 2$, and there is a debate about its behavior for higher redshifts. At redshift $z = 2$, the star formation is estimated to be a factor of 10 larger than the present value at $z = 0$.

The distribution of merger times can be estimated either by analyzing the present population of compact objects binaries or by involving the population synthesis. The first approach is limited to deal with the double neutron star binaries, and suffers from small number statistics. The second involves several uncertainties due to parametrization of binary evolution. However the two approaches yield similar results. The distribution of merger times for the double neutron star binaries can be well approximated by a distribution $\propto t^{-1}$. The lower cutoff for the DNS systems lies somewhere between 10 and 100 Myrs. The population synthesis leads to similar conclusions about the distribution of merger times for BHNS and BBH systems, however the low time cutoff may probably lie higher.

The evolution of the properties of binaries with cosmic time. The main factor that may affect the evolution of the binaries as a function of redshift are the changes in the distribution of metallicity. Metallicity affects strongly the mass loss rate in stars, and hence has a strong influence on the masses spectrum of compact objects. The lower the metallicity the higher the maximum mass of a black hole that may be formed in the course of stellar evolution. This leads to to stabilization of mass transfers and therefore to increase in the formation rate of compact object binaries.

Taking together the above factors we see that there are several reasons why the coalescence rate should increase strongly as we go to redshifts of $z = 1$–2. First the local star formation rate increases and the overall number of binary formation is larger. Second, the typical delay times for the DNS systems are low therefore their merger rate density will roughly follow that of the SFR. In the case of BHNS or BBH systems he typical delay times between formation and coalescence may be as large as 1–3 Gyrs. This delays the peak of coalescence rate density with respect to the star formation rate. Thus the delays are significant but not crucial. Third, the metallicity evolution may lead to higher compact object formation rate for high redshifts, and formation of larger number of massive BBH binaries.

This consideration can be put into detailed numerical codes to yield predictions about the rates. However even without such strong numerical support one can readily estimate with the back of the envelope calculation that the ratio of the coalescence rate (per unit volume per unti time) to the local one should be at least a few. The local coalescence rate can only be estimated with observations since neither the observational not the indirect approach mentioned earlier can yield the estimate of the rate with the accuracy better that plus minus an order of magnitude.

The Einstein telescope will provide a large sample of coalescences with the precise measurement of their masses and redshifts. This will be an extremely valuable tool for analysis of the cosmic compact object formation history. The measurement of their masses will yield information on the metallicity evolution as well as evolution of most massive stars. The Einstein telescope will yield a cosmic compact object census up to redshift $z = 2$, and will yield information about black holes and neutron star formed even at earlier epochs because of the delays between formation and coalescence.

There are two distinct routes to form BH binary. The first, conventional way, is to start with binary system of two main sequence stars and trace their evolution. There are several big uncertainties in this process. The first one is the initial mass ratio function: what is the distribution of the mass ratio in the binary of two main sequence stars, how it depends on the metallicity and spectral type. The second, and probably the biggest uncertainty, is related to the "common envelope" evolution, where the NS (or BH) and Helium core are emerged and evolve in the gaseous environment of the star. In this stage the NS/BH could merge with Helium core and binary is not formed. The third uncertainty is related to the direction and magnitude of the kick exerted on the newly born BH from the assymetric supernova explosion. All the above is reflected in the uncertainties on the rate of such binaries [11, 12].

The BH binaries could also be formed in the dense environment such as galactic nuclei. In the galaxies with SMBH ($M < 10^7\,M_\odot$), the relaxation time is less than a Hubble time, and a steep cusp of stars and stellar mass BHs can be formed. BHs as more massive and compact objects will segregate into central ≈ 1 pc region. Other two dense regions are massive globular clusters and nuclear star clusters in the centers of low-mass galaxies which may not have SMBH. The densities in those regions are high enough to have multiple encounters with formation and/or hardening of the BH binaries.

2.5.3 Intermediate mass black holes as seeds of galaxy formation

It is widely accepted that the massive black holes (MBHs) found in the centres of many galaxies grow from initial seeds through the processes of accretion and mergers following mergers between their host dark matter halos. However, little is known about the seeds from which these black holes grow. Open questions include — how and when did they form? What are their masses? Where are they? Current observations are consistent with both *light seed* scenarios, in which $\sim 100 M_\odot$ black hole seeds form at redshift $z \approx 20$ from the collapse of Population III stars [173, 174], and *heavy seed* scenarios, in which black holes of mass $\sim 10^5 M_\odot$ form from direct collapse of dust clouds [175, 176]. Mergers between MBHs in merging dark matter halos will generate gravitational waves. These are a major source for LISA [177], but LISA will only see mergers with total mass $\gtrsim 10^3 M_\odot$. LISA can therefore probe black hole seeds only in the heavy seed scenario and does not have the power to discriminate between the light and heavy scenarios.

The Einstein Telescope will have sensitivity in the 1–50Hz band in which gravitational waves from mergers involving $\sim$ 10–100$M_\odot$ black holes will lie. It will therefore provide complementary information to LISA and could directly observe the first epoch of mergers between light seeds. Present estimates, based on Monte Carlo simulations of galaxy merger trees [178, 179], suggest the Einstein Telescope could detect between a few and a few tens of seed black hole merger events over three years of operation [180]. Several of these events will be at high redshift, $z \sim 5$, by which time it is unlikely that $100 M_\odot$ black holes could have formed by other routes. ET and LISA in conjunction probe the whole merger history of dark matter halos containing black holes in the 10–$10^6 M_\odot$ range, which will provide detailed information on the hierarchical assembly of galaxies. ET on its own is not able to measure the distance to a gravitational wave source, but provided one additional, non-colocated, interferometer is in operation concurrently with at least two detectors at the ET site, the network will be able to determine the luminosity distance of a source to $\sim 40\%$ precision and the redshifted total mass of the system to $\lesssim 1\%$. Using a concordance cosmology, this distance estimate can be used to estimate redshift with comparable accuracy and so it should be possible to say that the $z \approx 5$ events are of *low mass* and at *high redshift*, and therefore are convincing candidates as Pop III seed mergers.

Just one detection by ET will rule out the heavy seed model. With several detections, we will be able to make statements about pop III seed black hole properties, such as their mass distribution, their early accretion history etc. [180]. These observations cannot be made be any other existing or proposed detector — it is science that is unique to ET. Such observations will be vital to our understanding of the assembly of structure in the Universe, and of the close link between black holes residing in the centres of galaxies and their hosts [173].

2.5.4 Cosmography with a population of standard sirens

The goal of modern cosmology is to measure the geometrical and dynamical properties of the Universe by projecting the observed parameters onto a cosmological model. The Universe has a lot of structure on small scales, but on a scale of about 100 Mpc the distribution of both baryonic (inferred from the electromagnetic radiation they emit) and dark matter (inferred from large scale streaming motion of galaxies) components is quite smooth. It is, therefore, quite natural to assume that the Universe is homogeneous and isotropic while describing its large-scale properties. In such a model, the scale factor $a(t)$, which essentially gives the proper distance between comoving coordinates, and curvature of spatial sections k, are the only quantities that are needed to fully characterize the properties of the Universe. The metric of a smooth homogeneous and isotropic spacetime is

$$ds^2 = -dt^2 + a^2(t)\frac{d\sigma^2}{1-k\sigma^2} + \sigma^2\left(d\theta^2 + \sin^2\theta\, d\varphi^2\right),$$

where t is the cosmic time-coordinate, $(\sigma, \theta, \varphi)$ are the comoving spatial coordinates, and k is a parameter describing the curvature of the $t = $ const. spatial slices. $k = 0, \pm 1$, for flat, positively and negatively curved

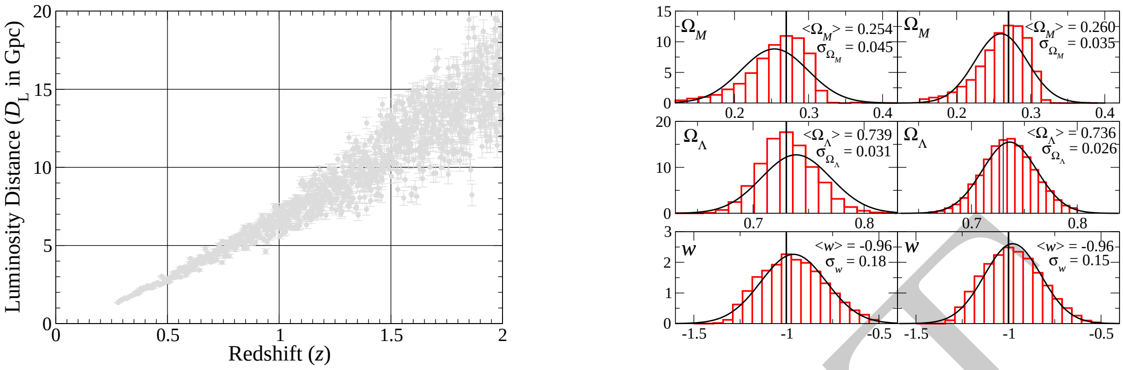

ee

Figure 30: The plot on the left shows one realization of a catalogue of binary neutron star (BNS) events that might be observed by ET. The plot on the right shows the distribution of errors in $\Omega_{\rm M}$, Ω_Λ and w obtained by fitting 5,190 realizations of a catalogue of BNS merger events to a cosmological model of the type given in Eq. (42), with three free parameters. The fractional 1-σ width of the distributions $\sigma_{\Omega_{\rm M}}/\Omega_{\rm M}$, $\sigma_{\Omega_\Lambda}/\Omega_\Lambda$, and $\sigma_w/|w|$, are 18%, 4.2% and 18% (with weak lensing errors in $D_{\rm L}$, left panels) and 14%, 3.5% and 15% (if weak lensing errors can be corrected, right panels).

slices, respectively. The evolution of $a(t)$, of course, depends on the parameter k, as well as the "matter" content of the Universe. The latter could consist of radiation, baryons, dark matter (DM), dark energy (DE), and everything else that contributes to the energy-momentum tensor.

The Friedman equation, which is one of two Einstein equations describing the dynamics of an isotropic and homogeneous Universe, relates the cosmic scale factor $a(t)$ to the energy content of the Universe through

$$H(t) = H_0 \left[\hat{\Omega}_{\rm M}(t) - \frac{k}{H_0^2 a^2} + \hat{\Omega}_\Lambda(t) \right]^{1/2}, \tag{41}$$

where $H(t) \equiv \dot{a}(t)/a(t)$ is the Hubble parameter ($H_0 = H(t_P)$ being its value at the present epoch t_P), $\hat{\Omega}_{\rm M}(t)$ and $\hat{\Omega}_\Lambda(t)$ are the (dimensionless) energy densities of the DM and DE, respectively. The above equation has to be supplemented with the equation-of-state of DM, assumed to be pressure-less fluid $p = 0$ [$\hat{\Omega}_{\rm M}(t) = \Omega_M(1+z)^3$, $\Omega_{\rm M} = \hat{\Omega}_{\rm M}(t_P)$] and of DE, assumed to be of the form $p = w\rho_\Lambda$ [$\hat{\Omega}_\Lambda(t) = \Omega_\Lambda(1+z)^{3(1+w)}$, where $\Omega_\Lambda = \Omega_\Lambda(t_P)$], with $w = -1$ corresponding to a cosmological constant. The goal of cosmography is to measure (H_0, $\Omega_{\rm M}$, Ω_Λ, w, k, ...), which essentially determine the large-scale geometry and dynamics of the Universe. In the rest of this paper we shall assume that the spatial slices are flat (i.e., $k = 0$).

Measuring the cosmological parameters Astronomers use "standard candles" to measure the geometry of the Universe and the various cosmological parameters. A standard candle is a source whose intrinsic luminosity L can be inferred from the observed properties (such as the spectral content, time-variability of the flux of radiation, etc.). Since the observations also measure the apparent luminosity F, one can deduce the luminosity distance $D_{\rm L}$ to a standard candle from $D_{\rm L} = \sqrt{L/(4\pi F)}$. In addition, if the red-shift z to the source is known then by observing a population of such sources it will be possible to measure the various cosmological parameters since the luminosity distance is related, when $k = 0$, to the red-shift via

$$D_{\rm L} = \frac{c(1+z)}{H_0} \int_0^z \frac{dz'}{\left[\Omega_{\rm M}(1+z')^3 + \Omega_\Lambda(1+z')^{3(1+w)}\right]^{1/2}}. \tag{42}$$

There is no unique standard candle in astronomy that works on all distance scales. An astronomer, therefore, builds the distance scale by using several steps, each of which works over a limited range of the distance. For

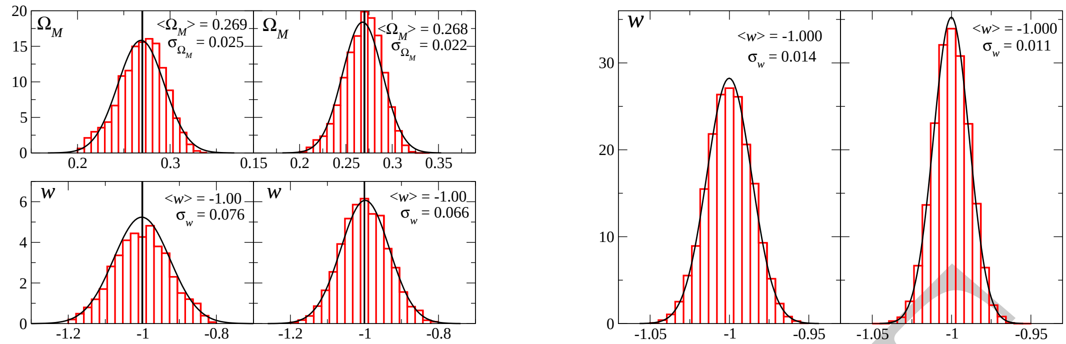

Figure 31: Same as the right plot of Fig. 30 except that one or more of the cosmological parameters are assumed to be known. The plot on the left assumes that Ω_Λ is known to be $\Omega_\Lambda = 0.73$, and fits the "data" to the model with two free parameters. The fractional 1-σ widths in the distribution $\sigma_{\Omega_{\rm M}}/\Omega_{\rm M}$ and and $\sigma_w/|w|$, are 9.4% and 7.6% (with weak lensing errors in $D_{\rm L}$, left panels) and 8.1% and 6.6% (if weak lensing errors can be corrected, right panels). The plot on the right is the same but assuming that w is the only unknown parameter. The fractional 1-σ width of the distribution $\sigma_w/|w|$ is 1.4% (with weak lensing errors in $D_{\rm L}$, left panel) and 1.1% (if lensing errors can be corrected, right panel).

instance, the method of parallax can determine distances to a few kpc, Cepheid variables up to 10 Mpc, the Tully-Fisher relation works for several tens of Mpc, the D_n-σ relation up to hundreds of Mpc and Type Ia supernovae up to red-shifts of a few. This way of building the distance scale has been referred to as the *cosmic distance ladder*. For cosmography, a proper calibration of the distance to high red-shift galaxies is based on the mutual agreement between different rungs of this ladder. It is critical that each of the rungs is calibrated with as little an error as possible.

Fitting a cosmological model to a CBC population The expected rate of coalescences per year within the horizon of ET is $\sim$ several $\times\, 10^5$ for BNS and NS-BH. Such a large population of events to which luminosity distances are known pretty accurately, would be very useful for measuring cosmological parameters. If, as suspected, BNS and NS-BH are progenitors of short-hard gamma-ray bursts (GRBs) [155], then it might be possible to make a coincident detection of a significant subset of the events in GW and EM windows and obtain both the luminosity distance to and red-shift of the source.

Since GRBs are believed to be beamed with beaming angles of order 40°, we assume that only a small fraction ($\sim 10^{-3}$) of binary coalescence events will have GRB or other EM afterglows that will help us to locate the source on the sky and measure its red-shift z. Eventually, we will be limited by the number of short-hard GRBs observed by detectors that might be operating at the time. As a conservative estimate, we assume that about 1,000 BNS and NS-BH mergers will have EM counterparts over a three-year period. For definiteness we consider only BNS mergers and take these to have component masses of $(1.4, 1.4)M_\odot$.

How well would we measure cosmological parameters with a catalogue of such sources? To answer this question we simulated 5,190 realizations of the catalogue containing 1,000 BNS coalescences with known red-shift and sky location, but the luminosity distance subject to statistical errors from GW observation and weak lensing. One such realization is shown in Fig. 6 (right panel). We assumed that the sources were all in the red-shift range $0 \le z \le 3.5$, distributed uniformly (i.e., with constant comoving number density) throughout this red-shift range. The luminosity distance to the source was computed by assuming an FRW cosmological model with $H_0 = 70\,{\rm km\,s^{-1}\,Mpc^{-1}}$, $\Omega_{\rm M} = 0.27$, $\Omega_\Lambda = 0.73$, and $w = -1$, but the *measured* distance was drawn from a Gaussian distribution whose width $\sigma_{D_{\rm L}}$ was determined by the quadrature sum of the errors due to weak lensing and GW observation. Weak lensing error in $D_{\rm L}$ was assumed to be 5% at $z = 1$ and linearly extrapolated to other red-shifts. GW observational error was estimated from the covariance matrix C_{km} of the five-dimensional parameter space of the unknown signal parameters $p_k = (M, \nu, t_0, \Phi_0, D_{\rm L})$:

$$C_{km} = \Lambda^{-1}_{km}, \quad \Lambda_{km} = \langle h_k,\, h_m \rangle\,, \quad h_k = \frac{\partial h}{\partial p_k}. \tag{43}$$

Here the angular brackets denote the scalar product, which, for any two functions $a(t)$ and $b(t)$, is defined as

$$\langle a,\, b\rangle = 4\Re \int_0^\infty \frac{{\rm d}f}{S_h(f)} A(f)\, B^*(f) \tag{44}$$

where A and B are the Fourier transforms of the functions $a(t)$ and $b(t)$, respectively, and $S_h(f)$ is the ET noise power spectral density. Note that since GRBs are expected to be strongly beamed, we did not take the angles (ι, ψ) associated with the unit normal to the plane of the inspiral as unknown variables. This assumption is justified: even if the opening angle of a GRB beam is as large as 40°, the unit normal to the plane of the inspiral would still be confined to only 3% of the area of a unit sphere. Averaging errors over (ι, ψ) with the constraint $\iota < 20°$ would then be little different from taking $\iota = 0°$. We did, however, average the errors over the sky position angles (θ, ϕ). We then fitted each realization of the source catalogue to the cosmological model given in Eq. (42), using the Levenberg-Marquardt algorithm [181, 182], in order to find a set of best fit parameters. It turns out that a catalogue of 1,000 sources is not quite enough for an accurate determination of all the parameters. However, assuming that H_0 is known accurately, the algorithm gave the best fit parameters in $(\Omega_{\rm M},\, \Omega_\Lambda,\, w)$ for each of the 5,190 realizations.

Accurate measurement of the Hubble constant at low redshifts ($z \simeq 0.01 - 0.5$) Taking H_0 to be the only free parameter and with only 50 sources up to a redshift of $z = 0.5$, ET itself would achieve an accuracy of 0.55% (using the kind of estimation explained here). For sufficiently low-redshift sources, the rest of cosmology is not very important. Having determined H_0 in this way, the higher-redshift sources can then be used to explore the cosmological parameter space more fully. In this way, GW astronomy will provide an independent measure of cosmography.

Thus, ET itself can use sources in the low-redshift Universe to measure H_0 with an error that is negligible compared to the uncertainties on the other parameters obtained from all sources combined, as we shall see below. In the rest of the discussion we will consider H_0 essentially known.

Measuring matter and dark energy densities The distributions $\mathcal{P}$ of the parameters obtained in the above way are shown in Fig. 30, where the vertical line is at the true value of the relevant parameter. The relative 1-σ errors in Ω_Λ, $\Omega_{\rm M}$ and w, are 4.2%, 18% and 18% (with weak lensing, left panels) and 3.5%, 14% and 15% (with weak lensing errors corrected, right panels). Although $\mathcal{P}(w)$ is quite symmetric, $\mathcal{P}(\Omega_{\rm M})$ and $\mathcal{P}(\Omega_\Lambda)$ are both skewed and their mean values are slightly off the true values. However, the medians are mostly coincident with the true values.

In addition to H_0 if Ω_Λ is also known (or, equivalently, if $\Omega_{\rm M} + \Omega_\Lambda = 1$), then one can estimate the pair $(\Omega_{\rm M},\, w)$ more accurately, with the distributions as shown in Fig. 30 with greatly reduced skewness and 1-σ errors in $\Omega_{\rm M}$ and w, of 9.4% and 7.6% (with weak lensing) and 8.1% and 6.6% (with lensing errors corrected). Finally, if w is the only parameter unknown, it can be measured to an even greater accuracy as shown in Fig. 30 with 1-σ errors of 1.4% (with weak lensing) and 1.0% (with lensing errors corrected).

Effect of unknown orientation and polarization In the previous section our study neglected the effect of different inclinations of the orbit to the line-of-sight. Varying the inclination has two distinct effects: On the one hand, as noted in Ref. [183], due to the strong correlation between the luminosity distance and inclination, the estimation of luminosity distance could get corrupted. On the other hand, binaries that are not face-on are, in general, elliptically polarized and have a non-zero polarization angle. Since polarization angle is correlated with the luminosity distance, there could be further degradation in the estimation of the luminosity distance.

In this section we will relax the condition that the inclination of the orbit is precisely known. However, we shall restrict the inclination of the binary's angular momentum with the line-of-sight to be within 20 degrees. We shall also assume that the radiation is described by an arbitrary polarization angle. Since the sky position is still assumed known, this gives us a 7×7 covariance matrix with a revised estimate for the error in the luminosity distance. As before, we construct catalogs of binary coalescence events but with the luminosity distance now drawn from a Gaussian distribution with revised widths. We fit each catalog to a cosmological model and then repeat the exercise 5,190 times to estimate the accuracy with which the various cosmological parameters can be measured.

As expected, the parameter measurments get worse if we assume two or more parameters to be unknown. For instance, errors in the estimation of Ω_{M}, Ω_Λ and w, are, respectively, $> 100\%$, 24% and 47% with weak lensing and $> 100\%$, 21% and 43%, if weak lensing can be corrected. Similarly, if Ω_Λ is assumed to be known then the errors in the estimation of Ω_{M} and w are, respectively, 12% and 9.5% if weak lensing is uncorrected for and 11% and 9.2% if weak lensing can be corrected. However, the results are more or less the same if dark energy parameter w is the only unknown quantity. Even when the inclination and polarization angles are taken as a free parameters, but inclination angle is restricted to within 20 degrees, the error in the estimation of w is 1.4% with weak lensing and 1.3% if weak lensing can be corrected.

Variation of dark energy with redshift We have seen that the Hubble constant H_0 can be measured with high accuracy using low-redshift sources, after which parameters like Ω_{M}, Ω_Λ, and the dark energy equation-of-state parameter w can be determined, where so far we have assumed that the latter is constant. One could go one step further and use prior information from, e.g., future Planck CMB measurements to get high-accuracy values for $(\Omega_{\mathrm{M}}, \Omega_\Lambda)$, and then measure the variation of w with time. Since CMB data would have a very wide prior on w and its first time derivative, this would constitute an independent measurement of the latter variables.

In practice, rather than looking at variation with time, it is more convenient to consider variation with scale factor or redshift:

$$\begin{aligned} w(z) &= w_0 + w_a(1-a) + \mathcal{O}\left[(1-a)^2\right] \\ &\simeq w_0 + w_a \frac{z}{1+z}. \end{aligned} \tag{45}$$

Since here we are mostly interested in the later stages of the universe's evolution, higher order terms will be ignored. With a redshift dependent $w(z)$, the Hubble parameter as a function of redshift becomes

$$H(z) = H_0 \left[\Omega_{\mathrm{M}}(1+z)^3 + \Omega_\Lambda\,(1+z)^{3(1+w_0+w_a)} e^{-3w_a z/(1+z)}\right], \tag{46}$$

and luminosity distance is still related to the Hubble parameter as

$$D_{\mathrm{L}}(z) = c(1+z)\int_0^z \frac{dz'}{H(z')}. \tag{47}$$

To estimate the constraints on cosmological parameters from future Planck CMB data, one can consider the Fisher matrix

$$F_{ij}^{\mathrm{CMB}} = \sum_{\ell=2}^{\ell_{max}} \sum_{XX',YY'} \frac{\partial C_\ell^{XX'}}{\partial p_i} \mathrm{Cov}^{-1}(D_\ell^{XX'}, D_\ell^{YY'}) \frac{\partial C_\ell^{YY'}}{\partial p_j}, \tag{48}$$

wherer p_i are the cosmological parameters to be evaluated; $C_\ell^{XX'}$ are the CMB power spectra and $D_\ell^{XX'}$ their estimates; and Cov^{-1} is the inverse of the covariance matrix at given angular size ℓ and channels X, X' (T for temperature, E for polarization). For a detailed discussion we refer to [184].

Given a collection of inspiral events, we can also associate a Fisher matrix to the set of events:

$$F_{ij}^{\mathrm{GW}} = \sum_k \frac{\partial_i(\ln D_{\mathrm{L}}(z_k))\partial_j(\ln D_{rmL}(z_k))}{\Delta \ln D_{\mathrm{L}}(z_k)}, \tag{49}$$

where ∂_i, ∂_j are partial derivatives with respect to cosmological parameters, and the k refer to individual events. This Fisher matrix can be combined with the one for the CMB as

$$F_{ij}^{\text{combined}} = F_{ij}^{\text{GW}} + F_{ij}^{\text{CMB}}. \tag{50}$$

Allowing for GRB beaming angles of 40°, one then finds $\Delta w_0 = 0.096$ and $\Delta w_a = 0.30$, which is comparable to projections from both the SNAP Type Ia supernova and the JDEM Baryon Acoustic Oscillations projects [184]; see Fig. 32. However, we stress that GW standard sirens are *self-calibrating* and have no dependence on a cosmic distance ladder.

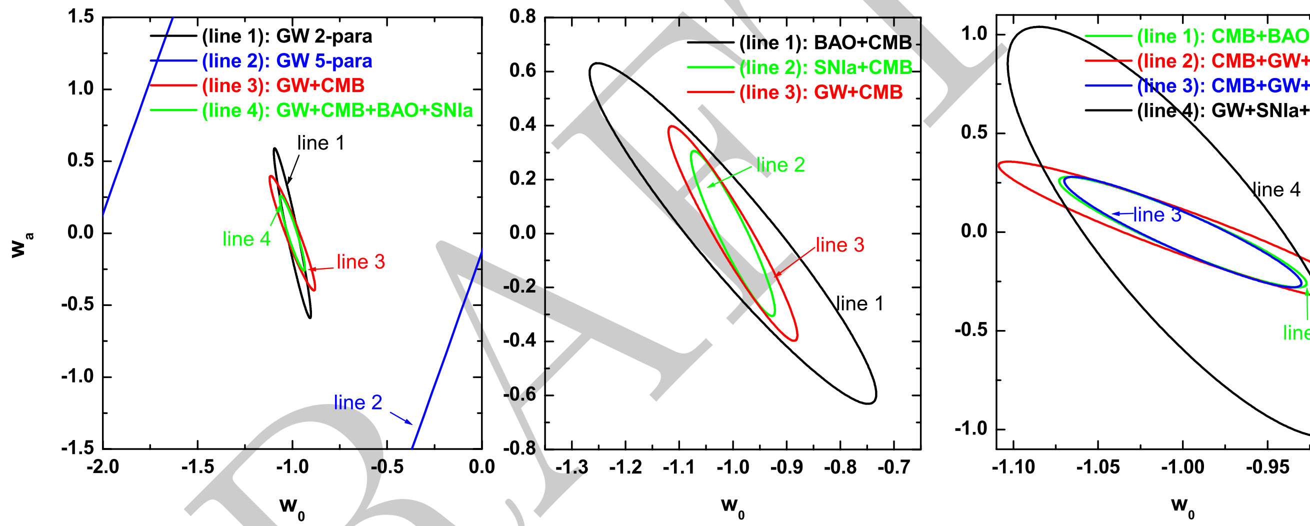

Figure 32: Investigating dark matter with GW standard sirens compared with other methods. Left: The accuracy in (w_0, w_a) with GW standard sirens, using projected Planck CMB accuracies as a prior for the other cosmological parameters (line 3); line 4 shows the minor improvements when also incorporating BAO and SNIa supernovae results. Middle: Assuming a Planck CMB prior throughout, one can compare accuracies from Baryon Acoustic Oscillations (BAO), SNIa supernovae, and GW standard sirens; they are comparable, but it should be noted that GW standard sirens are *self-calibrating*. Right: accuracies for various combinations of the GW, SNIa, BAO, and CMB methods.

2.5.5 Primordial gravitational waves

The cosmological stochastic background of GW [185] is an unique window on the very early Universe, as gravitational radiation propagates uninterrupted to us from cosmic events at the highest temperatures and densities, potentially up to the GUT scale 10^{16} GeV. The detection of any such background would have huge consequences for fundamental physics, possibly giving us direct indications of inflation, phase transitions or formation of topological defects. As shown in Figure 33, many types of cosmological stochastic background are potentially above the ET sensitivity curve. It may also be possible to extract detailed information about the cosmological events that produced GW if the spectrum has some characteristic shape.

Cosmological backgrounds are broadly of two types: wide-band, where $\Omega_{gw}(f)$ is approximately constant over a large range of frequency; and peaked, where Ω_{gw} varies strongly over f reaching a maximum at $f_{\rm peak}$. Wide-band sources are processes that extend over a large range of the cosmological scale factor $a(t)$, such as inflation and cosmic string evolution. Both these sources depend on unknown fundamental physics, and also have an approximate scaling symmetry. The detectability of a "flat" background spectrum depends only on the value of Ω_{gw} at a nominal frequency of 10 Hz.

Wide-band sources: inflation and strings There are many models of inflation, but they share a few essential features: exponentially expanding the scale factor in a short time; sourcing primordial density perturbations with amplitude $\mathcal{O}(10^{-5})$ and an approximately Harrison-Zeldovich ($n_s \simeq 1$) spectrum; and finally reheating the Universe to at least the temperature required for primordial nucleosynthesis (order of 10 MeV).

Tensor perturbations sourced during inflation can be described by an amplitude and spectral index n_t. Since they evolve similarly to the scalar perturbations, often only the *tensor-to-scalar ratio* r is considered. This is sensitive to the "energy scale of inflation" $V^{1/4}$ as $V^{1/4} \simeq (1.8 \times 10^{16}\,\mathrm{GeV})(r/0.07)^{1/4}$ [186]. In single-field models, the value of r also indicates the minimum distance the field travels during inflation via $\Delta\phi/M_P \simeq 0.46(r/0.07)^{1/2}$.

For a scale-invariant spectrum ($n_s = 1$, $n_t = 0$) the CMB determination of the scalar amplitude $S \sim 10^{-10}$ together with the current bound $r \lesssim 0.2$ translates to a very small value $\Omega_{gw}(f) \lesssim 10^{-15}$ for all frequencies accessible to interferometers [187, 188]. However, since the CMB bounds apply at $f \sim 10^{-18}$ Hz, a positive spectral index n_t could change the picture [189]: we have $\Omega_{gw}(10\,\mathrm{Hz}) = (10^{19})^{\bar{n}_t}\Omega_{gw}(10^{-18}\,\mathrm{Hz})$, where $\bar{n}_t$ is the averaged spectral index between these two frequencies [190]. In Fig. 33 we plot the possible signal for $r = 0.15$, $n_t = 0.2$.[3]

Alternatives to inflation There are two recognized alternatives to exponential inflation as a source of primordial perturbations: the 'pre-big-bang' scenario in string cosmology and the "ekpyrotic" and "cyclic" models involving a contracting phase and subsequent brane collision. For both, it is currently debated whether a realistic spectrum of scalar density perturbations can be achieved. The tensor or gravitational wave amplitude is known to be undetectably small in the "cyclic" model [191].

A potentially more interesting case arises from pre-big-bang scenarios in string cosmology [**?** **?**]. According to these models, the standard radiation-dominated and matter-dominated eras were preceded by phases in which the Universe was first large and shrinking (inflaton phase) and then characterized by a high curvature (stringy phase). The GW spectrum produced at the transition between the stringy phase and the RD era is described as $\Omega_{gw}(f) \sim f^3$ for $f < f_s$ and $\Omega_{gw}(f) \sim f^{3-2\mu}$ for $f_s < f < f_1$ [**?** **?**]. The cutoff frequency f_1, which depends on string related parameters, has a typical value of 4.3×10^{10} Hz. An upper limit on Ω_{gw} is imposed by the Big Bang Nucleosynthesis (BBN) bound down to 10^{-10} Hz, corresponding to the horizon size at the time of BBN. Measurements of the light element abundances combined with the WMAP data gives $N_\nu < 4.4$ [**?**], which translates to $\Omega_{gw} < 1.5 \times 10^{-5}$. Recent measurements of CMB anisotropy spectrum, galaxy power spectrum and of the Lyman-α forest give a bound of similar amplitude which extends down to 10^{-15} Hz, corresponding to the horizon size at the time of CMB decoupling [**?**].

However, attempts to reach a more realistic spectrum of scalar perturbations by considering specific forms of pre-big-bang cosmological evolution may lead to much smaller values of Ω_{gw} at frequencies accessible to ground-based detectors [192]. The spectrum and amplitude of primordial GW in such scenarios is strongly model-dependent.

Cosmic string evolution Cosmic strings (see *e.g.* [193]) in field theory are extended topological defects formed in phase transitions. Fundamental strings may also result from cosmological evolution, for instance in "brane inflation" models [194] strings are formed at a brane collision near the end of inflation [195]. After formation strings evolve by reconnection and oscillation of the resulting loops, which emit gravitational radiation

[3] Such optimistic values are however not consistent with most scalar field models.

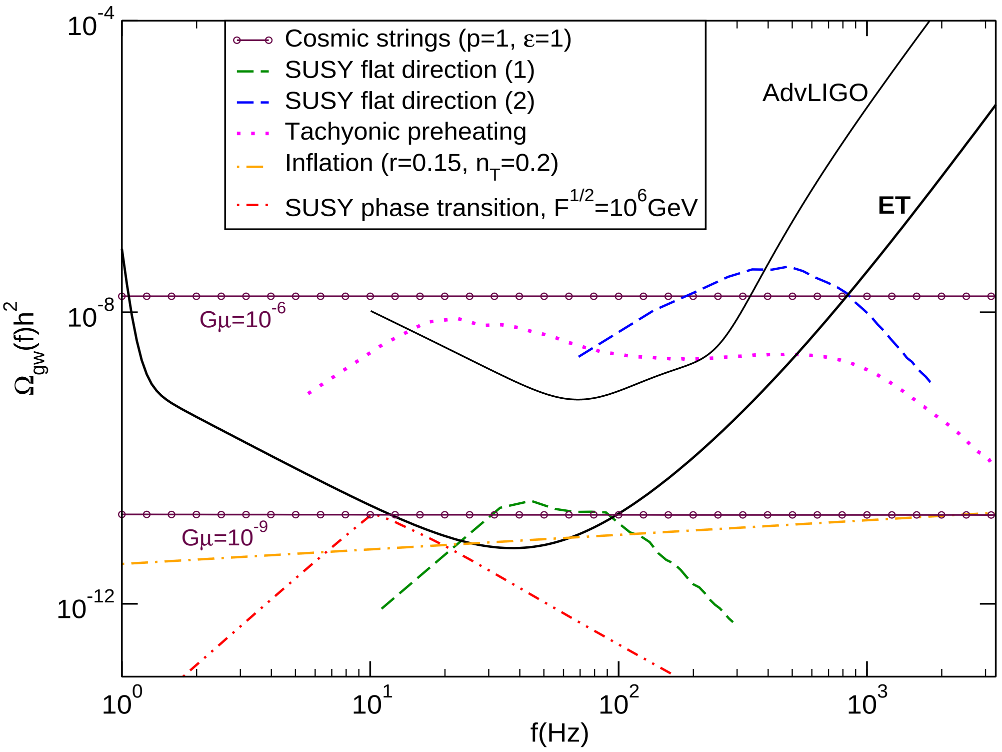

Figure 33: Cosmological stochastic GW backgrounds at Advanced LIGO and Einstein Telescope. The sensitivity curves correspond to an observation time of 1 year, S/N of 2.56, and co-located but not necessarily coaligned detectors (see end of Section 2.2.3). Models and parameter values are described in the main text. Data for tachyonic preheating and decay of SUSY flat directions were provided by J.-F. Dufaux; for phase transitions between metastable SUSY vacua, by N. J. Craig; the cosmic string GW spectra are based on a calculation of X. Siemens *et al.* [201].

(and possibly other quanta) and gradually shrink. The evolution is believed to have a scaling property and produces an almost flat spectrum in Ω_{gw} across frequencies accessible to interferometers.

The most important parameter is the string tension or energy per unit length $G\mu$, determined by the energy scale of the phase transition; in brane inflation this may take values from 10^{-6} down to 10^{-11}. The current limit from CMB and other cosmological probes is a few times 10^{-7} [196–198]. Fundamental strings also have a "reconnection probability" p significantly smaller than unity (the value for field-theoretic strings). The properties of both field-theory and fundamental string networks can be summarized by parameters $\alpha < 1$ (size of newly-created loops relative to the Hubble horizon) and $\Gamma \sim 50$ (gravitational-wave luminosity of string loops). These are subject to uncertainty from numerical simulations. There are two limits: the "large loop" case where α is comparable to unity, for which the "plateau" value of $\Omega_{gw}(f)$ may be estimated [199] as

$$\Omega_{gw}(f) \sim 10^{-8}(G\mu/10^{-9})^{1/2}p^{-1}(0.2\Gamma\alpha)^{1/2}. \tag{51}$$

The "small loop" case is motivated if the size of loops is determined by gravitational backreaction, giving $\alpha \simeq \Gamma G\mu \ll 1$; deviations from this value [200] are parameterized by a factor ϵ. In Fig. 33 we use a recent evaluation [201] of the GW spectrum for $p = \epsilon = 1$.

Peaked sources: phase transitions and reheating Peaked sources of stochastic background result from an event localized in cosmic time, typically a phase transition or reheating after inflation. There are many candidates arising from models of high-energy physics. Their detectability depends on the value of $f_{\rm peak}$ as well as the amplitude $\Omega_{gw}(f_{\rm peak})$; either side of $f_{\rm peak}$ the spectrum will decline as a power law [202]. The present-day frequency f is related to the frequency at the time of production f_* via

$$f = f_* \frac{a_*}{a_0} \approx (6 \times 10^{-8}\,\mathrm{Hz}) \frac{f_*}{H_*} \frac{T_*}{1\,\mathrm{GeV}} \left(\frac{g_*}{100}\right), \tag{52}$$

(see *e.g.* [203]), where a is the scale factor, T the temperature, g the number of relativistic degrees of freedom and H the Hubble rate, the suffixes "0" and "$*$" denoting the present time and time of production respectively.

Phase transitions and colliding bubbles First order phase transitions proceed by the nucleation of spherical bubbles in a "false vacuum" with latent heat (energy density) ϵ. The bubbles grow rapidly and may collide; after collision the bubble walls have a nonzero, rapidly-varying quadrupole moment and radiate gravitational waves. In the latter stages of the transition, gravitational waves may also be sourced by turbulence [204] as the energy difference ϵ is converted into heat.

The transition is characterized by the temperature T_* at which bubble nucleation occurs and the duration or characteristic timescale β^{-1}, assumed much shorter than a Hubble time H_*^{-1}. The present peak frequency and amplitude of GW are estimated as [205]

$$\begin{aligned} f_{\rm peak} &\simeq (5.2 \times 10^{-8}\,\mathrm{Hz}) \frac{\beta}{H_*} \cdot \frac{T_*}{1\,\mathrm{GeV}} \left(\frac{g_*}{100}\right)^{1/6}, \\ \Omega_{gw}(f_{\rm peak}) h_{100}^2 &\simeq (1.1 \times 10^{-6}) \kappa \left(\frac{\alpha}{1+\alpha}\right)^2 \left(\frac{v^3}{0.24 + v^3}\right) \left(\frac{H_*}{\beta}\right)^2 \left(\frac{100}{g_*}\right)^{1/3}, \end{aligned} \tag{53}$$

where α is a measure of the strength of the phase transition, κ is an "efficiency factor" for conversion of false vacuum energy to kinetic energy, and v is the speed of expansion of the bubbles. In the limit of a strongly first-order transition $\alpha \gg 1$, $v \to 1$ and $\kappa \to 1$, while β/H_* is expected to be of order 10^2. Turbulent plasma motion leads to similar values.

The electroweak phase transition with $T_* \sim 100\,\mathrm{GeV}$ is likely to produce GW with frequencies at or below the milliHz range accessible to LISA [206]. Similarly in the "Randall-Sundrum 1 model" there may be a first-order phase transition in the warped extra-dimensional geometry at temperatures of around $10^3\,\mathrm{GeV}$ [207]. A transition temperature of 10^6–$10^7\,\mathrm{GeV}$ corresponds to the sensitive range of ET [203]: this could be achieved for phase transitions between metastable SUSY-breaking vacua [208]. In Fig. 33 we plot one scenario with a hidden sector SUSY-breaking scale $\sqrt{F} = 10^6\,\mathrm{GeV}$.

Reheating and related phenomena At the end of inflation, the Universe is reheated by converting the inflationary energy density into radiation. In the "preheating" scenario the fluctuations of fields coupled to the inflaton grow exponentially rapidly via parametric resonance. The stochastic GW spectrum produced from preheating after chaotic inflation has a peak value $\Omega_{gw}(f_{\rm peak}) \gtrsim 10^{-11}$ [209, 210], however the peak frequency is well above the range of interferometers, unless coupling constants in the model take fine-tuned (extremely small) values.

Hybrid inflation ends due to the presence of a *tachyon* or "Higgs" field whose value sits at the top of a hill-shaped potential. The field decays by spinodal instability with a characteristic spectrum, giving rise to bubble-like regions which collide, fragment and finally thermalize. The GW spectrum resembles that of a phase transition, and for specific parameter values may be accessible to ET [211, 212]; its peak frequency and amplitude are estimated as

$$\begin{aligned} f_{\rm peak} &\simeq (6 \times 10^{10}\,\mathrm{Hz}) C g \lambda^{1/4}, \\ \Omega_{gw}(f_{\rm peak}) h_{100}^2 &\simeq (2 \times 10^{-6}) \left(\frac{v}{M_P}\right)^2 (Cg)^{-2}, \end{aligned} \tag{54}$$

for $g^2 \gtrsim \lambda$, where g is the coupling of the "Higgs" field to the inflaton, λ is its self-coupling and v its expectation value after symmetry-breaking; C is a constant determined by numerical simulation. When $g^2 \ll \lambda$ the relevant formulae are

$$f_{\text{peak}} \simeq (3 \times 10^{10}\,\text{Hz}) \frac{g}{\sqrt{\lambda}} \lambda^{1/4},$$
$$\Omega_{gw}(f_{\text{peak}}) h_{100}^2 \simeq (8 \times 10^{-6}) \left(\frac{v}{M_P}\right)^2 \frac{\lambda}{g^2}. \tag{55}$$

In Fig. 33 we plot the spectrum for the parameter values $\lambda = 2g^2 = 10^{-14}$, $v = 3 \times 10^{-7} M_P$.

The rapid decay of "flat directions" (scalar degrees of freedom) in supersymmetric models after inflation is a similar potential source of stochastic GW [213]. The characteristic momentum of fluctuations is of order the SUSY-breaking mass scale $m \sim$TeV giving a present-day frequency of 10^2–10^3 Hz. We plot in Fig. 33 the spectra for two choices of parameter values. The lower curve has $m = 100\,$GeV, reheating temperature $T_R = 10^8$ GeV and initial field value $\Phi_i = 2 \times 10^{18}$ GeV; for the upper curve, $m = 1\,$TeV, $T_R \geq 10^9$ GeV and $\Phi_i = 10^{18}$ GeV.

Conclusion Many diverse and exciting phenomena in the physics and cosmology of the early Universe may be probed by ET via the stochastic GW background, either almost immediately if a signal is well above the detection threshold, or with an extended observation period. It may be possible to estimate the parameters (*e.g.* mass scales and couplings) of the new physics responsible: observational evidence for a cosmological phase transition, or of the temperature of reheating, would be an epoch-making result.

2.6 Data Analysis and Computational Challenges

2.6.1 Nature of the ET data - many overlapping signals possibly creating a confusion background

Confusion background from compact binaries in ET With actual and advanced interferometers, whose horizon is only a tens or a hundreds of Mpc only, the detection of individual binaries is limited by the instrumental noise but with the third generation Einstein Telescope, which is expected to reach redshifts of $z \sim 1$ for NS-NS and $z \sim 2$ for NS-BH other problems may appear. For instance, after $z \sim 1$, gravitational lensing may become significant, altering distance measurements, and thus the quality of binaries as standard candles to proble cosmology and dark energy. Another problem at large distances is the formation of a confusion foreground, in which it may become difficult to resolve sources individually [17].

The GW signal falls into three statistically very different regimes, depending on the event rate and the duration of the waveform. The duty cycle (or the average number of sources present at the detector at the same time) is given by:

$$\Lambda(z) = \int_0^z \tau^o(z) \frac{dR_c^o}{dz}(z) dz \tag{56}$$

where $\frac{dR_c^o}{dz}(z) = \dot{\rho}^o(z) \frac{dV}{dz}$ is the coalescence rate per interval of redshift [**?**], and $\tau^o(z)$ is the typical duration of the inspiral in the detector frequency band, which depends strongly on the low frequency limit of the instrument and can last from a few minutes for advanced detectors with $f_L = 10$ Hz to a few days for the Einstein Telescope with planned low frequency bound between $1 - 5$ Hz

1. *Shot noise* ($\Lambda << 1$): This case describes when the number of sources is small enough that the interval between events is long compared to an individual event's duration. Measured waves are separated by long stretches of silence and can be resolved individually. This case pertains to instruments that are only sensitive to events at low redshift.

2. *Popcorn noise* ($\Lambda \sim 1$): As the reach of instruments increases, the time interval between events may come closer to the duration of single bursts. Events may sometimes overlap, making it difficult to distinguish between them.

3. *Gaussian* ($\Lambda >> 1$): For instruments with very large reach and excellent low frequency sensitivity, the interval between events can be small compared to the duration of an event. The signals overlap to create a confusion noise of unresolved sources.

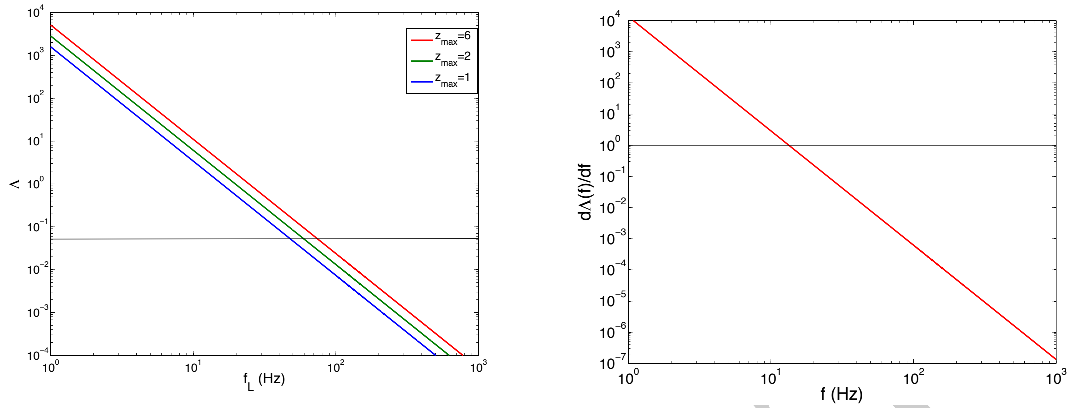

Figure 34: top: Duty cycle as a function of the low frequency limit for the population of binary neutron stars, and for maximal redshift of 6 (red), 2 (green) and 1 (blue) ($d\Lambda/df \sim f^{-8/3}$). A duty cycle larger than 1 means than the sources overlap in the time domain. bottom: Duty cycle per interval of frequency ($d\Lambda/df \sim f^{-11/3}$).

Fig. 34 gives the duty cycle for the population of BNS, as a function of the low frequency bound and for different values of the maximal redshift. When the maximal probed distance $z_{\max}$ improves, the number of sources increases, the waveforms start to overlap ($\Lambda > 1$) and the signal becomes more and more confused. Likewise, when the low frequency limit of the detector shifts toward lower values, the sources stay longer in our observation frequency window and overlap even at small redshift, creating a confusion background (Fig. 35).

For Einstein telescope, with a low frequency limit $f_L = 1$ Hz and an horizon $z_{\max} \sim 2$, the signal from BNS is clearly in the confusion regime. However, the sensitivity of ET is such that the sources appear mostly separated at the output of the detector. An example time series of the gravitational wave signal from BNS up to a redshift $z \sim 6$ is shown in the first plot of Fig. 36. The second plot shows the corresponding matched-filter (the strain amplitude is divided by the noise spectral density). We see that the waveforms overlap in the first plot but most of the sources are below the detector noise, especially at low frequencies, and it should be possible to disentangle sources with adapted data analysis techniques, such as the ones developed in the context of LISA.[214] or the Big Bang Observatory [215] . It has been shown that Markov Chain Monte Carlo based codes, such as the Block Annealed Metropolis-Hastings algorithm, are able to extract about 20,000 out of 30 million individual white dwarf binaries from the galactic foreground, approaching the theoretical limit of 25,000 resolvable sources. In a recent paper, [**?**] suggested that similar algorithms could be used for ET.

2.6.2 State-of-the-art in computing in the ET era

Author(s): S. Aoudia, L. Bosi, L. Storchi,

...

2.7 Computing:Status of Art

Computing has made great strides in recent years in order to provide each year even more fast processors. Since the invention of the integrated circuit in 1958, the number of transistors on a given chip double (roughly) every two years, as states the first Moore's law [216]. This exponential growth has allowed computers to get both cheaper and more powerful at the same time. In order to mantain this trend for the next decade the next technological steps need some rethinking of basic foundations such as:

- Process technology

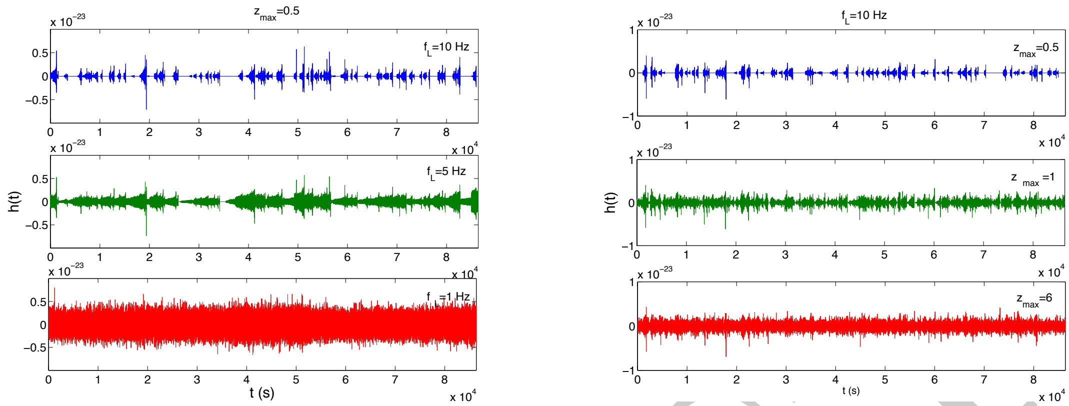

Figure 35: Evolution with the detector horizon $z_{\max}$ assuming $f_L = 10$ Hz (left) and with the low frequency limit f_L assuming $z_{\max} = 0.5$ (right) of a GW time series from a simulated population of binary neutron stars. The duration of the series is T=1 week.

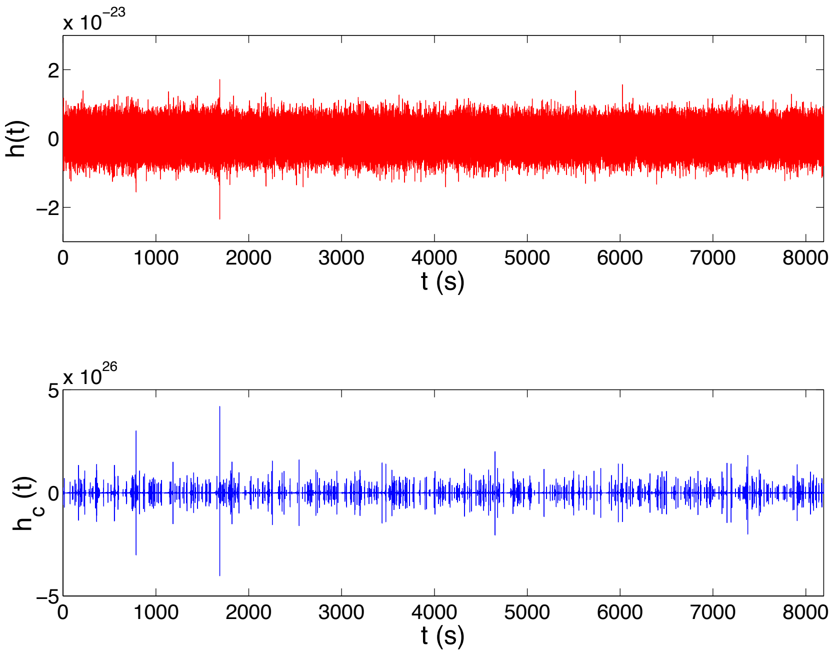

Figure 36: time series of the gravitational strain for $z_{\max} = 6$ and $f_L = 1$ Hz (top) and the same time series after the Fourier transform has been divided by the PSD of ET.

- Hardware Architecture
- Software Software

In this section we report about processors, computing infrastructure and architectures status of art, highligthing technical and physical problems that are leading major vendors to change Hardware and Software architectural paradigma.

2.7.1 Main difficulites on computing power increase

Quoting Mr Moore recent statment issued during an interview "..by about 2020, my law would come up against a rather intractable stumbling block: the laws of physics.." [217] we may be led to think that the Moore's Law is at the end. Today the integration scale (the typical size for the CMOS realization) is about 32-22nm that is comparable to few hundreds of atomic radii. It is so clear that one of the main limitation on continuing the actual processors renewal strategies is posed by the atomic limit. The difficulty on even more reducing the integration scale was evident and concrete already during the last 10 years. In fact major manufacturers introduced several technological innovations and hardware paradigma in order to provide even more fast processor, limiting the integration scale reduction and CPU frequencies increase.

We report on Computing power increase issue, introducing briefly the top500 and the last 10 years technological innovations.

The Top500 project [218] goal is to generate, twice a year, a list of the 500 most powerful computers in the world. The list is manteined by Hans Meuer of the University of Mannheim, Erich Strohmaier and Horst Simon of Lawrence Berkeley National Laboratory, and Jack Dongarra of the University of Tennessee. Dongarra invented Linpack benchmark [219] many years ago, used to rank the system within the list.

The Top 500 ranking has always been a good overview of the actual technology trends, and along the last ten/twenty years the list has showed an evident trends toward parallel and massively parallel systems. This trend has been confirmed by the appearance in the home computing system of superscalar and pipilened CPU firstly, and multi-core CPU after.

The actual top500 list emphasizes the following evolutive characteristics:

- Natural evolution from multi-core to many-core era
- Many-core architecture (i.e. GPU) together with multi-core X64 processors are in current use
- Moore's Law is alive and still works well
- Development of faster and more integrated interconnects as an obvious consequence of the increase in number nodes and cores

To stress those aspects it is essentials to cite the first ranked system on November 2010: the Tianhe-1A. This supercomputer is stationed at the National Supercomputer Center in Tianjin, it has achieved a performance level of 2.57 petaflop/s. This system equipped with 29376 GB of memory, is based on Nvidia graphics processing units (GPUs) as well as Intel Xeon 5600 series processors. The system collects together both the trends, fast interconnection (i.e. the Tianhe-1A is able to handle data at about twice the speed of InfiniBand), and many-core (i.e. the system is capable of such performance essentially thanks to the the acceleration given by Nvidia Fermi GPU processors). It is clear that a new programming paradigms and new algorithms are needed to get top performance from these computing infrastructure.

Looking for high performances, one has also to deal with **power consumption**. The power consumption of an HPC resource is a fundamental aspect on computing facilities setup. This requires an optimization in terms of efficiency, cost and resources reliability. In order to stress how this is today an extremely important and sensible theme, the Top500 has started to collect data related to power consumption of the 500 most powerful computer in the world.

To achieve greater performance per compute node, vendors have increased not just transistors and speed but consequently also the power density. Thus, a large-scale high-performance computing system requires continual cooling in a large machine room, or even a new building in order to work properly. So to achieve greater performances one has to consider direct and indirect (i.e. cooling system) costs. We have to remember the HPC systems failure rate increase is directly related to the working temperature.

Many-core seems to provide good performances also in terms of power consumption. In fact making the assumtion that The Tianhe-1A 2.5 PFlops system was built entirely with CPUs, it would consume more than **12 MW**. Thanks to the use of GPUs in a heterogeneous computing environment, Tianhe-1A consumes only **4 MW**, making it **3 times more power efficient**.

It is importaint to compare the power consumption of Tianhe-1A and Jaguar Cray XT5-HE, that is the second ranked system in top 500. In fact the Jaguar use 5-10 MW to achieve 1.7 PFlops while Tianhe-1A use 4 MW to achieve 2.5 PFlops. **This is a success of the many-core architecture providing 3-4 time more computing power per Watt!**

This enforce the evidence that computing hardware architecture are moving toward the many-core era direction.

2.7.2 20 years of Parallelization

In this section we introduce more details about architecture innovation introduced along last 20 years by hardware manufacturers. We intend to underline as the implicit and explicit parallelization concept has been used as a way to go around the miniaturization limitations and frequency increase.

A scalar processor is the simplest CPU that can considered. Is is capable of executing a single instruction per clock cycle and to manipulate one or two data items at a time.

A superscalar processor is instead capable of intrinsic parallelism. Each instruction processes one data item, but multiple instructions and data are processed concurrently, having multiple redundant functional units within each CPU. In fact modern superscalar processors includes multiple ALUs, multiple FPUs. Thus the dispatcher of the CPU reads instructions from memory and decides which ones can be run in parallel. An important step forward has been the introduction (around 1998/1999) of one or more **SIMD** units by AMD and Intel. Those units are used through the AMD's 3DNow and the Intel's Streaming SIMD Extensions (SSE) instruction set extension to perform basic vector operations (i.e. adding two vectors of float, in one step).

The capability of executing more than one instruction per clock cycle is another level of parallelism introduced into superscalar CPU. The basic idea is to split each instruction into several micro-instructions, each executed by an indipendent functional unit of the pipeline.

This approach permits a natural parallelism. In fact usually when there are several instructions to be executed, as soon as the first functional unit has finished the execution of the first micro-instruction, this is sent to the second unit. So the first functional unit of the pipeline is free to start the execution of the second instruction, and so on. Given a starting latency to fill the pipeline, the CPU reach a steady state where N instructions are executed together for each clock cycle, where N is number of functional units (so called depth of the pipeline).

Another step on improving the efficiency of CPUs, has been the introduction of **Simultaneous multithreading (SMT)**, roughly about 2003-2004. Maybe one of the most famous implementation of this technique is the Intel's Hyper-Threading Technology. The HT, or HTT, works duplicating some sections of the processor pipeline. In this way the hyper-threading processor appears as two "logical" processors to the host operating system. This allows the operating system to schedule two threads or processes simultaneously.

Starting from 2005 multi-core CPU have been introduced in the everyday computing architecture, both in the embedded and standard systems. This solution implements multiprocessing in a single physical package, namely the full processor, replicating the whole computing core. Different cores may or not share caches, and may implement message passing or shared-memory inter-core communication. The actual multi-core CPU implements up to four/six cores per package. In case of the multi-core CPU the performance gain is strictly related to the efficiency of the parallelized software. About that we have cite Amdahl's law[**?**], that connect the parallelization efficiency with the fraction of the software that can be parallelized to run on multiple cores simultaneously.

2.7.3 Manycore

The transition to many-cores systems seems to be the natural evolution of computational architecture. Many-core processoris have a larger number of cores respect to traditional multi-processor, roughly in the range of several tens of cores. The actual state of art in many-core architecture is represented by GPU processors, where in a single package hundreds of computing cores are implemented.

In the next part of the section, we would like to provide some information about major vendors technological decisions and roadmaps in order to give the feeling about many-core technological trends.

All major CPU processors manufactures, such as Intel and AMD, are researching and developing new innovative solutions in order to bypass the even more stringent technological challenges. In our work we have collected several information about major manufacturer production roadmaps and production planning.

As been previously reported in some sense GPU are the precursor of many-core architecture with several already marketed and used hardware devices. Even if these have been developed specifically for computer graphics this hardware is now widely used in other computing fields, proving a resounding success.

Moreover during 2010, Intel and AMD have published and made official communication about subsequent CPU generation. Also if in different way and implementation they report technological solution that are following the path of increasing number of computing core elements per CPU.

In detail AMD has declared to be close to release a new processors family based on Fusion [220]. AMD Fusion is the codename for next-generation microprocessor design and a product merging together AMD and ATI. Where AMD brings knowledge about CPU technology and ATI its own knowledge about Graphic Progessing Units, combining general processor execution as well as 3D geometry processing and other functions of modern GPUs into a single package. The core of this new architecture are the APU (Accelerated Processing Units). This technology is expected to debut in the first half of 2011.

Intel has recently declared during the New Orleans Supercomputing Conference its approach to the High Performance Computing, introducing the MIC (Many Integrated Core) solution [221], known with the name Knights Ferry. The Intel MIC architecture is derived from several Intel projects, including "Larrabee" [222] and such Intel Labs research projects as the Single-chip Cloud Computer [223, 224]. The architecture is based on chip containing 32 cores x86 at 22nm. Moreover Intel has declared for 2012 the production of an higher solution based on 50 core 4 hyper-threading processor. Obviously this solution can be compared directly with GPGPU, having an equivalent high number of cores. One of the key point of the Intel solution is the code portability, being a x86 compatible architecture. Moreover comparing Knights Ferry with GPU solution we have to remark that a CPU core is much more complex than a GPU core, providing for example SSE4, permitting 8 single precision operations per cycle per core.

In this context it is interesting to report also other experiences, such as Tilera products [225]. It provided the first innovative many-core solution based on x86 architecture. For example the 64-core TILEPro64 integrates 64 identical cores, having a complete full-featured processor, including cache memories and more.

The previous statements indicate a clear direction about new processor products: **CPU are evolving toward the direction of the many-core computing**. Each vendor is traducing this concept on different shapes (i.e. "homogeneous collections of general-purpose cores" rather than "computers using a variety of specialty cores"), but all agree on the need of increase significantly the parallelization level [226].

A so deep changes in the hardware architecture will require also a deep changes on software side and about the way of thinking algorithms. Without this effort it is impossible to extract the real power of these new computing resources.

2.7.4 Manycore as real scenario for future computing infrastructure

In order to understand the real capabilities of these new architectures, in Perugia group we started to explore the status of art of manycore devices. In particular we perform some test with NVIDIA C1060 (i.e. GT200) and with NVIDIA C2050 (i.e. the brend new Fermi GPU).

Our tests are based on a fully Multi-GPU implementation of a Coalescing Binaries Detection pipeline. This software includes specifically an input data conditioning, signal Post Newtonian generator up to PN 3.5 [227] and a complete matched fitlering procedure with colored noise [**?**].

Respect to CPU implementation of the same algorithms, results show an average gain factor (normalized by price) of about 50, using a single C1060 GPU. This can be translated in a number of applyied matched filtering per seconds of about **30**. Obviously this number depends on vector size. This numbers are about length of 2^23 samples. Using shorter vector it is possible to achieve higher gains. Performing the same test with new NVIDIA Fermi GPU (i.e. the Tesla C2050), this number increase up to **120 templates per second**.

In Perugia we implemented also a Multi-GPU version of the pipeline, which gives another increasing factor of 3.5 using 4 GPU, bringing us to an impressive result of about **400 templates per second** processed [228].

Another interesting gain factor is about FFT algorithm. Several benchmarks reports a gain factor of 50-80 using GPU respect to CPU architecture. This value has been renormalized by device prices.

Thus, we can state that using the already available many-core thecnologies the gain factor respect to the standard single core architecture is, conservatively speaking, about 100. Obviously an exhaustive analysis of the gain factor needs to deal also with power consumption and costs.

2.7.5 Computational challenges of handling massive template banks, long duration signals, etc.

Author(s): S. Aoudia, L. Bosi, L. Storchi,

...

2.8 Computing Challenges

In this section we try to use our analysis and our simulations in order to foresee for the next 12-14 years the computing solutions and power gain.

2.8.1 Moore's law

"Moore's Law is a violation of Murphy's Law. Everything gets better and better" [**?**] this is how Gordon Moore commented the law, that bears his name, in 2005. Moore's law describes trend in the history of computing hardware. The law has been originally thought to describes the number of transistors that can be placed inexpensively on an integrated circuit. But now we see this law can be applied also to the capabilities of many digital electronic devices, such as memory capacity, sensors and even even the number and size of pixels in digital cameras. There are in fact many other laws related to the Moore's one. Other laws prediction for example hard disk storage cost per unit of information, or network capacity, or pixels per dollar, and more.

Gordon E. Moore formulated the law by a simple observation. In 1965 he noted that number of components in integrated circuits had doubled every two years from the invention of the integrated circuit in 1958. Thus, he predicted that the trend would continue "for at least ten years". Years after the law has been reformulated to take into account an higher growth, and the final formulation state that integrated circuits would double in performance every 18 months. Thus "Moore's first law predict" an exponential rates for the transistor counts in a microprocessor: $P_n = P_0 \cdot 2^n$, where P_n is the predicted computer processing power in future years, P_0 is the actual computer processing power, and n the number of years divided by the doubling period, expressed in years. i.e. if we consider the transistor count the doubling factor is 2 (every 2 years), while if we consider the processors speed the doubling factor is 1.5 (every 18 months).

Moore's first law can be viewed just as an observation, but maybe there is even more. Maybe behind it there is a more deeper law, a law driving evolution of information and technology, of which the Moore's law is just a consequence. But up to now what it is clear is that this law has been widely accepted, and is used as a goal for both marketing and engineering departments of semiconductor manufacturers. We recall what has been reported in the previous section about top500 trend, that confirms the Moore's law.

What about future trends? As we are writing, seems to be well accepted, also within computer industry technology's "road map", citing Pat Gelsinger, SVP and co-GM of Intel's Digital Enterprise Group (DEG), "believes Moore's Law will continue to hold good through 2029" [229].

Although specialists agree that by 2019 the current strategy of ever-finer photolithography will probably have run its course, it is likely that some new type of technology will be needed to replace the current integrated-circuit production process, like new materials, optical or quantum computers.

In any case is not a simple exercise to translate transistor growth into practical CPU performances. This is particularly true for recent multi and many core systems. In this case it is always needed a great work on the software side in order to take advantage of the modern multi and many core CPU. One need often to substantially think back the software implementation.

There are other factors limiting the possibility of taking full advantage of the modern CPU, such as internal bandwidth and storage speed. In other words memory and disk access speeds have failed to keep up respect the CPU, and in fact to reduce the impact of this problems in processor and software design have been introduced different solutions, like: out-of-order execution, caching and prefetching strategies. This means also that there is still a big optimization margin on other computer components.

2.8.2 Future Possible Computing Scenarios

Next decades main key actions can be summarized as :

- Chip-Level Multiprocessing (CMP)- increasing parallelism for increased performance
- Special Purpose Hardware - Embed important functions relegated to software and specialized chips inside the microprocessor itself.
- Large Memory Subsystems - Memory access is a main bottleneck. In order to keep many high-performing cores, it is important to have a large quantity of memory on-chip and close to the cores.
- Microkernel - Microprocessors will need a sizable integrated intelligence, in order to coordinate all this complexity: assigning tasks to cores, powering up and powering down cores as needed
- Virtualization - Future microprocessors will need several levels of virtualization. virtualization is needed to hide the complexity of the hardware from the overlying software. The OS, kernel and software should not have to deal with the intricacies of many cores, specialized execution hardware, multiple caches, reconfiguration and so on.

We can assume that during next decades, these innovations will contribute on keep alive the Moore's law, that we can use to forecast the future computing power. On figure [**?**] we report the expected computing power gain respect to the epoch of evaluation. Thus, if we consider the actual computing power of a typical CPU, Moore's law predicts a gain factor of about 200 in 12 years and 700 in 14 years.

At least up today, this behavior is experimentally proved also by top500 performances graph shown in figure 38. As previously noted, the Linpack benchmark is used to rank the system within the list. Thus, the values reported in the graph can be considered a good estimation of the real power (i.e. sustained performances) of the 500 most powerful computer in the world.

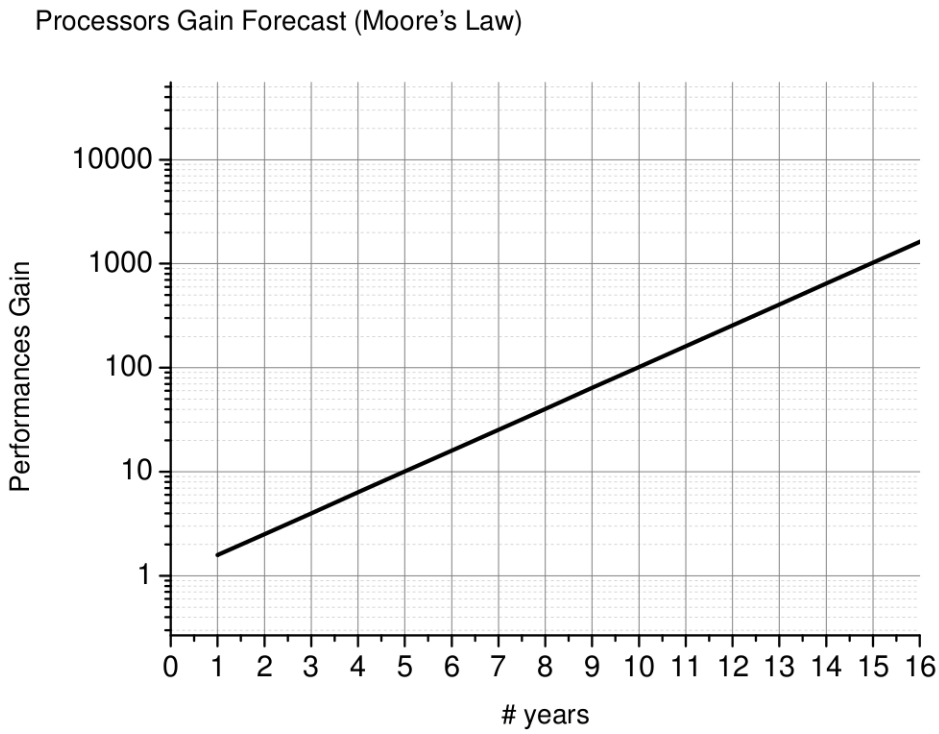

Figure 37: Moore's law projection of expected computing power gain respect to the epoch of evaluation.

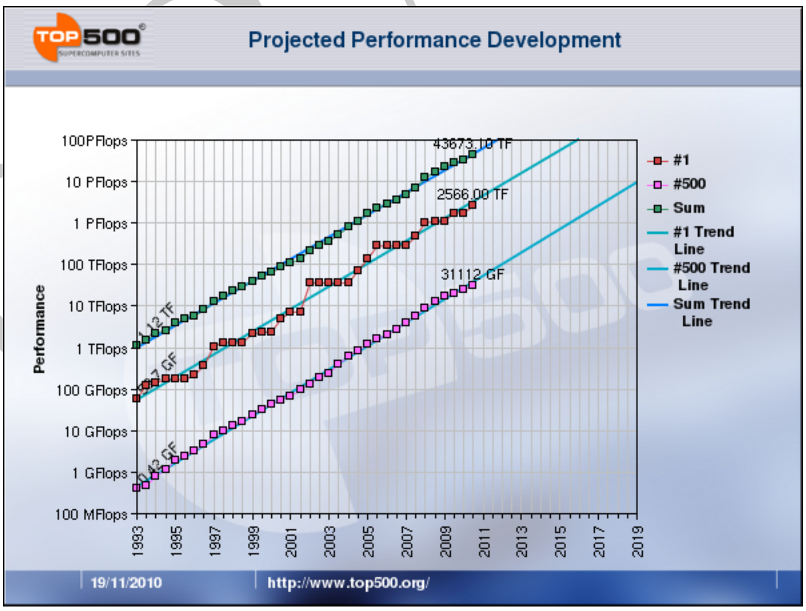

Figure 38: The Top 500 projected performance development.

In the figure 38 are reported three different sequences. The first one, labeled with **Sum**, represents the total amount of computing power of which all the 500 supercomputers in the list are capable. The second sequence, the one labeled with **#1**, is the power of the first ranked system. The last one, the sequence labeled with **#500**, is instead the computing power of the 500-th system in the list.

A simple execise to show to the reader how the first Moore's law works. If we consider the computing power of the last ranked system in the list ten year ago, this gives a number of approximately 100 GFlops. Today the 500-th system, namely a Xeon Cluster, has a power of more the 10 TFlops. This gives a gain factor of about 100, as the Moore's first law states. So, as it may seem incredible, experimental data confirms that in ten years we had and increase of a factor 100.

These information and in particular about GFlops are closely related with computational problem to be faced. In the ET case we can try to select some reference core algorithms and use the our many-core / Moore's law forecast factor to predict the realistic computing power in 10 years from now. These results can be used to understand the future investigation capabilities and limitation about some of the main ET data analysis area of interest.

A fundamental point that distinguish first and second generation gravitational wave detectors respect to ET science is the nature of the experiment. ET has to possess enough sensitivity and computing power to achieve its main goal, the GW observation and not detection. This means real-timand on-time analysis that will stress the computing infrastructure, requiering the handling of the two main data analysis aspects: detection and parameter recostruction problems.

2.8.3 Detection Stategies

Binariessystem

formed by pairs of neutron stars NS or an intermediate massive black hole IMBH with another NS or IMBH are the most important sources for ET [230]. In fact, the detection and the study of IMBH is an astrophysical challenge in itself.

In the context of full General Relativity, the exact equation describing the gravitational waves emitted by the motion of two compact objects is not really known. The only solution for that problem comes from the Post-Newtonian theory. In this last context, a significant progress had been made in the last few years and now we are able to have waveforms at the 3.5PN order in phase, 2.5PN order in spin-orbit (SO) effect and 2PN order for the spin-spin (SS) effects [231].

Waveform from a quasi-cicular coalescing binary is characterized by two sets of parameters, intrinsic and extrinsic ones. The extrinsic or kinematic parameters are all the parameters incorporated in the detection statistic. In our case, they are defined by the inclination i, the polarisation ψ of the source plus the fiducial time of coalescence t_c of the binary and phase at coalescence Φ_c. The intrinsic "dynamic" parameters are the reduced mass η, the chirp mass M_c, the algebraic values of the spins χ_1, χ_2 and the sky location of the source θ, ϕ[4].

in addition of these parameters, an other effect which will change the shape of the detected waveform is the Doppler shift effect of the frequency. The detector's motion can no longer be considered as negligible since the observation time could reach few days. This also suggests that a single ET detector could be able to determine the sky location of the source θ and ϕ even with moderate precision.

As the model waveform depends on a number of parameters, the most adequate way to search for the signal is to filter the data through a template bank covering the astrophysically interesting region of the parameter space[232, 233]. It represents a grid of theoretical waveforms (templates) placed, according to a fixed value of the minimal match MM, on the parameter space. Each point is associated with a template built from a specific values of the parameters. By matched filtering technique, one finds the maximal value of the likelihood which corresponds to the best mimicking template.

The problem with such technique of search is the large number of templates needed. For an ET-D configuration with a minimum match MM of 95% and for a total mass M range $[1M_o \;\; 300M_o]$ the number of templates ranges from 10^9 (with two parameters templates : η and M), 10^{13} (for a search with four parameters templates : η,

[4]Here we consider the algebraic values of the spins since we will limit ourselves to parallel and ant-parallel spins only without including the time evolution of spin directions

M_c and an all sky search θ, ϕ) and 10^{18} for spinning binaries (six parameters templates : two masses, two angles and two spins χ_1, χ_2).

In the Table-2.8.3, we summarize the computational time needed for flat search with different number of parameters.

Computers		GPU C2050	WLCG	Tianhe-1A	GPUs C2050 @ 2023
Processing power (TFlops DP)		0.5	2000	2567	100
Nbr of para	Nbr of templ	Computational time needed			
2	10^9	64 days	24 min	18 min	7 hrs
4	10^{13}	1760 yrs	182 days	128 days	9 yrs
6	10^{18}	179 10^6 yrs	5 10^4 yrs	4 10^4 yrs	9 10^5 yrs

Table 3: This table gives the computational time needed for a flat search with different number of parameters using : 1 GPU C2050, Worldwide LHC Computing Grid, the China's supercomputer Tianhe-1A and using the future performance of a single GPUs C2050 at 2023, respectively. The results show that using matched filtering search with six parameters template bank or more is not a realistic choice.

For a low SNR, one could suggest a hierarchical search, looking for a detection at first with a coarse grid and reconstructing the parameters around the detected template with a fine grid template bank in the second pass. However, this could be problematic if we have great SNRs (as in the case of ET). Many templates could have the same maximum value of the likelihood even with disparate values of the parameters (multi-sources, degeneresscence). This suggests to use a large parameter space ranges for the second step of search giving a large number of templates, or/and to use a multi-templates search technique (overlap of many sources) where also a huge number of templates will be needed.

The large SNR expected for ET and the relatively great number of overlapping expected sources make the most used search techniques, in the case of ground-based detectors, obsolete when the number of parameters $N > 4$). Thus, may be the most promising outcome is to adapt the algorithms used for the future space detector LISA such as MCMC, MHMC or Generics Algorithms GA to our purpose [234].

Another possible approach can be a two steps multi-band analysis. In this case the analysis is made first performing a detection phase with templates starting from higher cut-off frequency and assuming a small snr-lost, .e.g. of about 5%. In fact the template length is reduced exponentially starting from highest frequency. Starting for example from 10Hz we loose few percent in terms of signal-to-noise but we gain propotionally in terms of computing time. Thus, the first step can be considered similarly to a trigger zero, used for candidates selection. Then, in the second step, the whole template is analyzed for parameters reconstruction and observationi, using a finer template bank grid. Another possible optimization could be achieved using the Stationary Phase Approximation for template production of phase 1 and than the PN approximation or others during the phase2. This schema can be used also for other kind of generators.

Overview of the **isotropic analysis** (the radiometer analysis is almost based on the same framework) [235–237].

The analysis is based on the use of a network of detectors. For each detectors pair, first, one searches the times when both the detectors were taking science data, then split that time up into segments of length T (usually T 60 seconds). The interferometer pair are labeled with an index I=1, 2, ... , N, and for that pair, each segment is labelled by an index J = 1, 2, ... n_{segs}. Each of the segments analysed can be identified by the unique (I, J) pair. Since the segments will be Hann-windowed, only segments that overlap by 50% are used.

The bulk of the processing time is taken up by reading the data and finding the frequency dependent cross-correlation spectrum (the integrand of the cross-correlation estimator statistic, Y_{IJ}), and sensitivity integrand (the integrand of the theoretical error bar, σ_{IJ}) in each unique segment. The steps are:

- read the data for the segment for each IFO,
- downsample (to 2048 or 4096 Hz),

- high-pass filter to remove low-frequency components,
- put the data through a standard PSD estimation function,
- multiply the data with a Hann window,
- Fourier Transform the data,
- decimate the fourier transform to the same frequency resolution as the PSD (usually 0.25 Hz),
- calculate the overlap reduction function at the same resolution,
- calculate the optimal filter function,
- calculate the cross-correlation spectrum and sensitivity integrand,
- write some or all of these quantities to file.

Once this has been done one get the cross-correlation spectrum and sensitivity integrand for each unique segment given by the indexes (I,J). Then, the 'post-processing' could be started. The last is often repeated several times, without having to re-run the calculation of the spectra.

For each unique segment (I, J), the cross-correlation statistic, Y_{IJ} i and theoretical error bar, σ_{IJ}, are calculated.

For each pair, one finds the weighted sum of the cross-correlation statistics and theoretical error bars to give combined results Y_I and σ_I.

One then finds a weighted sum of the results from the individual pairs, to give an overall statistic Y and error bar σ. (Note, that normalization is done such that $Y = \Omega T$, where Ω is the amplitude of the GW spectrum [235]:

$$\Omega = \frac{f}{\rho_c}\frac{\mathrm{d}\rho}{\mathrm{d}f} \tag{57}$$

where $\mathrm{d}\rho$ is the energy density of gravitational radiation contained in the frequency range f to $f + \mathrm{d}f$, ρ_c is the critical energy density of the Universe, and f is frequency.

The final step is to use this statistic to find a Bayesian posterior PDF on the GW amplitude Ω, since this is a one-parameter problem (One marginalizes over any other unknown parameters, such as the calibration factors of the IFOs), one can simply calculate the posterior on a grid - there's no need to use MCMC or other statistical techniques.

Parallelization : they split the data from each IFO pair into 'jobs' which contain several segments (anything up to a few hundred segments). They then run the cross-correlation estimation (the items bit) for all the segments in one job on a single node, and these jobs are all run at the same time. So, the analysis which would take 300 hours of CPU time will usually complete within a few hours on the caltech cluster or on atlas. Once all the jobs are completed, they carry out the post-processing (very cheap computationally). - forecast: Stoc. problem size and Computing implications - for 300h x 2months 2pear of interferometers –> ET –> Isotropic/Radiomether –> 30Hour –> 1 Months –> IO Limit - 1h CPU time X 1 Day Knowing the actual detection algorithm parameterization, it is possible to estimate the computational cost and foresee the future capabilities give by computing infrastructure improvements. In particular we can evaluate the cross correlation problem. In this case we know that today the typical analysis is made in the frequency band 600-10kHz with 0.25 Hz of frequency resolution. With this information we can deduce the need to use a 20kHz as sample frequency and in order to achieve a frequency resolution of 0.25 [Hz] we need at least a data vector length of 1/0,25 s = 4 s. With these information we can estimate the typical data vector length equal to L= 4 x 20000 samples = 80000 samples.

If we consider the cross correlation algorithm and 1 Day of data, this computational problem is equal to perform roughly 43000 analysis cycle x cross correlated channels pair. The total ammount of processed data is 43000 x 8 * 80000 = 26GB per channels pair. We know that for 1 Day of data we need 1 h of CPU time, thus the estimated IO throughput is about 10MB/s per channels pair.

Moreover, We can try to estimate the GFlops considering a complexity manly due to FFT algorithm. The FFT complexity is $N\dot{l}og_2(N)$, under these hypothesis during a day we have a total value: $Nc\,N\,log_2(N)$. Considering as FFT reference library the fftw [238],it is possible to show that this algorithm expresses roghly 6 GFlops for vector data of 80000 sample.

Now in order to understand if this is a CPU or IO bounded problem we can test the two hypotesis. Under the hypotesis of a CPU bounded problem, we know from the previous evaluation made using real information that now we achieve 1MFlops x pairs channels. This data is 3 order of magnitude smaller than real one.

Usually the number of cross correlated channels is of the order of some tens, by that seem clear that this kind of analysis seems to be characterized by limitation due to data Input/Output from/to storage. Moreover the CPU power seems to be already enough to process data "in-time". A faster analysis could be realizing High throughput SAN (Storage Attached Network)

The **stochastic gravitational wave background** could be of cosmological (isotropic - like cosmic microwave background) or astrophysical nature (anisotropic following the spatial distribution of the sources).

It could be interpreted as the superposition of a number of plane waves having a frequency f and a certain direction Ω. We assume that the stochastic background is unpolarized, Gaussian, stationary but we allow an anisotropy in its distribution. The anisotropy of the signal will affect the statistical properties of data with the presence of a signature in the output of the detector.

The search methods for each nature of sources should depend on its angular distribution and its spectral properties.

The sky decomposition method is used for anisotropic background, the method provides maximum likelihood estimates of the gravitational wave distribution $P(\Omega)$ decompesed with respect to some set of basis functions on the sky [239]. This basis could be pixel basis or spherical harmonic basis defined with respect to the Earth's rotational axis.

For point sources the best choice is the pixel basis. For a diffuse background dominated by dipolar or quadrupolar distributions the best choice is the spherical harmonics. Note that for spherical harmonic decomposition and in the case of an isotropic signal, only the monopole moment contributes to the stochastic gravitational waves background strength function Ω_{GW}.

The likelihood estimator for anisotropic background gravitational wave signal is the quantity :

$$P_\alpha = (\Gamma_{\alpha\beta})^{-1} X_\beta \tag{58}$$

X_β is the components of the dirty map and $(\Gamma_{\alpha\beta})^{-1}$ are the components of the inverse of the beam pattern matrix $\Gamma_{\alpha\beta}$. It plies a role similar to that of the Fisher matrix. For spherical harmonic decomposition, the index α corresponds to the couple l, m.

$$X_\beta = \sum_t \sum_f \gamma^*_\beta(f,t) \frac{\tilde{H}(f)}{P_1(f,t)P_2(f,t)} C(f,t) \tag{59}$$

$$\Gamma_{\alpha\beta} = \sum_t \sum_f \gamma^*_\alpha(f,t) \frac{\tilde{H}(f)}{P_1(f,t)P_2(f,t)} \gamma_\beta(f,t) \tag{60}$$

The different functions appearing in the above formulas are defined and computed as following :

- The input $\tilde{H}(f) = (f/f_R)^\beta$ is the assumed spectral shape of the gravitational wave background. It is fixed at the start of the analysis by initializing the value of the reference frequency f_R (the most sensitive frequency) of the detector and the spectral index β for the power-law behavior of the gravitational wave spectrum (note that $\beta = 0$ corresponds to a constant gravitational strain power.

- $C(f,t)$ is the cross-spectra of the data calculated as the SFT of the time-series output data of the two detectors :
  - Down-sample output data to few kHz.
  - High-pass above few Hz to reduce contamination from seismic noise.
  - Windowed.
  - Discrete Fourier transformed to frequency domain.

Note that the frequency resolution (0.01 Hz) for $C(f,t)$ is much smaller than that one for $\tilde{H}(f,t)$ or for the spectral density function $P_i(f,t)$ $(i = 1,\ 2)$ and $\gamma_\alpha(f,t)$ which is fixed to 0.25 Hz. This is used to avoid unnecessary frequency resolution for these last functions, by averaging several frequency bins of $C(f,t)$ before to match Δf.

- $P_i(f,t)$ $(i = 1, 2)$ are the power spectra associated with the individual detectors computed according to Welch's modified periodogram using segments of 4-sec long (0.25 Hz) and 50% overlapping.
- $\gamma_\alpha(f,t)$ are the components of the overlap factor $\gamma(\Omega,f,t)$. they encode informations about the relative separation and orientation of the detectors as expressed by their beam pattern functions. They are analytically computed in the case of spherical harmonics decomposition.
- Choose a cutoff for the SVD regularization (fixe minimum eigenvalues for which the Fisher matrix is reversible).
- Choose $l_{\max}$. It consists of tradeoff between increasing the number of parameters to fit the data and minimizing the uncertainties.

The spherical harmonic analysis method can successfully recover simulated signals injected into simulated noise for several different types of stochastic gravitational wave backgrounds, for examples, isotropic sources, dipole sources, point sources, diffuse sources, etc.

However this method is more computationally intensive that isotropic and radiometer. The computation time will be proportional to some function of the maximum value $l_{\max}$, but roughly estimates show that the spherical harmonic search takes 10 times as much CPU time as the isotropic/radiometer searches.

$$ContinuosWavesAnalysis$$

We clasify as continuous waves (CW) a gravitational waves signal with duration longer than the typical observation time of a detector. The signal of these sources could be affected by a various processes. (i) By spin-down : the rotation frequency and then the emitted signal frequency slowly decreases due to the energy loss of the source (EM, GW...). (ii) The signal is frequency modulated by the Doppler effect associated to the relative source-detector motion. (iii) Signal is amplitude modulated due to the non-uniform antenna sensitivity pattern of the detector. (iv) There are also two further complications that can affect the GW signal from real sources : glitches which are brief spin-up due to star-quakes or interactions between crust and superfluid and timing noise which is random fluctuations of the rotation frequency or phase.

The analysis methods for CW can be divided among coherent, i.e. that take into account the signal phase when known (matched filtering, cross-correlation, MCMC) and incoherent, where the signal phase is discarded (periodogram, Radon transform, Hough transform). Typically, incoherent methods are more robust and less computationally demanding even less sensitive. The choice of a method (or combination of methods) depends closely on the prior information we have on the signal we are searching and on the available computing power. We can distinguish between two kinds of cases :

- Targeted search : cases where knowledges about the source parameters (position, frequency, spin-down) are available from electromagnetic observations of the source.
- Blind search : cases where all the source parameters are given within large intervals based on the available theoretical understanding of the astrophysical scenarios.

The targeted search could be schematized as following : (1) Extract the band of interest around the emission frequency : due to the Doppler effect, the amplitude modulation and the spin-down, the received GW is no longer monochromatic and covers a small frequency band (fraction of Hz) around the known emission frequency. (2) Correct Doppler and spin-down effect : if the spin-down parameters of a source are known with high accuracy we can remove both the Doppler and spin-down by multiplying data by the proper function $exp(-I\ \Delta\Phi_{\text{Doppler, spin-down}})$. (3) Matched filtering : apply matched filter of the new slowly varying signal (demodulated signal) over the unknown nuisance parameters (amplitude of signal as received on Earth, polarization and inclination angles, initial phase...) and over the uncertainty range of the known parameters (position angles, frequency, spin-down). An alternative to explicitly apply a matched filter for the nuisance parameters is the use of the so-called F-statistics [cite map]. (4) Select maximum of the values of the unknown parameters at filter output. (5) Compare it with noise distribution and claim detection or set an upper limit.

The computational cost for targeted searches rely on an accurate knowledge of the source parameters: position, frequency, spin-down. Considering that the frequency is very accurately known within a small bandwidth, one can substantially down-sample the data stream around the expected source frequency and the data analysis costs for such sources is therefore minimal (few templates). Even for sources observed in the electromagnetic domain, however, these parameters are known with finite accuracy and this can lead to a loss of sensitivity, especially for very long observation times. This will also increase the computational cost. For those NS's about which no information about the spin-down is available, we cannot set upper-limits on the signal strain and hence the computational costs become considerable. The number of templates is in the range $10^2 - 10^{10}$, for a year's worth of integration time. Therefore, even assuming a search in a narrow frequency range, around twice the radio frequency, the computational task is tricky. The situation is made worse by the lack of information about the frequency time derivatives, so that one would also have to scan the space of spin-down parameters, increasing the costs further. It is clear that more accurate data from radio observations are necessary in order to narrow down the uncertainty in the source parameters for making such searches feasible.

These results suggest that applying filtering method for a blind search is computationally not possible, since the minimal range for the source parameters is important (whole sky for angular position, whole bandwidth for the signal's frequency[5]...). Even for the more optimistic cases, the computational power required for such search is far from our actual computational capabilities (10^17 GFlops for circular orbit binaries) . A different approach with even a small loss of sensitivity but which ensures to reduce significantly the computational power is then needed.

Stack-slide One of the solution is the so-called hierarchical search (stack-slide search) where coherent and incoherent steps are alternated. In the incoherent step a rough exploration of the parameter space using short data segments is done with a low threshold which allows for many false alarms (some candidates are selected). In the coherent step each candidate is followed with a more refined search using long data segments but searching the parameter space only in the vicinity of the candidate detections of the first step.

Both search steps considered above share the following scheme : first, the data stream is divided into shorter lengths, called stacks. Each stack is phase corrected and FFT'ed, using a mesh of correction points sufficient to confine a putative signal to $\tilde{1}$ frequency bin in each stack. The individual power spectra are then corrected for residual frequency drift using a finer parameter mesh suitable to remove phase modulations over the entire data stretch. The corrected power spectra are summed, and searched for spikes which exceed some specified significance threshold.

From the computational point of view, the interesting feature of stack-slide method is the fact that it considers the available computational power as an initial parameter which fixes the values of the other parameters of the scheme. In fact, before the search begins, one have to specify the size of the parameter space to be searched (choose maximum frequency, region of the sky...), the computational power P that will be available to do the data analysis, and an acceptable false alarm probability. From these, one can determine optimal values for the maximum mismatch for a patch, the number of stacks, and the length of each stack. Optimization consists of maximizing the sensitivity function over these parameters given the definition of the total computational power as constraint.

[5] The computational power is proportional to the maximum frequency of the detector to the fourth power.

The advantages of a hierarchical search are, from one hand the fact that the low threshold on the first step allows detection of low-amplitude signals which would otherwise be rejected, and from the other hand the second step can search longer data stretches on a limited computing budget, because of the reduced parameter space being searched, thus excluding false positives from the first pass. For given computational resources, this technique achieves the best sensitivity if the thresholds and mesh points are optimally chosen between the first and second step of search.

Wide-area searches for continuous gravitational signals emitted by rotating neutron stars is an hard task and it cannot be addressed using optimal data analysis methods, due to the huge computational power needed. A possible alternative approach is e.g. proposed by cite(PHYSICAL REVIEW D, VOLUME 70, 082001)(Quantum Grav. 22 (2005) S1255.S1264), where thay developed a hierarchical method allowing a cut of data analysis computational requirement. This method is sub-optimal and the processing gain is paied by a small reduction in sensitivity. The method consists mainly on alternating coherent steps,based on FFT, and incoherent steps based on the Hough transform. The Hough transform is a feature extraction technique used typicaly in image analysis, computer vision, and digital image processing. The purpose of the technique is to find imperfect instances of objects within a certain class of shapes by a voting procedure. This voting procedure is carried out in a parameter space, from which object candidates are obtained as local maxima in a so-called accumulator space that is explicitly constructed by the algorithm for computing the Hough transform. In paper (Quantum Grav. 22 (2005) S1255.S1264) the computational requirements for a search over these many templates is also estimated. Analyzing the data in roughly real time requiresa computational power 10^8GFlops, moreover is reported the performances of the fastest supercomputers ca. 2010, 510^4GFlops.

Considering a foreseen factor of 200 we can expect in 2023 that the fastest super computer is capable of 10^7GFlops. This number is still an order of magnitude lower and we can conlude that with type of analysis the online will be still not achievable.

[R-Modes] After the supernova event, the newborn neutron star may spin down during up to one year due to R-modes instability (first investigated by Owen at al.[1998]) [**?**]. R-modes are non-radial pulsation modes of rotating stars that have the Coriolis force as restoring force with a characteristic frequency comparable to star rotation speed. These modes are driven unstable by gravitational radiation, inducing a differential rotation at second order in mode's amplitude, which leads the non linear evolution of the r-mode instability. This process generates Gravitational waves that are very difficult to be observed.

r-modes gravitational waves are interesting for ET Science, because could provide very foundamentals information about Formation Processes, such as initial condition, Neutron Star model and Equation of State and others like Neutrino emission models confirmations. In some sense R-mode gravitational wave observation can produce important and unique correlation with the nuclear physics of the neutron star and formation processes.

Using information reported in (Sá and Tomé model - Astrophys Space Sci (2007) 308: 557.561) we can acquire some characterizing data about this type of signals. The frequency domain of these waves is related to the angular velocity W by: $f = 2W/(3p)$. The frequency bound is given

- fmax ■ 1200 Hz, it depends on the initial value of the angular velocity $W0$
- fmin ■ (77-80) Hz, it depends on the final value of the angular velocity $W(tf)$ and K
- The GW duration is roughly $tf = (3.6\text{¸}7.1)10^6 s$

In ((Sà and Tomé model)) is also reported the Gravitational waves strain h(f) generated by R-mode: (formula)

We estimate the optimal signal-to-noise ratio for Einstein Telescope case, and it is given by the formula:

$$\frac{S}{N} = \frac{200}{\sqrt{2+K}} \frac{20Mpc}{D}$$

Given these results, we can make hypotesis about the ET horizon respect to rmodes gravitational waves. On douing that we consider the best and pessimistic cases realted to a very high K. Thus, if a NS borns with substantial differential rotation of $K = (10^5 - 10^6)$ the ovserved optimal SNR is about $[4 - 12]@1Mpc$. While if $K = 0$ we achieve $120Mpc$ close to GA.

Burst Analysis Currently, there are two successful methods for searching burst events: Omega and coherent wave burst. With coherent wave burst, the basic idea is to combine coherently time-frequency (t-f) maps from several detectors [240]. The sky position is encoded in the time delays between interferometers. If there was no time delay, then excess of power in some pixels in t-f map should be similar (modulo the antenna pattern). So one can determine the sky location of the signal from the antenna pattern and by doing multiple time shifts of the data corresponding to different sky positions. (The basic paper is Klimenko, Mohanty),

Doing analysis with networks of 2, 3, 4, 5 detectors, the computational cost will not be very different since we do not analyze each detector separately but generate triggers on combined data stream. So adding another detector should not be an issue by itself. If we do joint analysis with LIGO/Virgo, there is no point to combine the data if the sensitivity is very uneven (the weakest detector will bring noise to the analysis). In this case, it only makes sense to use the bandwidth where all detectors are reasonably sensitive. This would probably reduce the above bandwidth. At least, we can subdivide bandwidth into regions with comparable sensitivities and analyze each separately. If ET sees something but LIGO and Virgo do not, it would effectively be 1-detector analysis with no way to find the sky coordinates.

Recent use of that method in case of signal given by noise and glitches only (no gravitational waves), the computational cost is trivial. To process two years of S5 for 3 detectors with triple coincidence duty cycle of 40%, it would just take one week on Atlas (80 TFlops[6]) if it is not too loaded or broken. Also, during S6, burst search was run online for H1,L1,V1 producing coherent triggers about 5 minutes behind the real time doing computation on 1 dedicated computer. However, in the ET era there might be such a rate of events that it becomes much more computationally intensive. Also if each event is long duration or wide bandwidth, it might consists of millions pixels. Processing such huge clusters might be quite computationally intensive, however still feasible with the future computer's configurations.

Finally, one can emphasis that the computational cost depends on which detectors, what frequency band one want to explore and based on this one could estimate how many sky locations he can/should consider. But practically, the most important factor is the large false alarm rate that could not be predicted before the detector is switched on.

Note that for these kinds of search only sky location and the gravitational strength of the gravitational burst could be recovered, however, the likelihood method used in the search offers a convenient framework for introduction of constraints arising from the source models, Unlike for template searches where accurate waveforms are required, in principle, any useful information about sources can be used to constraint the likelihood functional. This allows customization of the generic burst algorithms in order to search for specific, but not very well modeled sources [240]. One obvious class of constraints is related to the different polarization states of the GW signals. For example, some of core collapse models predict waveforms with linear polarization or random polarization. Merging binary neutron stars or black holes are expected to produce elliptically polarized gravitational wave signals. Also the neutron star mergers can be the source of the short GRB signals, where relativistic jets are emitted along the rotation axis of the binary system and in this case the associated gravitational waves should have the circular polarization. The cWB algorithm allows searches with several types of the polarization constraints : circular, linear, ellipticla and random, or un-modeled search. Moreover, joining these results with neutrino observations will probably give a powerful tool to probe the physical scenarios behind such kind of sources.

For modeled bursts like GRBs from both core collapse, supernovae and some of mergers, the search is based on a matched filtering variant so-called time sliced matched filtering [241]. The application of matched filtering depends crucially on phase coherence in the true signal, in correlating it to a model template. For a magneto-hydrodynamical system powered by a Kerr black hole, turbulence in the inner disk or torus inevitably creates phase incoherence on long time scales, preventing the direct application of matched filtering by correlating to a complete wave form template with the detector output. To circumvent this limitation, the template is sliced into N segments on intermediate time scales, τ, for which phase-coherence may be sustained. Matched filtering is then applied using each slice, by correlating each template slices i with the detector output with arbitrary

[6] Atlas is composed by 1680 2.4GHz 64bit quad core CPUs which sums up to 64TFlops and 132 Tesla graphic cards which gives us a theoretical peak performance of 132TFlops. The real power processing of Atlas is less than the half of its peak value.

offset δ in time. So, the relevant parameters in this algorithm are three: a choice of coherence time τ which can be course grained, fine grained time of onset(s) δ of the (slices of the) burst and the mass of the black hole M. The mass is equivalent, for all practical purposes, to the duration of the burst. Changing the black hole mass changes the duration and also the strength of the signal, but the latter is automatically absorbed by the algorithm and requires no adjustments. For this kind of search, a computational cost can be extrapolated. For a single black hole mass parameter, it is about 6 hours of CPU time (core 2 duo) per 1 hour of detector data (sampled at 20 k Hz). For a range of black hole parameters with, e.g., 0.1% partition, a full parameter search amounts to a few thousand hours per 1 hour of detector data. In this case we can expect for about 2013 a gain factor of 200 considering the same architecture. Implementing Many-core tecnology factor we can consider a conservative 6 extra-factor (1200). The full parameter search will be roughly 10 times far from the "in-time" constrain using a "CPU" model, while trying a many-core implementation few hours of data will be analyzed in one hour. Thus for about 2014 the "in-time" analysis of full parameter search could be reasonable.

[**Reconstruction**] The genetic algorithm (GA) is a search technique that mimics the process of natural evolution based on the positive mutation principle. Initially, a group of organisms (templates) is chosen, each organism is characterized by a different set of genes (parameters). Then, the quality (log of the likelihood) of each organism is evaluated. Based on the value of their quality (templates with higher likelihood), a set of pairs (parents) are selected and their genotypes are combined to produce children (new templates). In the last step, one could, with a controlled probability, allow random mutations in the children's genes (by randomly changing the parameters of the new template to explore a large area of the parameter space). The new children will form the new parent and the procedure is repeated until one reaches steady state (maximum in the log likelihood). From the computational point of view and for the case of coalescing binaries, one could be able to recover the values of the coalescing time and the chirp mass in 1 hour of time with 1 CPU. For the other parameters except the direction of the spins 10 hours of time is needed with 100 CPU. An all parameters recovery will need few days of time with 100 CPU. The cost is purely dominated by the computation (time domain + FFT) of the templates (1 to 2 sec with 1 CPU for a waveform lasting 2 years).

2.8.4 Conclusions

– Observation Feedback on Theory – open to new algotithms possibility – Finally we would like to stress again that: to properly exploit the full power of the new incoming computing architecture, a great effort on the software side is strictly needed, regardless of the architecture we will use.

3 Site and infrastructures

3.1 Description

Responsible: WP1 coordinator, J.v.d.Brand

Interferometric gravitational wave detectors are large and complex and the selection of their site is an issue of great importance. The selected site should allow the highest possible level of scientific productivity at reasonable cost of construction and operation, and at minimal risk. Of paramount importance are the selection criteria that impact the scientific potential of ET. These include natural and anthropogenically generated seismicity and site geological constrains that affect critical parameters such as interferometer arm lengths. The first section of this chapter provides the requirements for the site and infrastructure of Einstein Telescope. An important aspect within these requirements is the allowed seismic motion, which is addressed according to source frequency. Seismic sources include the ambient seismic background, microseisms, meteorologically generated seismic noise, and cultural seismicity from anthropogenic activity.

The second section describes the background on one of the fundamental infrastructure limitations called Newtonian noise. Newtonian noise originates from fluctuations in the surround geologic and atmospheric density, causing a variation in the Newtonian gravitational field. New analytical formalisms and finite element models are presented for subterranean detectors giving an estimate for NN in ET for different geologies. Using these models we show that it is in principle possible to deploy seismic sensor arrays that monitor seismic displacements and filter the detector data using Wiener or Kalman filters.

The third section discusses the ET site selection. As part of the site selection and infra-structure program for ET, 11 European sites were systemically characterised to catalogue regions within Europe that would comply with the ET site demands. Among the data that were logged were the local seismic activity, already existing local infra-structure, and population density.

Finally, we discuss the subterranean infrastructure and cost aspects for caverns, tunnels, vacuum, and cryogenics for the ET site.

3.2 Executive Summary

Responsible: WP1 coordinator, J.v.d.Brand

Throughout the ET design study, the site selection and infrastructure design working group has seen an opulent evolution from a site study at 11 locations in 9 different countries, to a completely designed underground detector infrastructure. The site study has revealed several promising underground sites that comply with ET low seismic background performance requirements. In order to ascertain all site characterisation procedures were carried according to seismologic standards, measurements and data collection was carried out in collaboration with the Observatories and Research Facilities for European Seismology (ORFEUS) which is maintained by seismology department of the Dutch bureau of Meteorology.

The infrastructure definition contained several aspects such as the vacuum envelope, cryogenic infrastructure, tunnels, and caverns that are transverse through the detector optical configuration and suspension working groups. With the choice of combining a triple triangular detector with a xylophone detector topology, ET amalgamates an optimised planned disbursement for construction with a realistic proposal for a robust, highly sensitive, wide-band gravitational wave observatory. Through the design process, the vacuum system, caverns, and tunnel diameter are optimised such that the total infrastructure can be used for decades after its construction. The excavation of underground tunnels, caverns, and halls will occur over a period of approximately two years, where the ET observatory will be built in stages; the first construction stage containing a single 10 km xylophone detector. Later the second stage will incorporate the second and third 10 km xylophone detector.

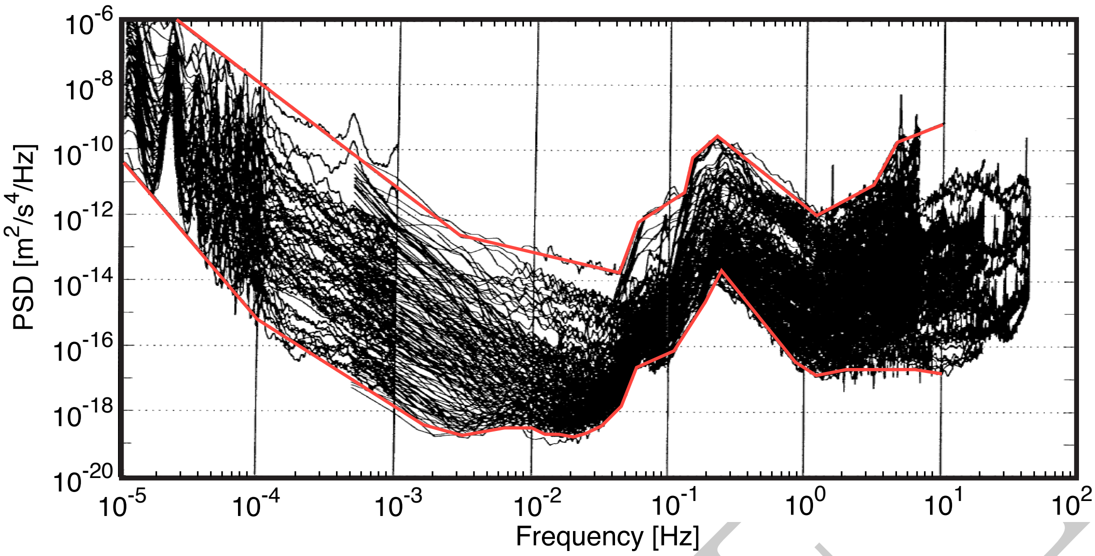

Figure 39: Overlay of network station spectra used in Peterson's background noise study [242] together with straight-line segments fitted to the high-noise and low-noise envelopes of the overlay.

3.3 Seismic motion

Responsible: D. S. Rabeling

Site specific noise sources, like seismic noise, will most likely influence the final sensitivity of ET. Most anthropogenically generated seismic noise propagates along the earth's surface, and attenuates with depth. Currently operating gravitational wave detectors have spent much effort developing seismic filter chains to suspend the main optics of the interferometer, preventing seismic induced vibrations to pass through and affect the detector sensitivity. Noise studies [243–246] often categorize noise sources according to frequency. Noise at frequencies below 1 Hz is termed 'microseismic' and its sources are dominantly natural (*i.e.* non cultural and non-local), depending on oceanic and large-scale meteorological conditions (*e.g.* monsoons and cyclones). Around 1 Hz wind effects and local meteorological conditions show up, while for frequencies above 1 Hz additional sources (besides natural) are related mainly due to human activity. Such noise is termed 'cultural noise' or 'anthropogenic noise'. It should be noted that the 1 Hz division is not absolute.

All seismic measurements and results in this chapter are presented as acceleration power spectral density (PSD)[7] versus Fourier frequency, where PSD values have units of squared acceleration $(\mathrm{m/s^2})^2/\mathrm{Hz}$. The largest PSD values are seen at low frequencies. The surface of the Earth experiences large external forces due to the gravitational attractions of the Moon and Sun. At very low frequencies this causes the surface of the Earth to rise and fall with amplitudes of about 0.5 m with respect to the center of the Earth. This tidal motion can be seen in Fig. 39 at a period of 2.3×10^{-5} Hz. Since the motion occurs at very low frequency the interferometer test masses will move *coherently* and differential test mass motion presents no problem. Large PSD values are observed at periods clustered around 0.2 and 5.5×10^{-2} Hz which correspond to microseisms. Note that a large dynamic range of more than four orders of magnitude (90 dB) is needed to accommodate signals between 1 and 0.01 Hz.

Peterson [242] catalogued acceleration noise power spectral density plots for frequencies up to 10 Hz from 75 seismic stations distributed worldwide. Several years of data were collected (about 12,000 spectra in total). From the upper and lower bound of the combined data of both surface and borehole sensors (100 - 340 m depth) he derived, what is now knows as, the new high/low noise model (NHNM/NLNM), which replaced his earlier low noise model [247]. The data and fit are shown in Fig. 39.

[7] In the literature various representations are used, such as the root power spectral density (RPSD), acceleration, velocity and displacement spectral densities.

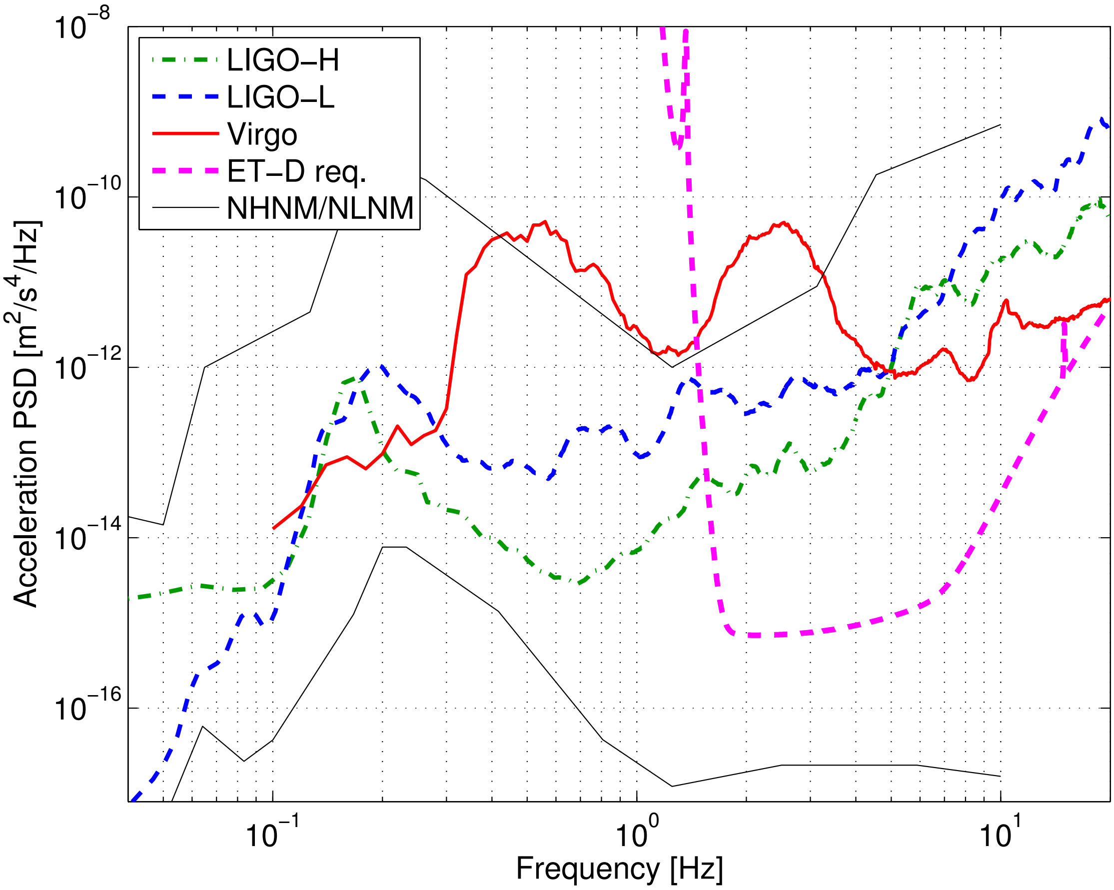

Figure 40: Seismic acceleration PSD at current gravitational wave detector sites. The magenta dotted line represents the most critical seismic performance limits, which are set by gravity gradient noise.

Microseismic ground motion is a prominent feature for frequencies around 0.17 Hz and 0.07 Hz. The small lower-frequency peak (periods of 10 - 16 s) correlates with the frequency of coastal waves, where the ocean wave energy is converted into seismic energy through either vertical pressure variations or from the surf crashing onto the shore. The larger peak, at about twice the frequency (periods of 4 - 8 s), originates from standing ocean waves that couple to the continental shelf. The standing waves are generated by superposition of ocean waves of equal period traveling in opposite directions and have recently been confirmed by satellite observations. Corresponding PSD values change up to 30 dB depending on the storm intensity, while the two frequencies shift upward as storms age.

Presently, the large interferometric detectors GEO600, LIGO, TAMA, and Virgo are placed on the surface of the earth and, consequently, are sensitive to seismic disturbances. In fact, their operation is limited by seismic displacement noise and their sensitivity rapidly deteriorates for frequencies below 10 Hz. At these low frequencies Virgo has realized excellent performance due to a suitable attenuation scheme. The required seismic noise reduction for second generation GW detectors will be achieved by improving passive and active vibration isolation systems. To further suppress seismic noise in third generation detectors the test masses will be suspended from even more sizeable and complex seismic attenuators, which scheme is discussed in chapter 4. Hild *et al.* calculated that, in order to obtain suitable suppression of the local seismic within the ET target sensitivity using the proposed suspension systems, a requirement is set on the tolerable seismicity of a site [248]. For comparison, Fig. 40 shows the seismic acceleration power spectral densities (PSD) of the Virgo and LIGO Hanford and Livingston sites.

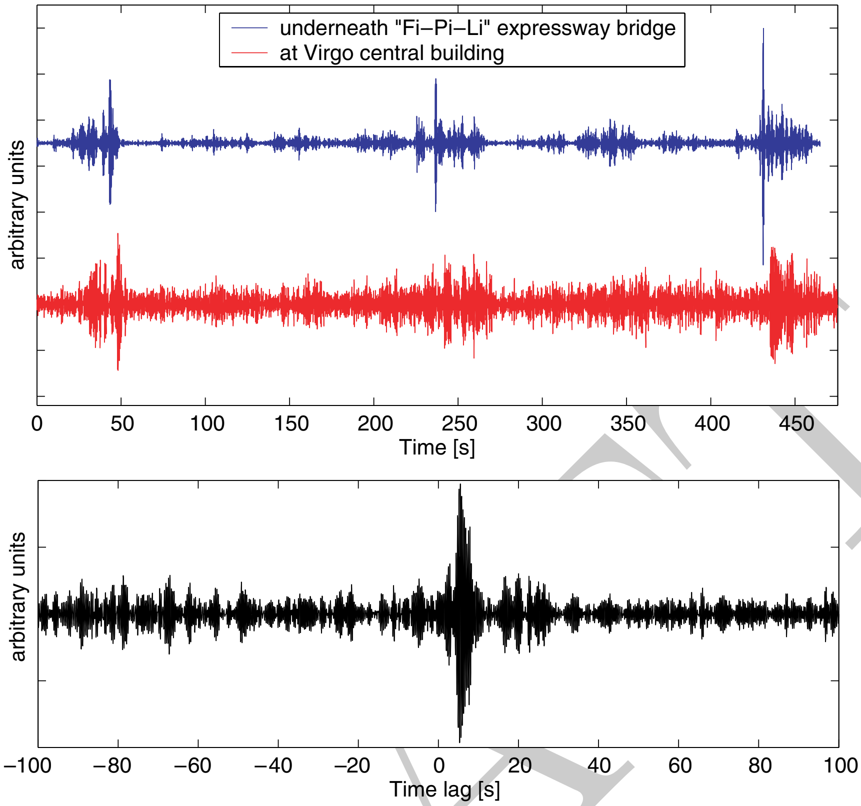

Figure 41: Top: Seismogram recorded on the ground underneath one of the nearby bridges (top signal) and the simultaneous seismogram recorded at Virgo (bottom signal). Three heavy trucks were crossing at approximately 5, 230, and 420s. Both signals have been bandpass filtered between 1 and 4 Hz. Bottom: Cross-correlation of the first 100s between the two seismic channels.

For Einstein Telescope the critical frequencies f are in the range 0.1 - 10 Hz, where the seismic noise is variable mainly due to microseismic and anthropogenic activity. It is therefore important to chose a site location far from oceans and human activities (both at present and in future). The NLNM yields a PSD of $1.38 \times 10^{-17} \mathrm{m}^2/\mathrm{s}^4/\mathrm{Hz}$ at 1 Hz corresponding to an acceleration of $3.7 \times 10^{-9} \mathrm{m/s}^2$. Like the NLNM many remote sites show an approximately flat PSD response for accelerations in the frequency band of 1 - 10 Hz. Corresponding displacements can be found by double integration of the accelerations yielding a $1/\omega^2$ frequency dependence. The conversion should take the integration bandwidth into account (often 1/3 octave is used corresponding to a range of ±10% about the center value). Note that when a Gaussian signal is passed through a narrow-band filter, the absolute peak signals of the filtered signal envelope will have a Rayleigh distribution (yielding a factor 1.253σ for $|\overline{x}_P|$). Using the above, we find that the lowest possible displacements, according to the NLNM, are about 0.1 nm/$\sqrt{\mathrm{Hz}}$ at 1 Hz and decrease with f^{-2}.

Anthropogenic noise

Responsible: D. S. Rabeling
As was discussed above, the NLNM is a composite of different stations and instruments with different geology and in various geographic regions. Therefore, it is not possible to duplicate its response at one specific location. It has been observed that lowest noise is obtained in continental sites with sensors placed in hard rock. Sensors with low PSD values are often at borehole and subterranean stations operated at remote sites, far from cultural, oceanic, and meteorologically induced seismic noise. For ET, this means that the distance to urban areas,

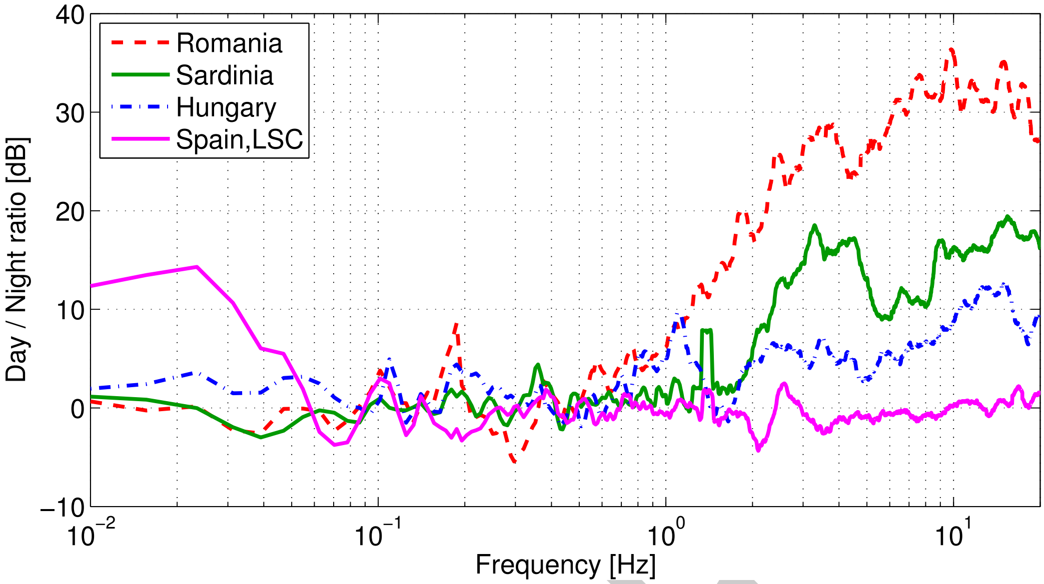

Figure 42: Midday versus midnight noise PSD ratios as a function of frequency at four different measurement sites. Cultural noise is visible for frequencies above 0.7 Hz.

highways, railways, airports, etc. needs be considered. The influence of traffic induced seismicity on gravitational wave detectors have been studied by various authors. Road noise depends on road structure and materials, traffic density and vehicle type and speed. Schofield *et al.* [249] reported that local traffic, from passenger vehicles to heavy trucks, induced vibrations at the LIGO Hanford, WA, site. Vibrations were measured for frequencies in the 1 - 50 Hz range, with maxima around 4 - 12 Hz. At the Virgo gravitational wave site, road noise was analysed using recordings of the seismic field at the Virgo site and correlating these recordings with measurements underneath a major high way overpass, 3 km away from the Virgo arms terminal building. Seismic noise originating from the nearby traffic was found in frequency ranges of 1-4 Hz, peaking at 3 Hz. The top plot of Fig. 41 shows the seismic recordings underneath the overpass and at the Virgo end building. The bottom plot of Fig. 41 shows the cross-correlation between the two signals during the first 100 seconds. Coward *et al.* [250] recorded ground vibrations at the AIGO site in Australia for vehicles passing the instrumentation as close as 24 m. Road noise was visible in the 5 - 30 Hz frequency band.

Even in remote areas, anthropogenic noise can still be recognised. Spectrograms for frequencies up to 60 Hz have been made by Young *et al.* [251] with seismometers at the surface and within boreholes in the USA for data collected over more than one year. Seismometers were placed in boreholes at Amarillo, TX, at depths of 5, 100, 200, 367, 1219 and 1951 m. The anthropogenic character was present at all depths and exceeded background by about 10 dB. Its source was identified from diurnal patterns and was prominent for frequencies between 1 and 40 Hz. At Datil, NM, seismometers were installed at depths of 0, 5, 43, and 85 m and cultural noise was absent, most probably due to the remoteness of the site. At Pinedale, WY, with seismometers at depths of 3, 13, 30, 122 and 305 m, diurnal patterns in cultural noise were obscured by a pattern of progressive day-time increase of wind noise.

As part of the ET site characterisation, the presence and spectral PSD values of anthropogenic noise were investigated. Fig. 42 shows an example of the day/night ratio obtained from four different site measurements. Respective high and low frequency disturbances can easily be recognised by comparing the listed day/night ratio values with local population density and the distance to seas and oceans, which are listed in table 4. Comparing these statistics, and comparing this with the population density map of Europe in Fig. 43 (data from REGIO database of EUROSTAT) corroborates the day/night ratio's found in table 4.

Table 4: Population density at the four different measurement sites. Population density figures are given in km^{-2}.

Location	Pop. Density [km^{-2}]	Dist. to ocean/sea [km]	Day/Night @ 10 Hz [dB]
Romania	180	300	33
Sardinia	10	10	16
Hungary	75	500	9
Spain	1.38	120	1

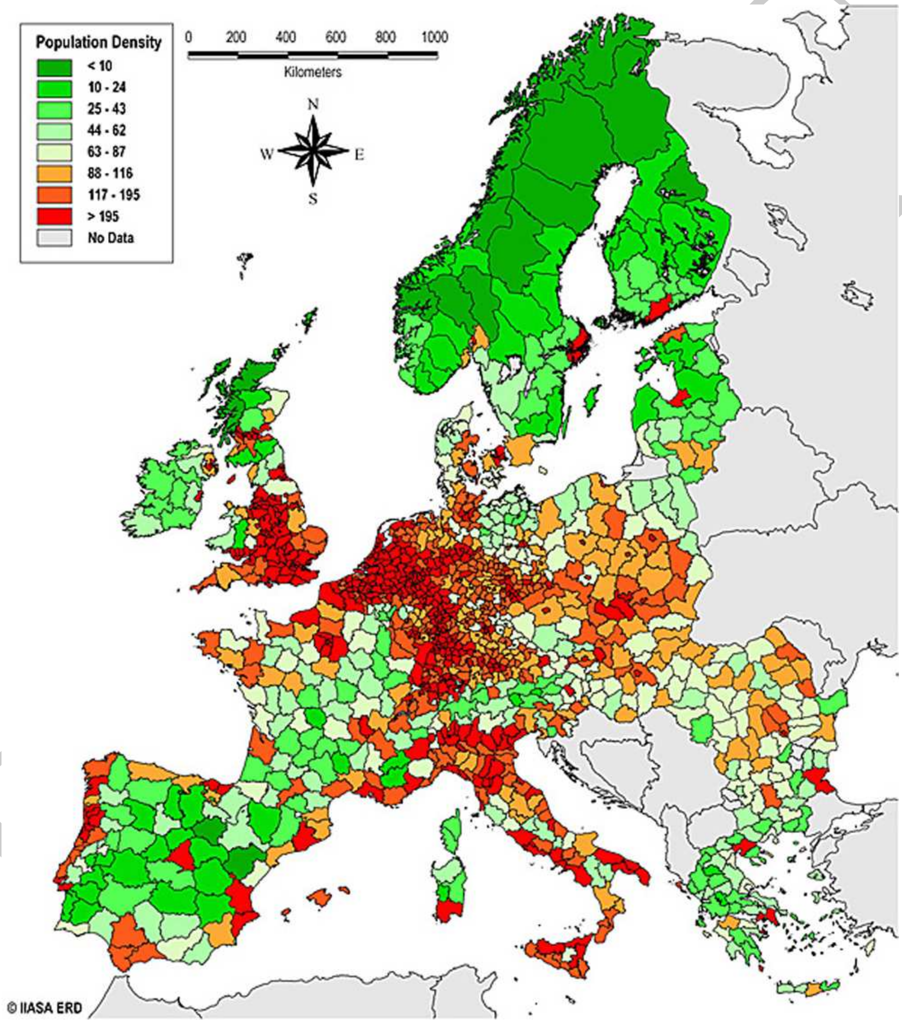

Figure 43: High frequency (1 - 10 Hz) seismic noise is driven by cultural noise. Density of population in Europe from the REGIO database of EUROSTAT [252].

Wind noise

Responsible: D. S. Rabeling
Wind noise has been studied by a number of authors to quantify the conversion of wind energy into ground motion. The presence of wind causes movement of surface objects, such as trees or structures, or directly through turbulent pressures on topographic irregularities. Of particular interest for ET are its frequency range,

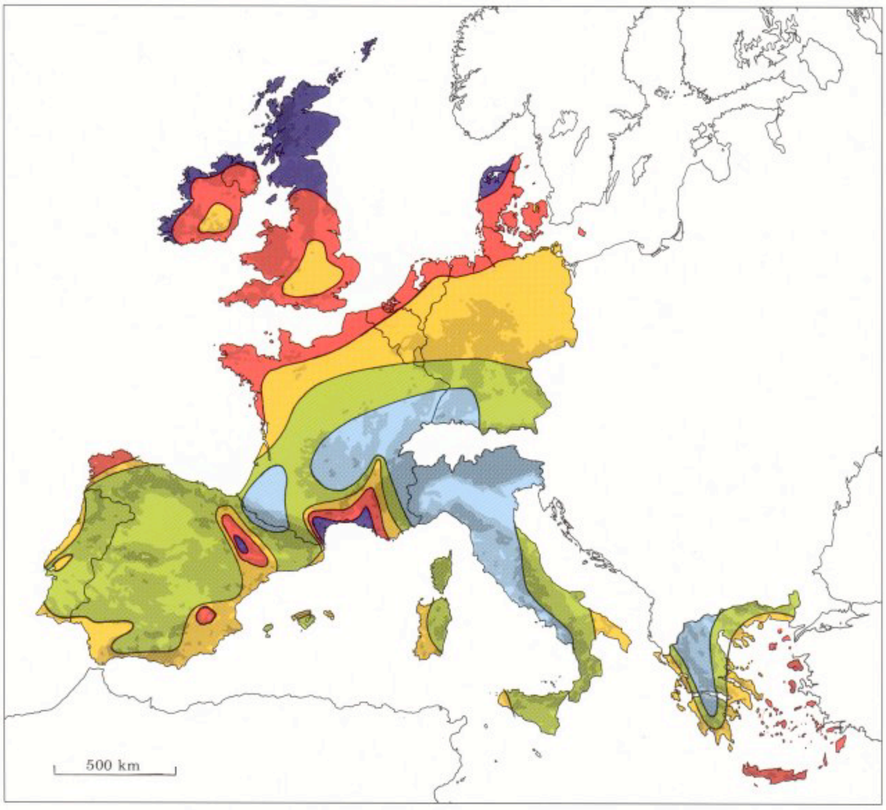

Wind resources[1] at 50 metres above ground level for five different topographic conditions										
	Sheltered terrain[2]		Open plain[3]		At a sea coast[4]		Open sea[5]		Hills and ridges[6]	
	$m\,s^{-1}$	Wm^{-2}	$m\,s^{-1}$	Wm^{-2}	$m\,s^{-1}$	Wm^{-2}	$m\,s^{-1}$	Wm^{-2}	$m\,s^{-1}$	Wm^{-2}
	> 6.0	> 250	> 7.5	> 500	> 8.5	> 700	> 9.0	> 800	> 11.5	> 1800
	5.0-6.0	150-250	6.5-7.5	300-500	7.0-8.5	400-700	8.0-9.0	600-800	10.0-11.5	1200-1800
	4.5-5.0	100-150	5.5-6.5	200-300	6.0-7.0	250-400	7.0-8.0	400-600	8.5-10.0	700-1200
	3.5-4.5	50-100	4.5-5.5	100-200	5.0-6.0	150-250	5.5-7.0	200-400	7.0- 8.5	400- 700
	< 3.5	< 50	< 4.5	< 100	< 5.0	< 150	< 5.5	< 200	< 7.0	< 400

Figure 44: European wind resources based on data collected for the European Wind Atlas [253].

the wind speed threshold for it to become evident, and its persistence with depth.

Withers *et al.* [254] performed measurements at Datil, New Mexico in the frequency band of 1-60Hz. This is a remote site that features sparse vegetation and distances to the nearest road and railroad were 12 and 90 km respectively. Measurements were performed at a depth of 0, 5, 43 and 85 m and the effect of wind noise was evident over the entire observed bandwidth with an ambient background threshold of $\sim$3 m/s. At a depth of 43m a reduction of 20 dB was found. Slightly higher reduction factors were found at 85m.

Young *et al.* [251] carried out similar measurements at Amarillo, Texas at a depths of 3, 13, 30, 122 and 305 m. Wind speed thresholds, for the presence of wind induced background noise, were found to be 3-4 m/s at depths of 0-5 m and 8-9 m/s at depths below 100 m. A strong correlation between seismic noise and wind was observed over a broad frequency spectrum range from 1 to 60 Hz. The noise was 34 dB above the NLNM at a depth of 3 m, and decreased to 10 dB above NLNM at a depth of 305 m. Koller et al. (2004) determined that many parameters relating to measured ground motion caused the amplitude ratio to vary, but that only wind speed affected the frequency at which the horizontal to vertical ratio curves peaked. Mucciarelli et al. (2005) found that, provided the sensor was sheltered from direct wind (inside a concrete box at 1.5 m depth), wind increased the amplitude of all components of seismic noise (vertical, east-west, north-south) in the band 0.1-10 Hz similarly, such that ratio was unchanged. This conclusion was valid for wind speeds up to 8 m/s.

The reductions in wind noise are a prime example that surface seismic noise contributions will decay with depth. For ET, the underground environment is expected to improve on all sources of seismic noise since surface seismic noise is exponentially reduced with depth, $e^{4d/\lambda}$, where d is the depth and λ is the wavelength of the seismic wave. Fig. 45 shows measurements at the Gyöngyösorozi mine by beker *et. al.* in the Hungary and indicate a factor of ∼10 suppression at 1 Hz at the depth of 400 m, and substantially more at higher frequencies. At Gyöngyösoroszi, the speed of sound at 400 m underground (hardrock) is ∼3 km/s, implying that the seismic waves in the 0.1-10 Hz band have long wavelengths that at the surface: 300 m - 30 km.

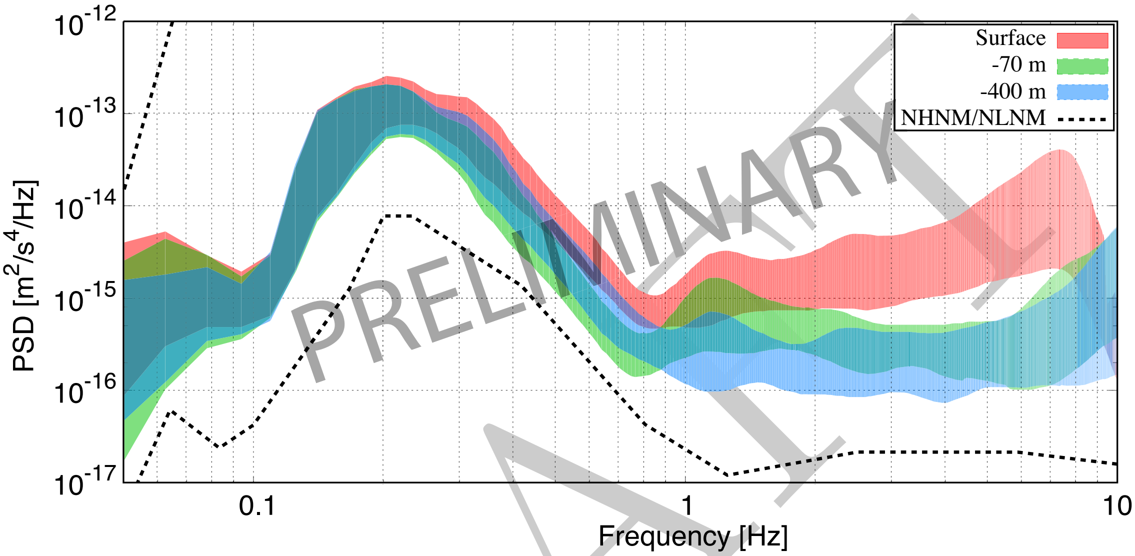

Figure 45: Measured reduction of seismic noise at the Gyöngyösorozi mine in Hungary for three different seismic sensors at depths of 0, 70, and 400m.

3.4 Newtonain noise

Responsible: G. Cella

Another source of noise within the gravitational wave detector that originates from the local seismic is gravity gradient noise. The seismic activity causes perturbations in the local gravity field, which couples directly to the interferometer test masses. Since no filter or shield can be built for gravitational coupling, suppressing this noise source is difficult and low seismicity sites should be identified. It is expected that an underground environment is to improve on all associated sources of seismic noise spectral amplitude, including seismically induced NN. Furthermore, the local environmental conditions underground are usually stable (and controllable) and anthropogenic-induced seismicity is much more controllable underground, where access is limited.

The following subsections discuss this issue.

In Subsection 3.4.1 a simple analytical estimations of NN is discussed. The power spectrum of NN is written as a function of a measurable seismic quantity, under the hypothesis of homogeneity for the medium, and neglecting any kind of effects from underground structures. This kind of approach is possible only with simplified models, however it can provide guidelines expecially when detailed informations about the geological structure of the site are not available.

A complimentary approach to analytical estimation, based on finite element models, is presented is Subsection 3.4.2. This is the natural way to give a refined evaluation of aspects that cannot be considered easily in the analytical approach, such as the effect of the infrastructures and of the geological details, for example inhomogeneities.

Finally, two NN subtraction schemes are presented. In Subsection 3.4.3 a subtraction scheme is presented to monitor the NN induced by the ambient seismic background, using a seismic sensor array. This is the approach that must be used when it is not possible to recognize a dominant and localized source of seismic noise.

On the other hand if a strong and coherent source of noise is known (for example a pump), a single accelerometer can be used to monitor the induced seismic field. Using optimal filtering, the NN transfer function is estimated from the source to the interferometer test mass, and can be subtracted from the data. Details about this subtraction procedure are presented in Subsection 3.4.4.

3.4.1 A simplified NN estimate

For a given distribution of masses, which can be described by a mass density function $\rho(\mathbf{x}, t)$, the acceleration experienced by a test mass located at $\mathbf{y}$ can be written as

$$\mathbf{a}^{NN}(\mathbf{y}, t) = G \int_V \rho(\mathbf{x}, t) \frac{\mathbf{x} - \mathbf{y}}{|\mathbf{x} - \mathbf{y}|^3} dV_x \tag{61}$$

where the integration is extended to the volume V of interest.

We are interested in the fluctuating part of this quantity when the medium is an elastic solid. From the expression of mass conservation we get

$$\dot{\rho} + \nabla \cdot \mathbf{J}_m = 0 \tag{62}$$

where the mass density current is given by $\mathbf{J}_m = \rho_0(\mathbf{x})\dot{\boldsymbol{\xi}}(\mathbf{x}, t)$, ρ_0 being the density of the medium in the static configuration and $\boldsymbol{\xi}$ its small displacement at a given point.

By inserting Eq. (62) inside Eq. (61) we find

$$\mathbf{a}^{NN}(\mathbf{y}, \omega) = G \int_V \nabla[\rho_0(\mathbf{x})\boldsymbol{\xi}(\mathbf{x}, \omega)] \frac{\mathbf{x} - \mathbf{y}}{|\mathbf{x} - \mathbf{y}|^3} dV_x \tag{63}$$

Note that this expression contains two different effects, as can be seen expanding the derivative. The terms proportional to $\rho_0 \boldsymbol{\nabla} \boldsymbol{\xi}$ describe the fluctuations of the local density connected to the compression of the medium, while $\boldsymbol{\nabla} \cdot \boldsymbol{\xi} \rho_0$ takes in account the effect of the movement of density inhomogeneities, for example at the surface boundary.

Starting from Eq. (63) a general theory about the connection between seismic measurements and NN can be developed. We will not give here the details, which can be found for example in [255]. The general idea is to decompose seismic motion in normal modes, which are supposed to behave as oscillators coupled to unknown stochastic forces. By measuring quantities connected to seismic fluctuations (for example the power spectrum of horizontal and/or vertical displacement, or the correlation between displacements at two different points) we can get informations about the excitation of these oscillators. Using Eq. (63) these can be converted to an estimate of NN.

By making some additional assumptions a simple estimate of strain equivalent power spectrum of NN S_h^{NN} can be done. We will present and discuss now this simplified result.

We model the ground as a homogeneous medium of given density ρ_0 and the longitudinal and transverse speeds of sound c_L, and c_T respectively. The mirrors of the interferometer are supposed to be underground, inside a cavity whose effect can be seen to be not important in the low frequency regime we are interested to.

As we said there will be two kind of contributions, connected to surface and bulk fluctuations. The main assumption of the model is that the fluctuations associated to surface Raileigh waves are dominant. In this case both the contributions are exponentially damped with the depth, over a typical scale of $\ell \sim v_s(2\pi f)^{-1}$ where v_s is the speed of sound and f the frequency.

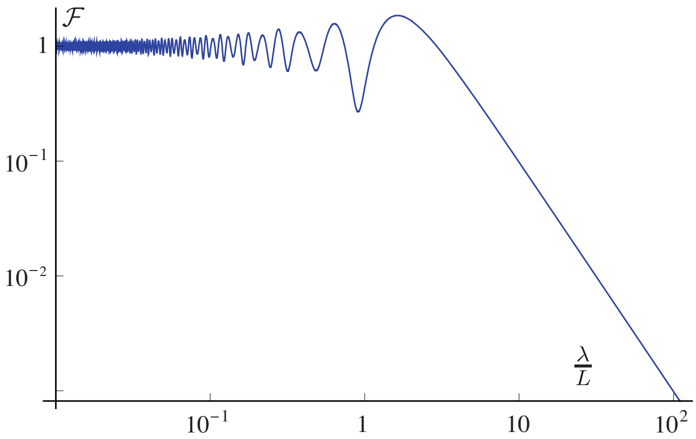

Figure 46: The geometrical suppression factor $\mathcal{F}$ as a function of the ratio between the mode's wavelength and the length L of the interferometer arm. $\mathcal{F}$ suppresses the NN at low frequencies. It is normalized to one in the high frequency region, where the contribution of the motion of each test mass is uncorrelated and adds in quadrature.

If we assume further that damping effects are negligible, so that each mode is excited essentially only at its natural frequency we can write now the final expression for the NN estimate as

$$\sqrt{\frac{S_h^{NN}(\omega)}{C_{vv}^{seism}(0;\omega)}} = \frac{4\pi G\rho_0}{L\omega\sqrt{2}} \times \left(\frac{2(\beta_T^2+1)e^{\beta_L K z} - (1+2\beta_L+\beta_T^2)e^{Kz}}{\beta_L(\beta_T^2-1)}\right)\mathcal{F}\left(\frac{\omega L}{c_T\sqrt{x}}\right)^{1/2} \tag{64}$$

where we choose to normalize the noise to the power spectrum of vertical surface seismic motion, $C_{vv}^{seism}(0;\omega)$. The function

$$\mathcal{F}(KL) = 1 + 2J_2(kL) - \frac{2}{kL}J_1(kL) - \frac{1}{2}J_2(KL\sqrt{2}) \tag{65}$$

which appears in Eq. (64) describes the coherence between the gravitational accelerations of different test masses. It is apparently real and it goes to zero in the low frequency regime. This is due to the fact that when the wavelength of seismic modes is large compared with the interferometer size each mirror feels the same acceleration, so that the length of the resonant cavities in the arms of the interferometer does not fluctuate. Practically it can be set to one in the frequency range of interest.

Setting $z = 0$ in Eq. (64) we can directly compare with previous estimates of NN on the surface [256–258], finding essentially an agreement.

The attenuation factor, which is the ratio between the NN amplitude at a depth z and the one on the surface, can be obtained comparing the intermediate factor between brages in Eq. (65).

It is plotted in Fig. 47 (left) for several selected frequencies, as a function of the depth.

For a given frequency NN can be zero at a peculiar depth. This in a sense is an artifact of our oversimplified model, and depend from our assumption that a mode contribute to the NN noise only at its resonant frequency. Another consequence of this assumption is that the vertical seismic correlation is proportional to $J_0\left(\frac{\omega r}{c_T\sqrt{x}}\right)$, so it decrease quite slowly (as $r^{-1/2}$) at large distances, which is also quite unrealistic.

We can take into account coherence effects by add some damping to the seismic modes considered in the model. This is equivalent to give a finite width to its resonant response. Just for illustrative purpose we can choose a Gaussian line shape parameterized by a width parameter Γ and compare the result for the NN estimate. We do not report the analytical details here, instead we present the result comparing the attenuation factor at different values of Γ in Fig. 47 (right).

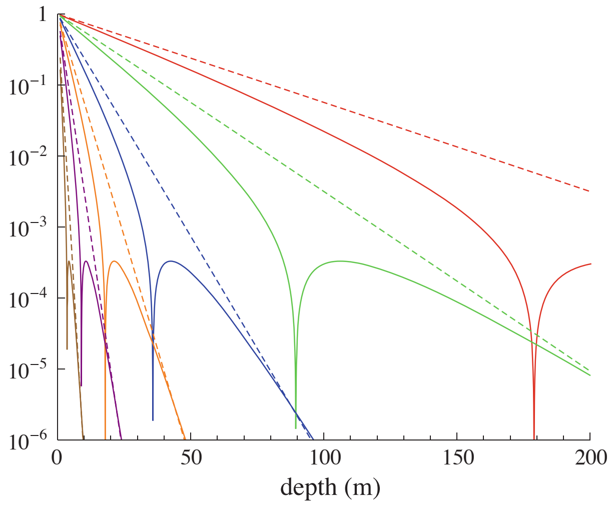

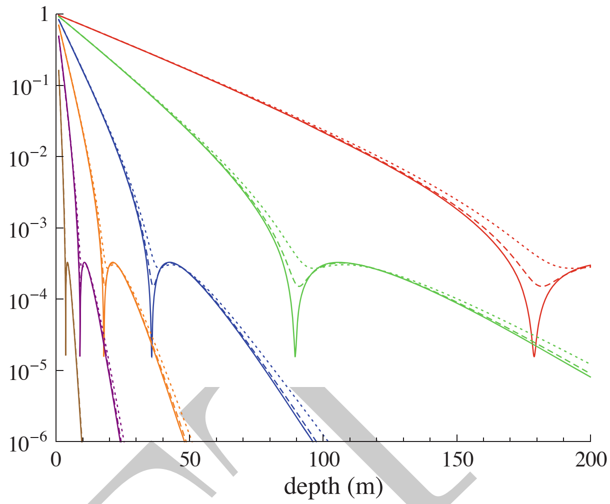

Figure 47: *Left.* The NN attenuation factor (vertical axis) predicted by Eq. (65) as a function of depth (horizontal axis) for selected frequencies. The correspondence is red 1Hz, green 2Hz, blue 5Hz, orange 10Hz, purple 20Hz, and brown 50Hz. Here $c_T = 220m/s$ and $c_L = 440m/s$ (continuous line) or $c_L = 880m/s$ (dashed line). The zero appears when the two exponentially damped factors in Eq. (65) cancel. Before and after this point the decrease will be dominated by one of the two, therefore the decay constant changes. *Right.* The effect of the quality factor (vertical axis) as a function of depth (horizontal axis, in m) for selected frequencies. The quality factor is modeled using Eq. (64) and corresponds roughly to $Q = 10^4$ (continuous line), $Q = 10^3$ (dashed line), and $Q = 2 \times 10^3$ (dotted line)

We see the expected smoothing effect, and also an apparent saturation of the attenuation factor for the smallest Q. This can be understood, because when the quality factor is small there are longer wavelength modes which are excited for a given frequency. Coherence effects have also an impact on the estimate of NN, which will not be discussed here.

3.4.2 Finite element models

Responsible: D. S. Rabeling

Complimentary to the presented analytical descriptions of seismic activity, it will be come important, whenever considering a non-homogeneous medium or complex geologies, to have an accurate description of the seismic wave field. Simulations of such systems were accomplished using the FE software package *Comsol* [259]. In the FE framework 3D continuum is subdivided into small hexahedral elements. Within each element the relevant physical parameters, like displacement and stress, are approximated by spline functions of arbitrary order. The following section shows how the FE software can be used to predict the NN contributions from surface and bulk waves in homogeneous media. The analysis provides the basis for simulation in non-homogeneous and/or stratified soils.

The displacement wave field that results from a seismic disturbance, is governed by the elasto-dynamic equations. The wave field in a homogeneous elastic medium can be expressed as a combination of plane body waves [260]. Two types of body waves exist, pressure (P) and shear (S) waves [261]. In the case of P-waves the movement of a ground particles is parallel to the direction of wave propagation. For S-waves the particle motion is perpendicular to the direction of the wave. The characteristics of seismic waves can be described by the ground properties, parametrized by the Young's modulus, E, the density, ρ, and the Poisson ratio, ν, describing the relationship between shear and strain forces. The wave velocities are then given by

$$c_P = \sqrt{\frac{E(1-\nu)}{(1-2\nu)(1+\nu)\rho}}, \text{ and } \quad c_S = \sqrt{\frac{E}{2(1+\nu)\rho}}, \tag{66}$$

for P and S-waves respectively. Typical values for hard-rock range from 3 - 6 km/s for c_P, and 1.5 - 4 km/s for c_S. In a medium that is bounded by another medium, such as air, or is comprised of layers, surface and head waves also exist. Head waves emerge in stratified media where modes propagating along an interface, cause energy to radiate into the low velocity zone. Surface waves are typically referred to as Rayleigh and Love waves. Love waves involve particle motion parallel to the surface and transverse to the direction of propagation. They produce no density variations and therefore have no effect on gravity gradients [258]. Rayleigh waves are polarized perpendicular to the surface and vanish with depth.

Solving the wave equation for harmonic Rayleigh waves results in the following displacement fields [262]

$$\begin{aligned} \xi_x &= iA(k_R e^{-\kappa_P z} - \zeta \kappa_S e^{-\kappa_S z}) e^{i(k_R x - \omega t)}, \\ \xi_z &= -A(\kappa_P e^{-\kappa_P z} - \zeta k_R e^{-\kappa_S z}) e^{i(k_R x - \omega t)}, \end{aligned} \tag{67}$$

where A is an arbitrary amplitude, t denotes time, ω denotes the angular frequency, z is the depth, k_R is the wave number of the Rayleigh wave, and $\kappa_S = \sqrt{k_R^2 - k_S^2}$ and $\kappa_P = \sqrt{k_R^2 - k_P^2}$ are decay factors related to the shear and pressure wave numbers. Finally, $\zeta = \sqrt{\kappa_P/\kappa_S}$. The horizontal Rayleigh wave speed, c_R, is slightly lower than the S-wave speed and when expressed in units of c_S is purely a function of ν. It can be found through $c_R/c_S = \chi$ where χ is the real root, in the range $0 < \chi < 1$ of the equation [262]

$$\chi^6 - 8\chi^4 + 8\left(\frac{2-\nu}{1-\nu}\right)\chi^2 - \frac{8}{1-\nu} = 0. \tag{68}$$

The above describes harmonic Rayleigh waves propagating far from the source. In reality, excitation of a medium results in a combination of all the different wave fields; body and surface. An important aspect for third generation GW detectors is the influence of cultural seismic noise. It has been shown [263] that the distribution of displacement waves from an excitation with a circular footing on a homogeneous, isotropic half-space largely consists of Rayleigh surface waves: 67 % of the energy, with 26 % and 7 % in shear and compression waves, respectively. One solution to reduce the cultural noise amplitude, is to move away from (sub)urban areas. Their amplitude decays exponentially and is negligible at a depth of a few Rayleigh wavelengths, $\lambda_R = 0.92 c_S/f$. Therefore, it seems natural to consider underground sites for third-generation GW detectors.

As waves propagate through the medium, their amplitude decreases. This attenuation can be attributed to two factors; material and geometric damping. Geometrical damping is a result of energy spreading over an increasing area. The frequency dependent material damping involves energy lost due to friction. Seismic wave attenuation for homogeneous media, can be described by [264]

$$A_2 = A_1 \left(\frac{r_1}{r_2}\right)^n e^{-\frac{\pi\eta f}{c}(r_2 - r_1)}, \tag{69}$$

where A_1 and A_2 are the wave amplitudes at distance r_1 and r_2 from the source, n is the geometric damping coefficient, f is the frequency and c the propagation speed of the wave. The material damping is represented by the loss factor η. The geometric damping coefficient can be determined analytically by assessing the type of wave involved and the source type. For radial surface waves $n = 1/2$ while radial body waves within the medium decay with $n = 1$.

To confirm the ground motion response calculated by a FE model, the arrival times and geometric damping of the wave fields can be studied. A homogenous half-space was simulated by creating a half-sphere model with no reflection of waves incident to the spherical boundary. In view of symmetry the model could be further simplified to a quarter half-space with symmetric boundary conditions on the vertical surfaces. A single vertical excitation force was applied uniformly within a circular area at the origin with a time dependent factor given

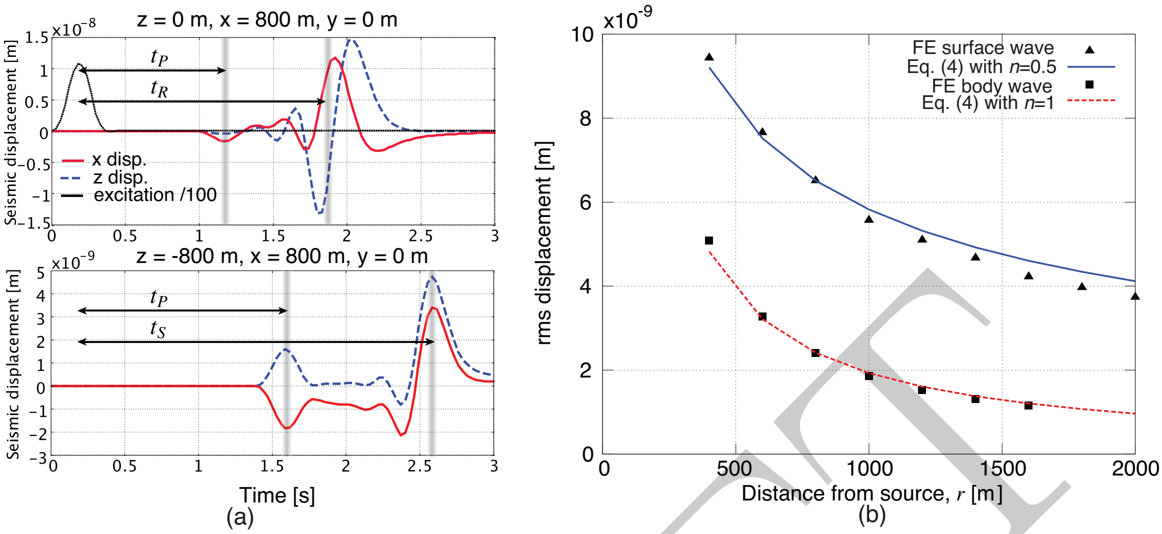

Figure 48: (a) FE ground displacement measurements at a surface and subterranean location after a pulse excitation. P, S and Rayleigh wave arrival times are indicated. (b) The FE results for the rms amplitude of the surface and body waves with increasing distance from the source. The geometric damping contribution to Eq. (69) is plotted for comparison.

by $F(t) = A\sin^2(\pi t/T_e)$ for $0 \le t \le T_e$ where T_e is the excitation period. The amplitude scaling factor, A, was adjusted to create a vertical displacement at the excitation point of 1 μm.

The model has parameters $E = 10$ GPa, $\rho = 2.0$ g/cm^3, $\nu = 0.25$ and a radius of 2.2 km. This results in wave speeds of $c_P = 800$ m/s, $c_S = 462$ m/s and $c_R = 420$ m/s. No material damping was implemented in this model.

Fig. 48a shows the FE results of seismic displacements along with expected arrival times at a location on the surface and at a depth of 800 m. Note the phase difference of $\pi/2$ between the x and z displacements of the Rayleigh wave. The rms wave amplitude with increasing distance from the source across the surface and within the medium are plotted in Fig. 48b. As expected from Eq. (69) the wave attenuation is proportional to $1/\sqrt{r}$ along the surface and $1/r$ within the medium.

With the above model, we can calculate the NN for a given distribution of masses, which can be described by the mass density function $\rho(\mathbf{r}, t)$. The resulting acceleration, experienced by a test mass (i.e. an interferometer mirror) located at $\mathbf{y}$, can be written as

$$\mathbf{a}(\mathbf{y}, t) = G \int_V \rho(\mathbf{r}, t) \frac{\mathbf{r}'}{|\mathbf{r}'|^3} dV, \tag{70}$$

where $\mathbf{r}$ is the position of the mass volume dV and $\mathbf{r}' = \mathbf{r} - \mathbf{y}$. In our FE analysis the acceleration is the summation of the contributions from each node i with mass m_i located at $\mathbf{r}_i$. The acceleration at the test mass is given by

$$\mathbf{a} = \sum_i \mathbf{a}_i = \sum_i G m_i \frac{\mathbf{r}'}{|\mathbf{r}'|^3}, \tag{71}$$

with G the universal gravitational constant. When a seismic disturbance is present, the nodes suffer a displacement denoted by $\xi_i(\mathbf{r}, t)$. The gravity gradient acceleration due to these displacements is given by

$$\mathbf{a}^{NN}(\mathbf{y}, t) = \sum_i (\nabla \otimes \mathbf{a}_i)^T \xi_i(\mathbf{r}, t). \tag{72}$$

Note that in the gravity gradient calculations presented here, the mass associated with each node is assumed to be constant. The corresponding analytical expression can be obtained by substituting $m_i \to \rho dV$ and evaluating the resulting integral.

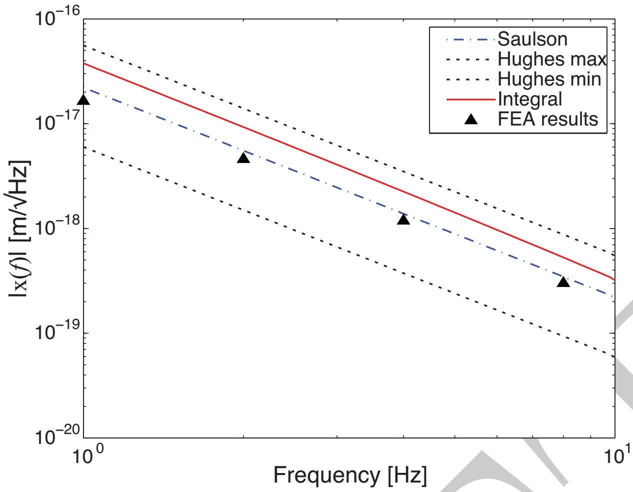

Figure 49: FE calculation of the Newtonian displacement noise amplitude for a surface detector. For comparison the results of Saulson, Hughes and Thorne, and the analytic integral are shown.

The calculation of GGN via FE models was validated by creating simple rectangular homogenous half-space models, equivalent to those discussed by Saulson for a surface detector [256]. The isotropic, elastic half-space with $\rho = 1.8$ g/cm^3, $\nu = 0.33$, $c_P = 440$ m/s and $c_S = 220$ m/s was excited on one boundary to yield plane harmonic pressure waves scaled to a flat ambient seismic noise spectrum of 1 nm/$\sqrt{\text{Hz}}$ between 1 and 10 Hz and the subsequent nodal displacements were recorded as a function of time. Boundary conditions were set such that no reflections occurred and seismic waves were continuous. With this input spectrum the gravity gradient displacement noise amplitude at the interferometer output was calculated and the result is shown in Fig. 50a and b. The FE results are compared with the analytic results of Saulson and Hughes and Thorne [256][258]. To facilitate comparison, an integral cut-off radius equal to that used in Saulson's analysis ($r_{\text{cutoff}} = \lambda/4$) was employed in the summation process. Fig. 49 shows that good agreement is obtained. To assess the effect of this cut-off the above model was calculated analytically with Eq. (72). Removing the cut-off leads to an increase of GGN by about a factor 2. The FE results approach those of the analytic expression in the limit that r_{cutoff} decreases to zero.

The pulse excitations and the half-sphere model described earlier, were used to investigate FE gravity gradient modeling (see Fig. 50). The nodal displacements were recorded as a function of time and the GGN was calculated at various depths on a vertical line at a distance $\lambda_P = 800$ m from the z-axis. In order to artificially separate the contributions of the surface and body waves to the GGN acceleration the nodes with a depth less than 200 m were summed separately to those deeper that 200 m. The respective surface and body contributions were combined to give a total acceleration. Note that for times shortly after the excitation, this distinction is not precise. The results for a test mass at the surface and a test mass at a depth of λ_P are shown in Fig. 50. Only the GGN acceleration in the horizontal direction is shown since it has the largest effect on the performance of an interferometer. The expected arrival times of the different waves are indicated in the figures and show that the Rayleigh wave dominates the GGN contribution of a detector on the surface. At a depth of λ_P the arrival of the S and P-waves can clearly be distinguished, the S-wave producing a larger contribution, attributed to the larger seismic displacements seen in Fig. 47a. The GGN contribution of a wave is initially negative as the wave approaches then changes sign as the wave passes by the test mass. It is interesting to note that the sign change of the surface contributions between a surface and underground detector. This is due to the sign change of the horizontal component of the Rayleigh wave for depths larger than $0.2\lambda_R \approx 80$ m. The figure also shows that GGN builds up before any seismic disturbance actually reaches the test mass and for short times is only dependent on surface contributions.

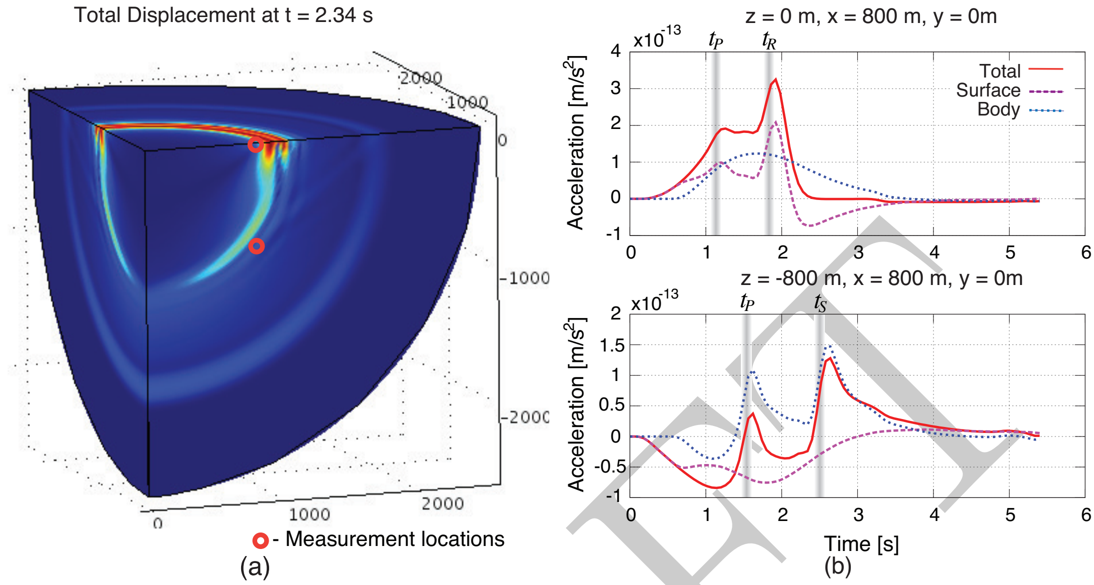

Figure 50: (a) Total displacement for a time domain simulation at 2.34 seconds after a 1 μm pulse excitation at the center of the half-sphere. (b) Time domain evolution of GGN acceleration at a surface (z=0 m) and underground (z=-800 m) test mass. Only the horizontal component of the GGN acceleration is shown. Arrival times of Rayleigh, S and P-waves are also indicated.

3.4.3 Ambient NN subtraction

Responsible: G. Cella

A possible approach to the problem of NN mitigation is its subtraction. The basic idea is to exploit the expected correlation between NN and a set of auxiliary quantities which are continuously monitored [265]. The natural candidates for these are seismic displacement, and we can imagine a basic scenario where a set of sensors (let's say displacement sensors) record several time series. We will consider here the simplest scenario, namely we suppose that the relevant quantities are stationary in a statistical sense. The time series recorded by the I-th sensor will be $X_I = s_I + \sigma_I$, where s_I is the seismic displacement evaluated at the sensor's position and σ_I its instrumental noise.

We will write the output of the interferometer as $Y = H + N$, where N is the NN and H the remaining part, which we suppose uncorrelated with the seismic motion. A simple way to state the problem is asking what is the linear combination of the interferometer's and sensors' time series

$$Y_s = Y(\omega) + \int d\omega' \sum_I \alpha_I(\omega, \omega') X_i(\omega') \tag{73}$$

which we can call subtracted signal which minimize the power spectrum at each frequency. The minimization variables are the functions $\alpha_I(\omega)$, which clearly represent linear filters that must be applied to the output of the sensors before adding them to the interferometer's data. The power spectrum $S_{Y_sY_s}$ of the linear combination

Eq. (**??**) is related to the correlation

$$\begin{aligned}\langle Y_s(\omega)^* Y_s(\omega)\rangle = \langle Y(\omega)^* Y(\omega)\rangle \quad &+ \quad \int d\omega'' \sum_l \alpha_l(\omega,\omega'')^* \langle Y_l(\omega'')^* Y_l(\omega')\rangle \\ &+ \quad \int d\omega'' d\omega''' \sum_{I,J} \alpha_I(\omega,\omega'')^* \alpha_J(\omega',\omega''') \langle Y_I(\omega'')^* Y_J(\omega''')\rangle \\ &+ \quad \alpha_l(\omega',\omega'')\langle Y(\omega)^* Y_l(\omega'')\rangle \end{aligned} \tag{74}$$

and minimizing this expression with respect to $\alpha_K(\omega',\omega'')^*$ we obtain a set of linear integral equations for the optimal filters

$$\langle X_K(\omega'')^* Y(\omega')\rangle + \sum_J \int d\omega'' \langle X_K(\omega'')^* X_J(\omega''')\rangle \alpha_J(\omega',\omega''') = 0 \tag{75}$$

In principle the expressoin of α_J's can be obtained by finding the inverse of the kernel $K_{KJ}(\omega,\omega') \equiv \langle X_K(\omega)^* X_J(\omega')\rangle$, formally

$$a_I(\omega',\omega) = -\sum_K \int d\omega'' K^{-1}_{IK}(\omega,\omega'')\langle X_K(\omega'')^* Y(\omega')\rangle \tag{76}$$

If non stationary noise is present, we should define what is the relevant quantity that must be maximized, as the definition of the optimal apparatus sensitivity cannot be given it term of noise spectrum only. In the stationary case we can write

$$\langle X_I(\omega)^* Y(\omega')\rangle = 2\pi\delta(\omega-\omega')C_{SN\,I}(\omega) \tag{77}$$

Here the I, J entry of the array C_{SS} is the cross correlation between the seismic noise measured by the Ith and Jth sensors. Similar $C_{\Sigma\Sigma IJ}$ is the correlation between the intrinsic noises of the Ith and Jth sensors. Finally,

$$\langle Y(\omega)^* Y(\omega')\rangle = 2\pi\delta(\omega-\omega')[C_{NN}(\omega) + C_{HH}(\omega)] \tag{78}$$

is the decomposition of interferometer's power spectrum in a NN contribution plus all which is uncorrelated with it. Putting all this inside Eq. (76) and 74 we get the optimal filters

$$\alpha_I(\omega,\omega') = -\delta(\omega-\omega')[C_{SS}(\omega) + C_{\Sigma\Sigma}(\omega)]^{-1}_{IJ}[C_{SN}(\omega)]_J \tag{79}$$

which in the stationary case considered are time invariant, and the amplitude efficiency $\epsilon(\omega)$ of NN subtraction, which we define in terms of the ration between the power spectra of the subtracted ($S_{Y_S}(\omega)$) and un-subtracted ($S_Y(\omega)$) interferometer's signal spectral amplitude

$$1-\epsilon(\omega) = \sqrt{\frac{S_{Y_S}(\omega)}{S_Y(\omega)}} = \sqrt{1 - \frac{C^{+}_{SN}(\omega)[C_{SS}(\omega) + C_{\Sigma\Sigma(\omega)}]^{-1}C_{SN}(\omega)}{C_{nn}(\omega)}} \tag{80}$$

Note that $(1-\epsilon)^2$ gives the ratio between the power spectra of the NN contained in the subtracted and un-subtracted signal.

Equation (80) tells us that to achieve a good subtraction efficiency three conditions are needed. First of all the sensors should be coupled as much as possible to NN, in other words C_{SN} must be as large as possible. Second, the intrinsic noise of the sensor described by $C_{\Sigma\Sigma}$ should be small. Third, the correlation between quantities measured by different sensors, described by C_{SS}, must also be low. It is important to observe that the second term below the square root is always positive, so the procedure will never reduce the sensitivity at each frequency.

The quantities C_{SS}, C_{SN} and C_{NN} can be estimated using a given model. C_{NN} is clearly given by Eq. (**??**), and C_{SS} by Eq. (**??**). A similar formula can be derived also for C_{SN} . Note that only C_{SS} can be measured easily, so there is no real hope to fully test the subtraction procedure without building a NN sensitive detector.

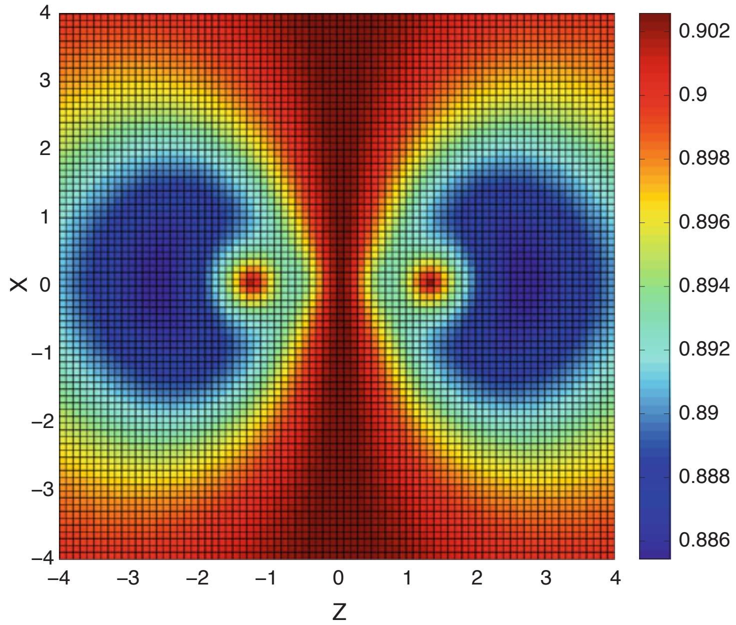

Figure 51: The percentage reduction of NN on a single test mass with three sensors, for the model described by Eq. (74). The test mass is at the origin of the coordinate system, and the sensors measure the local density fluctuations. NN acceleration is sensed along the z axis. Two sensors are fixed at their optimal positions, which are located at the circular spots at $(x, z) = (0, \pm)$. the quantity $1 - \epsilon$ (see Eq. (73)) is plotted as a function of the position of the third sensor. There is axial symmetry around the z axis, so only the $x - z$ plane is displayed.

One issue to be investigated is connected with the optimal way in which the set of sensors available must be displaced on the field. This can be studied theoretically using a given model, and optimizing Eq. (80) over the positions and the orientations. For illustrative purposes we report the results of a simple optimization study, done using a model with seismic correlations characterized by a single (frequency dependent) correlation length $\xi(\omega)$.

We consider a single test mass inside an infinite medium, and we suppose that each sensor can monitor the mass density ßuctuation at its position. The ith sensor is also affected by a intrinsic noise $\sigma_i(f)$, without correlations between $\tilde{\sigma}_i$ and $\tilde{\sigma}_j$ when $i \neq j$. We model the density ßuctuations as a Gaussian stochastic field described by an exponential cross correlation function

$$\langle \tilde{\rho}(\omega, \mathbf{x})^* \tilde{\rho}(\omega', \mathbf{x}')^* \rangle = 2\pi\Gamma(\omega)^2 \delta(\omega - \omega') \exp\Big(-\frac{|\mathbf{x} - \mathbf{x}'|}{\xi(\omega)}\Big) \tag{81}$$

The correlation functions relevant for the subtraction are easily evaluated, obtaining

$$\begin{aligned} C_{SS}(\omega)_{IJ} + C_{\Sigma\Sigma}(\omega)_{IJ} &= \Gamma(\omega)^2 \exp(-|\mathbf{u}_i - \mathbf{u}_j|) + \sigma^2(\omega)\delta_{IJ} && (82) \\ C_{SN}(\omega)_I &= 4\pi\xi G\Gamma(\omega)^2 \cos\theta_I \Psi(u_I) && (83) \\ C_{NN}(\omega) &= \frac{16}{3}\pi^2\xi^2 G^2 \Gamma(\omega)^2 && (84) \end{aligned}$$

where $\mathbf{u}_I = \xi^{-1}\mathbf{r}_i$ is the position of the I-th sensor measured in ξ units, θ_I the angle between the axis along which the Newtonian acceleration is measured and the sensor's position vector and

$$\Phi(u) = \frac{1}{u^2}\Big[2 - e^{-u}\Big(2 + 2u + u^2\Big)\Big] \tag{85}$$

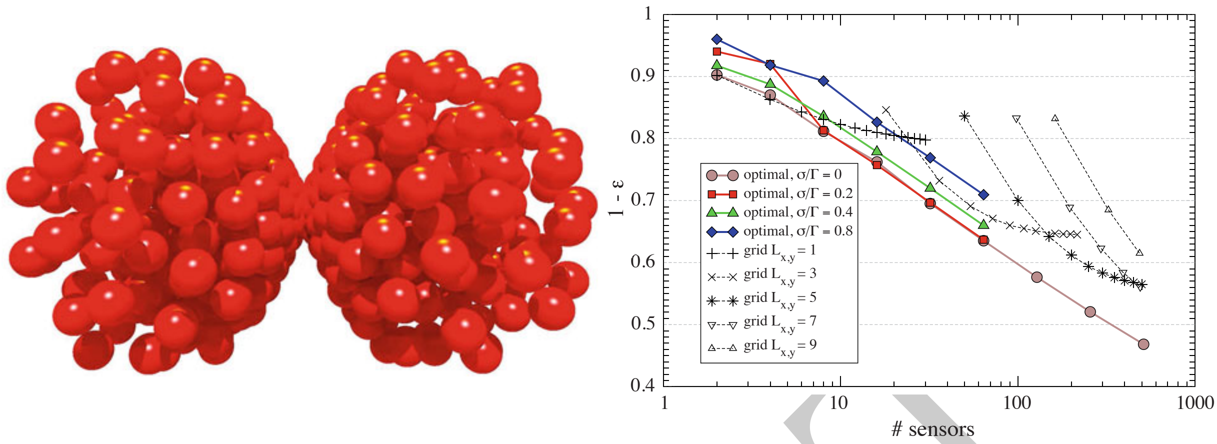

Figure 52: Left). The optimal positions for 512 sensors, evaluated accordingly with the model (74). Each sensor is supposed to measure the local fluctuation of density, and is represented as a sphere with the center on its position and radius ξ. The single test mass considered is at the center of the two clouds, and the NN is measured along the approximate axis of symmetry of the distribution. Right). The percentage of NN on a single test mass as a function of the number of auxiliary sensors, accordingly with the model (74). The sensors are supposed to measure the local fluctuation of density. Solid lines correspond to optimal configurations, evaluated for different intrinsic noises of the sensors. Dashed lines correspond to regular grids with sizes $L_x = L_y$ and L_z. The grid is centered on the grid and the number of sensors given by L_x, L_y, L_z. The NN is sensed along the z axis, and $\sigma = 0$ in this case.

For a given arrangement of the sensors Eq. (80) becomes

$$1 - \epsilon = \sqrt{1 - 3\left(e^{-|\mathbf{u}_I - \mathbf{u}_J|} + \frac{\sigma^2}{\Gamma^2}\delta_{IJ}\right)^{-1} \Phi(u_I)\Phi(u_J)\cos\theta_I \cos\theta_J} \tag{86}$$

With two sensors only the optimal positions are on the Newtonian acceleration axis, at a distance $d \simeq \pm 1.281\xi$ from the est mass (we will consider only the $\sigma = 0$ case). The $\cos\theta$ factor is maximized along the axis, while $\Phi(u)$ has a maximum at $u \simeq 1.451$. In this optimal case $1 - \epsilon \simeq 0.902$. If we add a third sensor, we can evaluate $1 - \sigma$ as a function of its position, which the other two fixed. This is represented in figure 51, assuming that the NN is measured along the z axis. We can see how the subtraction efficiency changes with the position of the sensor, measured in unit of the correlation length. There is no improvement if we put the third sensor near the others, due to the complete correlation of the new measurement with the others. We do not gain anything from far from the test mass or at $z = 0$, because in this case the measure is uncorrelated to NN. the best positions are along the z axis, at a distance roughly doubled from the center.

The model is quite crude so these are only indicative results, which however shows one expected feature. The separation between the sensors must be optimized accordingly with the typical correlation length ξ of the contributions to NN we want to subtract, which depends on the frequency band where the subtraction is needed.

Another important point to understand is how the subtraction procedure improves with the number of sensors, and how much it is sensitive to a non optimal placement of the sensors. This is important because in a practical implementation the possibility of optimizing the placement will be limited, especially if the number of sensors will be large. It must be remembered that the optimization of the sensors' positions is a global process and all the parameters must be changed at the same time.

Remaining in the framework of the simple model considered we optimized Eq. (86) for a different number of sensors. We used a simulated annealing procedure to be reasonably sure to find a global minimum. A typical result for the optimal configuration of the sensors is shown in the left illustration of Fig. 52. We considered 512 sensors, adjusting their positions. Each sphere in the plot has a radius length ξ, and is centered on a sensorÕs

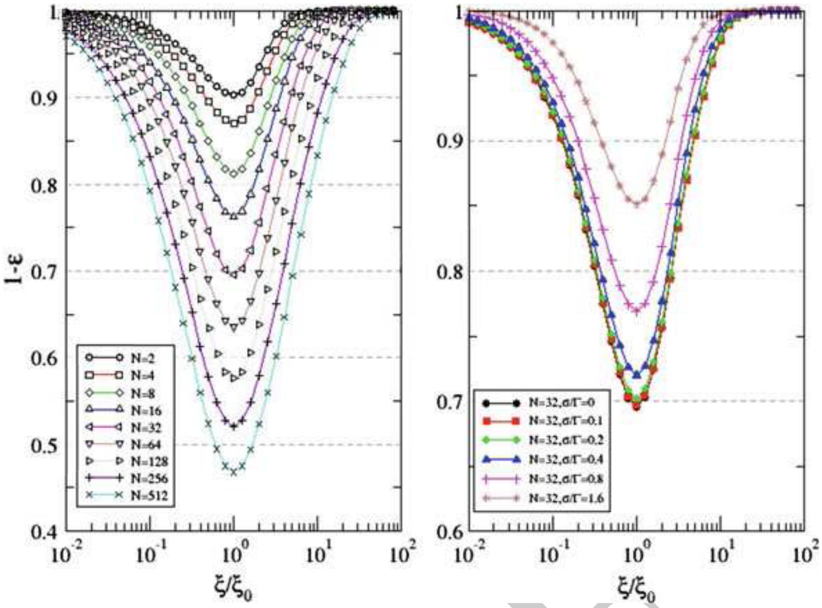

Figure 53: On the left, the reduction of NN for a configuration of the sensors optimized for $\xi = \xi_0$, as a function of the ratio $\xi(\omega)/\xi_0$, where $\xi(\omega)$ correspond to the observed frequency. The different plots correspond to different number of sensors. On the right, for N =32 sensors in the configuration optimized at $\xi = \xi_0$, the reduction of NN is plotted as a function of $\xi(\omega)/\xi_0$. The different plots correspond to different values of the intrinsic noise of the sensors.

position. We see that the spheres attempt to cover the region which is maximally coupled to NN acceleration (the test mass is between the two clouds), but they attempt also not to overlap in order to minimize the correlation between sensors. Fig. 8 correspond to the optimal configuration in the $\sigma = 0$ case. We do not show similar plots for $\sigma > 0$, however in that case we found that the overlap between the spheres increases with σ/Γ. This is expected because in that case a correlation between detectors can be compensated by the average of intrinsic noises.

In the right plot of Fig. 52 we show the relative reduction of NN as a function of the number N of auxiliary sensors. The reference plot is labeled with circles, and it corresponds to the optimal configuration in the $\sigma = 0$ case. We see that the reduction of NN is quite modest, and improves slowly with N. This is partly due to the chosen model, which is quite bad from this point of view, a scan be seen with the following argument. Each sensor can be used at best to subtract the contribution to the NN of a sphere of radius ξ centered on it. The number of non overlapping spheres at distance ξ from the test mass scales as n^2, while the contribution of each of them to NN scales as n^{-2}. We have to sum all the contributions in quadrature, so i fall the spheres with $n < N$ are monitored we expect for large n that $1 - \epsilon \sim \sqrt{\sum_k^\infty k^{-2}} \sim n^{-1/2}$ or as the number of sensors N_s scales as n^3, $1 - \epsilon \sim N_s^{-1/6}$.

Different models are expected to allow better subtraction performances, especially when the loss of coherence described by the scale ξ is less relevant. This could be the case in some geological scenarios, while in others the simplified model presented can give an adequate description. It is an important issue, which is currently under careful investigation.

Coming back to the right plot in Fig. (52), the plots labeled with squares, triangles and diamonds gives $1 - \epsilon$ for the optimal configuration in presence of some amount of instrumental noise. As expected there is a reduction of the subtraction performances. Finally, we showed in the same figure for comparison the results which can be obtained with a non optimal configuration, namely a regular grid of detectors with different sizes $L_x = L_x$ and L_z , centered on the test mass. The optimization here is done only on the grid size, and $\sigma = 0$. The best regular grids correspond to the shapes which are best overlapped to the region coupled to NN, which means

$L_z > 2L_{x,y}$.

The optimization of the positions of sensors can clearly be done at a given coherence length $\xi(\omega)$, while the subtraction procedure will be applied to an entire range of frequencies (we can assume for definiteness ξ proportional to the frequency). This means that the subtraction will be optimal at a chosen frequency only.

In Fig. 53 (left) we plotted the NN reduction as a function of the ratio $\xi(\omega)/\xi_0$ between the coherence length at the observed frequency and the one ξ_0 which correspond to the optimized sensors' configuration. Different plot correspond to a different number of sensors, and $\sigma = 0$. A sensible reduction of the subtraction performance is evident when ξ changes by one order of magnitude. This reduction is somewhat decreased by a large number of sensors.

The effect of noise can be seen in Fig. 53 (right). Here the number of sensors is fixed at 32, and different plots correspond to different values of σ/Γ. The plot suggest (with some extrapolation) that to achieve an hundred fold NN suppression, rock density (and position) ßuctuations need to be measured in real time with resolution less than 1% of the actual motion (in quiescent times in a quiet location), i.e. $\sigma/\Gamma < 10^{-2}$. Because the available seismometers have been mainly developed to detect seismic events, their sensitivity is just below the normal rock activity level. A well defined subtraction pipeline has to be tested with models in order to give a precise estimate, however our conservative expectation is that seismic sensors 100 times more sensitive must be developed for NN suppression to become useful. Preliminary studies in this direction are being done at Homestake, specifically in the direction of laser strain meters and high sensitivity dilatometers. We expect that these developments, if successful, will also yield important side results in geology.

3.4.4 NN subtraction from periodic sources

Responsible: D. S. Rabeling

Active NN subtraction schemes have been studied both at the LIGO and Virgo laboratories [Beker, Harms, Adhikari]. Methods for active NN subtraction involve placing a witness sensor (seismometer) that monitors the noise source and estimates the noise transfer function by methods of minimising a cost function (difference between the measured noise and the estimated transfer function times the seismometer signal). The cost function that is commonly used in filter design optimisation, is the mean-square error (MSE). Minimising the MSE involves only second order statistics (correlations) and stems from the theory of linear filtering, which has many practical applications. In general, the idea is to recover a desired signal $d(n)$ given a noise observation $x(n) = d(n) + v(n)$ using some linear filter with coefficients $\mathbf{w}$. Minimising the cost function

$$J = E\{e^2(n)\} = E\{(d(n) - \hat{d}(n))^2\} = E\{(d(n) - \mathbf{w}^T\mathbf{x}(n))^2\} \tag{87}$$

with the provisions that the derivative of J with respect to $\mathbf{w}$ and the second derivative to $\mathbf{w}$ are zero and positive respectively, provides the Wiener, or optimal filter solution, which is useful for filter coefficients that are constant in time. If we assume that the seismic spatial distribution, generated by pumps and electricity generators, can be approximated by a Gaussian distributed impulse acting vertically onto the soil, we can use the finite element results to attempt to estimate and subtract the NN from our gravitational wave data channels.

Figure 54 shows the results of a typical time domain NN simulation. The top and bottom plots on the left show the seismic excitation and the resulting displacement amplitudes at the centre of the homogeneous half space and at a depth of 800m respectively. The top and bottom plots on the right of Fig. 54 show the resulting Newtonian acceleration for a test mass placed on the surface of the half space, 800m from the excitation point and the Newtonian acceleration for a test mass placed at a distance of ∼1130m and 800m below the surface. Note that, in both cases, as soon as the excitation occurs a Newtonian acceleration is present at the test mass.

The left and right plots in Fig. 54 can be interpreted as individually measured quantities, *i.e.* a NN signal in our GW detector (right) and a seismic disturbance that is measured at it's source (left). Since the disturbance is impulse like, we can estimate the NN impulse response due this disturbance from this specific source.

Figure 55 shows the time domain estimation and subtraction results obtained using the data displayed in Fig. 54. After the initial Wiener coefficients have been obtained, a periodic signal is placed at the center of the half sphere.

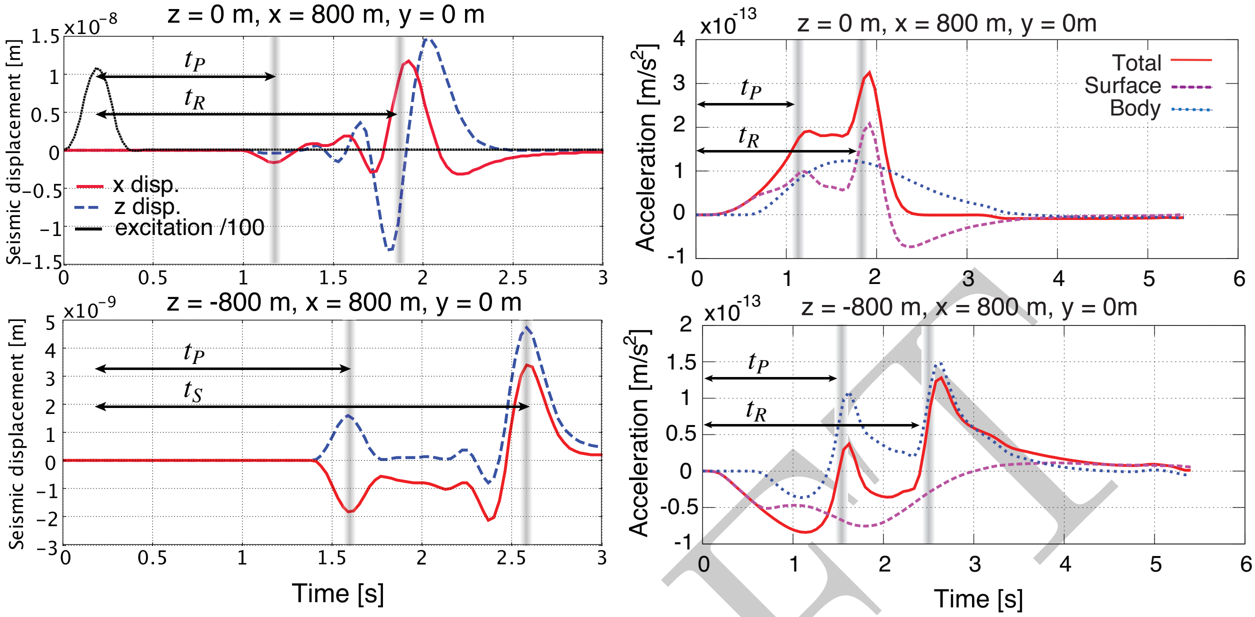

Figure 54: Results of time domain finite element simulations for NN. Top left) Element displacement after a 1 μm pulse excitation at the center of the half-sphere. Bottom left). Element displacement at an underground location (x=800 m, z=-800 m) after pulse excitation at the center of the half-sphere. Top right). Newtonian acceleration at the surface of the half sphere due to a pulse excitation. Bottom right). Newtonian acceleration at an underground location (x=800 m, z=-800 m) due to a pulse excitation.

Using the knowledge of the noise transfer function we can estimate the NN due to the excitation close to the seismic sensor. As can be seen, typical estimates allow subtractions of at least an order of magnitude.

After ET becomes operational, it will be of great importance to minimise localised anthropogenically generated seismicity. This does not stop at restricting access to areas close to the interferometer test masses. Thorne *et. al*. investigated how the interferometer is affected by NN originating from humans, animals, airplanes, etc [266]. Within the subterranean environment this extends to placement of electricity generators, pumps, and cryo-coolers to keep the facility operational. These devices will be sources of seismic noise and will therefore generate continuous NN.

3.5 Site selection

Responsible: D. S. Rabeling

As described in the previous sections, ground motion may prove a limiting factor for the low frequency performance of ET. A preliminary site investigation was carried out to make a comparative analysis of various (underground) locations throughout Europe and across the globe. The following paragraphs will discuss the measurement procedures and a list of locations that have undergone investigation. In order to ascertain all site characterisation procedures were carried according to seismologic standards, measurements and data collection was carried out in collaboration with the Observatories and Research Facilities for European Seismology (ORFEUS) which is maintained by seismology department of the Dutch bureau of Meteorology. This will include a summary of the results from each location as well as the data collected at these sites.

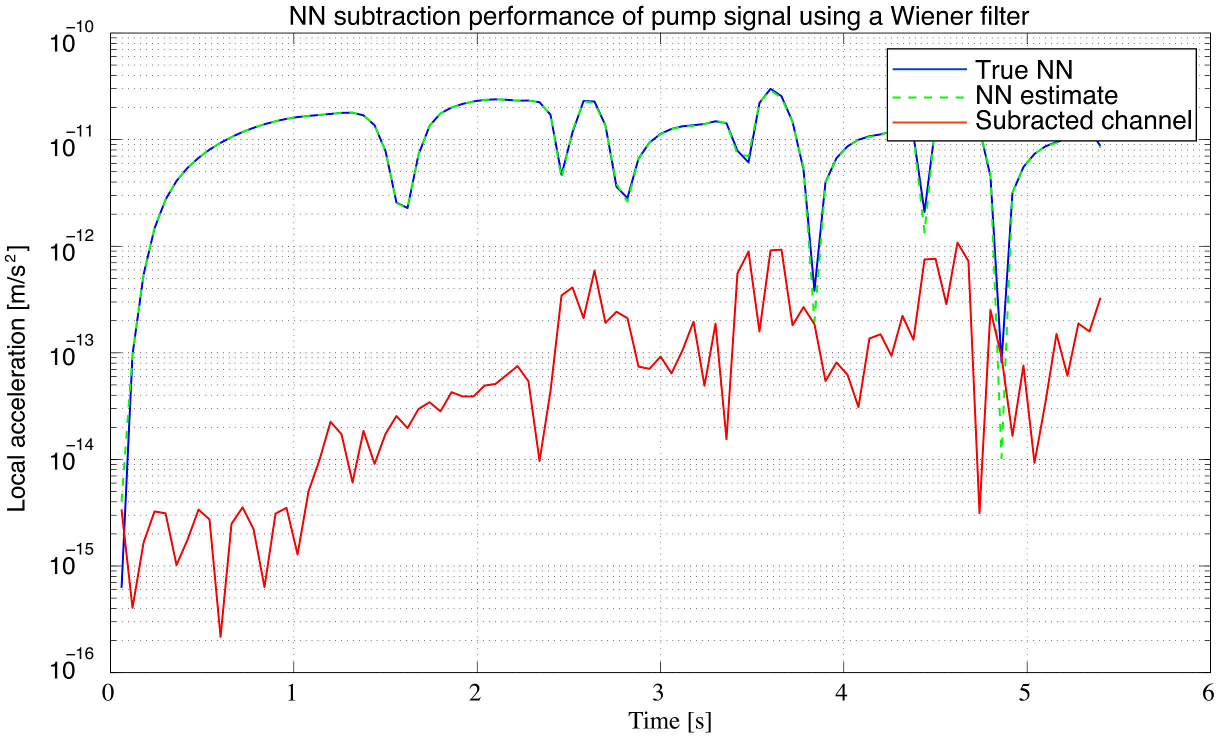

Figure 55: Typical subtraction performance of NN using a Wiener filter. The NN originates from seismic excitations by a pump or electricity generator. NN estimates allow a subtraction of an order of magnitude

3.5.1 Measurement methodology and data analysis

Responsible: D. S. Rabeling

In order to measure the ambient seismic background requires low noise broadband seismometers. All seismic measurements were carried out using two measurement stations, each station consists of a Trillium 240 (T240) accelerometer and a data acquisition system. The T240 is a broadband low noise seismometer with a flat velocity response from 4 mHz to 35 Hz and a self noise below the Low noise model from 0.01 to 10 Hz. The seismometer is placed on top of a granite tile that is fixed to the solid rock floor with tile glue. A thermal and acoustic insulation cover is then placed over the seismometer. The read-out of the seismometers is done using a portable data acquisition system consisting of a 19 inch rack mounted computer with a national instruments 18 bit DAQ card, a low noise amplifier, a battery UPS and a power supply to both the seismometer and amplifier.

The seismometer produces a sensitive measurement of the ground velocity in 3 directions (north, east and vertical) and a number of diagnostic signals. The velocity channels are amplified by a factor of 105 to increase the resolution of the read-out system and passed through a low-pass filter with a -3 dB point at 30 Hz. The sampling rate is 128 Hz and every 128 seconds of data are written away into a single ascii data file using a LabView program.

The noise budget for each seismic measurement station has two major contributors; the self-noise of the T240 and the amplifier and ADC noise. The ADC noise in terms of an acceleration PSD, denoted by $PSD_{noise}(f)$, can be modeled using the following equation [Sleeman].

$$\mathrm{PSD}_{\mathrm{noise}}(f) = \left(\frac{2A}{2^n}\right)^2 \cdot \frac{1}{12 \cdot f_N}, \tag{88}$$

where A is the full-scale amplitude to the input of the ADC, f_N if the Nyquist frequency (related to the sampling frequency, $f_N = f_s/2$) and n the number of quantization levels (or bits). Fig. 56 shows the outcome of Eq. (88) with the seismic stations DAQ parameters ($n = 16$, $A = 10$ and $f_N = 64$), along with the T240 self-noise provided by the manufacturer and the measured DAQ and amplifier noise. The latter was obtained by short-circuiting the amplifier input with a impedance equal to the of the seismometer output (300Ω). The DAQ and amplifier noise is consistent with the expected values from Eq. (88), the dip in measured noise above 10 Hz is due to the seismometer response function. This suggests that this noise source is limited by the ADC noise. The total noise of the system stays below the NLNM between 0.03 and 8 Hz and is dominated by the T240 self-noise, except between 0.3 and 20 Hz.

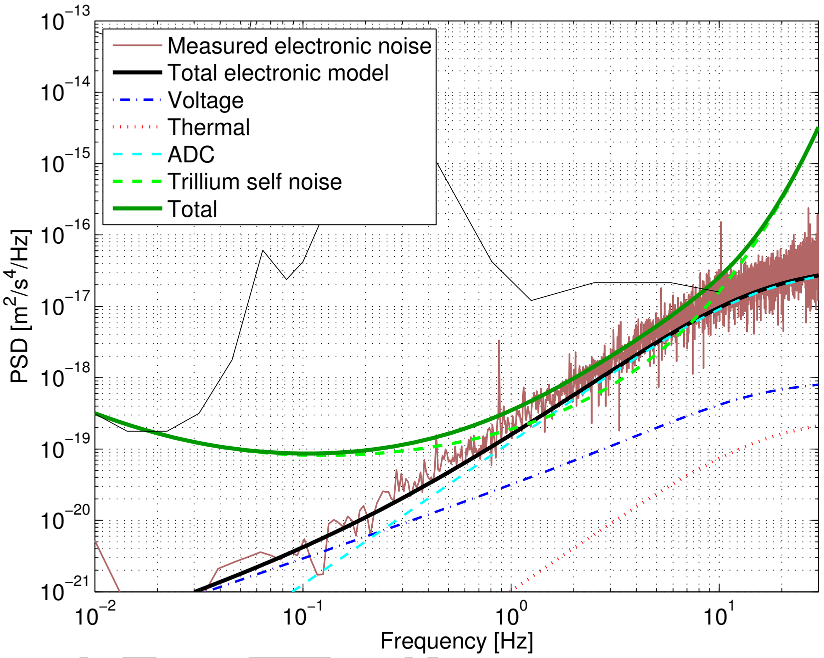

Figure 56: Noise characterization of the seismic data acquisition system. The theoretical DAQ limit is calculated from Eq. 88 and the Trillium 240 self-noise as provided by the manufacturer. The total noise is below the low noise model between 0.03 and 8 Hz.

On site measurements are made over a period of 5 to 6 days. Care is taken to ensure that the measurement time includes at least a weekend and a number of week days. To characterize seismic measurements the amplitude of each frequency component of the velocity channels are calculated using Fourier analysis. In all of the following results a fast Fourier transform (FFT) was performed on stretches of 128 seconds of data to obtain a acceleration PSDs in units of $(\mathrm{m}^2/\mathrm{s}^4)/\mathrm{Hz}$. The PSDs are averaged over a period of half an hour. Averaged PSD values are smoothed by taking the average of the PSD values in a constant relative bandwidth of 1/10 decade. (So for low frequencies the averaging is over only a few points, for high frequencies the averaging is over much more points). A means of comparison is required to give an impression of the relative amplitude of the seismic noise. To do this the new high and low noise models are used. These models indicate theoretical values for extremely high and extremely low seismic noise locations respectively. Spectral variation plots are used here to not only show the amplitude of the seismic signal but also how much time, as a percentage, is spent at a certain level. This is indicated by the color of the plot. The spectral variation plots also contain three solid line plots to indicate the mode and the 90 and 10% levels. The mode is the most common PSD value in each frequency bin, and 90 and 10 % levels indicate the point under which the PSD will stay for 90%, 10% of the time respectively.

3.5.2 Measurement sites

Responsible: D. S. Rabeling

The following section provides a brief description of all locations included within the site characterisation and classification program. The locations that were incorporated are displayed on the map of Fig. 57. The selection criteria for these sites was based on the availability of a suitable underground measuring location. Gaining safe access to underground locations with little or no nearby (underground) activity proved very challenging. The majority of the sites are therefor already existing underground laboratories or decommissioned mines that are undergoing environmental rehabilitation or being converted for tourist purposes. Initial selection procedures were based on general suitability for an ET detector and surface measurement of seismic data. The main purpose of this research was to ear-mark 3 or 4 locations for an extensive seismic and geological study. A followup site selection study would address in more detail the suitability of constructing an ET at or near the location or in similar geological conditions.

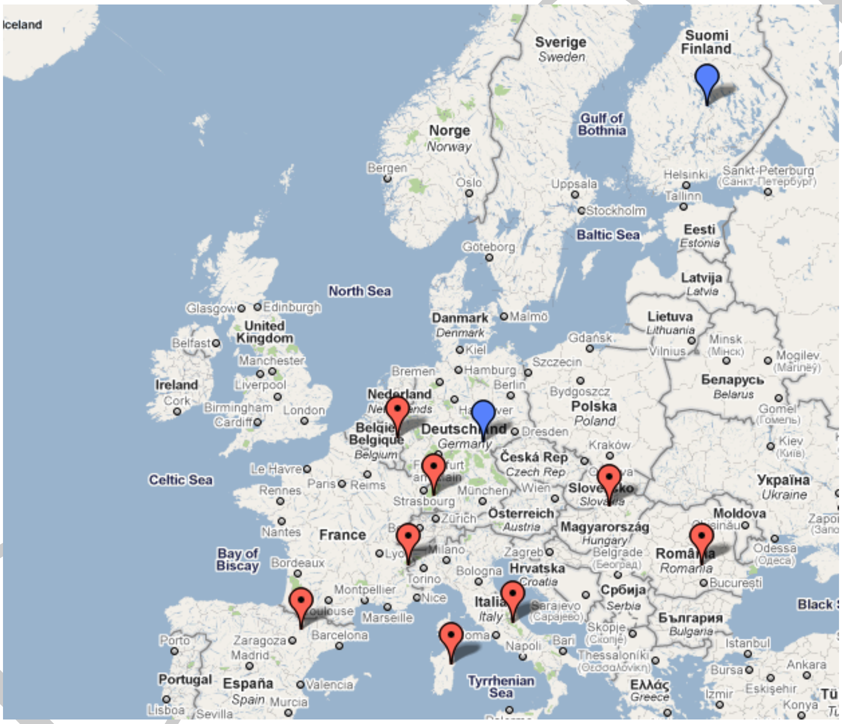

Figure 57: Map displaying the European locations presented in this report. Red icons with a dot indicate locations where measurements where taken at underground locations, blue icons indicate where data was obtained via the Orfeus network from surface installations.

- *Italy: Gran Sasso.* The Gran Sasso National Laboratory is the largest underground combined laboratory in the world for experiments in particle physics, particle astrophysics and nuclear astrophysics. It is located between the towns of L'Aquila and Teramo, about 120 km from Rome. The underground facilities are located on one side of the ten kilometer long freeway tunnel through the Gran Sasso Mountain at an average depth of 1400 m. They consist of three large experimental halls, each about 100 m long, 20 m wide and 18 m high and service tunnels, for a total volume of about 180,000 cubic meters.
- *Italy: Sardinia.* The island of Sardinia is centrally positioned with respect to the European tectonic plate, which results in a seismically much quieter more stable domain than the Italian main land. Measurements were performed in a mine near Lula, 50 km south of Olbia on the north-eastern side of the Island. This former lead-zinc mine is currently being rehabilitated to allow safe passage into the mine for tourists.

- *Italy: Sicilie.* The Italkali salt mine is an active mine situated near the town of Realmonte on the southern coast of Sicily, 10 km east of Agrigento. Salt is excavated by creating large caverns, some exceeding dimensions of 100 m in length and 35m in height. Measurements were taken at a depth of 60 m below the surface, at an elevation of 30 below sea level. Both stations were installed in a storage cavern about 50 meters apart. One seismic station was on a large concrete pad with the other was placed straight onto the salt floor.
- *The Netherlands: Heimansgroeve.* The Heimansgroeve is an old quarry situated at the southern tip of the Netherlands. It contains the oldest rock sort found in the Netherlands, Carboniferious, about 360 - 300 million years old. The stone consists of slate and carbonic sandstone and holds a seismic observatory maintained by The Royal Netherlands Meteorological Institute, some 10 meters below the surface.
- *Hungary: Gyöngyösoroszi.* The Gyöngyösoroszi mine is situated some 107 km North-East from Budapest in the Mátra mountains. This old zinc-lead mine has horizontal access with underground depths ranging from 100 to 350 m at an elevation of ∼400 m. Local rock type consists of andezit and andezit tufa. A ecological rehabilitation of the neighborhood and mine was started last year. The mine contains a number of long straight drifts of which the longest is 3 km. There is a permanent Seismological Observatory of the Hungarian Academy of Sciences at Piszkéstetö on the site of the Konkoly Thege Astronomical Observatory. It is situated about 4 km from the mine entrance.
- *Romania: Slanic.* Slanic-Prahova is located, 40 km NE of Ploiesti, or 100 km north of Bucarest in Romania. The salt layers in the area allow large caverns (30m wide and 35m high) to be dug. The salt exploitation ended in 1971, however another salt mine is still active in the same salt deposit. For the time being the mine contains a low background laboratory in one of the caverns. Access into the mine is via an elevator, able to carry up to 10 tons. The current network of galleries of Unirea salt mine are very large, extending an area of 70 000 m2 with 2.9 million m3 having already been excavated.
- *France: Frejus.* The underground laboratory LSM "Laboratoire Souterrain de Modane", is located along the road tunnel between the Frence Modane and Italy. The overburden at this site is 1700 m of hard-rock or 4800 meters of water equivalent. The LSM, in operation since 1982, already hosts two particle physics experiments requiring an extremely low-background environment to study neutrino properties and to search for Dark Matter.
- *Spain: Canfranc.* The Canfranc Underground Laboratory (LSC, "Laboratorio Subterráneo de Canfranc") is located on the Spanish side of the Pyrenees, under the mountain of "El Tobazo" and has various particle physics programs aimed at very low background experiments for the study of neutrino properties and the search for Dark Matter. It has 2500 m water equivalent overburden at depths of around 900 m and can be accessed via the roadway or decommissioned railway tunnels.
- *Germany: Black Forest.* The Black forest observatory is a geophysical observatory in operation since 1972, owned and operated by Karlsruhe University and Stuttgart University. It is located in an abandoned silver mine and contains gravimeter, seismometers, tilt-meters as well as electromagnetic and weather sensors. The local rock type is granite and the overburden is up to 180 m.
- *Finland: Sumiainen.* The Finish bedrock is amongst the oldest and most stable in Europe, ranging from 3.5 to 2.6 billion years old, making it cheap and relatively trivial to construct underground caverns and tunnels. For this reason much of the infrastructure in Finish cities is built underground. Finland's isolation from major oceans and small population density could prove ideal for a low seismic background environment. No site was visited but data from an already installed surface seismic observatory in central Finland, near Sumiainen, was acquired.
- *Belgium: Mol* Near Mol in northern Belgium an underground laboratory has been constructed to investigate the long-term effects of construction in the "Boomse" clay layer. Clay is impenetrable to water and has self healing properties. For these reasons it has been proposed as an excellent candidate for the long-term storage of highly active nuclear waste. The HADES underground laboratory administered by EURIDICE is situated at a depth of 230 m in a clay layer roughly 150 m thick. In 2002 a new gallery

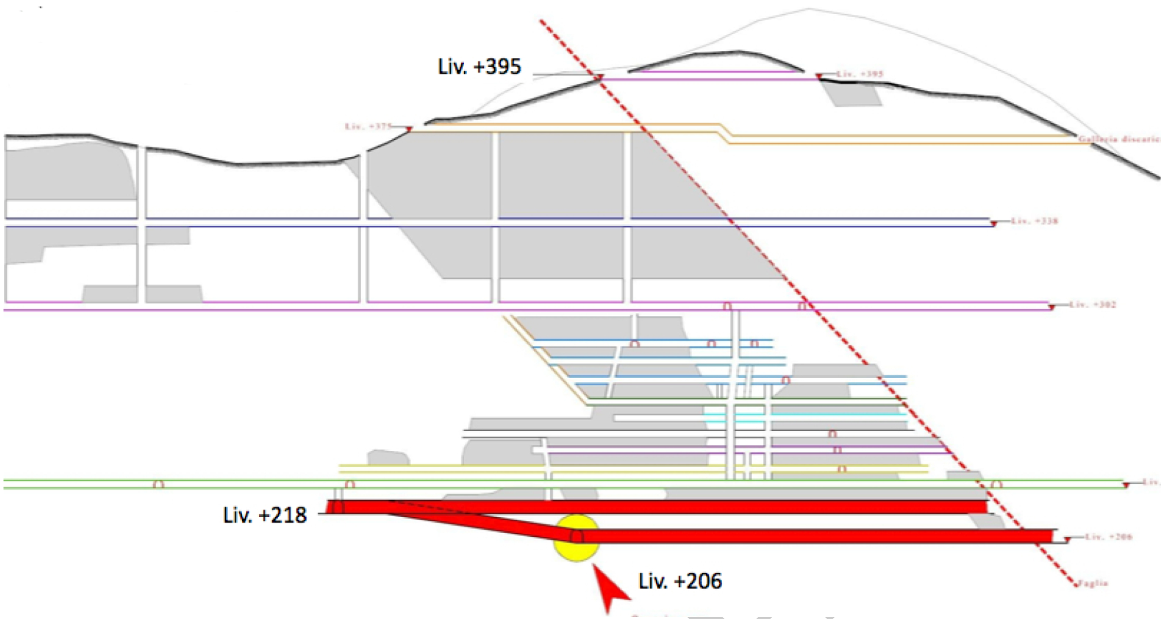

Figure 58: Underground map of the Sos Enattos mine, Sardinia. The yellow spot indicates the measurement location, at an elevation of 206 m and depth of 189 m.

was constructed, in a cylindrical form with a diameter of 4 m and a length of 80 m. A seismic station was setup in the new gallery and measurements were taken during the Christmas break of 2010.

3.5.3 Results from a selection of sites

Responsible: D. S. Rabeling

The following section discusses, in more detail, three sites that have been selected for further investigation. Seismic measurement results will be presented and discussed, then summarized in the following section.

Sos Enattos mine, Sardinia, Italy

The Sos Enattos mine, Lula, Sardinia, is a former lead and zinc mine of schist rocks composed of sphalerite ([Zn,Fe]S) and galena (PbS). It is situated 50 km south of Olbia on the north-western side of the island, 20 m from the coast. A map of the mine is shown in Fig. 58. The experimental areas where the seismometer stations were placed was at a depth of 189 m, at an elevation of 206 m above sea level, which are indicated by the yellow circles in Fig. 58. Data was collected during the period of June 31, to July 5, where the most significant results, obtained by applying the analysis method described in a previous section, are presented below.

The spectral variation plots, data taken from the Sos Anattos mine, are shown in Fig. 59. The primary and secondary microseismic peaks are visible at 0.08 and 0.2 Hz respectively and are within an order of magnitude or touching the low noise model. This is due to the relatively large distance to the atlantic ocean (1000 km to west coast of France). At higher frequencies, between 0.4 and 0.8 Hz an extra "tertiary" microseismic peak can be seen. This is due to similar effects that cause the primary and secondary micro-seismics, but its origin stems from the Mediterranean sea and are typical of other Italian sites [267].

When inspecting the spectrograms in Fig. 60, it becomes clear that, in the frequency range from 2 to 20 Hz, there is a relatively large variation in the spectral density. It is easy to see that PSD variations at these

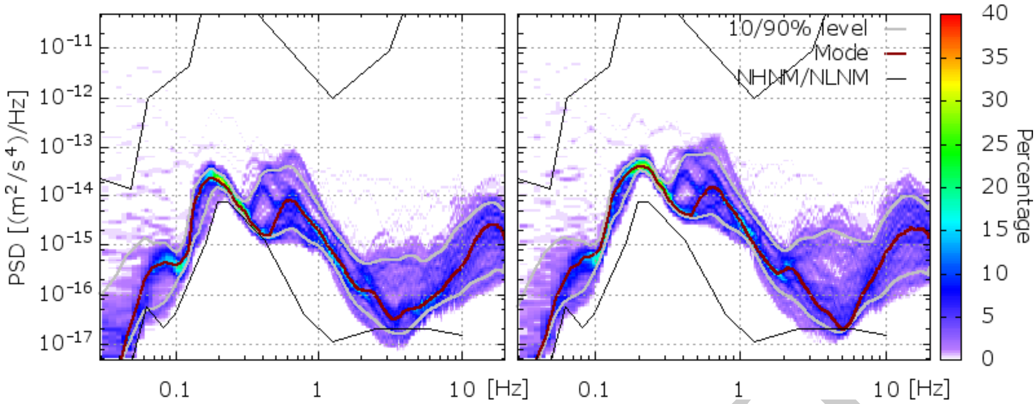

Figure 59: The horizontal (left) and the vertical seismometers component (right) power spectral densities, plotted as a spectral variation from the Italy - Sardinia site. The "tertiary" microseismic peak as a result of microseismics from the Mediterranean sea is evident from 0.4 to 0.8 Hz. Large variations at higher frequency are a results of work in the mine and anthropogenic activity.

frequencies occur according to a daily pattern, indicating that sources of seismic noise at these frequencies are from anthropogenic nature. More over, in the 2 - 8 Hz range the heightened activity seems to occur during the late morning hours before noon, on all days except sunday. This coincides with the miners schedule of underground works and tourist activity during these hours.

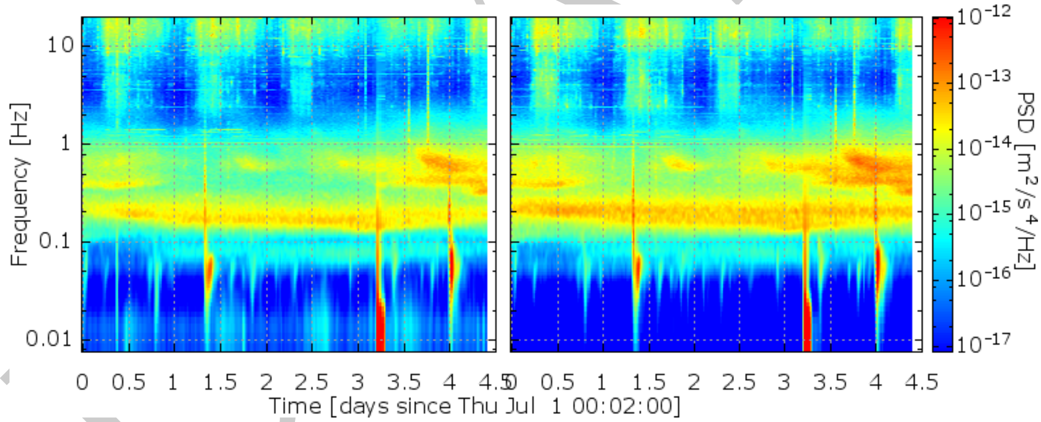

Figure 60: The spectrogram of the horizontal (left) and vertical (right) component from the Italy - Sardinia site. Day and night variation is visible as is the morning underground activity on Thursday, Friday and Saturday.

LSC, Canfranc, Spain

The Canfranc Underground Laboratory is located under the mountain "El Tobazo" in the Northern Pyrenees, along the 8.5 km road tunnel spanning the French-Spanish border. Situated underneath 850 m of rock providing an overburden a 2500 m water equivalent, makes it suitable for low background experiments. Access to the laboratory is via either the road tunnel or the parallel decommissioned railway tunnel.

Seismic measurement stations were set up at two separate locations along the tunnels. The first was just behind the access door to the low background laboratory, running along the railway tunnel. Due to the continuous background activity of pumps and ventilators close to the laboratory, as well as near-by construction work at the main laboratory, the data from this station was deemed unsuitable for background seismic measurements. The second seismometer station was installed in a gallery connecting the road and railway tunnels, which acts as an emergency escape route. The latter location was half way along the tunnel and 1 km away from the laboratory. This meant that this station was suitably removed from human and/or mechanical activity (besides a lightly travelled road tunnel, 50 m away) at a depth of 900 m.

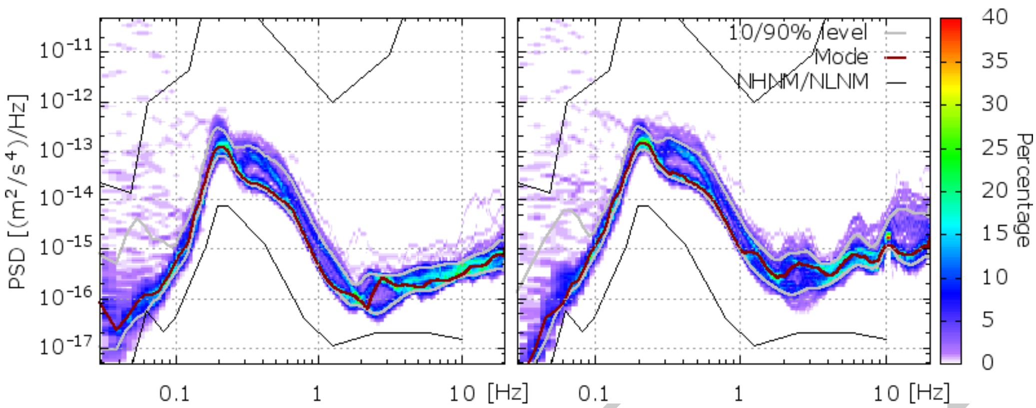

Figure 61: The horizontal component (left) and the vertical component (right) power spectral density plotted as a spectral variation from the Spain - Laboratorio Subterráneo de Canfranc site. The large microseismic peak is a result of the sites proximity to the atlantic ocean. The small spectral variation at high frequencies is due to the low population density of the area.

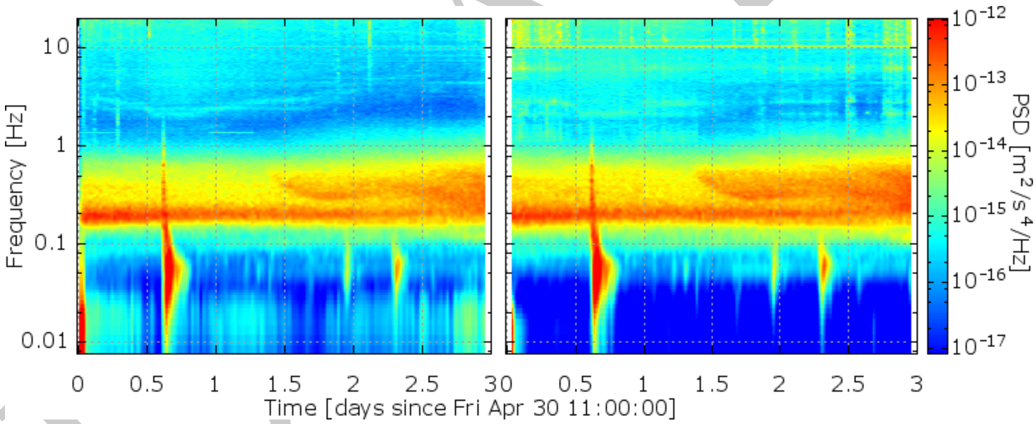

Figure 62: The spectrogram of the horizontal (left) and vertical (right) component from the Spain - Laboratorio Subterrńeo de Canfranc site. No difference in day and night activity is distinguishable indicating there are no anthropogenic sources contributing to seismicity at this site.

The results from the second Canfranc seismic measurements are are shown in Fig. **??** in the form of spectral variation plots. The microseismic peak around 0.2 Hz is evident consistent with the relatively close proximity to the Atlantic ocean. At higher frequencies (2 - 20 Hz), where seismic noise is predominately a results of anthropogenic noise, the seismicity is low. The variation in the PSD values at these frequencies is low, having just half an order of magnitude between the 10 and 90 % levels. In the spectrograms there is no clear day and night variation that usually indicates anthropogenic activity, a results of the very low population density of the area and the considerable depth of the site.

Gyöngyösoroszi mine, Hungary

The Gyöngyösoroszi mine in Hungary is a former lead and zinc mine that is currently being rehabilitated for environmental reasons. This provided an excellent opportunity to enter safely into the mine without any large scale mining activity nearby. The mine is situated 107 km north-east of Budapest in the Mátra mountains at an elevation of 400 m above sea level. The surrounding geology is Andezite. Access into the mine is on a electric locomotive through a horizontal tunnel.

Two separate seismometer stations were installed at locations along the main drifts. At each site the miners had excavated a small hollow into the tunnel wall so that the instruments could be safely installed without being inundated by the small, but steady, flow of water and mud. The first location was 1435 m from the entrance with a rock overburden of 70 m. The second location was 3750 m from the entrance at a depth of 400 m. A permanent seismic station of the Hungarian Academy of Science was situated at the surface, just 2.5 km away from the deepest station. Data was also obtained from this station and compared with the two underground sites. The results were presented earlier in Fig. 45 and show and order of magnitude decrease in seismic noise between the surface and depth locations at frequencies above 1 Hz.

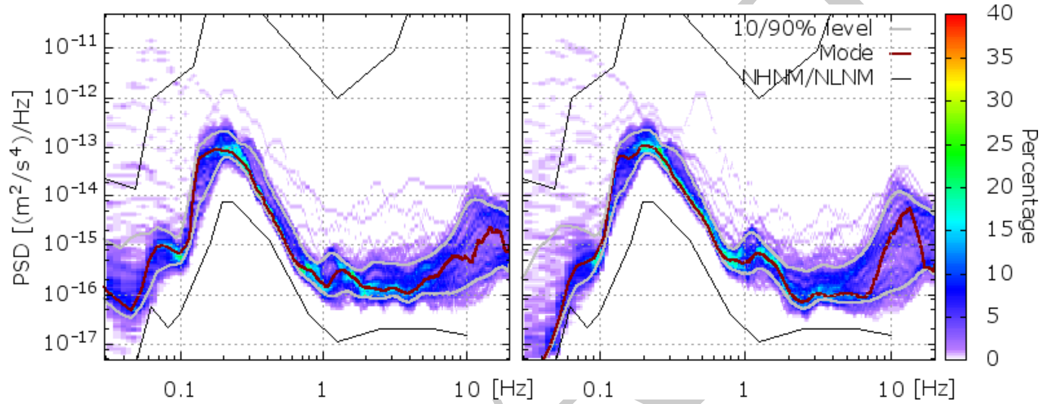

Figure 63: The horizontal component (left) and the vertical component (right) power spectral density plotted as a spectral variation from the Hungary - Gyöngyösoroszi mine site. The microseismic peak drops off quickly providing a low noise at 1 Hz. Large spectral variation at higher frequencies is due to anthropogenic activity.

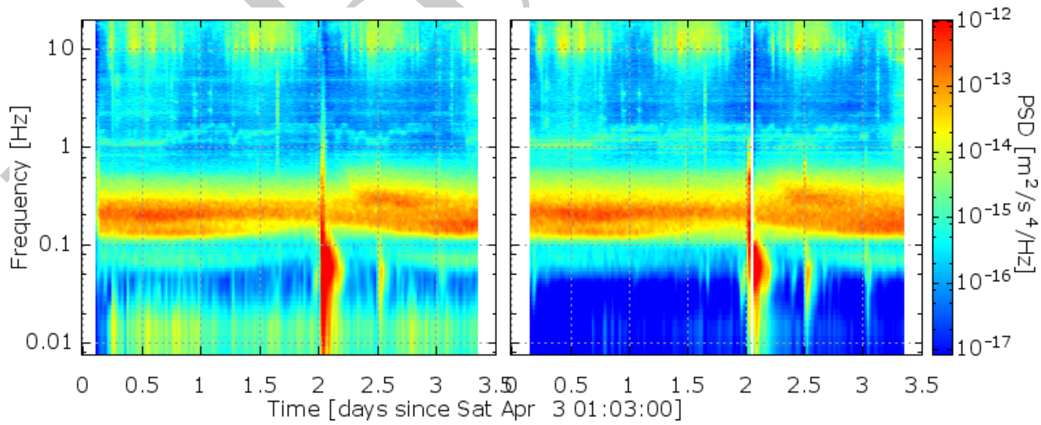

Figure 64: The spectrogram of the horizontal (left) and vertical (right) component from the Hungary - Gyöngyösoroszi mine site. The large event after 2 days is an Earthquake in Mexico with a magnitude of 7.2. Day and night variations due to anthropogenic noise at higher frequencies is still visible.

The spectral variation plot of the Gyöngyösoroszi seismic results are plotted in Fig. 63. The microseismic peak at 0.2 Hz is again obvious and its tail drops off faster than, for example, the Spanish site. From 1 to 8 Hz the acceleration PSD of the horizontal component stays flat and just 1.5 orders of magnitude above the NLNM. At higher frequencies the upper limit of the spectral variation increase by another order of magnitude. This is due to anthropogenic activity that is penetrating down to the measurement site. Evidence of this can be seen in the spectrogram plotted in Fig. 64, where a clear day and night pattern is visible.

3.5.4 Summary of measurement results

Responsible: D. S. Rabeling

The preliminary site investigation set out to explore the possibilities of finding a suitably seismically quiet environment for a third generation GW detector. Seismic measurements were taken at a dozen sites throughout Europe and data was also analyzed from a series of existing seismic observatories. It has been shown in the previous paragraphs that a number of sites can provide consistent low seismic background environments. Three candidate sites where selected according to their seismic suitability. The results of all three sites and results from the site of the existing GW detector Virgo, are plotted for comparison in Fig. 65. It is clear to see that moving to a quiet location can improve seismic disturbance effects by several orders of magnitude. In the case of the Virgo site, up to 5 orders of magnitude improvement in terms of seismic acceleration power. A follow on study is proposed at, or in similar geographical conditions to, these sites to investigate long-term seismic and geological properties and address the issues of housing large underground facilities.

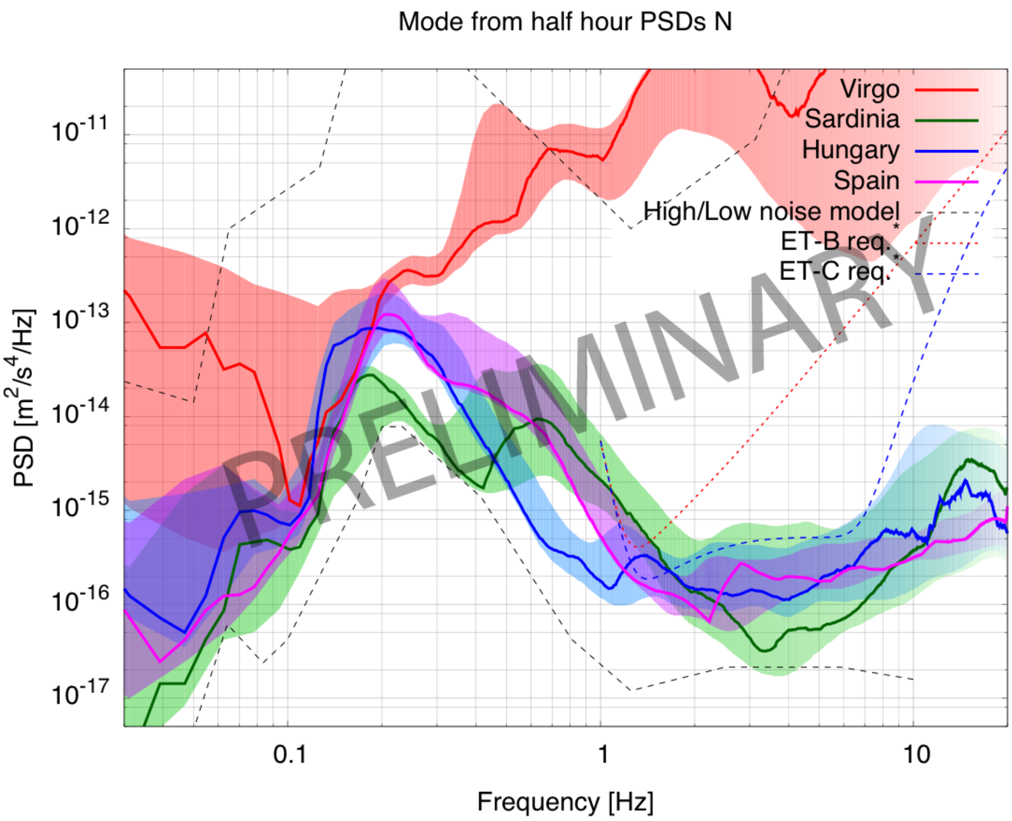

Figure 65: Spectral variation results of the three candidate site, plotted for comparison is the site of the current GW detector Virgo. The solid lines correspond to the mode, while the upper and lower limits of the transparent regions are the PSD levels that weren't exceeded for 90 and 10 % of the time respectively.

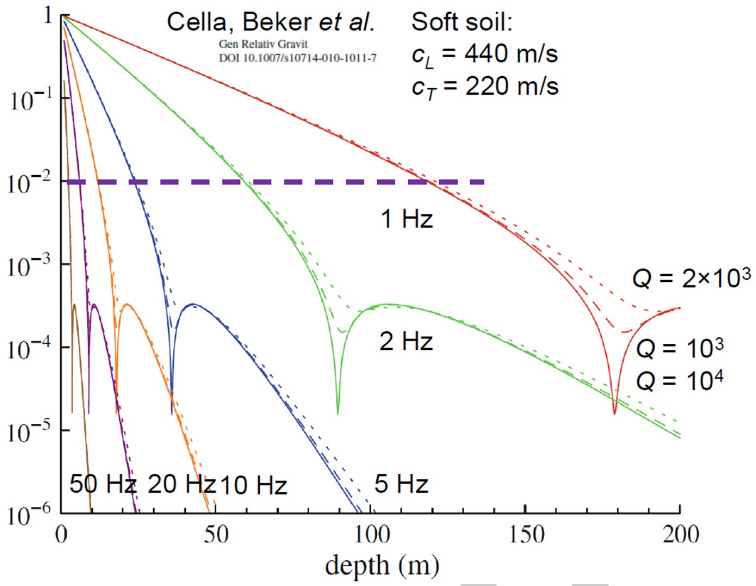

Figure 66: Attenuation factor for gravity gradient noise at an underground location for various depths in soft soil with $c_L = 440$ m/s and $c_T = 220$ m/s.

3.6 Infrastructure realization

Responsible: Jo v/d Brand

Einstein Telescope will have excellent sensitivity of about $10^{-22}/\sqrt{\text{Hz}}$ at low frequency. This is achieved with advanced suspension systems with a frequency cut-off below 1.8 Hz in combination with site locations that feature low seismic noise. Fig. 65 shows that various excellent candidate sites for ET have been identified in Europe. ET will be constructed underground in order to benefit from low seismic and gravity gradient noise. It is well known that the major part of the seismic noise in the frequency range 1 to 10 Hz is generated at the surface. The corresponding GGN is then partly suppressed at underground locations due to surface averaging effects. The GGN attenuation factor is shown in Fig. 66. Dedicated studies [255] show that it will be a challenge to obtain sites with low GGN properties. The calculations show large differences in attenuation between 1 and 2 Hz. The required depth is driven partly by the wave length of the seismic waves. Roughly $\lambda/4$ is required for about a factor of 100 suppression. The wavelength scales with the seismic velocity. While for soft soil typical values of 440 m/s are found for the longitudinal velocity c_L, these values increase to 6000 m/s for hard rock such as granite. Consequently, while the depth of ET could be limited to a few hundred meters when constructed in soft soil, significantly larger depths may be required when considering siting in hard rock. The ET site studies were performed at various underground locations in hard rock (Frejus, Canfranc, Gran Sasso, Sardinia and Hungary in Europe, Homestake in the USA, and Kamioka in Japan), in salt (Slanic Salt Mine in Romania, and Realmonte in Sicily), and in Boom clay (the HADES facility for storage of nuclear waste in Mol, Belgium). The lowest seismic noise was obtained in hardrock. Note that homogeneity and seismic correlation length of the medium are expected to be important parameters for future GGN subtraction schemes.

The realization of ET requires the construction of substantial underground infrastructure. Fig. 67 shows an impression of one of the corner stations. In ET there are three such corner stations connected by 10 km long tunnels. These tunnels house the interferometer arms and have an inner diameter of 5.5 m. In the following we discuss aspects of the construction of the tunnels, underground caverns, and the vertical shafts.

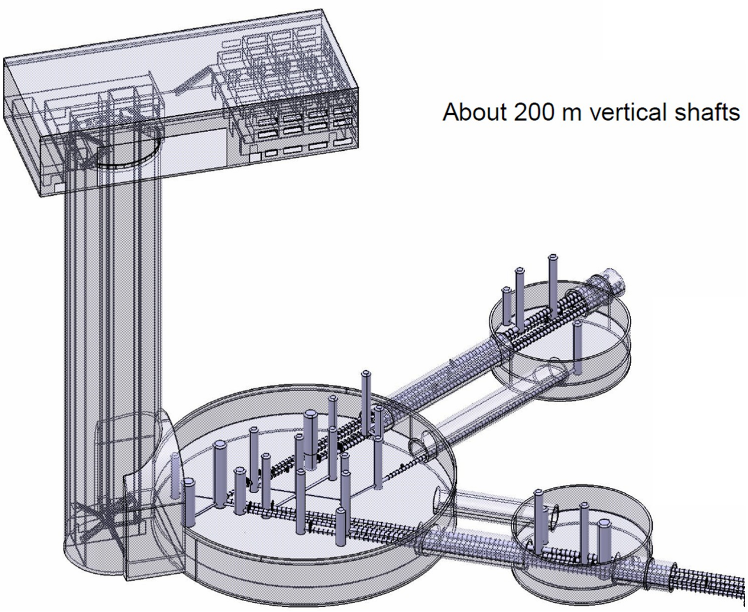

Figure 67: Corner station of Einstein Telescope. In total 3 such corner stations are connected by 10 km tunnels.

3.6.1 Tunnel construction

At present there is a significant worldwide demand for the creation of underground tunnels. For the construction of high speed trains alone, in 2010 about 1000 km of lines is taken in operation, while the current demand for 2020 is estimated at 3500 km [?]. For the construction of underground tunnels, two major technical approaches can be distinguished: tunnel boring machines (TBM) and drill and blast (D&B). Fig. 68 schematically shows the two techniques.

Tunnel construction with TBMs

The TBM technique is state of the art, and excavation rates of 20 - 25 m per day are routinely obtained. The geology must be well understood through site surveys and one must realize that given the large size of the machine (typically 400 m for the TBM and train combination) it is difficult to adapt to changes (for example in geology).

Fig. 69 shows an outline of a gripper TBM from Herrenknecht [268]. This TBM has a 9.58 m diameter and a length of 441 m. A power of 7.8 MW is required to drive the machine. The TBMs needed for ET would have a diameter of 6.5 m.

The investment costs are large (*e.g.* about 20 M€ for the TBM shown in Fig. 69) and set-up times are long. In the case of ET several TBMs would be required in order to keep the construction time limited to 2 years. Sizeable diameters are needed for the vertical shafts in order to lower the equipment. A typical TBM cycle would involve boring 2 m of tunnel, followed by clearing out the rock. The tunnel wall support with anchors, shotcrete and steel arches is then implemented next. Per day shifts 1 and 2 would involve the above cycle, while shift 3 would be dedicated to the service and repair of the TBMs.

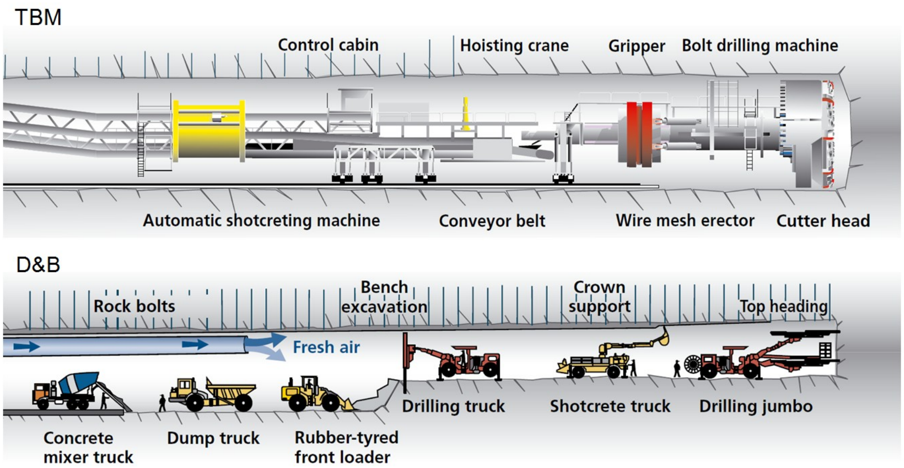

Figure 68: Underground tunnels can be constructed with tunnel boring machines (TBM), or by using the conventional drill and blast method (D&B).

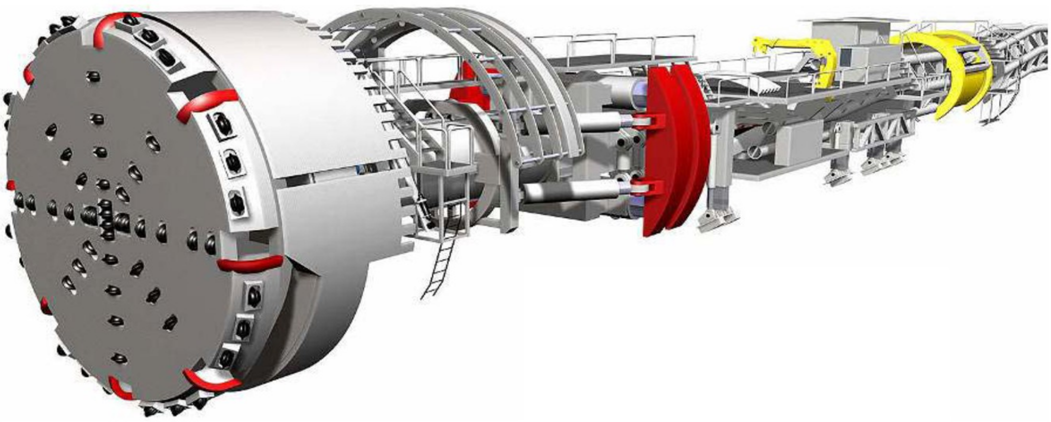

Figure 69: Schematic representation of a gripper tunnel boring machine from [268].

Tunnel construction with D&B

The drill and blast technique is highly adaptable, but excavation rates are limited to 6 - 10 m per day. A cycle consists of drill, charge, and detonate. After ventilation, various tasks as support and muck removal take place. In good rock conditions 1 cycle can be accomplished in an 8 hour shift.

In order to cope with the relatively low advance rate, various teams have to work in parallel. Advanced multi-head drilling tools have been developed (see Fig. 70) in order to increase the advance rate. Fig. 71 shows that support of the tunnel walls can be provided in parallel with the multi-head drilling activities.

Practical experience with tunnel construction

There is a vast amount of experience available with tunnel construction in various soil types and under various conditions. When long tunnels (typically with lengths exceeding 6 km) are considered and smooth walls are needed (*e.g.* for high speed trains) then TBMs are often selected. Underground infrastructure such as train tunnels are designed for a lifetime of about 100 years. Thus, special wall treatment is needed to ensure such a long lifetime.

Figure 70: Special tooling has been developed for the D&B technique for tunneling.

Figure 71: Support of the tunnel walls can be erected in parallel to the drilling process.

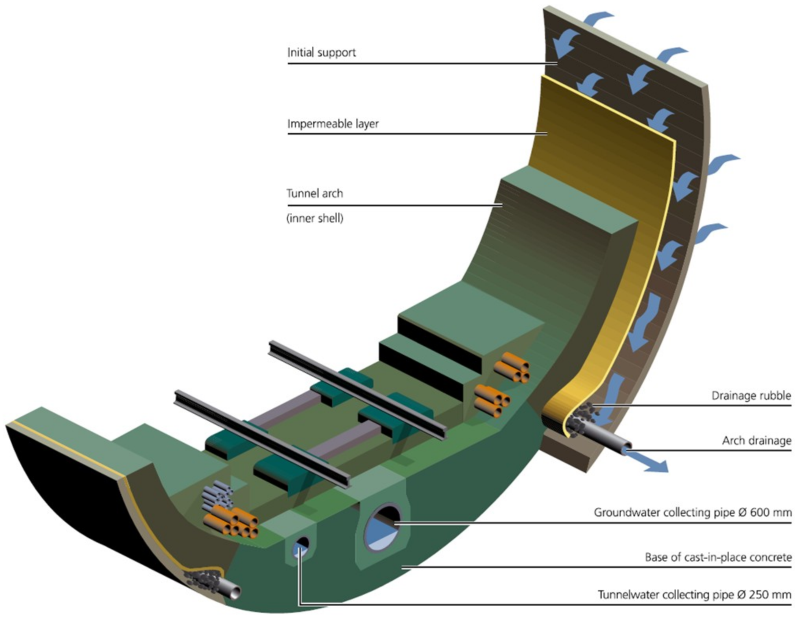

Figure 72: Wall segments used in the construction of the Gotthard-Basistunnel. This project represents the world's largest underground construction.

Fig. 72 shows a wall segment that has been used in the construction of the Gotthard-Basistunnel. The Gotthard-Basistunnel represents the longest tunnel project in the world: a total tunnel length of 98.135 km has been constructed with TBM and 53.705 km with D&B. The lining is designed to handle corrosive water containing chloride, sulphates, *etc.* The impermeable layer avoids swelling of the concrete, corrosion of the anchors, and sintering in the drainage system. The drainage system is designed to prevent groundwater pressure buildup.

Construction of tunnels at large depth has various implications. Fig. 73 shows that in general rock temperature increases with depth. For train tunnels these temperatures can be handled (since the trains act as pistons), but it may cause troubles for ET. Sizeable and costly ventilation systems must be installed. These systems also dilute dust and remove methane and radon (detection systems for these gases must be installed). Other problems encountered in construction at large depth include rockfall, rockbusts and possibly large deformations.

For ET the issue of micro tremors may be significant. In the context of the Gotthard-Basistunnel project, the Swiss Seismological Service, SED, recorded an accumulation of seismic activity in the area of the MFS Faido (see Fig. 74). Events were recorded in the period between March 2004 and June 2005. Normally, this is a region with very low seismicity. A local seismic network was set-up at the multi-purpose station, MFS Faido, consisting of 9 stations at the surface, including one station from the SDSNet. The stations were installed in a circular arrangement 10 to 15 km around the MFS Faido. In addition, 2 seismic stations were placed in the tunnel. The hypo-centers of the micro tremors were reconstruction in 3D. It was clear that this seismicity was related to the underground tunnel construction. The tremors were observed over at least a 2 year period.

Several water dams are located in the vicinity of the Gotthard-Basistunnel. TPS and GPS measuring systems were installed around these dams in order to monitor surface ground motion. Fig. 75 shows that several mm displacements have been measured at these dams. The movements are correlated with the TBM activity at Nalps North and were first observed in December 2005. It is believed that although these dams are several km away from the underground construction, the movements are due to changes induced in the ground-water levels.

In general the construction of the Gotthard-Basistunnel went according to expectations. However, a major problem occurred in 2003 when crossing the horizontal fault zone at Bodio. The TBM got stuck for more than 6 months and had to be excavated. This was possible since the project features 2 tunnels (an East and a West

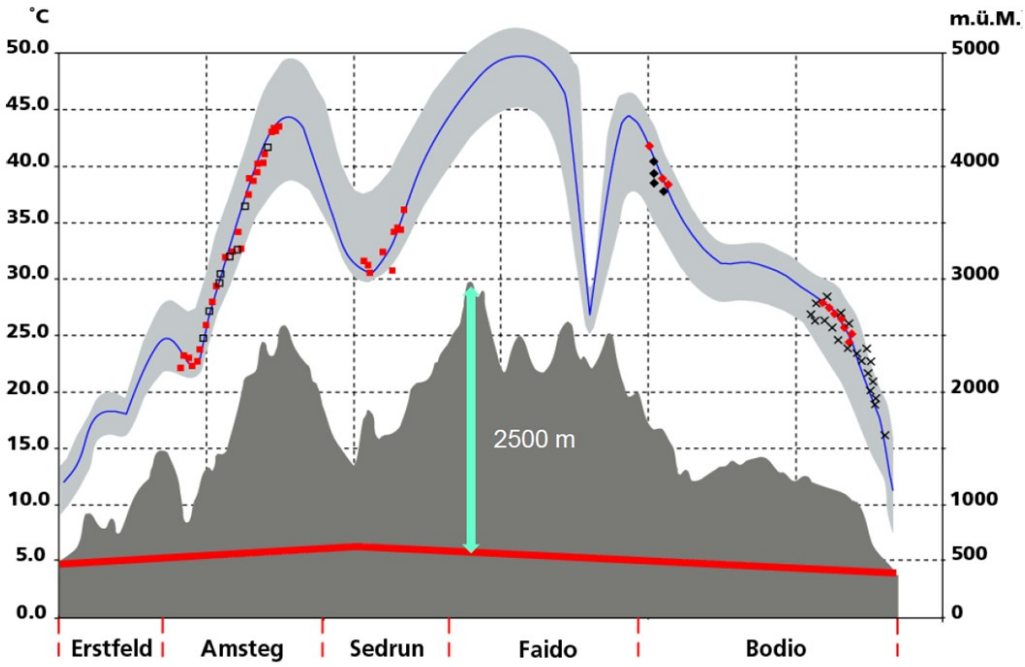

Figure 73: Rock temperature distribution in the Gotthard-Basistunnel. Temperature is shown on the left vertical axis and depth on the right axis (m.ü.M = meters above sea level). Erstfeld, Amsteg, *etc.* are locations along the tunnels.

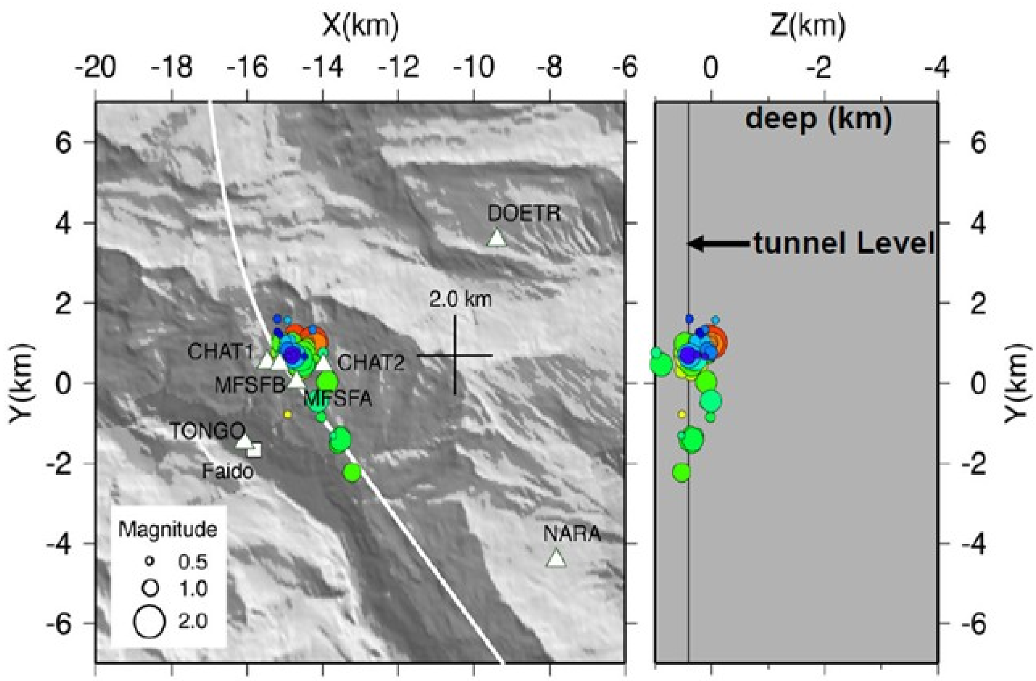

Figure 74: A seismic network set-up near Faido for the Gotthard-Basistunnel project measured various micro tremors over a 2-year period.

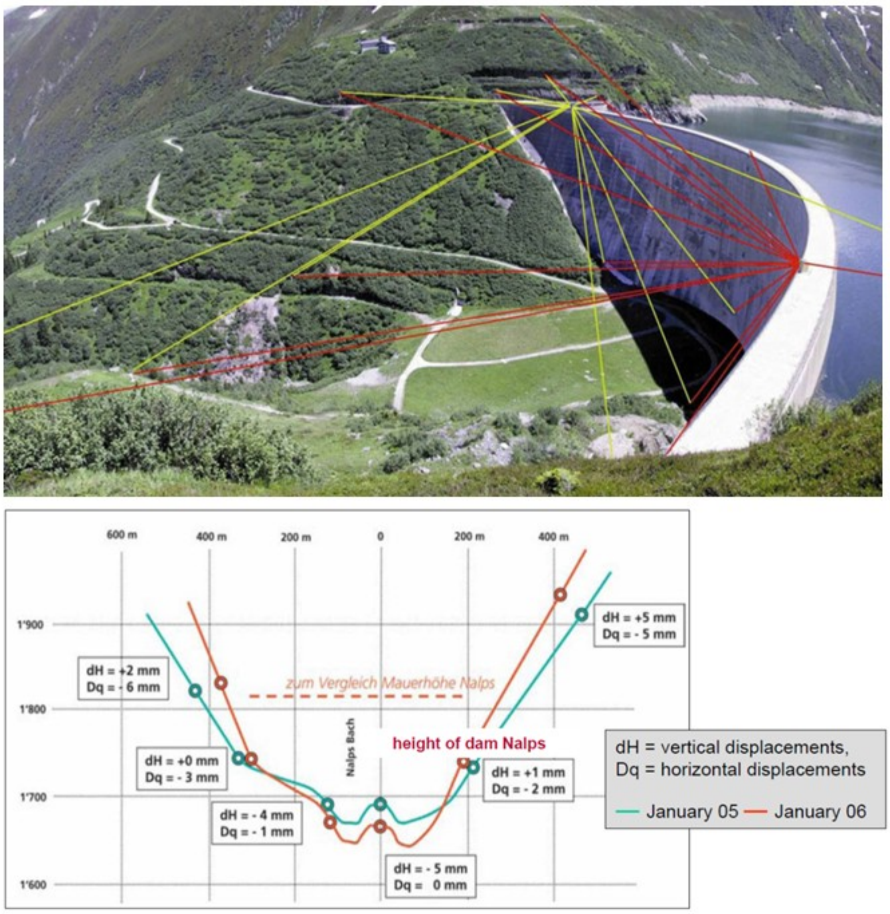

Figure 75: Horizontal and vertical displacements measured at the water dam Nalps are related to the Gotthard-Basistunnel project.

railway tube).

TBMs can also be used to drill tunnels in soft soil. In that case special types of TBMs (*e.g.* mixshield) must be used that have a submerged wall, a working chamber, air cushion and pressure bulkhead. The tunnel walls require advanced lining, while the TBM servicing requires special manpower (divers). In general, tunnel construction in soft soil is considerably more expensive than in hardrock.

The tunnel for the HERA ring (6.6 km circumference) at DESY in Hamburg, Germany and the LHC (the LEP) tunnel (26.7 km circumference) at CERN in Geneva, Switzerland have been constructed with TBMs. The 6 km tunnel for the LCGT project in the Kamioka mountain in Japan will be constructed by D&B.

3.6.2 Caverns

Einstein Telescope will have a total of 9 underground caverns. Each corner station will have a large cylindrical underground cavern with a diameter of about 65 m and a height of 30 m. Each corner station will have 2 smaller caverns with diameters of 30 m and a height of 30 m.

Figure 76: The construction of the Robert Bourassa hydropower station in Quebec, Canada. Drill and blast was used to excavate the powerhouse with dimensions 296 m by 25 m by 47 m. More than 11,000 rock bolts were used.

ET's caverns will be constructed by D&B. Worldwide various such underground structures have been constructed. Fig. 76 shows the underground hydropower station in Quebec (Canada).

For the LHC project at CERN, the caverns to host the Atlas and CMS experiments have been constructed by D&B. The left photo in Fig. 77 shows the waterproofing foil used in the CMS cavern at CERN. The right photo shows the completed cavern. The Atlas cavern is located at a depth of 92 m and has a length of 55 m, a width of 32 m, and a height of 35 m. The CMS cavern is located at a depth of 20 m and has a length, width and height of 53, 27 and 25 m, respectively.

The construction of the Atlas cavern took 4.5 years and that of the CMS cavern 6.5 years. It is clear that for ET the various caverns must be constructed in parallel in order to avoid excessive construction times.

Figure 77: The construction of the CMS cavern for the LHC project at CERN, Geneva.

3.6.3 Shafts

Presently, it is not clear whether ET will have horizontal or vertical access. In the case of vertical access, there is a significant increase in complexity of the construction methods needed for shafts with depths exceeding 200 m.

In the following, we present a discussion that is based on vertical access, similar to for example the LHC experiment at CERN (see Fig. 78).

Each corner station will be accessed through a 20 m diameter vertical shaft. For excavation of the tunnels, the TBMs (in case this technique is adopted) will be lowered through these shafts. After tunnel construction, the shafts will be equipped with concrete elevator modules, staircases and will carry all services (power, water, compressed air, ventilation ducts, *etc.*). Additional shafts with a 10 m diameter are foreseen at the center of the arms.

The top of the shafts will be integrated in large surface buildings. There the equipment of the ET interferometers, such as the vacuum system, will be prepared. Subsequently, the various modules will be lowered through the shafts into the caverns using hoisting devices.

3.6.4 Final remarks on construction

Cost analysis shows that tunnels, shafts and caverns constitute the main cost drivers for the ET project. It is obvious that the cost of underground construction is site dependent and contains large uncertainties at this stage of the project.

In follow up studies it is imperative that risk management of the project is assessed. Worldwide many problems occurred during underground construction. Furthermore, in our discussions with insurance companies it became clear that part of the risk cannot be insured (*e.g.* water leaks in tunnels). The Technical Committee on Geotechnical Reports of the Underground Technology Research Council has established guidelines for a so-called geotechnical baseline report (GBR) for construction. It is customary that a project starts by defining such a GBR in order to establish a baseline on risks (*e.g.* from geology) for industry and client. After site selection such a GBR must be realized. It contains as much as possible detailed site information based on geophysical surveys, lidar surveys, drilling samples, probabilistic assessment of rock mass behavior, *etc.* and requires close collaboration between the client, industry, and geophysicists.

Figure 78: The construction of the CMS access shaft for the LHC project at CERN, Geneva. This shaft has an 18 m diameter and the entire CMS experiment was lowered through it. To facility its construction, the ground at the shaft walls was frozen.

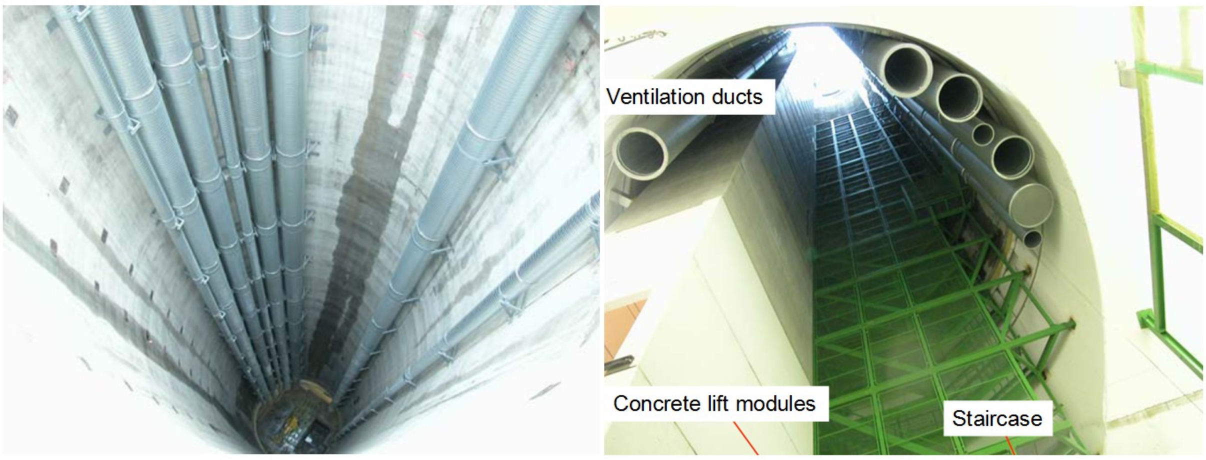

Figure 79: Completed access shafts for the LHC project at CERN, Geneva.

3.7 Vacuum systems

Author(s): C.Bradaschia, G. Parguez, A. Pasqualetti

3.7.1 Vacuum Systems

Introduction In laser interferometers for GW detection most of the instrument has to be kept under High-Vacuum or Ultra-High-Vacuum (HV, UHV) for several reasons:

- reduce the noise due to vacuum fluctuations along the beam path to an acceptable level
- isolate test masses and other optical elements from acoustic noise
- reduce test mass motion excitation due to residual gas fluctuations
- reduce friction losses in the mirror suspensions
- contribute to thermal isolation of test masses and of their support structures
- contribute to preserve the cleanliness of optical elements.

A vacuum system of this kind (Fig. 80) is composed of several UHV pipes with kilometric length and several cylindrical vertical HV/UHV tanks (towers) containing the optical elements and their support structures (Fig. 81). In general it is necessary to have the whole vacuum system constituting one single volume, without physical separations (windows) on the laser beam path. HV volumes (the towers) contain parts of the apparatus not easily compatible with UHV pipes where, on the contrary, the large majority of the laser beam has to travel. The separation between HV and UHV is obtained by differential pumping or by cryogenic traps, stopping the migration of water and other high vapor pressure components.

The vacuum enclosure will be built of stainless steel (304L); this material is preferred for its easy availability, its price, the large experience in machining and welding, the mechanical properties (ductility), the chemical properties and the achievable outgassing rate. The same choice has been made in the past for Virgo, LIGO, GEO600.

Average base pressure in the arm pipes The noise due to vacuum fluctuations (index instabilities due to statistical fluctuations of the number of molecules in the volume occupied by the laser beam in the arms cavities) has been calculated by several people for Virgo and LIGO [**?**]. It is (at first approximation) inversely proportional to the square root of the beam volume (or to the square root of the beam average radius or to the square root of the arm length or to the square root of the average pressure). The following baseline parameters have been used:

- arm length: 10 km
- beam waist: 40 mm (TEM00) @ 5 km
- beam average radius on mirrors: 120 mm
- best sensitivity: $\sim 3\,10^{-25}$ $\mathrm{Hz}^{-1/2}$ @ 300 Hz.

As it is common practice in matter of vacuum, we will take a safety factor of at least 10 with respect to the pressure producing a phase noise at the limit of the best sensitivity. The residual gas composition will be dominated by hydrogen with presence of water and other gases; we will aim to keep the residual pressure at level of $1\,10^{-10}$ mbar (H_2 and H_2O, each at $5\,10^{-10}$ mbar, would generate an overall noise level of about $2\,10^{-25}$ $\mathrm{Hz}^{-1/2}$, see Fig. 82). The vacuum system will be extremely clean from heavy organic molecules, both to limit the phase noise and to prevent pollution of the optical components. Hydrocarbon partial pressure shall be at the level of 10^{-14} mbar.

To reach these conditions it will be necessary:

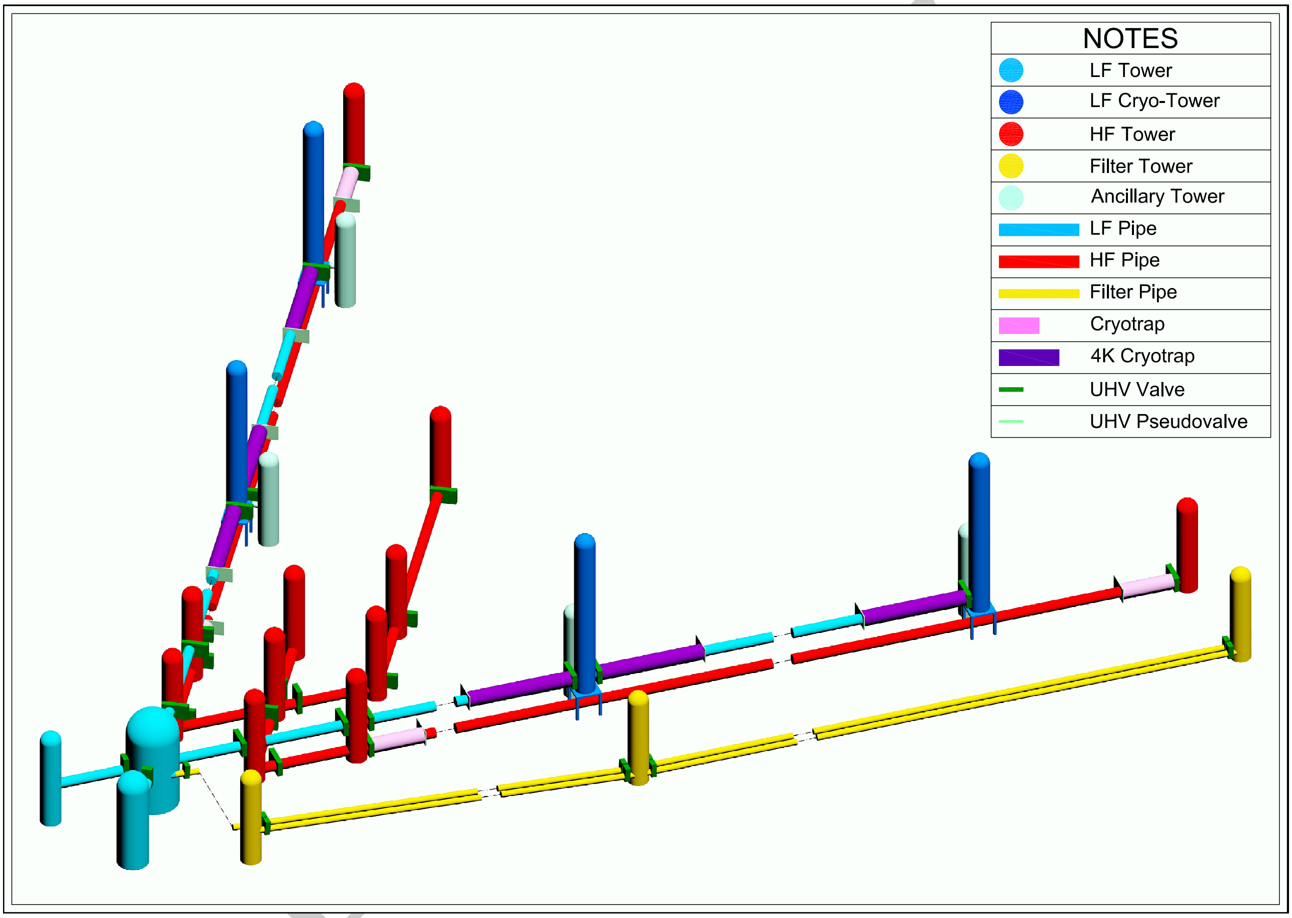

Figure 80: Schematic of the ET vacuum system lay-out, out of scale. Only one xylophone detector is shown, out of three.

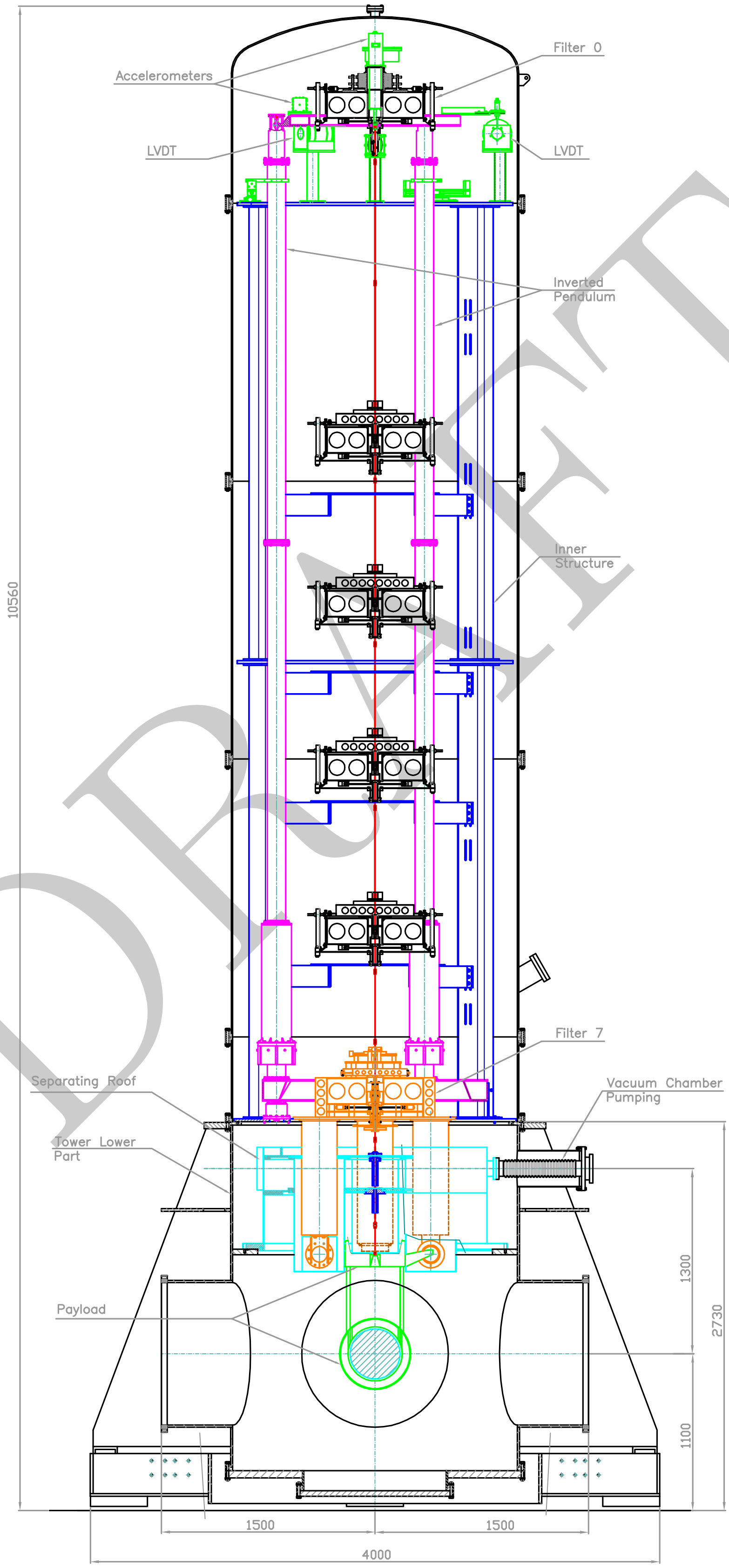

Figure 81: As an example the cross-section of a Virgo a mirror tower is shown.

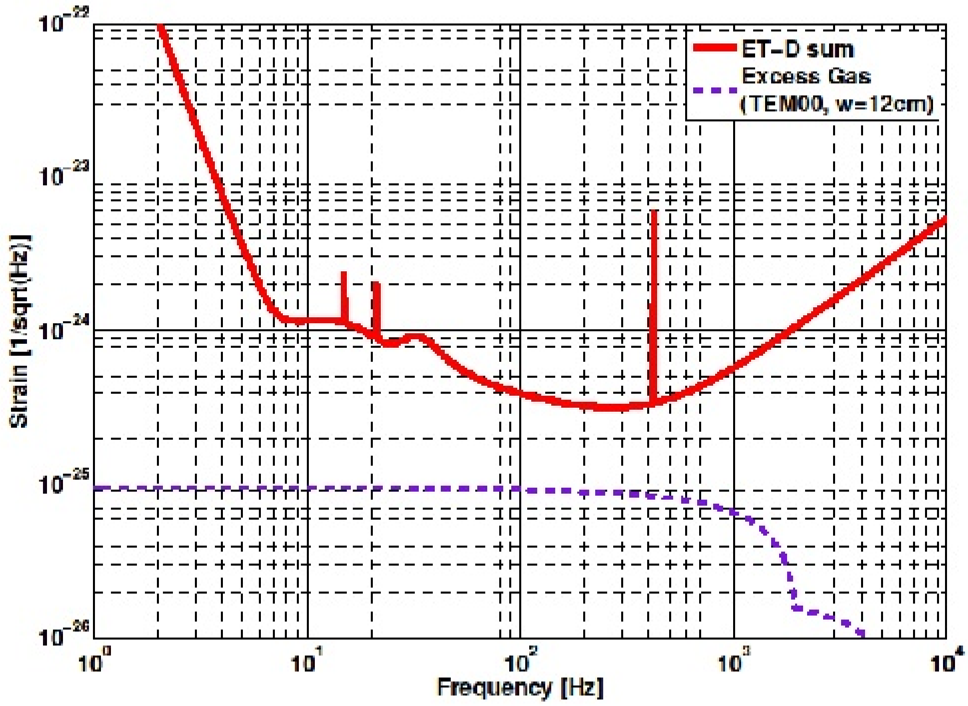

Figure 82: Phase noise given by selected gases compared to the expected sensitivity, computed for the appropriate beam profile. (Gas composition: Hydrogen [$1\,10^{-10}$ mbar], Water [$5\,10^{-11}$ mbar], Nitrogen [$1\,10^{-11}$ mbar])

- to fire (one week in an air oven at 450°C) the stainless steel vacuum enclosure elements (or the raw material sheets) in order to reduce the H_2 outgassing rate at the level of 10^{-14} mbar l /cm^2 s
- to bake for one week at 150°C the pipes already assembled and under vacuum in order to eliminate the water molecule layers sticking to the pipe inner wall.

Liquid nitrogen cryotraps will be necessary to separate the baked UHV pipes from the water dominated unbaked mirror towers, in HV regime. Concerning the phase noise, the path length of the beams in HV will be kept short, that is a negligible noise contribution, when compared to the kilometers in the UHV arm pipes. Large gate valves will be put at each end of the arm pipes, in order to preserve vacuum when venting a tower. For the same reason each tower will be separable from the rest of the vacuum enclosure by suitable gate valves. The reference cavities being less sensitive to vacuum noise require a residual pressure at the level of 10^{-7} mbar. Their pipes will not be fired at 450°C nor baked at 150°C.

The arm pipes Due to the multi interferometer/xylophone choice for ET, several beams will run along each side of the triangular tunnel, we assume four main beams and two filter cavity beams, taking into account all the three detectors (six interferometers) composing the full ET.

The chosen baseline configuration includes four pipes, one for each main beam: two with a 0.9 m diameter for the HF interferometers and two 0.75 m diameter pipes, for the LF interferometers. In addition, two 0.69 m pipes for the two filter cavity beams belonging to each LF interferometer. HF interferometers will be equipped also with a 700 m long filter cavity, running in a dedicated tunnel, inside a 0.6 m diameter pipe.

The pipes will be arranged inside the tunnel cross-section as shown in Fig. 83: the filter cavities at the bottom, under a movable floor, the two HF beams on the floor at the tunnel sides and the two LF beams on top of them (see below the "Tower" paragraph).

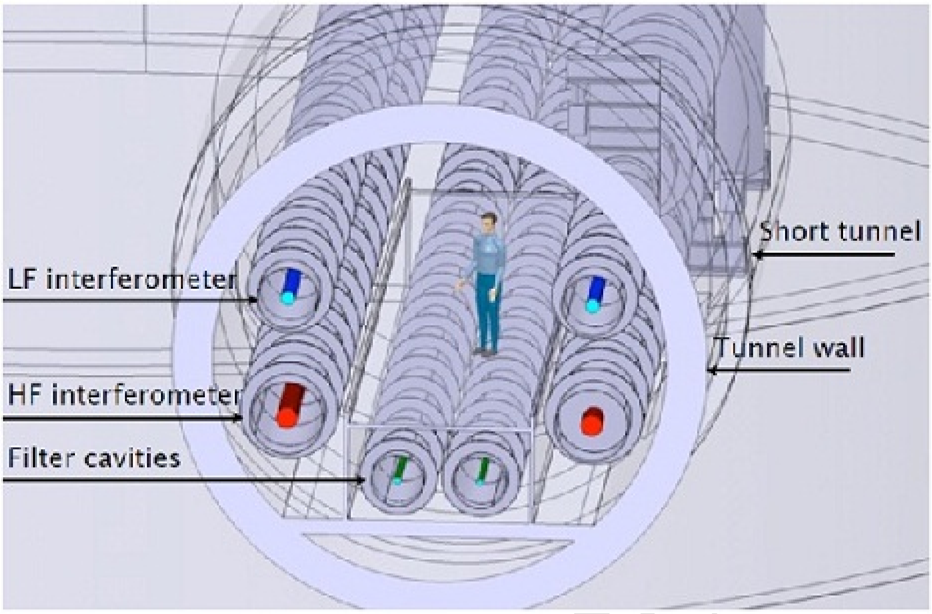

Figure 83: Arrangement of the vacuum pipes in the tunnel cross-section.

The pipe construction procedure merges Virgo and LIGO experience, even if the final choice will be performed in due time, with the appointed company. The pipes will have thin walls (3 – 4 mm) with external stiffening rings, every 1 – 2 meters. Two ring s will be larger, serving as attachment for the supports (see below).

20 m long pipe elements will be fabricated by continuous spiral welding in a suitable clean factory installed on site. At one end of each element a suitable bellows will be added to accommodate thermal expansion, during bake-out; winter/summer temperature excursion should be negligible under ground. At both ends 2 mm thick lips will be added, to allow UHV compatible welding of adjacent elements, without inert gas protection on the inner side of the weld (this technique has been successfully applied in Virgo).

Simple supports "a la LIGO", using steel cables and adjustable stretching screws will be sufficient, coping with the relatively high stability of an under ground tunnel.

The pipes will be aligned in the tunnel using optical instruments and laser beams, since GPS will not be applicable under ground. The requested straightness error for the arms is of the order of 10 mm. Periodical surveys will be necessary every few years, in order to detect dangerous pipe displacements due to ground movements.

Each 10 km pipe will contain a few hundreds of metallic baffles for diffused light mitigation. They shall be made out of stainless steel with a suitable conical shape and serrated inner edge (Fig. 84) against diffraction. The radial width of the baffles, between 50 and 100 mm, and their position will be determined by a suitable simulation [269] [270].

Pipe Assembly The 20 m pipe elements will be lowered to the corner caverns with the ends sealed by suitable end-caps and equipped with thermal insulation; each element will weight about 1.5 t. The element will be put on and bolted to a simple carriage made of two parallel 20 m long beams supported by small train wheels. In this way pipe elements can be pushed to their position one after the other by an electric tractor running on 5 km long rails reaching up to mid arm. The rails, two for each pipe, are supported by frames extending to the whole tunnel cross-section. These same frames have the function, as said before, of supporting the pipes. In alternative the element could be suspended to a 20 m long beam running, as a bridge crane carriage, attached to a 5 km long rail. The rail, one per pipe, is supported by the already mentioned frames. Also in this case

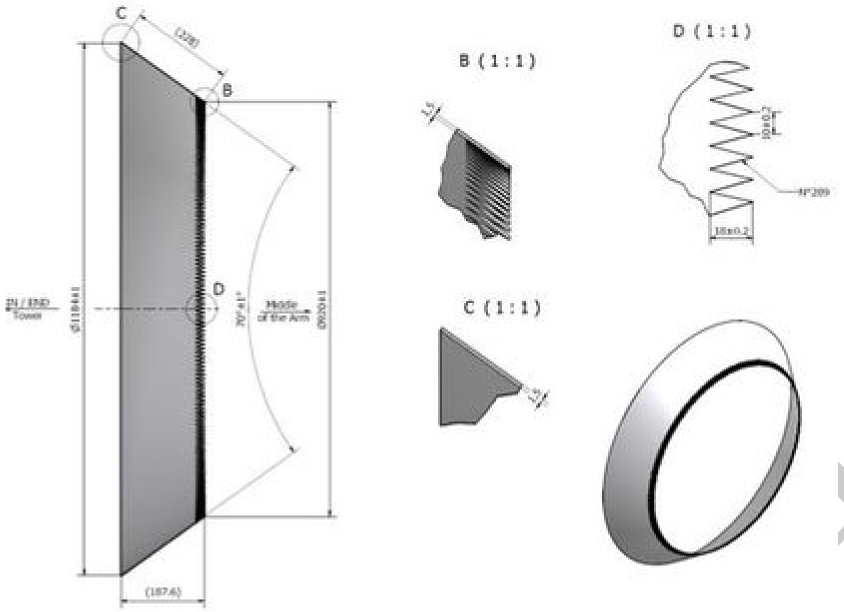

Figure 84: As an example the Virgo pipe conical baffles are shown.

pipe elements can be pushed to their position one after the other by an electric tractor or by a traction line.

Every 500 m, along the tunnel, there is an enlarged room to accept pumping, bake-out and control equipment; those rooms are used also to weld the pipe elements at ease in a wide area, under a clean tent.

The first pipe element is stopped with the rear end under the tent; when the front end of the second element is close, the sealing lids are removed, after starting appropriate clean air flows. The corresponding end lips of the adjacent elements are precisely adjusted and welded. The beams of the two carriages (under or above the pipe, according to the chosen option) are rigidly bolted together, taking care of appropriate compression/extension of the bellows.

The two modules are shifted forward until the rear end of the second module is at the welding position; now the front end of the third module is adjusted and welded as before. This procedure is continued until the 25^{th} module is welded and the 500 m long section of pipe is completed.

The ends of the assembled pipe section are closed with vacuum tight lids, the section is evacuated and tightness tests are performed. The closing lids will be strongly fastened to the tunnel wall, in order to keep the 6.4 t axial load due to atmospheric pressure.

The 500 m long section will be then vented and shifted by 20 m to its final position.

Every pair of upper support cables (as said, in the LIGO style) are attached to the corresponding support ring, the cables are tightened, the bolts of the pipe elements to the carriages are removed, the elements are lifted (lowered, in the case of suspended transportation) by 10 mm in 1 mm steps. The 500 m long train composed by 25 carriages is sent back to the end cavern, to start the assembly of the second 500 m pipe section. The lower support cables are attached to the support rings and suitably tightened.

The clean tent and the welding equipment are transferred to the next enlarged room and the assembly of the second 500 m pipe section is started. Once completed and vacuum tested, taking advantage of the bellows and of the support cables, the front lip of the new 500 m section is adjusted to the rear lip of the previous section and welded. This final weld is the last to be performed in that particular enlarged room.

The procedure continues contemporarily extending the installed pipe from mid arm to both arm ends.

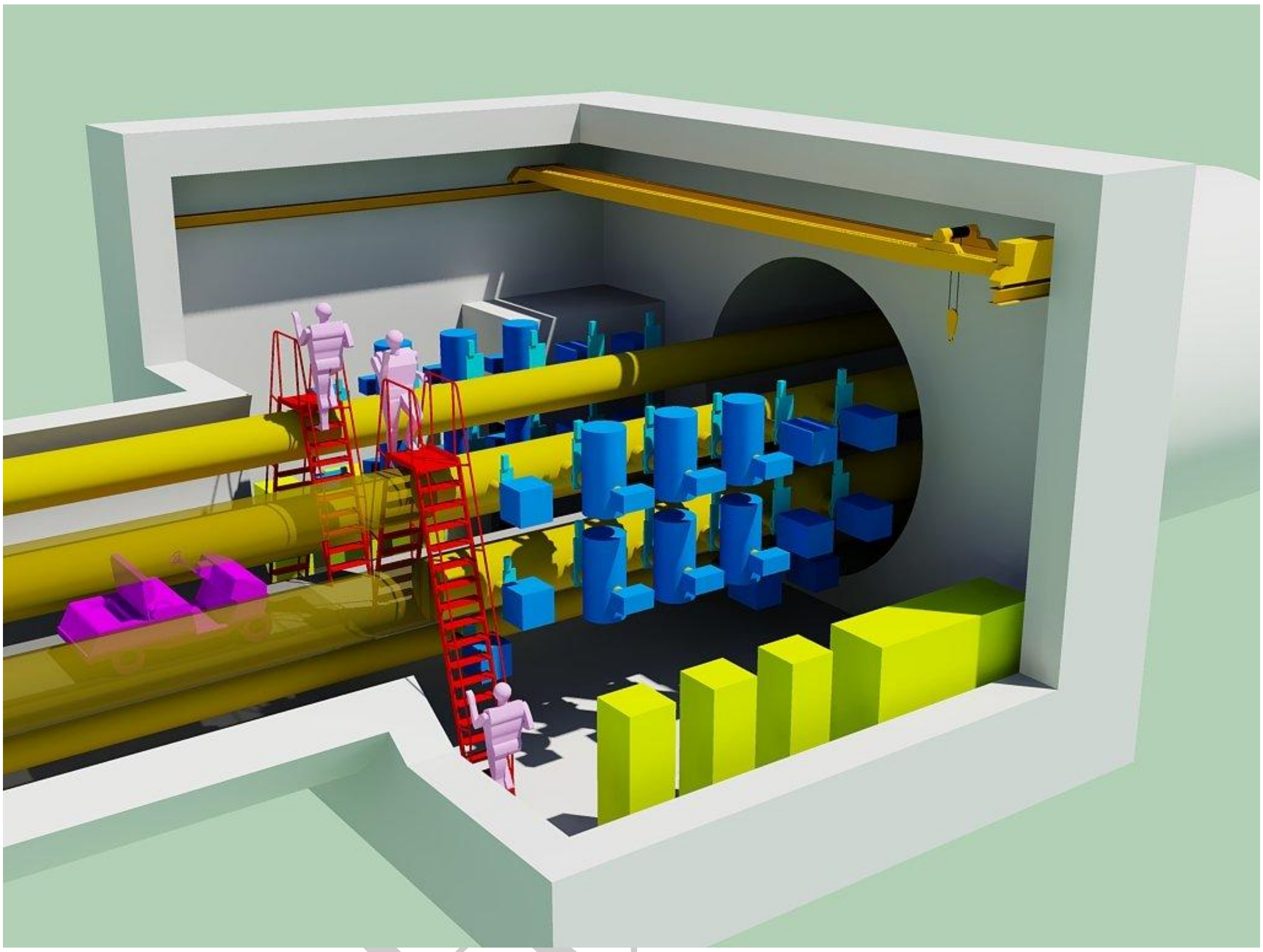

Figure 85: 3D view of a pumping station: the blue objects represent the pumps and sensors, the yellow ones the cabinets for pumps control (1 per tube) and baking power supply (1 cabinet for all). A separate small room is reserved for the high voltage electrical transformer.

Concerning the pipes arrangement in the tunnel, it is necessary to have the possibility to inspect and repair the welds between pipe elements. This could be achieved leaving a clearance of about 0.5 m between the "nude" pipes and the tunnel wall (at least every 20 m). We should consider also the case of needs of (small) maintenance interventions on the tunnel wall lining.

A pumping station room is sketched in Fig.85 . In practice it is an enlargement of the tunnel for a width of 12 m and a length of 10 m, allowing the installation of the pumps, which are hold in their position by a metallic frame not reported in the sketch. Three cabinets housing the electronics of the vacuum equipment are included, together with an electrical power supply for baking (60 VDC 300 Kwatt).

A bridge crane shall be present, and the room shall probably need a conditioned humidity and temperature, to allow electronics efficiency.

Pipe pumping system The pipe pumping system has been conceived to be composed of standard modules, grouped together, in order to limit the number of pumping stations along the arms.

The goal total residual pressure (hydrogen and other gases) of $1\,10^{-10}$ mbar can be obtained, after firing and bake-out (see a previous paragraph), with one 5000 l/s pumping group, every 500 m, both in a 0.9 m and in a 0.7 m diameter pipe, the smaller gas load due to the smaller diameter being compensated by the relatively reduced conductance.

Below is described the pumping system for one single pipe.

Each permanent pumping group will consist of three identical modules, each made of one 2500 l/s Ti sublimation pump (TSP), connected to the pipe through a 250 mm gate valve (the Ti will be sublimated not in the tube but in a separated chamber), coupled to a 300 l/s ion pump. The former to pump active gases, the latter to pump inert gases. At such a low pressure TSPs are expected to require not more than one yearly regeneration. NEG pumps are being considered as a possible alternative to TSPs. Some redundancy is necessary to cover the Ti pumps regeneration periods.

Besides the permanent pumping group, every pumping station will include suitable vacuum gauges and two 2000 l/s turbo, backed by a scroll pump, for initial evacuation and bake-out.

The Filter cavity pipes, requiring a 10^{-7} mbar residual pressure, will be equipped only with the turbo/scroll groups, possibly reinforced with 77 K cryo-pumps.

Every 10 km pipe will have three RGA's, at each end and in the middle, to monitor the vacuum quality and for easier diagnosis in case of problems.

Pipe bake-out system In order to perform the 10 days bake-out under vacuum at 150°C, the pipe could be heated by electrical current flowing in its walls, closing the circuit by a suitable Al bar or cable. Closing the circuit with the pipe of the adjacent twin interferometer would save the Al conductor cost, but does not seem practical. The use of DC will assure a uniform current and temperature distribution on the pipe walls and improve human safety. Typical arrangement of the circuit could be, similar to Virgo, a series of double ring circuits with one DC source every 500 m delivering 1000 A at 50 V along 250 m in each direction. Such a system will deliver 200 W per meter of pipe, which has been experimentally demonstrated to be sufficient to reach 150°C, if the pipe is wrapped in a suitable 10-20 cm thick thermal insulation layer. Each DC source will consist of a transformer/rectifier supplied by medium voltage AC (15 kV). This choice is dictated to reduce the cross section of cables to distribute 2 MW along 10 km. 15 kV equipment will be confined in dedicated rooms.

In this configuration, delivering 300 W per meter of tunnel, in absence of ventilation, a very crude estimate considering a 6 m aperture tunnel, drilled in isotropic rocks (assumed $\rho = 2500$ kg/m^3, k = 2.0 watt/m K, C = 800 joule/kg K) gives an increase of room and wall temperature by about +13°C after a 10 days bake-out. This situation, being at the limit of what could be tolerable, suggests to exploit several remedies like baking at a lower temperature for more days and improving the thermal insulation properties, in order to reduce the temperature increase of the tunnel walls. A suitable air cooling system will be designed to reduce further the ambient temperature (possibly renewing once per hour the tunnel air volume). The overall power release inside the tunnel could be reduced also performing bake-out in sequence on shorter pipe sections, separated by "pseudo-valves", vacuum tight, but able to sustain null pressure difference.

Cryotraps As stated above, HV volumes (e.g. the towers) will communicate with the UHV pipe through liquid nitrogen cryotraps, to prevent migration of water and other high vapor pressure contaminants. In order to allow the beam passage the cryotraps will consist of a large hollow muff, containing liquid nitrogen, suspended inside an increased diameter pipe section, with a design very similar to the one adopted for LIGO, Virgo and Advanced Virgo (Fig. 86). The lateral surface will be thermally isolated by a few cylindrical metal screens; the heat exchange at both ends will be limited by suitable circular baffles, leaving passage for the beam. The propagation of mechanical noise due to liquid nitrogen bubbling will be limited installing cryotraps at least 20 m away from the mirror towers; this will help to avoid excessive cooling of the mirrors (to avoid condensation, in no circumstance a mirror should be the coldest point in the environment). Cryotraps will have valves at each end, in order to be confined during warming-up for regeneration (not more than once per year). The traps will be 7–10 m long for pipes with diameters of 0.6 – 1.0 m. The liquid nitrogen consumption has been evaluated to be about 10 liters per hour per trap. In correspondence of the cryogenic towers for the 4 K mirrors of the LF interferometer, the cryotraps will be much longer (50 m) and will include liquid helium sections to strongly limit

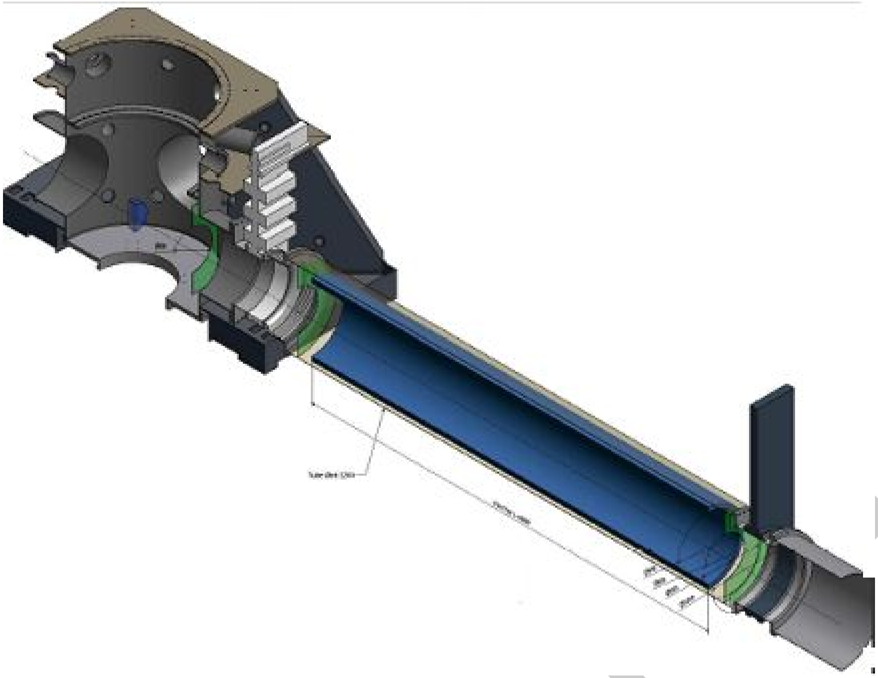

Figure 86: A liquid nitrogen cryotrap.

the mirror heat exchange as described in the following section. We refer to the same section for a description of the supply plant for cryogenic liquids.

Towers Mirror towers upper part will have a 2–3 m diameter to contain easily the pendulum chains of Superattenuators and the inverted pendulum legs; the structure will be an evolution of the Virgo towers (Fig. 81). The lower chamber of the towers will have a diameter up to 3 m, to contain large payloads. The HF interferometer towers will have a large bottom lid to allow installation of payloads from a clean basement, under a filtered air shower. The height will be 10 m for the main mirrors of the warm HF interferometer. Auxiliary mirrors or benches requiring lower isolation, will be located in shorter towers. The towers containing the cryogenic mirrors of the LF interferometer, to achieve full seismic isolation performance down to 2 Hz, will be up to 20 m tall. In these towers, sitting on top of the HF interferometer, the payload installation will be performed through a lateral port. This order of superposition has been chosen to have the low power LF beam passing through the HF mirror suspensions (at room temperature) and not the high power HF beam passing through the low temperature LF mirror suspensions. The lower part of the cryogenic towers will be described in the next section. Each cryo-tower will be coupled to an ancillary tower to support the heat extraction chain preventing seismic noise propagation.

Tower pumping system Mirror towers will be made of two or three vacuum compartments in order to separate by differential vacuum the lower mirror chamber from the less clean suspension mechanics in the upper chamber. The horizontal separating walls will have a low conductance hole for the passage of the pendulum chain support wire. The mirror chamber will be equipped with a permanent pumping group consisting of one 2500 l/s Ti sublimation pump coupled to a 300 l/s ion pump. In addition one 2000 l/s turbo, backed by a scroll pump, will be operated for initial evacuation. The tower upper chamber(s) will be pumped by suitable turbo/scroll groups.

An effort will be performed to build the suspension mechanics and electronics with ultra clean and low outgassing components, in order to pump permanently also the upper chamber with ion pumps. The use of large cryo-pumps is being considered to increase pumping power and to eliminate moving parts from the vicinity of mirrors.

Valves A great number of UHV gate valves with large aperture, up to 1 m will be necessary. They will be all metal with only the gate gasket out of vacuum outgassed Viton. Every tower will be separable from the rest of the vacuum system by such valves. Every cryotrap will also be separable for regeneration; the HV side will be equipped with a Viton gasket valve, while the UHV side will be equipped with a totally metallic "pseudo valve", vacuum tight, but tolerating only a few mbar pressure difference.

3.7.2 Cryogenic service infrastructures

Author(s): F. Ricci We present two possible approaches for the cryo-plants to be set up mainly for the LF-Interferometer. In fact the HF- interferometer includes just cryo-traps installed at the tube ends for fulfilling the ultra high vacuum requirements. These traps already present in the LIGO detector and now planned also for Advanced VIRGO , are based on the use of liquid nitrogen. Similar cryotraps for the ET HF- interferometer have been already presented in a previous section and from here after we focus on the cryogenic requirement of the LF - interferometer. The cryo-plant for the LF-interferometer will provide the refrigeration power needed to bring the mirror temperature in the 4 K range. This porpoise can be pursued either by setting up a system based on a battery of cryo-coolers or in alternative using the classic approach of liquid helium cryostats. In the next we sketch the main characteristics of ET cryostats on the base of the evaluation of the expected thermal inputs. Then we present and compare the two alternative cryo-plants.

3.7.3 The ET cryostats

Author:F. Ricci

In order to reduce the thermal noise impact on the ET sensitivity curve its is sufficient to cool at cryogenic temperature the four test masses of the LF- detector. The heat is extracted from the mirror via the suspension fibers attached at the other end to the marionette. Moreover the marionette is suspended to the super attenuator which attenuates the seismic noise up to few hertz. Thus, it is extremely important to preserve the mechanical isolation between the mirror and the cooler system. On the other hand an efficient thermal link between the payload and the cooling system plays is crucial for the design optimization: we have to design links as short as possible and optimize the thermal contacts, in order to avoid refrigeration power loss. In figure 87 we report a sketch of the cryo-mechanical system to be adopted for ET-LF.

The whole payload that we will describe in the suspension chapter is hosted in the lower part of the vacuum tower hosting the 17-m long super-attenuator chain. The vacuum tower basement is a cryostat with two thermal screens: the blue line schematizes a surface at ~ 4 K, while the red one is the shield at intermediate temperature (~ 80 K). The upper part and lower part of the tower are separated by a roof crossed by the Ti-6Al-4V thin rod which holds the whole payload [8] The blue line define a volume that has to be vacuum tight. It will permit to cool and warm up faster the whole payload by adding pure Helium gas in this experimental volume. Few mbars of helium will provide an efficient heat exchange during the cooling phase of the payload from room to cryogenic temperature. Once the equilibrium temperature is achieved, the helium gas is pumped out before the laser light injection. The basement of the main tower hosting the mirror is connected to an ancillary tower shown in the figure. The ancillary tower is hosting the cold box, which will keep the mirror at cryogenic temperature. The box can be either a simple liquid helium container in the case of a cryoplant based on cryofluids or the cold head of a cryo-refrigerator in the case of a cryocooler plant.

A thermal line of 20 m maximum length connects the cold box to the last stage of the mirror suspension. It can be made of a braid of a high purity material as the electrolytic copper or the grade 6 aluminum (99.9999 % purity). Both of them are metals characterized by thermal conductivity value of 2 kW/m/K in the range 1-10

[8] The interface between the upper and lower suspension is described in the section (4.4.3.

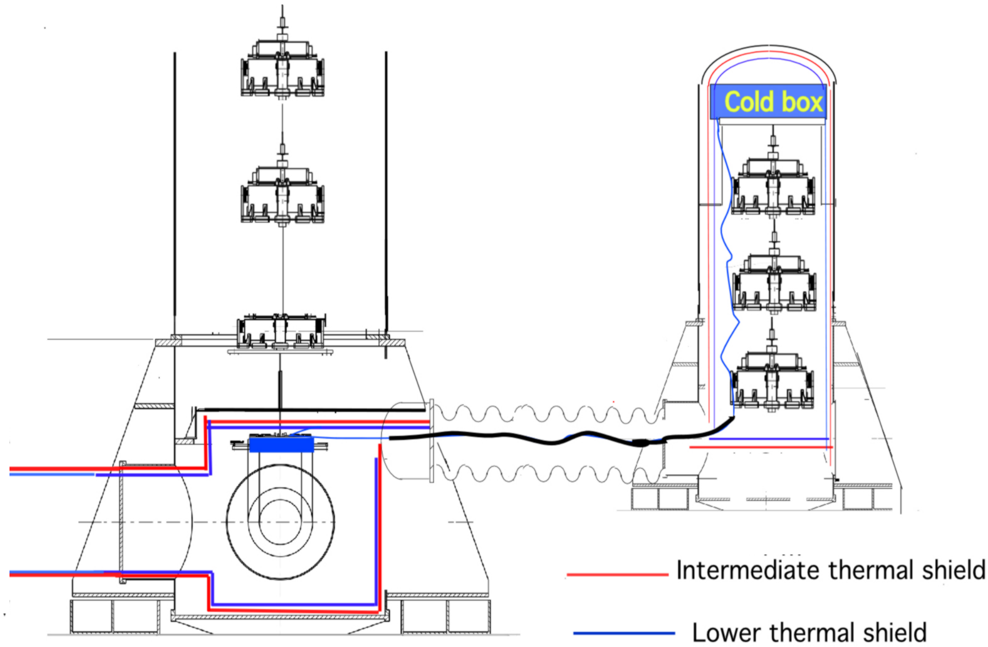

Figure 87: Scheme of the cryostats needed for cooling a test ass of the LF-interferometer.

K. In fact a braid of 20 m length, made of 8 wires 1 mm diameter can support an heat flow of 200 mW for a temperature difference of$\sim$ 1K at the link ends.

To damp the vibration associated to the cooling system, the soft braid is mechanically coupled to the auxiliary super attenuator chain, hosted in the ancillary tower and fully complaint with the cryogenic environment.

In order to define the requirement of the cryo plant we have to estimate the cryostat thermal inputs, which depend on the cryostat dimension and the quality of the thermal insulation.

Assuming that the inner vacuum chamber has to host a mirror with a half meter diameter, we derived the order of magnitude of the thermal input for the cylindrical cryostats whose dimensions are reported in the following table:

Table 5: Cryostat dimensions

Container	Diameter [m]	Height [m]
Payload vacuum chamber	1.5	3
Auxiliary tower	1	2

The thermal super insulation is a standard technique used in the modern cryostats. The thermal shield is formed by highly heat reflective thin layers, set under vacuum for increasing radiation reflection and decreasing radiation heat transfer through the insulation. The most known implementation is based on layers of porous (self-vented) mylar sheets, which are aluminized on one side. The sheets are wrapped around the surface to be insulated and form a multilayer blanket. The mylar is an hydroscopic material incompatible with the HUV requirements of ET. As a consequence the proposed solution implies to separate the chamber hosting the mirror to the insulation vacuum of the cryostat. A dedicated pumping system (rotary-roots-turbo-molecular group) will provide the vacuum insulation.

Wrapping 25 and 75 layers of self vented aluminized mylar around the two thermal shield, we achieve the condition to limit the thermal input below 1 W for the 4 K shields and around 50 W for the intermediate ones. We assume in this evaluation that the thermal input due to laser light absorbed by the mirror and the thermal radiation emitted by the the km tube is in the range of few tens of milliwatts thanks to low silicon absorption at the laser wavelength and to the helium cryotraps described in 3.7.4.

It is forth-worth to evaluate in more details these data in the context of the ET technical design study.

3.7.4 The LF-interferometer cryotraps

Author(s) G. Gemme

Motivations.
The main heat inputs into the cold mirror of the LF interferometer are the thermal radiation coming from the warm surface of the vacuum tube, and the heat load due to the absorption of a small fraction of the laser light into the mirror surface. The latter can be estimated considering that the laser power circulating in the optical cavity is 18 kW, and that a reference value for the absorption coefficient of the mirror optical coating at the working wavelength is around 1 ppm. This gives an approximate value of 20 mW of absorbed laser power.

The radiation from the warm surface of the vacuum tube to the mirror can be estimated by the modified Stefan-Boltzmann equation

$$\dot{Q}_r/A_1 = \sigma F_e F_{1-2}(T_2^4 - T_1^4) \tag{89}$$

where $\dot{Q}_r/A_1$ is the heat transfer rate by radiation per unit area of the mirror surface, $\sigma = 5.67\,10^{-8}$ (W/m^2/K^4) is the Stefan-Boltzmann constant, F_e is the emissivity factor, and F_{1-2} is a geometric configuration factor relating the two surfaces, whose temperatures are T_2 (warm) and T_1 (cold). From eq.89 the heat flux on the mirror at $T_1 = 10$ K, coming from the vacuum tube at $T_2 = 300$ K can be as high as $\dot{Q}_r/A_1 \sim 460$ W/m^2. This huge heat flux is not compatible with the cryogenic environment and needs to be reduced by several orders of magnitude.

In order to reduce the thermal radiation from the beam duct into the cold mirror, two strategies are viable, as shown by eq.89: the reduction of the emissivity factor and/or the reduction of the geometric configuration factor, i.e. the reduction of the solid angle under which the warm surface is seen by the cold surface.

The emissivity factor can be reduced by an appropriate choice of material for the wall of the tube, or trough the deposition on the warm surface of a low-emissivity coating. This solution might be realizable, but usually conflicts with the requirements of the ultra-high-vacuum environment, since low-emissivity coatings may result in increased out-gassing rates and thus spoil the required vacuum level.

The reduction of the geometric configuration factor, on the other hand, can be obtained by building in the region adjacent to the mirror cold sections of the vacuum tube, that "move away" the warm section of the tube from the mirror, and in this way reduce the solid angle under which the warm surface is seen by the cold mirror. The temperature(s) and length(s) of these sections must be chosen in order to minimize the ration heat transfer to the mirror, and, at the same time, the overall cost of the cryogenic plant. Moreover, they will also serve as cryogenic pumps. In particular, in the region immediately adjacent to the mirror, a zone *colder* than the mirror itself is needed to avoid the condensation of the residual gas on the surface of the mirror, that could lead to the growth of a layer of contaminants and spoil its optical characteristics.

Heat load on cryogenic mirror - simple analytical calculation.
The equilibrium temperature of the mirror is reached when the power extracted by the cooling system is equal to the power absorbed by the mirror ($\dot{Q}_{abs} = \dot{Q}_{coolsys}$). The power extracted by the cooling system mostly flows through the four silicon suspension wires (a small fraction is exchanged with the surroundings through thermal radiation) to the penultimate mass (the marionette) and then is removed by the heat sink directly connected to the cooling system. The equilibrium temperature of the mirror T_{mir} can be calculated by a simple analytical model if we assume that the temperature of the penultimate mass is kept fixed at the design value of 5 K:

$$\dot{Q}_{abs} = \frac{4S_w}{L} < k_{Si} > (T_{mir} - T_{mario}) \tag{90}$$

$$< k_{si} > = \frac{1}{\Delta T} \int_{T_{mir}}^{T_{mario}} k_{si}(T) dT \tag{91}$$

where S_w is the section of the silicon suspension wire, L is its length and $k_{si}(T)$ is the thermal conductivity of silicon. In the following calculations we shall use the thermal conductivity shown in fig.88 [271]. From this figure we see that $< k_{si} > \sim 1.4\,10^3$ (W/m/K) in the temperature range of interest (5–10 K). We also take the design values for the silicon suspension wires (diameter: 3 mm, length: 2 m). The maximum power that can be extracted from the mirror, keeping its temperature at the design value of 10 K, is approximately 100 mW. Since

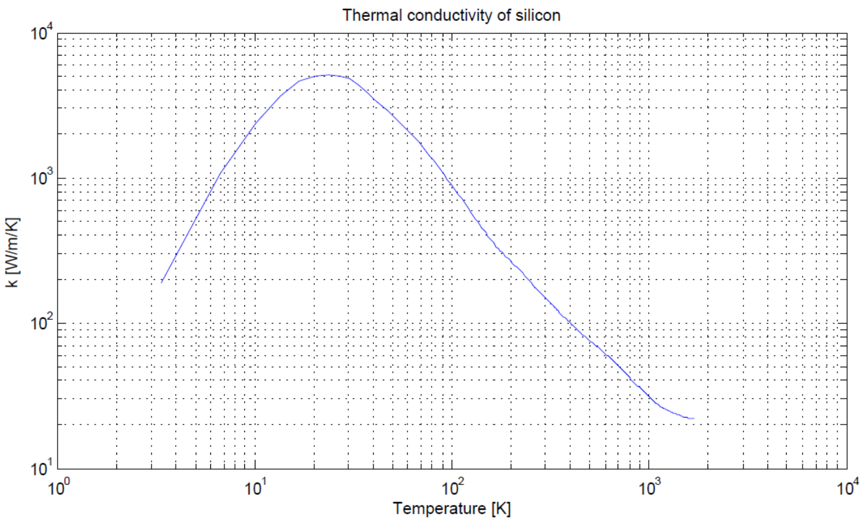

Figure 88: Thermal conductivity of silicon (from [271])

the laser power absorbed by the mirror is approximately 20 mW, we can conclude that the thermal radiation heat load must not exceed $\sim$ 80 mW.

Heat load on cryogenic mirror - finite element model.
The back-of-the-envelope calculation of the previous paragraph was checked by a finite element model of the mirror and its suspension system, as shown in fig. 89 The parameters used in the model are summarized in table 6.

The calculation was done setting on the front surface of the mirror a fixed heat source, representing the power coming from the laser and absorbed by the mirror, of 20 mW, with superimposed a variable heat source, representing the additional heat load due to thermal radiation. For the sake of simplicity the temperature of the penultimate mass was set at the fixed value of 5 K. The thermal conductivity of silicon shown in fig.88 was used in the model [271].

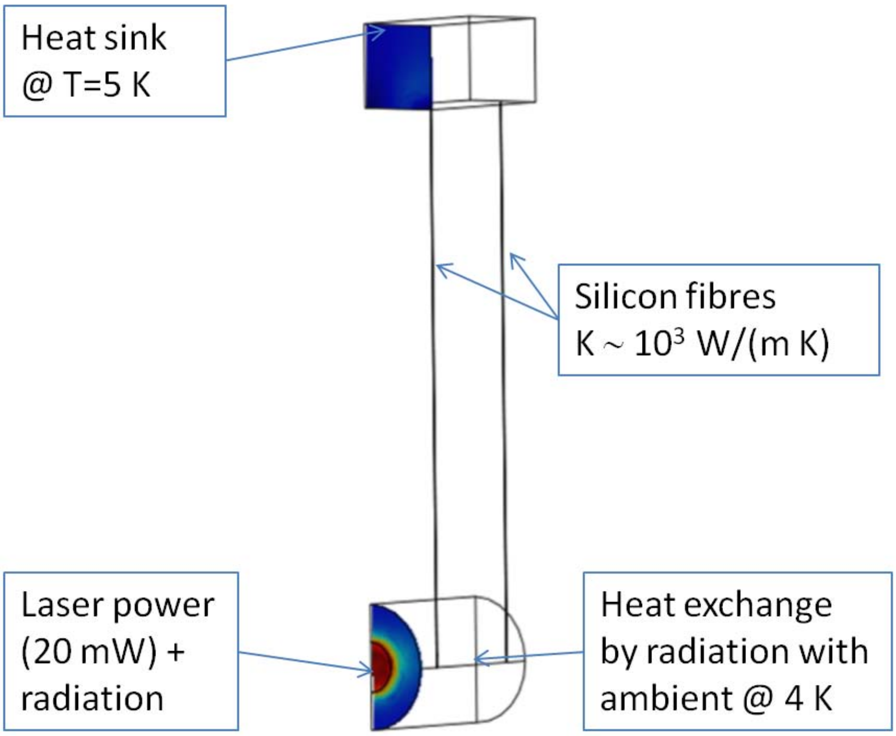

Figure 89: Finite element model and boundary conditions

Table 6: Finite element model parameters

Mirror temperature	10 K
Mirror diameter	45 cm
Mirror mass	211 Kg
Silicon fibers length	2 m
Silicon fibers diameter	3 mm
Marionette temperature	5 K
Power in cavity	18 kW
Absorbed power	20 mW
Beam radius	9 cm

The solution of the problem was calculated sweeping the variable heat source in the 0–0.1 W range, with steps of 10 mW, and looking at the temperature in the central area of the mirror. The results are shown in fig.90. They confirm the order-of-magnitude values found in the previous section. The temperature of the central area of the mirror does not exceed 10 K when the thermal radiation is lower than 70 mW, corresponding to 90 mW of total power absorbed by the mirror.

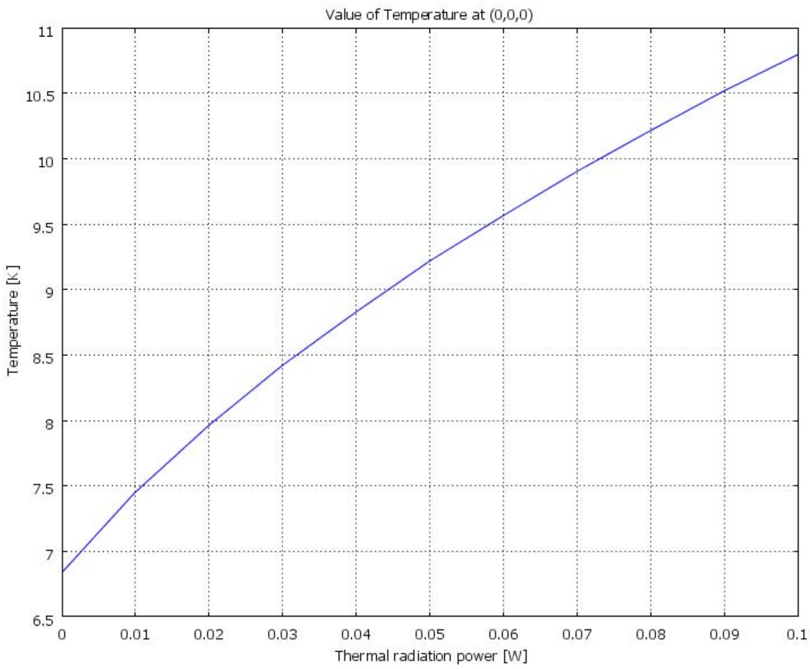

Figure 90: Temperature at the center of the mirror vs. thermal radiation power

Given this result, we have to find out how to design the cryotraps in the region adjacent to the mirror to keep the thermal radiation from the warm surface of the vacuum tube at a value not greater than few tens of milliwatts.

Thermal radiation from vacuum tubes - Direct exchange.

Radiative transfer of heat from one area to another depends, among other things, upon the fraction of the radiant energy emitted by one area which is intercepted by a second area. This fraction is identified by several names, such as the configuration factor, the interchange factor, the angle factor, or the geometric view factor, and is a function of the geometrical relation of the areas involved. The configuration factor is defined as the fraction of diffusely radiated energy leaving surface A that is incident on surface B, and it is represented by the F_{1-2} factor that appears in eq.89.

The notation adopted here is that used in [272] and in [273]. The configuration factor from a differential area element dA_1 to a second element dA_2 is denoted by dF_{d1-d2}. In general, such a factor is given by

$$dF_{d1-d2} = \frac{\cos\theta_1 \, \cos\theta_2}{\pi S_{1-2}^2} \, dA_2 \tag{92}$$

where the quantities on the right-hand-side are shown in fig.91

For the case of A1 and A2 both finite, the configuration factor is

$$F_{1-2} = \frac{1}{A_1} \int_{A_1} \int_{A_2} \frac{\cos\theta_1 \, \cos\theta_2}{\pi S_{1-2}^2} \, dA_2 \, dA_1 \tag{93}$$

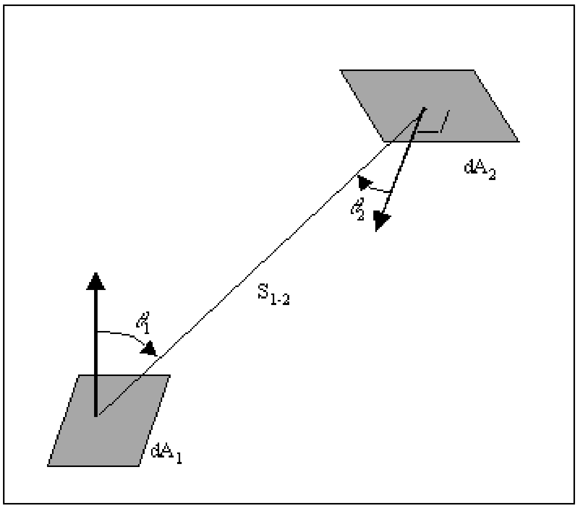

Figure 91: Defining geometry for configuration factor (from [273])

leading to the reciprocity relation

$$A_1 F_{1-2} = A_2 F_{2-1} \tag{94}$$

For each section at fixed temperature we need to calculate the geometric factor of the interior surface of circular cylinder of radius R to a disk of radius r where $r < R$. The disk is perpendicular to axis of cylinder, and the axis of the cylinder passes through center of disk (see fig.92) [274, 275] .

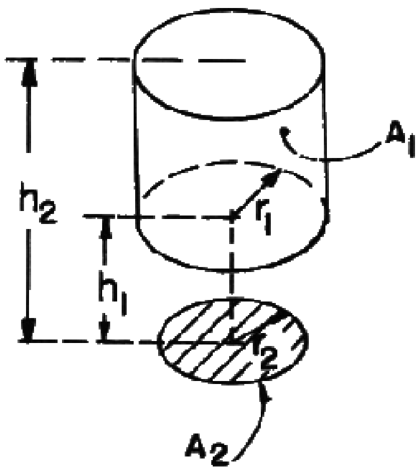

Figure 92: Defining symbols in eq.95 and eq.99 (from [273])

With the definitions:

$$R = \frac{r_1}{r_2} \tag{95}$$

$$H_1 = \frac{h_1}{r_2} \tag{96}$$

$$H_2 = \frac{h_2}{r_2} \tag{97}$$

$$X = H^2 + R^2 + 1 \tag{98}$$

the equation is:

$$F_{1-2} = \frac{1}{4R(H_2 - H_1)} \left[(X_1 - X_2) - (X_1^2 - 4R^2)^{1/2} + (X_2^2 - 4R^2)^{1/2} \right] \tag{99}$$

We can now explicitly calculate the configuration factor for the geometry schematically shown in fig.93 and

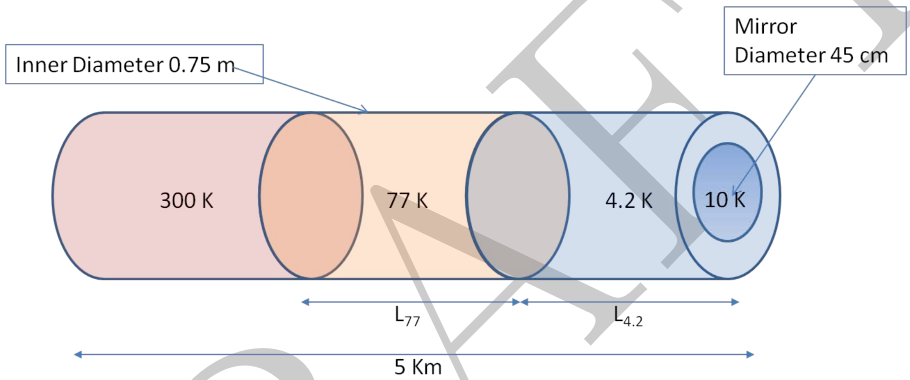

Figure 93: Conceptual scheme of the vacuum tube with cryotraps

making use of eq.89 we can calculate the thermal radiation power on the mirror as a function of the lengths of the two cold sections, at 4.2 K and 77 K. The result is shown in fig.94 We see that to keep the thermal radiation power in the range ~ 10 mW, we need a 4.2 section of few meters and a 77 K section of few tens of meters. For example, with $L_{4.2} = 10$ m and $L_{77} = 50$ m, we are in a situation were the *direct* transfer of thermal energy from the warm tube to the mirror is approximately 3 mW, well below the maximum allowed value.

Thermal radiation from vacuum tubes - specular and diffuse reflection.
The calculation of the thermal energy *directly* transferred to the mirror is not sufficient. For the correct evaluation of the thermal radiation on the cold mirror the reflective properties of the surfaces must be taken into account. These are rather complicated to specify as the reflected energy depends not only on the angle at which the incident energy impinges on the surface but also on the direction being considered for the reflected energy. Two important, and relatively simple, limiting cases can be used for calculating heat exchange: *diffuse* surfaces and *specular* surfaces.

For a diffuse surface the incident energy from the direction (θ, ϕ) that is reflected produces a reflected intensity that is uniform over all (θ_r, ϕ_r) directions. When a diffuse surface element irradiated by an incident beam is viewed, the element appears equally bright from all viewing directions. In the previous paragraphs, all the surfaces involved in the calculation of the configuration factors - in particular the inner surface of the vacuum tube - were assumed to be diffuse emitters.

Mirror-like, or specular, surfaces obey well-known laws of reflection. For an incident beam from a single direction, in a specular reflector, the reflected beam is at the same angle away from the surface normal as the incident beam, and is in the same plane as that formed by the incident beam and surface normal. When reflection

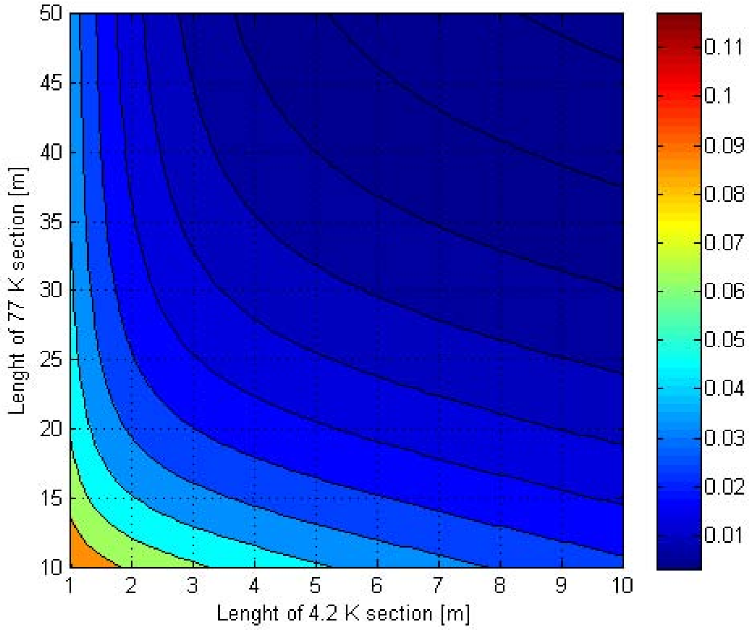

Figure 94: Thermal radiation on the mirror vs. lengths of 4.2 K and 77 K sections.

is diffuse, the directional history of the incident radiation is lost upon reflection. With specular reflection the directional history of the incident radiation is not lost upon reflection. Consequently, when dealing with specular surfaces, it is necessary to account for the specific directional paths that the reflected radiation follows between surfaces.

An important parameter for deciding whether a surface falls in the diffuse or specular limit is the surface roughness, or more precisely the ratio of the root-mean-square roughness to the wavelength of the radiation. For long-wavelength radiation a smooth surface tends toward being optically smooth, and the reflections tend to become more specular. Thus, although a surface may not appear mirror-like to the eye (i.e. for the short wavelengths of the visible spectrum), it may be specular for longer wavelengths in the infrared.

On actual engineering surfaces it is reasonable, as a first approximation [272, 276], to represent the reflectance ρ as being divided into diffuse δ and mirror specular μ components:

$$\rho = \delta + \mu \tag{100}$$

In addition, we assume an opaque gray body, whose radiation is emitted diffusely according to Lambert's cosine law [272]. The emitted flux depends on the absolute temperature, T, of the surface, the surface emissivity, ϵ, and the Stefan-Boltzmann constant, σ, in the combination$\epsilon\sigma T^4$. Kirchoff's law states that the same surface element will absorb only the fraction ϵ of the incident radiation, while reflecting the fraction $\rho = 1 - \epsilon$, so that

$$\epsilon + \delta + \mu = 1 \tag{101}$$

In the diffuse limit ($\mu = 0$, $\rho = \delta$), we let G represent the radiant flux incident on a unit surface. Then for a diffusely emitting surface with a diffuse reflectance, δ, the radiosity, J, given by

$$J = \epsilon\sigma T^4 + \delta G \tag{102}$$

represents the diffusely distributed radiant flux leaving a unit surface element [277]. The net inward radiative heat flux, q, is then given the difference between the irradiation and the radiosity:

$$q = G - J \tag{103}$$

Using eq. 102 and eq. 103 we can eliminate J and obtain a general expression for the net inward heat flux into the opaque body based on G and T. From eq. 101 with $\mu = 0$ we get $\epsilon = 1 - \delta$, thus q is given by:

$$q = \epsilon \left(G - \sigma T^4 \right) \tag{104}$$

This equation was solved for the geometry given in fig. 93 by a finite-element model. The geometric dimensions of the system were the same as in Table 6, with the lengths of the cold sections $L_{77} = 50$ m and $L_{4.2} = 10$ m. The results are shown in fig. 95: We see that for $\epsilon \geq 0.1$ the heat transferred to the mirror is essentially

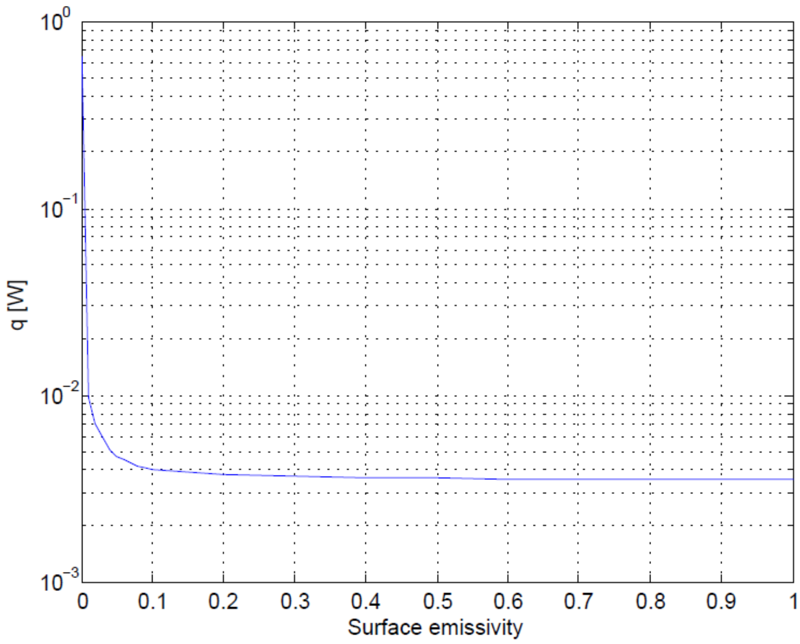

Figure 95: Thermal radiation heat transfer in the diffuse reflection limit

the direct contribution from the warm tube. Only for small values of $\epsilon < 0.1$ (high reflectivity $\delta > 0.9$) the contribution to the heat transfer from the surface reflectivity increases dramatically.

The case when the pipe walls are specularly reflecting was discussed in [278, 279]. A large heat load caused by thermal radiation through a metal shield pipe was observed in a cooling test of a cryostat for a prototype of the cryogenic interferometric gravitational wave detector (CLIO) in Japan. The heat load was approximately three orders of magnitude larger than the value calculated by the Stefan-Boltzmann law. The phenomenon was studied both by simulation and by experiment and it was found that found that it was caused by the conduction of thermal radiation in a metal shield pipe due to multiple specular reflections in the pipe.

A simple model for the evaluation is illustrated in fig. 96 [280].

In the case we are considering the aspect ratio of the pipe is sufficiently large to make the number of reflections

$$N \sim \frac{L}{d} \tan\theta \tag{105}$$

a number large compared to unity. At each reflection the radiation intensity is reduced by an amount $\rho(\theta) = 1 - \epsilon$ the specular reflection coefficient of the wall. The total reduction in intensity due to reflections at a given angle of incidence in the tube is determined by ρ^N.

The efficiency of transfer of radiation, η emitted by an on-axis point source is then

$$\eta = \int_0^{\frac{\pi}{2}} \rho^N \sin\theta \, d\theta \tag{106}$$

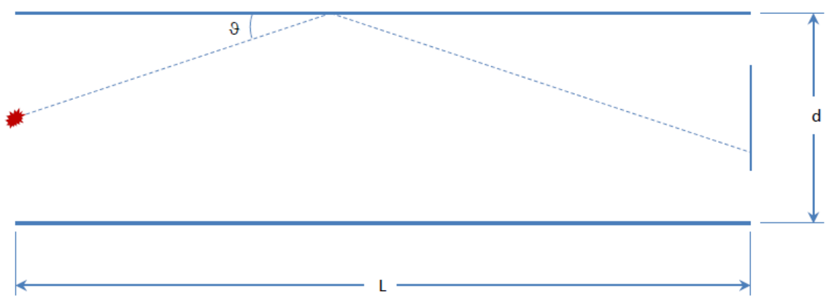

Figure 96: Thermal radiation ”light-pipe” geometry for an on-axis source

The plot of the radiation heat transferred to the mirror by specular radiation is shown in fig. 97. We see that

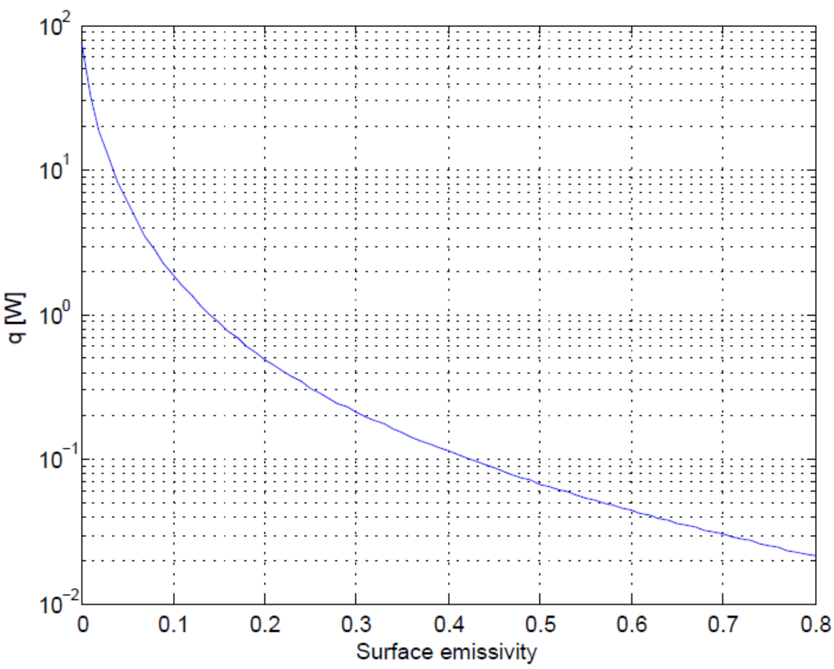

Figure 97: Thermal radiation heat transfer in the specular reflection limit

a huge amount of heat reaches the mirror for almost all the values of the emissivity.

Mitigation strategies.

- The *direct* radiation heat from the tube at 300 K to the cold mirror is strongly suppressed with cold sections (cryogenic shields, or cryotraps) near the mirror. With a section 10 meters long, cooled at liquid helium temperature, and a section 50 meters long, cooled at liquid nitrogen temperature, the direct heat transfer can be reduced in the milliWatt range. Obviously a reduction of the surface emissivity of the *warm* pipe can be helpful.

Figure 98: The displacement noise spectrum of the second stage cold point of the CRYOMECH PT407 and of the Sumitomo SRP-052A as function of the frequency.

- For the given cold pipe aspect ratio $L/d \sim 80$, the contribution of *diffuse* reflectivity of the surface of the cold sections becomes important only for reflectivity $\delta > 0.9$ ($\epsilon < 0.1$).
- Specular reflection in the cryogenic shields can increase the radiation heat transfer by two or three orders of magnitude. The effect can be controlled by placing absorbing baffles on the radiation paths inside the cold pipe; by coating the inner surface of the cold pipe with an high emissivity layer ($\epsilon > 0.9$); increasing the surface roughness of the cold pipe to suppress the mirror-like reflections

3.7.5 The cryogenic infrastructure based on pulse tube cryo-coolers

Author:F. Ricci

A simple approach to cool down the mirrors is based on the use of cryocoolers [281]. In particular, Gifford-McMahon (GM) refrigerators have been developed since a long time and are widely used in various fields of science and industries because of their convenient handling. However, their cooling power is provided by the motion of a displacer which causes large vibrations at the cold head, an aspect which makes them not suitable for all applications where a low acoustic noise level is necessary.

In more recent times, the pulse tube (PT) cryocoolers have been developed. The particular thermal cycle of PT refrigerators gives them a two or three times higher efficiency than GM cryocoolers for loads temperatures between 55 and 120 K, and requires no moving elements at low temperature. This latter characteristic is quite important: because of it, we expect PT refrigerators to be intrinsically more reliable and less noisy than classic GM coolers [282]. Thus, a pulse tube cryocooler seems to be an interesting option for our purposes. However, because of the gas pulse flowing in its cold head, also this kind of refrigerator injects mechanical noise in the cooled sample, at a level which is still far too high for the elements of a gravitational antenna. Indeed, in order to detect gravitational waves, current detectors have reached displacement sensitivities of the order of $10^{-18} m/\sqrt(Hz)$ and an increase by at least two orders of magnitude is foreseen for ET, where we have to implement the use of low temperatures.

The starting point of the system design is the choice of the pulse tube refrigerator model. We compared two different models of cryo-coolers, the Cryomech PT 407 and the Sumitomo SRP-052A. For both systems, we measured the acceleration of the 4 K cold head.

Our data show that the vibration noise level generated by the Sumitomo is lower by a factor ~ 10 than that by the Cryomech. Moreover, our model of Sumitomo has the additional advantage of having the room temperature throttle valve separated from the main body of the refrigerator, with the possibility to keep it far from the cryostat obtaining a further attenuation of the noise produced by this element. However, the first harmonic generated by the pulse tube is around 1 Hz and it is not attenuated efficiently by the super attenuator chain. In order to overcome this difficulty, the plan is to apply the technologies developed for gravitational interferometers and to reduce the vibrations of the cold finger of a PT cryocooler by an active control system. In the past we designed a vibration free cryostat [283] for limiting the cryocooler vibration, according to the issues discussed above. The cryostat scheme is sketched in figure 99. It is based on the idea to attenuate the cryocooler vibrations by directly acting on it. The cold head vibration is monitored by an optic bundle fiber, a displacement sensor acting as low temperature, while the actuation is based on three piezoelectric stacks set at room temperature outside the cryostat vacuum. The cryocooler cold head is clamped to a platform placed on dampers and it is connected to the cryostat by a soft bellow designed to mechanically decouple it from the cryostat. The feedback correction signal is sent to the three piezo-actuators which are loaded by the platform and can push the cold head platform elastically coupled to cryostat mechanical structure.

At present the attenuation achieved controlling just the vertical degree of freedom is of the order of $3 \cdot 10^{-3}$. A further improvement is expected by controlling the horizontal degrees of freedom and by reducing the recoil

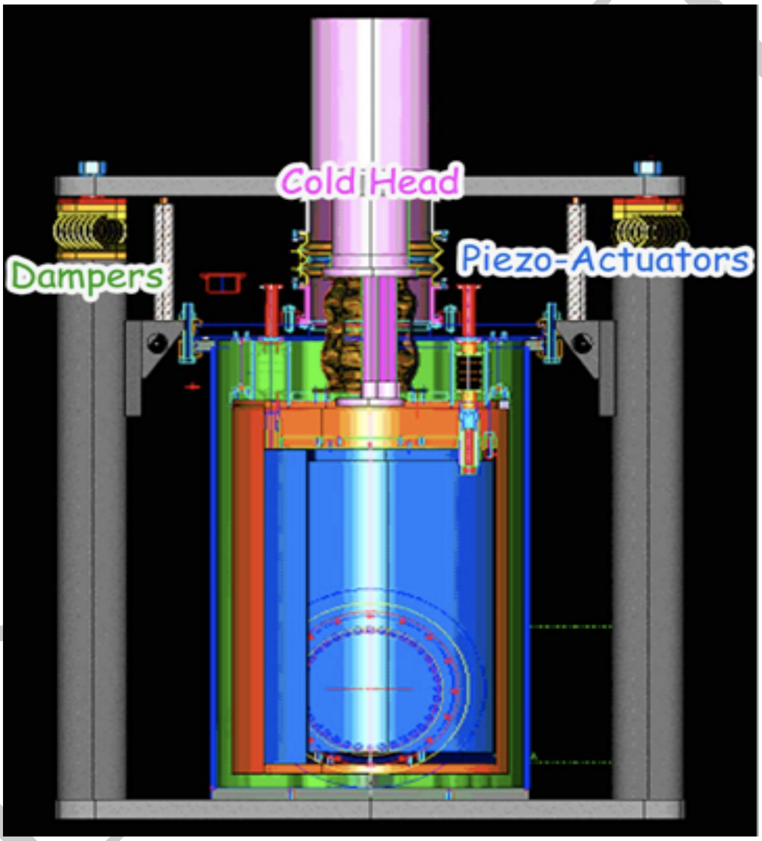

Figure 99: A simplified scheme of the vibration free cryostat.

effect on the structure holding the monitor sensor of the 4 K stage. However this active attenuation system is not sufficient and in parallel to this R & D effort industrial studies a are under way [284] , new proposals have been presented [285] to reduce the the cryo-cooler vibration. We discuss some of new ideas in the R& D section 3.7.9.

The cryo-plants based on PT cryo-coolers implies to install for each tower hosting a test mass a doublet of one stage and two stage PT cryocoolers. A similar solution is used to cool the ancillary tower. It will permit to speed up the cooling process providing a redundancy during the data taking phase. Each PT cold head is driven by a helium compressor via a couple of high pressure flexible line of a maximum length of 30 m. A larger number of cryocoolers (10 [to be CHECKed in function of the cryotrap length and its thermal input]) are needed for the helium cryotraps (see 3.7.4). Each compressor operates at a pressure $\sim$ 22 bar, it requires 5 l/min of refrigerated water and it absorbs an electrical power drawn at 50 Hz between 5 - 8 kW depending on the model. Although they are classified as silent models the typical acoustic noise level at 1 m distance is $\sim$ 53 dB(A). To reduce the noise trouble, due to the presence of compressors, an underground hall must be

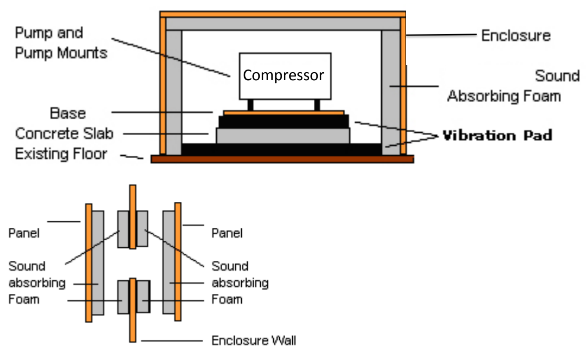

Figure 100: The standard mounting of a compressor to damp the vibrations.

created as a separated part of the main cavern hosting the super attenuator towers . The wall of this hall has to be treated by a sound insulation system, to avoid noise transmission between the compressor hall and the test mass area (see fig 100). Seen the number of compressors for each tower and the requested amount of water flow and electric power great emphasis must be put on the safety issues concerning this auxiliary hall of $\sim$100 m^2 surface. We have to notice also that the gas pulse vibration is transmitted also along the high pressure helium flexible lines. Thus, the line require a specialized design and construction: it will include an acoustic sheath covering the flexible tube and massive concrete slabs to anchor several sectors of the gas lines.

Although this solution has been adopted in LCGT, we stress that the vibration issue is one of the most limiting factors of a low temperature GW experiment and it requires a R&D activity to be carried on in collaboration with the specialized industries.

3.7.6 The cryogenic fluid approach

Author:F. Ricci

Cryogenic fluids in the form of liquid helium and liquid nitrogen are required to circulate for cooling the cryostats of the test masses and the associated cryotraps. The heat load requirement at a particular temperature is a prime important factor to select a helium refrigerator/liquefier and to define the dimensions of the nitrogen

Table 7: Summary of pro and contra of the cryocooler approach

In favor
higher duty cycle
limited manpower
Against
high level of vibration
high electric power consumption in the underground environment
Infrastructure requirements
distribution of high pressure lines
compressors hosted in auxiliary caverns
efficient water refrigeration system

plant. The cryogenic systems of ET should operate in different modes cool down, steady state and warm up for each test mass tower, The cooling time is a trade off between the need to limit the detector down time and the stress due to the thermal gradients During cool down the recommended flow rate of helium gas will be approximately $\sim$ 1 g/s. The heat load requirement of cryogenic systems including the transfer loss at steady state is approximately $\sim$ 20 W at 4 K [to be CHECKed in function of the cryotrap length and its thermal input] helium refrigerator/liquefier. A helium refrigerator/liquefier having refrigeration capacity of 160 W at 4 K in refrigerator mode and 50 L/h in liquefier mode without LN2 pre-cooling and 200 W at 4.5 K in refrigerator mode and 100 L/h in liquefier mode with LN2 pre-cooling, is sufficient to guaranty the cooling in the vertex area of the triangular interferometer. In this evaluation a redundancy factor has been included so that the system will satisfactorily cater the refrigeration load at different state.

As we anticipated before, to reach a full flexibility of the system, the possibility of performing the cool-down and the regeneration with the main refrigerator has been foreseen too. The cryogenic system will include a distribution valve box and the cryogenic piping up to the interface of the ET cryostat. The distribution valve box contains a 1000 L liquid helium control dewar, a heat exchanger, an electrical heater, a Joule-Thompson cryogenic valve and relevant instrumentation for pressure, temperature and flow rate measurements. The cryogenic system has to deliver, in a controlled way, the cooling helium from the refrigerators to the client. It includes mainly a 80 K gas helium circuit and a 4.5 K helium circuit, that can be interconnected through bypass valves; both shut-off valves and control valves are used. The 1000 L liquid helium dewar is used as buffer to stabilize the thermal loads and as re-cooler of the helium coming from the main refrigerator. A 45 kW electrical heater on the return line of the 80 K circuit and a 1 kW electrical heater on the return line of the 4.5 K circuit are foreseen to test the cryoplant with dummy loads and also to compensate dynamic thermal loads. An electrical heater and a cooling system are planned to make the system appropriate to operate an high temperature regeneration (470 K) and to cool it down again to room temperature.

The redundancy of several elements is added to improve the reliability and the effectiveness of the cryoplant during the experimental conditions and to make it more flexible.

The European industries have demonstrated there ability to construct complete refrigeration systems both for the needs of the huge accelerator and the associated detectors. Thus, the main refrigerators for ET will be realized with proven industrial technologies and tailored on the GW detector needs. It will be based on Claude cycle and it will provide the coolant helium at the required temperature for cooling the mirror. For the liquid helium distribution, we recall here that long and low thermal loss lines were developed at CERN already in the context of the LEP project. Since this time several improvements in design with respect to earlier lines of similar construction, made it possible to achieve reproducibly linear heat in-leaks of $\sim$ 30 mW/m. At present the LHC refrigeration system is connected to the 27 km long accelerator thanks to high performances helium transfer lines, which exhibit a variety of types, sizes, design choices and layouts.

In the ET case the refrigerator will be installed on the surface building and the liquid helium has to be sent by long transfer lines to the underground detector, like the case of the LHC cryoplant. The transfer lines are based on the four-fold coaxial corrugated tube design Each line is made of austenitic stainless steel and the coaxial assembly provides an inner channel for the supply of liquid or gaseous helium an annular channel acting as a shield for the return of cold vapor , and a common vacuum enclosure for thermal insulation. Low thermal conductivity spacers, made of teflon PTFE are set between the outer tube, return channel and supply pipe. The outer corrugated tube of the return channel is also super-insulated by several layer of aluminized mylar.(see figure 101

Figure 101: A cross section of a flexible transfer line developed at CERN in collaboration with Kabel Metalelectro [286]

In order to reduce the quantity of impurities in the helium and to recover the gas, a Purification and Recovery System is implemented in the cryogenic plant. It is composed by a helium vaporizer, a high pressure recovery compressor and a helium cryogenic purifier system. An atmospheric gas bag (100 m^3), high pressure containers (20 bottles at 20 MPa, 10 N m^3 each) for impure gas helium, 3 medium pressure tanks (30 m^3 at 2 MPa) for pure gas helium, a liquid nitrogen container (50,000 L) and dedicated transfer stainless steel pipe lines are provided for the fluids storage. The helium to be recovered is collected in the gas bag; if its temperature is too low to enter in the gas bag, the cold helium is sent to a vaporizer where it is heated to the ambient temperature before entering the helium gas bag. The helium coming from the gas bag is sent to the recovery compressor and stored in the high pressure (20 MPa) bottles from which is delivered to the impure gas storage. The impure gas helium flows to the purifier and then it is stored in medium pressure (up to 2 MPa) pure helium buffers connected to the cycle compressors.

The cryoplant will be installed in a building close to the main experiment building on surface. To reduce the noise trouble, due to the presence of compressors, a cryogenics compressor hall will be created as a separated part of the technical supplies building. The wall of this hall will be treated by a sound insulation system, to avoid noise transmission between the compressor hall and the other building.

3.7.7 Cryogenic plant control

Author:F. Ricci

The cryoplant design and the technical solutions to be adopted are focused on the optimization of the system performances and it will be conceived to implement all the required operative scenarios in a fully automatic mode.

The facility control system, based on a master/slave architecture, will be split into three plants (each for interferometer vertex) and three distinct supervisory systems will be provided with engineer and operator workstations.

The three control systems will be independent, but inter communication signals will be exchanged among the station units. The internal structure of the cryogenic control system will be based on PLCs (Programmable Logic Controllers), equipment of proven reliability in the industrial environment. A PLC will act as master of the local unit PLCs, with the purpose to coordinate the cryoplant activities and interface the logic unit with the upper subsystem level. Feedback control will be necessary to control for example the speed of the turbines or other parameters like temperature and pressure of the helium in different part of the cryogenic system; since the time constraints are not strict (response times of the order of seconds), the control routines will be executed without problems by PID (Proportional-Integral-Derivative) controllers inside the PLCs. A commercial off-the-shelf Supervisory Control and Data Acquisition system will be employed to monitor the plants, for operator intervention, commissioning, test purposes and data storage.

3.7.8 A future development: lowering the temperature with Helium II

Author:F. Ricci

The use of the liquid helium II (He II) appears to be an alternative way to cool at low temperature the mirrors. It limits the vibration noise associated to the other cryogenic fluids [287] and it provides a powerful way for extracting the heat from the mirrors. Modern large engineering projects for high-energy physics require thermostatic control of working components at the level of 1.8 - 2 K and are constructed with lengths of channels containing He II. The uniqueness of He II is that it contains a superfluid component with zero entropy, which moves through other liquids and solids with zero friction to an extent dependent on the temperature of the liquid. He II is a liquid of extremely low viscosity and very high heat capacity, which prevents small transient temperature fluctuations. Moreover, thanks to its very high thermal conductivity is able to conduct away heat a thousand times better than any metallic conductor like copper.

In He II, the heat from a hot surface is carried away by the superfluid component, so in any design with complicated geometry and helium flows, the entire heat load acts on the phase interface. The boiling mechanism involves evaporation from surfaces ad in a flow of ordinary boiling liquid, the heat influx is uniformly distributed in unit volume of the two-phase mixture. In stratified He II, the heat influx is associated with the interface between the phases, so the He II evaporation rate is increased by a substantial factor. A major feature of boiling in He II is that the evaporation of the superfluid component predominates. The heat load is transported by convection in the superfluid component, and this consequently evaporates more rapidly than does the normal component.

When a two-phase flow of He II moves in a heated channel, a droplet structure or mist is formed in the vapor space as the amount of liquid in the stratified flow decreases. In a stratified flow of an ordinary liquid in a large-diameter tube, an increase in the bulk vapor content leads to the vapor becoming superheated and the liquid evaporating completely. In He II one prevents the vapor becoming superheated by encouraging the spontaneous formation of a droplet structure with a large heat-transfer surface, which provides a constant temperature over the channel cross section.

An efficient and quiet configuration for cooling the mirror by He II is the *bain de Claudet*. Here the idea is to provide superfluid helium at atmospheric pressure and to insure continuous refilling from the container of the helium in the normal state. In this way the He II bath is kept in a quiet hydrodynamic status well far from the boiling point. In this case the cold box on top of the super attenuator of the ancillary tower is an heat exchanger filled by superfluid helium at atmospheric pressure and operating in the stationary condition of zero mass flow, which implies $\rho_s v_s = -\rho_n v_n$ in absence of the vapor phase, where ρ and v are the density and the velocity of the normal (n) and superfluid (s) components.

The He II mirror cooling approach requires also a deeper analysis of the impact of the acoustic losses of the fluid to the dynamic behavior of the suspended test masses. This effect should depend on the hydrodynamic regime of the helium II. In particular we need to consider the interaction mechanism between the two liquids (normal and superfluid), which determines the heat transport. In the case of a superfluid helium vortex formation this is described by the Gorter-Mellink force per unit length, which results a function of the velocity difference $|\vec{v}_n - \vec{v}_s|$. For a one dimensional helium flow f can be written as

$$f = \frac{\rho_n \rho_s}{(\rho_+ \rho_s)^2} \eta_n |\vec{v}_n - \vec{v}_s| \tag{107}$$

where η_n the viscosity of the normal fluid.

Moreover the design of the heat exchanger providing a sufficient refrigeration power is not straightforward. In fact the velocity difference of the two fluids depends strongly on the geometry of the heat exchanger, the nature of the material in contact with the fluid and the status of the contact surfaces. In conclusion in order to assess the validity of the cooling approach for the cryogenic design of the ET detector, we need to develop a complete hydrodynamic model including vapor phase and extra interaction terms as well as a deep R& D activity and prototyping.

3.7.9 R & D in Cryo-coolers

Author: F Ricci

As we pointed out in the previous section the focus of the R&D activity for cryo-cooler will be on the reduction of the vibration generated by the pulse tube. The pulsed force due to the gas deforms the tube of the cold head displacing the cold plate of several microns. These effect has been simulated via finite element software showing that in function of the the cold geometry the longitudinal expansion of the tube can be of the same order the horizontal displacement. Thus, there is a large margin of improvement on the active attenuation damping of the harmonics associated to the gas pulse.

Moreover it has been proposed to modify the mechanical design of the cold head to reduce the displacement vibration. Several attempt have been done already by several groups in the world, using different tube material, adding glass fiber support or using coaxial geometry [288].

An interesting idea has been proposed by Suzuki to utilize the vibration as counter force to compensate the pulse tube expansion with the constraint to adopt a compact configuration. In practice adding to the same cold head a couple of tubes pressurized by a gas wave with opposite phase to the other couples we can obtained a cancellation effect. In the figure 102 we show a first test carried on at KeK they tied improved the cancellation by adding more than one couple of tubes with suitable phase difference.

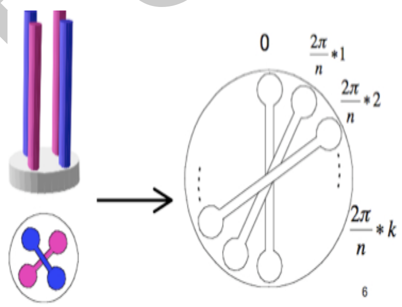

Figure 102: The pulse tube scheme proposed and tested by T. Suzuki at Kek [285]

As we discussed in the previous section 3.7.8, there are significant advantages to lower the temperature below the λ point and we can succeed to lower the temperature by modifying the cryoplant based on cryogenic liquids. However, the same temperature can be achieved using cryo-coolers. The standard two-stage PT operate with ^{4}He as working ßuid. Consequently the minimum no-load temperature of these PTs was above 2 K, because the thermodynamic properties of 4 He near the superfluid phase transition prevent cooling to lower temperatures. A regenerative cryocooler can cool below 2 K when ^{3}He is used as working ßuid instead of ^{4}He. This approach was pursued and a minimum stationary temperature of 1.27 K was achieved and at 4.2 K the cooling power was found to be larger than with ^{4}He [289]. This result has to be regarded as the starting pint of a possible evolution of the ET cryo-cooler plants, which requires higher refrigeration power and less vibration. To succeed in getting a significant improvement without spoiling the refrigerator performance a strong interaction with the PT experts and specialized cryogenic industry has to e set up.

3.8 Safety Issues

Safety and health would have the highest priority in the engineering of a deep underground laboratory and would be fully integrated into the design of laboratory activities at every stage of planning, design and construction. An underground laboratory would also provide an ideal laboratory for research and development leading to advances in underground safety systems and technology. Scientists and engineers could carry out safety and health research within a deep, controlled underground setting. Particular attention would go to advances in key areas such as underground communication, ventilation, access, emergency egress and refuge design. During all phases of operation (*e.g.* from construction to science operation) safety policies and guideline will have to be in place with regards to:

- Construction of the ET infrastructure: During the construction of the ET infrastructure the safety of both engineering and scientific personnel has to be insured. Hazards at this phase include explosions, strata collapse, vehicle collisions, fires, inundation, drowning and asphyxiation.
- Commissioning and scientific operation: During this phase it is assumed that construction has been completed. Hazards that have to be addressed are: strata collapse, explosions, water inundation and drowning, electrocution, fire, cryogens (*e.g.* rapid expansion > asphyxiation), and chemicals like sulphide minerals etc.
- Escape routes and fire doors: compartmentalising
- Cost examples from other underground facilities

3.9 Computing infrastructures

Author(s): T. Dent, S. Aoudia ...

3.10 Cost estimate

Preliminary cost analyses have been performed in order to optimize the cost-to-performance ratio for the ET Reference Design. Various components costs were estimated, options compared and significant cost-driven changes were implemented will maintaining the scientific performance goals. The estimates were based on numerous European-wide tenders and using the lowest reasonable price for the dedicated specifications. In addition, estimates were made of the explicit work force needed to support the respective activity. Four classes of cost are distinguished

- Site specific costs
- Infrastructure costs
- Detector costs
- Operating costs

The total estimated value for the ET Reference Design is xx MEuro (in 2010 €). An important result of the value costing is that it provides a basis for determining the relative value of various components and work packages. This enables an equitable division of commitments of the partners in the ET consortium.

The site specific costs for the ET Reference Design are related to the direct costs for providing the infrastructure to site the observatory and are estimated at xx MEuro (2010 value level). These costs include the underground civil facilities, services (electricity and water distribution), buildings and surface construction. These costs are site dependent and have been considered for a range of European sites. It should be noted that the actual site-specific costs will depend on the location where the observatory is constructed, and the facilities that already exist at that location.

The infrastructure costs include the direct costs for the safety and security systems, the vacuum system and the cryogenic infrastructure.

The explicit labor required to realize the construction project is estimated at xx million person-hours. It includes administration and project management, installation and testing. Part of the labor will be contracted and part will come from existing labor in collaborating institutions.

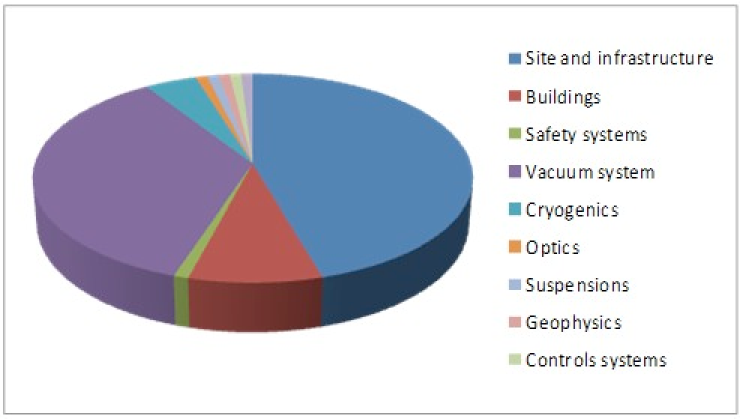

Figure 103: Cost breakdown of the ET Reference Design in single interferometer mode.

The cost breakdown of the ET Reference Design in single interferometer mode is shown in Fig. 103. This configuration constitutes the phase I instrumentation of ET and features a single xylophone interferometer. Phase II will be realized later and features a triple xylophone interferometer configuration.

The figure shows that the main cost drivers are the underground site infrastructure and the vacuum system. A breakdown of these main cost components is given in Figs. 104 and 105. Fig. **??** shows that the main cost drivers are the tunnels and caverns. Note that the cost of tunneling is site dependent. For the estimates we have used €260 / m^3 for the excavation costs. Several underground sites in Europe have been identified that comply with such costs, although a significant bandwidth applies. The number is also compliant with the site costs for LCGT in Japan.

The vacuum vessel constitutes the main cost driver for the vacuum system. In addition, the bake-out equipment is a significant cost driver. In order to realize the vacuum system at the estimated cost, it will be needed to set-up 3 vessel construction facilities at the ET site.

The budget estimate is structured as follows.

1. Facilities
   (a) Manufacturing facilities
      i. Factories: vacuum tube construction
      ii. Shops: mechanical, electronics workshops
      iii. Preassembly: cleanroom facilities
      iv. Testing
   (b) Conventional facilities
      i. Sites: main site and two satellite sites

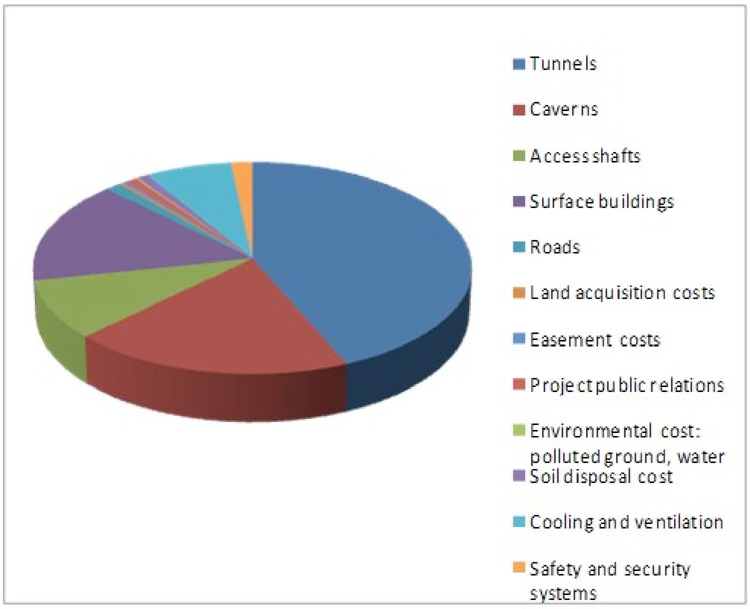

Figure 104: Partitioning of the site specific costs of the ET Reference Design.

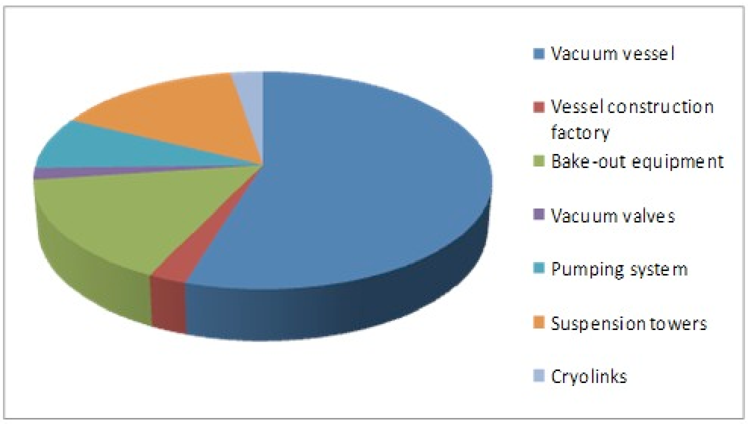

Figure 105: Partitioning of the costs for the vacuum system of the ET Reference Design.

ii. Buildings
iii. Tunnels
iv. Caverns
v. Main shafts
vi. Midway shafts
vii. Utilities
viii. Environmentals

Estimates for the cost of Einstein Telescope Reference Design in single interferometer mode (phase 1) are given in Table 1.1.

Project table 1.1. *Budget estimate for the Einstein Telescope Reference Design in single interferometer mode (phase 1).*

Subsystem	Cost [Euro]
Site and infrastructure	10,000
Buildings	10,000
Safety system	10,000
Vacuum system	10,000
Cryogenics	10,000
Optics	10,000
Suspensions	10,000
Geophysics	10,000
Control system	10,000
Computing	10,000
Total	**10,000 PlEuro**

Site requirements that impact construction cost must be considered. These include topography and geological subterranean conditions. Factors such as horizontal VS vertical access to the underground facilities greatly affect the construction costs. Site availability and acquisition cost can vary greatly. Availability of existing support infrastructure is important. Underground laboratories as Laboratorio Nazionali del Gran Sasso LNGS (Italy), Laboratoire Souterrain de Mondane LSM (France), Laboratorio Subterraneo de Canfranc LSC (Spain) and Institute for Underground Science, Boulby mine (UK) provide extensive facilities for scientific and technical staff. This includes accommodations for resident staff (housing, schools, etc.), and visiting staff (lodging, transportation, etc.). For the same reason active or closed down mines may provide valuable facilities such as hosting shafts, electrical infrastructure, water pumps, and safety systems. In addition, they may provide local technical support and experienced technical staff. Other factors that determine the (cost of) the main infrastructure design include groundwater conditions, hydrology and drainage which have an impact on the design of buildings and tunnels, accessibilities such as roads, railroad, distance to nearby supporting technical facilities, site utilities installations as power, water, and sewage. Finally, labour cost and proximity of soil waist and borrow areas must be considered.

Aside from construction costs, there are various factors impart the operation cost. These include the cost of electrical power, cost of local labour, heating and cooling requirements, maintenance, and travel time and cost for visiting staff. Environmental, health and safety plans must be put in place to assure the safety of users, staff and visitors to ET. These plans must comply with the relevant governmental and European standards and regulations. It is important to elevate the life-safety level above that in the mining and underground construction industries to one appropriate for researchers, students, and the public.

Risk must be minimized in the realization of ET. Risk factors include acquisition risk, risk from environmental sources such as earthquakes, floods and storms. Special attention must be paid to potential future man-made noise and vibration from development or industrial projects.

3.11 Technologies to be developed

Author(s): D.Rabeling, C. Bradaschia, P. Puppo

- GGN subtraction schemes
- ...

3.12 Appendix A: Seismic measurement results

All the seismic measurements have been made possible with the dedication and help from a vast number of locals. To all the people that have provided their expertise, time and assistance we would like to extend a sincere thank you. Due to the extent of the research it is impractical to list all those people but we would like to thank a few people in particular. For fruitful discussions and advice as well as facilitating measurements at the Heimansgroeve we thank Reinoud Sleeman and his colleagues from the KNMI. We also acknowledge their help in obtaining data from the Virtual European Broadband Seismograph Network (VEBSN). The measurements in Hungary were generously supported by Istvan Racz of the RMKI, Budapest, and the mining company MECSEK-ÖKO. For assistance during the measurements in Romania we are grateful to Romul Mircea Margineanu and the Salrom mining company. The Frejus tunnel measurements were kindly facilitated by Michel Zampaolo of the Laboratoire Souterrain de Modane. We thank Alessandro Bettini and Jose Jimenez of the Canfranc Underground Laboratory for their help during measurements in Spain. We are grateful to Fulvio Ricci, his colleagues from University "Sapienza" and the miners of IGEA spa, for access to the Sardinian site. We would also like to thank Eugenio Coccia and Benedetto Gallese for their help during measurements at the Gran Sasso underground laboratory. We are very grateful to Rudolf Widmer-Schnidrig, Thomas Forbinger and Walter Zuern of the Black Forest Observatory for the interesting discussions and access to their laboratory. We acknowledge Guido Nuijton for his thoughts on sites in Finland. For measurements carried out at the CLIO site in Japan we thank, Kazuaki Kuroda, Uchiyama Takashi, Osamu Miyakawa and Miyoki Shinji. Ricardo de Salvo and friends at the Italkali mine in Sicilie kindly assisted the measurements there. Finally we would like to acknowledge the help of EURIDICE staff members, Philippe van Marcke and Kris Moerkens, during measurements in Belgium.

Germany - Black forest

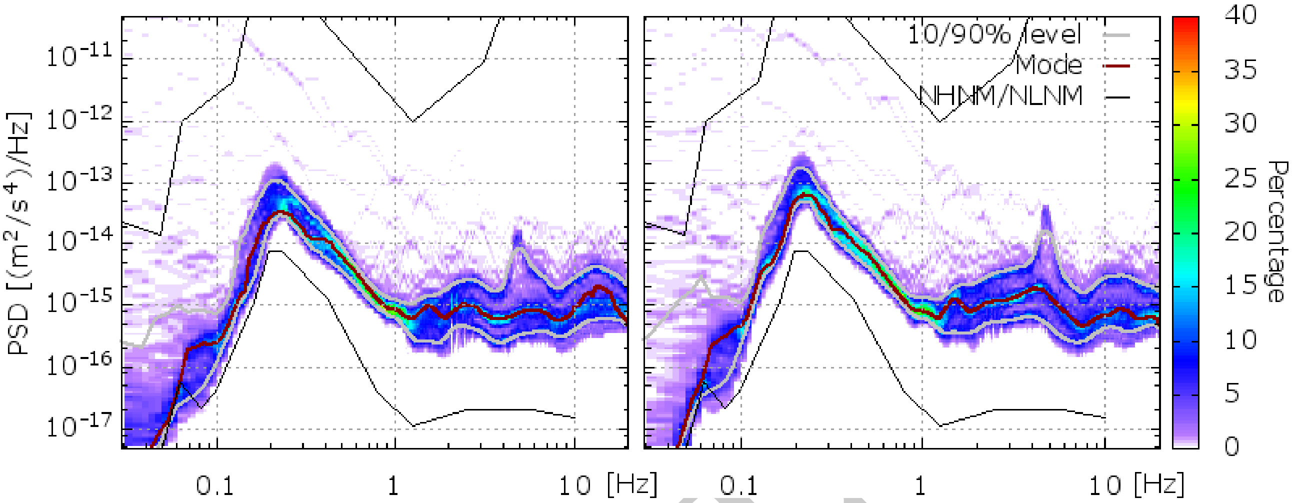

Figure 106: The horizontal component (left) and the vertical component (right) power spectral density plotted as a spectral variation from the Germany - Black forest site.

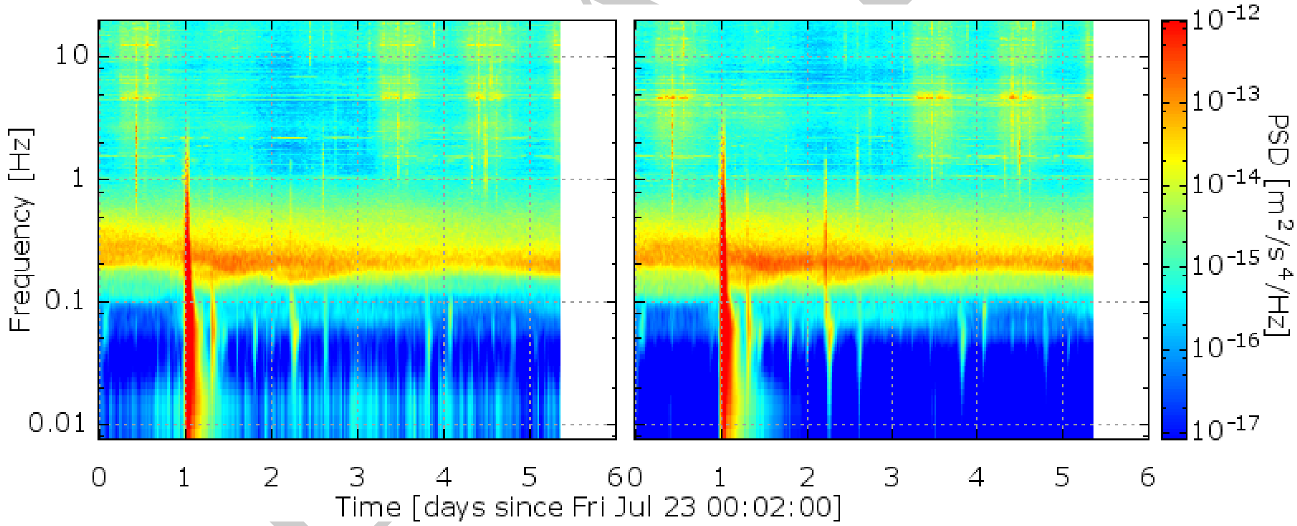

Figure 107: The spectrogram of the horizontal (left) and vertical (right) component from the Germany - Black forest site.

Spain - Laboratorio Subterréneo de Canfranc

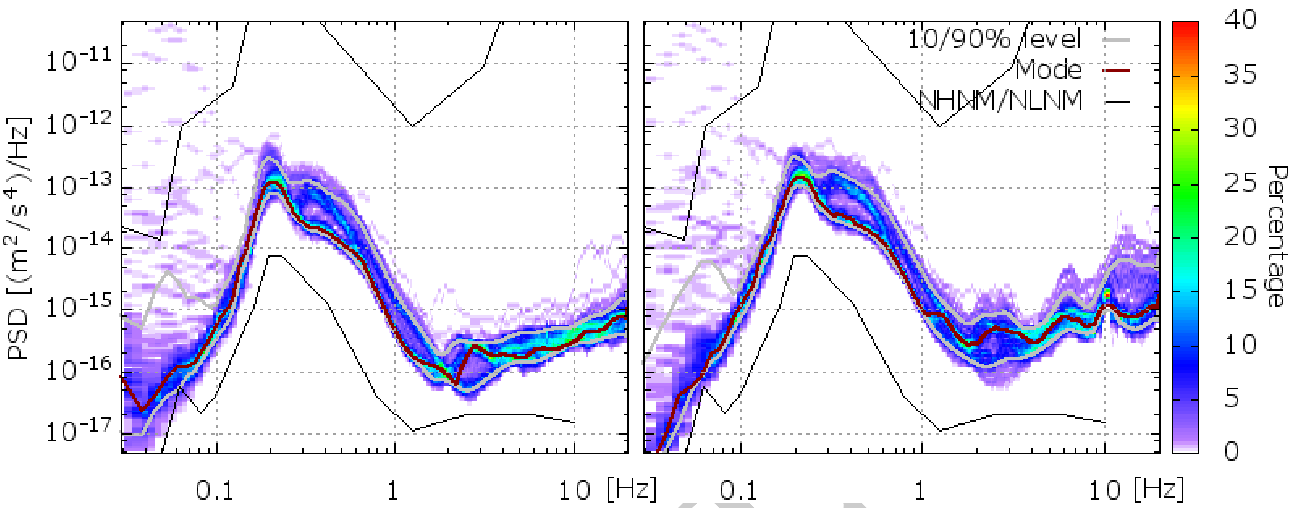

Figure 108: The horizontal component (left) and the vertical component (right) power spectral density plotted as a spectral variation from the Spain - Laboratorio Subterréneo de Canfranc site.

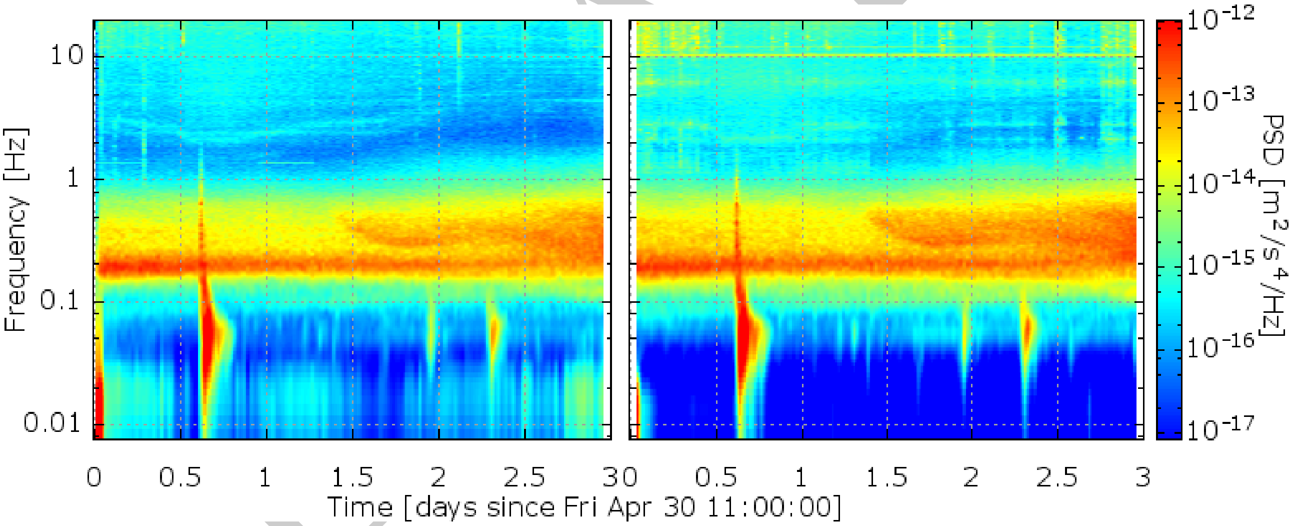

Figure 109: The spectrogram of the horizontal (left) and vertical (right) component from the Spain - Laboratorio SubterrÃ¡neo de Canfranc site.

Finland - Sumiainen

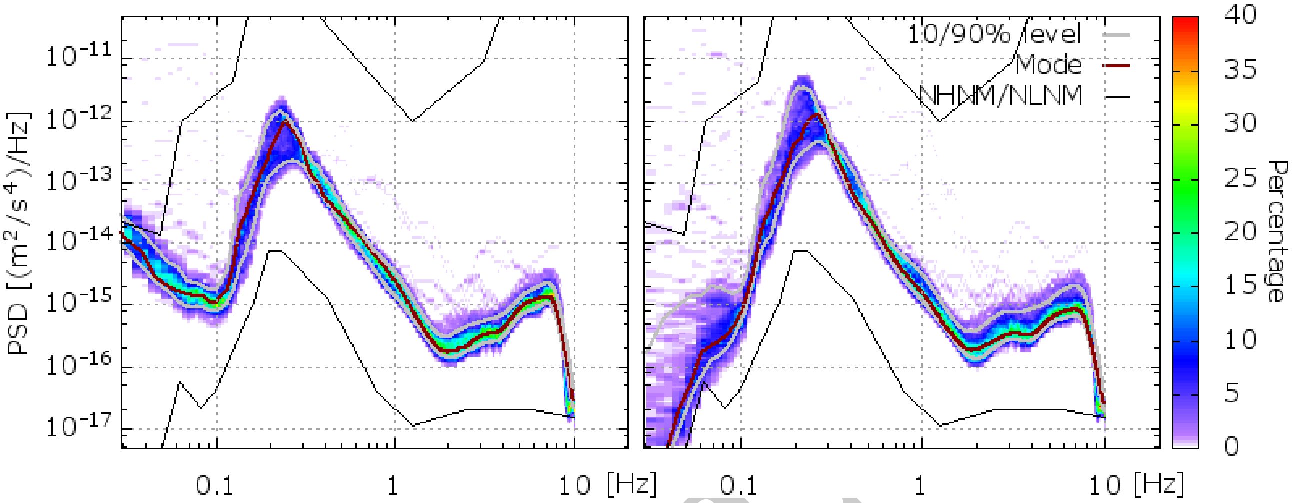

Figure 110: The horizontal component (left) and the vertical component (right) power spectral density plotted as a spectral variation from the Finland - Sumiainen site.

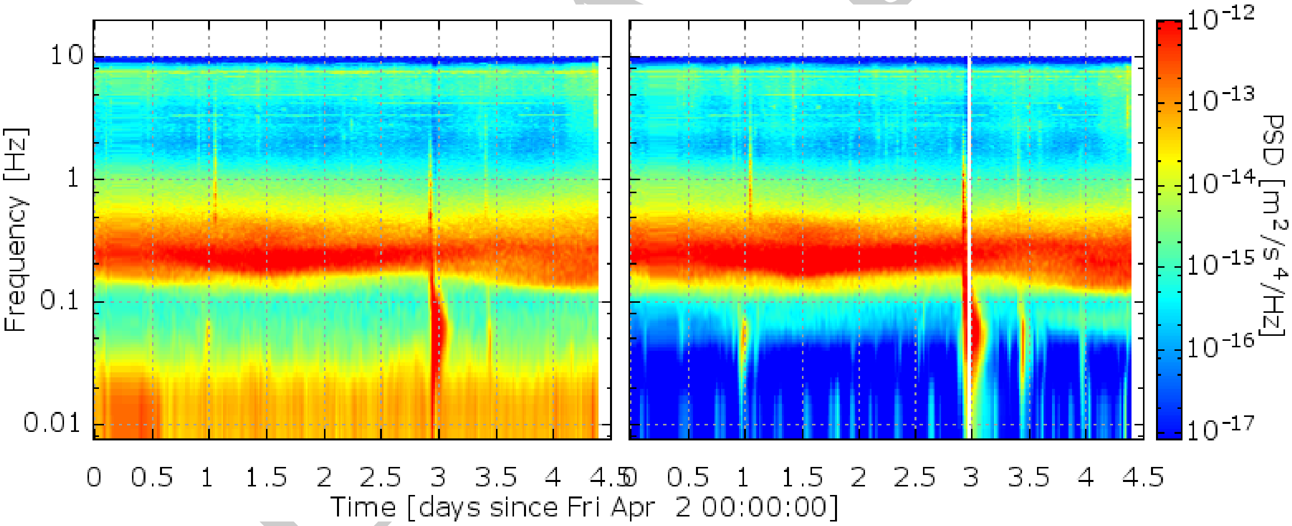

Figure 111: The spectrogram of the horizontal (left) and vertical (right) component from the Finland - Sumiainen site.

France - Frejus

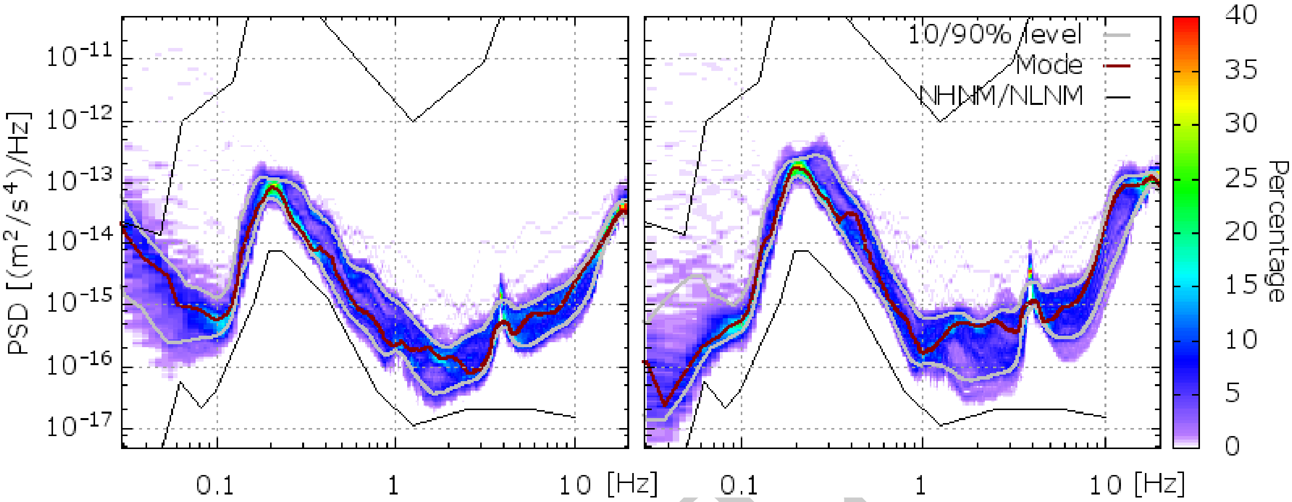

Figure 112: The horizontal component (left) and the vertical component (right) power spectral density plotted as a spectral variation from the France - Frejus site.

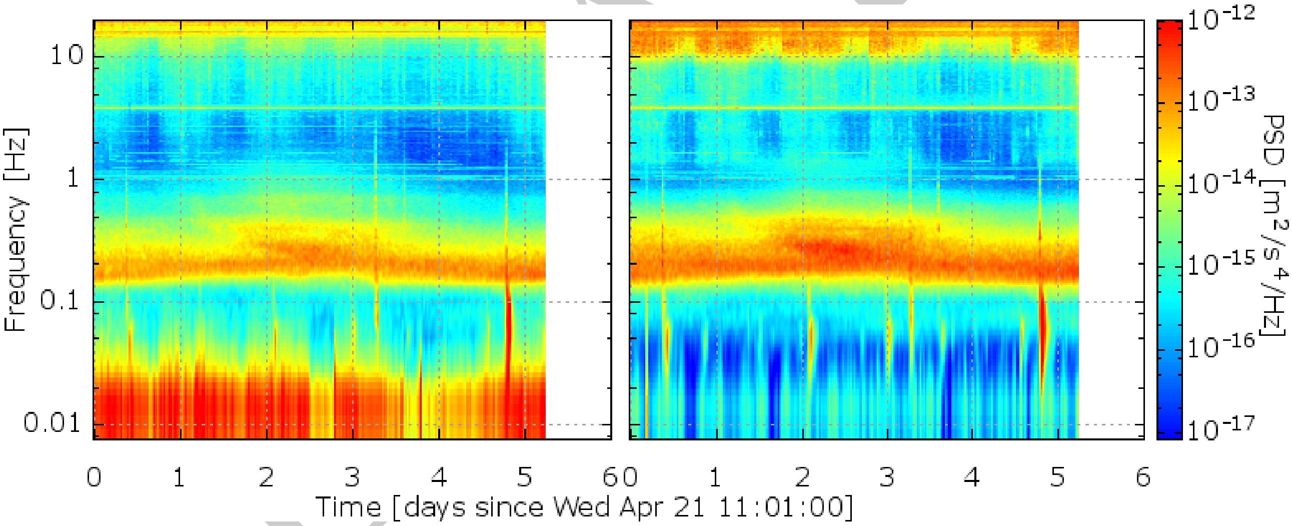

Figure 113: The spectrogram of the horizontal (left) and vertical (right) component from the France - Frejus site.

Italy - Gran Sasso

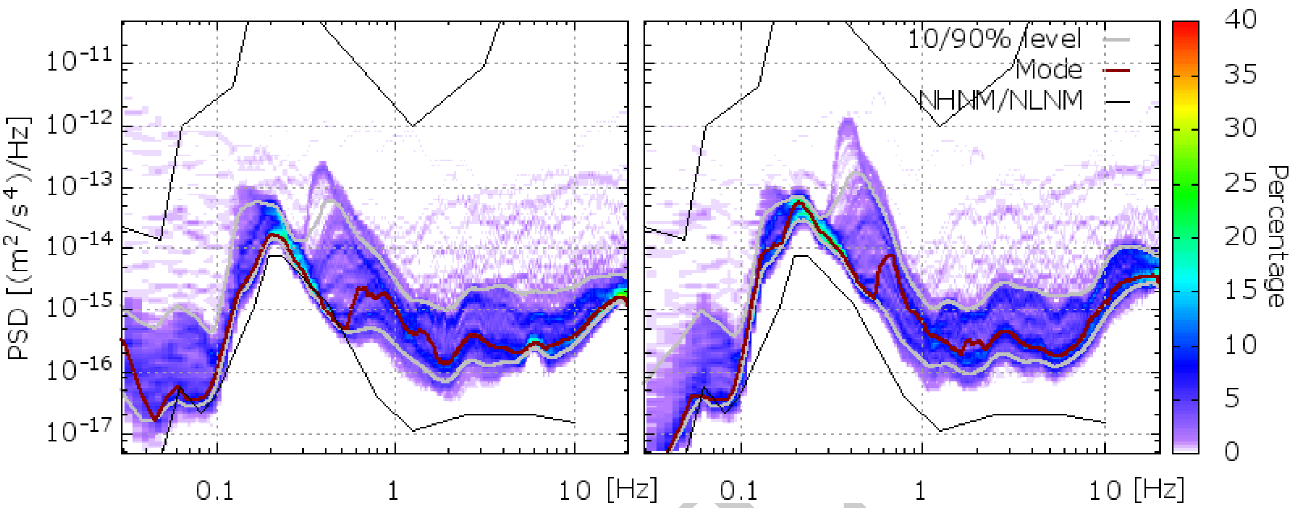

Figure 114: The horizontal component (left) and the vertical component (right) power spectral density plotted as a spectral variation from the Italy - Gran Sasso site.

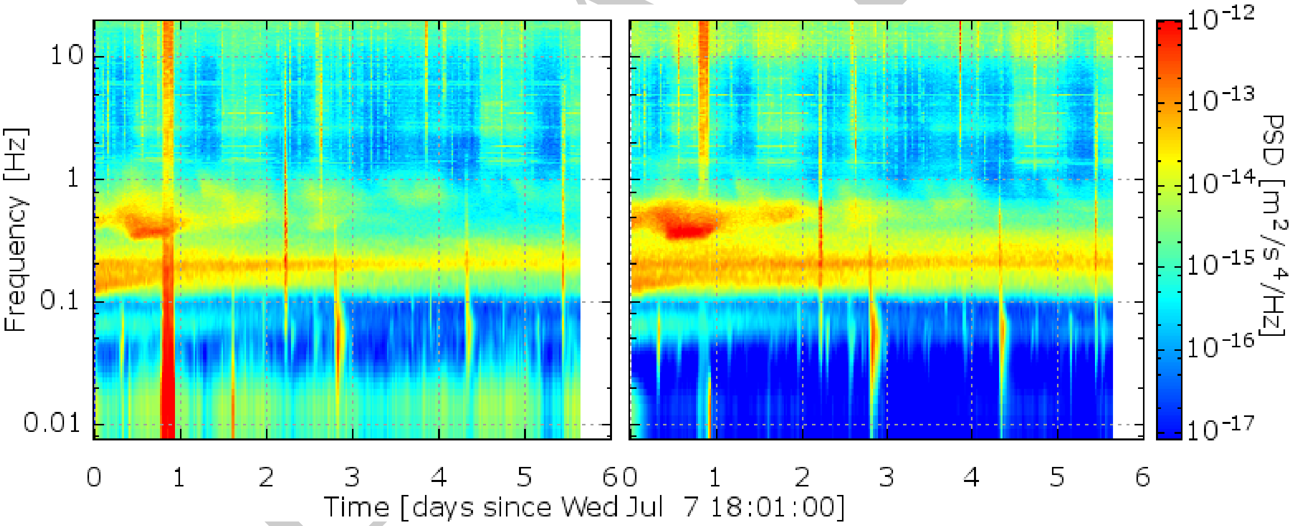

Figure 115: The spectrogram of the horizontal (left) and vertical (right) component from the Italy - Gran Sasso site.

Japan - Kamioka mine

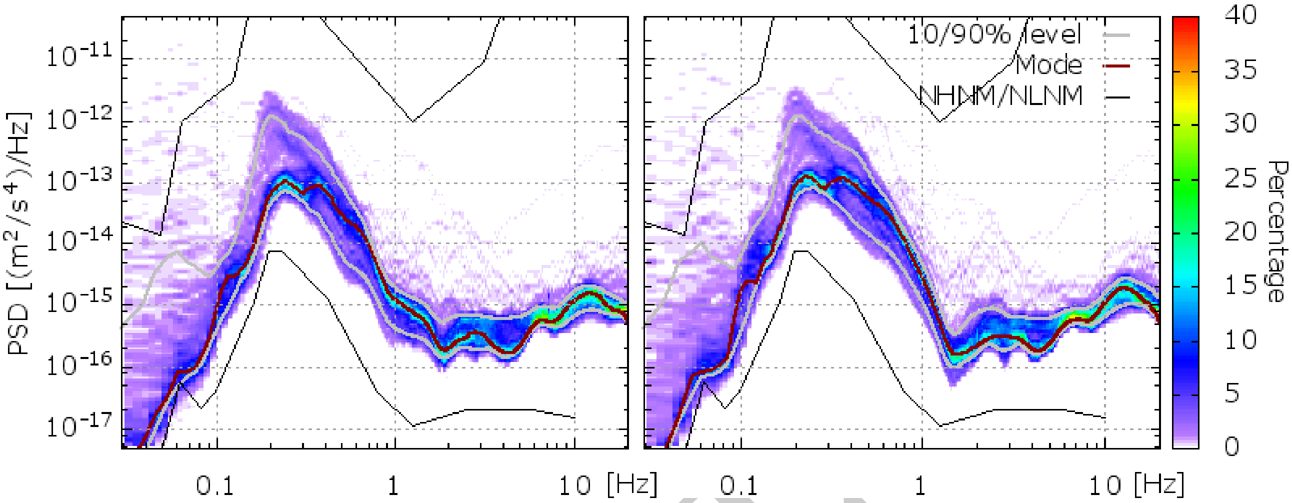

Figure 116: The horizontal component (left) and the vertical component (right) power spectral density plotted as a spectral variation from the Japan - Kamioka mine site.

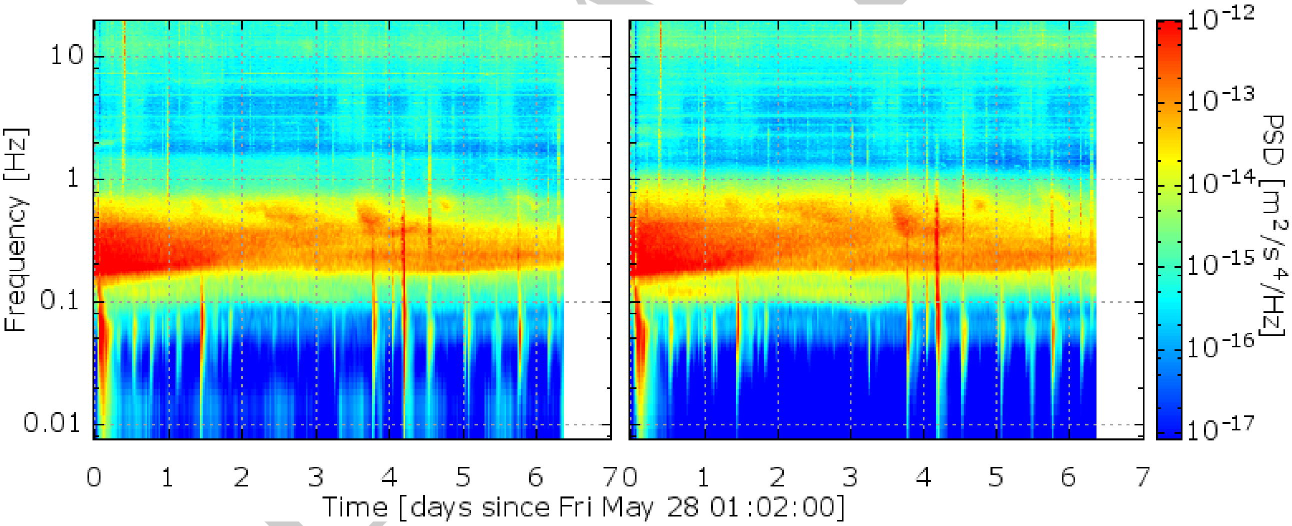

Figure 117: The spectrogram of the horizontal (left) and vertical (right) component from the Japan - Kamioka mine site.

Germany - Moxa

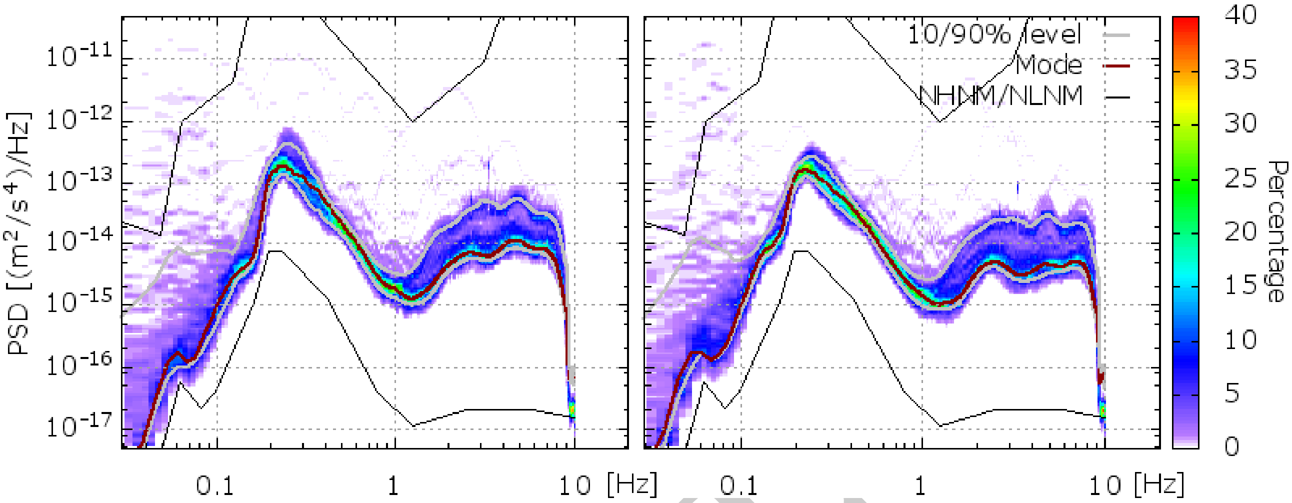

Figure 118: The horizontal component (left) and the vertical component (right) power spectral density plotted as a spectral variation from the Germany - Moxa site.

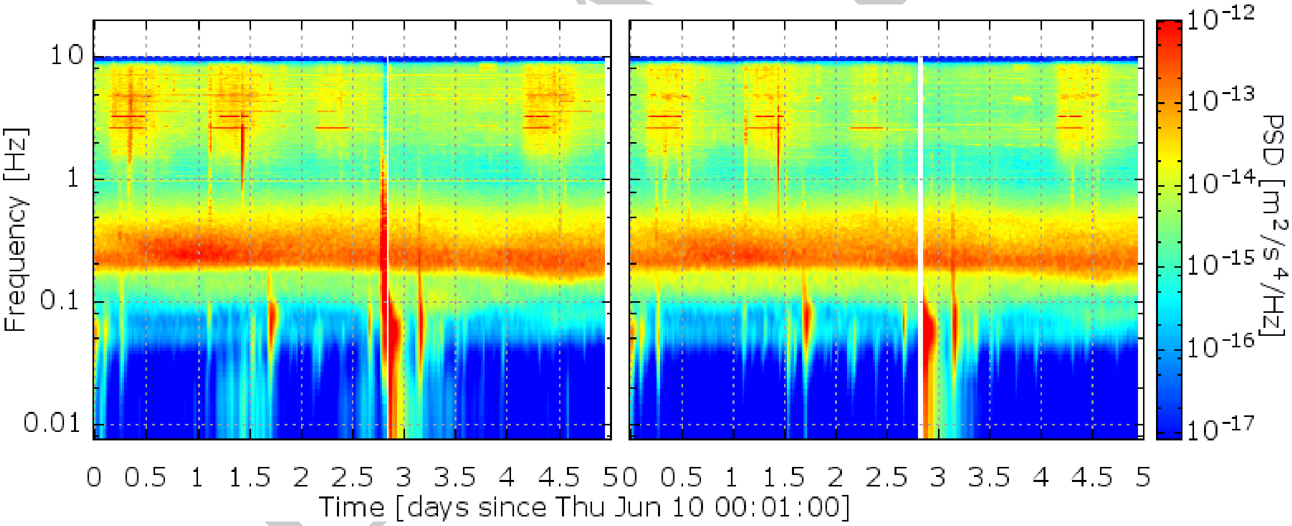

Figure 119: The spectrogram of the horizontal (left) and vertical (right) component from the Germany - Moxa site.

Netherlands - Heimansgroeve

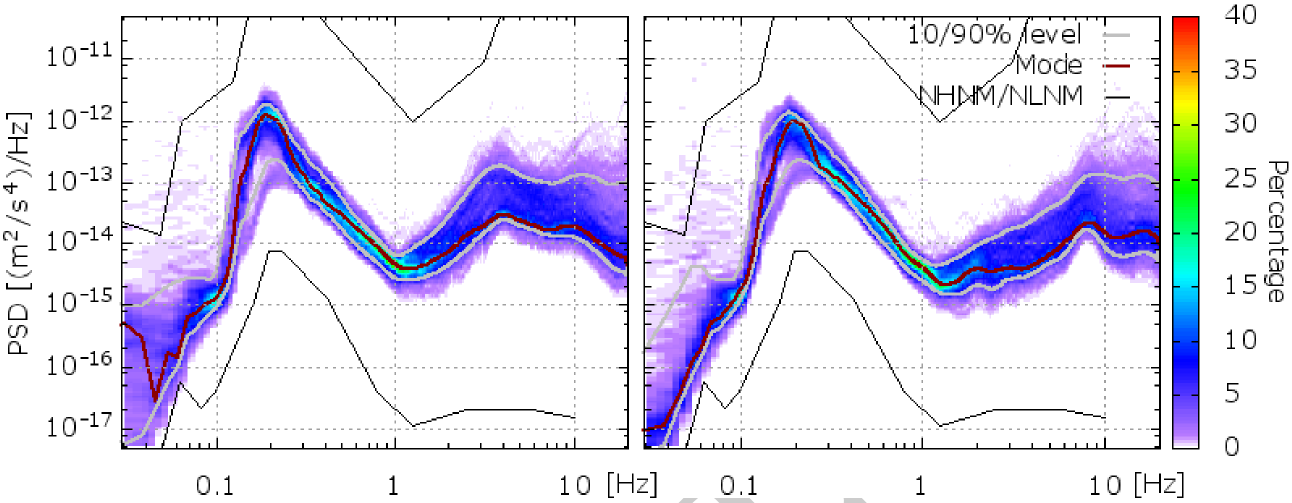

Figure 120: The horizontal component (left) and the vertical component (right) power spectral density plotted as a spectral variation from the Netherlands - Heimansgroeve site.

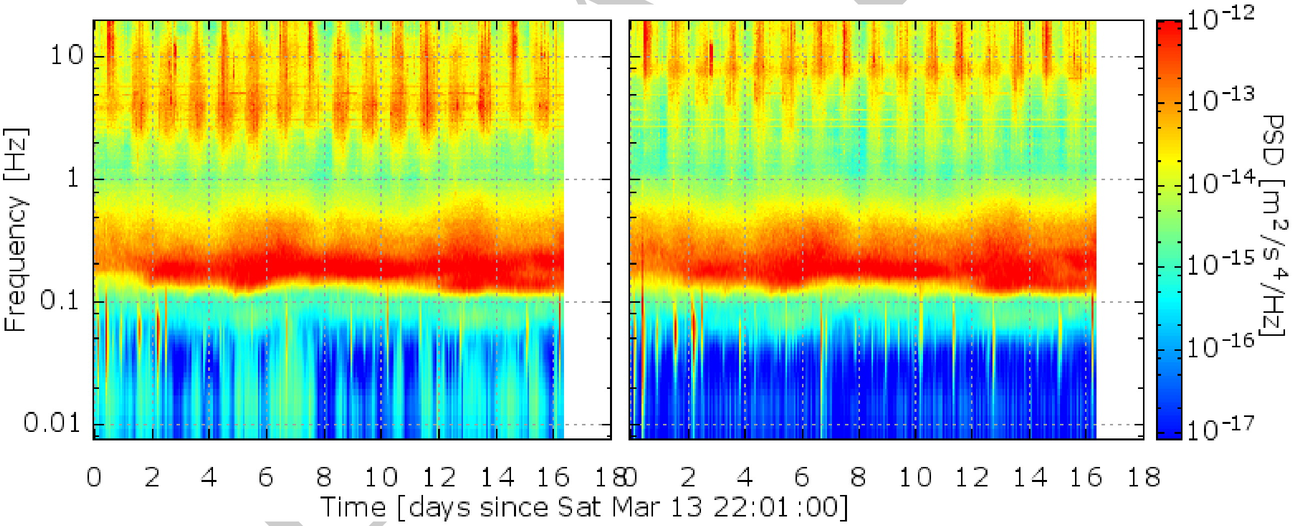

Figure 121: The spectrogram of the horizontal (left) and vertical (right) component from the Netherlands - Heimansgroeve site.

Romania - Slanic-Prahova

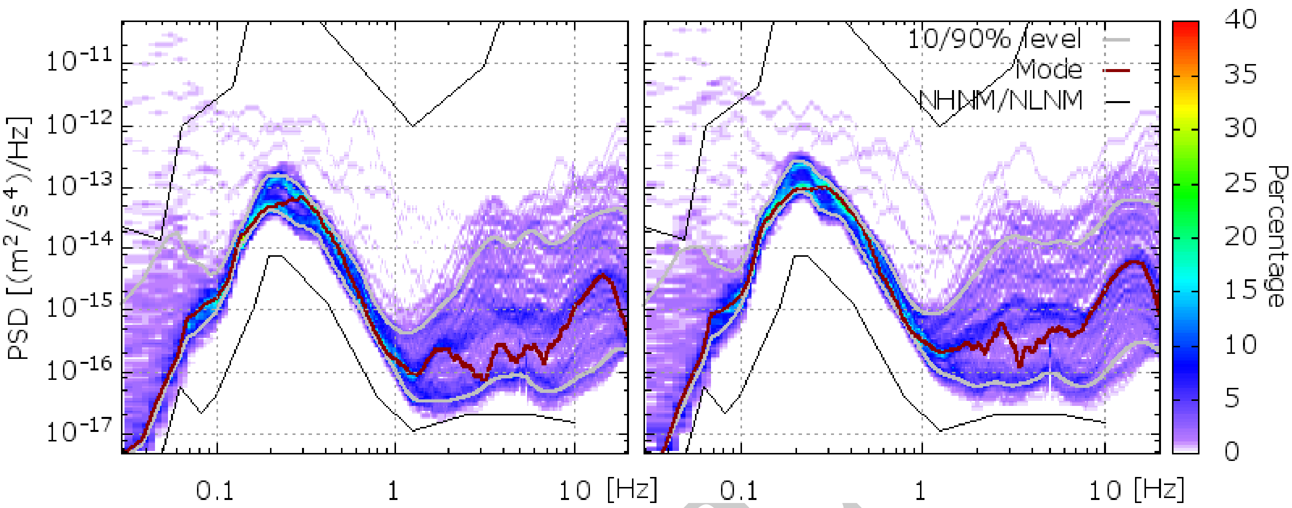

Figure 122: The horizontal component (left) and the vertical component (right) power spectral density plotted as a spectral variation from the Romania - Slanic-Prahova site.

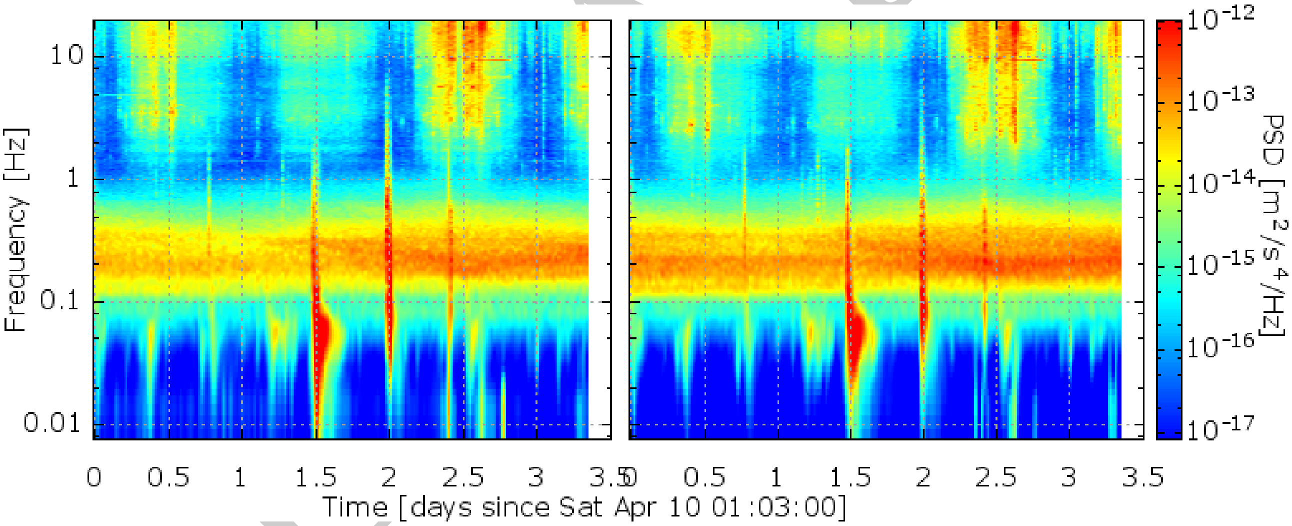

Figure 123: The spectrogram of the horizontal (left) and vertical (right) component from the Romania - Slanic-Prahova site.

Belgium - Mol

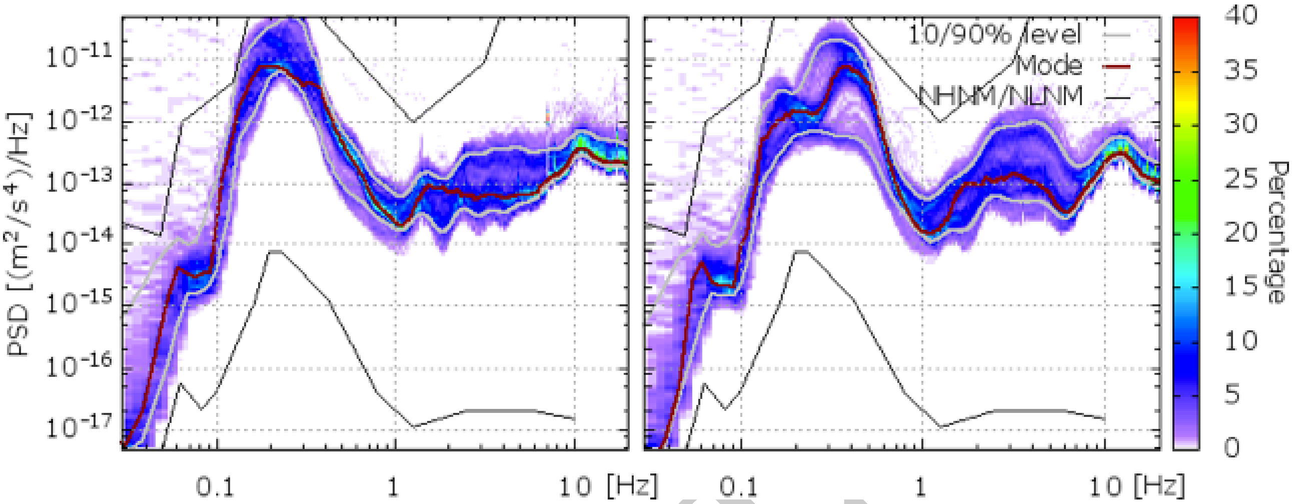

Figure 124: The horizontal component (left) and the vertical component (right) power spectral density plotted as a spectral variation from the Romania - Slanic-Prahova site.

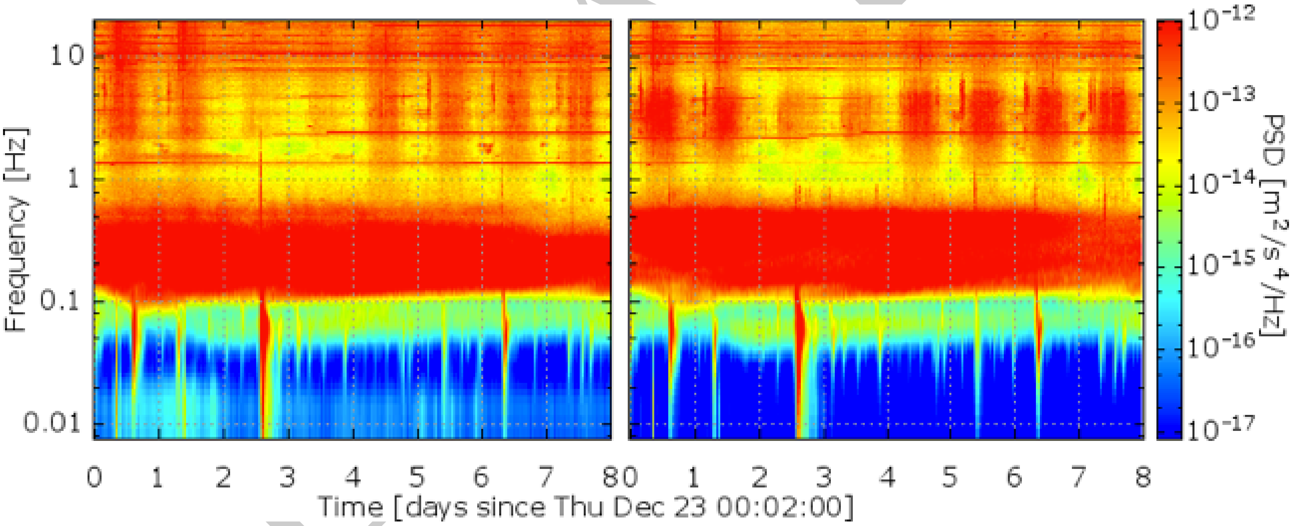

Figure 125: The spectrogram of the horizontal (left) and vertical (right) component from the Romania - Slanic-Prahova site.

3.13 Appendix B: ET infrastructure drawings

4 Suspension systems

4.1 Description

Responsible: WP2 coordinator, F. Ricci

The suspension system in the gravitational-wave detector isolates the test masses from the seismic vibrations of the ground and it ensures that test masses are nearly in a free fall state in the frequency bandwidth of interest.. The suspension is a cascade of mechanical filters providing the necessary attenuation from seismic and acoustic noise and by means if which we implement the control strategy necessary to keep the interferometer at its working point.

The last stage of the suspension plays also an other important role: all the mechanical elements which are connected to the mirror are designed not to degrade the intrinsic mechanical losses of the mirror itself. This is necessary because of the well known relation between mechanical dissipations and thermal motion in macroscopic systems. The thermal noise contribution is reduced by developing sophisticated suspension systems with materials with low mechanical dissipation and low friction mechanical clamps. However, to achieve the goal sensitivity of third generation detectors at low and intermediate frequency, a further reduction of thermal noise contribution is obtained by cooling the mirror and its last stage at cryogenic temperature. Cryogenic operation introduces a number of complications, but the benefits in the reduction of thermal noise is enhanced also by selecting materials with improved properties at low temperatures.

A major challenge for cooling the mirror is to provide an efficient path for heat conduction while still maintaining good thermal noise and mechanical isolation performance. The cooling system needs to provide adequate heat extraction from the test masses, for both steady state operation and for cooling from room temperature in a reasonable time, without adding noise or short-circuiting the mechanical isolation. This constraint has an important impact on the design of a last stage of cryogenic suspension.

In the next sections we analyze in sequence these aspects and we will try to synthesize a perspective solution for each of them and present also possible alternative approaches. We conclude with an overview of the related technologies to be developed.

4.2 Section summary

We organized the design study of the ET suspension focusing the activity on four main arguments:

- The upper part of the suspension, the *superattenuator* (SA), providing the need seismic and acoustic insulation. This issue is discussed and the solution is presented in the Upper Stage section 4.4.
- The last stage (payload), crucial for the defining the thermal noise performances and the mirror control and presented in paragraph 4.5
- The local control strategy and the related instrumentation, analyzed in 4.5.7,4.5.8,**??**,4.5.9, **??**
- A overview of the main technologies to be developed for achieving the ET scientific goal, (see sec. 4.6)

We notice that to clarify some of the open problems, several R & D programs have been carried out but with limited resources. in particular a bigger effort should be done in the domain of the material studies and of the low temperature sensing devices. Nevertheless we succeed in preparing a reference solution and a set of alternative scenarios for driving the ET technical design. However the solution selection requires intensive experimental activity and the coordination efforts will be significantly effective only if continuous activity in the laboratories is sustained and coordinated in collaboration with the Japanese project LCGT.

4.3 Achievements

The preliminary activity of the WP2 was centered on the definition of ET suspension requirement. In particular we collected and compared the mechanical and thermal properties of the materials at room and low temperature. Both silicon and sapphire potentially offer superior performance at cryogenic temperatures. In particular silicon samples can be obtained in large cylindrical blocks of mass higher than 100 kg. Its attractive thermal and thermo-mechanical properties makes it a strong candidate for the mirror and the suspension fiber in the future detector operating at cryogenic temperatures.

The low and high frequency interferometers (LF-ET and HF-IT) proposed in the ET design study require different suspension systems. In the following we will show that the SA as it is operating within the VIRGO interferometer is already compliant with the HF detector requirements. On the other hand for LF-ET a dedicated effort is required. in fact, to extend the detection bandwidth of the Einstein Telescope in the low-frequency region starting from a couple of Hz, a better seismic attenuation in the ultra-low frequency range is needed. The super attenuator dynamics in the low frequency range, where the inner normal modes of the mechanical filter chain are confined, has been simulated by using the electro-magnetic equivalent circuit and a detailed simulation campaign devoted to this design study has been performed. On the base of it we concluded that we can fix to six the number of filters because a better attenuation performance in the high frequency range is not necessary any more since the safety margin is large enough in Advanced Virgo and even larger in an underground environment. Then, a SA 17 m high with 6 magnetic anti-spring filters ("equal-spaced" configuration) tuned with a vertical cut-off frequency around 300 mHz, represents the reference solution for LF-ET interferometer.

As we anticipated in the previous paragraph, the last stage of the suspension system is crucial in defining the suspension thermal noise performances. In particular for the LF-ET case we deal with a system of coupled oscillators with masses at different temperature. Thus, the thermal noise evaluation required to develop a specific model, which includes interacting masses at different thermal equilibrium. The study of the thermal noise of this system has been carried on by using two different methods and the suspension thermal noise curves have been compared with the ET-D goal sensitivity curve driving the design of the last stage of the mirror suspension. Thus, the conceptual design of the payload for LF and HF -ET has been completed. It includes for LF-ET the analysis of the heat flow, the definition of the fiber material and geometry and the heat path from the mirror to the cold box via the marionette trough the suspension fibers and the dedicated heat sinks.

The LF-ET payload will be set-up in the lower part of the vacuum tower hosting the 17-m long super-attenuator chain. The vacuum tower basement is a cryostat separated to the upper part by a roof crossed by the Ti-6Al-4V thin rod, which holds the whole payload. An ancillary tower is hosting the cold box set on top of an cryo compatible attenuator chain. The box will keep the mirror at cryogenic temperature: it can be either a simple liquid helium container in the case of a cryoplant based on cryofluids or the cold head of a cryo refrigerator in the case of a cryocooler plant. Both the solutions are discussed and compared in more details in the infrastructure section. The final choice will depend on the outcome of a dedicated R & D effort.

A sophisticate control systems will be implemented in order to hierarchically control test mass positions to bring the interferometer to operation. The actuation system meant to align the test masses as interferometer's mirrors and to automatically maintain the operation point by using automatic signal derived from the circulating light will reasonably use internal forces exerted through the last stages of the suspension as in present detectors. The actuation based on a coil-magnet system for ET is reviewed in details and its limit associated to the $1/f$ potential noise is assessed; the alternative electrostatic approach is also discussed. Moreover, the low temperature use of optical conduits and bundle fiber served as position sensors have been tested for coarse mirror control together with short-arm optical levers and small interferometric systems for fine position control with alignment accuracy within 10 nrad RMS. Hence low frequency cryogenic accelerometers have being developed for this purpose.

Finally we notice that the outcome of this complex study on the Et suspension system is not limited just to the definition of a reference solution. We identified also some crucial technologies to be developed mainly in the domain of the slicon fiber and cryo-device construction, areas of potential interest also for industrial world.

4.4 Upper stages mechanics

Author(s): S. Braccini, F. Frasconi

4.4.1 LF interferometer

- Attenuation requirements
- The Virgo Superattenuator
- Seismic isolation measurements with the Superattenuator (SA)
- SA modifications for Low Frequency ET
- Noise from SA mechanical micro-glitches
- SA control strategy and improvements for ET
- APPENDIX - Cryogenic compatibility of materials for Superattenuator construction

a) Attenuation Requirements As shown in figure 126, Virgo is operating close to its design sensitivity also in the low frequency range. Looking at the detector noise budget, it turns out that its response is not limited by the mirror seismic noise passing through the anti-seismic suspension (*Superattenuators*). A set of measurements aimed to check if the present *Superattenuator* performance is compliant with the higher sensitivity of the next generation antennae, in particular with the Einstein Telescope, has been performed. The mechanical transfer function requirements for seismic noise isolation of the mirror in future detectors can be obtained starting from their design sensitivity curve expressed in terms of the mirror displacement. To this purpose, in figure 127, the design sensitivity curves of Advanced Virgo [290], the upgraded $3km$-long interferometer expected to enter in action in 2014 at the Virgo site, and those ones for the two reference solutions of the Einstein Telescope, are compared. The maximum acceptable transfer function amplitude of the seismic isolation system in different antennas is plotted as a function of the frequency in figure 128. This is given by the ratio between the detector displacement sensitivity curves reported in figure 127 and the linear spectral density of seismic noise measured on site at ground level. At the Advanced Virgo site (the same of Virgo) the linear spectral density of the ground seismic displacement has been measured to be roughly isotropic and well approximated, between a fraction of Hz and a few tens of Hz, by the function A/f^2, where f indicates the spectral frequency and A is around $10^{-7}\ m \cdot Hz^{3/2}$ [292]. A conservative value of A around $5 \times 10^{-7}\ m \cdot Hz^{3/2}$ has been considered to take into account possible fluctuations in some spectral regions, and the fact that the residual displacement due to seismic noise affects all four mirrors of the two Fabry-Perot cavities. Since the Einstein Telescope site has not yet been chosen, the requirement has to be considered as provisional. The linear spectral density seismic noise of $5 \times 10^{-9}/f^2$, measured in the Kamioka mine, where the new cryogenic Japanese interferometric detector is planned to be installed [293], is taken as a reference value. The recent progresses of Einstein Telescope working group for site selection are promising [294]. In particular, a measurements campaign of seismic noise for different underground sites in Germany provides seismic spectra smaller by a few units or comparable with that one measured in Kamioka mine. This makes the chosen reference seismic floor conservative for our goals (the requirements are likely more stringent than necessary).

It is important to stress that the transfer function requirements are valid both for vertical and horizontal seismic noise, that have a similar magnitudes. While for horizontal direction the argument is straightforward, in the vertical case the plot represents the maximum fraction of vertical seismic noise that can be transferred to the mirror along the beam direction without affecting the antenna sensitivity. As shown in the following section, only a fraction of the mirror vertical motion is transmitted along the beam because of unavoidable mechanical coupling and Earth curvature (making 10 km far plumb lines not parallel each other).

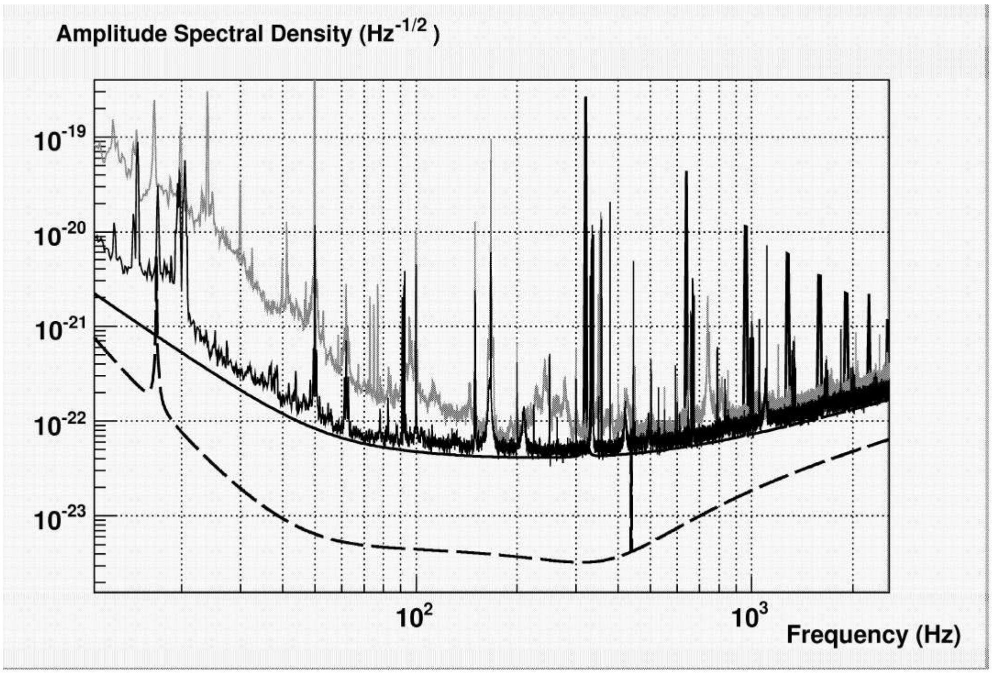

Figure 126: Virgo sensitivity achieved after a few months of the second scientific run ($VSR2$ - black experimental curve), compared with the sensitivity reached in 2007 during the first scientific run ($VSR1$ - grey curve). The continuous curve is the Virgo design sensitivity, discussed in [291], while the dotted curve is the design sensitivity of Advanced Virgo, the next generation detector.

b) The Virgo Superattenuator (SA) Since it will be shown that the *Superattenuator* as it is operating within the VIRGO interferometer is already compliant with the third generation detector requirements above 3 Hz, it is important to provide a detailed description of the apparatus. The *Superattenuator* working principle is based on a simple idea. Exciting in horizontal direction the suspension point of a simple pendulum at frequency f higher than the pendulum normal mode f_0, it is easy to prove that the oscillation is transmitted to the suspended mass with an attenuation proportional to $(f_0/f)^2$. Therefore a device suspending a mirror based on the working principle of a simple pendulum, represents a good isolation system for seismic noise at frequency f $> f_0$. A better attenuation performance is achievable considering an $n - stage$ pendulum. With this system an oscillation at a frequency f higher than the frequencies of the chain normal modes ($f > f_0 > f_1 > ... > f_n$), is transmitted to the suspended mass with attenuation proportional to f^{-2n}. In particular, the ratio between the linear spectral density of the last mass displacement (the optical component) and the linear spectral density of the suspension point displacement (where the excitation is applied), decreases as A/f^{2n} where $A = f_0^2 \cdot f_1^2 \cdot f_2^2 \cdot \cdots \cdot f_n^2$ and n is the number of stages. In this way a very large attenuation of seismic noise horizontal component can be obtained in the frequency range above the highest pendulum resonance, simply increasing the number of stages. The longer are the pendulums, the lower are the resonant frequencies of the system and higher is the attenuation response at a given frequency.

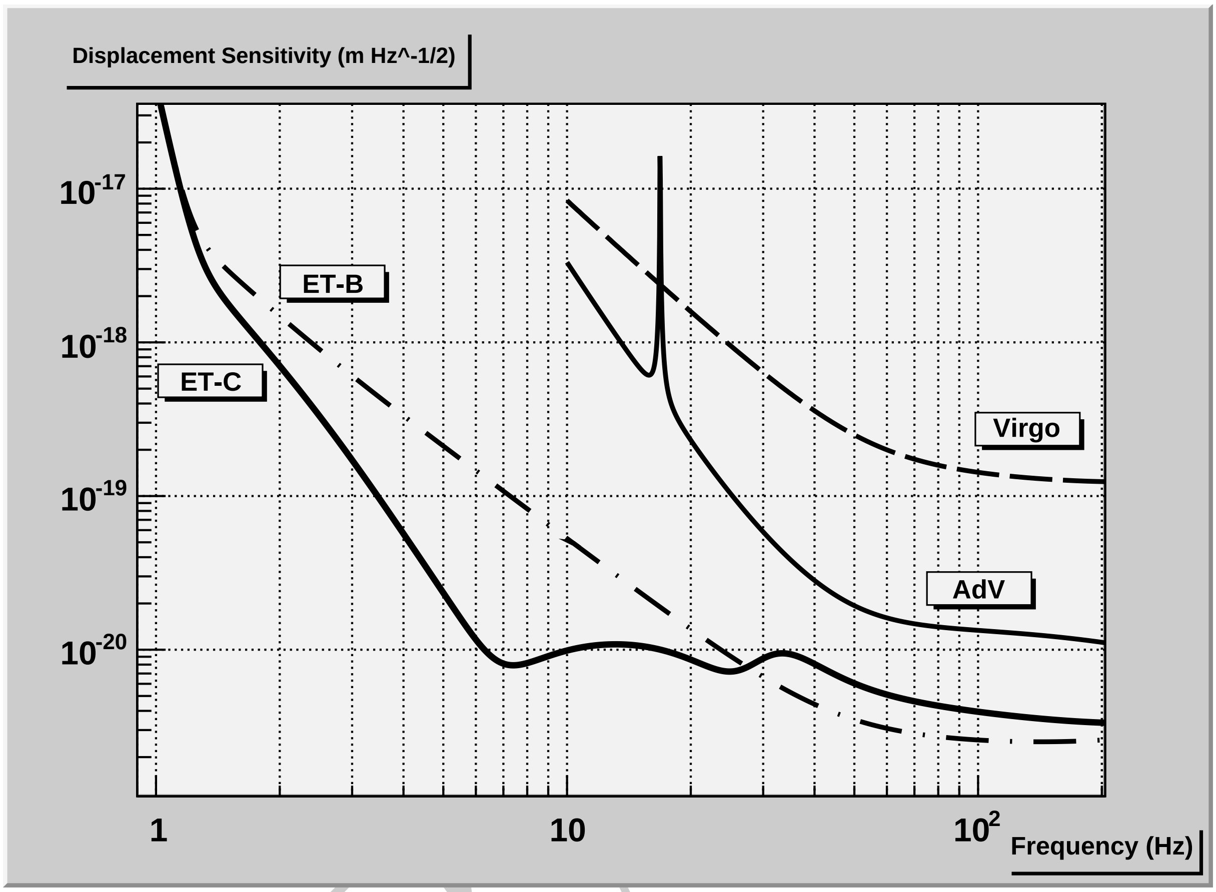

Figure 127: Displacement design sensitivities of Virgo, Advanced Virgo (AdV), and of the two reference configurations of the Einstein Telescope: the high-frequency interferometer (ET-B) and the *'xylophone'* design (ET-C), optimized for the low frequency detection. While the detection bandwidth of Virgo and AdV starts from 10 Hz, Einstein Telescope aims to extend the detection bandwidth in the low frequency region starting from a few Hz.

Unfortunately, due to different directions of the plumb line on the curved Earth surface, the end mirrors, suspended 3 km away in our interferometer and 10 km in Einstein Telescope, are misaligned (each with respect to the other) by about 3×10^{-4} rad and 10×10^{-4} rad respectively. For this reason it is necessary to tilt one mirror with respect to the other by the same amount, making at least one mirror misaligned with respect to the local plumb line. With this setting up the mirrors are not perfectly perpendicular to the laser beam and then any vertical vibration will be partially transmitted to the interferometer horizontal axis (laser beam direction). In addition any vertical vibration will be partially transmitted to the interferometer horizontal axis because of an unavoidable coupling among different degrees of freedom. Thus vertical motion will cause a phase change of the laser beam. It is thus clear that a vertical attenuation of seismic noise comparable with the horizontal one is fundamental to reduce the frequency detection threshold. With a multistage pendulum this goal can be achieved by replacing each suspension wire with a spring to form a cascade of oscillators also along the vertical direction. The spring should support a heavy load and, at the same time, it should be soft enough to exhibit a low resonant frequency. With this technical solution it is possible to confine the vertical resonances of the chain in a low frequency range obtaining a strong attenuation starting from a few Hz.

Even the unavoidable mechanical couplings between rotations and horizontal beam direction can cause a phase change on the interferometer laser beam. In order to confine these rotational mode frequencies well below the detection band, each pendulum mass has to be replaced by a structure having a high momentum of inertia.

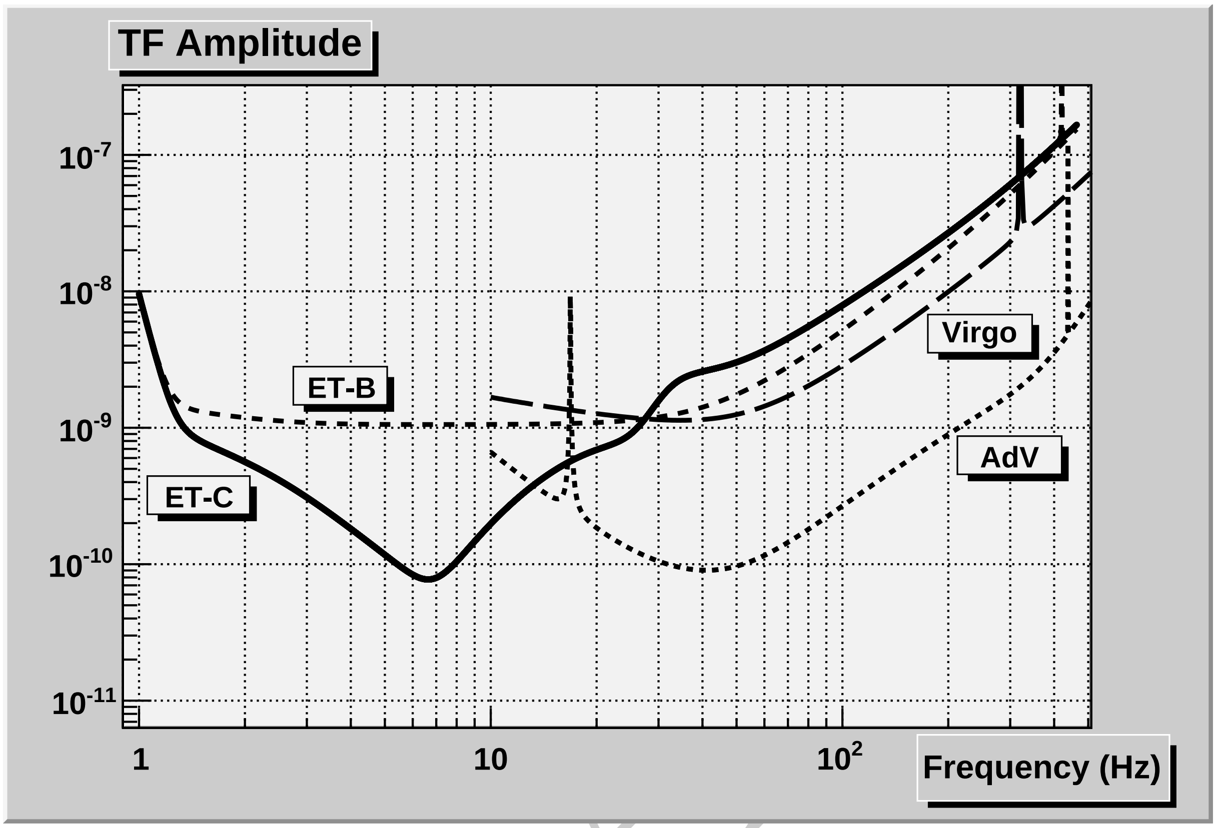

Figure 128: Seismic vibration transfer function requirements for different antennas. The curves represent the ratio between the displacement sensitivities reported in figure 127 and the conservative linear spectral density of seismic noise at the level where the interferometer is located. Since seismic noise will be at least a couple of orders of magnitude smaller in underground environment, Einstein Telescope, despite its better sensitivity, is less demanding in terms of seismic attenuation at high frequency.

In addition, the diameter of the suspension wire, connecting two consecutive stages, has to be small enough to reduce its restoring torque which opposes the rotation of the chain and determining its rotational frequencies. An interconnection of the stages at small distance and as close as possible to their centres of mass, guarantees low frequency tilt modes (i.e. rotational modes around the two horizontal axes) and a negligible coupling effects on the horizontal displacement of the suspended mass.

Keeping in mind all the considerations reported above, the VIRGO *Superattenuator* has been conceived having a mechanical structure based on the working principle of a multistage pendulum [**?**]. Each mirror, indeed, is suspended to a 8 m-long SA chain with 6 mechanical filters (see fig.129). The system consists of three fundamental elements: the Inverted Pendulum (IP), the mechanical seismic Filters (SF) connected each other by metallic suspension wires and the Last Stage (LS) or optical payload. The suspension system is described here below, while more detailed information of each single chain element can be found in reference [295].

The Inverted Pendulum top stage The top stage of the *Superattenuator* is designed to fulfil three main functions:

- to introduce a very low frequency (about 40 mHz) horizontal filtering stage, limiting the amount of seismic energy feeding into the SA and thus reducing the SA excitation resonant modes and improving its overall attenuation performance;
- to provide the SA with a suspension point positioning system: the amplitude of the slow tidal drifts over

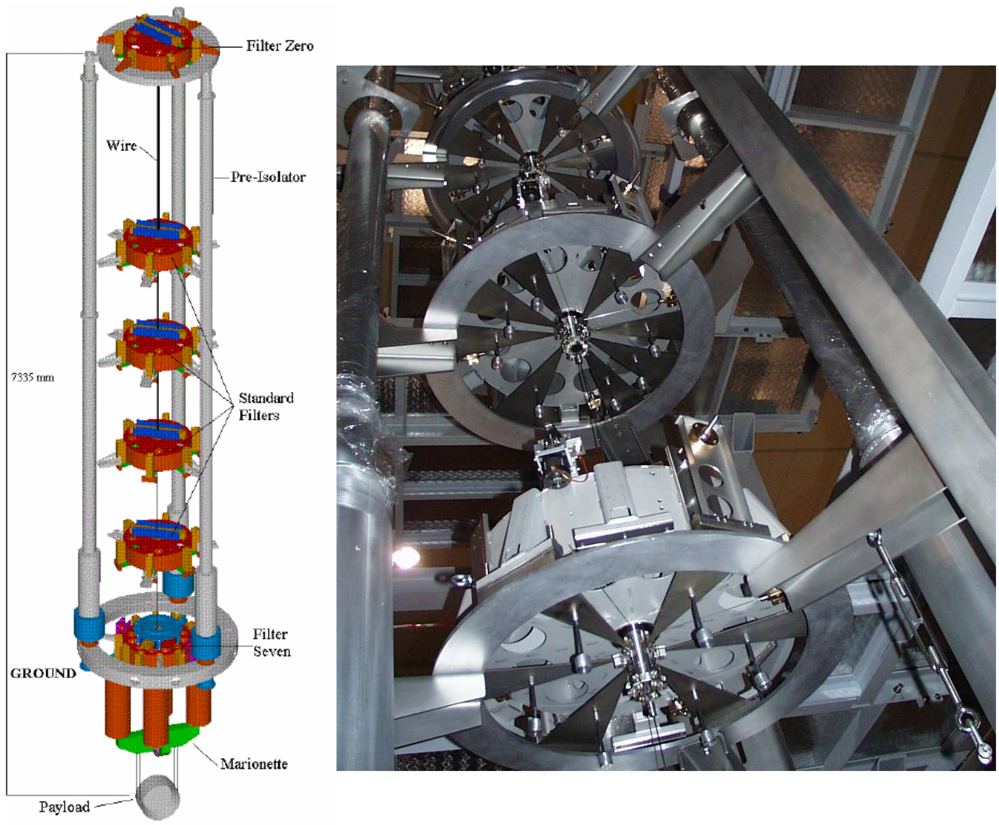

Figure 129: The VIRGO *Superattenuator* suppresses the transmission of ground seismic vibrations to the suspended mirror. The mechanical filter chain and the three legs of the inverted pendulum are visible. In our attenuation measurements the excitation is applied to the filter chain suspension point.

three km is far beyond the dynamic range of the actuators exerting the locking forces upon the mirror. Therefore tidal drifts are compensated by moving softly the SA suspension point: the tidal strain over 3 km can be as large as a few hundred microns in 6 hours;

- to provide a soft suspension stage on the top of the chain to allow active mode damping of the chain resonant modes and seismic noise depression by means of inertial sensors, positioning sensors and electromagnetic actuators. The main goal is to reduce the *swing* of the optical payload down to a fraction of micron allowing a low-noise control of the mirror in the interferometer.

To fulfil all the above requirements in the horizontal plane a device based on the working principle of an Inverted Pendulum (IP) has been built. An IP is a suitable device for several reasons. An ideal Inverted Pendulum can be conceived as a mass-less vertical bar of length l connected to ground by means of an elastic joint with stiffness k and supporting a mass M on its top. In such a pendulum the gravity acts as an anti-spring and the resonant frequency can be tuned to have a very low resonant frequency (about 40 mHz in VIRGO). The required force to displace the suspended chain from an IP resonating at 40 mHz is very low: the needed force, in DC mode, for moving a 1 ton SA chain by 1 cm is less than 1 N. Therefore soft electromagnetic actuators can be used to control the mirror position. For this reason the IP is a good platform to act upon for the active damping of the SA normal modes.

The present VIRGO Inverted Pendulum (see fig. 129 left side) is a three-leg metallic structure interconnected on their top with a steel ring (the Top Ring). The Top Ring surrounds the first filter of the chain (hereafter called Filter Zero) to which is rigidly connected. The Filter Zero together with the Top Ring form a platform suspended by three thin wires (31 mm long) accommodated on top of the legs. The elasticity of the structure is due to three flexible metallic joints. They are screwed onto the legs to form an interconnection element between the upper part and the bottom one of the aluminium pipes. A bottom steel ring, on which the Inverted Pendulum is anchored, completes this metallic frame. Each leg is essentially a light hollow cylinder made of aluminium with an inner diameter of 125 mm and an outer diameter of 130 mm. The total length of the leg, from the bottom of the flexible joint to the suspension point of the SA is about 6.2 m. The leg is composed by two sections flanged together and reinforced with titanium inserts.

The three legs are made in Aluminium to minimize their weight. Nevertheless the leg mass is about 26 kg. An extension below the flex joint is necessary to tune the *percussion point* avoiding an isolation performance spoiling. The flex joint is therefore mounted on top of a 0.8 m high rigid support. A proper counterweight is attached to a high bell-shaped 0.9 m long skirt bolted to the bottom of the leg.

The Inverted Pendulum structure is surrounded by a rigid metallic frame (called Ground Reference Structure - visible in fig.129 right side), holding the parts of sensors and actuators that needs to stay "on ground". It is provided with [296], [297]:

- three motorized sleds set on the external structure in front of the legs top. Each sled is connected to the corresponding leg top through a soft spring. The motors are used to set the IP roughly in its working point, so that to minimize the correction signals in the closed loop operation;
- 3 horizontal $LVDT$ position sensors set in pin wheel configuration. The secondary windings stay on the ground reference structure, while the primary ones are rigidly connected to the top stage;
- 3 horizontal coil-magnet actuators, set in pin wheel configuration. The coils, arranged as a Maxwell pair, stay on the ground reference structure, while the magnets are rigidly connected to the top stage;
- 3 horizontal accelerometers, set on the top stage;
- 2 vertical accelerometer, set on the Filter Zero crossbar;
- 1 vertical $LVDT$, measuring the position of the Filter Zero crossbar with respect to the top stage;
- 2 vertical coil-magnet actuators, acting between the Filter Zero body and its crossbar.

The Seismic Filters In the VIRGO *Superattenuator* each pendulum mass has been replaced by a rigid metallic structure drum shaped acting as an oscillator in vertical direction too. A sequence of six mechanical filters is able to isolate the optical components from seismic noise in accordance with the working principle of a multistage pendulum (see fig. 129). A detailed description of the design and performance of a single filter can be found in reference [298]. A seismic filter is a rigid steel cylinder (70 cm diameter, 18.5 cm high for a total weight of about 100 kg) suspended as close as possible to its centre of mass (see fig. 130 left side). On the outer circumference of its body bottom part, a set of triangular cantilever spring blades is clamped. Each blade (3.5 mm thick and 385.5 mm long) is bent at a constant curvature radius and with different base width according to the load to be supported. A nominal load, ranging between 48 kg and 96 kg hung on the blade tip, forces it in flat and horizontal position. The blade tip is connected by a 1 mm diameter wire to a central column, inserted through a hole in the centre of the filter body. Any movement of the central column, apart from the vertical direction, is prevented by two sets of four centreing wires accommodated on the top and on the bottom of the filter body.

A crossbar, bolted on the upper part of the central column, is used as a mechanical support for the magnetic anti-spring system described in the next sub-paragraph. The central column and the crossbar, connected to the blade spring, represent the moving part of the mechanical filter from which the load of the lower stages is suspended by a steel suspension wire. By connecting each filter to the next one, a chain of mechanical oscillators in vertical direction has been achieved.

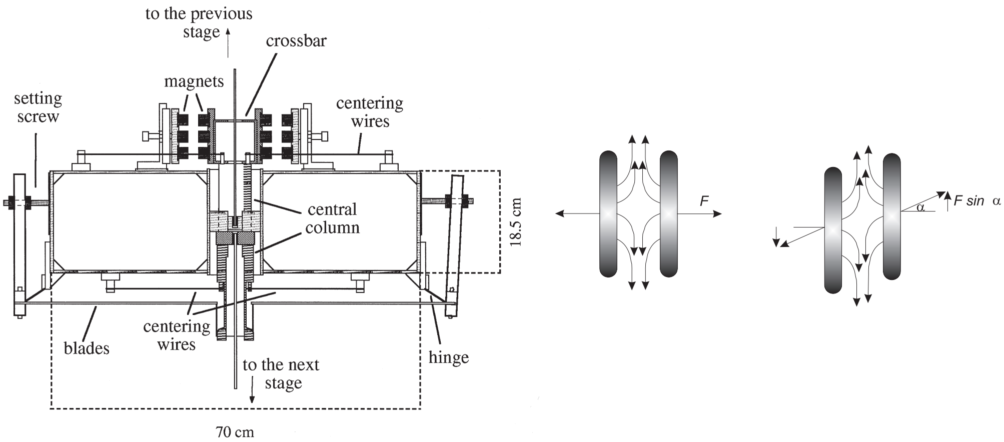

Figure 130: The VIRGO seismic filter: a technical drawing (*left side*). The working principle of the magnetic anti-spring system accommodated on the seismic filter crossbar (*right side*).

According to the previous description of our filtering system it is clear that the total load of the chain is suspended by the triangular steel blades. The base width of the triangle ranges from 180 to 110 mm in accordance with the load to be supported. For the same reason the top filter is equipped with 12 blades while the last one needs only four blades.Once properly loaded the main vertical resonant frequency of each filter is about 1.5 Hz.

Maraging steel has been used in place of standard steel for blade construction in order to minimize micro-creep effects [299],[300] due to the high load applied. The same material has been used to machine the suspension wires with nail-head at both ends [301]. Since the suspended load decreases going from the top to the bottom of the chain, the wire and the nail-head diameters change along the chain in the ranges 4-1.85 mm and 8-6 mm, respectively. In this way it has been possible to confine the violin vibration mode within the high frequency band and to reduce its angular stiffness which determines the rotational frequency around the vertical axis.

The two nail-heads of the wires connecting a filter on the chain to the previous and to the next one are screwed in the central part of its body at a relative distance of 5 mm, very close to the filter centre of mass. As mentioned above, this guarantees a small return torque to rotations of the filter around the horizontal axis and thus a low tilt frequency.

The magnetic anti-spring The suspension wire length of 1.15 m in the VIRGO *Superattenuator* sets the pendulum resonant frequency of each stage at about 0.5 Hz. In the vertical direction the stiffness of the triangular blade springs fixes the natural resonant frequency at about 1.5 Hz. In order to reduce the vertical stiffness of the blades, and then to confine the main vertical resonant frequency of each filter below the pendulum one, a system of magnetic anti-springs [298],[302] has been adopted (see fig. 130 left side). It consists of two sets of permanent magnets (the first assembled on the crossbar and the second one on the filter body), facing each other with opposite horizontal magnetic moment (namely in a repulsive configuration). In this way the two matrices screwed on the crossbar are forced to move in vertical direction only.

When the magnets are perfectly faced the repulsive force has a null vertical component, but as soon as a matrix is moved in the vertical direction, a vertical component of the magnetic force appears. Considering a small relative displacement (Δy), compared with the distance (d) between two matrices of magnets and with their transverse dimension, the vertical component of the repulsive force (F_y) is proportional to Δy:

$$F_y \approx F_0 \cdot (\Delta y/d) \tag{108}$$

where F_0 is the module of the repulsive force (see its working principle in fig. 130 right side). Such device is equivalent to a vertical spring with a negative elastic constant (anti-spring) whose module is F_0/d. Its rest position is thus the position for which the two couple of matrices are perfectly faced. On a seismic filter the magnetic anti-springs act on the crossbar in parallel with the blade springs, so that the vertical modes frequency of the chain are confined below the highest frequency of the horizontal ones. As detailed all along this part of the document, the magnetic anti-spring (a very clean and contact-less system) represents the reference solution for the third generation detector and no improvement is needed.

The Steering Filter The last mechanical filter of the VIRGO seismic attenuation chain is the Steering Filter [303]. It has been designed to suspend and orientate the payload, a multi-body mechanical system whose core is a test-mas of the gravitational-wave detector, by means of forces exerted within the suspension. The payload clearly plays a role in the overall dynamics of the system and its presence has been included in all the projections shown in this section of the report, assuming a basic design similar to that actually developed for VIRGO (fig. 129). However a dedicated section will be devoted to the issues related to this system provided its crucial role in dealing with test-masses as mirrors of the interferometer. In the VIRGO experimental apparatus the steering filter has been equipped with four Aluminium legs (about 900 mm long and 250 mm in diameter) bolted on the filter body bottom part. These legs are the mechanical support of the coils mounted in front of the permanent magnets screwed on the marionette wings and used to control the payload position.

In addition the Steering Filter is equipped with different vacuum compatible stepping motors. Two of them are dedicated to the filter alignment around its vertical axis. The first one is accommodated on top of the filter body and it is used to move the filter and the payload with respect to the upper part of the *Superattenuator* while the second one is mounted at the bottom of it to change the relative position of the filter with respect to the payload. This last one is used to optimize the coil-magnet distance for the actuation on payload. A second pair of vacuum compatible stepping motors completes a set of remote controlled devices mounted on this mechanical filter. By moving some small masses attached to a mechanical trolley on top of the filter body, a fine adjustment of the tilt (rotations around the two horizontal axes) can be performed.

c) Seismic isolation measurements with the Superattenuator (SA) The attenuation performance of the *Superattenuator* has been measured by using the VIRGO interferometer. In particular, a direct measurement of the mechanical transfer function has been obtained exciting the top stage, where the mechanical filters chain is suspended, with sinusoidal forces. The measurement consists in detecting the presence of a spectral line with the same excitation frequency at the level of the mirror, i.e. at the interferometer dark port. The ratio between the linear spectral density at the excitation frequency of the mirror and that one of the top stage displacement (measured by means of the accelerometers) provides a measurement of the *Superattenuator* mechanical transfer function magnitude. When the line is not detected at the level of the interferometer, only an experimental upper limit of the transfer function amplitude can be given. We remind that the linear spectral density of the noise floor of the top stage sensors or of the interferometer dark port, does not depend on the time length of the measurement while the amplitude of a spectral line increases with square root of the time interval. The

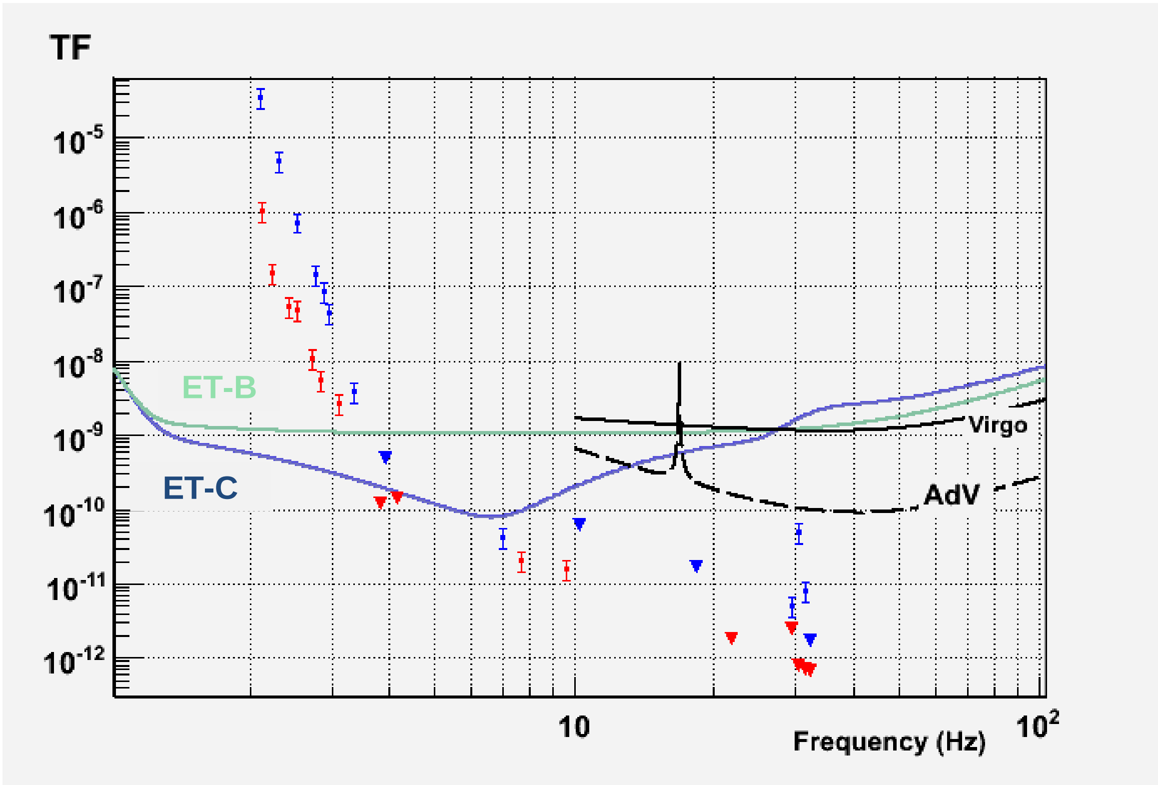

Figure 131: The measurement of the transfer functions at different frequencies. In red are reported the measurements where a vertical excitation of the top stage is applied. In blue are the measurements with the excitation in horizontal direction. The upper limits are indicated by triangles, while the direct measurements (when a signal is detected at the level of the mirror) are indicated with the bars. For the discussion of the error bars see reference [304].

longer is the integration time, the higher is the capability to distinguish a spectral line from the interferometer noise floor. Moreover, in those measurements where the peak is not distinguished at the level of the mirror, the upper limit of the transfer function, given by the ratio between the noise spectral floor and the top stage peak at the excitation frequency, improves (i.e. becomes smaller) increasing the integration time. In this case, the linear spectral density of the excitation line (denominator) becomes larger, while the interferometer noise floor (numerator) does not change.

A campaign of measurements has been performed exciting the suspension top stage both in horizontal laser beam direction and in vertical direction. The excitation is applied to the suspension point through the coil-magnet actuators used in the Inertial Damping of the chain resonance modes. The experimental results have been compared with the requirements of the future generation detectors (as reported also in figure 128) and plotted in Fig.131.

Above 3 Hz all the measured transfer functions (upper limits or direct measurements) turn out to be within the requirements of Einstein Telescope. Changes to the *Superattenuator* structure (such as a length extension of the filter chain) will be needed in Einstein Telescope only in the case the detection threshold frequency will be moved below 3 Hz. In reference [303], where a stage by stage (indirect) measurement of the *Superattenuator* total transfer function (valid at any frequency) has been provided (and compared with simulation), a very steep behavior around 3 Hz is well visible. Considering this as a reference result, it is clear that even changing by a couple of orders of magnitude the input seismic noise as well as the attenuation requirements, the crossing frequency between the transfer function and the requirement curve should remain around 3 Hz.

In addition, around 30 Hz and in the 7-9 Hz region, our measurements put in evidence some peaks above the interferometer noise floor while excitation is applied on the top stage. This is an indication of noise transmission a couple of orders of magnitude larger than expected from simulation and indirect measurements (stage by stage). However, also in these cases, the transfer function has been measured to not exceed the detector requirements. Other mechanisms could cause the detected tiny motion of the mirror by-passing the extremely high mechanical attenuation, as discussed in [304],[305]. The extension of the multistage pendulum length, linked to the need of moving down below 2 Hz the cross-over between the horizontal seismic noise and the antenna sensitivity (see next section), is welcome for a better separation of the top-stage control and the optical payload control preventing cross-talks.

It is important to stress that, during our measurements campaign, the pre-isolator stage (described above) has been excluded from the transfer functions measurements. So that an additional attenuation factor, of the order of $20 - 40\ dB$, has to be considered as safety margin. With this additional attenuation factor, one can conclude that the cross-over for the Einstein Telescope requirements is expected to be around 2.8 Hz by using the present *Superattenuator* scheme. The cross-over is dominated by horizontal seismic noise.

d) SA modifications for Low Frequency ET In order to extend the detection bandwidth of the Einstein Telescope in the low-frequency region starting from a couple of Hz, a better seismic attenuation in the ultra-low frequency range is needed. To this purpose a detailed simulation campaign devoted to this design study has been performed. The SA dynamics in the low frequency range, where the inner normal modes of the mechanical filter chain are confined, can be well simulated by using the electro-magnetic equivalent circuit (a series of oscillators). A maximization algorithm, called *Simplex* [306], based on the possibility to change the masses and the mechanical filter chain lengths, has been developed. It searches for a maximum attenuation performance at a fixed frequency that, in our case, was 2 Hz. Since the transfer function has a smooth shape, it turns out that the larger is the attenuation at 2 Hz, the lower is the "cross-over frequency" with the requirements curves (see fig. 132). As showed in the direct measurement performed with the VIRGO interferometer (see section 4.1.1.c), the cross-over between seismic noise at the mirror level and the requirements is dominated by the residual horizontal seismic vibrations. For this reason the motion of the cross-over at lower frequency, pass through the attenuation performance improvement of the horizontal seismic vibration in the low frequency range. An important preliminary conclusion of our design study is that, fixing the length and the number of mechanical filters, the optimal configuration (*i.e.* that one minimizing the cross-over frequency or maximizing the attenuation performance at 2 Hz) is that one where the filters are separated along the chain by the same distance. This "equal-spaced" configuration represents the optimal one even because the vertical transfer function is not influenced by the filter positioning along the chain. Moreover it has been proved that increasing/decreasing the number of filters or changing their masses do not play a fundamental role in determining the cross-over frequency between the horizontal transfer function and the requirements. The results obtained are plotted in fig.132 and fig.133 while in the corresponding captions complementary information is available. The only way to move in the low frequency region the cross-over frequency extending the Einstein Telescope bandwidth below 3 Hz, is to increase the SA chain total length. The simulation results for different configurations can be found in figure 134 and described in [305], while the best solution seems to be represented by a SA with 6 filters and a total length of $17m$ (identical the VIRGO configuration, where 5 mechanical filters suspended from an horizontal pre-isolator stage plus the marionette are assembled forming a filter chain about $9m$ long). As shown in fig.136, with this solution the cross-over frequency has been placed around $1.7 - 1.8$ Hz, that is considered enough for our purpose. Indeed, Newtonian noise and other technical noise are assumed to prevent an effective detection above a couple of Hz. With this configuration, the vertical cut-off frequency of the whole system is set below 1.8 Hz by tuning each mechanical filter having the main vertical frequency around 300 mHz (see fig. 135). The corresponding vertical transfer function is plotted in fig.136. Since the residual seismic noise along

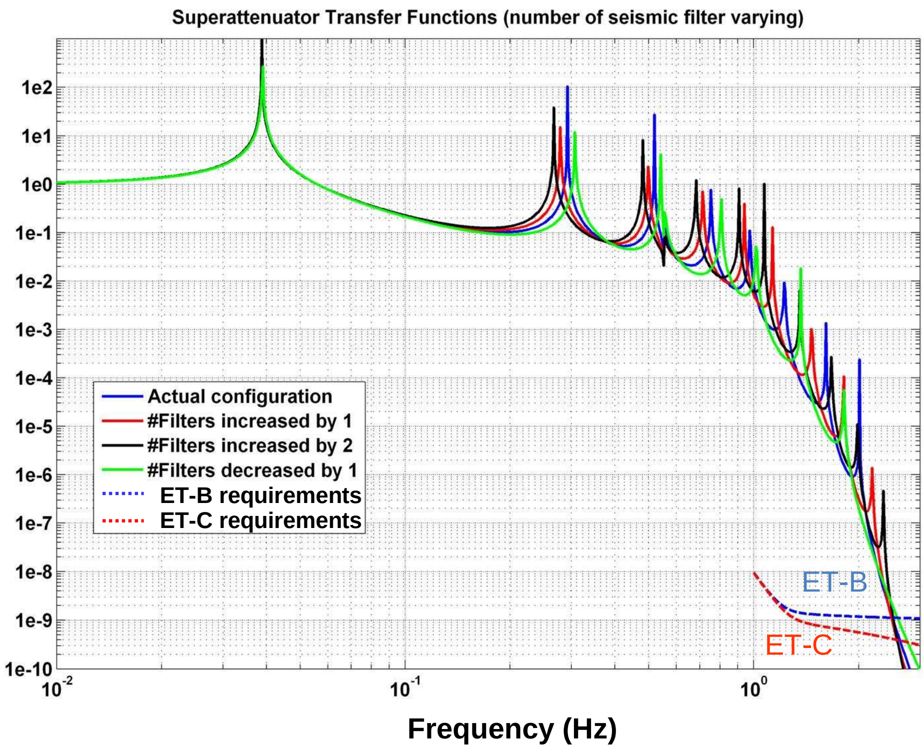

Figure 132: Simulation results of the SA horizontal transfer function with the present chain length (9 m). Changing the number of ("equal-spaced") filters the resulting horizontal transfer function is compared with the ET requirements (for High Frequency - $ET - B$ - and low frequency or "xylophone" configuration - $ET - C$). Adding or removing filters along the chain length do not have remarkable role in the positioning of the cross-over frequency with the requirements.

the vertical direction, at the level of the mirror, is expected to limit the Einstein Telescope sensitivity again around $1.7 - 1.8$ Hz, a coupling factor of 10^{-3} has been considered. This is due to the fact that the Earth curvature makes plumb lines at a 10 km distance not parallel each other. At least one mirror has to be inclined with respect to the local plumb line performing the alignment of the cavities. This transmits the residual vertical mirror motion along the beam with the mentioned coupling factor (10^{-3}). Many mechanical filters of the VIRGO *Superattenuators* are already working since years around 300 mHz with an excellent stability. By using the VIRGO interferometer data, it has been observed that the long-term change of the chain main resonant frequencies induced by the temperature variation under vacuum are well inside the line-width of the chain vertical resonances. No effect on the interferometer control is due to this potential disturbance. Moreover, even if the temperature variations induce a motion of the suspension chain and then a vertical breath of the mirror (a few mm per $^{\circ}C$ is the measured value for the VIRGO *Superattenuator*), this effect is well within the specifications of any interferometer (vacuum tank provides an excellent temperature stability - fraction of $^{\circ}C$ peak to peak). The standard SA, presently in operation on the VIRGO interferometer, is already well inside the third generation specifications for this point of view too.

In addition, it is important to remind that the requirements in the tens of Hz range are less stringent in Einstein

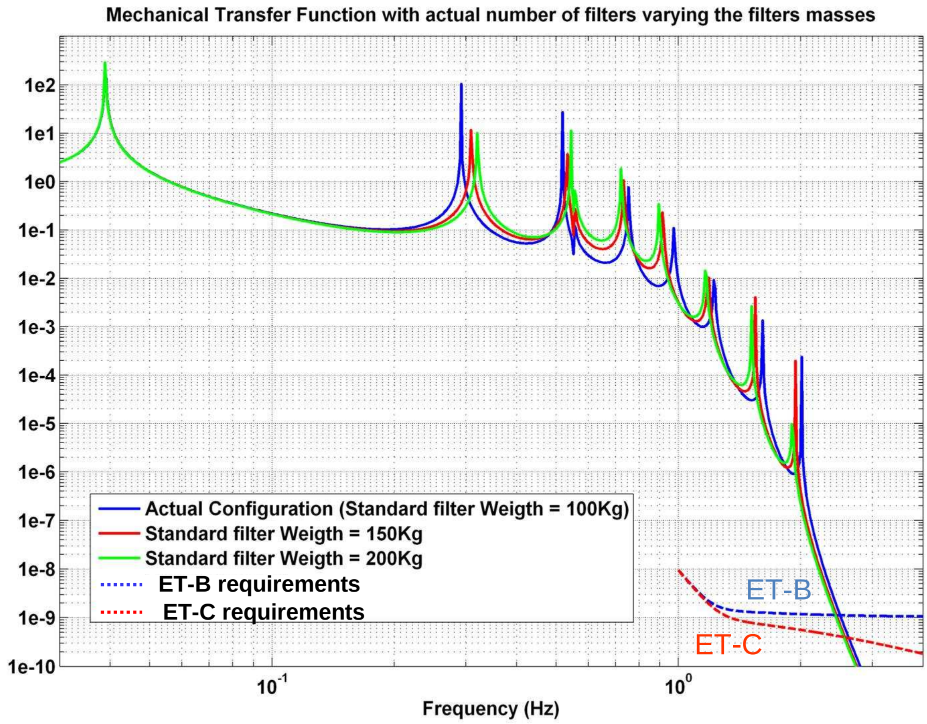

Figure 133: The horizontal transfer function of the present SA (6 filters weighting 100 kg each one for a total length of about 9 m) is compared with the same transfer function changing the mass of each filter (150 kg and 200 kg). Also in this case the cross-over frequency with the ET requirements is not remarkably affected by the change of the filter mass.

Telescope than in Advanced Virgo (see section 4.1.1.a) and thus, fixing to six (a choice lead by the reduction of the cross-over frequency) the number of filters, a better attenuation performance in the high frequency range is not necessary any more since the safety margin is large enough in Advanced Virgo and even larger in an underground environment. In conclusion, a SA 17 m high with 6 magnetic anti-spring filters ("equal-spaced" configuration) tuned with a vertical cut-off frequency around 300 mHz, represents the reference solution for the Einstein Telescope.

e) Noise from SA mechanical micro-glitches As well known from literature [307] dislocations in the blade-spring of the anti-seismic filter, wires, and other elastic elements under stress follow a "self-organized criticality dynamics" inducing a mechanical shot-noise force along the vertical direction. This force due to micro-glitches exhibits an "$1/f$-spectrum", and it is sometime called "creep noise". This noise mechanism could affect the interferometer sensitivity. For this reason the VIRGO interferometer has been used to set upper limits on the noise floor induced by this spurious mechanism. As sketched in fig.137, the dynamics of the optical payload along the vertical axis can be seen as the motion of three rigid bodies (mirror, reference mass and marionette) connected by three constraints (suspension wires). As a consequence, the payload vertical motion attached to the elastic blade spring of the last filter of the chain exhibits three fundamental modes along the

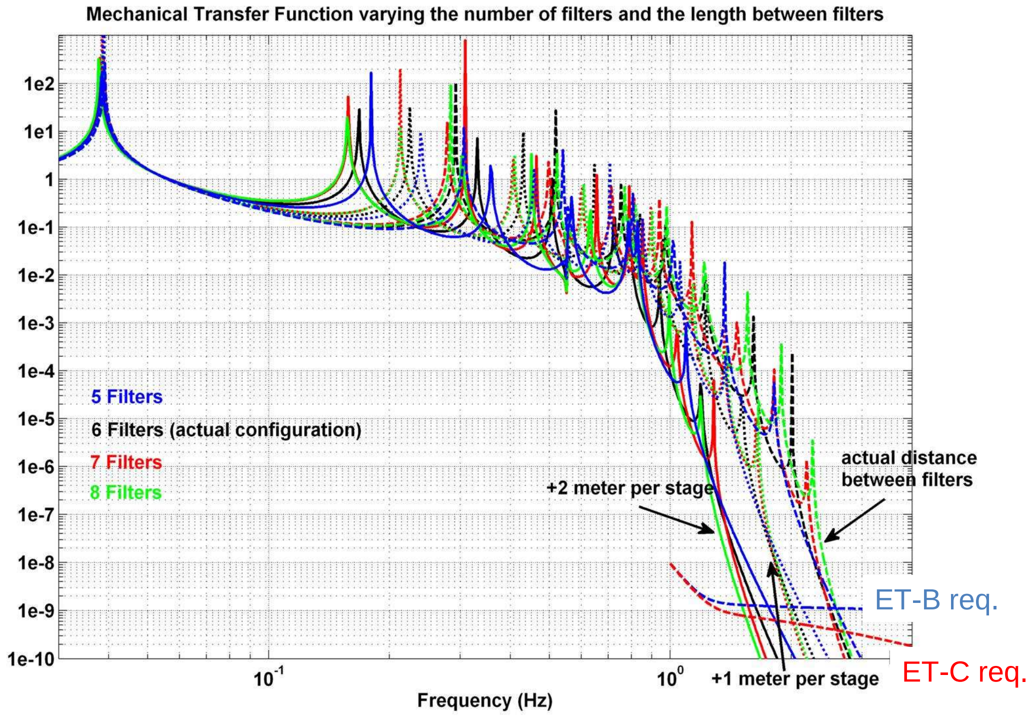

Figure 134: Simulation results for different configurations. The horizontal transfer function of the SA is plotted changing the number of filters and keeping fixed their relative distances ("equal-spaced" geometry) along the chain (changing, as a consequence, the full length of the SA).

vertical direction involving mainly (but not only) the vertical displacement of the reference mass, mirror and marionette respectively (see fig.137). These vertical modes are well visible on the VIRGO interferometer output port, namely they appear as peaks on the output photo-diode placed in front of the detector dark fringe (see fig.138). This means that the modes are excited by some spurious vertical force of unknown origin. The micro-creep, such as thermal noise or the electro-mechanical noise floor coming from the coil-magnet actuators are only possible excitation mechanisms. Using the coil-magnet actuators steering the marionette it is possible to excite the three vertical normal modes of the payload. More in general, it is possible to measure the transfer function between the vertical force acting on the marionette and the mirror longitudinal displacement (measured with very high accuracy by the VIRGO interferometer). The measured transfer function (mirror displacement along the beam, expressed in m over the vertical force applied on the marionette, expressed in N) is plotted in fig.139. In order to set an upper limit on the vertical force presently acting on the marionette, one can make the ultra-conservative hypothesis (likely not realistic) that the vertical spurious force is dominant in all the band, namely it is responsible of the present sensitivity of the detector. With this assumption, dividing the present sensitivity (expressed in displacement along the beam) by the mentioned transfer function (mirror displacement vs. vertical force) the linear spectral density of the maximum vertical force acting on the marionette compatible with the measured sensitivity can be plotted (see fig.140). The deeps due to the three vertical modes of the payload (where the denominator - the transfer function - is large because of the resonant frequencies) are well

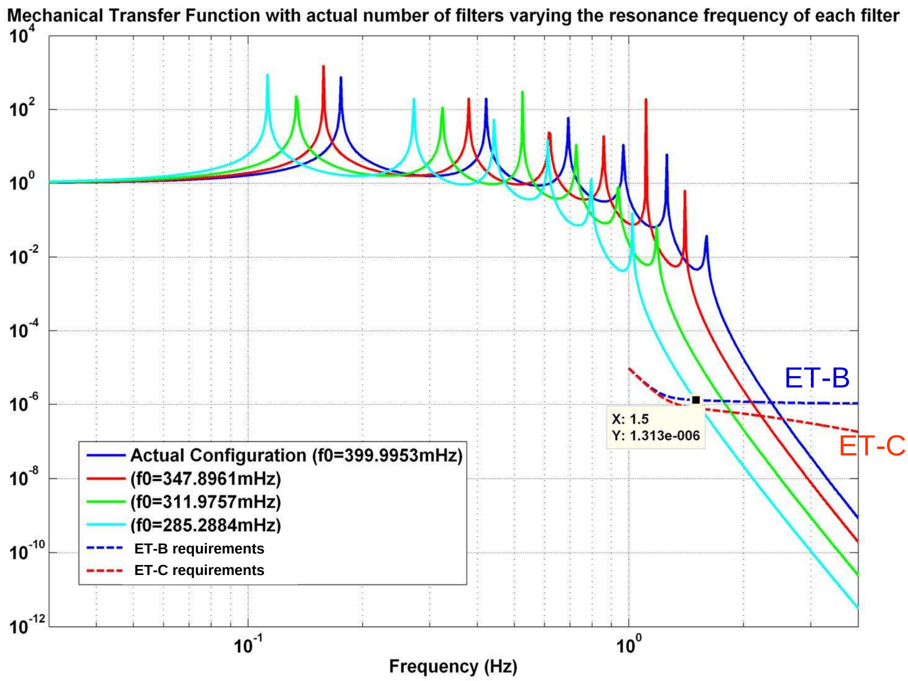

Figure 135: Vertical Transfer Function of the SA considering the six stages (as it is now, i.e. with the pre-isolator or "Filter Zero" plus other five mechanical filters). The different curves have been obtained changing the filter vertical resonant frequency. With filters working around 300 mHz it is possible to move the cross-over below 2 Hz.

visible. As mentioned above, the micro-glitches are expected to induce a shot-noise, namely a "$1/f$-colored force" thus one can set also the maximum "$1/f$-like force" compatible with the present sensitivity (see line at fig.140). By multiplying the plotted $1/f$-force by the measured transfer function (mirror displacement divided by vertical force on the marionette) one can thus obtain the linear spectral density of the maximum displacement induced by the micro-glitches on the mirror. This upper limit is compared in fig.141 with the sensitivity of the VIRGO and AdV. From this figure, one can see that the upper limit just set is sufficient to exclude a dominant contribution in AdV. An important remark is that the micro-glitches are expected to increase when the operation vertical frequency of the anti-seismic filters is reduced. On the other hand, as described in section 4.1.1.d, we know that working with seismic filters tuned around 300 mHz is a must to achieve the required vertical attenuation in the Einstein Telescope. However, several last filters of the *Superattenuator* chains are already working around 300 mHz and thus our result, excluding a dominant effect due to micro-glitches in Advanced detectors at the level of last filter blades , is valid also at this tuning frequency. The present upper limit is thus surely valid also in Einstein Telescope. On the other hand this upper limit is far (several orders of magnitude) from the third generation sensitivity, especially in the ultra-low frequency range. Since the micro-glitches of the elastic blades taking place on the upper stages of the chain are strongly filtered by the anti-seismic filter underneath, it is obvious that possible problems coming from micro-glitches (if present) can affect the sensitivity of the

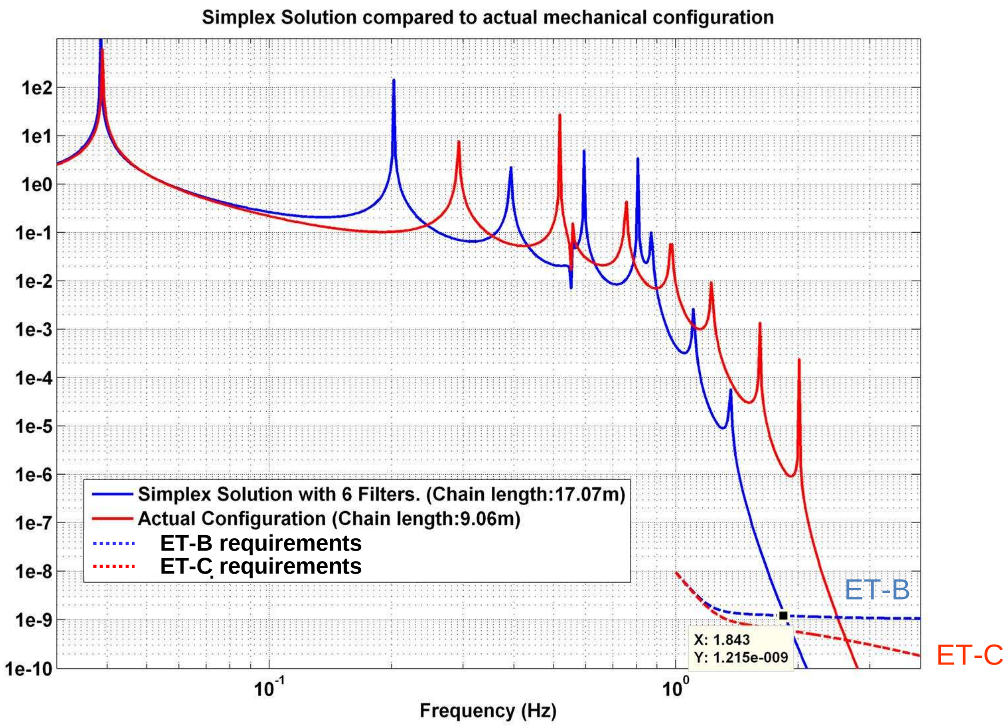

Figure 136: The proposed reference solution for the *SA* configuration of the Einstein Telescope. Other slightly different configurations are discussed in [305].

third generation antenna only if they take place at the level of the last filter(s) of the chain. A dedicated *R&D* programme to minimize micro-glitch effects on the cryogenic payload (see Appendix) and, if necessary, on the last stage(s) of the *Superattenuator*, is mandatory. In any case this is not expected to affect our anti-seismic isolation strategy, at least on the upper isolation chains.

f) SA control strategy and improvements for ET The Suspension Control System plays a crucial role in the interferometer operation. At the top level, it provides DC positioning control and damping of chain normal modes along horizontal, vertical and yaw degrees of freedom. At the bottom it provides the handle to apply residual correction from ground onto the horizontal and yaw degrees of freedom through the steering filter usually left actuation-free. Given the payload suspension point controlled with suitable accuracy, another section of the control is devoted to apply internal forces to the payload and to the interferometer control. The overall structure, described by more than 80 vibrational modes model, is presently (VIRGO/VIRGO+) controlled by 18 coil-magnet pairs actuators while its status is monitored by using about 20 sensors.

Such controls make use of two main classes of error signals: *local controls* and *global controls*. Local controls use error signals generated by local sensors, accommodated on or close to the suspension structure. Global controls are those whose input signal is generated by sensors located ”far” from the suspension mechanics or traced by the interferometer signal. Typical local control sensors are accelerometer located on suspension and position

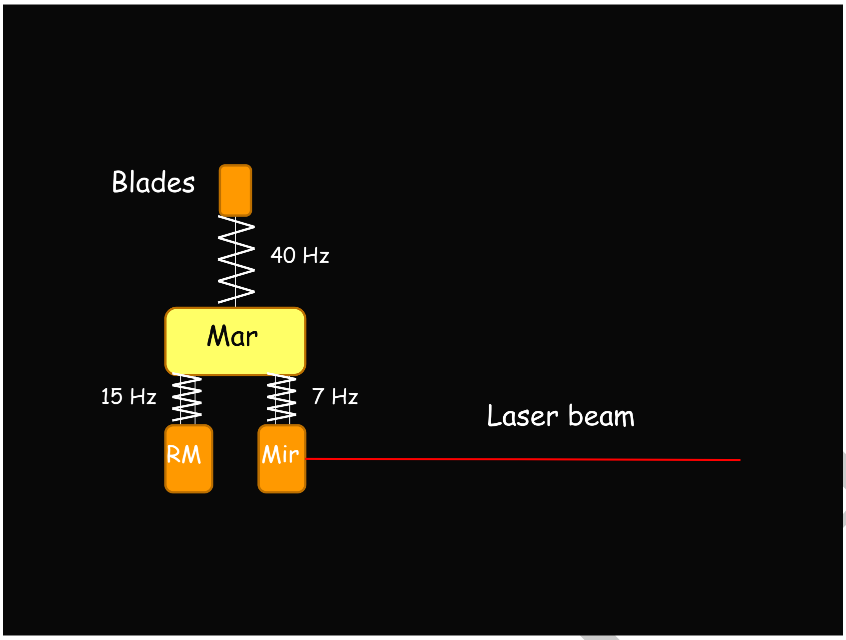

Figure 137: The three vertical modes of the optical payload suspended from the blades of last filter of the chain. For the vertical dynamics the two thin wires in a cradle configuration suspending the reference mass and the mirror can be thought as single vertical springs. As mentioned in the text, the vertical normal modes involve mainly (but not only) displacements of each payload element suspended from the blades: Marionette (Mar - 40 Hz), Reference Mass (RM - 15 Hz) and Mirror (Mir - 7 Hz).

sensors measuring displacement between suspension and suspension enclosure like linear variable differential transformers ($LVDT$), while for the payload control CCD cameras and PSD optical levers. Usual global control sensors are photo-diodes or quadrant photo-diodes providing information on suspended optical elements along three directions related to the interferometer beam (longitudinal displacement and two transverse tilts).

In order to ensure drift-less control and to provide suitable response of the system during far earthquakes, with the VIRGO set-up, remote sensors and interferometer signals are combined with local sensors. Significant examples are the drift-less local control of mirrors alignment and the Global Inverted-Pendulum Control ("$GIPC$"). Long suspensions in their *rest* position, without any applied force, are usually up to a several millimetres far from their nominal working point. For this reason the control system has a large dynamics, accomplished by using suitable large dynamics sensors and actuators. Once the RMS accuracy of the suspension point (at the top of the mechanical structure) is brought to $\sim 0.1\ \mu m$, large angular oscillations or DC misalignment can still be present at the level of the payload and local controls are engaged to slow down mirror motion to $\sim 1\ \mu m/s$ while aligning it from 50 μrad down to 10 $nrad$ accuracy. In section 4.5 some specific issues involving local controls of the payload will be further commented. In fact for ET the role played by the payload and its controls will be crucial in the overall suspension performance even more critically than for VIRGO.

In VIRGO we successfully tested multi-dynamical range actuators, to apply locking force through the payloads, which are capable of switching between operational modes without introducing discontinuities in the feedback. Meeting injected noise requirements should not be an issue using such devices. To cover the whole huge dynamical range actuation forces are distributed along the chain. Whatever will be the final mechanical design for ET suspension it looks unfeasible taking into account less than four actuation points (presently inverted pendulum, steering filter, marionette and mirror).

Digital controllers used in suspension control system are quite complex: about 250 poles for each suspension

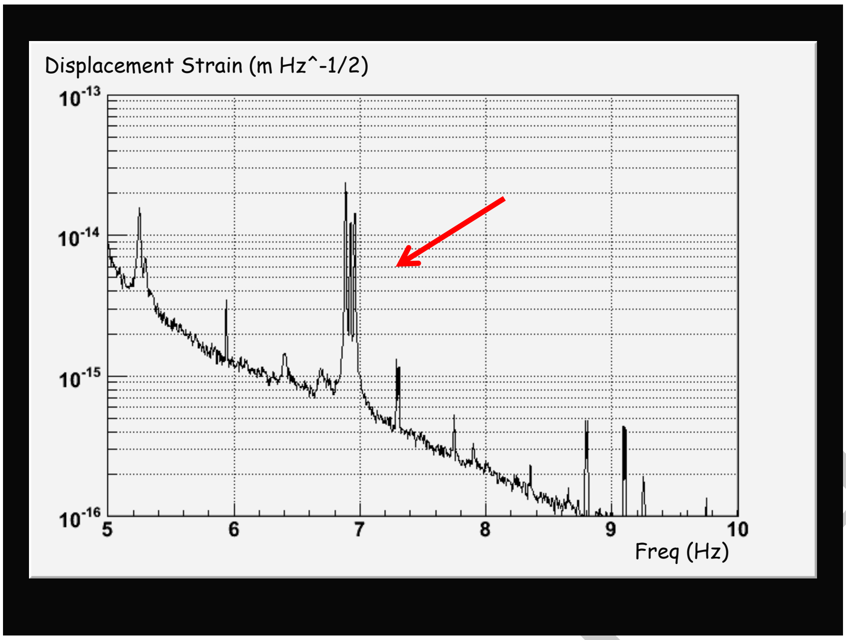

Figure 138: The photo-diode signal at the dark port of the VIRGO antenna expressed in strain sensitivity. The four peaks around 7 Hz correspond to the vertical modes where the mirror displacement is mainly involved. A peak for each one of the four mirrors accommodated along the two Fabry-Perot cavities appears in the dark port (each at a slight different frequency around 7 Hz).

requiring about 150 $MFLOPS$ computation capabilities (sustained). One of the key points for a second generation system will be providing tools to ease control engineers life. Today control loops performances are a function of who actually implements the control algorithm. While this approach showed to slowly converge to a nearly optimal control modern control techniques allow optimal control using almost automated procedures much more human independent than $Nyquist$ like techniques used so far.

APPENDIX - Cryogenic compatibility of materials for Superattenuator construction In this appendix some guide lines to select materials and components for the construction of a *Superattenuator* working in a cryogenic environment are reported. Doing this it will help in the understanding process of the interface problems linked to the presence of a cryogenic payload suspended from an anti-seismic system. During our investigation, based on data coming from literature and on some lab tests performed by Virgo collaboration, no preliminary hypothesis on the operating temperature has been done keeping the maximum flexibility. Even if some construction materials (stainless steel, $OFHC$ copper, etc.) can be used down to liquid helium temperature this does not represents a limiting factor of our investigation. However, for each element of the chain, it is necessary to perform a careful characterisation test of the thermal expansion coefficient. The presence of very sophisticated optics, indeed, requests a particular attention to avoid the environment contamination that needs to be carefully controlled. The conclusions of our activity, summarised in the following, are discussed in detail in [308].

- *Actuators*: the position of different elements of the suspension system, especially those ones close to the optical payload, must be moved for the interferometer control. Some commercial stepping motors designed for Ultra High Vacuum (UHV) and cryogenic applications are available, but they should be tested and qualified by a dedicated characterisation measurement performed in the standard working conditions. An AML motor has been tested successfully at Virgo down to a few Kelvin [$F.Frasconi$, *Private communication*]. Cryogenic lubricants should also be selected, avoiding those ones having chemical com-

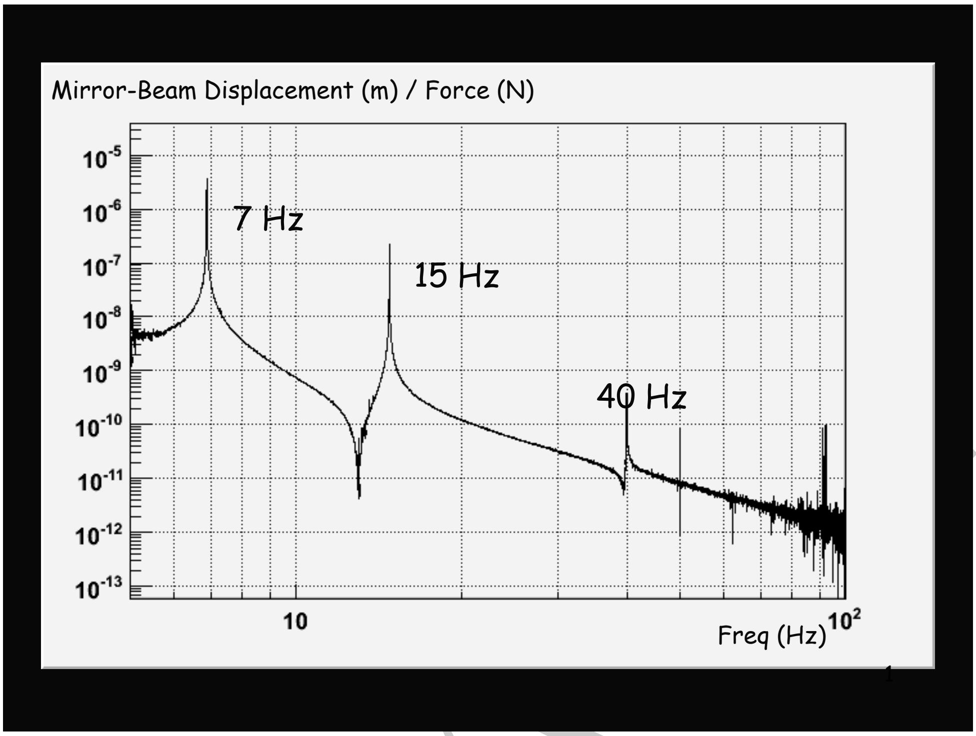

Figure 139: The transfer function between the mirror displacement along the beam (expressed in m) and the vertical force acting on the marionette (expressed in N). The vertical to horizontal coupling-factor (i.e. how much the mirror displacement in vertical is transmitted horizontally along the beam) is obviously already included in our measured transfer function and does not require any additional evaluation.

position based on hydrocarbon and fluorine for possible contamination issues.

- *Cabling*: the great variety of control systems and sensors in Einstein Telescope will require a large number of electrical connections, that should have low thermal conductivity (to reduce heat exchange), low electrical resistivity (to reduce dissipation), high flexibility (to reduce noise injection) and low contamination. An optimization of conductors and insulator dimensions as a function of current and operating temperature is required. As detailed in [308], some low out-gassing samples tested in Virgo can be used at low temperatures: Pyre-Ml insulated wires, alumina insulated wires, Gore-Tex ribbons. While $Kapton$ and $PTFE$ insulation have been already tested for satellite applications.
- *Adhesives*: during the construction of the interferometer there will certainly be the need to bond several elements of Einstein Telescope. For this reason some adhesives could be selected and used. They must be able to withstand thermal cycling and match the thermal expansion coefficients of the bonded elements. The adhesives properties are strongly dependent on the specific batch and on the curing recipe (time and temperature). As shown in [308] several solutions are available for testing them down to liquid helium temperature, including epoxy and ceramic adhesives. Even if some of them have been tested on optical surfaces, the bonding strength, the thermal expansion coefficient, ageing and contamination issues on long time scales must be measured by a dedicated research activity devoted to a precise characterisation of each adhesive.
- *Magnets*: the properties of magnetic materials are strongly dependent on the temperature. Ferrite and Alnico materials are not suited below 200 K because they change magnetic properties. Neodymium-Iron-Boron magnets show an increasing magnetic field going from room temperature down to 140-120 K

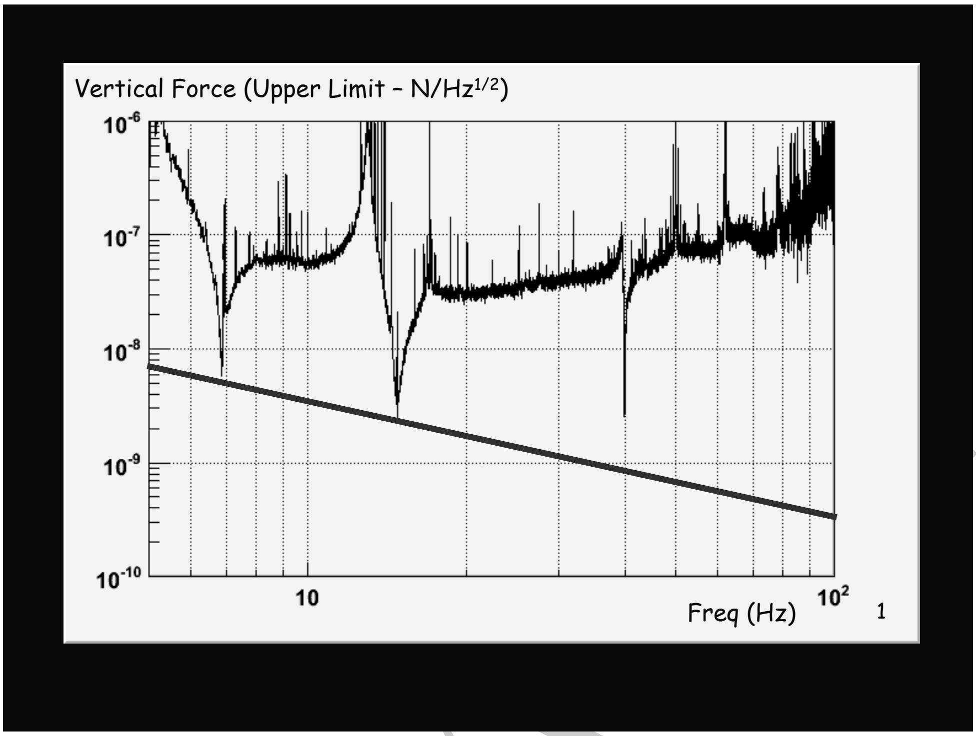

Figure 140: The linear spectral density of the maximum possible vertical force acting on the marionette compatible with the VIRGO sensitivity. This is given by the simple procedure described in the text. Since the "$1/f$-behavior" of the micro-glitches force is assumed, one can find what is the maximum force having an "$1/f$-profile" at the level of the marionette compatible with the VIRGO sensitivity. This is given by the minimal "$1/f$-shape" line touching the curve that gives the general upper limit on the vertical force just plotted.

while decreasing its value at lower temperature. Samarium-Cobalt magnets show a magnetic field slowly decreasing with decreasing temperature and they have been successfully used down to liquid helium temperature. A critical point is the "Barkhausen noise" that requires a dedicated $R\&D$ activity for a precise characterisation. From literature we know that at room temperature, Samarium-Cobalt magnets show a smaller "Barkhausen noise" than Neodymium-Iron-Boron magnets.

As mentioned in section 4.1.1.e, another important topic deals with the creep noise of suspension elastic elements generated by the high stress applied. It has been already shown in the same section (4.1.1.e) that the noise due to the dislocations motion and to their avalanche formation are typical events triggered by the temperature increasing, important only in the last stage(s) of the *Superattenuator*. The natural question is: what is the situation of this micro-glitch noise in a cryogenic environment? Even if creep is associated to an increment of the environmental temperature, cryogenic creep is not necessarily negligible, as observed for $OFHC$ copper. Data from literature on this subject and relative to steels as reported in [309] are insufficient and scattered. Since most part of previous studies investigated transient creep, it is suggested to perform very long term tests before using this material in a cryogenic environment. In [309] typical apparatus to measure creep in a cryogenic environment are outlined. An $R\&D$ program is required only if in the final design of Einstein Telescope some elastic elements will operate at low temperature.

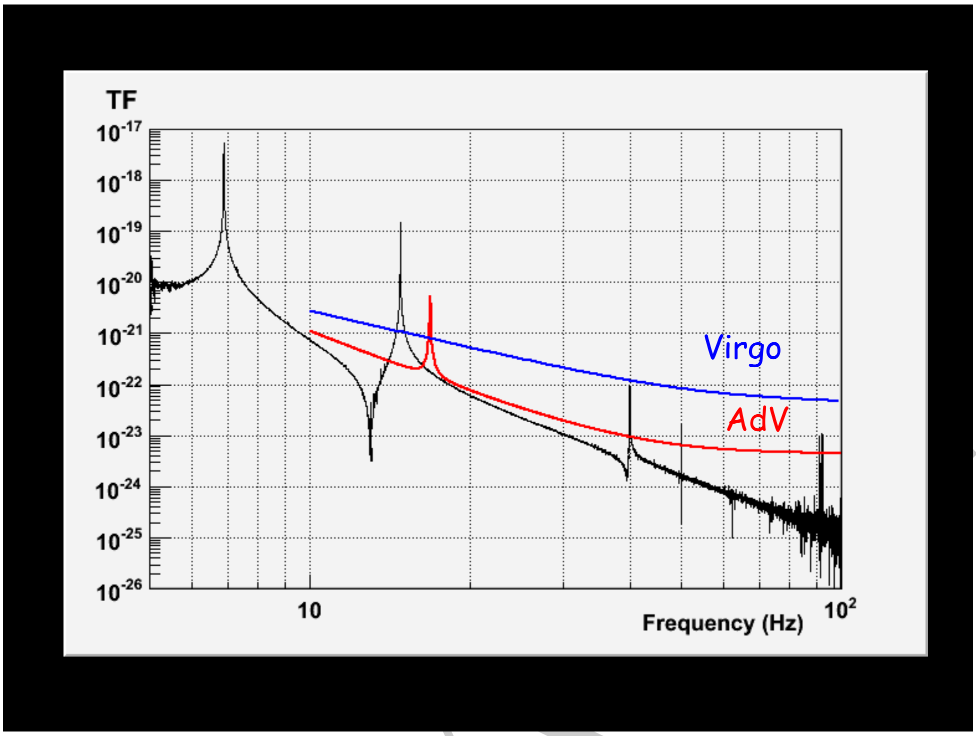

Figure 141: The upper limit of the micro-creep noise floor taking place in vertical on the blades of the last stage is given by the "$1/f$-force" upper limit plotted in the previous figure and the mentioned transfer function (stating how this force is transmitted along the beam). The upper limit of this noise floor is compared with the design sensitivity curves of VIRGO and AdV. The upper limit, except around the resonant peaks, is enough to state that AdV will not be affected by this source of noise.

4.4.2 HF interferometer

As detailed in section 4.1.1.c the measurements campaign performed with the VIRGO interferometer and devoted to evaluate the attenuation performance of the *Superattenuator*, demonstrated that, above 3 Hz, a multistage pendulum suspended to a three legs mechanical structure, as pre-isolator stage, is compliant with the ET requirements. The results reported in figure 131 have been obtained by using a *Superattenuator* with *six* seismic filters (for a total length of about 9 m) hung to a platform accommodated on top of the Inverted Pendulum which has been by-passed during the suspension point excitation phase of the measurements. This represents a good safety margin from attenuation point of view, because passing the seismic noise through the mechanical structure of the Inverted Pendulum, it will be additionally attenuated by a factor around $20 - 40$ dB.

Starting from the long experience acquired in operating a similar mechanical system for seismic noise suppression, a base line for the LF and HF Detectors of the ET Project has been tracked. It is based a seismic attenuation system designed for the VIRGO interferometer with common peculiarities: the first one can be conceived extending the detection bandwidth below 3 Hz by improving the chain total length up to 17 m (see details in section 4.1.1.d), while for the second a VIRGO-*like Superattenuator* can be built. The advantages of this choice are different:

- even considering a conservative cut-off frequency of the whole system around 5 Hz, it turns out that there will be a wide overlap between the HF Detector bandwidth the LF Detector one (following our indication starting around 2 Hz);

- the construction technology, mainly based on the use of magnetic anti-spring, has been deeply tested in vacuum for a very long time period (about ten years);
- the behavior of high stressed elastic elements (blades and wires) has been studied as reported in section 4.1.1.e;
- many mechanical and electro-mechanical elements are compatible with cryogenic environment (see the Appendix of the previous section);
- the upgrades, presently in progress for the VIRGO *Superattenuator*, can be used for this application too.

In this context and considering the ET requirements the choice of the VIRGO *Superattenuator* as seismic isolation system for the third generation of gravitational wave detector, seems to be the natural one.

4.4.3 Upper-lower suspension interface

As described all along this document, the ET Project is based on two different detectors. The first one aimed to the detection of gravitational wave signals in the low frequency range (*LF Detector*) and the second one for the detection of high frequency signals (*HF Detector*). The LF experimental apparatus will have a detection bandwidth as wide as possible in this specific region adopting, as seismic isolation system, the VIRGO *Superattenuator*. The main difference is represented by the length of the multistage pendulum (for details see section 4.1.1.d), an important parameter to move the cut-off frequency of the whole system to the best value in accordance with the ET requirements (around 2 Hz for a total chain length of about 17 m). The main characteristic of the LF Detector is that the suspension upper part will be at room temperature while the payload is maintained at cryogenic temperature for beating the thermal noise limit. These working conditions will not be present in the HF Detector where a seismic isolation system based on the VIRGO *Superattenuator* 9 m high will be operated at room temperature thanks to its attenuation performance above 3 Hz compliant with the ET requirements.

For this project a complex vacuum system has been studied with both detectors within the same tunnel and in particular with the pipes for LF Detector running on top of those ones of the HF Detector. This configuration will include a cooling shield containing the payload within the vacuum tower basement of the LF Detector. While the test mass and the penultimate stage of the suspension will be accommodated within the cryostat, a suspension wire made of $Ti-6Al-4V$ will be used to suspend the payload from the *Superattenuator* upper part at room temperature (see section 3.4). This interconnection element has a key role in preserving the thermal isolation between the payload and the suspension upper part. Moreover, the cryostat structure will have a hole through which this suspension wire will pass. This hole should be large enough to avoid possible wire friction during standard working condition, but it should not create an important and undesirable thermal input for the cryostat operation. The penultimate stage, indeed, will be directly connected through a thermal link to an ancillary suspension where a "*cold box*" will be installed. In this way the heat extraction from the mirror is obtained via the suspension fibres attached to the penultimate stage, and then through the thermal link toward the ancillary suspension.

Since the hole in the cryostat structure will be also used for pure helium gas exchange during the cooling down process (pure helium gas will be injected within the experimental volume to speed up the cooling down/warming up procedure), it will be equipped with a mechanical shutter (vacuum tight) driven by a stepping motor (remotely controlled for opening/closing procedure) to be installed in the roof structure separating the tower upper part from the bottom one. This mechanical solution together with an adequate pumping system and a well defined evacuation procedure will be important steps to reach the needed vacuum level.

4.5 The mirror last stage suspension

Author: F. Ricci

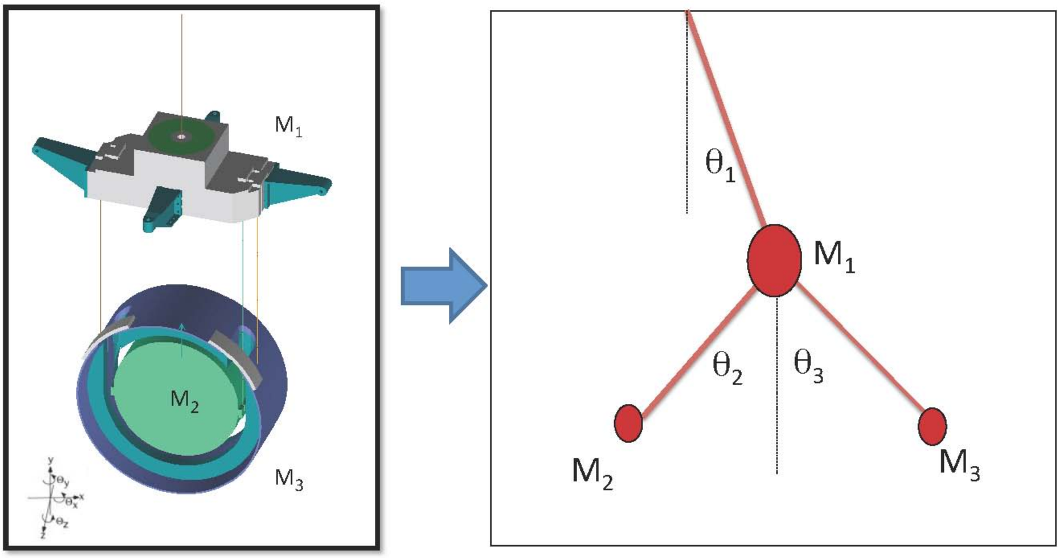

Figure 142: Left: Sketch of the Virgo-like Last Stage suspension. Right: Scheme using the point-like masses M_1: Marionette, M_2: Mirror, M_3 : RecoilMass

The Last Stage Suspension (LSS) is the system designed to couple the test mass to the *Superattenuator* chain, to compensate the residual seismic noise and to steer the mirror through internal forces exerted from the last Superatenuator element (4.4.1) [**?**].

The main components of a Virgo-like LSS are the Marionette, the Recoil Mass (RM) and the Mirror as shown in figure (142). The marionette (M_1) is the first stage used to control the mirror position with coil-magnet actuators operating between the upper suspension stage and marionette arms; the recoil mass (M_3) is used for the Mirror (M_2) steering and its protection, it carries the coils of the e.m. actuators acting on the mirror rear side.

Using the last stage it must be possible to perform the alignment in dc of the test masses, to compensate the residual seismic noise below 1 Hz and to steer the optical components maintaining the relative position of the interferometer mirrors. It includes a dedicated set up for controlling the position and orientation of the suspended masses to the respect of the local reference frame It is useful also for dumping large oscillation eventually excited during the adjustment phase.

The last stage must be ultra high vacuum compatible, made of no-magnetic and no-electrostatic materials to avoid extra dumping factor and spurious couplings. In particular the choice of the suspension material and its shape is crucial for limiting the thermal noise contribution of the interferometer sensitivity.

The mechanical and electromagnetic design is conceived following specific requirements:

- The mechanical resonance frequencies of the last stage elements must be as high as possible to avoid spurious thermal noise contributions to the interferometer output
- The steering of the optical elements needs to be performed in an ultra-high vacuum (UHV) space.
- The payload components (marionette, reaction mass and e.m. actuators) has to be conceived in such a way to limit the dust contamination of the optical element during the assembly phase and in operation (class 1 clean-room compatibility)
- It is necessary to limit the cross-talk effects among the various degrees of freedom to be controlled. This implies an accurate design of the electromagnetic actuators and a careful design of the suspension point of the mechanical elements.

In particular, to fulfill the last requirement crucial and simplify the Multi Input Multi Output (MIMO) control, we have to keep

- the center of masses alined along the super attenuator axis
- parallel the principal axis of the ellipsoid of inertia of each suspended body to the interferometer optical axis, its transversal direction and the gravity line

Other requirements are derived on the base of the experience accumulated in Virgo, as the optimization of the mass values for limiting the recoil effect and the to avoid along the main beam the insert of composite bodies (as for example a mirror clamped to an external frame).

In the next sections, we model the thermal noise of the mirror suspension and we describe the mechanical designs for LF- and HF-ET. Then we focus on the control issues and the related actuators and sensors. Finally we discuss the technologies to be developed.

4.5.1 Material selection for the last stage suspension

Author: R. Nawrodt

The last stage suspension is the most critical point of the whole suspension chain. It determines the thermal noise of the suspension elements. Thus, low mechanical loss materials in combination with a monolithic suspension technique as used in GEO600 [310, 311] and the Advanced Detectors [312–314] is preferred. Here the material of choice is fused silica which fulfills these requirements and has been studies in great detail in the past.

In the low temperature detector the suspension elements have to fulfill a second crucial duty - they have to extract the thermal load that is put into the optical component by the laser beam. This additionally demand rules out fused silica as a suspension element due to its very small thermal conductivity at low temperatures as an amorphous material (see figure 143). In contrast, crystalline materials have a very high thermal conductivity at low temperatures.

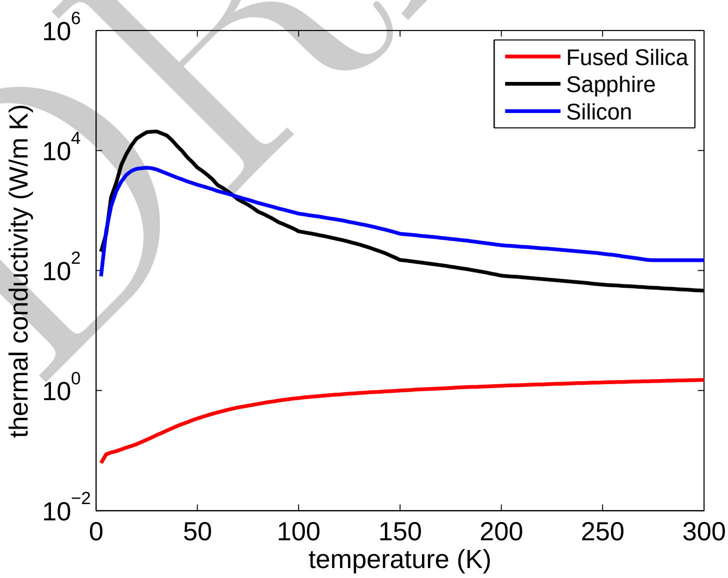

Figure 143: Thermal conductivity of bulk fused silica, sapphire and silicon. The plotted values are obtained from Touloukian [315, 316] as 'recommended' curves.

Both materials - silicon and sapphire - show a large thermal conductivity in the temperature region of interest (typically below 20 K which will be shown later by means of thermal noise considerations in section 5.9.5).

Sapphire has a higher thermal conductivity as silicon below 20 K. Sapphire fibers for heat extraction have been investigated in detail by Japanese groups for CLIO and LCGT [317–319].

A third point for the selection of the suspension material is the possibility to bond the suspension element to the test mass. As will be shown later the most likely substrate material will be silicon for the Einstein Telescope due to its availability in large pieces. Sapphire samples are not available in large enough pieces which are needed for the LF detector (see section 5.9.1). The bond strength of sapphire-silicon [320] bonds is smaller than silicon-silicon [320, 321] bonds based on hydroxid-catalysis-bonding. The reason for the weaker bonds in a sapphire-silicon configuration is so far unknown - beside direct chemical effects during the bonding process imperfections in the polished surfaces of the bonded samples are very likely to be the origin of this effect. Besides the weaker bonds the different coefficients of thermal expansion might cause stress during operation at low temperatures which might reduce the reliability of the sapphire-silicon bonds.

All these considerations lead to a preferred design based solely on silicon. Silicon suspension elements are currently under investigation in the form of fibers [322] and ribbon-like structures [323]. Details about the ongoing work can be found in section 4.6.

The thermal conductivity of crystalline materials is dependent on different effect:

- the concentration of impurities,
- the sample dimension,
- the phonon density at the given temperature.

These properties define the shape of the thermal conductivity curve in dependence on temperature. At higher temperatures thermal phonons collide with other phonons or impurities which leads to a finite thermal conductivity. At lower temperatures the effect of phonon-phonon collision becomes weaker due to the reduced density of phonons. The impurities dominate this region. At sufficient low impurity concentrations the thermal phonons begin to collide with the sample boundaries before other collisions. The phonons propagate now ballistically and the thermal conductivity becomes geometry dependent. At even lower temperatures the thermal conductivity decreases due to a lack of available phonons for carrying heat. This general behavior of a crystalline material can be seen from figure 143.

A very high impurity density is present in polycrystalline samples. Here, the grain boundary act as very efficient scatter centers and reduce the thermal conductivity of the sample (see figure 144). In order to get high thermal conductivity suspension elements polycrystalline samples need to be avoided.

The effect of impurities and phonon-phonon scattering by means of N- and U-processes on thermal conductivity has been studied in detail in the past [324, 325]. For very pure silicon samples it was observed that the natural composition of isotopes acts as scattering centers as well. If these scattering centers are removed by enriching the silicon with one isotope the thermal conductivity can be even further increased (see figure 144).

The impact of the sample geometry on the thermal conductivity will become important for the design of suspension elements. These elements are naturally thin in at leas one dimension. If one dimension of the suspension element gets into the region of the mean free path of the phonons the thermal conductivity becomes size limited.

A detailed theoretical model of thermal conductivity in semiconductors including scattering of phonons at other phonons, impurities and boundaries can be found in [327].

It is clear from this observation that for all calculations that include the thermal conductivity of small samples great care must be taken. A conservative value for the total thermal conductivity was assumed with a value of 1000 W/m K at 10 K has been chosen in the following calculations to incorporate already phonon-boundary and impurity scattering.

Besides thermal conductivity the specific heat capacity as well as the coefficient of thermal expansion (CTE) play an important role in order to build a low noise suspension. The heat capacity of crystalline materials follows Debye's T^3-law. Thus, at very low temperature we expect very small values for the heat capacity (see fig. 145(a)).

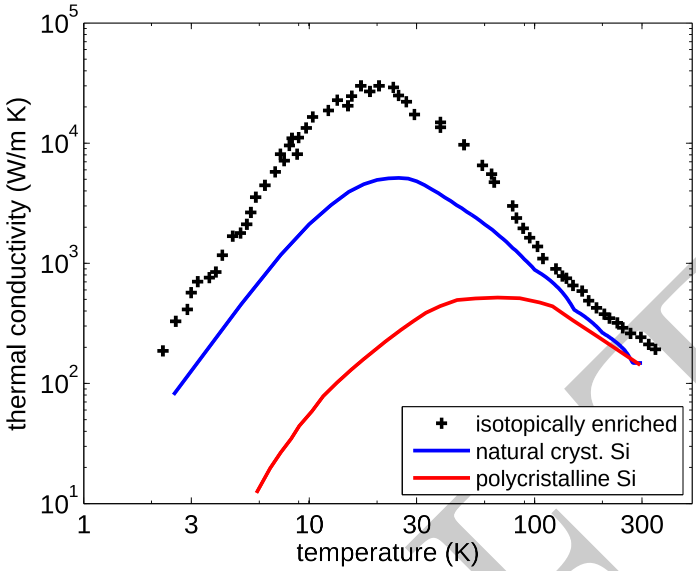

Figure 144: Thermal conductivity of silicon. The results for natural and the polycrystalline silicon are obtained from [315] for the isotopically enriched sample from [326].

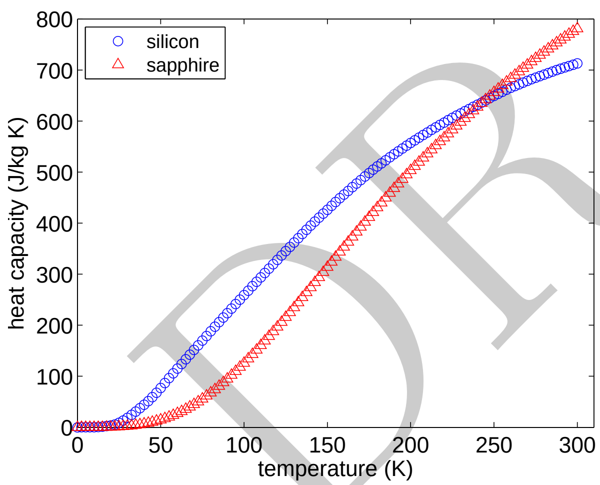

(a) Heat capacity ([328, 329]).

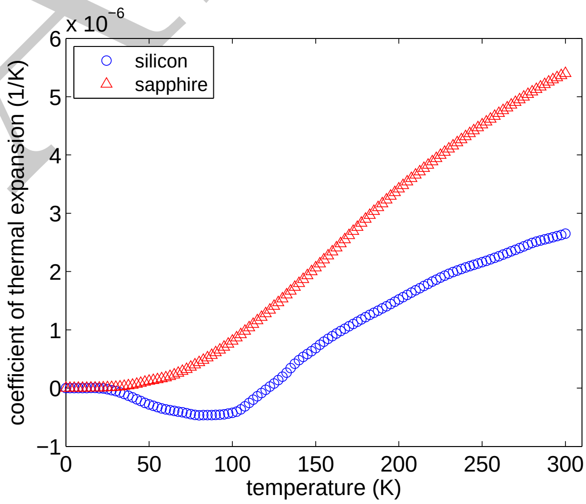

(b) Coefficient of thermal expansion ([330, 331]).

Figure 145: Heat capacity and coefficient of thermal expansion for silicon and sapphire as a function of temperature. The heat capacity of both materials follows the predictions of the Debye-law that states a T^3 behaviour. The coefficient of thermal expansion also decreases with decreasing temperature. Silicon shows a special behaviour having two distinct temperatures (around 18 K and 125 K) where the coefficient of thermal expansion vanishes. All values have been obtained from.

The CTE determines the level of thermo-elastic loss and thus thermo-elastic noise of the suspension elements. Here, fluctuations of the local temperature is directly transfered into a position fluctuation by means of the CTE. In order to get a low level of thermo-elastic noise it is necessary to choose an operational temperature that provides a low CTE. Fig. 145(b) summarises the temperature dependence of the CTE for sapphire and silicon. The general trend shows that lower temperatures lead to smaller CTE. Silicon has a special behaviour where the CTE changes its sign at 125 K and at around 18 K. Thus, at these two point the CTE is zero and thus the contribution of the thermo-elastic noise in theory zero. However, due to the demand that the suspension element has to extract the residual heat from the optical absorption in the test masses they will not be in a thermal equilibrium and thus a homogeneous temperature distribution along the fibre/ribbon cannot be expected. The lower the overall temperature of the suspension element is the smaller the total thermo-elastic noise contribution.

Brownian thermal noise of the suspension is strongly dependent on the mechanical loss of the suspension element. The mechanical loss is usually studied by means of a ring-down experiment. For different materials this parameter has been studied in the past in detail (see e.g. [323, 332–336]) both for bulk materials (see section 5.9.1) and suspension elements made from fused silica (see e.g. [337–341]). There is only little known about the intrinsic loss of silicon or sapphire samples with dimensions close to the ones used in suspension elements. Silicon studies have revealed that thin silicon flexures can reach a mechanical loss as low as 4.4×10^{-7} at about 80 K [323] and even 3.5×10^{-8} at around 10 K [336]. The mechanical loss of a thin silicon flexure studied down to 10 K is presented in figure 146(a). The mechanical loss drops by around 3 orders of magnitude during cooling from room temperature to below 10 K. The behaviour of the mechanical loss is dominated by the thermo-elastic damping at higher temperatures. At around 125 K the vanishing CTE causes a dip in the mechanical loss curve.

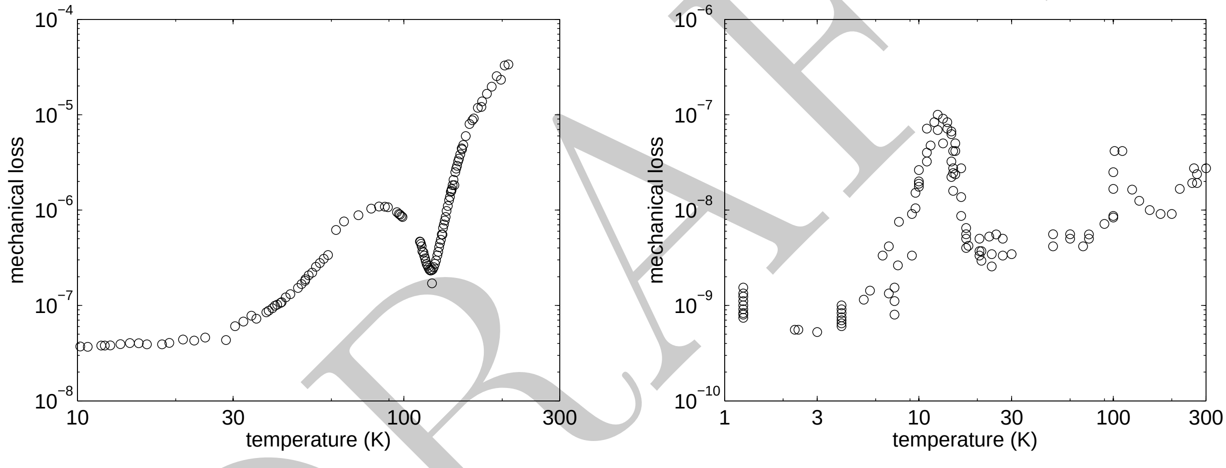

Figure 146: Comparison of the mechanical loss of silicon. (a) - silicon flexures [336] at 19.6 kHz, (b) - bulk silicon [332]. Loss peaks in the bulk material measurement are associated with impurity induced losses that can be avoided.

Compared to the mechanical loss of bulk silicon this value is slightly higher. The reason for this higher mechanical loss is currently assumed to be associated with surface losses. The investigation of the origin of these surface losses is within the focus of the current R&D (see section 4.6). Losses of about 10^{-8} are believed to be within the range of achievable values by the time ET will be built.

Figure 147 summarises the different loss contributions of a fibre suspension element typically needed for ET. While at room temperature thermo-elastic loss contributions dominate the low temperature suspension element is limited by intrinsic mechanical loss and surface loss which is assumed to be frequency independent as a first approximation. Thus, at cryogenic temperatures the mechanical loss can be estimated to be frequency independent as well and around 1×10^{-8} for typical suspension elements.

Currently, there are two possible techniques under investigation for the fabrication of silicon suspension elements. The first technique is the so-called micro-pulling technique [322]. Here, a thin fibre with typical diameters in the lower millimeter range is drawn from a silicon melt. The fabricated fibres are not perfectly single crystalline - but recent work has improved the crystallinity of the fibres. Currently, these fibres are produces with a length of 30 cm for the initial investigations. In principle there is no limit for the maximum achievable length and thus

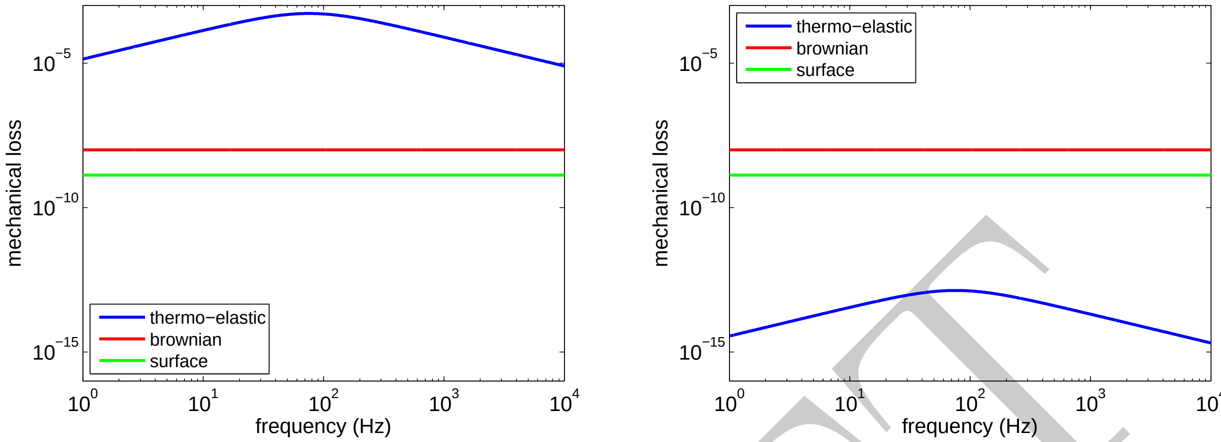

(a) 300 K.

(b) 10 K.

Figure 147: Comparison of the loss contributions of a suspension fibre with a diameter of 3 mm that has been proposed to be used for the low frequency detector of ET.

this technique is promising to be used for the low temperature suspensions for ET. For technical details of the fibre pulling technique see the section 4.6.1.

The second attempt is to use suspension structured etched out of single crystals or wafers. This technique provides suspension elements with a rectangular or quadratic cross section due to selective etching of the crystalline silicon in different directions. This technique utilises different well established processes from the fabrications of MEMS (micro-electro mechanical systems). A very well known and accurate silicon processing exists to fabricate structures out of crystalline silicon. Figure 148(a) shows such a typical element. A thin silicon flexure was fabricated from Si-wafers with a rectangular cross-section. The thickness of the flexure is in the range of a few 10 microns while the width and the length are in the range from 5 to 70 mm. The selective etching technique is just limited by the wafer size and in principle it is possible to create much longer elements. These structures have been used to investigate the intrinsic losses of silicon flexures [323] as well as intrinsic losses of coating materials applied to them [342–344].

There exist different etching techniques to fabricate such structures. The most frequently used ones are selective wet chemical etching and dry etching. These two technique provide different surface qualities strongly depending on the exact process parameters. Fig. 148(b) indicates that the minimum obtainable loss from these devices at low temperatures is strongly surface dependent. The origin of the surface losses in silicon are so far not fully understood and within the focus of the research carried out by several institutions involved in this design study (see section 4.6.3).

The promising flexure structures that are currently available and that are showing very low mechanical losses have an anisotropic stiffness due to their geometry. While in one direction the suspension element is soft (e.g. in beam direction) it is very hard in the perpendicular direction. This might lead to problems in the control of the interferometer (see sections 4.5.7 and following). Therefore, the investigation of the fabrication of crystalline fibres as well as novel control strategies including anisotropic properties need to be done. A summary of ongoing R&D activities regarding the suspension elements can be found in section 4.6.

4.5.2 The suspension thermal noise model

Author: P. Puppo

To calculate the thermal noise curve of this system along the horizontal and vertical degrees of freedom, we

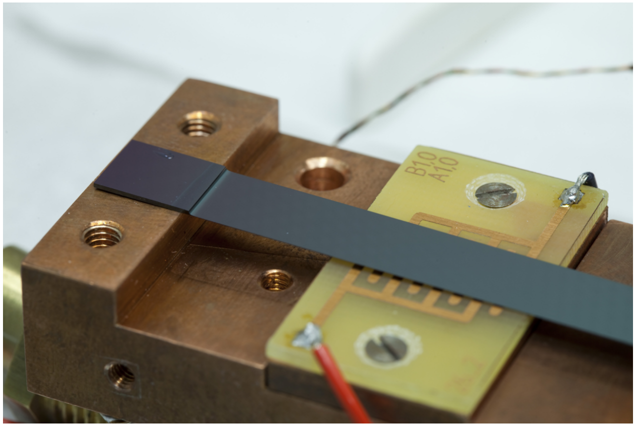

(a)

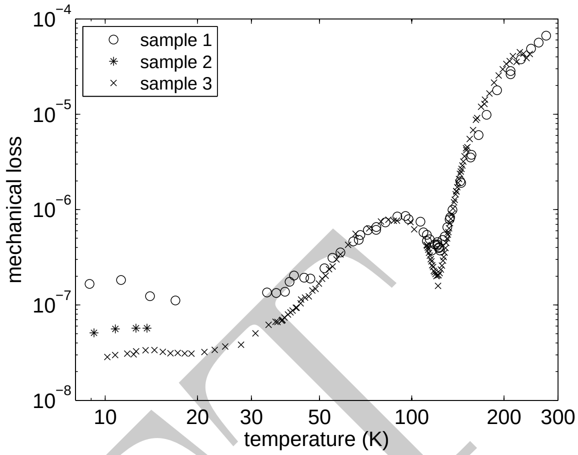

(b)

Figure 148: (a) Silicon flexure etched out of a silicon wafer. (b) - Mechanical loss obtained from different surface qualities. Depending on the surface preparation different roughnesses have been obtained (sample 1 - 330 nm, sample 2 - 33 nm, sample 3 - 6 nm; RMS roughness over 100 μm).

can write the Lagrangian by supposing the 3 elements as point-like masses so that the Virgo-like last stage suspension is a cascade of three pendula: to the first pendulum (the marionette) the mirror and the recoil mass (RM) are hung as branches (see figure (142)). As a consequence the rotations about the coordinate axes are not included. This choice can be reasonable if we suppose a negligible coupling of such degrees of freedom with the interferometer output coordinate.

The study of the thermal noise of this system can be carried on by using two different methods: the Fluctuation Dissipation Theorem (FDT) and the modal expansion methods [345, 346]. For both these models we write the motion equations from the Lagrangian and the dissipation functions.

The FDT approach uses the mechanical impedance matrix $\hat{Z}$ to calculate the thermal noise on the i_{th} mass of the system by the formula:

$$S^i_{therm}(\omega) = \frac{4k_bT}{\omega^2}\mathcal{R}e\left\{(\hat{Z}^{-1})_{ii}(\omega)\right\} \tag{109}$$

In the modal expansion method, the motion equations are diagonalized and the normal modes frequencies and coordinates are found in function of the free oscillators ones. In this way it is possible to infer the frequencies, the displacements and the losses of each pendulum from the measured ones on the system modes. The main difference between this model and the FDT treatment, is that it allows us to insert the Langevin stochastic thermal forces independently acting on each pendulum. In this way we can study it even in a steady thermal state in which every oscillator has a different stationary temperature.

This behavior can be schematized by setting each mass of the i_th pendulum at steady thermal state T_i as if it has a constant heat exchange with a thermal bath at the same temperature. In this case each pendulum is subject to a different thermal stochastic force:

$$< F^2_{thi} >= \frac{k_bTM_i}{\tau_i}; i = 1, 2, 3 \tag{110}$$

Using the modal expansion model it can be shown that the thermal displacement noise of the i_{th} mass is also affected by the thermal noise of the other masses of the pendulum chain, mainly by the marionette's stage via its dissipation mechanisms. The FDT and the modal study of the thermal noise lead to similar results if the temperature of the whole suspension is supposed homogeneous. A complete study of both the models can be found in the reference [345], here we will illustrate the main calculation lines of this method.

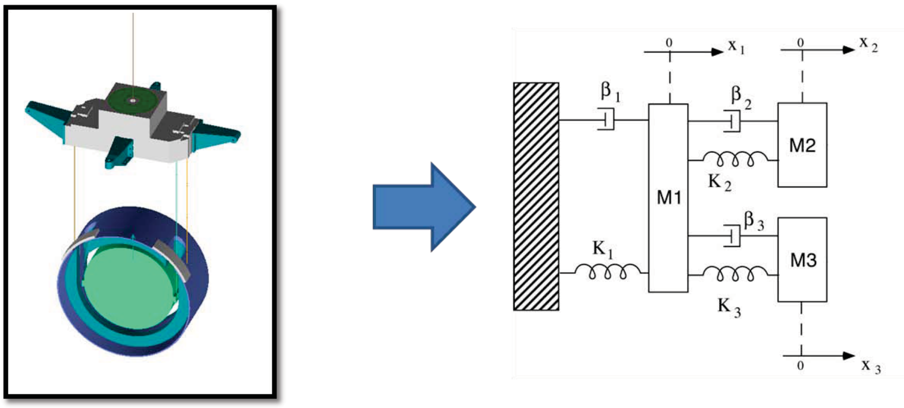

Figure 149: A Virgo-like last stage suspension is a cascade of three pendula. To the first pendulum (the marionette, M_1) the mirror M_2 and the recoil mass M_3 are hung as branches.

4.5.3 Normal mode formalism

In the mode expansion, the eigenvectors of the characteristic matrix of the system are the coordinates Y_-, Y_0, Y_+ of the modes and its eigenvalues are the modal frequencies $\omega_-, \omega_0, \omega_+$, thus every normal quantity is a function of the uncoupled ones. Moreover, the stochastic normal forces F_-, F_0, F_+, acting on each mode, are found in function of the uncoupled ones [345].

Within this formalism, the mirror coordinate X_2 is expressed in terms of the normal eigenvectors and its thermal noise is calculated with its power spectrum. We find:

$$\left\langle X_{th2}(\omega)^2 \right\rangle = \left\langle f_{th1}{}^2 \right\rangle |T_{n1}(\omega)|^2 + \left\langle f_{th2}{}^2 \right\rangle |T_{n2}(\omega)|^2 + \left\langle f_{th3}{}^2 \right\rangle |T_{n3}(\omega)|^2 \tag{111}$$

where $T_{ni}(\omega)$ are generalized transfer functions depending on the uncoupled mechanical parameters of the pendula [345] .

This result is fully equivalent to the FDT calculation shown in the equation (109) at homogenous temperature, however the explicit dependance on the temperatures T_i (in the $\langle f_{thi}{}^2 \rangle$) is the new result which permits to calculate the thermal noise of a suspension at a thermal steady state but with the stages at different temperatures.

4.5.4 Thermal noise computation of LSS for the LF interferometer

We have studied the thermal noise of a Virgo-like last stage suspension for the LF cryogenic interferometer characterized by the parameters summarized in the table (8). In this case the working temperature of the mirror is 10 K corresponding to the minimum mechanical losses of the mirror coating ($Ti : Ta_2O_5$ see section 5.9) and the material for the mirror bulk and its suspension wires is silicon (see section 5.9). The marionetta and the RM masses have been chosen in order to reduce the marionette recoil effects as much as possible. For this reason the marionette mass must be the sum of the masses of the mirror and the RM at least. The materials used for making the suspension wires have a loss angle of 10^{-8} (silicon) for the mirror and the RM and 10^{-5} (Ti6Al4V alloy [347]) for the marionette; their length is 2 m. The diameter of the silicon wire has been chosen to be 3 mm: with this value the temperatures of the marionette and the mirror in the steady state are $5\ K, 10\ K$ with a silicon wire having an thermal conductivity which is about 10 times worst that that one of the highly pure material. These value can take into account the presence of the thermal resistances due to the contacts between the mirror and its suspensions.

The obtained thermal noise curves have been compared with the ET-D goal sensitivity curve where the low frequency region refers to the low frequency interferometer with a power of 18 kW stored in the cavities. The results are sketched in figure 150.

	Marionetta	Recoil Mass	Mirror
Masses for ETDLF (kg)	422	211	211
Wire Diameter (mm)	3	3	3
Wire length (m)	2	2	2
Wire Material	Ti6Al4V	Silicon	Silicon
Loss Angle	10^{-5}	10^{-8}	10^{-8}
Temperature (K)	2	10	10

Table 8: Parameters used in the design of the mirror last stage suspension for the LF interferometer.

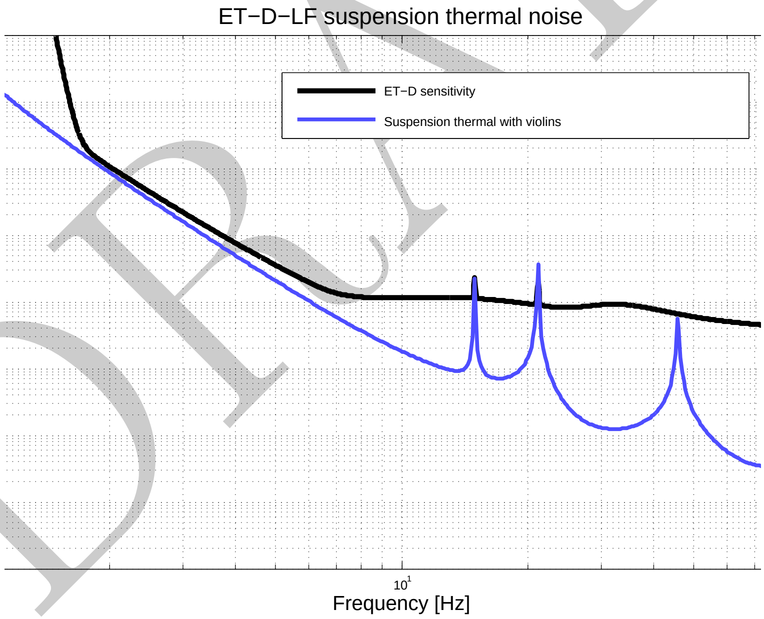

Figure 150: ET-D-LF sensitivity curve (Black) compared with the suspension thermal noise calculated with the parameters of the table 8 (Blue)

4.5.5 The payload of the HF interferometer

Author(s): P. Puppo, F. Ricci

The design of the last stage of the mirror suspension system of ET-HF is greatly based on the experience on Virgo and Advanced Virgo. The marionetta will be almost the same as in Advanced Virgo, while the recoil mass design of can be adapted to different mirrors lengths. We will accommodate in it the thermo compensation plate (CP), an other optical element s essential for compensating the thermal lensing induced in the test mass mirror by the huge laser power stored in the HF Fabry-Perot cavities. A Marionetta Recoil Mass is being developed: facilitates installation and operation for large diameter mirrors, could improve thermal noise matching for Test Mass Mirrors, it is necessary for larger mirrors (i.e. the BS). . In the marionette design the requirements for cleanliness, vacuum compatibility, mechanical precision, magnetic and electrical properties apply. Moreover several new aspects must be considered: the use of the fused silica fibers and the change of geometry of the mirror.

Moreover, monolithic suspensions currently being tested in GEO and with a 21 kg mirrors in Virgo should be developed for a 200 kg test mass (4.6.2). In the case of the monolithic suspensions, the silica wires must be attached to the marionette by a new kind of clamps which must not introduce further mechanical losses in the interface between the silica and the marionette surface. These new clamps have to be placed in such a way the fibre bending point lays on the horizontal plane passing through the center of mass of the marionette to minimize the coupling between different degrees of freedom. As the wire bending section is different by the clamping section, because of the tapered fibre tip (see section 4.6.2), this is carefully taken into account in the new design. The coupling between the marionetta and the fibre also influences the mounting procedure of the payload and consequently the new assembly tool design. Moreover the change of the position of suspension wires of the new reference mass, and, in case of need, of the balancing motor, are taken into account.

In the new reference mass (RM) design the requirements for cleanliness, vacuum compatibility, mechanical precision and magnetic and electrical properties apply. The new design takes into account the bigger thickness and mass of the mirrors, the implementation of the mirror control and the thermal compensation system.

The RM surrounds the mirror in order to protect it by accidents and hosts its actuators. It is equipped with safety stops designed taking into account the different shape and increased mass of the mirrors suspended with a monolithic structure. The design is conceived to host the ring heater and compensation plate foreseen in the thermal compensation system. To this aim, the dielectric parts of the RM must work at high temperature because of the possible contact with the heaters. The presence of a compensation plate could deeply affect the dynamical behavior of the last stage suspension: the centers of mass of mirror and RM must coincide to reduce the coupling among the various degrees of freedom. The structure required to carry the compensation plate will make more difficult to satisfy this requirement.

The actuators have to be dimensioned to fulfill the displacement requirements for the locking purposes and consequently are related to the optical configuration. There are two different options for the mirror actuation by the reaction mass: the coil-magnet actuators and the electrostatic actuators. We present them in the following sections (4.5.8, 4.5.9)

In the case of the coil-magnet actuation (see section 4.5.8), which is currently the reference solution, it is necessary to use a dielectric material to avoid eddy current dissipation and magnetization effects. The mechanical strength of the new insulating material must allow to use the reaction mass also as a safety structure for the mirror.

The dielectric material must be chosen to be UHV and cleanliness compatible. The use of a dielectric material could give rise to the problem of the mirror static electric charging by friction with the RM. A solution can be the use of dielectric materials having a finite high resistivity that avoids the formation of stray currents but reduces the presence of static charges. A possible choice is the TecaPeek CF30, a kind of polymeric plastic, loaded by carbon and grafite particles to increase its density and have a slight electrical conductivity which is useful to avoid the static charges formation.

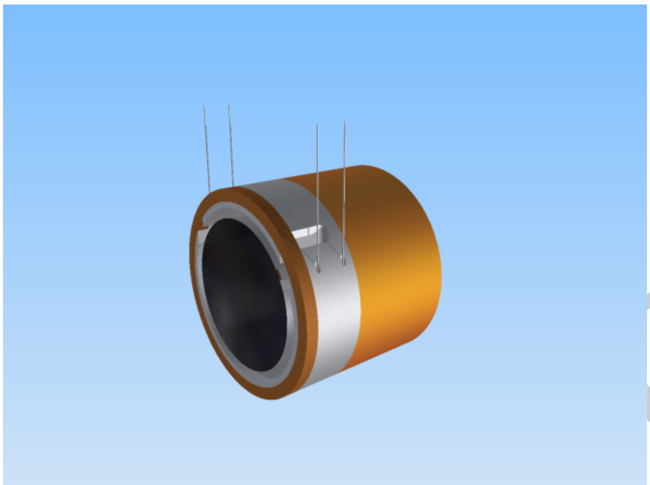

Figure 151: Schematic picture of the new mirror reaction mass. The various colors indicate the different materials used.

The ET configuration for the last stage suspension system can include a new element: the Marionette Reference Mass (MRM). The new element will permit

- to suspend a larger diameter mirror avoiding any mechanical interference between the marionette and the pots installed on the separating roof of the Ultra High Vacuum (UHV) chamber;
- to simplify the payload installation and its preliminary alignment procedure;
- to guarantee a high level of mirror cleanness without spoiling mechanical performance of the suspension system.

The MRM will be installed, as an additional suspended element, within the UHV chamber between F7 and marionette re-placing the F7 legs. It will host the actuator coils for steering the marionette. In this way a more compact design of the payload will be conceived and the IVC structure could be revised to accommodate a mechanical filtering system for the air flow entering within the UHV chamber. Following these project guidelines, the payload integration on the suspension system will benefit of:

- a wider clearance for the monolithic payload assembly, including the possibility to install a larger diameter mirrors;
- a more compact payload pre-aligned on bench will reduce the permanence time of two operators within the high vacuum chamber for the installation and its fine positioning;
- a quasi-laminar flow of clean air within the UHV chamber volume to be used during the assembly phase (TBC).

Monolithic fused silica (FS) suspension of the four 200 kg Fabry-Perot cavity mirrors will be realized for ET HF, exploiting the experience achieved developing the Virgo+ payload. The optimal geometry and technology is being pursued with the objectives of minimizing the pendulum thermal noise, fulfilling the requirements for an optimal control of the test mass, ensuring safety and reliability. For Virgo+ a large amount of work has been made to reduce the risk in the welding procedure. The fibers (once welded directly to the mirror) are now welded to intermediate components (called ears) silicate bonded to the lateral flats of the test mass. The former procedure induced a lot of thermal stress on the bonded surfaces that could damage the silicate bonding and eventually break it. Another problem is that the fibers pass through a dangerous manipulation procedure that can open cracks on their surface decreasing their breaking strength. To recover these problems a new technique has been developed: two lateral supports with vertical grooves are attached using silicate bonding to the mirror lateral flats. Fibers are produced apart from a fused silica bar previously welded to an upper clamp and a lower anchor. The fibers are then placed in position clamping the upper part to the marionetta and inserting the lower anchor below the lateral supports bonded to the mirror. In the end the anchor and the supports are bonded together through silicate bonding or *water glass*. Although this solution has been successfully implemented for Virgo it would be easier (and with lower mechanical dissipation) to avoid the lateral bonding of the supports to the mirror.

The suspension scheme tested for Virgo and to be applied for AdV trying to reduce the most critical part induced by silicate bonding the lateral supports on the lateral mirror flats. The supports can be machined out from the mirror , the lower surface of the support is polished to perform a silicate bonding which will be discussed in the following section 4.6.2. The suspension scheme proposed is the following: one fused silica part called "anchor" will be welded to a $sim7$ mm fused silica bar and to an upper clamp. Using the CO_2 laser machine the fiber will be produced from the bar welded to the clamps, the whole clamp-fiber will be placed in position on top to the marionetta and on the bottom under the mirror support. The contacting surfaces of the two parts (both with a polishing) will be bonded onsite using the silicate bonding or *water glass* procedure as for Virgo. To this aim it is necessary to find a geometry of the lateral supports easy to machine, and to demonstrate that the surface quality is sufficiently good for thermal noise performances.

The role of the upper clamps coupling with the marionette in order not introduce further frictions and recoil losses is very important. For this purpose a stainless steel box has been carefully designed with the aim to host the silica upper clamp and to attach it to the marionette without introducing further losses. The steel box is formed by two pieces. An external one fastened to the marionette by four screws. An internal one in direct contact with the fused silica and fastened by lateral screws to the external one. The silica core is kept fixed in its box by an upper lid fastened by screws. The steel inner box is also designed as the support of the upper clamp during the fiber pulling (see section 4.6.2) and then is coupled to the tool used to insert the fibre on the marionette lateral side, as foreseen by the assembly procedure.

4.5.6 The payload of the LF interferometer

Author(s): R. Nawrodt, P.Puppo, F. Ricci

Assuming for ET an optic configuration with mirror losses of the order of 10^{-6} and a stored light power of ~ 18 kW, we deal with the need to implement a cryogenic system able to extract tens of milliwatts of heat from the mirror during the working steady state. This requirement is compatible both by defining a cooling strategy based on closed loop cryo-coolers or by setting up a dedicated liquid helium plant.

Moreover for the employment at low temperature in a GW detector we need to design the suspension system in such a way

- to transmit the refrigeration power to the mirror without spoiling the control procedure of the mirror degrees of freedom
- to extract the heating power coming from the laser light in the more efficient and quicker way.

The materials used for building a cryogenic payload must follow these requirements, thus those materials with a very high thermal conductivity, good mechanical and optical properties at low temperature can be taken into account. Silicon is one of the best candidates both for the mirror and its suspensions in this case, indeed it has a very high thermal conductivity and very low thermal expansion rate. On the other hand the silicon material has very low mechanical losses at cryogenic temperatures.

For this reason in our analysis we have considered a last stage suspension designed as it is in the Virgo interferometer with a silicon mirror suspended to silicon fibers in a monolithic way.

The choice of the materials for building the marionette and the recoil mass must fulfill the requirements given by the work at cryogenic temperatures. In figure 152 it is shown how a cryogenic suspension should work during the interferometer operation, i.e. when the payload has been cooled down and the laser is turned on. The laser power absorbed by the mirror ($\dot{Q}_{laser}$) is extracted via its suspension wires and passing through the marionette reaches the refrigerating system. To this aim the marionette is directly connected with very efficient, soft heat links to the cooling power.

In a similar way as for the mirror the reaction mass is cooled down via its suspension wires and, if there is not extra thermal input on that, it reaches the thermal equilibrium and acts as a thermal shield for the mirror. The choice of the wires for the recoil mass must fulfill the request of having a good mechanical and thermal performance. For this reason, the use of a silicon suspension also for this part is a possible option.

In the scheme there is also the reaction mass of the marionette (MRM), absent in the present Virgo-like payloads. This part is an intermediate element between the marionette and last filter of the higher suspension which can act as a mechanic and thermal decoupler and as a thermal shield. In our study the MRM is not included because it has a negligible contribution to the thermal noise of the mirror [345].

The thermal equilibrium is reached when the power extracted by the cooling system is equivalent to that one absorbed by the mirror ($\dot{Q}_{abs} = \dot{Q}_{coolsys}$). At this condition most part of the power absorbed by the mirror flows through its suspension wires (a small fraction is lost in radiation), and then it is removed by the heat link directly connected to the cooling system. The equilibrium temperature of the mirror T_{mir} can be calculated by the simple analytical model relating it to the temperature of the thermal bath T_{bath} of the cooler via the power flow through the mirror wires:

$$\dot{Q}_{abs} = \frac{4\Sigma_w}{L} < K_{si} > (T_{bath} - T_{mir}) \equiv \frac{1}{Z_{therm}} \Delta T \tag{112}$$

$$\tag{113}$$

$$< K_{si} >= \frac{1}{\Delta T} \int_{T_{bath}}^{T_{mir}} K_{si}(T) dT \tag{114}$$

where Σ_w is the wire section, L its length and $K_{si}(T)$ is the thermal conductivity of silicon. For a given thermal input $\dot{Q}_{abs}$, the thermal impedance Z_{therm} is important to yield the final temperature of the mirror: this is the quantity which sets up the performance of our system and influences the choice of the material and of the geometry of the mirror suspension wire.

On the other hand, also the transient phase to reach the steady state must be taken into account, because we do not want too much long cooling times. For this reason the thermal capacity of the whole system plays also a role. Thus the presence of all the masses of the system is important for determining its thermal behavior.

To this aim some studies with a finite element simulation have been helpful. In figure 153 it is shown the FEM model developed to perform such a study. The reaction masses are not present, for reasons of computing time, and their screen effect is simulated by the surrounding system at 10 K. For similar reasons as for the reaction masses, the marionetta arms are not present. The mirror is suspended with a silicon fiber of 1 mm diameter and the reaction mass with a steel wire of 0.6 mm diameter. The silicon thermal properties vs temperature are included in the model. The mirror is heated with a power of 1 W distributed around its center with a gaussian shape to simulate the laser mode. The cooling power, directly linked to the marionette, comes from 2 pulse tube cryocoolers with a cooling capacity (W) depending on the temperature: at a temperature of the cold finger of 4.5 K the power is 1 W, while at 20 K the cooling power is about 10 W. At the thermal equilibrium the cold finger temperature is 4.5 K. A similar behavior is obtained using the liquid helium with a temperature of the thermal bath of 1.8 K. The simulation results agree with the formula (114) when $T_{bath} = T_{cold\ finger}$ and give the thermal distribution on the whole payload, as shown in figure (154) where it is evident that the final temperatures of each payload elements are not the same.

This result cannot be neglected when the thermal noise of the last stage suspension system is calculated for two main reasons: the thermal properties of the suspension wires change as the second equation in (114) shows; a different temperature upper stage can differently influence,depending on its temperature and mechanical losses, the thermal noise of the mirror. For these main reasons we presented in the previous paragraph 4.5.2 the thermal noise model generalized to the case of the stages at different temperatures.

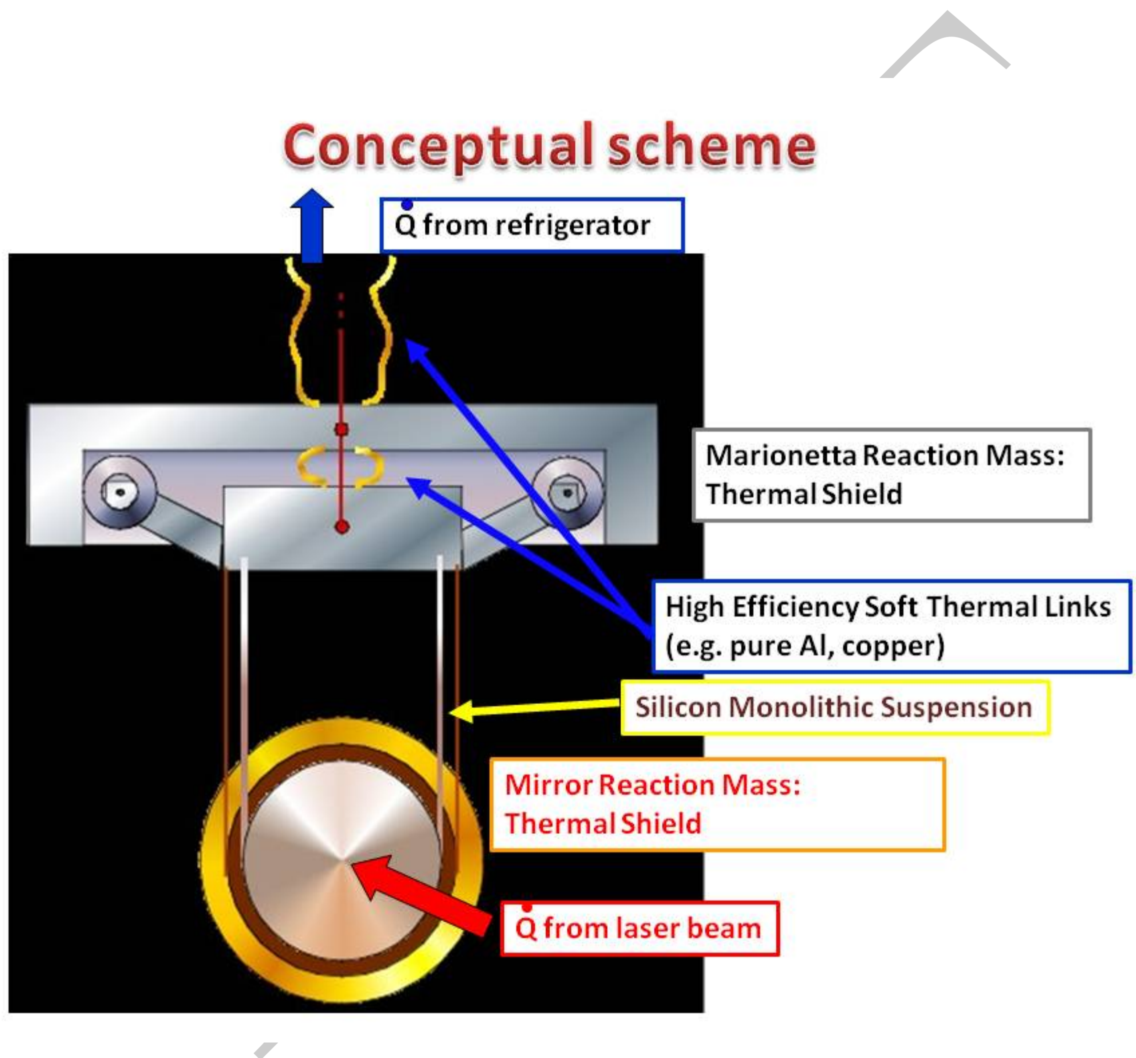

Figure 152: The conceptual scheme for a cryogenic suspension

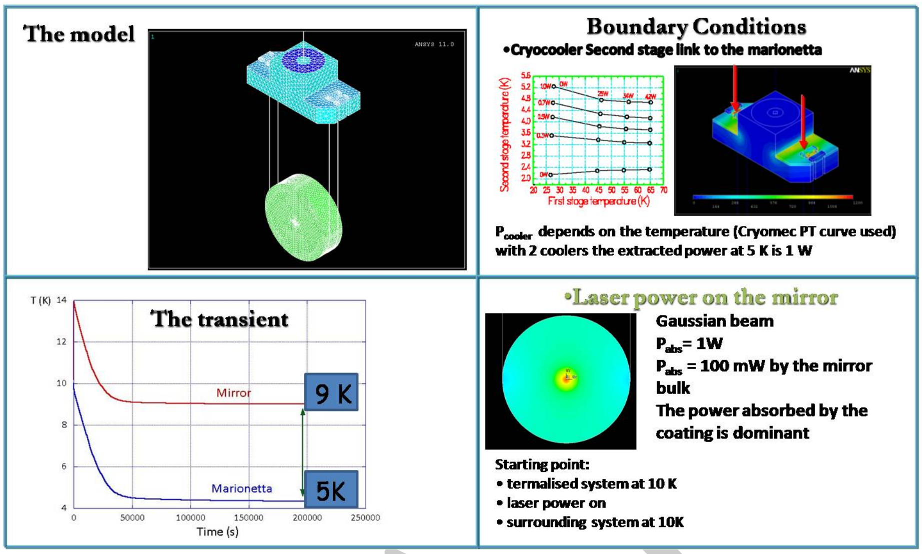

Figure 153: The reaction masses are not present in the simulation, their screen effect is simulated by the surround system at 10K. The marionetta arms are not present, silicon thermal properties vs temperature are included in the simulation.

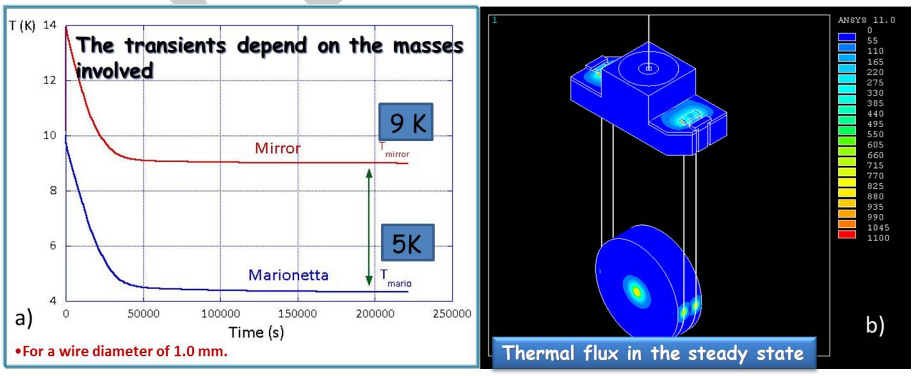

Figure 154: FEM results: a) time evolution of the mirror's and marionetta's temperatures, b)thermal distribution on the whole payload

4.5.7 The payload local control for ET

Author: F. Ricci E. Majorana

The local control of test masses plays a crucial role in gravitational wave detectors with independent test masses. Payload local control system is meant to slow-down and align the test masses as interferometer's mirrors, driving their dynamics within the gain range of automatic error signals (wavefront sensing for angles and locking for longitudinal position). As said, in order to preserve the quasi-inertial state guaranteed at the level of payload suspension point by the superattenuator, only internal forces should be used (as in VIRGO).

As said in the context of overall suspension control, the actual VIRGO+ performance will be easily tunable towards Advanced detector performances, ET digital/analogic chain (Fig. 155) needs to be improved, namely by reducing by more than one order of magnitude the overall low frequency noise re-injection during locking force reallocation to payload stages. The related R&Ds will naturally follow the developments of advanced detector implementations.

However, ET system will be complicated by the presence of cryostats surrounding the vacuum chambers hosting the payloads Fig. 155, whose design will not be trivial.

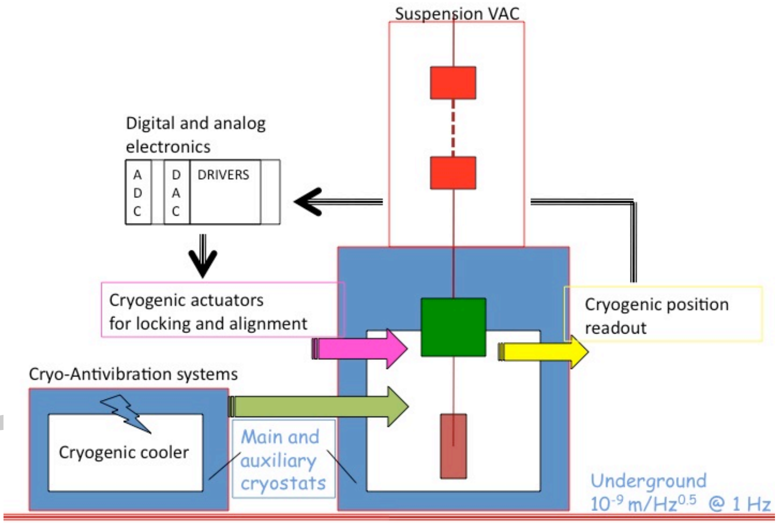

Figure 155: Schematic picture of ET suspension assembly concerning local control role.

The main issues that drive ET-related R&Ds concerning local controls leading to the identification of final solutions are listed below.

- Sensing access to the mirror position without significant perturbation of cryostat performance in mirror cooling.
- Non-perturbing or reliably reproducible effect of cryogenics onto mirror position-sensing apparatus.
- Compliance with cryostat links and its vibration control system.

For a cryogenic detector the viewports are sources of thermal input, a safe engineering approach is to limit the number of viewports to be installed.

The fiber-optic lever technique is the simplest method for non-contact and high-precision displacement detection. Its principle was originally recognized by Frank and Kissinger, then analyzed by Cook and Hamm. The sensor utilizes the internal reflection properties of step-index fibers that have significant motion sensitivity as a displacement transducer.

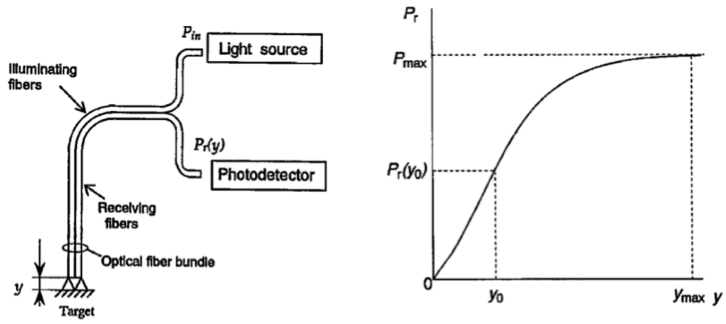

Figure 156: On the left sensor we show a schematic illustration of a basic optical fiber displacement. On the right we plot a typical curve of the receiving light power versus the gap y between the fiber bundle end and the target surface.

The system consists of a light source, a bifurcated optical fiber bundle, and a photosensor. The light radiated from the light source enters the illuminating fibers and then radiates to a target. It forms a diverging cone or annular ring on the target surface. The reflected cone is differentially subtended as a function of the target distance, by receiving fibers and is transmitted to a photosensor. Consequently, the target distance is sensed by the photosensor as the subtended power. The device has been used successfully at low temperature during the cryogenic payload test carried on at the VIRGO site.

To that extent, imaging systems (e.g. CMOS or CCD cameras), the use of optical conduits and bundle-fiber-served position sensor devices have also been considered for *coarse* mirror control together with short-arm optical levers and small interferometric systems for *fine* in order to provide the required dynamics of error signals (from several *mrads* to *nrads*). The scheme of payload local control will be studied in compliance/integration with the spurious low-frequency vibration injection arising from cryogenic system. Hence low frequency cryogenic sensors (accelerometers) are being developed for this purpose.

Normally, as done in VIRGO, the centers of mass of the suspension bodies are close to bending points of suspension wires. That is a condition which is particularly relevant for the marionette. For ET the payload will necessarily be controlled also transversally to the beam direction in order to prevent the mirror roll through the transmission of residual transversal disturbance reaching the marionette suspension point. Hence dedicated actuators and sensors will be added to the simple scheme of VIRGO. In must be remarked that given the delicate balance demanded to payload marionettes further balancing counterweights (transversal) will be also needed.

Even though the thermal contacts allowing the cooling down of the payload will transmit a vibration that can be made smaller than ground seismic vibration by using passive or active systems, from the point of view of the dynamical state of marionette's suspension point, isolated by the ground through the superattenuator that will appear as a mechanical short-cut and expectedly dedicated inertial sensing/control system will be needed at the level of superattenuator/payload interface.

4.5.8 The coil - magnet actuators

Author: F. Ricci, P. Falferi

The actuators acting on the marionette and the reaction mass are designed to allow active control of the locking and alignment during operation.

Small and fast corrections of the mirror position can be obtained, through the marionette, if the mechanical transfer function of the system is taken into account. For example, due to the response of pendulum mechanical filters, the displacement amplitude of the mirror face with respect to that applied to the marionette arms decreases with the frequency. Then, in order to avoid self-oscillations at higher frequencies, a significant increase of the feedback gain, at the edge of the dynamics of the electronics, is needed. Furthermore, when forces are applied to the marionette, the spectral components of the feedback energy can be absorbed at the mechanical resonant frequencies of the SA, making the desired control more complex. Then, the need of direct actuation of the mirror for fast position control has motivated the use of a reaction mass.

In the present Virgo configuration two magnets are placed on the marionette x oriented arm and have the axis in the direction z. The other two, attached on the marionette z arm, are oriented along y. Through these two pairs of actuators, and choosing properly the sign of the currents flowing into the coils, it is possible to steer, around θ_x and θ_y , and displace, along y and z, the mirror and the reaction mass as a whole. Longitudinal and angular forces can be applied to the mirror by coil-magnet actuators, which are attached to the reaction mass and the mirror respectively.

In order to design the coil - magnet actuators for the marionette and the mirror of the LF interferometer, several constraints must be taken into account.

Here we considered only the effect of the magnetic noise produced by the magnet at 4.2 K and its magnetization change due to the cooling, the current noise of the coil and the power dissipated by the current flowing in the coil.

The force exerted onto the magnet by the coil is $F = \alpha\mu I$ where μ is the magnetic moment of the magnet, I the current in the coil and α depends on geometrical factors. It can be shown that the interaction force has a maximum at an optimal distance between coil and magnet and can be considered constant for small displacements around this position and for small misalignment of the magnet axis with respect to that of the coil [348]. As μ and I play the same role in determining the actuator force, similar considerations hold for both the quantities.

As regards the magnetization, measurements [?] have been carried out on a cylindrical SmCo magnet [349], 10 mm diameter and 4 mm height, axially magnetized, of the same type used in the Virgo marionette. The magnetic field at room temperature at the top surface of the magnet is 0.36 T. For convenience, all the low temperature data have been taken at 4.2 K, in liquid helium at atmospheric pressure. The measurements of magnetization change have been performed with a fluxgate magnetometer with cryogenic probe and the magnetic noise measurements with a commercial SQUID system coupled to a superconducting pick-up coil fixed coaxially on the magnet 157. A detailed description of the experiment is reported in [?] and here we summarize just the results having an impact on the ET design study.

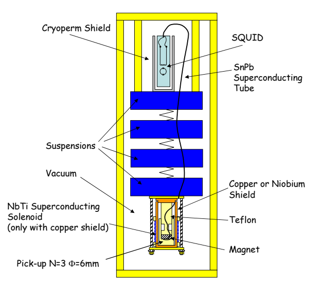

Figure 157: Experimental set for the magnetization noise measurements at 4.2 K.

Figure 158 shows a typical flux noise spectrum (calculated at the SQUID loop and expressed in units of $\Phi_0/\sqrt{Hz}$, $\Phi_0 = 2.07 \times 10^{-15}$ Wb), produced by the magnet in the niobium shield and obtained by combining two spectra taken with different frequency range and averages.

In order to determine the different noise contributions, several noise measurements have been realized in different configurations. The analysis of these measurements has suggested the following interpretation of the noise spectrum of figure 158.

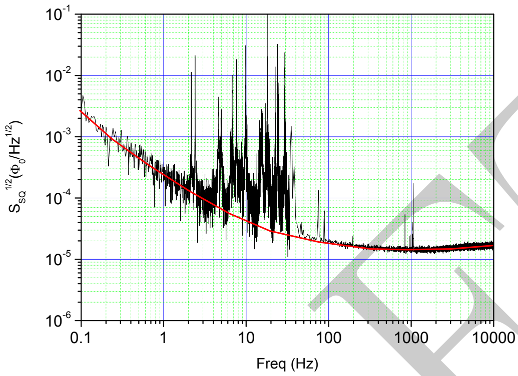

Figure 158: The magnetic flux noise spectrum produced by the SmCo magnet and referred at the SQUID loop. The spectrum is obtained by combining two spectra taken with different frequency range and averages.

At frequencies higher than 200-300 Hz the noise is dominated by thermal magnetic noise that is magnetic field fluctuations arising from the thermally agitated motion of electric charges of the conductor (SmCo in this case). This noise can be related to the temperature of the metal via a Nyquist type relation. A similar noise level has been obtained with the stainless steel cylinder. Vibrational peaks are present between 2 e 100 Hz (as expected, suspensions are effective between 100 and 1000 Hz). Between 0.1 and 4 Hz the noise, of the 1/f-type, is due to the magnet and tends to decrease with time.

We have also measured the noise produced by the magnet when it is subjected to a dc or low frequency (0.1 Hz) magnetic field with magnitude comparable to that needed to produce a force of the order of 1 mN. All the tests have shown that the application of magnetic field does not change the noise of the magnet.

The frequency range 2-100 Hz is dominated by vibrational peaks but the shape of the magnet intrinsic noise can be easily guessed and is described by the red curve in figure 158 that we consider as reference noise level for the following calculation of the force noise acting on the mirror.

As the force of the actuator is proportional to the magnetic moment of the magnet and this is proportional to the magnetic flux picked-up by the pick-up coil connected to the SQUID, we have

$$\frac{{S_{\Phi p}}^{1/2}}{\Phi_p} = \frac{{S_F}^{1/2}}{F} \tag{115}$$

where ${S_{\Phi p}}^{1/2}$ is the flux noise at the pick-up in $Wb/\sqrt{Hz}$, Φ_p is the dc flux at the pick-up in Wb, ${S_F}^{1/2}$ is the maximum force noise of the actuator in $N/\sqrt{Hz}$ when the maximum force F is generated.

Then, from the noise spectrum of figure 158 expressed as the equivalent flux noise at the pick-up ${S_{\Phi p}}^{1/2}$, the dc flux that crosses the pick-up Φ_p, and the maximum force F needed, the force noise that the actuator exerts on the mirror (or the marionette) can be estimated.

For example, considering one of the mirror actuators with a maximum force needed of 0.1 mN and the mirror (200 kg) as a free mass one can calculate, from the force noise, the displacement noise spectrum and then the equivalent strain noise spectrum on the basis of the 10 km arm length ET-D LF model. The comparison with the ET-D LF total noise is shown in figure **??**.

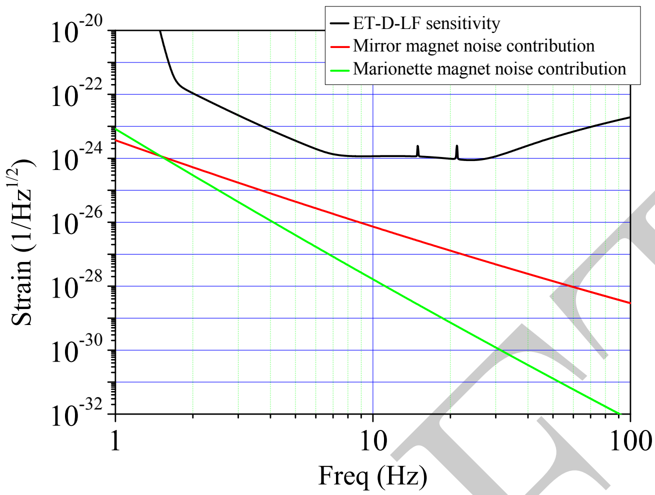

Figure 159: Magnetic noise contribution to the strain sensitiviy in the case of maximum force of 0.1 and 0.5 mN compared to the ET D sensitivity curve.

In the same figure it is also shown the strain noise contribution considering one of the marionette actuators with a maximum force needed of 5 mN. This rough estimation has been obtained by assuming the marionette as a free mass and the resonance frequency of the mirror pendulum (about 0.3 Hz) much less than the considered noise frequencies.

As is evident from this figure we can conclude that the displacement noise at the mirror level, induced by the coil-magnet actuators of the marionette and mirror, is negligible.

To design the actuators acting directly on the mirror a further constraint, related to the thermal noise of the mirror pendulum mode, has to be considered. The random magnetic force exerted by the actuators has to be kept below the intrinsic noise limit of the system, i.e., the mirror thermal noise force S_{f_T} :

$$S_{f_T} = 4k_B T Re\Big[Z(\omega)\Big] = 4k_B T \frac{\Phi M {\omega_o}^2}{\omega} \qquad (116)$$

where $Z(\omega)$ is the mechanical impedance of the suspended mass and Φ is the loss angle of the mechanical system assumed to be frequency independent. Here, the second equality holds in the simplified case of a simple pendulum.

The e.m. actuators are used in the digital control loop to keep the interferometer locked. During the operation, these kinds of actuators have to adjust the mirror position along a 1 μm range. As the force acting on the mirror is a linear function of the current I flowing in the coils, we have introduced the actuation factor $\alpha_m = F^{(m)}/I$. The control loop, which concerns these magnetic actuators, is conceived to compensate the fast changes in the mirror position and orientation. The quantized electronic noise of the digital feedback loop drives the random motion of the mirror. The noise spectral density of the current driving the reaction mass coils is intrinsically related to the noise injected into the control loop by the readout. The simplest readout scheme is a system of two components: a photodiode and a mixer. This second element is needed to demodulate the signal of the interferometer. To characterize the noise figure of the photodiode we can introduce the parameter D^2 defined as

$$D^2 = \frac{< i_d >^2}{S_{in}}$$

where $< i_d >$ is the mean current flowing into the mixer which follows the photodiode readout and the current noise spectral density of the photodiode:

$$S_{in} = 4e^2 D^2 \tag{117}$$

Using the two previous equations (116), (117) and imposing the inequality $4e^2 D^2 {\alpha_m}^2 << S_{f_T}$, we get the upper limit for the actuation factor

$$\alpha_m << \frac{1}{e\ D}\sqrt{k_B T M \frac{{\omega_o}^2 \Phi}{\omega}} \tag{118}$$

A typical figure of the ET parameters is: $\Phi \sim 10^{-8}$, $M \sim 200$ kg, $\omega_0/2\pi \sim 0.3$ Hz, $D \sim 10^8\ \sqrt{Hz}$, and $T \sim 10$ K. Then, from the equation (118) we derive the upper limit at $\omega/2\pi \sim 1$ Hz:

$$\alpha_m{}^{(max)} \simeq 4 \times 10^{-4} \quad N/A$$

Moreover, we have to point out that in a cryogenic apparatus we need to limit the power dissipated in vacuum by the current flowing into the actuator coil. It useful to report here the observation done on a prototype of cryogenic payload cooled at 10 K . The payload has the typical dimensions of the VIRGO and it holds a fake 20 kg mirror made of silicon. It is equipped with actuator coils made of copper, by means of which we measured the electro-mechanical transfer function of system at low temperature. To do that we need to drive the actuators with an electric current of few mA. Despite of the significant decrease of the copper resistivity with temperature, the heat radiated in vacuum cause a large drift of the temperature of silicon mass as it is shown in the figure 160. These measurements suggested us to design the ET coils made of Nb Ti with the core made of copper. In this way at cryogenic temperatures we will take advantage of the superconducting transition of the metallic alloy.

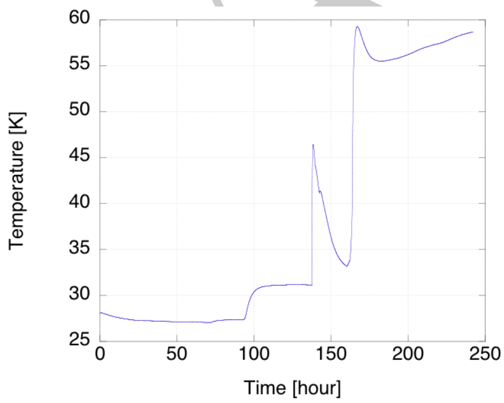

Figure 160: The temperature drift of the 20 kg silicon mirror hold in a prototype of cryogenic payload during the mechanical transfer measurements.

In conclusion, the maximum force exerted on the mirror will be in the range of 10 μN providing to use magnets of small magnetic moment in order to limit the viscous dissipation effect due to the eddy currents on marionette and reaction mass. However, in order to achieve the condition in which, at low frequency, the ET sensitivity is limited by the internal friction of the mirror pendulum mode, we must use a dielectric material both for the reaction mass and the marionette arms.

4.5.9 The electrostatic actuators

Author: R. De Rosa

Electrostatic Actuators (EA) are an interesting alternative for the control of the test masses, respect to the widely used coil-magnet pairs.

Such solution was already applied for the GEO 600 detector [350] and it is under study also for other detectors, currently adopting coil-magnet pair actuators. The use of EA offers several advantages. The first one is the possibility to keep the mirrors under control without the need of gluing the magnets on the mirror bulk, saving, in this way, the mechanical quality of the test masses and, as a consequence, reducing the final thermal noise [351]. Another advantage is the strong reduction of the coupling with external magnetic fields, that is an important issue for magnetic actuators, since no direct coupling is anymore possible in the case of EA. Another possible advantage, mainly for third generation detectors, is linked to the possibility to control the suspended test mass, in science mode, only from the previous suspension stage, avoiding the need of a reference mass. In this case an electrostatic actuator, fixed on ground, represents the simplest way for the lock acquisition without adding any extra noise when the control is transferred to the upper stage.

The working principle of an electrostatic actuator is simply described by standard electrostatic, giving, for a device of capacitance C, polarized at fixed voltage V, a resulting force along the x axis equal to:

$$F_x = -\frac{1}{2}\left|\frac{\mathrm{d}C}{\mathrm{d}x}\right| V^2 = -\alpha V^2 \tag{119}$$

where the capacitance is supposed to vary by changing the system characteristics along the x axis while the minus sign is due to the characteristic of such forces, that are always attractive. In the case of actuator for suspended dielectric mirrors, such devices mainly consist in a set of close conductive strips, arranged in a suitable geometry, alternately polarized at two different voltages. The strips, together with the dielectric suspended test mass, placed at distance a x with respect to the actuator plane, constitute a capacitor, with a capacitance variable by changing the distance of the test mass with respect to the actuator.

The deduction of the theoretical expression of the capacitance, for such system, is described in [352]. It can be written as: For the simplest geometry, i.e. a set of N parallel conductive strips with period b, rectangular in shape, of length L and width a, laying on a substrate with relative dielectric constant ϵ_s, placed at distance x from the test mass having a relative dielectric constant ϵ_m, the capacitance can be written as:

$$C(x) = C_\infty \alpha_m \left(\tilde{a}, \tilde{x}, \epsilon_m\right) \tag{120}$$

where $\tilde{a} = a/b$ is the normalized strip width, $\tilde{x} = x/b$ is the normalized distance, α_m is a function of the listed parameters describing the effect of the mirror at distance x, and C_∞ is the capacitance of the isolated actuator (i.e. with $x \to +\infty$). This expression is calculated in the approximation of infinitely long strips and taking into account only the contribution of the first image charges, both for the substrate and for the mirror. As a consequence the capacitance of real devices become different from the this value for small values of x with respect to b due to the increasing weight of border effects and image charges as the distance decreases [352].

The force expression (119) has to be modified to consider also the presence of a stray electric charge q on the dielectric mass. In this case, by making the simple approximation that the electric field is proportional to the polarization voltage applied to the actuator, it is possible to write:

$$F_x = -\alpha V^2 + \beta V \tag{121}$$

where the factor β is, in general, a function of the charge q, the distance x and the geometry of the actuator. The effects of this term were already observed on a similar set-up [353], and some techniques for its mitigation were already developed [354]. To reduce the effect of the stray charges, it is also possible to modulate the driving signal, to obtain a zero averaged contribution of the linear term of the actuation force even in presence of charges on the test masses [355]. This driving technique was already successfully experimented in the control of a bench top Michelson interferometer with a suspended mirror controlled by a such EA [356].

To clarify this approach, let $A(t)$ be the driving signal we want to apply on the test mass, A_{DC} the voltage bias and $f_M = \omega_M/2\pi$ the modulation frequency of the full driving signal. The square root is computed and sent, with the modulation, to the actuator driver. In this way the voltage applied to the actuator is:

$$V = G\sqrt{A_{DC} + A(t)}\cos\omega_M t \tag{122}$$

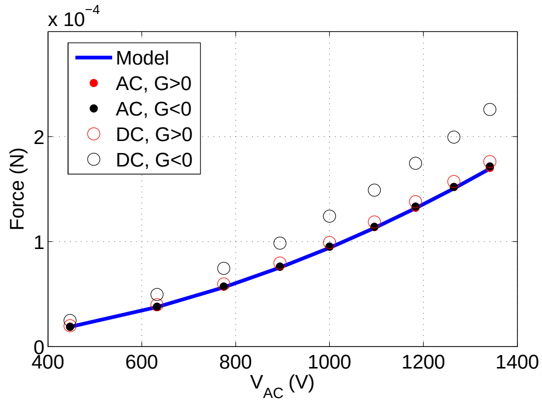

Figure 161: Comparison between the model and the force measured, in different bias conditions, for a excitation with $f = 0.1$ Hz.

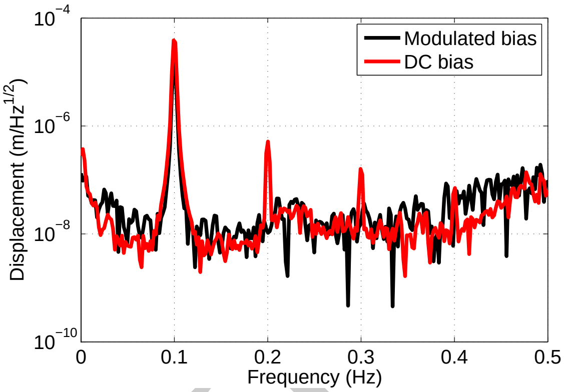

Figure 162: Spectra of the test mass displacement with the same actuation force, at $f = 0.1$ Hz in two different bias conditions.

where G is the gain of the EA driver. With this voltage, the force exerted on the test mass becomes:

$$F = -\frac{1}{2}\alpha G^2 \left(A_{DC} + A(t)\right)\left(1 + \cos 2\omega_M t\right) + \beta G\sqrt{A_{DC} + A(t)}\cos\omega_M t \tag{123}$$

If the modulation frequency is chosen at enough high frequency to have negligible effects on the test mass motion and the frequency content of the driving signal is much smaller with respect to f_M, the main contribution of the force (123) only consists of a DC bias term plus a term proportional to the driving signal $A(t)$. This is the required behavior for such actuator.

The characterization of an EA with such driving technique is described in [355]. The most interesting results are related to some observed deviation from the theoretical model. The measurements are shown in figure 161. The filled dots represent the force measured in AC bias, both with positive or negative G, while the open circles are the force measured in DC bias with different sign of G. The deviation from the foreseen behavior, clearly visible for all the points in DC bias, in particular in the case of negative G, is due to the presence of spurious charges on the dielectric suspended mass. In fact in this case, equation (123) becomes:

$$F = -\alpha G^2 \left(A_{DC} + A_{AC}\cos\omega t\right) + \beta G\sqrt{A_{DC} + A_{AC}\cos\omega t} \tag{124}$$

and a not negligible contribution could arise from the last term. Moreover this contribution depends on G as confirmed by the results. The two opposite polarizations, for the AC bias, give instead the same results, as the experimental measurements are practically overlapped. This confirms the effectiveness of the alternate bias technique that is insensitive to any static stray charge present on the test mass.

Following the (124) a larger disagreement would be expected also for the case of DC bias with positive G, but one should consider that the description of the electrical field between the EA and the test mass is very roughly approximated in the model; moreover a slight dependence of β from the sing of G is expected. More investigations are need in this direction which also require some upgrade in the experimental set-up, as the possibility to change the distance between the EA and the test mass without opening the chamber and changing, in this way, the amount of charges on the mass. The displacement spectra, in case of measurements in DC bias conditions, also show additional lines placed at multiple frequency respect to the one injected by the signal. These lines disappear if the measurement is performed in AC bias as shown in figure 162.

Starting from theoretical model, and on the basis of the previous results, it not too difficult to effectively design the electrostatic actuation system for ET. By assuming a mirror mass of 200 Kg (it is slightly higher for LF-ET, but the difference is not very relevant), a wire length of the last stage of 2 m and a conservative residual motion of the test mass $x \sim 10\mu$m, the minimum force required for damping the mirror motion is:

$$F \sim m\omega_0^2 x = 250\mu\text{N} \tag{125}$$

Since the beam radius is about 9 cm and the mirror diameter is 45 cm (in the worst case) the maximum reasonable residual space useful for the EA is about 10 cm. Moreover the distance between the test mass and the actuator has to be at least 5 mm, in order to reduce the damping from the residual pressure, and this also fix the period of the electrodes strip, that has to be close to the mirror-actuator distance to enhance the field fringes. From these figures it results that each actuator can be composed by 5 strips large 4 mm arranged in concentric arches. For such pattern the model provide $\alpha = 1.8 \cdot 10^{-10}$ N/V^2. By using the equation (119) it results that the required force, using 4 pattern, can be achieved with a maximum voltage of about 600 V, that is a good value for voltage amplifiers with low electronic noise and large bandwidth. After the lock acquisition the actuation noise can be easily reduced by reducing the voltage bias of the actuator until few volts, hence by reducing the noise of two order of magnitude. Of course, in case of full locking reallocation at the marionetta level the electrostatic actuator can even be switched off and no actuation noise is introduced.

4.6 Technologies to be developed

Author(s): M. Lorenzini, S. Reid

4.6.1 R&D on the production of high purity silicon crystal fibre for the LF interferometer

Author(s): M. Lorenzini, S. Reid

In designing the ET low frequency cryogenic interferometer, fused silica monolithic suspensions are no longer suitable, due to a broad dissipation peak in silica around 40 K which spoils its performances. Among the suggested materials, silicon is very promising due to its very low intrinsic mechanical loss [357] [358] and thanks to the high thermal conductivity, suitable to remove the heat deposited into mirrors by the laser.

Suspension elements must therefore be realized starting from pure silicon material. A study [322] has been carried out on crystalline silicon fibres grown starting from a melt of pure silicon and using the μ-pulling down technique, to investigate the possibility of employing this technique in the realization of silicon suspension elements in a cryogenic interferometer. The interest in this technique is manyfold. Besides of mechanical applications, silicon is a very important material for many technological fields, such as electronics, photovoltaic industry, and integrated photonics. Let see some aspects in more details. The photovoltaic industry for solar cell production is a rapidly expanding market. Many efforts are spent worldwide in order to increase the efficiency of solar cells or to diminish the production costs. In both respects the production of silicon fibers can play an important role because new geometrical schemes can be tested and the silicon fibers are produced directly in a ready-to-use shape, thus cutting the processing costs and loss of material. Another important potential application of Silicon fibers is for the transmission and processing of signals in integrated photonic circuits. Silicon has important optoelectronic properties, such as its high thermal conductivity, high optical damage threshold, and low losses in a wide spectral range from 1.2 to 6.6 μm. Recently Stimulated Raman Scattering (SRS) has been used to demonstrate Raman laser in integrated wave-guides in the near infrared (NIR) or for image amplifiers in the mid infrared (MWIR). The production of optical fibers with a silicon core would be an important complement to this emerging research field, but up to now silicon fibers have had a limited success due to the low crystal quality of the fibers. In fact a new production technique that has recently been presented is not capable to produce single crystal silicon-core fibers [359] and the presence of several domains and interfaces increase the transmission losses of the optical device. The availability of single-crystal Silicon fibers would be a great advance in this field, too.

The method of production consists in placing the melt in a vitreous carbon crucible, heated with a radio frequency generator. A seed of crystalline silicon is then inserted in an orifice at the bottom of the crucible and pulled downward. The melt cools down in a controlled way passing through the nozzle and a fibre is grown (figure 163). About 15 crystalline silicon fibres have been grown with thickness ranging from 0.3 to 3 mm and length up to 310 mm (figure 164). Produced fibres showed a good diameter regularity for most of their length, except for some abrupt change in thickness probably due to instabilities in the RF generator. The crystalline orientation was determined using the Laue X-ray diffraction method: as a result, the fibres were not single crystals, but are composed of several single crystal parts.

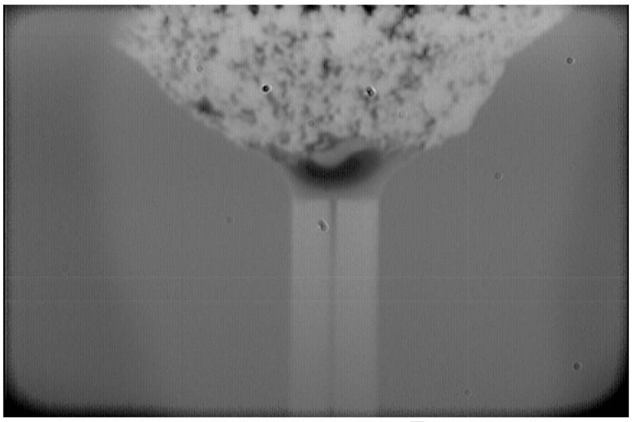

Figure 163: A closeup view of the crucible nozzle during the production of a fibre.

The loss angle of the fibres was evaluated at room temperature using a ring-down technique, and was dominated by the thermoelastic contribution. The thermoelastic loss peak allowed to experimentally measure the thermo-mechanical parameters of the realized fibres (see table 9). In order to get rid of surface contaminants (mainly SiC) the produced fibres were superficially etched before the measurements, using a HNA isotropic etching (in a 75%HNO_3, 20%HF, 5%CH_3COOH solution).

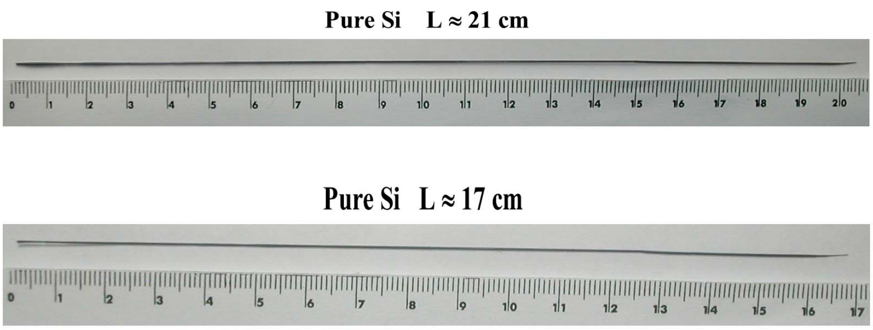

Figure 164: Two silicon crystalline fibres produced using the μ-pulling down technique.

The longest fibre among the produced ones was 310 mm long. After this study, the technique has been improved and new unpublished results have been obtained [360]. They recently succeeded in growing single-crystal Silicon fibers up to 10 cm long. In all cases the diameter is around 3 mm with small fluctuations (around 0.1 mm) along the whole length of the fiber. A successive X-ray analysis confirmed the single-crystal character of the fibers, and the only crystal phase detected is that of pure Si. Moreover a SEM analysis did not detect the presence of any impurity in the crystal material within the sensitivity of the instrument. It is presumably feasible to grow Si fibers with diameter from 0.5 mm up to 5-10 mm and virtually unlimited length. In the used facility the maximum length possible is limited to 40 cm by the dimensions of the pulling machine.

A problem was highlighted in the cited study, concerning the welding of the produced fibres to other parts. Due to the very high thermal conductivity, it turned out to be very hard to weld the fibres tip to silicon pieces. The alternative to the welding consists in using the parts to be welded as seeds for the growth of the fibre. Similarly, the crucible can be removed at the end of the pulling, leaving intact the contained material: in this way, a fibre with a thick head can be obtained. This procedure seems to be promising to realize a monolithic silicon suspension and needs to be investigated experimentally.

Table 9: Measured room temperature parameters for two crystalline Si fibres. Values are pretty close to the ones reported in literature for silicon.

length [mm]	E [GPa]	α [K^{-1}]	κ [W m^{-1} K^{-1}]
111.5 ± 0.5	150 ± 11	$(2.54 \pm 0.13) \times 10^{-6}$	146 ± 13
308.0 ± 0.5	174 ± 12	$(2.56 \pm 0.11) \times 10^{-6}$	138 ± 11

This study proved the feasibility of thin silicon crystalline fibres suitable to be employed as suspensions for a cryogenic silicon mirror. The investigation of the loss and thermomechanical behaviour of these fibres is an important step in the technical development of the optimal suspension design. More studies are needed to evaluate the fibres parameters in cryogenic conditions.

4.6.2 R&D on the bonding of silicon for the production of quasi-monolithic silicon suspensions

Author: S. Reid

[perhaps necessary to plot thermal conductivity simulations for typical suspension geometries to above section?]

It will be necessary to identify the optimum method by which the silicon suspension elements may be attached to the silicon mirrors, whilst maintaining high thermal conductivity (for cryogenic operation) and low mechanical loss (to minimize thermal noise). The technique of hydroxide-catalysis bonding [ref Gwo patent] was implemented in the GEO600 gravitational wave detector in order to create quasi-monolithic suspensions of the fused silica mirrors and is being used in the upgrades for Advanced LIGO and Advanced Virgo. The resultant bonding material has been demonstrated to have very low mechanical losses [ref Sneddon, Smith, Cunningham] in addition to mechanical strength (shear) being reported being > 27 MPa. Studies also suggest that hydroxide catalysis bonding is unaffected by temperature cycling [ref Elliffe], which will also be crucial for the long-term operation of ET-LF, where the use of cryogenics is required to achieve the desired displacement sensitivity at low frequency.

Various studies have already been carried out to investigate the use of hydroxide catalysis bonding for jointing silicon components [321**?** **?**]. This includes a detailed study of the mechanical strength of bonds at both room temperature and cryogenic temperature (77 K) [**?**], which is summarized in Figure 165. The average bond strength at cryogenic temperature is similar to that at room temperature, albeit with a slightly larger dispersion. No correlation was observed between oxide layer thickness and bond strength above ~ 50 nm, therefore the oxide layer thickness should be minimized to this level to minimize potential thermal noise.

Studies are also ongoing into quantifying the thermal conductivity of bonded silicon components at low temperatures. Measurements of the thermal conductivity suggest that bonded silicon components at low temperature can be modeled as pure silicon with an thin (~ 700 nm) interfacing glass-like layer. These results, as shown in Figure 166, suggest that hydroxide catalysis bonding can facilitate the necessary extraction of heat, deposited on the mirrors by the incident laser beam, through to the silicon suspensions elements and towards the cooled upper-stage.

[we need to choose a bond area and calculate actual heat flow expected - and compare to heat flow through typical fibre geometry as a function of temperature]

4.6.3 R%D on surface losses in silicon

Some lines about possible surface loss mechanisms and ideas how to lower surface loss. Resp: Nawrodt, before Amsterdam meeting.

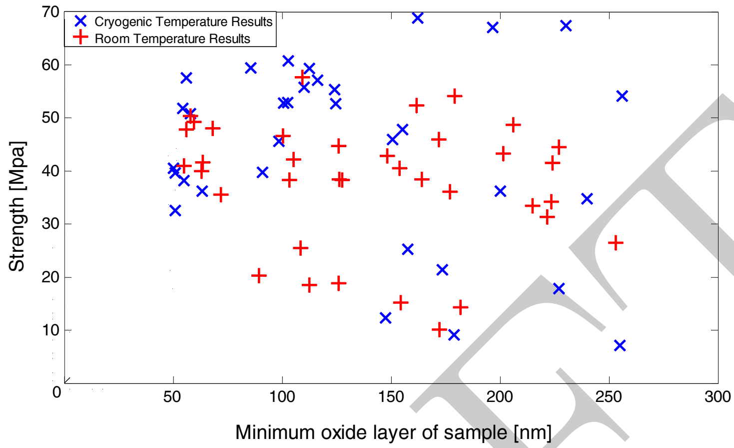

Figure 165: Plotted strength results for various silicon-silicon bonds at room and cryogenic (77 K) temperatures.

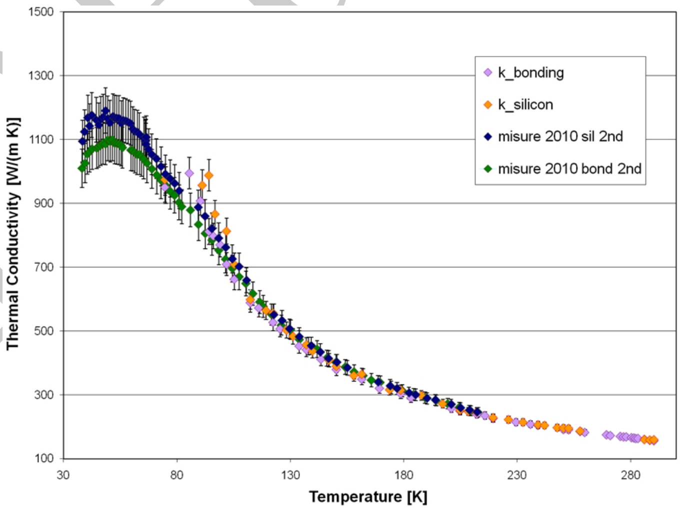

Figure 166: Measured thermal conductivity through silicon rods (1" diameter, 28 and 48 mm lengths) carried out in Florence. Bonded samples fabricated in Glasgow.

4.6.4 R&D on a new generation of monolithic accelerometer for the suspension control.

Author(s): F. Acernese, F. Barone

The development of inertial sensors, with high sensitivity and large measurement band is a key point for the inertial damping to perform on the suspension system of third generation interferometric detectors.

In particular we developed a low noise high resolution horizontal monolithic folded pendulum (FP) sensor [361, 362]. The design is based on the use of micro-machining techniques (to reduce the sensor size to dimensions suitable for placing it in sea floors or in boreholes) and the application of laser optics techniques for the implementation of the sensor readout system (to improve the sensitivity and the immunity to environmental noises) [363], [364].

An accurate description of the dynamics of a Folded Pendulum is given by the simplified Lagrangian model developed by J.Liu et al. [361], based on the mechanical scheme shown in Figure 167. The FP model consists of two vertical beams of lengths l_1 and l_2 and masses m_{a_1} and m_{a_2}, respectively. The central mass is modeled with two equivalent masses, m_{p_1} and m_{p_2}, located near the hinge points at distances l_{p_1} and l_{p_2} with respect to the pivot points of the pendulum arm and of the hinging point of the oscillating mass.

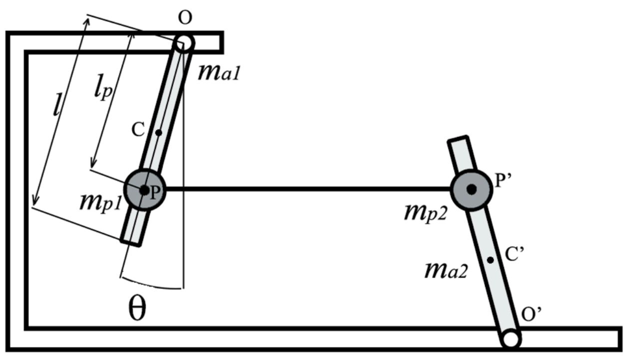

Figure 167: Folded Pendulum Mechanical Model

Assuming that the center of mass of the pendula is in $l_i/2$ and using the approximation of small deflection angles, then the FP Transfer Function can be easily obtained by solving the Lagrange Equations. Defining the coordinate of the pendulum frame (fixed to the ground) as x_s and the coordinate of the FP central mass as x_p (see Figure 167), then the FP transfer function is

$$\frac{x_p(\omega)}{x_s(\omega)} = \frac{\omega_0^2 - A_c\omega^2}{\omega_0^2 - \omega^2} = 1 + \frac{(1-A_c)\omega^2}{\omega_0^2 - \omega^2} \tag{126}$$

where

$$\omega_0^2 = \left(\frac{g}{l_p}\right) \cdot \frac{(m_{a_1} - m_{a_2})\frac{l}{2l_p} + (m_{p_1} - m_{p_2}) + \frac{k}{gl_p}}{(m_{a_1} + m_{a_2})\frac{l^2}{3l_p^2} + (m_{p_1} + m_{p_2})} \tag{127}$$

is the square of FP resonant angular frequency and

$$A_c = \frac{\left(\frac{l}{3l_p} - \frac{1}{2}\right)(m_{a_1} - m_{a_2})}{(m_{a_1} + m_{a_2})\frac{l^2}{3l_p^2} + (m_{p_1} + m_{p_2})} \tag{128}$$

is the parameter related to the center of percussion effects [361].

The tuning can be obtained changing the values of the masses m_{p_1} and m_{p_2}, adding a tuning mass, M_l, at a distance D from the pendulum suspension point.

A better physical interpretation of the dependence of the FP resonant frequency from its physical and geometrical parameters, can be obtained if Equation 127 is rewritten as

$$\omega_0^2 = \frac{(m_{a_1} - m_{a_2})\frac{gl}{2l_p^2} + (m_{p_1} - m_{p_2})\frac{g}{l_p} + \frac{k}{l_p^2}}{(m_{a_1} + m_{a_2})\frac{l^2}{3l_p^2} + (m_{p_1} + m_{p_2})} \tag{129}$$

Defining the equivalent gravitational constant, K_g, as

$$K_g = (m_{a_1} - m_{a_2})\frac{gl}{2l_p^2} + (m_{p_1} - m_{p_2})\frac{g}{l_p} \tag{130}$$

the equivalent elastic constant, K_e, as

$$K_e = \frac{k}{l_p^2} \tag{131}$$

and the equivalent mass, M_e, as

$$M_e = (m_{a_1} + m_{a_2})\frac{l^2}{3l_p^2} + (m_{p_1} + m_{p_2}) \tag{132}$$

then the FP resonant frequency, $f_o = \frac{\omega_o}{2\pi}$, can be rewritten as

$$f_0 = \frac{1}{2\pi}\sqrt{\frac{K_g + K_e}{M_e}} \tag{133}$$

It is easy to recognize in Equation 133 the classic expression of the resonant frequency of a spring-mass oscillator with an equivalent elastic constant $K = K_g + K_e$.

The FP mechanical prototype is a monolithic system, shaped with precision machining and electric discharge machining (EDM) [363, 364]. In fact, the monolithic mechanical design has the great advantage of avoiding the shear effects at the contact surface among mechanical parts that can generate hysteresis and dissipation in a non monolithic structure [361]. The result is a very compact sensor, with a high Q-factor (the Q factor of the material) and a good thermal sensitivity that guarantees a very good sensor directivity: coupling factors of less than 10^{-4} among the different degrees of freedom have been obtained in monolithic structures [362].

The four torsional flexures, connecting the pendulum arms to the central mass and to the frame, have an elliptical profile with $100\,\mu m$ minimum thickness with ellipticity ratio of $\epsilon = 16/5$. The pendula arms are designed to minimize the mass and the moment of inertia without reducing rigidity and symmetry. The values of the masses of the pendulum arm, of the inverted pendulum arm and of the central mass are $m_{a_1} \approx 40\,g$, $m_{a_2} \approx 50\,g$ and $(m_{p_1} + m_{p_2}) \approx 600\,g$, respectively.

The tunability of the monolithic FP natural frequency was obtained machining several drilled holes for fixing suitable shaped and positioned tuning masses, as predicted by Equation 127. In fact, tuning the FP at its lowest possible natural frequency maximizes the sensor measurement band at low frequencies. But, the lower is the natural resonance frequency, the lower is the restoring force of the pendulum to external perturbations. Furthermore, a lower natural resonant frequency permits to relax the specifications of the control system for force feedback sensor configuration. The drawback of soft restoring forces is that the test mass easily touches the frame, saturating the sensor. Therefore, the gaps between the central mass-arms and arms-frame was made of $2\,mm$ large. In this way the dynamics of the monolithic FP sensor is quite large, but still far from the elastic limit of the material. These large gaps have another vantage when the FP works in air. In fact, the Q of the instrument in air is strongly influenced by the damping effect of the air present in these gaps, that largely reduces its value. This effect reduced the value of Q from $Q = 3000$ in vacuum to values of $Q = 3$ in air [362]. Our technical choice allowed us to obtaining a measured value of $Q = 140$ in air, perfectly acceptable for an use of monolithic FP as sensor.

The measurement of the transfer function was made using a standard measurement procedure used in control theory to obtain the transfer function of a linear system using white noise. For this task the central mass,

m_p, was excited with white noise (input signal) through the coil-magnet actuator while the output signal, that quantifies the central mass motion, was read with the optical lever readout. Then the transfer function of the monolithic FP is obtained by simply dividing the output spectrum by the input one. The results of this first test are shown in Figure 168, where both the theoretical model and the experimental points are reported. It is evident the very good agreement of the data, that give enough confidence for the applications of the theoretical model. The analysis of these data show the natural *design* resonance frequency of the monolithic FP is $720 \pm 5\,mHz$ with a $Q \approx 140$ in air.

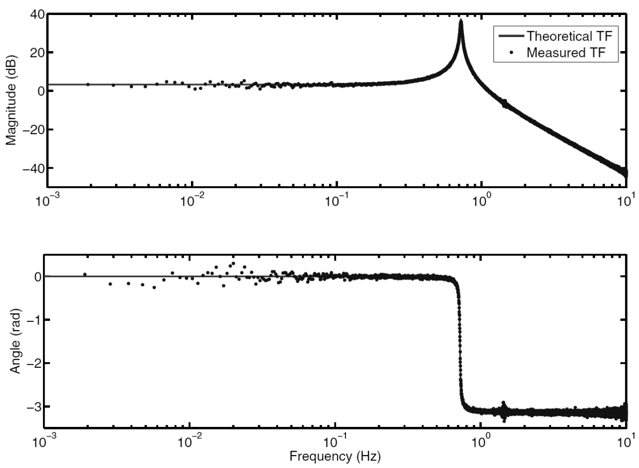

Figure 168: Theoretical and experimental Transfer Function of the horizontal monolithic FP.

To test the tuning procedure, we used tuning masses of different weights, in order to implement a rough or fine calibration, positioned in the opening of the test mass. The FP sensor was positioned on a platform for leveling. The tuning masses were moved in small steps, of less than $1\,mm$.

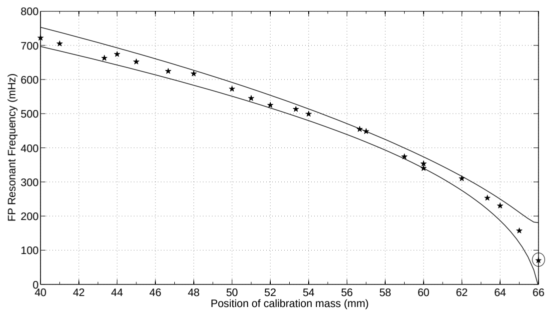

Figure 169: Measured resonance frequencies of the horizontal monolithic Folded Pendulum sensor. The best measured frequency, $f_r = 70\,mHz$, is circled.

We made different sets of measurement to evaluate the stability of the measurement procedure. In Figure 169 the measured frequency versus the tuning mass position is shown. The data were interpolated using Equation 127 with adaptive parameters $(m_{p_1} + m_{p_2})$ and k. Figure 169 shows the very good agreement between the experimental data and the 3σ error bars of the theoretical model. The three sets of measurements performed over 10 days fall on the same curve within errors. The interpolation parameters with an error bar with a level of significance $\alpha = 0.05$ are in good agreement with the experimental ones, such as the distributed masses and the angular stiffness interpolated are in good agreement with the measured ones in this case, too.

The second step was a direct measurement of the Q of the monolithic FP sensor. For this task we performed a set of measurements in air in order to obtain an experimental curve expressing Q as function of the monolithic FP resonance frequency, f_o. We are well aware that these measurements are largely dependent also on the environmental conditions, but they are important to obtain an empirical physical law for our prototype, useful to predict the values of Q at different resonance frequencies. For this task we used a tuning mass of $M_l = 120\,g$. The results of this set of measurement are reported in Figure 170, where it appears evident that all the measurements follow a linear law. In fact fitting the data we obtained a confidence factor equal to $R = 0,95$.

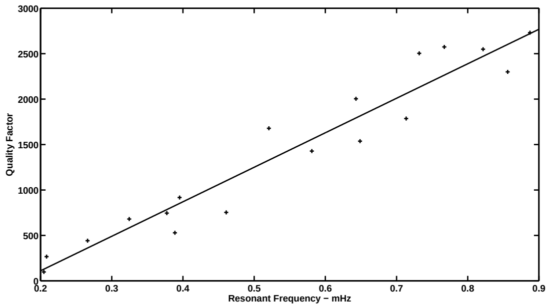

Figure 170: Mechanical quality factor versus resonant frequency for FP sensor in air.

4.7 Rough cost evaluation of the suspension system

Author(s): S. Braccini, F. Frasconi, E. Majorana, M. Lorenzini, R. Nawrodt , P. Puppo, S. Reid, F. Ricci

Impact on infrastructure

- clean rooms
- silica fiber facility
- silicon fiber facility
- assembly tools
- payload transport

ET- HF

- there are already good cost estimation for the SA
- there are already good estimation for the pay cost

ET- HF

- cost estimation for the SA to be reviewed
- cost estimation for the pay to be reviewed
- extra SA for the ancillary tower
- extra cost for active vibration dumping

5 Optical design

5.1 Description

Responsible: WP3 coordinator, A. Freise

Modern gravitational wave detectors are based on km-scale laser interferometers. Also the Einstein Telescope is using a sophisticated laser interferometer to convert the signal of a passing gravitational wave into a readout signal that can be processed electronically. The basic interferometer design is still similar to that of the original interferometer by Michelson (used more than 100 years ago in the famous Michelson and Morley experiment to disprove the existence of a so-called aether). However, to achieve better sensitivities the interferometry has been refined and extended continuously, especially during the last two decades, driven by the gravitational wave community. As a result, modern interferometers are now able to reach unprecedented sensitives beyond the Standard Quantum Limit of interferometry. At the same time the optical design has become a more challenging task. Modern interferometers couple all involved optical system into one closely coupled, complex machine.

The focus of WP3 is to identify and develop an optical layout for the core interferometer of a third generation detector which includes advanced optical technologies required to reach the target sensitivity of the ET detector. The term 'optical layout' includes a number of layers of complexity in optical design: first of all the core interferometer is the part of the detector which converts the gravitational wave signal into a measurable optical signal. Second, the core interferometer by design couples all auxiliary subsystems together. Thus part of the WP3 studies was dedicated to how the signal and all possible noises couple into the detector output. And third the optical layout largely defines the type of instrument, i.e. it defines the shape of the detector, the type of interferometry used, as well as which advanced optical technologies are included.

In order to achieve the envisaged sensitivity of the Einstein Telescope, once again the interferometry must be pushed beyond the state-of the art. For the first time a number of advanced technologies such as cryogenic mirrors, squeezed light and alternative beam shapes are to be combined in one system. This section describes in detail the design process towards the optical layout of ET which forms the baseline for the design of the infrastructure as well, as the mirror suspension systems.

5.2 Executive Summary

Responsible: WP3 coordinator, A. Freise

All the currently active GW detectors are L-shaped, with orthogonal arms; although this geometry maximises the sensitivity of the single detector with respect to the arm length, other geometries are possible. In particular, triangular-shaped detectors have been proposed in the past and also the LISA geometry is triangular. Two L-shaped detectors, forming a 45 degrees angle, could fully resolve the two polarisation amplitudes of the incoming wave. Obviously in an underground site, the realization of orthogonal L-shaped detectors is difficult, due to the high cost of the infrastructure. If the angle between the two arms of each detector is reduced to 60 degrees, three detectors can be accommodated in a triangular-shaped underground site, minimizing the required number of caverns. An analysis of a triangular-shaped third generation GW observatory is described in sections 5.3 and 5.4 with the conclusion that if a site that can accommodate a triangular observatory is found, the triple co-located interferometers will be the best choice and the triangular shape has been adopted as the baseline for the current ET design.

Each detector within a triangular observatory can in principle be composed of one or several interferometers of different topology. It can be shown that one interferometer per detector is not ideal. Spanning the wide detection band envisaged for ET is technically extremely challenging: Different noise types dominate the various frequency bands and often these noises show opposite response for changing the involved design parameters. Sometimes the reduction techniques for different noise types are incompatible. A well-known example for a parameter that affects different frequency regions differently is the correlation of the two quantum noise components: photon shot noise and photon radiation pressure noise. In order to improve the shotnoise-limited sensitivity at high frequencies one needs to increase circulating optical power of the GW detector, which at the same increases the radiation pressure noise and therefore worsens the low frequency sensitivity. Vice versa, lowering the circulating power reduces the radiation pressure effects and improves the low frequency sensitivity, while the shotnoise contribution will raise and reduce the high frequency sensitivity. This dilemma can be resolved by following the path of electromagnetic astronomy, where telescopes are built for a specific, rather narrow-banded detection window (visible, infrared etc) and later on the data from different frequency bands are combined to cover the desired bandwidth. Building two detectors, each optimised for reducing the noise sources at one specific frequency band, can form a xylophone observatory providing substantially improved broadband sensitivity. We have developed a 2-band xylophone detector configuration to resolve the high-power low-temperature problem of a single band ET observatory as described in section 5.8. Based on this design envelope of three xylophone detectors in a triangular setup, a more detailed design of the optical layout could be performed. This formed the basis for the investigation into the required cavern size and associated infrastructure impact, see section **??**.

Currently the Michelson interferometer topology is used in laser-interferometric gravitational wave detectors. However, alternative topologies, such as the Sagnac interferometer or so-called 'optical bars', have been suggested and would fit equally well into a triangular-shaped, xylophone based detectors. The main attraction of alternative interferometer topologies is that they allow the implementation of different quantum noise reduction schemes. While classical interferometers are limited by the Standard Quantum Limit, a noise floor composed by photon shotnoise and radiation pressure effects, clever interferometer designs and the use of squeezed light allow us to push beyond that limit. A detailed study of a wide range of possible quantum noise reduction schemes has been undertaken and is reported in sections 5.5, 5.6 and 5.7. As the outcome of this study and taking into account technical considerations, a Michelson-based topology with Signal Recycling and squeezed light injection has been selected for the Einstein Telescope baseline. The study also showed that Sagnac-based speedmeter topologies are an appealing alternative and should be studied further.

With a baseline of the optical layout decided the designed progressed into essential subsystems. The core element of these laser interferometers are the large principal mirrors of the arm cavities. The thermal noise of these mirrors represents one of the main limits to the achievable sensitivity. Towards the realisation of second-generation interferometric detector, a major research effort is underway to study and improve all aspects of these mirrors, especially the quality of the dielectric coatings. This work has been extended here to determine the requirements for the Einstein Telescope. A further challenge is to identify the best material and design choices for the cryogenic mirrors to be used in the low-frequency interferometer. Two solution based on Sapphire and silicon as mirror bulk material have been identified and carefully studied in section 5.9 alongside fused-silica mirrors for the high temperature interferometer. This work is complemented by tables stating the optical, mechanical and thermal properties in appendix 5.16.

The following sections 5.10, 5.11, 5.12 and 5.13 provide details about auxiliary optics system, such as the injection optics, providing the laser beam to the main interferometer, the detection system, responsible for converting optical into electrical signals and the control systems required to maintain a stable operating position of the entire interferometer. The design of these systems is a direct application and extension of the work done for and experienced gained with the first and second generation of detectors and we expect future changes to these systems based on the experience gained when the advanced detectors start operating.

Based on the detailed baseline design of the optical layout as well as the main subsystems, section 5.14 provides a cost evaluation of optical system for the Einstein Telescope. We also provide a guide to future R+D activities by outlining in section 5.15 which of the technologies require major R+D efforts before they could be incorporated in a technical design of the Einstein Telescope.

5.3 Review on the geometry of the observatory

Author(s): ***Andreas Freise***, *Stefan Hild*

This section briefly reviews the reasoning behind the shape of current gravitational wave detectors and then discusses alternative geometries which can be of interest for third-generation detectors. We will use the terminology introduced in the review of a triangular configuration [365] and discriminate between the *geometry*, *topology* and *configuration* of a detector as follows:

- The *geometry* describes the position information of one or several interferometers, defined by the number of interferometers, their location and relative orientation.
- The *topology* describes the optical system formed by its core elements. The most common examples are the Michelson, Sagnac and Mach–Zehnder topologies.
- Finally the *configuration* describes the detail of the optical layout and the set of parameters that can be changed for a given topology, ranging from the specifications of the optical core elements to the control systems, including the operation point of the main interferometer. Please note that the addition of optical components to a given topology is often referred to as a change in configuration.

5.3.1 The L-shape

Current gravitational wave detectors represent the most precise instruments for measuring length changes. They are laser interferometers with km-long arms and are operated differently from many precision instruments built for measuring an absolute length. Viewed from above they resemble an L-shape with equal arm length. This geometric form follows directly from the nature of gravitational waves: gravitational waves are transverse, quadrupole waves, thus a length change measured along any axis occurs with opposite sign along the axis orthogonal to the previous and the direction of propagation. This key feature allows to make a differential measurement between two orthogonal interferometer arms, yielding twice the amplitude of a single arm. More importantly a differential measurement allows us to potentially discriminate between gravitational wave signals and those types of noise common to both arms, such as, for example, laser amplitude noise. To achieve this the interferometer arms generally have to have approximately the same length. The most simple L-shaped interferometer allowing to do this type of measurement is the symmetric Michelson interferometer, on whose topology all current interferometric detectors are based.

The long arm length of the detectors represents the simplest way to increase the signal-to-noise ratio in the detector because the 'tidal' effect of the gravitational wave increases with the base length over which the measurement is taken, while the fundamental noises are connected to the interaction of light with the optical components or the photo detection and thus do not scale with the length of the interferometer arms. We can summarise, provided specifications of the vacuum system housing the interferometer and the performance of mirror position control systems are good enough, an increase in arm length will increase the sensitivity of the detector proportionaly.

Using the framework developed in [41] we can compute the sensitivity of a laser interferometer with two arms to gravitational waves, taking into account the geometry of the detector, the location of the source and the changes of both over time. The equations show directly that the arms of the detector do not have to be perpendicular, the right angle, however, provides the maximum response of an ideal detector to gravitational waves, which more generally can be written as

$$h(t) = F_+(t)h_+(t) + F_\times(t)h_\times(t) = \sin\zeta\, f(t, \psi, \dots) \tag{134}$$

with ζ the opening angle of the interferometer arms, F_+ and $F_\times$ the beam pattern functions and $f(t, \psi, \dots)$ a functions of the remaining parameters describing the geometry (the location of the detector and of the source in space and time and the wave polarisation angle).

In summary we can say that for a gravitational wave of given direction and polarisation, a properly aligned symmetric L-shape is an ideal optical layout for an interferometric detector; the arms should be as long as possible and the sensitivity is maximised for an opening angle of 90°. It should be noted that this does not put severe constraints on the type of interferometer topology used. In fact, most common interferometer types can be used in a form that features two large symmetric arms in an L-shape while potential other interferometer arms or sections are shortened such that they can be considered as part of one corner of the detector.

5.3.2 Interferometer Topologies

To date no laser interferometer topology other than the Michelson has been used for gravitational wave detection. However, some very advanced noise reduction techniques proposed for future detectors are based on topologies of the Sagnac interferometer, the Fox-Smith cavity or the Mach-Zehnder interferometer [366–368].

It is worth noting that a triangular geometry as discussed above is conceivable with different interferometer topologies. In particular it is possible to use different topologies while maintaining the L-shape of the single interferometers as displayed in figure 173. Therefore, for example, three Sagnac interferometers or three cavities could be used to form a triangle. Such detector designs can provide similar benefits as described above for the triple Michelson geometry so that the triangular geometry is largely independent of the topology of the individual interferometers.

The case for alternative topologies is largely based on ideas for the reduction of quantum noise. In general, the signal-to-noise ratio of a single interferometer is different for each topology, with the actual difference depending also on the type of noise under investigation. However, it is not possible to identify a topology with a meaningful signal-to-noise ratio or sensitivity since these vary dramatically with the interferometer *configuration*.

During the design and construction of the first generation of detectors the Sagnac topology has been investigated and prototypes have been build [369] but eventually it did not show significant advantages over the Michelson topology [370]. More recently it has been proposed to use the Sagnac topology as a *speed meter* [366] to reduce the quantum noise. The Sagnac topology can be hosted in different ways in a triangular geometry: each Sagnac as an equilateral triangle, or as an L-shaped zero-area Sagnac. Noise couplings due to the Sagnac effect favor the zero-area Sagnac topology: it can be shown that for a typical choice of optical parameters this extra noise couplings do not impose stringent new requirements in the case of a zero-area Sagnac interferometer.

We note that Michelson-based detectors currently offer the advantage of using the experience as well as the advanced optical technologies of the first two detector generations.

5.3.3 The triangle

At any given moment an L-shaped detector can only detect one linear combination of polarisations of a gravitational wave. However, for estimation of source parameters from the measured signal, the full polarisation information can be essential. Thus it is of considerable interest to design a detector able to detect both polarisations (and thus the full content) of a gravitational wave at all times. This can be achieved by combining two co-located L-shaped detectors which are positioned at 45° to each other. Already more than 20 years ago it was recognised that a triangular geometry would provide the same sensitivity to both polarisations as detectors at 45° while requiring less enclosed space and fewer end stations [371]. In particular, the sensitivity of the two geometries shown in Figure 172 differs only by 6% [365]. The difference in the sensitivity to different polarisations between a single L-shape and a triangular geometry can be best illustrated with a plot of the so-called antenna pattern as shown in Figure 171.

Using co-located detectors yields another advantage. Both layouts shown in Figure 172 represent detectors with redundancy. Redundancy here can be understood in relation to the continuous operation of the detector as an observatory, or as a feature of the data streams generated by the full system. Redundancy in operation is achieved by having multiple detectors which generate an equal or similar response to gravitational waves. This is desirable in observatories which are expected to produce a quasi-continuous stream of astrophysical meaningful data over an substantial amount of time. Typically laser interferometers cannot produce science data during upgrades and maintenance work. Thus only alternate upgrading and data taking of redundant detectors can avoid long down-times, for example during detector upgrades.

Such redundancy is obviously provided in the case of the 4 L-shaped detectors, where two detectors are always identical but can be operated independently. However, one can easily show that the triangular geometry provides exactly the same redundancy [365]. For example, for three equal L-shaped interferometers oriented at 0°, 120°

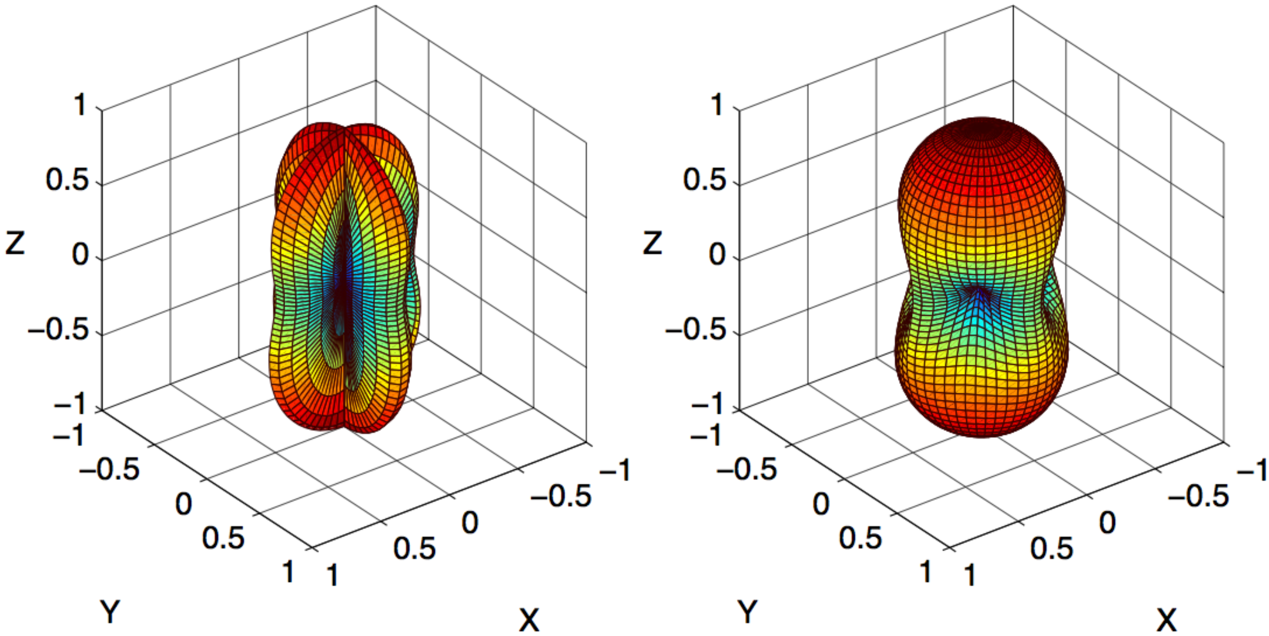

Figure 171: The response of a detector to a linear polarised gravitational wave as a function of the detector orientation. Both plots show the normalised sensitivity to a wave travelling along the z-axis. Each data point represents the sensitivity of the detector for a specific detector orientation defined by the detector normal passing the respective data point and the origin. The colour of the data point as well as its distance from the origin indicate the magnitude of the sensitivity. The left plot depicts the response of a single Michelson, while the right plot gives the response of a set of three interferometers in a triangular geometry.

and 240°, one obtains:

$$-h_{0^\circ} = h_{240^\circ} + h_{120^\circ}\,, \tag{135}$$

where the sign of the operation is defined by which ports of the interferometers are used to inject the laser light. Thus the two interferometers at 120° and 240° create exactly the same response as the one at 0°. This allows to construct so-called null-streams (or null-data streams) [372]. Null-streams are a powerful data analysis method that allows to identify noise which is uncorrelated between the detectors. Even though this does not increase the sensitivity of a detector, it can add significantly to the robustness of the data processing pipelines and thus lead, for example, to shorter delays between an event and the generation of a trigger for follow-up searches with optical telescopes. The triangular geometry represents the minimal setup in one plane that can resolve both polarisations and provides redundancy for the generation of null-streams.

5.4 Review on the topology of the detector

Author(s): ***Helge Mueller-Ebhardt***, *Keiko Kokeyama*

The topology of a gravitational-wave detector is determined by the optical system formed by its core elements [365]. Examples of basic topologies are the Michelson interferometer, the Sagnac interferometer and the Mach-Zehnder interferometer. The specific optical layout of a detector includes more details about the actual realization, i.e. leses, telescopes, folding mirrors, mode cleaners, control system, injection system, detection system. Those issues are addressed in Sec. ???. Finally, the configuration fixes the set of parameters that can be changed for a given topology, ranging from circulating optical power, bandwidths and detunings of cavities to the detection angle of a homodyne detection (cf. Sec. ???). In a laser-interferometric gravitational-wave

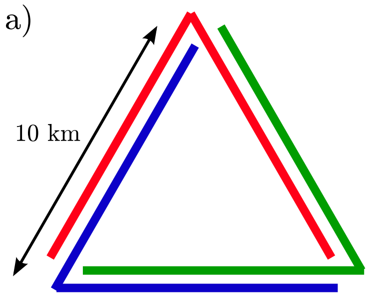

Figure 172: a) Triangle geometry: three L-shaped detectors with 10 km arm length are positioned in a equilateral triangle. **b)** Four L-shaped detectors at 0° and 45°. The integrated length of all interferometer arms in both configurations is 60 km and two interferometer arms can share the same structure. Note that for avoiding noise correlations between two detectors the neighbouring interferometer arms would probably be housed in a separate vacuum tubes.

detector, there are different types of noise sources, which are usually categorized into quantum noise sources (cf. Sec. 5.4.2) and classical noise sources (cf. Sec. 5.4.3). In terms of the noise, the main difference in the sensitivity of the different topologies comes from the spectral distribution of the quantum noise, as it is described in details in Sec. 5.5.1, even though there could also arise differences in the susceptibility to the classical noise, due to the fact that there are e.g. a different number of mirrors or different shapes of cavities.

5.4.1 Different topology options

In the following we will list the different main interferometer topologies that can be use for gravitational-wave detection and describe their basic optical systems. A full gravitational-wave detector could actually consist of more than one of those main interferometers and could also be equipped with additional techniques in order to achieve a specific susceptibility to the quantum noise as it will be described in Sec. 5.5.1. Note that in principle all of the mentioned interferometer topologies can be fitted into a L-shape or into another two-arm shape under

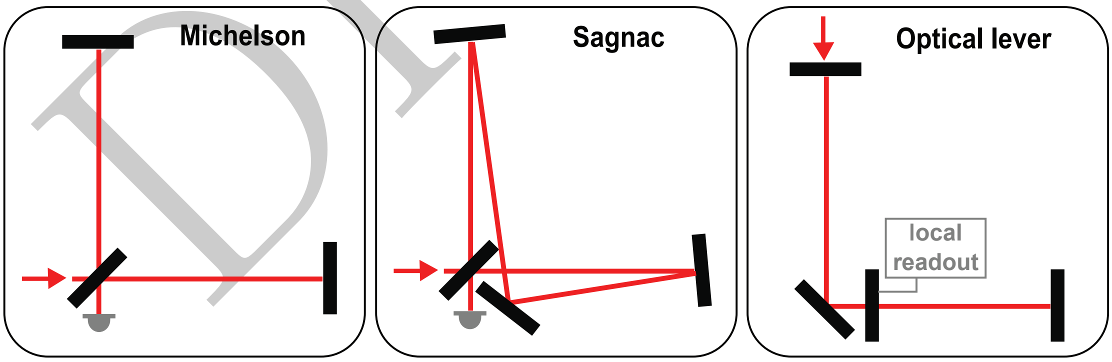

Figure 173: Different (basic) topology options: simple Michelson interferometer topology (left panel); zero-area Sagnac interferometer topology (middle panel); optical bar topology (right panel)

an arbitrary angle, as shown in Fig. 173.

- **Michelson interferometer** (basic): a laser beam is split at a beam splitter and send along two perpendicular interferometer arms (cf. left panel of Fig. 173). The ends of these arms (north and east) are marked by highly reflective identical end mirrors, which reflect the beams back into themselves so that they can be recombined at the beam splitter. Generally, the Michelson interferometer has two outputs, namely the so far unused (south) port and the (west) input port. Both output ports can be used to obtain interferometer signals, however, most setups are designed in such a way that the signals are detected at the south port. For the detection of gravitational waves, the Michelson interferometer has to be sensitive to small perturbations in the difference of the two arm lengths and the phase relation is chosen in such a way that this signal interferes constructively at the south port. Usually the south port is kept nearly dark, with all light reflected back to the west input port, then also called the bright port of the interferometer. A power-recycling mirror can be positioned at the bright port in such a way that it forms a resonant cavity for the carrier light together with the mirrors of the two interferometer arms. Furthermore, each interferometer arm can be replaced by equal Fabry-Pérot cavities, formed by an input mirror and an end mirror. An additional mirror can also be placed at the interferometer's south port, known as the signal-recycling mirror. Another possibility is to send the output signal at the west port into an additional resonator, a so-called sloshing cavity. Furthermore, polarizing optics can be used in order to send the beam back into the interferometer. The Michelson interferometer is the standard topology for interferometric gravitational-wave detectors. The great advantage of this is, that there is a lot of experience gathered.

- **Sagnac interferometer** (basic): a laser beam is split into two beams at the beam splitter which travel both through the whole interferometer but in opposite directions. The two beams are recombined at the beam splitter. The interferometer has only one output port, namely the so far unused (south) port. A Sagnac interferometer is by construction always operated at a dark port, where all carrier light is reflected back to the input port. The arms can be folded in such a way that both beams circulate around a zero area (cf. middle panel of Fig. 173) in order to make the interferometer insensitive to rotations and forming two perpendicular interferometer arms. Those arms can be replaced by ring resonators, either of rectangular or triangular shape. For the Sagnac interferometer topology, an additional mirror at the input port can realizes power-recycling and an additional mirror at the output port can realize signal-recycling. Up to now a Sagnac interferometer has never been adopted as a large-scale interferometric gravitational-wave detector. Only some features have been tested in table-top experiments and a theoretical study has started to explore noise couplings in a Sagnac interferometer [373].
- **Optical bar**: The optical bar topology is an optical realization of a mechanical resonant bar gravitational-wave detector. It essentially consists of two coupled optical resonators, which are shape as an L and coupled through a light, partially transmissive mirror as shown in the right panel of Fig. 173. An additional local meter is applied to the central mirror, reading out its motion. The local meter could in principle be any device but its sensitivity is essentially determining the sensitivity of the optical bar detector. It is even not obligatory for the local meter to be an optical device, moreover it could be a SQUID-based microwave meter as a speed meter, or some other high precision superconductive sensor. The optical bar topology can be transformed into an optical lever topology by inserting an additional mirror into each arm of the L, forming a resonant cavity together with the corresponding end mirror.

5.4.2 Requirements on the topology due to quantum noise

The so-called free-mass standard quantum limit (SQL) [374, 375] on high-precision measurements is imposed by the Heisenberg uncertainty principle, when it is applied to free-falling test masses. The spectral representation of this quantity, which falls off with one over frequency in amplitude and only depends on the test-mass' weight and arm length of the detector, has become a standard reference for the quantum noise of interferometric gravitational-wave detectors. With the help of this reference one is able to compare the quantum noise of different topologies and configurations having the same test-mass weight and arm length. The quantum noise of a gravitation-wave detector consists of two parts: the quantum measurement noise, i.e. the direct imprecision of the measurement, and the quantum back-action noise. For interferometric gravitational-wave detectors, the direct measurement process consists of counting the number of photons by recording the photo current of the photo diode. The photons of a coherent beam arrive according to a Poissonian distribution. The photon counting error represents the direct measurement noise, which is usually called photon shot noise. The power of this noise source is inversely proportional to the circulating laser power. The measurement's back action is clearly given by the laser light's fluctuating radiation pressure which imposes a force onto the mirror and causes the radiation-pressure noise in the measurement output. The power of this noise source is in contrast to the photon shot noise directly proportional to the circulating laser power. Since the suspended mirrors in a gravitational-wave detector can be approximated as free falling test masses in the direction of the incident laser beam – due to a very low eigenfrequency of the pendulum created by the mirror's suspension – and the two quantum noise sources are uncorrelated they result in the free mass standard quantum limit. In this case, the radiation-pressure noise dominates the spectral density of the quantum noise at lower frequencies while the shot noise dominates at higher frequencies. Therefore, one in general needs to trade-off between high optical power for a low shot noise and not too high optical power in order to cope with the radiation-pressure noise. One way out of this problem is the xylophone configuration [376], where the detection band of the gravitational-wave detector in split into two or more frequency bands, for which different configurations (or even topologies) are responsible for.

On the other hand, the SQL is actually not a real limitation on the quantum noise strength of a gravitational-wave detector. Several methods for overcoming the SQL, which are suitable for laser interferometric gravitational-wave detectors, have been proposed. They have different, and often very special, requirements on the optical topology. The quantum-noise reduction techniques can be divided into two main groups, where the classification is not chosen in terms of the topology, but by the technique of how the quantum noise is reduced: the first one is based on the principle, that the goal of the gravitational-wave detectors is not the measurement of the test-mass position, which is a quantum variable and thus cannot be measured continuously with a precision better than the SQL, but rather the detection of a gravitational-wave strain as a signal, which can be treated as a classical (tidal) force acting on the test mass mirrors [377]. It was shown that by introducing cross-correlation between the quantum measurement noise and the quantum back-action noise, arbitrary high sensitivity (in terms of the quantum noise) can be achieved [378] – assuming the absence of optical losses. The correlations are actually used here to quantum-mechanically cancel the back-action noise in the measurement output. Thus, this method relies clearly on **noise-cancellation techniques**. The second group of methods is based on the idea that the spectral distribution of the SQL itself is not a fixed constant, but depends on the test object dynamics, i.e. on the (mechanical) susceptibility of the test mass, which relates the test-mass motion to all forces acting on it. Therefore, the free-mass SQL can be beaten by using a more responsive object and increasing thus its signal displacement – the harmonic oscillator as an example has much stronger response to near-resonance forces and therefore a better sensitivity than the free-mass SQL around the resonance frequency. Therefore, the sensitivity gain is obtained not by delicate cancellation of the quantum noise, but by a classical **signal amplification**. More details about quantum-noise-reduction techniques are given in Sec. 5.5. In that section we will also see that with those topologies there are different detector options for the main interferometer: the position meter, the optical spring interferometer, the speed meter, the optical transducer. Furthermore, all those main interferometer detectors can then be additionally equipped with the input-squeezing technique (for details cf. Sec. ???) and the variational readout technique (cf. Sec. 5.5.1).

5.4.3 Requirements on the topology due to technical noise sources

Apart from the quantum noise there are many other noise sources, usually called classical or technical noise sources, degenerating the sensitivity of a laser interferometric gravitational-wave detector. In the third generation of detectors these classical noise sources have to be dealt with different techniques which might have additional demands on the topology as we shall review in the following.

Suspension thermal noise. The suspension thermal noise will be a serious noise source in third generation gravitational-wave detectors. For more details refer to Sec. ???. Here we will only describe its influence on the topology: in order to avoid high thermal noise, the fibers of the suspended optics – especially those in a cryogenic environment – have to be as cool as possible. If the detector consists of more then one interferometer, then the question arises how the collinear interferometer arms are arrange in the tunnel. One of the interferometer arm could be placed above the other. Then it might be unavoidable that the laser beam of the interferometer lying upon the other intersects at some point with the suspension fibers of the other interferometer. In that case it is necessary that this laser field is not too strong in order not to heat up the suspension fibers and increases the thermal noise.

Mirror internal thermal noise. *Author(s): Keiko Kokeyama, Andreas Freise* The noise coming from thermal effects influencing the test-mass mirrors is dominating the noise spectrum in the mid frequency regime. There exist several different contributions to the total thermal noise of which the (coating) Brownian thermal noise is the largest in current interferometer topologies utilizing arm cavities. The obvious way of lowering thermal effects is cooling the mirrors down to cryogenic temperatures. Such cryogenic test-masses allow only for limited amount of optical power passed through the mirror substrates and coatings which influences the design of the detector. Another way to lower the thermal noise is to change the mode shape of the laser beam inside the interferometer (cf. Sec. 5.15). The higher-order Laguerre-Gauss (3,3)-mode (LG_{33}) which is proposed for thermal noise reduction in advanced gravitational-wave detectors [379, 380] requires that no triangular cavities are used because of the astigmatism issue. The optical parameters of a $LG_{l,m}$ mode at the $2|l| + p$ order are degenerate with the other modes at the same order. As they have the identical optical parameters, they can degenerate in the resonant cavity, and they are decomposed by the astigmatism effect, i.e., when a beam experiences a non-zero angle of incident in respect to the mirror normal. Because the mode decomposition significantly degrades the mode purity inside the cavity, a two-mirror linear-cavity where the angle of incident is always zero is preferable as an optical resonator for the LG_{33} mode.

- Parametric instability as discussed in Sec. ??? requires what in terms of the topology? *Author(s): Kazuhiro Yamamoto*

Any kind of displacement noise. *Author(s): Sergey Tarabrin* Most of the dominant noise sources in laser interferometric gravitational-wave detection can be related to the class of displacement noise: seismic noise, gravity-gradient noise, various thermal noise sources, even the quantum back-action noise. Each method of suppression or elimination of displacement noise is usually suited for control of only one kind of noise: seismic isolation, measurement and partial cancellation of gravity gradients, cryogenics, quantum-noise-reduction schemes. Displacement-noise-free interferometry (DFI) is the method of displacement noise cancellation which aims at simultaneous elimination of the information about all position fluctuations of the test masses, but leaving a certain amount of information about gravitational waves. All known DFI schemes can be divided into two categories: schemes with complete and partial displacement noise cancellation. Complete displacement noise cancellation relies on the distributed nature of gravitational waves. While displacement noise imprints on the optical phase only at the moments of the laser beam reflection at the test masses (localized effect), gravitational waves affect the laser beam along its optical path (distributed effect). From the viewpoint of some local observer the interaction of the gravitational wave with the interferometer adds up to two effects [381]: the motion of the test masses in the gravitational-wave tidal force-field (which is indistinguishable from the action of fluctuating forces, therefore it is a localized effect) and the direct coupling between the gravitational wave and light (distributed red-shift effect). DFI implies the cancellation of displacement noises along with the localized part of the gravitational-wave effect, leaving the distributed red-shift effect in the interferometer response. Since the latter one has the order of $O[h(L/\lambda_{\rm GW})^2]$ (where h is the gravitational-wave amplitude, L is the interferometer linear scale and $\lambda_{\rm GW}$ is the gravitational wavelength), DFI has much weaker gravitational-wave susceptibility than conventional gravitational-wave detectors in the long-wavelength regime $L \ll \lambda_{\rm GW}$. Complete displacement noise cancellation can be achieved in an interferometer with large enough number of the test masses by properly combining several response signals [382]. For instance, 2- and 3-dimensional setups composed of two Mach-Zehnder interferometer topologies sharing the beam-splitters [383]. The gravitational-wave response of the 2-dimensional scheme has the order of $O[h(L/\lambda_{\rm GW})^3]$, while the one of the 3-dimensional scheme is of the order of $O[h(L/\lambda_{\rm GW})^2]$. For comparison, the gravitational-wave response of the conventional Michelson interferometer is $O[h(L/\lambda_{\rm GW})^0]$. Implementation of the time-delay devices, while improving the strength of the gravitational-wave response, limits the sensitivity by adding the noise [384]. Another class of DFI schemes with partial displacement noise cancellation aims on keeping strong enough gravitational-wave susceptibility, with either $O[h(L/\lambda_{\rm GW})^0]$ or $O[h(L/\lambda_{\rm GW})^1]$ leading orders in the response. This can be achieved with linear Fabry-Perot cavities, ring cavities, etc. A single Fabry-Perot cavity, double-pumped through both mirrors, allows elimination of their displacement noise in the proper linear combination of the responses, however, the sensitivity remains limited due to laser noise and displacement noise of all the auxiliary optics [385]. Modification of this scheme with two cavities placed symmetrically allows complete displacement noise cancellation but does not allow laser noise cancellation [386]. In a symmetric double Michelson interferometer with the arm-cavities the sensitivity is limited by the noise of the local oscillators used for detection of the transmitted waves in the arms; in addition, this scheme requires placing several mirrors on a single common platform rigidly that is very impractical [387]. Double pumping of the resonant ring cavity allows cancellation of its mirrors noise and laser noise, but cannot deal with displacement noise of the mirrors and beam-splitters used to produce the pumping waves [388]. To summarize, all detectors with either complete or partial displacement noise cancellation consist of combinations of many different topologies and therefore differ in general significantly from the conventional detectors especially in terms of the complexity and either have very weak gravitational-wave susceptibility or impractical requirements (like rigid platforms) to operate or suffer from uncancelled noises, thus making them hardly advantageous over the conventional non-DFI topologies.

Holographic noise. *Author(s): Sergey Tarabrin* It is currently widely assumed that the holographic principle, developed by G. 't Hooft and L. Susskind, should be the fundamental constituent part of any unified theory of quantum gravity. It says that that the physical theory defined in the space-time of dimensionality D is equivalent to another theory defined on the boundary of dimensionality $D-1$. The most known mathematical realization of holographic principle is the AdS/CFT correspondence by J. Maldacena: string theory in anti-de Sitter space-time is equivalent to conformal field theory on its boundary. It follows from the holographic principle that if the volumetric system can be described by the theory on the boundary, then the maximal number of volumetric degrees of freedom should not exceed the number of their "images" on the boundary. Since the "classical" field-theoretical informational content of the region of space is defined by its volume, such a description contains much more degrees of freedom than allowed by the holographic entropy bound. Therefore, our 3-dimensional world must be "blurry" in order to match the number of degrees of freedom inscribed on some 2-dimensional holographic surfaces. The holographic uncertainty is a particular (highly speculative) hypothesis proposed by C. Hogan about how the holographic principle works in a flat space-time [389]. He posited that in order to preserve the holographic nature of space time, it must have diffractive nature described by the wave functions of transversal position distribution of matter-energy [390], i.e. transversal coordinates of two particles (test masses) separated by a distance L in a longitudinal direction should no longer commute: $[\hat{x}_1, \hat{x}_2] = il_{\mathrm{P}}L$, where the commutator is defined on the light-like geodesics only. The corresponding uncertainty relation reads $\Delta x_1 \Delta x_2 \geq l_{\mathrm{P}}L$ meaning that the relative transversal positions of two test masses cannot be measured with infinite precision. The holographic uncertainty relation implies that the measurement of the transversal position of a single test mass with the optical signals will yield uncertain results with $\Delta x \geq \sqrt{l_{\mathrm{P}}L}$, where L stands for the distance the light wave travels between the two measurements. This holographic fuzziness with associated uncertainty Δx should be seen in precise interferometry, otherwise it would be possible to distinguish more test-mass configurations than is allowed by the holographic entropy bound. Thus, in a Michelson interferometer measurement of the beam-splitter transversal position relative to the direction of the incident laser beam should yield uncertain results. Uncertain measurement results produce the fluctuating time series, i.e. the noise, called holographic noise. The minimal level of expected holographic noise corresponds to the Gaussian space-time wave functions which minimizes the holographic uncertainty relation, much like in usual quantum mechanics. In the frequency region $f \ll c/L$ holographic noise power spectral density is frequency-independent and equals to $S(f) = 2t_{\mathrm{P}}L^2/\pi$, or effective metric strain $h(f) = \sqrt{S(f)/L^2} = \sqrt{2t_{\mathrm{P}}/\pi} = 1.84 \times 10^{-22}/\sqrt{\mathrm{Hz}}$ with t_{P} standing for Planck time. Holographic noise prediction is thus fixed with no free parameters, therefore the hypothesis can be either confirmed or ruled out experimentally. Holographic noise signatures are currently being looked for in the noise spectrum of GEO-600 interferometer. However, the available sensitivity does not allow to make unambiguous conclusions. Since the space-time wave function universally defines the transversal distribution of mass-energy, holographic noise should exhibit particular cross-correlation features. Namely, the two closely positioned interferometers should produce correlated measurements of the holographic displacement, because they occupy nearly the same space-time volume and thus holographic motion of their test masses (beam-splitter, in particular) is defined by nearly the same wave function. If the two interferometers are aligned along their arms and are displaced by $\Delta L \ll L$ along one of them, then the cross-correlation spectral density equals to $S(f) = 2t_{\mathrm{P}}L^2[1-(\Delta L/L)]/\pi$. This expected feature of the holographic noise is to be tested in the Fermilab holometer which is currently under construction [391]. For the Michelson interferometer with the arm-cavities in the arms effective metric strain equals to $h(f) = N^{-1}\sqrt{S(f)/L^2} = N^{-1}\sqrt{2t_{\mathrm{P}}/\pi} = N^{-1}1.84 \times 10^{-22}/\sqrt{\mathrm{Hz}}$, where N is the average number of photon round trips inside the cavities. The reason for the N^{-1} factor is that the cavities effectively lengthen the arms for the gravitational waves (this holds true for the frequencies $f \lesssim c/2LN$), thus amplifying the response to the gravitational waves, but do not change the beam-splitter holographic displacement spectrum [389]. With planned transmittances of the arm-cavities input mirror and the end mirror of 7000 and 10 ppm, respectively, the number of photon round-trips inside the ET cavities equals to $N \approx 277$, thus lowering the holographic metric strain to $h(f) \approx 0.66 \times 10^{-24}/\sqrt{\text{Hz}}$. The development of sound theoretical models and experimental test are under way. If it turns out that the holographic noise is a serious issue for the Einstein telescope gravitational-wave detector, the optical design (as e.g. cavity finesse) has to be adopted.

5.4.4 Alternatives to laser interferometry: atomic sensor

Author(s): Sergey Tarabrin

It is in principle also possible to utilize light pulse atom interferometry to detect gravitational waves. Light pulse atom interferometry can be thought of as a comparison of time kept by internal atom clocks and optical wave of the laser. The incoming gravitational wave changes the rate of time which can be seen in an interferometer phase shift. The major advantage of the atom-light interferometry over conventional optical interferometry is that the atoms, playing the role of inertial sensors, are not subjected to the external fluctuations in comparison with the mirrors, and thus do not require sophisticated vibration isolation techniques. A phase shift measurement in atomic interferometer consists of three steps [392]: first, the atomic cloud is prepared, cooled to sub-microkelvin temperatures and then launched. Atoms in the cloud are in the $|\text{ground}\rangle$ state and are freely falling after the launch. In the second phase light pulses are applied. The "beamsplitter" $\pi/2$-pulse places atoms in the superposition of two states: $1/\sqrt{2}|\text{ground}\rangle + 1/\sqrt{2}|\text{excited}\rangle$. Since the internal state of the atom is correlated with its momentum, atoms in ground and excited states acquire different velocities, and thus both states become temporarily and spatially separated. After some time the "mirror" π-pulse exchanges the two components of the superposition: $|\text{ground}\rangle \to |\text{excited}\rangle$, $|\text{excited}\rangle \to |\text{ground}\rangle$, so that the atoms will finally overlap. Finally, the second "beam-splitter" $\pi/2$-pulse makes the two branches of the atom wave function interfere, in full similarity to a Mach-Zehnder interferometer. The third phase of interferometry is detection. The interference pattern can be extracted by measuring the population of atoms in a given state, for instance, in the excited state. The measured phase shift results from both the free-fall evolution of the quantum state along each path in interferometer and from the local phase of the laser which is imprinted on the atoms at the moments laser pulses are applied. Since laser sources and atomic interferometer can be separated by a significant spatial distance, the incoming gravitational wave modulates the latter, thus causing the modulation of the arrival time of the laser pulses which enters the measured atomic phase shift. A terrestrial based gravitational-wave detection with light-atom interferometry can be realized in a vertical shaft with the linear scale of ~ 1 km. Two atomic interferometers of the linear scale of 10 m are placed on the top and the bottom of the shaft and are operated by the common lasers. With the reasonable measurement repetition time ground-based setup will have the peak susceptibility to the gravitational waves around 1 Hz that is very interesting form the astrophysical point of view. Such a setup allows performing the differential measurement between two atomic interferometers which significantly suppresses vibrational and optical noise of the lasers. The vibration of the optical trap which leads to different launch velocities is of less importance, since the initial "beam-splitter" pulse is applied after the atoms are launched. However, spread in velocities will enter the measurement error through the gravity-gradients, since in the nonuniform gravitational field atoms moving along different trajectories experience different gravitational forces. Gravity-gradients seem to be one of the major limiting factors towards the increase of the sensitivity. Other noises sources come from the variations of the magnetic field which change the atoms energy levels, coupling of the Earth rotation to the fluctuating transversal velocity of the optical trap. One of the dominating noise sources with the technique currently available is the atomic shot noise. It can be lowered by implementation of the sources with more intense atom fluxes and/or preparation of the atoms in squeezed states. Although light pulse atom interferometry has already found applications in atomic clocks, metrology, gyroscopes, gradiometers and gravimeters, its implementation in gravitational-wave detection requires detailed and comprehensive study and further development of the noise-lowering techniques. With the current technologies available atomic interferometers cannot provide the same level of sensitivity as the well-developed optical interferometers.

5.5 Quantum noise reduction techniques

Author(s): ***Helge Mueller-Ebhardt***, *Keiko Kokeyama*

Already the second generation of laser-interferometric gravitational-wave detectors (such as the Advanced LIGO detector [393] and the the Advanced VIRGO detector [290]) is expected to be limited by the quantum noise — the shot and the back-action noise — nearly within the full detection band. Within the context of the third generation of detectors this aspect becomes even more important, since there is an enormous effort in increasing the quality of the technical components of the interferometer – such as the mirror and beam splitter materials as described in Sec. ???; the suspension systems (see Sec. ???); the stability of the laser source (Sec. ???) – in order to decrease the strength of all the technical noise sources by a large amount. Beside parameters such as the circulating optical power and the test-mass weight, the spectral distribution of the quantum noise mainly depends on the topology of the detector including the injection strategy at the bright port as well as the detection strategy at the dark port of the interferometer. Therefore, the choice of the topology and configuration of the detector are severe for the design of future gravitational-wave detectors. Especially because parameters as the optical power and the test-mass weight will always be limited due to technical reasons, the design of future gravitational-wave detectors is calling for quantum-noise-reduction techniques. As we have seen in Sec. 5.4, there are different topology options available which can all be fitted into an L-shaped geometry. With the different topologies one can build up different types of detectors, having specific quantum noise features, as we have reviewed within this design study. Many of them have actually great potential in reducing the quantum noise, but there is a big discrepancy in terms of readiness: some are far away from being ready to be implemented into gravitational-wave detectors, others have been already demonstrated experimentally as a proof of principle or have been even already implemented into gravitational-wave detectors. In the following we will report on the sensitivity of

- optical-spring interferometer
- speed-meter interferometer
- optical-inertia interferometer
- optical transducer with local readout
- (frequency-dependent) input-squeezing interferometer
- variational-output interferometer

even though not all of them can be fitted into the same optical layout. It has turned out that one of these techniques is probably not able to reduce the quantum noise in the required broadband way, but certain combinations among these techniques are possible. Additionally, one is not restricted to build a detector from only a single interferometer, but from two or more interferometers covering different frequency bands as a xylophone interferometer [376]. Within the design study, there have been carried out many optimizations of the quantum noise of different detectors towards different astrophysical sources. In the following there example noise curves given which are optimized towards the detection of neutron star binary inspirals, as carried out in Ref. [394]. Furthermore, those examples are attempts to realize the ambitious sensitivity goal of the Einstein telescope gravitational-wave detector – in terms of the quantum noise – with a single interferometer, where the total circulating optical power is limited to 3 MW, the arm length to 10 km and the test-mass weight to a few hundred kilograms.

5.5.1 Quantum noise features of different topologies

The first candidate among the different types of detectors is the **simple position meter**: here we gather the Michelson interferometer topology w/o or w/ arm cavities, w/o or w/ power-recycling, w/o or w/ tuned signal-recycling (cf. Sec 5.4.1). The installation of a power-recycling cavity (by putting an additional mirror at the bright port of the interferometer) and the use of cavities in the arms of the interferometer, both increase

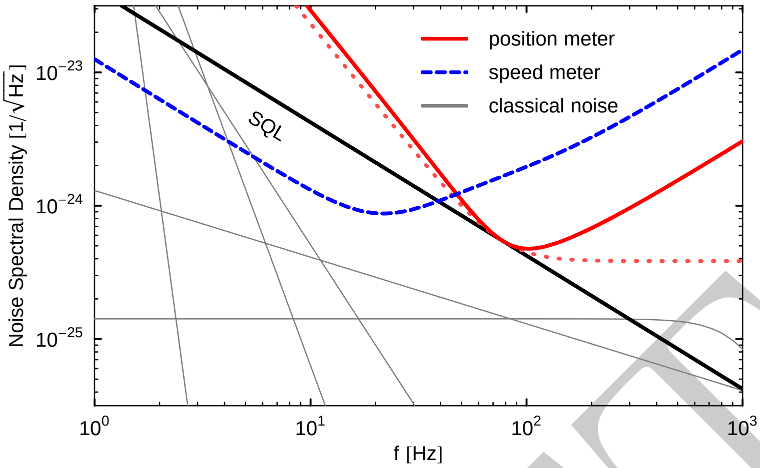

Figure 174: Example quantum noise spectral densities for position meter (solid curve), with adiabatically eliminated cavity mode (dotted curve) and for a speed meter (dashed curve): 10 km arms; 3 MW optical power; 120 kg test-masses. Example noise budget (gray curves): seismic and gravity gradient noise reduced by a huge amount compared to advanced detectors; suspension thermal noise (coating thermal noise) reduced by a factor of 10 (4.5) in amplitude compared to estimations for Advanced LIGO detector.

the circulating optical power inside the interferometer, therefore force up the interaction strength between the laser field and the test-masses and reduce the shot noise (dominating at high frequencies) but at the same time increase the radiation-pressure noise (dominating at low frequencies). From another point of view (namely when the required circulating optical power in the arms is fixed) the power-recycling technique can help to lower the required input power, while using arm cavities can additionally lower the optical power which has to pass the beam splitter preventing thermal effects in the transmissive optics to become a major problem and also minimizing the bright port / dark port coupling due to the beam splitter motion [395]. The use of arm cavities additionally increases the signal-susceptibility within the finite bandwidth of the optical arm resonators, but decreases it above the optical bandwidth making the shot noise spectral density raise towards higher frequencies and therefore decreasing the bandwidth of the gravitational-wave detector. Signal-recycling, as proposed by Meers [396], can increase the bandwidth of the gravitational-wave detector by creating an effective bandwidth. Here an additional mirror, the so-called signal-recycling mirror, is placed at the dark output port of the interferometer, reflecting parts of the signal modulation fields back into the interferometer and forming a signal-recycling cavity either together with the end mirrors of a simple Michelson interferometer or with the input mirrors of the interferometer's arm cavities. The signal becomes recycled which basically means that it is amplified due to an increase in interaction time between the laser field and the mirrors. If the signal-recycling cavity is tuned with respect to the laser frequency, the optical resonator (or the two coupled optical resonators in a Michelson interferometer with arm-cavities) have an (effective) bandwidth — which can be greater than the original bandwidth of the arm-cavities. In such a detector the quantum noise depends mostly on the optical power circulating in the interferometer, the bandwidth and length of the cavities and the test-mass weight, which altogether define the measurement frequency, i.e. the frequency where the quantum noise touches the standard quantum limit. The strength of the quantum noise is basically shuffled between high and low frequencies by shifting the measurement frequency towards higher frequencies. All first generation laser-interferometric gravitational-wave detectors (LIGO [2], VIRGO [397] and TAMA [398]) so far have been constructed as simple position meters. In Fig. 174 we see example quantum noise curves for a simple position meter and the standard quantum limit for such a detector with 10 km long arms and 120 kg test-masses. The quantum noise spectral densities are plotted for 3 MW circulating optical power in the arms for a detector with an effective 50 Hz cavity-bandwidth (solid curve) and for a detector with adiabatically eliminated cavity mode (dotted curve). Furthermore, the different contributions of an example classical noise budget for a third generation detector with classical noise reduction techniques as described within this design study (cf. Sec. ???) is additionally adumbrated in Fig. 174 and shows a big gap between this assumed classical noise budget and the standard quantum limit. It is obvious that such a simple position meter would be totally dominated by the quantum noise, i.e. a waste of efforts in the classical noise reduction, and therefore not suitable to reach the sensitivity goal of the Einstein Telescope gravitational-wave detector. For more details refer to e.g. Ref. [394] and references therein.

When the signal-recycling cavity is neither resonant nor anti-resonant with respect to the carrier frequency, the technique is called detuned signal-recycling. In this case the sensitivity of the interferometer is enhanced around the (effective) optical resonance frequency. The signal-recycling technique was already successfully tested in a 30 m prototype gravitational-wave detector [399, 400], in table-top experiments [401, 402] and has been implemented into the GEO600 detector [403]. Additionally, the optomechanical coupling in the arm cavities of a Michelson interferometer with detuned signal-recycling can induce a restoring force onto the differential motion of the arm-cavities mirrors — the optical spring effect [404], which can up-shift the mechanical resonance frequency into the detection band. We will call such a device an **optical spring interferometer** [404–407]. Here the sensitivity of the detector is further enhanced around the second resonance, the optical spring resonance.

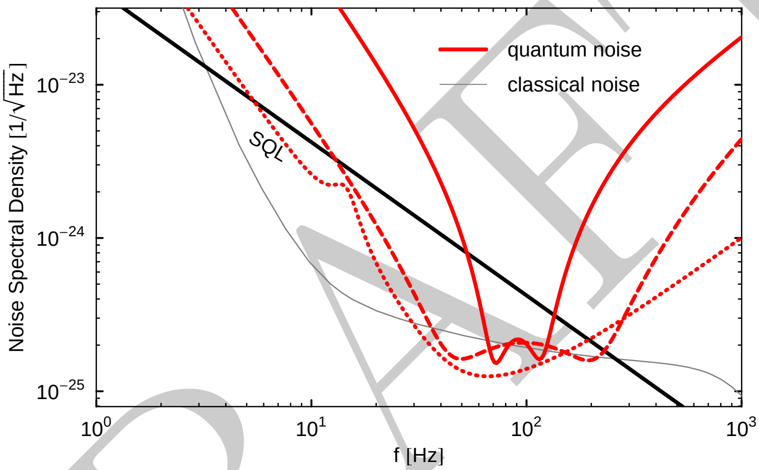

Figure 175: Example quantum noise spectral densities for Michelson interferometer with arm cavities (10 km; 3 MW optical power; 120 kg test-mass mirrors) and detuned signal-recycling (136 Hz effective detuning; 16 Hz effective bandwidth; $2\pi/3$ detection angle) – no input-squeezing (solid curve), no optical loss. Dashed curve: with 10 dB frequency-dependent input-squeezing (208 Hz effective detuning; 120 Hz effective bandwidth; $0.44\,\pi$ detection angle) and 75 ppm loss in each 10 km filter cavity. Dotted curve: variational output with 10 dB frequency-independent input-squeezing (4 Hz effective detuning, 180 Hz effective bandwidth) and 75 ppm loss in each 10 km filter cavity.

This quantum-noise reduction technique belongs to the second group of methods as defined in Sec. 5.4.2. The optical spring effect has been demonstrated e.g. in a 40 m prototype gravitational-wave detector [402] and in several table-top experiments [408]. Furthermore, the Advanced LIGO detector [393] will very likely make use of the optical spring effect in order to improve the sensitivity. In Fig. 175 example noise curves for such an optical spring interferometer are given. For the optical spring interferometer the optimal quantum noise – optimal for the specific wave-form of neutron star binary inspirals – becomes very narrow peaked around 100 Hz [394]. Also for different astrophysical sources the optimal quantum noise spectral density is rather narrowband than broadband. Note that the concept of the optical spring interferometer can be extended to double optical spring interferometer [407] or even multiples optical spring interferometer, where a second (or multiple) additional frequency-shifted carrier is injected into the interferometer, creating additional optical springs which can be used to enhance the sensitivity and additionally stabilize the optomechanical system within the detection band.

A third detector option is to use an optical **speed meter** [409]. The idea of using speed meter detectors was to totally avoid the quantum back-action of the measurement. At first glance it seems to be very promising to reach this goal by measuring the speed of the test-masses, because it is usually proportional to the momentum, which, as a conserved quantity, cannot introduce any back-action noise. But once the detector couples to the speed, it has been shown that in this case the conjugate momentum is actually not only proportional to speed [410] of the test object. Nevertheless, a speed meter is able to surpass the standard quantum limit broadbandly by removing the (frequency-independent) radiation-pressure noise from the measurement output. The dashed curve in Fig. 174 shows a typical example for a quantum noise curve of a speed meter interferometer – here with 10 km long arms, 120 kg test-masses, 3 MW circulating optical power in a 35 Hz-bandwidth cavity. There exist different proposed designs of how to realize a speed meter with different topologies: it is possible to turn a Michelson interferometer topology into a speed meter by adding a sloshing cavity [411, 412] to the interferometer at the dark output port, where the signal sloshes back and forth, realizing a time-delayed sensing of the test-mass position. Another option is to use polarizing optics and build up a speed meter from a Michelson interferometer topology by either re-sending the signal into the interferometer multiple times [413] or by circulating the light through the two arms [414] of the Michelson-like setup. The most obvious way to realize an optical speed meter, however, is by using a Sagnac topology (cf. Sec 5.4.1) with triangular or rectangular ring cavities in the (folded) arms [366, 415, 416]. Ignoring the influence of optical losses, all those different speed meter realizations have the same quantum noise performance [366] even though they have different technical advantages and disadvantages. The specific quantum-noise feature of a speed meter is that it has a flat response to the

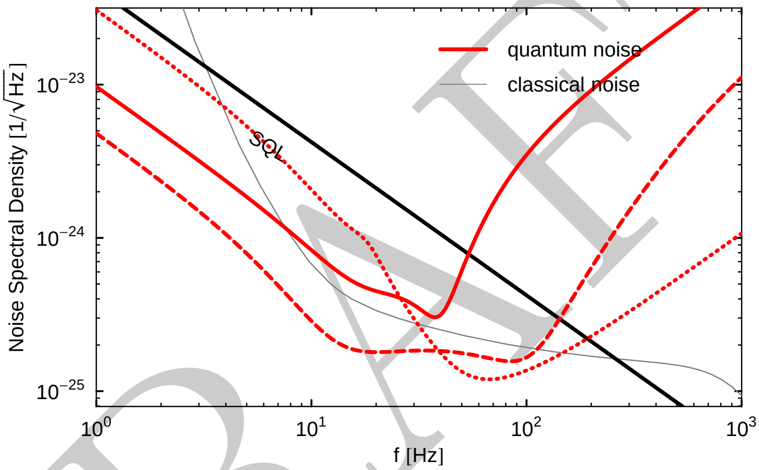

Figure 176: Example quantum noise spectral densities for Sagnac interferometer with ring cavities (10 km; 3 MW optical power; 100 Hz bandwidth; 120 kg test-mass mirrors) and detuned signal-recycling (42 Hz effective detuning; $0.475\,\pi$ detection angle) – no input-squeezing (solid curve), no optical loss. Dashed curve: with 10 dB frequency-dependent squeezed input (150 Hz bandwidth; 95 Hz effective detuning; $0.475\,\pi$ detection angle) and 75 ppm loss in each 10 km filter cavity. Dotted curve: variational output with 10 dB frequency-independent squeezed input (50 Hz bandwidth; 0.5 Hz effective detuning) and 75 ppm loss in each 10 km filter cavity.

radiation-pressure noise at low frequencies [366], providing a constant back-action free detection quadrature. The measurement can therefore be made shot-noise limited at lower frequencies but with a decreasing signal transfer [369] (cf. Fig. 174). A detuned signal-recycling cavity turns a speed meter interferometer into an **optical inertia interferometer** [415]: the optomechanical coupling influences the dynamics of the test-masses – it modifies their dynamical mass by introducing an optical inertia. In Fig. 176 we see the quantum noise of a signal-recycled Sagnac interferometer, which provides high sensitivity mainly in the low-frequency regime, due to the speed meter effect, while the detuned signal-recycling broadens the sensitivity curve by opening it a little more to the high-frequency regime [394]. Note that the optical inertia can become in principle even negative and then can cancel the mechanical inertia. The hope is that in this way one can create a test object which has a high resonance-type mechanical susceptibility in a broad frequency band. Such a situation can also be found in the double optical spring interferometer, by exploiting the frequency dependence of the two optical springs [417].

Finally, the last option for the main interferometer, which we want to review here, the **optical transducer** [418–421], is totally different compared to the others in terms of the readout method: the idea of such schemes is not to measure the phase shift of the laser field via monitoring the outgoing modulations fields at the dark port of an interferometer but to measure the redistribution of optical energy directly inside an interferometer by converting the gravitational-wave strain via radiation pressure into real mirror motion. This motion should then be sensed by an additional highly sensitive local meter. The overall sensitivity to gravitational waves for such a transducer scheme depends not only on the transducer ability of the main interferometer but also on the sensitivity of the local meter. Several optical realizations have been proposed: the initial idea was to construct an optical bar, as an optical analog to an mechanical bar resonator. Later this topology was extended to the optical lever scheme [420], where the interaction strength is enhance by the use of arm cavities. Furthermore, it had been realized before that also a detuned signal-recycled Michelson interferometer with arm cavities effectively functions as an optical bar at low frequencies, where the gravitational-wave strain is converted into mirror motion of the input mirrors of the arm cavities. In this case even the realization of a local meter is straightforward: a second frequency-shifted carrier can be inserted into the interferometer, which is anti-resonant in the arm cavities, and therefore forming a small interferometer with the arm-cavity input mirrors as its end mirrors. This local readout scheme [421] is a combination of an optical bar interferometer and a optical spring interferometer, where the two outputs can be combined in an ideal way to enhance the sensitivity at lower frequencies (optical bar) and simultaneously at higher frequencies (detuned signal-recycled Michelson).

All these different main interferometer detectors can be equipped with a technique which is usually called **input-squeezing**. The use of squeezed states of light for improving the sensitivity of gravitational-wave detectors was first proposed in 1981 by Caves [422]. He showed that the quantum noise limited sensitivity in a shot noise dominated interferometer can be enhanced by the injection of broadband (frequency-independent) squeezed fields into the interferometers signal port. Accordingly at a point, where the interferometer performance will be limited by the amount of the achievable circulating light power and the thermal load in its optics squeezed field injection can be used to either relax the high power requirement or increase the sensitivity further. The reduction of shot noise by the aid of squeezing was later experimentally shown in Refs. [423–425] (cf. Sec. ???). However, at first view the enhancement of an interferometers sensitivity with frequency independent squeezing (squeezed light with a fixed quadrature angle) can only be achieved in a certain frequency range. This is a direct consequence of the Heisenberg uncertainty principle. Considering a simple position meter, the quantum noise in its phase quadrature (shot noise) can be reduced by the amount of squeezing. Unfortunately, the quantum noise in the amplitude quadrature (radiation pressure noise) will be increased by the same amount enhancing the noise at low frequencies. Later it was revealed by Unruh [426] and others [427–429] that squeezed field injection with frequency dependent squeezing angle allows an overall quantum noise reduction including the radiation pressure noise. Motivated by the work of Unruh and Jackel & Reynaud the use of additional input and output optics — namely filter cavities — was proposed by Kimble *et al.* [378]. Applying these filters (commonly referred to as Kimble-filters) converts a conventional interferometer into a broadband quantum non-demolition interferometer (cf. Sec. ???). The filters allows the preparation of squeezed states providing a frequency-dependent squeezed quadrature which is adapted to the interferometers quadrature rotation. The injection of such a prepared squeezed state leads to a quantum noise reduction over the entire detection band. The investigation of Kimble *et al.* was restricted to simple position meters. It was shown by Harms *et al.* [430] and Buonanno & Chen [431] that such filters applied to optical spring interferometers also allows a broadband quantum noise reduction by squeezed light. Unfortunately, quite generally two low-loss, narrow-bandwidth, and therefore long-baseline optical filter cavities are necessary to prepare the squeezed states in an optimum way. The generation of frequency-dependent squeezing utilizing one filter cavity was experimentally characterized by Chelkowski *et al.* [432] followed by the shot noise reduction of a table-top dual-recycled Michelson interferometer demonstrated by Vahlbruch *et al.* [433]. Another way to achieve an enhancement in the high frequency range without drastically worsen the low frequency sensitivity by avoiding the use of multiple long base-line filter cavities was proposed by Corbitt *et al.* [434]. Here, the use of a tuned Fabry-Perot cavity with two partly transparent mirrors was suggested acting has high-pass filters (termed amplitude filters within this context) for the squeezed field. In reflection of this filter cavity the squeezing at sideband frequencies beyond the filter cavity bandwidth is preserved whereas at low frequencies the squeezing is lost and replaced by ordinary vacuum noise. Since any optical loss of the filters mainly affects the transmitted part, the baseline of the filters can be chosen comparatively small. It has already been realized quite early that there is a transition region between the reduced noise at high frequencies and the non-increased noise at low frequencies, were the sensitivity is degraded. Later, this degradation was explained by information loss at the end mirror of the filter cavity and an additional homodyne detection was proposed to capturing this information [435]. Furthermore, it has been proposed to inject additional squeezed vacuum though the filter cavity end mirror and thus suppress also the low-frequencies radiation-pressure noise [436]. However, these techniques are more useful for simple position meters and are intended to be installed as a low-cost add-on during the life cycle of the second generation detectors [437], since the rotation of the squeezing ellipse around the optical resonance of optical spring interferometers cannot be compensated by these filters leading to a deceased sensitivity which can be even below that of the interferometer w/o input-squeezing. For speed meter interferometer the quantum noise can be reduced by input-squeezing analogously to a position meter with filter cavities [412]. But here it is also possible to achieve an enhancement at lower frequencies without drastically worsen the high frequency sensitivity avoiding the use of filter cavities [416]. Furthermore, it has been experimentally verified that the shot-noise limited sensitivity of a zero-area Sagnac interferometer can be enhanced by input-squeezing [416]. In Fig. 175 and Fig. 176 one finds examples of quantum noise spectral densities (dashed curves) for optical spring and speed meter interferometer with frequency-dependent input squeezing in the ideal case of no optical loss.

Additionally, all main interferometer detectors can be equipped with a balanced homodyne detection and with the **variational-output** technique, which was invented conceptually in the early 1990s by Vyatchanin, Matsko and Zubova [438, 439] and later substantiated by Kimble *et al.* [378]. Here filter cavities are used to make the quadrature angle of the detected output field frequency dependent and therefore realize a broadband evasion of the radiation-pressure noise. Even though the most efficient combination of frequency-dependent input-squeezing and variational-output for the optical spring interferometer cannot be realized with Kimble-filters, different semi-optimal configuration have been found [431]. Especially at low frequencies, variational output with frequency-independent input-squeezing can in principle improve the sensitivity much more than frequency-dependent input-squeezing, but on the other hand optical losses in the filter cavities for the variational-output become even more severe [378, 440]. When the radiation-pressure noise is strong, it is required to bring enough of the quadrature without signal-content into the output in order to cancel the radiation-pressure noise and this introduces significantly higher noise due to optical losses. Moreover, optical losses in the filters remove parts of the at low frequencies already weak signal from the output. In Fig. 175 and Fig. 176 there are examples for quantum noise spectral densities (dotted curves) of variational readout interferometers in the ideal case of no optical loss given. For more details refer to Ref. [394].

5.5.2 Chosen design topology and configuration

The actual design topology and configuration for the Einstein telescope gravitational-wave detector has to be carefully chosen among the possible candidates. Not only the ideal quantum noise performance of the different candidates (cf. Sec. 5.5.1) has to be taken into account, also degradation due to optical loss and technical problems in the realizability have to be considered [394]. Neither realization of an optical speed meter interferometer is actually enough explored and each has certain technical problems: INPUT FROM ANDREAS FREISE AND STEFAN HILD IS NEEDED! Moreover, theoretical studies and considerations of the feasibility of certain advanced techniques including realistic optical loss suggest that the desired sensitivity for the total observation band of the Einstein telescope gravitational-wave detector cannot be covered by a single interferometer. The variational readout technique applied to an optical spring interferometer as well as to a Sagnac interferometer with detuned signal-recycling could in the ideal situation provide a single broadband detector [394] but considering realistic values for optical losses (in particular, the quantum inefficiency of the photo detector) destroy the quantum correlation, abolish thus the quantum noise cancellation and degenerate the signal (see dotted curve in Fig. 175 and Fig. 176). Optical transducer detectors are much less sensitive to optical loss [440] and require much less power for the detection. But an important implementation issue is the fact that the actual sensitivity of the detector depends strongly on the sensitivity of the local meter, a completely not yet developed part (cf. e.g. Ref. [440] and references therein).

It has been suggested to split the detection band into two frequency bands, each covered by a single interferometer, which are optimized on that specific frequency band, forming altogether a so-called xylophone interferometer [376] covering the full detection band. Especially from the technical point of view it might be unavoidable to consider separately a low-power, cryogenic interferometer optimized for the low-frequency band and a higher-power, room-temperature interferometer covering the high-frequency band, avoiding in this way that high-power laser beams have to be transmitted through cryogenic optics (cf. Sec. ???). For the high-frequency interferometer the obvious choice is an upscaled but otherwise only moderately advanced version of a second generation interferometric gravitational-wave detector, a simple position meter. Furthermore, at the moment the most favored candidate for the low-frequency part of the full detector is, especially in terms of feasibility, an squeezed-light enhanced optical spring interferometer, which can be optimized in order to fit the low-frequency classical noise profile. This requires the injection of frequency-dependent squeezed states of light, created by two filter cavities. Filter cavities are a key feature in the development of quantum-noise-reduction methods for future gravitational-wave detectors, therefore, we will discuss technical aspects of the filter cavities in Sec. ???. For a later upgrade state of the detector, a speed meter seems to be a promising alternative for the low-frequency part – after a successful prototyping stage. More details of the chosen configuration will be given in Sec. ???.

5.6 Quantum noise reduction with squeezed states of light

Author(s): ***Andre Thuering***, *Helge Mueller-Ebhardt, Keiko Kokeyama*

At first glance, quantum physics imposes a fundamental limit on metrology–the science of measurement–, and thus imposes a corresponding limit on the sensitivity of GW detectors. A fundamental problem in optical interferometry is the stochastic distribution of photons arriving at the photodiodes. This statistical fluctuations obscure the tiny power variations caused by GW signals. Fortunately, quantum physics also provides a solution to this problem via the concept of quantum entanglement.

"Quantum metrology" uses quantum entanglement to improve the measurement precision beyond the limit set by measurement counting noise. The first such proposal was made by C.M. Caves in 1981 when he suggested the use of squeezed states of light as an (additional) input for laser interferometric GW detectors [422]. Caves's initial proposal was motivated by the limited laser power available at the time. Indeed, squeezed states allow for improvement in the sensitivity of a quantum noise limited interferometer without increasing the circulating laser power.

Squeezed states [442–445] belong to the class of so-called *nonclassical* states of light. Generally, nonclassical states are those that cannot be described by a classical (positive valued) probability distribution using the coherent states as a basis (the P-representation) [446]. Let us first consider the coherent states. If light in a coherent state is absorbed by a photodiode, mutually independent photon 'clicks' (in terms of photo-electrons) are recorded, a process that is described by a Poissonian counting statistics. Due to quantum mechanics, every individual 'click' is not predictable, but rather the result of a truly random process. If the number of photons per time interval is large ($N \gg 1$), its standard deviation is given by $\sqrt{N}$, see Fig. 177 a (i). This uncertainty gives rise to *shot-noise*. For a *squeezed* light beam, the detection of photons are not time-independent but instead contains quantum correlations. Nevertheless, the photon statistics still cannot be predicted by some external clock. They instead show auto-correlations that give rise to a reduced standard deviation, as shown in Fig. 177 a (ii). The correlations might be described in the following way. Whenever the quantum statistics might drive the actual photon number above the average value N, a similar number of photons destructively interferes with the main body of photons providing a (partial) compensation of the fluctuation. These quantum correlations *squeeze* the interferometer's shot-noise below its natural value. Another complementary way of describing the properties of squeezed states is based on the phase space quasi-probability distribution using the amplitude and phase quadratures of a light wave (the Wigner function) [443, 446].

A squeezed state that contains only quantum-correlated photons with no coherent amplitude is called a *squeezed vacuum state* [446]. If such a state is overlapped with a coherent laser beam on a semi-transparent beam splitter, two beam splitter outputs are generated which are quantum correlated. As a consequence, the overall (bi-partite) quantum state cannot be written in terms of products of the two beam splitter output states. Such a quantum state is called non-separable or *entangled*. This is exactly what happens if a squeezed state is injected into the signal output port of a laser interferometer for GW detection (Fig. 177 b). The two *high-power* light fields in the interferometer arms get entangled and the light's quantum fluctuations in the two arms are correlated with

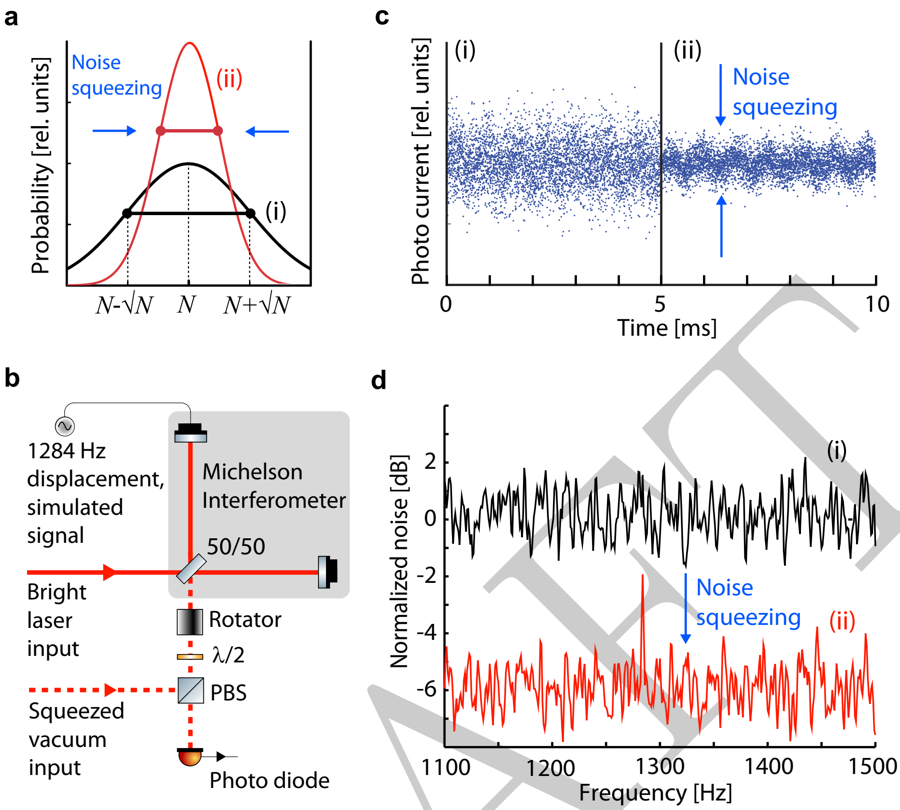

Figure 177: Squeezed light enhanced metrology (a) For large photon numbers N, squeezed light shows a photon counting statistic with a standard deviation smaller than $\pm\sqrt{N}$. In all panels, (i) correspond to shot-noise and (ii) to 6 dB squeezed noise. (b) A squeezed vacuum beam is injected into the dark signal port of a Michelson interferometer, in addition to the conventional bright laser input. The squeezed beam leads to path entanglement of the light fields in the two arms and to an improved signal to noise ratio, as shown on the right. Without squeezing, the optical path length modulation at 1284 Hz is neither visible in the time series of the photo-electron current (c, simulation by B. Hage, AEI) nor in its noise power spectrum (d, measurement, courtesy of H. Vahlbruch, AEI [441]). In (c) as well as in (d), the signal is clearly visible when squeezing is applied (ii).

each other. Although the fluctuations are not predictable from the outside, they provide an improved signal-to-noise ratio in the interferometer. Recall that an interferometer measures the optical path length change in one interferometer arm with respect to the other arm. If the quantum noise in the two arms is correlated it will cancel out. This entanglement interpretation was not discussed in the initial proposal by Caves. Nevertheless, it shows that the application of squeezed states in interferometers is a real application of quantum metrology by its very own definition. The entanglement produced by splitting a squeezed state at a semi-transparent beam splitter was tomographically characterized and quantified in [447]. Fig. 177 c shows a simulated signal from a photodiode, without (i) and with (ii) *squeezing*. The tiny modulation in the interferometer's output light due to the (simulated) passing GW is visible only with the improved signal-to-noise ratio. Fig. 177 d shows the analogue in frequency space, i.e. after a Fourier transform of the photo current was applied.

The above paragraph shows that squeezed states can be conveniently combined with the extremely high photon numbers of coherent light to improve a laser interferometer, as proposed in [422] and shown in Fig. 177 b. In fact, the stronger the squeezing factor [443, 446] the greater the path entanglement and the signal-to-noise improvement.

Shortly after Caves proposed squeezed states of light for laser interferometers in 1981, the first experimental demonstration of squeezed light [448] and proof of principle demonstrations of quantum metrology were achieved

[423, 424]. In parallel, it was theoretically discovered that squeezed states offer even more advances in metrology than 'just' reducing the quantum shot-noise. From the early days of quantum physics, when fundamental aspects of the measurement process were discussed, it was clear that, in general, a measurement disturbs the system to be measured [375]. The measurement of quantity A (say a position of a mirror) increases the uncertainty of the non-commuting quantity B (say the mirror's momentum). Both observables are linked by a Heisenberg Uncertainty relation. For repeated measurements of A, the increased uncertainty in B disturbs the measurement of A at later times. This is referred to as *quantum back-action noise*. Here, the back-action arises from the fluctuating radiation pressure due to the reflected light [449]. It is significant if the mirror's mass is low and a large photon number is reflected. In the 1970s, ideas were developed that showed how, in principle, back-action noise for continuous measurements can be avoided. Such schemes were called quantum-non-demolition (QND) measurements [450, 451]. However, for laser interferometric GW detectors using *quasi-free* falling mirrors it remained unclear if QND schemes exist. In [422, 449] it was concluded that back-action noise of a free mass position measurement can in principle not be avoided and, together with photon counting noise, defines a *standard quantum limit* (SQL). In [427, 452] it was argued, however, that measurements below the SQL of a free mass are indeed possible. The discussion remained controversial [453] until Jaekel and Reynaud [429] were able to convincingly show that the cleverly arranged squeezed states in a GW detector can simultaneously reduce the shot-noise and the radiation pressure noise, by almost arbitrary amounts (as long as most of the photons belong to the light's coherent displacement).

So far no experiment has achieved a position measurement with sensitivity even at, let alone below, its standard quantum limit. Eventually this will be achieved, possibly first in future gravitational wave detectors. Advanced detectors are in fact designed to have a sensitivity at or just below their SQLs. Once the SQL is reached a new level of quantum metrology is achieved, because the position-momentum uncertainty of the mirror becomes correlated with the quadrature uncertainty of the reflected optical field. In this way, entanglement between the mechanical and the optical system can be observed [454]. This is all the more remarkable from the perspective of GW detectors since we are talking about mirrors with masses of 40 kg, planned for the upcoming improvement to LIGO - the Advanced LIGO [312], and even in the order of a 100 kg concerning the envisaged LF-detector of ET. Eventually, even two such mirrors might be projected via entanglement swapping [455] into an entangled state [456]. Obviously quantum metrology opens the possibility for further studies of the peculiarities of quantum physics at a macroscopic scale.

5.6.1 Squeezed light for Gravitational wave astronomy

Laser interferometers for GW astronomy are facing extreme sensitivity requirements that can only be achieved if all available tools, inclusive of quantum metrology, are combined in an elaborate measurement device. Squeezed light must be generated in a non-linear interaction. Squeezed light was first produced in 1985 by Slusher et al. using four-wave-mixing in Na atoms in an optical cavity [448]. Shortly after, squeezed light was also generated by four-wave-mixing in an optical fibre [457] and by parametric down-conversion in an optical cavity containing a second order non-linear material [458]. In these early day experiments, squeezing of a few percent to 2 to 3 dB were routinely observed (For an overview of earlier experiments and squeezed light generation in the continuous-wave as well as pulsed regime please refer to Ref.[459]).

GW detectors are operated with high-power, quasi-monochromatic continuous-wave laser light with an almost Fourier-limited spatial distribution of a Gaussian TEM_{00} mode. For a non-classical sensitivity improvement, squeezed light in exactly the same spatio-temporal mode must be generated and mode-matched into the output port of the interferometer [422], providing interference with the high-power coherent laser beam at the interferometer's central beam splitter. High-power lasers for GW astronomy are based on optically pumped solid-state crystals in resonators [460], suggestive of a similar configuration for a "squeezed light resonator". Fig. 178 (a) shows a schematic setup for generation of squeezed light that is built upon one of the very first squeezing experiments [458], a setup that has been used in many experiments thereafter [461–464]. The setup uses a solid state laser similar to those used as master lasers in high-power systems. After spatial mode filtering, second harmonic generation (SHG) in an optical cavity containing a second-order non-linear crystal is applied to produce laser light at twice the optical frequency. The second harmonic light is then mode-matched into the

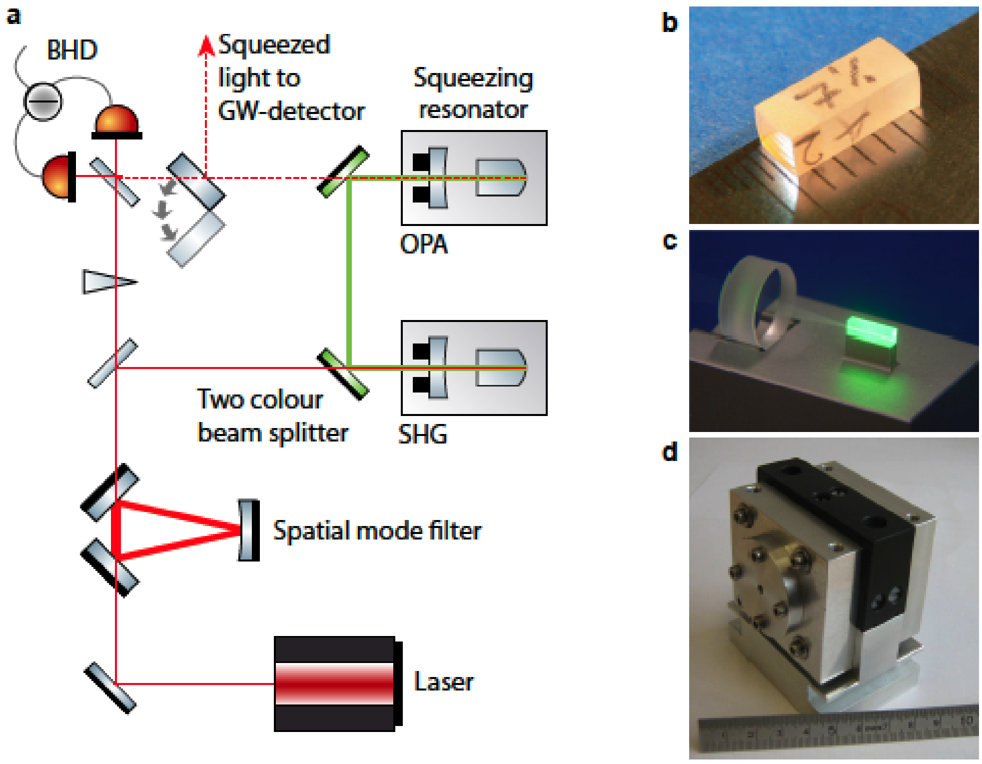

Figure 178: Generation of squeezed light (a) A continuous-wave laser beam at the GW detector wavelength is first spatially filtered and then up-converted to a field at half the wavelength (second harmonic generation, SHG). That beam is then mode-matched into the 'squeezing resonator' in which a tiny fraction of the up-converted photons are spontaneously down-converted by optical parametric amplification (OPA) producing a squeezed vacuum state. The squeezing factor is validated by a balanced homodyne detector (BHD). SHG as well as OPA are realized by a non-linear crystal (b), here a 6 mm long MgO:$LiNbO_3$ crystal, inside an optical resonator (c) formed by an external cavity mirror and the dielectrically coated crystal back surface. The two non-linear resonators may be constructed in an identical way and are put into temperature stabilized housings (d).

squeezing resonator to pump a degenerate optical parametric amplifier.

Fig. 178 (b-d) show photographs of the non-linear crystal, the optical arrangement and the housing of a squeezing resonator. The crystal is temperature stabilized at its phase matching temperature. At this temperature the first-order dielectric polarization of the birefringent crystal material with respect to the pump is optimally overlapped with the second-order dielectric polarization of the resonator mode at the fundamental laser frequency. This ensures a high energy transfer from the pump field to the fundamental Gaussian TEM_{00} resonator mode, i.e. efficient parametric down conversion.

Initially, the resonator mode is not excited by photons around the fundamental frequency, i.e. it is in its ground state, characterized by vacuum fluctuations due to the zero point energy [446]. Note that the process is typically operated *below* oscillation threshold in order to reduce phase noise coupling from the pump [465]. This setup produces a squeezed vacuum state [446]. The down-converted photon pairs leaving the squeezing resonator exhibit quantum correlations which give rise to a squeezed photon counting noise when overlapped with a bright coherent local oscillator beam. The squeezed field is detected by interfering it with a coherent local oscillator beam, either in a balanced homodyne detector (BHD), see Fig. 178 (a), or when injected into a GW detector and detected with a local oscillator from the GW detector along with an interferometric phase signal, see Fig. 177. The closer the squeezing resonator is operated to its oscillation threshold, and the lower the optical loss on down-converted photon pairs, the greater the squeeze factor is. For instance, the observation

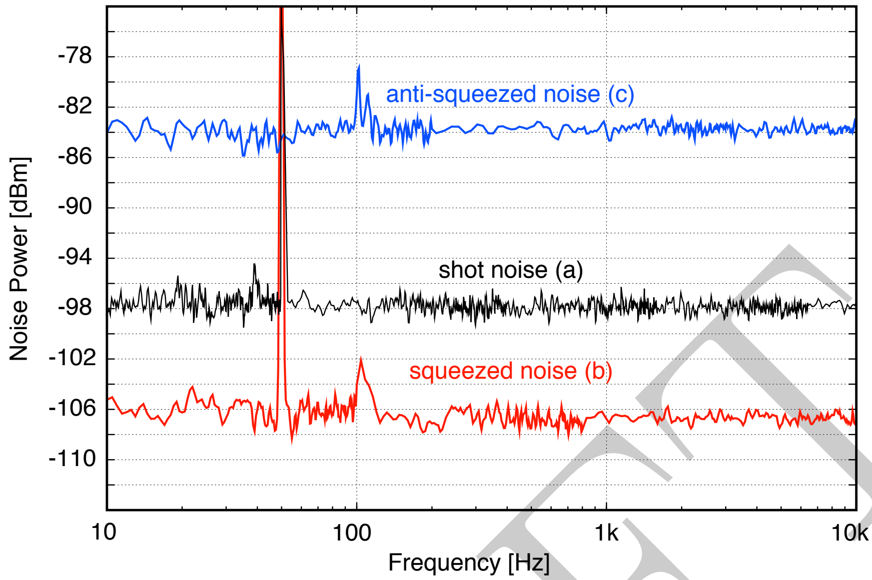

Figure 179: Quantum noise squeezing The spectral analysis of measured noise powers without (i) and with 'squeezing' (ii). The horizontal sections of traces (i) correspond to shot-noise, serving as reference levels (0 dB), respectively. Current best performance of a squeezed light laser for GW detection shows an up to 9 dB squeezed noise over the complete detection band of ground-based GW detectors [466].

of a squeezing factor of 2 is only possible if the overall optical loss is less than 50% [459]. **A 90% nonclassical noise reduction, i.e. a squeezing factor of 10, or 10 dB already limits the allowed optical loss to less than 10%.**

Although squeezed light was demonstrated in the 1980s shortly after the first applications were proposed [448, 457, 458], several important challenges pertaining to the application of squeezed states to GW detectors remained unsolved until recently.

First, squeezing has always been demonstrated at Megahertz frequencies, where technical noise sources of the laser light is not present. At this frequencies, the laser operates at or near the shot-noise limit. In the 10 Hz to 10 kHz band where terrestrial GW detectors operate, technical noise masked and overwhelmed the observation of squeezing. For example, acoustic, laser relaxation oscillatiion thermal and mechanical fluctuations can be many orders of magnitude larger than shot noise. Until recently, it was not certain that a laser field could even be squeezed and matched to the slow oscillation period of GWs. Second, it was previously not known whether squeezed light was fully compatible with other extremely sophisticated technologies employed in GW detectors, such as signal-recycling. Third, the technology to reliably produce stable and strong squeezing with large squeeze factors was lacking. Long term observation of strong squeezing was a technical challenge until recently.

These challenges have all been overcome in the past decade. All the open questions have now been satisfactorily addressed. This development is very timely since many known advanced classical interferometric techniques have almost been exhausted. Many remaining classical improvements are becoming increasingly difficult and expensive) to implement.

Generation of squeezing in the audio-band A major breakthrough in achieving squeezing in the audio band was the insight that the dominant noise at audio frequencies that degrades squeezed light generation couples via the coherent laser field that was used to control the length of the squeezed light laser resonator, whereas noise coupling via the second harmonic pump field is insignificant [467, 468]. This led to the first demonstration of audio-band squeezing at frequencies down to 200 Hz [469], see Fig. 179 a. There the length of the squeezing resonator was stabilized without a bright control beam by using the phase sensitivity of the squeezing itself – a technique known as quantum noise locking [470]. Subsequently a coherent beam control scheme was invented [471] for simultaneous control of both the squeezing resonator length and the squeezing angle [446]. Shortly thereafter another noise source was identified and mitigated, which allowed for squeezing of more than 6 dB throughout the audio-band down to 1 Hz [472]. This noise source arose due to tiny numbers of photons that were scattered from the main laser beam and rescattered into the audio band squeezing mode after having experienced a frequency shift due to vibrations and thermal expansions of potential scattering surfaces, an effect known as *parasitic interferences*. Since bright laser beams cannot be completely avoided, the recipe for the generation of audio-band squeezing turned out to be fourfold: avoiding scattering by using ultra-clean super-polished optics, avoiding rescattering by carefully blocking all residual faint beams caused by imperfect anti-reflecting surfaces, reduce the vibrationally and thermally excited motion of all mechanical parts that could potentially act as a re-scattering surface and avoid pointing fluctuations [473].

Compatibility of squeezing with other interferometer techniques Current detectors achieve their exquisite sensitivity to GWs due their kilometre-scale arm lengths, the enormous light powers circulating in the enhancement resonators (arm, power- and signal-recycling cavities), and sophisticated pendulum suspensions that isolate the test mass mirrors from the environment (Fig. ??). When these techniques were developed, squeezing was not envisioned to become an integrated part of such a system. Building on existing theoretical work [430, 474], a series of experimental demonstrations of squeezed state injection into GW detectors were carried out. These included compatibility with power recycling, with signal recycling [425, 433], and with the dynamical system of suspended, quasi-free mirrors [475, 476].

Generation of strong squeezing Squeezing has significant impact in quantum metrology if large squeezing factors can be produced. Squeezing of 3 dB improves the signal-to-noise ratio by a factor of $\sqrt{2}$, equivalent to doubling the power of the coherent laser input. Squeezing of 10 dB corresponds to a ten-fold power increase. Remarkably, the experimentally demonstrated squeezing factors have virtually exploded in recent years [477–479], culminating in values as large as 12.7 dB [416]. All the squeezing factors above 10 dB were observed with monolithic resonators and at MHz frequencies. However, reduced optical loss in non-monolithic resonators and a careful elimination of parasitic interferences should in principle enable such factors also in the GW band. An 8 to 10 dB improvement based on strong squeezing seems realistic for future GW detectors in their shot-noise limited band [416].

So far, strong squeezing values have been reported for a wavelength of 1064 nm. However, the procedure of squeezed light generation is also applicable for the wavelength of 1550 nm that will be required for future, cryogenic GW detectors. Recently, the generation of squeezing at a wavelength of 1550 nm was reported in a first proof-of-principle experiment [480]

The first squeezed light laser for GW detection Based on the previous achievements reviewed here, very recently, the first squeezed light laser for the continuous operation in GW detectors was designed and completed [441, 466]. Up to 9 dB of squeezing over the entire GW detection band has been demonstrated (Fig. 179b). This laser produces squeezed vacuum states and is fully controlled via co-propagating frequency-shifted bright control beams. This 9 dB squeezing factor is limited by technical effects: The squeezing resonator has to have an adjustable air gap to allow for an easy way to apply length control. The anti-reflection coated surface in the resonator introduces additional loss and reduces the escape efficiency. Moreover, a Faraday isolator has to be used in the squeezed beam path in order to eliminate parasitic interferences. This rotator produces a single pass photon loss of about 2%. This squeezed light source is designated for continuous operation in the GEO600 GW detector. A squeezed light source based on a design that should have less sensitivity to retro-scattered light [481] is being prepared for deployment on one of the most sensitive detectors, the 4 km LIGO detector in Hanford, Washington.

5.7 Filter cavities

The necessity of filter cavities for a broad band quantum noise reduction with squeezed state of lights was described in Secs 5.5.1, 5.6 and 5.6.1. In the following Sections, technical requirements for these optical filters are discussed. An important point is the required baseline length of these filter cavities in view of their optical round-trip loss (Sec. 5.7.1). The tolerances of the determined design parameters will be discussed in Sec. 5.7.3. Furthermore, in Sec. 5.7.4 the optical layout with regard to the round-trip loss that will be mainly caused by scattering at the used imperfect mirrors is treated. Finally, the degradation of the squeezing level due to noise couplings (e.g. displacement noise in the filter cavities) will be analysed in Sec. 5.7.5 leading to further estimates for the requirements.

5.7.1 Restrictions for the baseline length of the filter cavity

In this Section we start with a description of the influence of optical round-trip loss on the filter cavities' performance in dependence of their baseline length and half-bandwidth. The required half-bandwidth $\gamma_{\rm fc}$ and detuning $\Phi_{\rm fc}$ (note that we will define them as angular frequencies) of the filter cavities giving the optimal frequency dependent squeezing angle are determined by the interferometer configuration and its induced phase-space rotation of light fields entering the interferometers output port. The determination of these values is presented in Sec. 5.7.2 in detail.

Generally, any round-trip loss will degrade the squeezing level at sideband frequencies being resonant in the filter cavity. For a given power round-trip loss $l^2_{\rm rt,fc}$ (mainly caused by scattering) the resulting loss in reflection of the filter cavity increases with a decreasing baseline length $L_{\rm fc}$ of the filter. As well, for a certain length $L_{\rm fc}$ and a certain round-trip loss $l^2_{\rm rt,fc}$ the loss imposed on the squeezed field increases with a decreasing half-bandwidth $\gamma_{\rm fc}$ that needs to be realized. Starting from the expression for the half-bandwidth of a lossy cavity

$$\gamma_{\rm fc} = \frac{c}{2L_{fc}} \arccos\left(1 - \frac{(1-\rho_{\rm c}\sqrt{1-l^2_{\rm rt,fc}})^2}{2\rho_{\rm c}\sqrt{1-l^2_{\rm rt,fc}}}\right) \tag{136}$$

one can derive the filter cavity's coupling mirror power reflectance $R_{\rm c} = \rho^2_{\rm c}$ that is required to achieve the targeted half-bandwidth. One obtains

$$\rho_{\rm c} = \frac{1}{\sqrt{1-l^2_{\rm rt,fc}}}\left[2 - \cos(\mathcal{F}') - \sqrt{\cos^2(\mathcal{F}') - 4\cos(\mathcal{F}') + 3}\right] \tag{137}$$

with

$$\mathcal{F}' = \frac{2\gamma_{\rm fc}L_{\rm fc}}{c} = \frac{\gamma_{\rm fc}}{\rm FSR_{fc}} = \frac{\pi}{\mathcal{F}_{\rm fc}}\,. \tag{138}$$

Graph e) in Fig. 180 shows the value for $R_{\rm c} = \rho^2_{\rm c}$ according to Eq. (137). In the underlying calculations the baseline length $L_{\rm fc}$ and the round-trip loss $l^2_{\rm rt,fc}$ were considered with 10 km and 75 ppm, respectively. The tuning of the filter cavity was exemplary set to $\Phi_{\rm fc} = \gamma_{\rm fc}L_{\rm fc}/c$. It can be seen, that for small half-bandwidths $\gamma_{\rm fc}$ the reflectance $R_{\rm c}$ comes close to unity. Correspondingly, the resulting Finesse rises as shown in Graph d). It can be seen from Eq. (137) that there are two fundamental restrictions for the choice of the filter cavity length. First, for great values of the Finesse (i.e. for small half-bandwidths) we obtain

$$\lim_{\gamma_{\rm fc}\to 0} \rho_{\rm c} = \frac{1}{\sqrt{1-l^2_{\rm rt,fc}}} > 1 \tag{139}$$

which does not represent a physical solution. Thus, there must exist a value $L_{\rm min}$ such that for $L_{\rm min} < L_{\rm fc}$ we always have $\rho_{\rm c} < 1$. The expression for $L_{\rm min}$ can be derived to

$$L_{\rm min} = \frac{c}{2\gamma_{\rm fc}} \arccos\left[2 - \frac{2-l^2_{\rm rt,fc}}{2\sqrt{1-l^2_{\rm rt,fc}}}\right]\,. \tag{140}$$

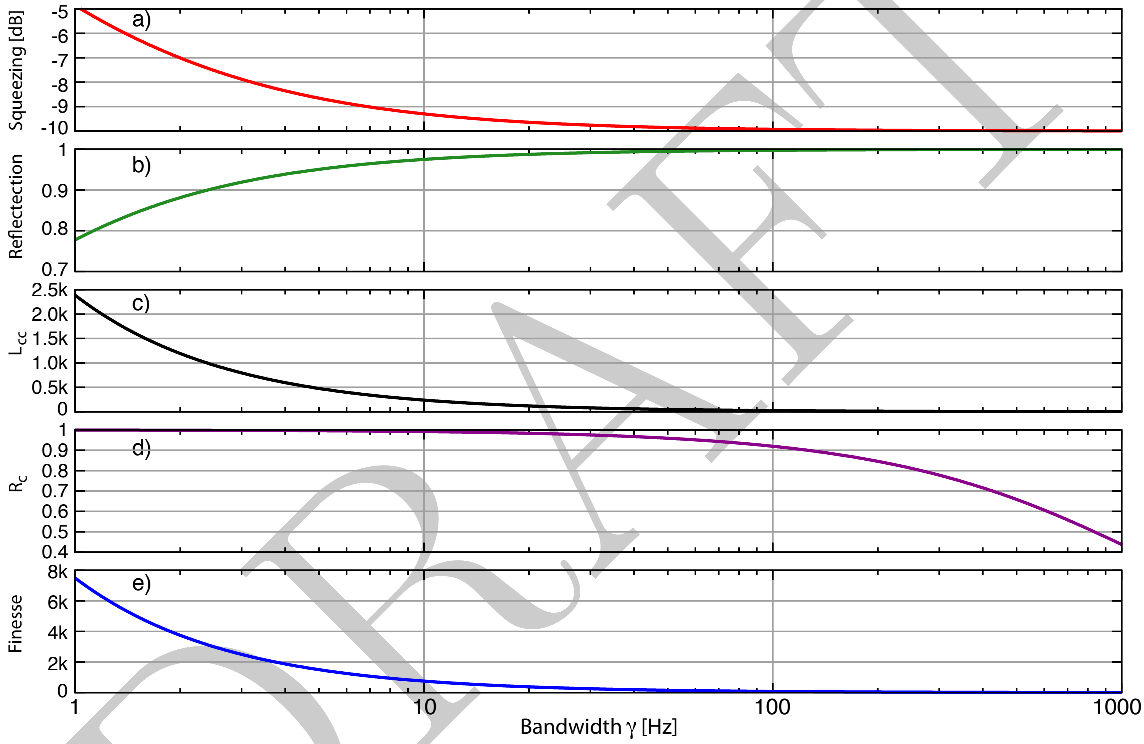

Figure 180: Filter cavity properties in dependence of its half-bandwidth $\gamma_{\rm fc}$. a) the remaining detectable squeezing level in reflection of the filter cavity and b) its reflectance at the frequency $\Omega = \Phi_{\rm fc} L_{\rm fc}/c$. In c) the value for $L_{\rm cc}$ is shown according to Eq. (141). Curve d) shows the Finesse and e) the coupling mirror reflectance $R_{\rm c}$ given by Eq. (137). For all traces a filter cavity length $L_{\rm fc} = 10\,{\rm km}$ and a round-trip loss $l^2_{\rm rt,fc} = 75\,{\rm ppm}$ was assumed. An initial pure 10 dB squeezed state was considered. It can be seen that the impact of the round-trip loss becomes significant for $\gamma_{\rm fc} < 2\pi \cdot 10\,{\rm Hz}$.

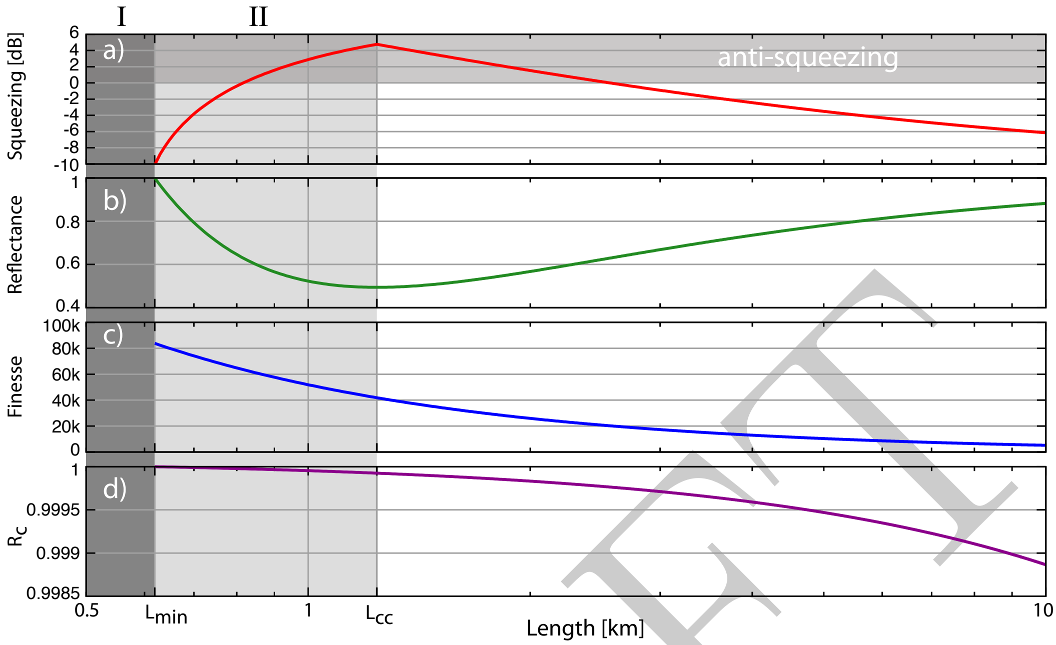

Figure 181: The figure shows the filter cavity performance in dependence of its baseline length L_{fc}. Graph a) shows the remaining squeezing level in reflection of the filter cavity at its resonance frequency. Graph b) shows the according reflectance of the filter cavity. Graph c) and d) show the filter cavity's Finesse and coupling mirror reflectance R_c, respectively. The two grey shaded areas in the left highlight the region where $L_{fc} < L_{cc}$ (area II) and where $L_{fc} < L_{min}$ (area I). In the considered example ($\gamma_{fc} = 2\pi \cdot 1.4\,\text{Hz}$, $\Phi_{fc_1} = 2\pi \cdot 6.6\,\text{Hz} \cdot L_{fc_1}/c$, $l^2_{rt,fc} = 75\,\text{ppm}$) the critical length L_{cc} is about 1239 m. The top grey shaded area in graph a) highlights the anti-squeezed region. Due to the unbalanced loss for upper and lower squeezing sidebands in the detuned filter cavity, for high resulting loss (i.e. for a cavity reflectance much smaller than one) the detected noise can be even enhanced when compared to the vacuum noise (refer to Fig. 182). In the considered example the detected noise is already enhanced (anti-squeezed) for filter cavity baseline lengths smaller than approximately 2.5 km.

Second, for $L_{fc} < L_{cc}$ we obtain $\rho_c > \sqrt{1 - l^2_{rt,fc}}$ and the filter cavity becomes under-coupled. But even in the most general case, the interferometer represents an over-coupled cavity. Hence, an under-coupled filter cavity with $L_{fc} < L_{cc}$ can not provide the phase-space rotation required for the generation of the optimal squeezing angle.

To keep $\rho_c < \sqrt{1 - l^2_{rt,fc}}$ the filter cavity length needs to be

$$L_{fc} > L_{cc} = \frac{c}{2\gamma_{fc}} \arccos\left[2 - \frac{1 + (1 - l^2_{rt,fc})^2}{2(1 - l^2_{rt,fc})}\right] \tag{141}$$

Please note that for $L_{fc} = L_{cc}$ the filter cavity is critical coupled (impedance matched) and the loss in its reflection is maximum. Therefore, to preserve the squeezing in reflection of the filter cavities its length should be chosen with $L_{fc} \gg L_{cc}$. This fact becomes obvious when looking at graph a) and b) of Fig. 180. They show the squeezing level in reflection of the filter cavity and the according reflectance of the filter cavity at its resonance frequency, respectively. At small half-bandwidths the value for L_{cc} (graph c)) is of the order of the filter cavity's baseline length $L_{fc} = 10\,\text{km}$ and hence the reflectance and accordingly the remaining squeezing level are considerably reduced.

In Fig. 181 the filter cavity performance is shown depending on its baseline length L_{fc}. In the corresponding calculations we assumed the target half-bandwidth with $\gamma_{fc} = 2\pi \cdot 1.4\,\text{Hz}$ and the target detuning with

Fig. to be added

Figure 182: Some nice phasors showing the effect of unbalanced loss...

$\Phi_{\mathrm{fc}_1} = 2\pi \cdot 6.6\,\mathrm{Hz} \cdot L_{\mathrm{fc}_1}/c$. Note, that these values are approximately the requirements for one of the filter cavities that needs to be realised in the ET-LF detector [?]. Again, the round-trip loss was considered with 75 ppm and the initial squeezing level with 10 dB. Graph a) demonstrates, that even with a filter cavity length of 10 km the amount of squeezing is already reduced by a factor of about 4 dB. For lengths smaller than about 2.5 km the unbalanced loss for upper and lower squeezing sidebands results in a noise enhancement (anti-squeezing) when compared to vacuum noise in reflection of the filter cavity. At the crtical length $L_{\mathrm{fc}} = L_{\mathrm{cc}} \approx 1239\,\mathrm{m}$ this enhancement becomes maximum and corresponds to about 5 dB anti-squeezing. For lengths smaller than L_{cc} the noise level drops and squeezing can be achieved again (grey shaded area II) until it reaches at $L_{\mathrm{fc}} = L_{\mathrm{min}}$ the initial level of 10 dB. However, in this region the filter is under-coupled and does not yield the required phase-space rotation of the squeezed field. This can be understood when considering the extrem case for $L_{\mathrm{fc}} = L_{\mathrm{min}}$. Here, R_{c} is equal to one and the filter cavity can be replaced by an ordinary mirror that has no frequency dependence. Again, it can be deduced, that a filter cavity length $L_{\mathrm{fc}} \gg L_{\mathrm{cc}}$ needs to be realised in order to preserve the squeezing. In addition, the high finesse of a short cavity might pose a problem for the lock acquisition in the environment of a gravitational-wave detector where the optics needs to be suspended.

So far in Figs. 180 and 181 the squeezing level was shown in reflection of the considered filter cavities at its resonance frequency. Here the (frequency dependent) imposed loss is maximum. Now, for exemplification Fig. 183 shows squeezing spectra obtained after the reflection at two subsequent filter cavities FC_1 and FC_2. The considered half-bandwidths and tunings of these filters are those needed for the ET-LF detector. The length of the cavities were considered with $L_{\mathrm{fc}_1} = L_{\mathrm{fc}_2} = 2\,\mathrm{km}$ (red curve), $L_{\mathrm{fc}_1} = L_{\mathrm{fc}_2} = 5\,\mathrm{km}$ (blue curve) and $L_{\mathrm{fc}_1} = L_{\mathrm{fc}_2} = 10\,\mathrm{km}$ (green curve), respectively.

The calculations and exemplary filter properties considered within this Section imply, that in 3rd generation GWADS detectors such as the Einstein Telescope, where filter cavities with half-bandwidths in the range of $\gamma_{\mathrm{fc}} \approx 2\pi \cdot 1 - 2\pi \cdot 5\,\mathrm{Hz}$ will be required, the baseline length of these filters needs to be in the order of a few kilometers. This contrasts to the results presented in [436] for the aLIGO detector. As for the aLIGO configuration filter cavities with half-bandwidths in the order of $2\pi \cdot 50 - 2\pi \cdot 200\,\mathrm{Hz}$ will be required, a considerable sensitivity increase by the injection of frequency dependent squeezed light can already be achieved if filter cavities with lengths in the order of 100 m are utilised. Certainly, our exemplary calculations are based on a conservative assumption of 75 ppm for the round-trip loss of the filter cavities, but even if optimistic values of $l^2_{\mathrm{rt,fc}} = 20\,\mathrm{ppm}$ are considered, the corresponding values for the critical lengths will be $L_{\mathrm{cc,fc}_1} = 330\,\mathrm{m}$ and $L_{\mathrm{cc,fc}_2} = 84\,\mathrm{m}$, respectively. As shown in Figs. 180 and 181 the respective length L_{fc} should be at least 10 times greater than L_{cc}. I.e. for the ET-LF detector the length of the two required filter cavities should be realised with 10 km. In contrast, it can be shown that for the ET-HF detector a filter with a length of about 500 m is sufficient. This filter will be required for an optimisation of the squeezed quadrature in the radiation pressure noise dominated frequency band. However, in this frequency band other noise sources dominates the quantum noise. By that it is satisfactory to adapt the squeezing level to the level of these noise sources which will be possible with a comparatively short filter cavity.

The foregone investigation demonstrated that the round-trip loss ultimately restricts the minimal allowed baseline length and consistently the performance of the filter cavities. As it is expected that the round-trip loss of the filters will be dominated by scattering at imperfect mirror surfaces, the optical layout needs to be designed such that the amount of scattering is as much as possible reduced. The scattering in different optical layouts is treated in Sec. 5.7.4.

5.7.2 Determination of the required filter parameters

In publications by Purdue and Chen [?] and Harms [?] treating the frequency dependent squeezed light injection, some analytical expressions were derived showing first the need for filter cavities and second allow for a calculation of the required number, bandwidth and tuning of filter cavities. In these articles the interferometers

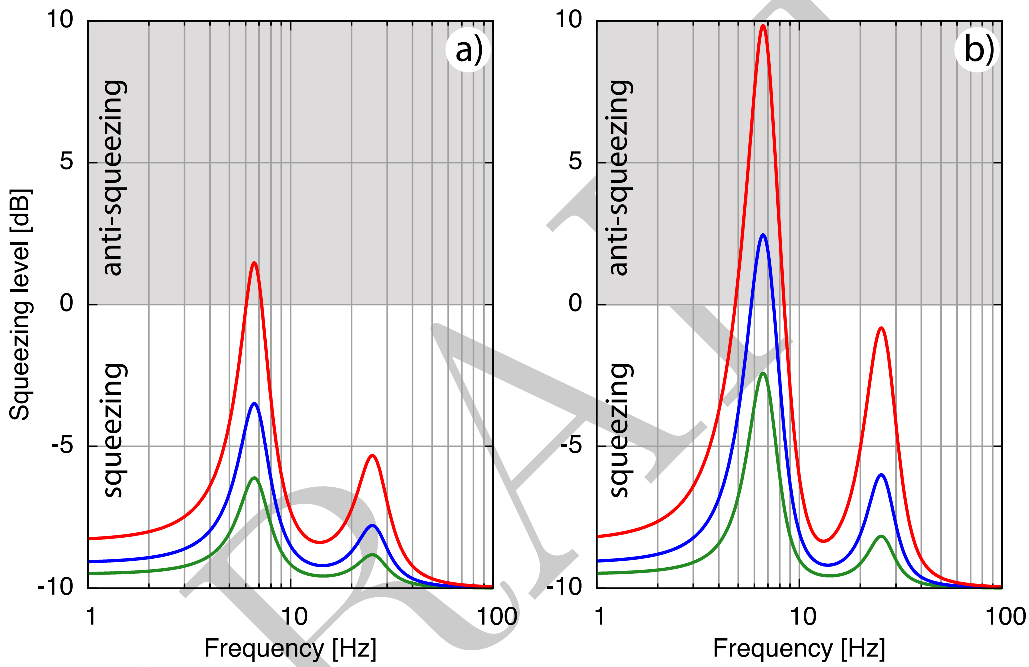

Figure 183: The figure shows the remaining squeezing level after subsequent reflection at two filter cavities FC_1 and FC_2. In graph a) an initial pure 10 dB squeezed state was considered and 75 ppm round-trip loss in each cavity. Additionally, in graph b) optical loss of 9 % outside the filter cavities was considered. Thus, an initial pure 20 dB squeezed state is necessary to achieve 10 dB detectable squeezing. In both cases, three length of the cavities were considered. The green curves are obtained for $L_{\mathrm{fc}_1} = L_{\mathrm{fc}_2} = 10\,\mathrm{km}$, the blue one for $L_{\mathrm{fc}_1} = L_{\mathrm{fc}_2} = 5\,\mathrm{km}$ and the red one for $L_{\mathrm{fc}_1} = L_{\mathrm{fc}_2} = 2\,\mathrm{km}$. The filter parameters are approximately those that are required for a broadband quantum noise reduction in the ET-LF detector, i.e. $\gamma_{\mathrm{fc}_1} = 2\pi \cdot 1.4\,\mathrm{Hz}$, $\Phi_{\mathrm{fc}_1} = 2\pi \cdot 6.6\,\mathrm{Hz} \cdot L_{\mathrm{fc}_1}/c$ and $\gamma_{\mathrm{fc}_1} = 2\pi \cdot 5.7\,\mathrm{Hz}$, $\Phi_{\mathrm{fc}_1} = -2\pi \cdot 25.4\,\mathrm{Hz} \cdot L_{\mathrm{fc}_1}/c$, respectively. Please note, that from this comparison it can be deduced, that the tolerable loss in the filters needs to be determined also in view of the injected anti-squeezing.

quantum noise transfer function was derived using the Caves-Schumacher two-photon formalism [**?**]. The interferometer's quantum noise transfer function is then described by a 2×2-matrix $\mathbf{T}$ (refer to Eq. (3) in [**?**]). From this matrix the required frequency dependent squeezing angle $\lambda(\Omega)$ can be derived according to Eq. (16) in [**?**]

$$\lambda(\Omega) = \arctan\left(-\frac{T_{11}\cos\zeta + T_{21}\sin\zeta}{T_{12}\cos\zeta + T_{22}\sin\zeta}\right). \tag{142}$$

Here, Ω is the angular sideband frequency and ζ the read-out angle. It was shown in [**?**], that with a combination of Fabry-Perot cavities the required frequency dependent angle $\lambda(\Omega)$ can be realized. It has the form [**?**]

$$\tan\lambda(\Omega) = \frac{\sum_{k=0}^{n} B_k \Omega^{2k}}{\sum_{k=0}^{n} A_k \Omega^{2k}}\,\text{, with } |A_n + \mathrm{iB_n}| > 0 \tag{143}$$

From the corresponding characteristic equation

$$\sum_{k=0}^{n} (A_k + \mathrm{iB_k})\,\Omega^{2k} = 0 \tag{144}$$

the required bandwidth and tuning of the filter cavities can be obtained. They are given by the $2n$ roots (in n pairs with a positive imaginary part) of Eq. (144). However, these calculations are based on the assumption of a lossless main interferometer, an infinite small signal-recycling cavity length, an expansion in powers of the light's angular frequency and the approximated expression for a cavity's half-bandwidth $\gamma = c\tau/(4L)$. Thus, in general they allow just for a precise estimation for the required parameters. Furthermore it is demonstrated in Fig. 184, that it is not sufficient to realize filter cavities having the bandwidth and tuning determined by Eq. (144). First, the impact of optical loss was considered. Therefor, the phase-space rotation in reflection of a cavity with a half-bandwidth $\gamma = 2\pi \cdot 1.44448\,\mathrm{Hz}$ and a tuning according to $f_{\mathrm{res}} = 6.628\,\mathrm{Hz}$ is calculated for different values of the round-trip loss. The lenght was set to 10 km. The results are shown in the left graph of Fig. 184. It can be seen, that the deviation of the phase-space rotation related to the lossless case increases with inreasing optical loss. Similar, the rotation in reflection depends on the baseline length of the cavity. This fact is shown in the right graph of Fig. 184. Here, the round-trip loss was set to 75 ppm for all cases.

Especially under consideration of optical intra-cavity round-trip loss and a finite baseline length of the filter cavities as well as the signal-recycling cavity there is no possibility to determine the optimal filter cavities' parameters analytically. Thus, the parameters for the filter cavities were fitted with respect to the residual phase-space rotation of injected squeezed field. Fig. 185 compares the results for the parameters determined in accordance to Eq. 144 (red curve) and those determined by the fit (black curve) for the ET-D LF detector. The corresponding filter cavity parameters are listed in Tab. 10

	tuning [Hz] (fitted / analytical)	half-bandwidth [Hz] (fitted / analytical)
FC_1	-25.4255 / -25.3592	5.76766 / 5.68148
FC_2	6.6167 / 6.6280	1.53135 / 1.44448

Table 10: Comparison of the parameters obtained from the fit and the analytical calculation in the case of optical loss. The loss in the interferometer was considered with 37.5 ppm per surface, the filter cavities' round-trip loss was considered with 75 ppm, their length with 10 km.

5.7.3 Robustness of the design parameters

In this Section we illustrate the effect of a deviation of the determined design parameters. We will concentrate on the most obvious quantities, that will potentially change the properties of the filter, i.e.

1. the reflectance factors of the used mirrors,

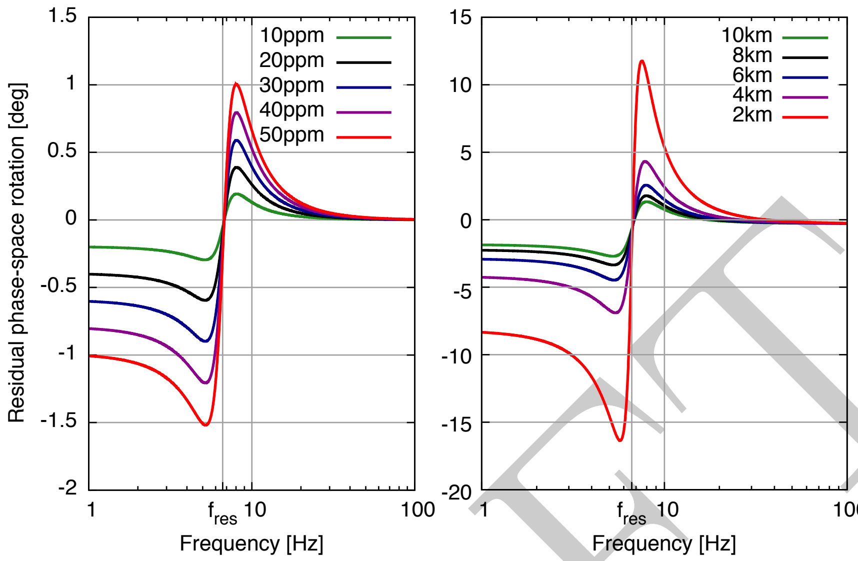

Figure 184: The figure demonstrates, that the phase-space rotation of a Fabry-Perot cavity is not only determined by its resonance frequency and bandwidth (here exemplary set to 6.628 Hz and 1.44448 Hz, respectively, for all cases), but also by its round-trip loss (left) and its baseline length (right).

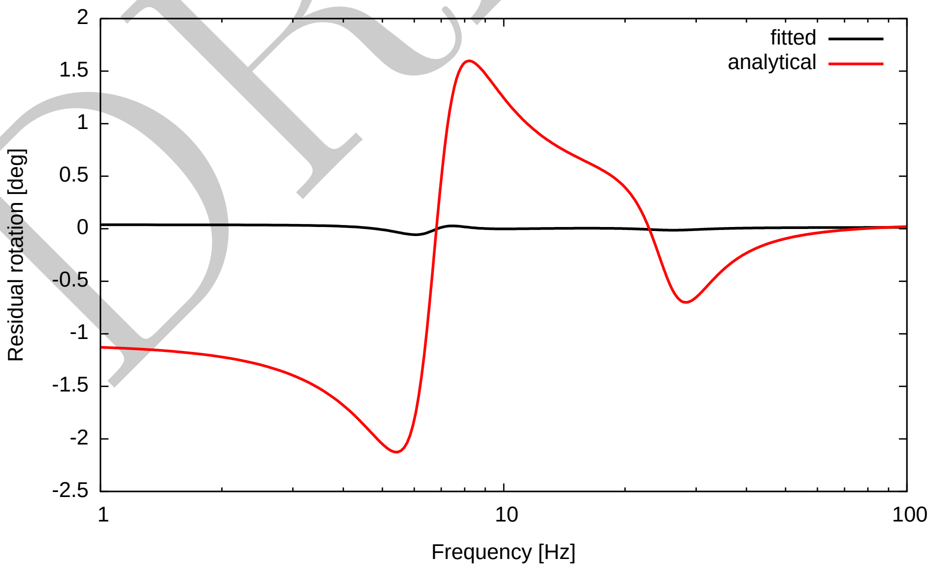

Figure 185: The figure shows the residual rotation of the injected squeezing, if the filter cavities are realized with parameters determined in accordance to Eq. (144) (red curve) and those determined by a fit (black curve). After fitting the parameters, the residual rotation is less than 0.2 deg.

2. the round-trip loss,
3. the macroscopic length and
4. the resonance frequency.

The first three quantities affect the bandwidth of the filter cavity and thus the required phase-space rotation around the targeted resonance frequency. A deviation from the design values of these quantities could not be compensated if the filter cavity is realised as single resonator. An adaption of the filters bandwidth would be possible if coupled resonators– e.g. a linear coupled three-mirror cavity– are utilised. Although it should be always possible to tune the filter cavity to the required resonance frequency, for the sake of completeness we treat a potential mismatch within this section. From the results the requirements for the length stabilisation with regard to displacement noise could be determined. This will be described in Sec. 5.7.5 in detail.

We start from the set of design parameters for the length, the detuning and the mirrors reflectance factors yielding the bandwidth and phase-space rotation of the two filter cavities that are required for ET-C LF. These parameters are listed in Table 11. The analysis of the impact on the achievable squeezing levels for a certain mismatch of the bandwidths will give the allowable tolerances of theses parameters.

Paramter	FC_1	FC_2
length L_{fc} [km]	10	10
half-bandwidth γ_{fc} [Hz]	$2\pi \cdot 1.4$	$2\pi \cdot 5.7$
resonance frequency f_{res} [Hz]	$2\pi \cdot 6.6$	$-2\pi \cdot 25.4$
detuning Φ_{fc} [°]	≈ 0.1369	≈ 0.3026
round-trip loss $l_{rt,fc}$ [ppm]	75	75
coupling mirror reflectance R_c	99.8864 %	99.5323 %

Table 11: adapt parameters to previous tab.Design parameters / estimates for the two filter cavities FC_1 and FC_2 needed in the ET-C LF detector.

To demonstrate the effect of a mismatched bandwidth we calculate the squeezing spectra after reflection at two subsequent resonators– the required filter cavity and an auxiliary cavity which models the interferometer. For the filter cavity the design parameters (and a certain deviation of them) as listed in Table 11 are assumed. The auxiliary one has a bandwidth and detuning that models the transfer function and thus the phase-space rotation of the interferometer. Consistently, no phase-space rotation occur after subsequent reflection at these resonators if their bandwidths are matched. Note, that the auxiliary resonator is assumed to be loss-free so that the imperfections in the squeezing spectra can be clearly traced back to the respective deviation of the filter cavities design parameters. For an first illustration of the effect of a mismatched filter cavity's bandwidth, Fig. 186 shows the squeezing level (top) and the residual phase-space rotation (bottom) after subsequent reflection at both cavities. Note, that here *both* cavities were assumed to be loss-free.

Fig. 187 shows the performance of the filter cavities (FC_1 and FC_2) required for the ET- LF detector. Their bandwidth was varied according to a deviation of 1 % to 5 % from the designed value. In these plots, the round-trip loss of the filter cavities was considered with 75 ppm.

If a tolerable degradation of the squeezing by less than 2 dB (related to the squeezing levels achievable with the design parameters) is targeted, a deviation of the bandwidth less than 5 % is acceptable. From this value, the tolerances for the design parameters can be duduced.

5.7.4 Choosing the optical layout of the filter cavity

Author(s): K. Kokeyama, A. Freise, H. Lück

As was shown in the last section, a filter cavity has a strict requirements for phase noises and optical losses of the filter cavities in order not to degrade the squeezing level. Since scattering noises can be a dominant sources

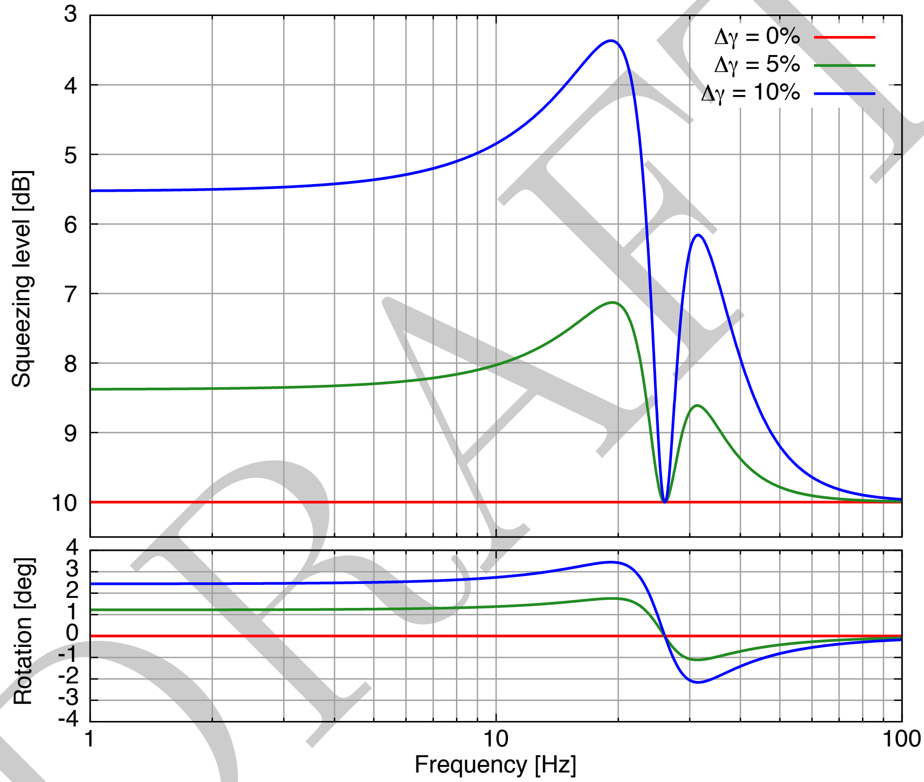

Figure 186: The figure illustrates the effect of a deviation of the required bandwidth. The lower graph show the resulting residual phase-space rotation of the squeezing ellipse, the upper graph the accordant squeezing levels. Please note, that the filter cavities are assumed to be loss less. Thus, the degradation of the squeezing level can be clearly traced back to the residual phase-space rotation.

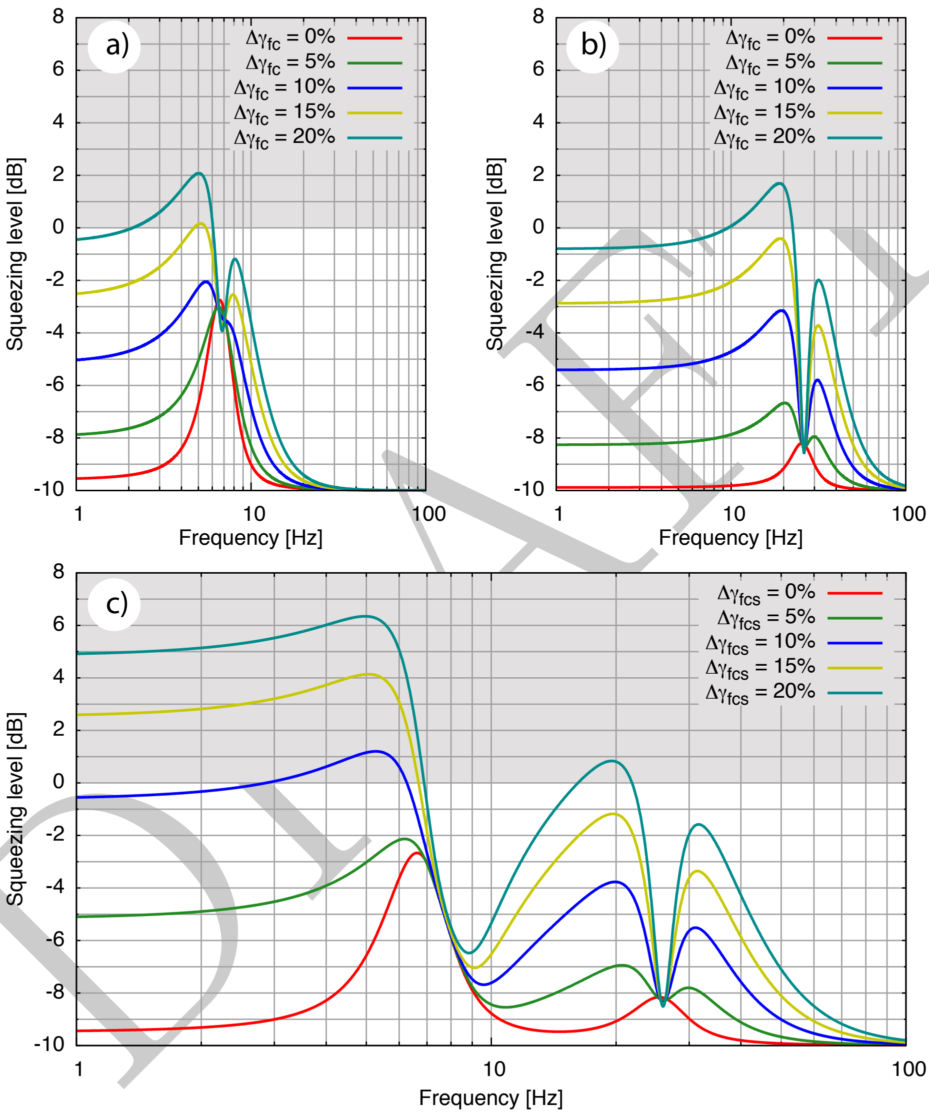

Figure 187: The figure shows the squeezing spectra for a deviation of the designed bandwidth of a) the single FC_1 and b) the single FC_2. Graph c) shows the spectra if both filter cavities are considered.In all cases, the filter cavities' round-trip loss was considered with 75 ppm.

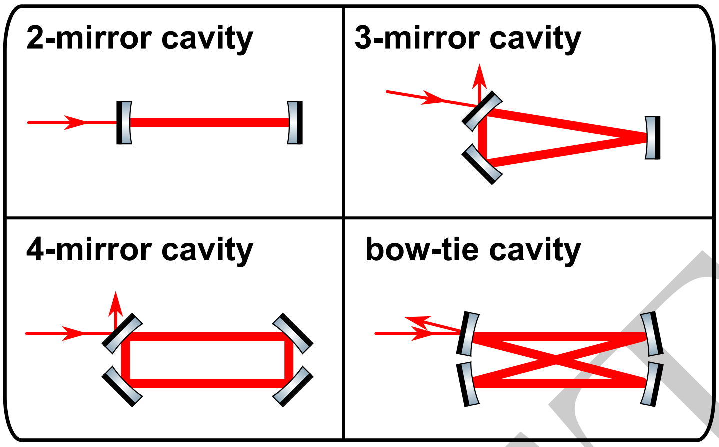

Figure 188: The scattering-light effect for these four geometries is analyzed.

of phase noises and optical losses for filter cavities as well as ET arm cavities, we analyzed the scattering light noises and compare the geometrical advantages or disadvantages for four kinds of cavity geometries. Deviations from a perfect mirror surface scatter the stored light in the cavity, and the scattered field propagates arbitrary spurious paths around the cavities. The scattered field possibly couples into the cavity fundamental mode and amplified by the cavity. The enhanved field produce the phase noise or optical losses.

Here, we assume four simplified scenarios of scattering process to estimate the scattered light levels of ET cavities, and compare the four geometries: a two-mirror cavity, triangular-cavity, rectangular cavity, and bow-tie cavity, as shown in Fig. 188.

To evaluate the effect of the scattered light noise, we calculate how much the scattered field coupling into the cavity mode. The coupling factor between the scattered field is defined as a convolution between them. In other words, the convolution term between the scattered fields and the cavity resonant field is the cross term when the light field is detected by a photo detector because this cross term will appear on the photo detector:

$$X = \int_{-\infty}^{\infty}\int_{-\infty}^{\infty} \psi_{\rm sc}(x,y,z_{\rm sc})\psi^{*}_{\rm cav}(x,y,z_{\rm cav})\mathrm{d}x\mathrm{d}y, \tag{145}$$

where $\psi_{\rm sc}(x,y,z_{\rm sc})$ is the scattered light field, $z_{\rm sc}$ is the location when the scattering process occurs with z axis as a main beam propagation direction, and $z_{\rm cav}$ is the locations of the target field coupled by the scattered light. $\psi_{\rm cav}(x,y,z_{\rm cav})$ is the Gaussian field which is the resonant mode in the cavity,

$$\psi_{\rm cav}(x,y,z_{\rm cav}) = \sqrt{\frac{k_0}{\pi z_R}}\frac{iz_R}{z+iz_R}\exp\left[\frac{-ik_0(x^2+y^2)}{2(z+iz_R)}\right] \tag{146}$$

where z_R is the Rayleigh range of the cavity resonant mode and k_0 is the wave number of the laser source.

Now we consider following four kinds of scattering-coupling scenarios for each geometry; direct back scattering, diagonal path scattering I and II, and Gaussian tail effect.

Direct back scattering When the main beam is reflected by a mirror, some of the main light field is scattered back by the non-uniform distribution of the mirror surface. The scattered field couples with the cavity resonant mode in the opposite direction in respect to the propagation direction of the main beam, just after being scattered by one mirror. In general, when the wavefront of the scattered light is changed by deformations of the mirror surfaces, the scattering into any direction is given by the Fourier transform of the mirror surface roughness. When the mirror surface roughness with a longer spacial wavelength, the scattering angle will be

Path color for left panel	ϕ_1	ϕ_2	Coupling direction
gray	large	small	normal
pink	small	small	opposite
blue	small	small	opposite
green	large	small	normal

Table 12: Scattering conditions for the four paths shown on the lower left panel in Fig. 189. The amplitude of the scattered light depends on the scattering angle when the light is scattered at a mirror and assumed using the BRDF for each path. The small or large scattering angle has larger and smaller efficiency, respectively.

Path color for right panel	ϕ_1	ϕ_2	Coupling direction
gray	large	large	opposite
pink	small	large	normal
blue	small	large	normal
green	large	large	opposite

Table 13: Scattering conditions for the four paths shown on the lower right panel in Fig. 189.

bigger. A typical mirror surface has more long spacial frequencies than short spacial frequencies, therefore, the scattering angle will be very small. Although arbitrary scattering angles are considered here for simplicity, numerical evaluation will show that no coupling into the main mode is expected even if the big angle scattering occurs.

To evaluate the coupling factor, the scattered field is written as

$$\psi_{\mathrm{sc}}(x,y,z) = \psi_{\mathrm{cav}}(x,y-z)\ \exp\bigl[-2ik_0M(x,y)\bigr]m(x,y,\alpha) \tag{147}$$

where

$$m(x,y,\alpha) = \exp\Bigl[-2ik_0x\tan\alpha + \frac{ik_0(x^2+y^2)}{2r_C}\Bigr], \tag{148}$$

$M(x,y)$ is a surface map of the mirror where the scattering occurs, and $m(x,y,\alpha)$ describes the phase delay due to the mirror angle α in respect to the mirror normal, and the radius of curvature of the mirror r_C is taken into account as the phase delay due to the reflection surface geometry.

Substituting Eq. (147) into Eq. (145), we obtain the coupling coefficient as

$$\begin{aligned} X_1 = \frac{k_0z_R}{\pi(z^2+z_R^2)}\int_{\infty}^{\infty}\int_{\infty}^{\infty}\exp\Bigl[-\frac{k_0z_R(x^2+y^2)}{z^2+z_R^2} \\ -ik_0\Bigl\{\frac{x^2+y^2}{2r_C}+2M(x,y)+2x\tan(a)\Bigr\}\Bigr]\mathrm{d}x\mathrm{d}y. \end{aligned} \tag{149}$$

Diagonal path scattering I In the rectangular cavity, diagonal lines of the rectangular geometry can be scattered light paths as depicted in the left panel of Fig. 189. When the main beam illuminates a mirror, scattered light is produced by the mirror surface distribution. We assume that the light field is scattered and propagate along the diagonal path as a spherical wave. Although spherical waves are averaged and weakened after propagating some distance, we use spherical wave form as a rough approximation and for a simple analytical expression. The spherical field is scattered again by a mirror at the diagonal line end, and the field couples into the cavity Gaussian mode again either in the normal or opposite direction of the main beam propagation. The efficiency of the scattering power is large when the scattering angle is small, and small when the scattering angle is large, therefore, the amplitude of the scattered field depends on the propagation path. Here we assume the amplitude using a bidirectional distribution function (BRDF) which is a function of the scattering angle, see below.

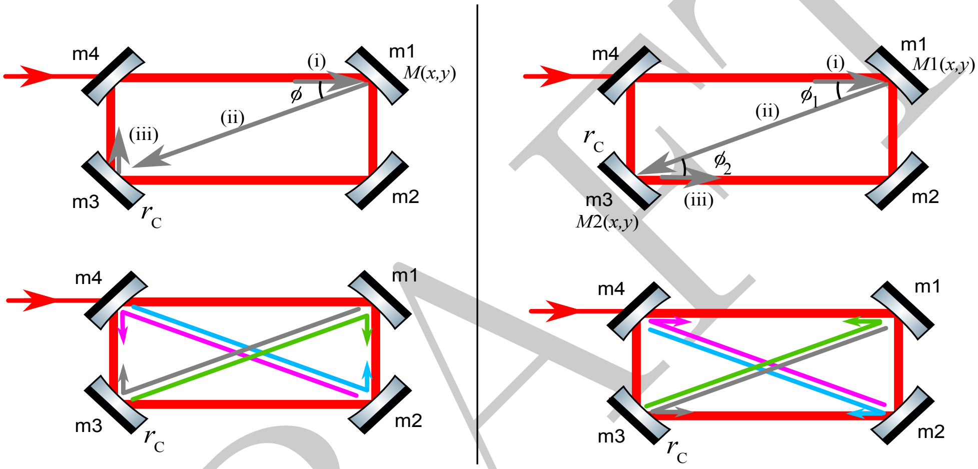

Figure 189: Upper left panel: scattering process of diagonal path with the small angle at the second scattering. (i) Laser light is scattered when the main beam is reflected by m1. The mirror surface distribution of m1 is $M(x, y)$. (ii) The scattered light propagates along the diagonal line of the rectangular as a spherical wave. (iii) the scattered field is scattered again at a small angle in respect to the main beam axis and couples into the Gaussian mode of the cavity. Lower left panel: all the possible incidents of diagonal path I process. Depending on the scattering incident mirror, ϕ is large (blue and magenta arrows), or small (gray and green arrows). Upper right panel: scattering process of diagonal path with the large angle at the second scattering. Processes (i) and (ii) are the same as the left panel. (iii) the scattered field is scattered again at a large angle by mirror m3 with its mirror map $M2(x, y)$ and couples into the Gaussian cavity mode. Lower right panel: all the possible incidents of diagnal path II process. Similar to the diagonal-I process, ϕ_1 and ϕ_2 depend on the paths. For example, both ϕ_1 and ϕ_2 are small for the gray process, on the other hand, ϕ_1 is large and ϕ_2 is small for the magenta process. The amplitude of the scattered light strongly depends on the scattered angle which is summarized in Table. 12 and Table. 13 for all the possible paths.

After the light field is scattered by the first mirror and propagate the diagonal path, there are two possibility to be scattered again at the second mirror. The diagonally propagating field is scattered again with small or large scattering angle or large angle, as depicted in the left or right panel of Fig. 189, respectively. As the incident at a small scattering angle has larger scattering efficiency compared with one at the large scattering angle because the most field is scattered to a small angle due to the longer spacial frequency of a typical mirror surface, as mentioned above. In total, eight paths are considered here. For each path, the scattered angles and the coupling direction are summarized in Table. 12 and Table. 13.

The scattered field is written as

$$\psi_{\rm sc}(x,y,z) = \frac{\eta(\phi_1)\eta(\phi_2)}{R_d}\ \exp\Big[-ik_0\big\{R_d + \frac{x^2+y^2}{2r_C} \\ +M_1(x,y)+M_2(x,y)\big\}\Big]. \tag{150}$$

where R_d is a distance of the diagonal path and r_C is a radius of curvature of a mirror when the scattered filed couples into the cavity. $M(x,y)$ is the mirror surface map of the mirror where the scattered light occurs. The amplitude of the scattering, $\eta(\phi_{1,2})$, are assumed using the BRDF which describes the scattering intensity distribution of a mirror as following: The amplitude of the field scattered at angle ϕ is written as

$$\eta(\phi) \quad = \quad \sqrt{P(\phi)}. \tag{151}$$

where $P(\phi)$ is the field power that reaches the reflection mirror surface at the end of the diagonal path. The power can be estimated using the BRDF as,

$$P(\phi) \sim P_0 {\rm BRDF}(\phi) dS \tag{152}$$

where P_0 is the incident light power, dS is the solid angle of the second mirror which recieves the scattered light, from the first mirror. As BRDF of a ET mirror is unknown, we use a typical BRDF in a laser-interferometric gravitational wave detector measured by LIGO pathfinder [482]:

$${\rm BRDF}(\phi) \quad = \quad \frac{1000}{(1+5.302\times 10^8\phi^2)^{1.55}}. \tag{153}$$

Note that this is a BRDF of a silica mirror and can be overestimate for the advanced mirrors of ET. Also, the BRDF is valid when the incoming beam is perpendicular to the mirror surface, which is different from our situation. The bidirectional reflection distribution might be alter in our case in which the incoming beam and the mirror normal have an angle.

Substituting Eq. (150) into Eq. (145), The coupling coefficient is derived as

$$X_2 = \sqrt{\frac{k_0 z_R}{\pi}}\frac{\eta(\phi_1)\eta(\phi_2)}{R_d(z_R+iz_{\rm cav})}\int_\infty^\infty\int_\infty^\infty \exp\Big[-ik_0\big\{R_d + \frac{x^2+y^2}{2r_C} \\ -\frac{x^2+y^2}{2(z_{\rm cav}-iz_R)} + M_1(x,y)+M_2(x,y)\big\}\Big]{\rm d}x{\rm d}y. \tag{154}$$

Diagonal path scattering II We consider three-time scattered process for the diagonal path scattering (added later).

$$X_3 \tag{155}$$

Gaussian tail effect In the rectangular and bow-tie cavities, the tail of the Gaussian field may reach a wrong mirror, for example as shown in Fig. 190 (a), and is partially reflected. This reflected field couples into the main Gaussian beam. Note that this is also a simplified picture. As shown in Fig. 190 (b), the wave front at the edge of the main field faces to the different direction compared with the wave front at the center of the

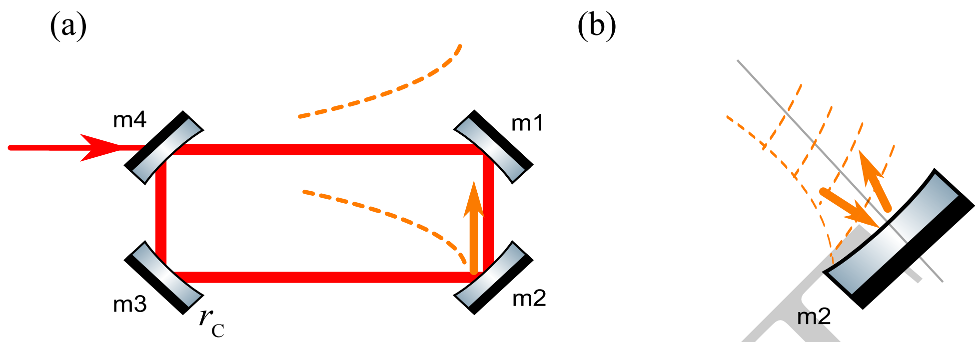

Figure 190: (a) An example image of the Gaussian tail effect. This process will occur at each mirror. (b) Image of wave fronts at the tail of Gaussian field. In the rigorous picture, the incident angle and the reflection angle is slightly different from the approximated picture of (a).

beam, therefore, the reflection angle may differ from the main beam path. However, for a simple estimation, we approximate that the Gaussian tail field is reflected and directly couples into the main mode. The rectangular or bow-tie cavity has four field to be considered since this process can occur at each mirror.

When a mirror (therefore the coupling point) is L m away in x direction to the main beam, the coupling field is written as

$$\psi_{\rm sc}(x,y,z) = \psi(x+L_s, y, z_{\rm sc}). \tag{156}$$

The coupling coefficient is

$$\begin{aligned} X_4 = & \frac{-k_0 z_R}{\pi(iz_{\rm cav}+z_R)(iz_{\rm sc}-z_R)} \\ & \int_\infty^\infty \int_\infty^\infty \exp\left[-ik_0\left\{\frac{x^2+y^2}{2(iz_R - z_{\rm cav})} + \frac{(L_s+x)^2+y^2}{2(iz_R - z_{\rm sc})}\right\}\right] {\rm d}x{\rm d}y. \end{aligned} \tag{157}$$

Numerical evaluation In order to calculate X_1-X_4, we assume that the round trip of a cavity is about 10 km, and a waist position of the laser beam is at the middle point of the round trip for the all geometries, as shown in Fig. 191. The triangular cavity is an isosceles triangle with two 5km arms and with a 1 m base, and the beam waist is at the middle of the short path. The rectangular cavity has the long and short paths of 5 km and 1 m, respectively and the beam waist is at m2 in Fig. 191. The bow-tie cavity have four paths of 2.5 km and the separation between the closer mirrors is assumed as 1 m. For mode-matching, flat or a radius of curvature r_C was assumed for each mirror. ET fake mirror maps simulated using a sum of Zernike polynomials with maximum 1 nm amplitude were used [483].

•X_1: Fig. 192 shows the plot of X_1 over the mirror angle α for various mirror positions, i.e., scattering positions (z=1, 1000, 2500, and 5000). X_1 is strongly depends on the angle between the mirror normal and the propagation direction of the beam, α. The coupling coefficient becomes rapidly zero when the angle is larger than 10^{-3} degrees. Since the mirror angles of all the ring cavities have much larger α, the direct back-scattering is negligible in ET cavities. However one has to be careful not to have mirror surface structures which may generates additional scattering light.

•X_2: X_2 is numerically evaluated using a ET fake mirror map. Taking the statistical sum of the eight scattered fields, the total amplitude of the scattered filed is 2.5×10^{-12}, while the laser power is normalized to be unity at each mirror.

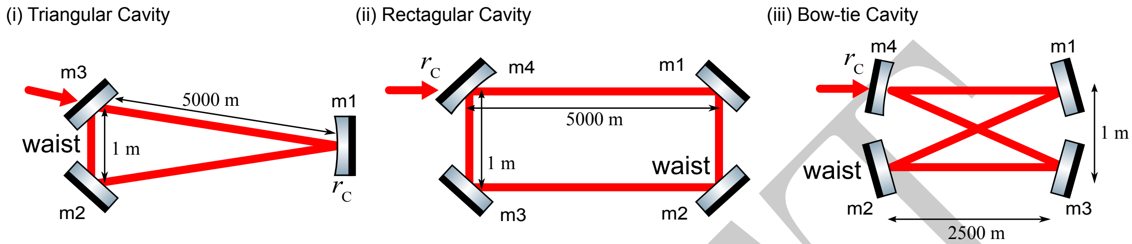

Figure 191: Cavity designs used for the numerical calculation. The cavities have a round trip length of approximated 10 km, and a beam waist at the middle point of the path.

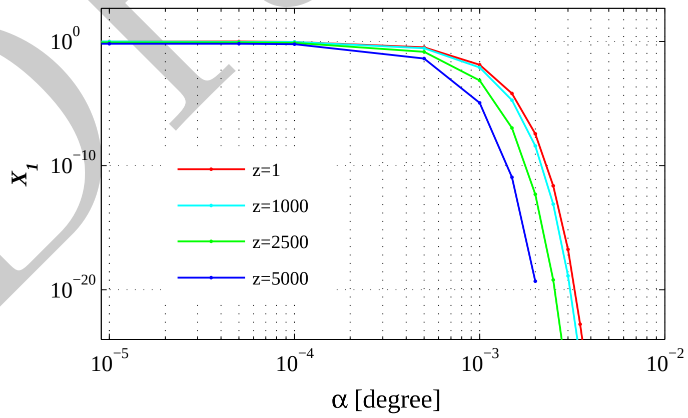

Figure 192: The coupling factor X_1 (direct back scattering) over the mirror angle where the scattering process occurs. The coupling factor rapidly goes to be zero after 10^{-3} degrees.

Type	direct-back scattering	Diagonal I	Diagonal II	Gauss. Tail
Two-mirror	N/A	N/A	N/A	N/A
Triangular	0	N/A	N/A	N/A
Rectangular	0	2.5×10^{-12}		0
Bow-tie	0	N/A	N/A	0

Table 14: Summary of the scattering process for each geometry without an amplification factor of the cavity. The numbers are in amplitude while the light power is normalized to be unity inside the cavity.

•X_3:

•X_4: X_4 is found to be negligible with the beam and cavity parameters considered here. The separation of the shorter paths in rectangular or bow-tie cavities of 1 m in the numerical evaluation, which turned to be enough. Although this length should be careful not be too close.

Table. 14 shows the summary of the numerical evaluation. The two-mirror cavity is the best configuration from the scattered-light point of view there is no spurious path in the geometry. For the other three configurations, the direct back scattering and the Gaussian tail effect are found to be negligible with the ET fake mirror maps. One has to be careful to the scattering field propagating along the diagonal paths in the rectangular cavity. In order to block the diagonal paths, putting baffles inside the rectangular geometry will be useful to prevent from the scattered light propagating along the paths.

Cavity enhancement Cavity enhancement and a cavity finesse restriction will be added. The phase noise restriction in the next subsection will be refered.

5.7.5 Noise couplings

In this Section several noise mechanisms that potentially limit the detected squeezing levels are discussed. First, we discuss the effect of phase noise in the squeezing path. Assuming a self-homodyning readout (DC readout) of the interferometers signal field, the DC part of the interferometer's output field serves as local oscillator. The quadrature of the signal field, that is read out is determined by its relative phase with regard to this local oscillator. In order to reduce the quantum noise of this measurement, the relative phase of the injected squeezed field needs to be chosen such that the squeezed quadrature coincides with the readout quadrature. This required phase relation gets disturbed due to e.g. vibrating optical components in the squeezing path (displacement noise) or residual high frequency phase modulations that probably will be required for control purposes. If the measurement time is greater than the period of the phase jitter period, the homodyne read out is not a pure measurement of a certain quadrature Φ (e.g. the squeezed quadrature) but the integral over some span of $\Phi + \delta\Phi$. In this case, a certain fraction of the noise in the anti-squeezed quadrature is mixed into the measurement that was intended to be a measurement of the squeezed quadrature. It is obvious, that such a *phase diffused squeezed state* results in a degraded squeezing level. Accordingly, an upper limit for the overall tolerable phase noise in the squeezing path needs to be deduced with regard to the targeted quantum noise reduction of 10 dB.

The influence of phase noise on the squeezed field can be nicely illustrated by the accordant Wigner functions. We start from the Wigner function of a squeezed state that has a certain orientation (determined by the quadrature angle φ) in phase-space. It is given by

$$W(X_{1,\varphi}, X_{2,\varphi}, \varphi) = \frac{1}{2\pi\sqrt{V_s V_a}} \exp\left[-\frac{X_{1,\varphi}^2}{2V_s} - \frac{X_{2,\varphi}^2}{2V_a}\right]. \tag{158}$$

Here V_s and V_a denotes the variances in the squeezed and anti-squeezed quadrature, respectively (e.g. for a pure 10 dB squeezed state $V_s = 0.1$ and $V_a = 10$ if normalised to the variance of the vacuum state $V_{\mathrm{vac}} = 1$).

The orientation in phase-space is accounted for by setting

$$X_{1,\varphi} = X_1 \cos(\varphi) - X_2 \sin(\varphi) \tag{159}$$
$$X_{2,\varphi} = X_1 \sin(\varphi) + X_2 \cos(\varphi) \,. \tag{160}$$

Here, the local oscillator serves as reference for the phase-space with its amplitude (X_1) and phase quadrature (X_2). The corresponding probability distribution in the amplitude quadrature (X_1) can be obtained from the Wigner function by integrating over X_2. One obtains

$$P_{X_1} = \int_{-\infty}^{\infty} W_d(X_1, X_2) dX_2 \tag{161}$$
$$= \frac{1}{\sqrt{2\pi V_{X_1}(\varphi)}} \exp\left[-\frac{X_1^2}{2V_{X_1}(\varphi)}\right] . \tag{162}$$

with the variance of the amplitude quadrature

$$V_{X_1}(\varphi) = V_s \cos^2(\varphi) + V_a \sin^2(\varphi) \tag{163}$$
$$= \frac{1}{2}\left[V_s + V_a + (V_s - V_a)\cos(2\varphi)\right] . \tag{164}$$

Now, to describe a phase diffused squeezed state, the quadrature angle φ needs to be replaced by a probability density for the phase denoted as $\Phi(\varphi)$. Then, the Wigner function is given by

$$W_d(X_1, X_2) = \int \Phi(\varphi) W_d(X_1, X_2, \varphi) d\varphi \,. \tag{165}$$

Again, the corresponding probability distribution in the amplitude quadrature (X_1) can be obtained from the Wigner function by integrating over X_2

$$P_{X_1,d} = \int_{-\infty}^{\infty} W_d(X_1, X_2) dX_2 \,. \tag{166}$$

Accordingly, the variance of a phase diffused squeezed state is given by

$$V_{X_1,d} = \int_{-\infty}^{\infty} \Phi(\varphi) V_{X_1} d\varphi \Leftrightarrow \int_{-\infty}^{\infty} P_{X_1,d} X_1^2 dX_1 \,. \tag{167}$$

In Fig. 193 four Wigner functions (top) and the corresponding probability distribution in the X_1-quadrature (bottom) are shown. We assumed and Gaussian distributed phase noise, i.e

$$\Phi(\varphi) = \frac{1}{\sqrt{2\pi\sigma^2}} \exp\left(-\frac{\phi^2}{2\sigma^2}\right) . \tag{168}$$

We have considered phase noise with a standard deviation σ of 0 (no phase noise), 0.3, 0.6 and 0.9 (from left to right in Fig. 193). The initial squeezed state (left figures) was assumed with $V_s = 0.1$ and $V_a = 10$, i.e. as a pure 10 dB squeezed state. The degradation of the squeezing level due to phase noise becomes obvious from the comparison with the probability distribution of a vacuum state (grey traces in the bottom graphs). The probability distribution are labelled with the corresponding squeezing level. For strong phase noise the initial squeezing is destroyed and the noise in the amplitude quadrature is even enhanced when compared to the vacuum noise (shot noise).

The illustration in Fig. 193 implies, that the larger the anti-squeezing level, the larger the effect of phase noise. In fact, in order to achieve the targeted quantum noise reduction of 10 dB, a squeezed light source needs to

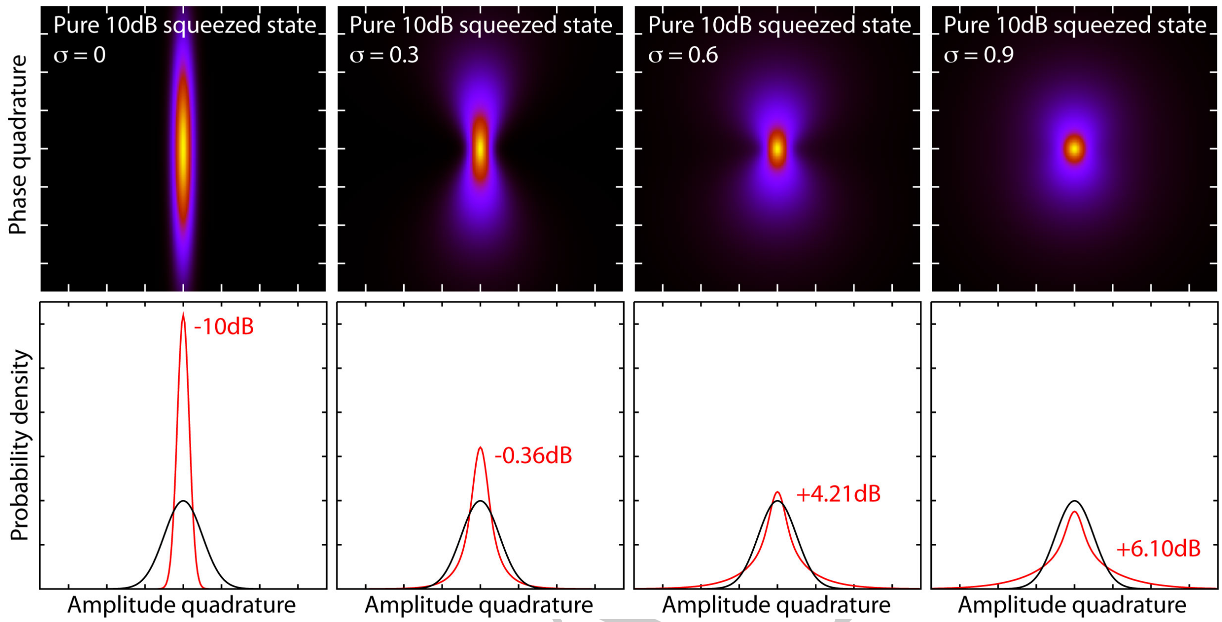

Figure 193: Illustration of the influence of a Gaussian distributed phase noise on the squeezed state. **Top:** Wigner functions for phase noise with a standard deviation σ of 0, 0.3, 0.6, 0.9. The initial, pure squeezed state was assumed with 10 dB. **Bottom:** The probability distribution of the phase diffused squeezed states and the corresponding squeezing levels (red curves and red labels, respectively) in the amplitude quadrature (X_1). For comparison, the distribution of a vacuum state is shown (grey curves).

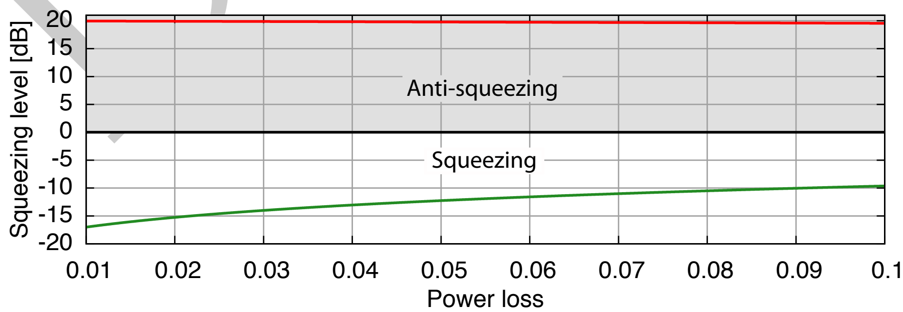

Figure 194: The degradation of the squeezing and anti-squeezing levels due to optical loss for an initially pure (no loss) 20 dB squeezed state.

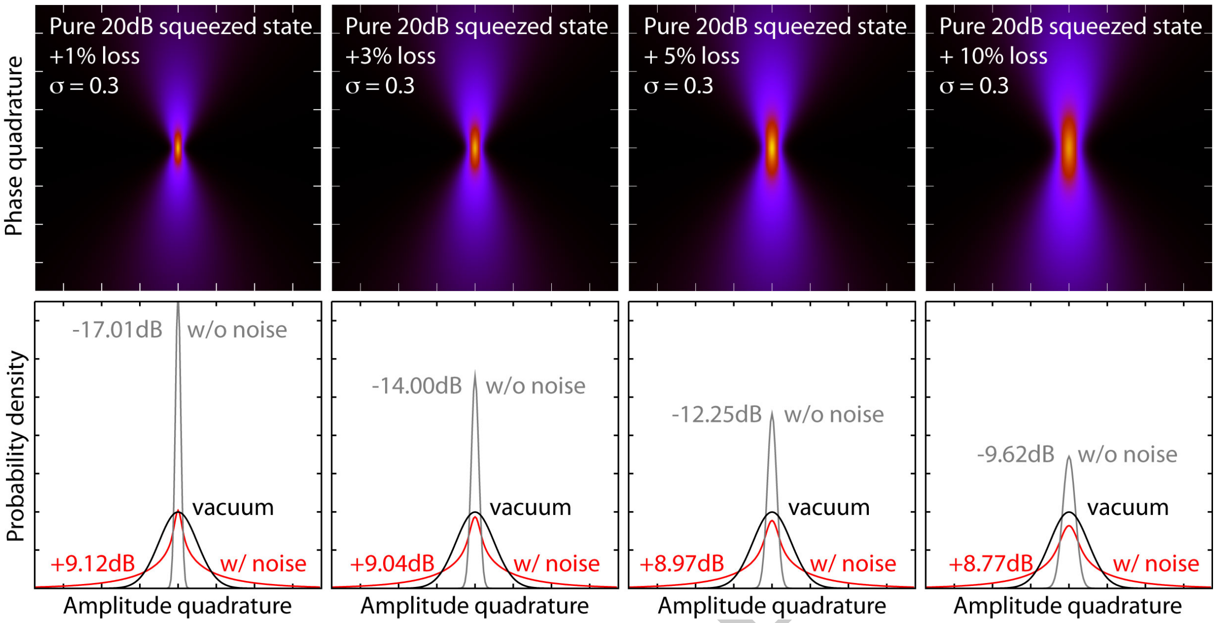

Figure 195: Degradation of a pure 20 dB squeezed state due to optical loss and phase noise.

be utilised that generates considerably more than 10 dB (anti-)squeezing to compensate for possible loss. If an overall optical loss of up to 10 % in the squeezing path (including 1 % loss in the squeezed light source itself) is assumed, an initially pure 20 dB squeezed state needs to be generated. The degradation of the squeezing (and anti-squeezing) level with optical loss is shown in Fig. 194. Whereas the squeezing level is strongly affected by optical loss, the anti-squeezing level is not considerably reduced. Considering an overall optical loss of 10 % the squeezing level is reduced from 20 dB to about 9.6 dB, but the anti-squeezing level is still about 19.5 dB. In Fig. 195 the effect of phase noise on a initially 20 dB squeezed state is illustrated at which optical loss of 1 %, 3 %, 5 % and 10 % was considered. Here the phase noise was assumed with a standard deviation of $\sigma = 0.3$. Again, the top graphs show the Wigner functions and the bottom graphs the probability distribution in the amplitude quadrature. Here, in each case three traces are plotted. The red trace is the distribution of the phase diffused squeezed state and the black one that of a vacuum state. The grey curves correspond to the distribution without phase noise, i.e. the degradation of the squeezing level only due to the considered optical loss can be deduced. Again, it can be seen that the high phase noise destroys the squeezing. In each case, the resulting noise level is considerably enhanced when compared to the shot noise level. Please note the following: although the squeezing levels in the undisturbed case are ≥10 dB, the high anti-squeezing level of almost 20 dB leeds to higher noise levels when compared to the pure 10 dB squeezed state (refer to Fig. 193). I.e, in presence of phase noise the achievable squeezing level can be optimized by reducing the anti-squeezing (and thus the squeezing) generated by the squeezed light source. On the other hand, that means that in presence of considerable phase noise a compensation of optical loss in the squeezing path is not possible by enhancing the squeezing (and thus the anti-squeezing) generated in the squeezed light source.

In the foregone investigation for illustration purpuses comparatively high values for the phase noise was considered. Such high values are not expected to be present in a suitable experimental environment. However, the upper limit for the overall phase noise in the squeezing path depends on the squeezed state, that is generated by the squeezed light source. Table 15 lists the allowed phase noise (i.e its standard deviation) for several conditioned squeezed states. The states were constituted for several values of the optical power loss l^2 such that the squeezing level without phase noise is 10 dB. The required squeezing that needs to be generated inside the squeezed light source can be calculated according to

$$V_s = 0.1 - l^2 \quad \text{and} \quad \mathrm{V_a} = \frac{1}{\mathrm{V_s}}. \tag{169}$$

We relates the upper limit $\sigma_{\max}$ for the phase noise to a squeezing level that is reduced to 9 dB due to the phase noise. As the phase noise is assumed to be Gaussian distributed with zero mean, Eq. (167) can be solved giving

$$V_{X_1,d} = \frac{1}{2}\left[V_s + V_a + (V_s - V_a)\exp\left(-2\sigma^2\right)\right] . \tag{170}$$

Soving Eq. (170) for σ yields

$$\sigma = \sqrt{-\frac{1}{2}\log\left[\frac{2V_{X_1,d} - V_s - V_a}{V_s - V_a}\right]} . \tag{171}$$

From this equation the tolerable phase noise characterised by σ_{max} can be calculated for the targeted variance $V_{X_1,d} = 0.1$ and squeezing level of 10 dB, respectively.

optical loss [%]	initial squeezing [dB]	squeezing [dB]	anti-squeezing [dB]	$\sigma_{\max}$
1	-10.41	-10	10.37	0.049
3	-11.41	-10	11.29	0.044
5	-12.79	-10	12.58	0.038
9	-19.59	-10	19.19	0.018
10	$-\infty$	-10	∞	0
20	$-\infty$	-6.99	∞	0

Table 15: The table lists the squeezing and anti-squeezing levels and the tolerable phase noise for several values of optical loss.

From the tolerable $\sigma_{\max}$ we will deduce in following investigations

- the allowed displacement noise in the filter cavities
- the requirements for the filter cavities' length stabilization
- the requirements of frequency noise of the squeezed light source related to main interferometer beam

5.7.6 Length control of the filter cavities

We will analyse

- the realisation of a locking scheme without introducing too much optical loss (due to pick-off mirrors needed for detection ports).
- the potential of using the orthogonal polarisation for error signal generation.
- the restrictions to RF sidebands. They need to be in the same mode as the squeezing, therefore generated in the squeezer by means of the coherent control beam.
- A ring -vs- a linear filter cavity design. If linear filter cavities are used additional Faraday rotators are required.

5.8 Optical layout

*Author(s): **S. Hild**, A. Thuering, A. Freise*

5.8.1 A xylophone design for ET

Spanning the detection band over four orders of magnitude in frequency, as is ask for third generation GW observatories such as ET, is technically extremely challenging: Different noise types dominate the various frequency bands and often show opposite response for different tuning of the same design parameter.

In the following we give some examples of fundamental issues of a broadband third generation interferometer that could be resolved by using a set of xylophone detectors:

- **High Power vs Cryogenic Temperature**: Using a single broadband ET observatory as described in [248] features the challenge of the simultaneous use of high optical power (a few megawatts) to achive the required high frequency senstivity and test masses at cryogenic temperatures in order to provide the required suppression of thermal noise. Eventhough tiny, the residual absorption of the dielectric mirror coatings deposits heat in the mirrors which is difficult to extract, without spoiling the performance of the seismic isolation systems. A possible solution for this problem would be to build a xylophone observatory consisiting of a high frequency detector featuring high power and high temperature and a low frequency detector featuring low power and cryogenic temperatures.
- **Shot Noise vs Radiation Pressure Noise**: As already briefly described in above it is will be hard to obtain the desired bandwidth with a single detector due to inverse scaling of photon radiation pressure noise and photon shot noise with the circulating power. Therefore, again it might be useful to split ET into a low-power low-frequency and a high-power high-frequency companion.
- **Mixing Interferometer Topologies**: Xylophone configurations will also allow to mix alternative interferometer topologies, such as Sagnac interferometer [366] and optical levers [410], with the standard Michelson interferometer. For example one could imagine to acompany a standard high-frequency Michelson interferometer with a low-frequency optical lever detector.

The xylophone concept was first suggested for Advanced LIGO, proposing to complement the standard broadband interferometers with an interferometer optimized for lower frequency, thus enhancing the detection of high-mass binary systems [484, 485].

One may think that a xylophone might significantly increase the required hardware and its cost by the need to build more than one broadband instrument. However, such an argument does not take the technical simplifications that it would allow, the better reliability of simpler instruments, and the more extensive scientific reach allowable into account. For example splitting a third generation observatory in to a low-power, low-frequency and a high-power high-frequency interferometer, has not only the potential to resolve the above mentioned conflict of PSN and PRPN, but also allows to avoid the combination of high optical power and cryogenic test masses. To reduce thermal noise to an acceptable level in the low frequency band, it is expected that cryogenic suspensions and test masses are required. Even though tiny, the residual absorption of the dielectric mirror coatings deposits a significant amount of heat in the mirrors. Since this heat is difficult to extract, without spoiling the performance of the seismic isolation systems, it imposes a limit on the maximum circulating power of a cryogenic interferometer.

The baseline for ET is a 2-band xylophone detector configuration, composed of a low-frequency (ET-LF) and a high-frequency (ET-HF) detector. Both interferometers are Michelson interferometers featuring 10 km armlength and an opening angle of 90 degree. Due to their similar geometry both detectors will share a single facility. Table 16 gives a brief overview of the main parameters of the analysed low-frequency (ET-LF) and high-frequency (ET-HF) detector. Figure 196 shows sketches of the corresponding core interferometers and the filter cavities. The full layout of the two core interferometers of a single ET detector is depicted in Figure 197.

5.8.2 Arm cavity design

The size and shape of the laser beam inside the interferometer is defined by the surface shape of the cavity mirrors; the beam sizes at the IM and EM as well as the position of the cavity waist are determined by only two parameters, the radii of curvature (ROC) of IM and EM. Since inside the two Fabry-Perot cavities of the

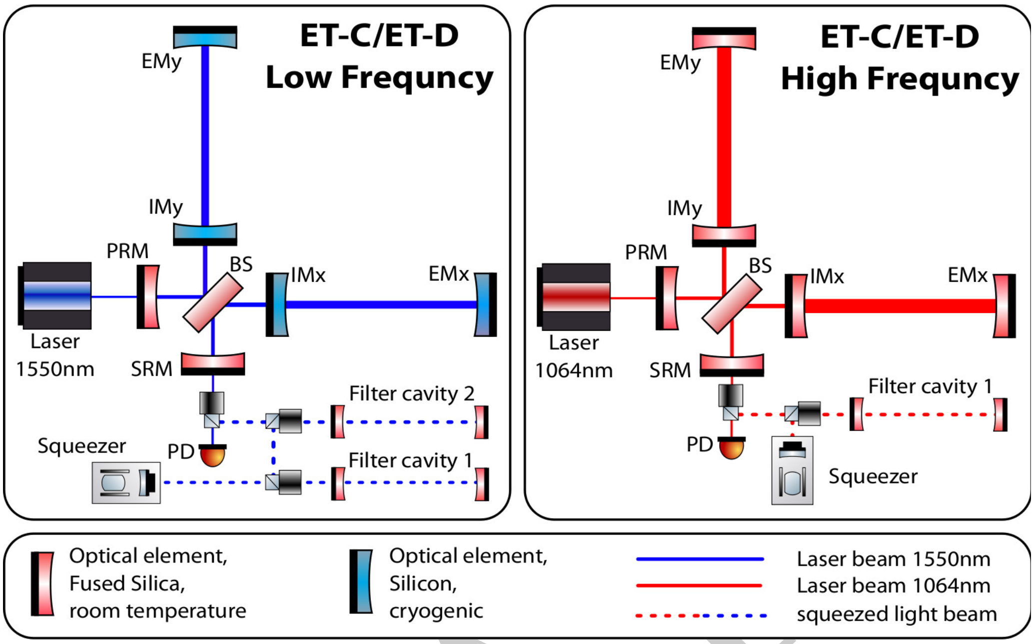

Figure 196: Simplified sketch of the ET low and high frequency core interferometers of a single ET-detector.

Parameter	ET-D-HF	ET-D-LF
Arm length	10 km	10 km
Input power (after IMC)	500 W	3 W
Arm power	3 MW	18 kW
Temperature	290 K	10 K
Mirror material	Fused Silica	Silicon
Mirror diameter / thickness	62 cm / 30 cm	min 45 cm/ TBD
Mirror masses	200 kg	211 kg
Laser wavelength	1064 nm	1550 nm
SR-phase	tuned (0.0)	detuned (0.6)
SR transmittance	10 %	20 %
Quantum noise suppression	freq. dep. squeez.	freq. dep. squeez.
Filter cavities	1×10 km	2×10 km
Squeezing level	10 dB (effective)	10 dB (effective)
Beam shape	LG_{33}	TEM_{00}
Beam radius	7.25 cm	9 cm
Scatter loss per surface	37.5 ppm	37.5 ppm
Seismic isolation	SA, 8 m tall	mod SA, 17 m tall
Seismic (for $f > 1$ Hz)	$5 \cdot 10^{-10}\,\mathrm{m}/f^2$	$5 \cdot 10^{-10}\,\mathrm{m}/f^2$
Gravity gradient subtraction	none	none

Table 16: Summary of the most important parameters of the ET-D high and low frequency interferometers. SA = super attenuator, freq. dep. squeez. = squeezing with frequency dependent angle.

Michelson interferometer the GW interacts with the laser light, creating signal sidebands, the two arm cavities can be seen as the heart of the ET interferometers. The characteristics of the arm cavities have not only a high impact on the detector sensitivity and bandwidth, but also on the overall detector performance.

The choice of the beam size on the arm cavity mirrors is a trade-off process taking the following considerations into account:

- For a given cavity length there is a minimal achievable beam size, which is determined by the divergence of the beam.
- Above this minimal beam size, any further increase in beam size leads to and additional reduction of the various thermal noise contributions.
- Finally the upper limit for the manageable beam size is given firstly by the maximum available mirror substrate size and secondly by the approaching the cavity instability.

Beam waist of the arm cavity beam eigenmode

In the case of a two-mirror cavity the size of the beam can be computed conveniently from the stability parameters g_1, g_2 given as:

$$g_{1,2} = 1 - \frac{L}{R_{C\,1,2}} \tag{172}$$

with L the length of the cavity and $R_{C\,1,2}$ the radius of curvature of the input and end mirror respectively.

The waist size w_0 of the cavity eigenmode can then be computed as :

$$w_0^2 = \frac{L\lambda}{\pi}\sqrt{\frac{g_1g_2(1-g_1g_2)}{(g_1+g_2-2g_1g_2)^2}} \tag{173}$$

In many cases symmetric or near symmetric cavity layout will be used (or can be used to estimate design options). In that case we set $g = g_1 = g_2$ which leads to a much simpler equation:

$$w_0^2 = \frac{L\lambda}{2\pi}\sqrt{\frac{1+g}{1-g}} = \frac{L\lambda}{2\pi}\sqrt{\frac{2R_C}{L} - 1} \tag{174}$$

Beam size on the arm cavity mirrors

Typically we are interested in the size of the beam on the mirror, rather than the waist size directly. The beam size can be computed similarly as the waists; for the input mirror we get:

$$w_1^2 = \frac{L\lambda}{\pi}\sqrt{\frac{g_2}{g_1(1-g_1g_2)}} \tag{175}$$

And in the case of a symmetric cavity we obtain:

$$w^2 = \frac{L\lambda}{\pi}\sqrt{\frac{1}{1-g^2}} = \frac{\lambda}{\pi}\sqrt{\frac{RL}{2-\frac{L}{R}}} \tag{176}$$

Arm cavity mirror size

A common method to define the mirror size is to demand the optical power loss due to clipping (light being lost because it 'falls over the edge of the mirror') to be less than 1 ppm. The computation of the scaling factors is described in [486] and results in:

mode	LG00	LG33
mirror radius to beam radius	2.63	4.31

Minimal mirror sizes for ET

Using the currently discussed options for ET we can compute minimal mirror sizes for various options, by using $L = R_C$ resulting in $w_{\min} = \sqrt{\frac{L\lambda}{\pi}}$.

setup	min beam radius [cm]	min mirror diameter [cm]
LG33, 1064nm	5.8	50.2
LG00, 1550nm	7.0	37.0

Realistic mirror sizes for ET

Using the minimal beam sizes is obviously not optimal in terms of thermal noise. Therefore we intend to push the beam sizes for ET towards the maximum feasible size, which corresponds to about 60 cm substrate diameter for fused silica mirrors and 50 cm for the silica mirrors. Assuming 9.3 km long arm cavities, we can derive the following arm cavity characteristics.

IFO	λ	beam shape	mirror diameter	R_C	w_0	z_0	w	z_R
ET-HF	1064 nm	LG_{33}	62 cm	5147.7 m	2.27 cm	4650 m	7.25 cm	1521.3 m
ET-LF	1550 nm	TEM_{00}	45 cm	5489 m	3.11 cm	4650 m	8.0 cm	1964 m

5.8.3 Central interferometer design

The central interferometers consist of the two recycling cavities and the central Michelson interferometer formed by the beam splitter and the arm cavity input mirrors. The design of the central interferometer is mainly determined by two constraints. First of all it should allow for the implementation of non-degenerate recycling cavities. Second, the central interferometer has to serve as mode matching telescope for the arm cavities.

The non-degenerate recycling cavity design used by the advanced detectors (see Figure 215) can probably not be directly adapted for ET, because no beam splitter substrates of the required dimensions would be available. For example the high frequency interferometer featuring an opening angle of 60 degree would require a beam splitter with a diameter of 115 cm.

Therefore we plan to investigate design options, making us of input mirror substrates including a focussing lens with a focal length of 0.5 to 1 km and shifting the input mirrors away from the beam splitter. Figure 197 illustrates how such a configuration would like. Please note that the arm cavity mirrors are the only full sized optical elements and that beam splitter and recycling mirrors can be significantly smaller. In addition in this scenario no additional folding mirrors are necessary in the recycling cavities.

Layout option for LG00, 1550nm

The optical parameters of a possible solution based on a arm cavity length of $L = 9.3$ km and a LG00 mode at 1550 nm are provided below:

- focussing element in or near the ITM with a focal length of $f = 685$ m
- distance ITM-BS: 700 m
- distance BS-MPR: 10 m
- beam size on BS: 0.95 cm
- beam size on MPR: 0.86 cm
- Rayleigh range in central interferometer: 47.0 m

The recycling cavity formed by MPR and ITM has a length of 710 m and a FSR of 211 kHz. The round-trip Gouy phase is given by ≈ 9.7 deg which corresponds to a mode separation frequency of 11 kHz.

Layout option for LG33, 1064nm

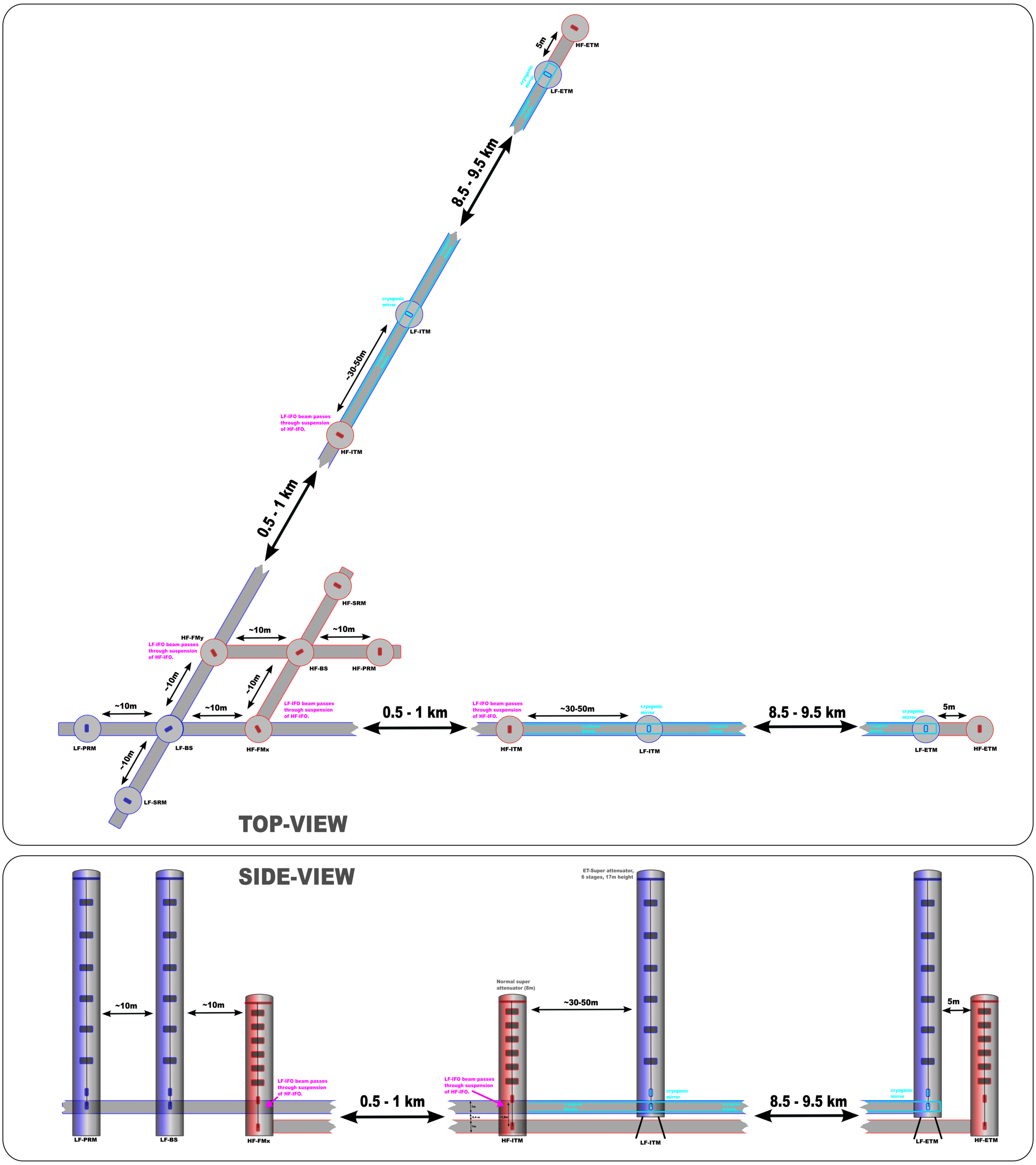

Figure 197: Simplified drawing of the low and high frequency core interferometers of a single ET-detector. Injection and detection optics as well as filter cavities have been omitted for clarity. Please not that the complete ET observatory consists of three such detectors.

Using the same distances and focussing elements for the interferometer with a LG33, 1064 nm beam, we also obtain reasonable numbers:

- beam size on BS: 0.89 cm
- beam size on MPR: 0.81 cm
- Rayleigh range in central interferometer: 40 m
- Gouy phase: 7.6 deg
- mode separation frequency: 9 kHz

These layout options are not yet optimised in any way but they show that a separation between beam splitter and input optics in the order of 700 m represents a useful baseline. The numbers for the beam sizes at the beam splitter and recycling mirrors in both cases need to be checked against a detailed thermal noise computation.

Furthermore, the design needs to be evaluated for losses originating from astigmatisms inside the recycling cavities as well as for scattered noise issues.

5.9 Main interferometer optical components

Author(s): ***K. Kokeyama****, A. Freise, etc.*

As the optical components for ET HF/LF interferomers, silicon, sapphire, and fused silica substrates have been proposed. The substrate materials show different properties and performances depending on the environment especially on the temperature, the material should be properly investigated. The most important elements to be considered are the thermal properties and the surface qualities attained by the material. The thermal and mechanical properties of silicon, sapphire, fused silica will be summarized in Appendix 5.16.

5.9.1 Bulk material selection

Authors: J. Franc, K. Kokeyama, R. Nawrodt

Different materials have been proposed in order to reduce thermal noise of the optics of future gravitational wave detectors. Three main candidate materials are the most promising ones to construct a 3rd generation detector: Fused Silica, Sapphire and Silicon.

Fused Silica is the favorite substrate material for an interferometer or components of an interferometer that operates at room temperature. It is the substrate material of the advanced detectors and will be used as test masses in Advanced LIGO and Advanced Virgo. Due to the extensive use of fused silica for first and second generations of gravitational wave detectors, this material has been extensively characterised at room temperature. For example, fused silica exhibits very low optical absorption (as low as 1 ppm/cm at 1064 nm and below) with high homogeneity and low birefringence. Driven by the research effort for the Advanced detectors a state of the art polishing and coating technique exists that provide excellent specifications. Micro-roughnesses of better than 0.05 nm RMS and flatnesses of better 8 nm RMS on ⌀ 150 mm have been achieved. Moreover, Fused Silica is available in large pieces with an extremely high purity. Additionally, there exist techniques to fabricate quasi-monolithic suspensions based on pulled fused silica fibres and silicate bonding. These techniques have demonstrated their reliability for years in the GEO600 detector [310, 311]. This convincing result triggered the implementation of this technique in Advanced LIGO [312–314] as well as Advanced Virgo [487, 488]. Fused Silica has a very low mechanical loss at room temperature exceeding 4×10^{-10} at 100 Hz [341]. The coefficient of thermal expansion is extraordinary low at room temperature providing a small thermo-elastic noise of the bulk material. However, the mechanical loss increases as the temperature is decreased (see e.g. [489, 490]) reaching values as high as 10^{-3} at 10 K. This would result in a high substrate Brownian noise and makes Fused Silica not suitable for optics operated at low temperatures. Additionally, the thermal conductivity of Fused

Silica decreases to 0.4 W/mK at 10 K [491] which is more than 1000 times smaller than for typical crystalline materials.

The second candidate material is Sapphire. This material are under consideration as a test mass material for LCGT (Large-scale Cryogenic Gravitational-wave Telescope) in Japan [492]. Hence, Sapphire mirrors have been investigated regarding their performance at cryogenic temperatures. Sapphire has a small coefficient of thermal expansion. Below 20 K it can be approximated by $\alpha = 7.5 \times 10^{-13} T^3 [K^{-1}]$ [493]. This leads to a very small thermo-elastic noise at low temperature regime. The mechanical loss of Sapphire has been determined from Q-factor measurements. At 4.2 K losses of 4×10^{-9} and at 20 K of 10^{-8} have been observed [494]. The measured sample was a CSI (Crystal System) Hemlite grade. Additional excellent properties like the high thermal conductivity at low temperatures make Sapphire a good candidate as a bulk material for cryogenic optics. The optical absorption at 1064 nm has been measured by the LCGT group to be about 90 at 5 K [492]. They report that the absorption is temperature dependent reaching 168 ± 24 ppm/cm at room temperature. The value of the absorption is an important property influencing effects like thermal lensing and cooling the mirror. In both cases - at room temperature and cryogenics - the sapphire substrate has about ten to hundred times higher absorption than that of typical Fused Silica. This may cause the thermal lensing effects in a cryogenic interferometer based on Sapphire because the strain due to the thermal lens effect is proportional to the absorption, thermal coefficient of refraction, and input power. However, this does not completely deny the sapphire option, as there are investigations to lower the sapphire absorption by annealing [495]. As artificial sapphire crystals are broadly used in industries (e.g. as laser rods, heat sinks, etc.) there are many Sapphire manufacturers available. The biggest currently available crystal is $\varnothing\, 330 \times 200$ mm, 65 kg manufactured by an American company Crystal System (CSI) [496]. This size is not enough for a potential use in the ET LF interferometer. Here, a mirror with a minimum mass of 211 kg is proposed due to the suppression of the radiation pressure noise. This corresponds to a mirror of about $\varnothing\, 620 \times 180$ mm which is far away from a current availability. Additionally, the quality of such a large crystal is supposed to be not enough yet. When the c-axis of the crystal and the beam axis are different, optical losses occurs. Therefore the cylinder shape of the mirror must be produced precisely along the c-axis. Also, the deviation between the beam axis and the c-axis increases the birefringence. The currently measured birefringence of sapphire with 250 mm diameter indicated that the birefringence level exceeds the LCGT requirement of the fringe contrast by three times [497]. As an another current technical issue, there is no known way to bond sapphire wires onto the sapphire substrate with sufficient strength which would be important for the fabrication of a low thermal noise quasi-monolithic suspension [320]. To suspend the mirror and to extract the heat from the substrate, the bonding should be done with the enough strength while keeping the thermal conductivity. Despite all the issues, it is still anticipated to have large crystals using the high-quality smaller crystals as a seed crystal and growing to a bigger crystal with keeping the quality [496], and sapphire mirrors will be employed by the LCGT interferometer within several years.

The third candidate material that has been proposed as a future detector material is silicon [334, 498]. Silicon has excellent mechanical and thermal properties and is available in high quality due to the large market of the semiconductor industry. The coefficient of thermal expansion is zero at two special temperatures around 18 and 125 K [499]. At these temperatures the contribution of thermo-elastic noise will therefore vanish. The mechanical loss of silicon has been studied by Q-factor measurements. It was experimentally shown that Silicon bulk samples can reach mechanical losses as low as 5×10^{-10} at 2 K, 1×10^{-9} at 10 K, 4×10^{-9} at 20 K and 5×10^{-9} at 30 K [332]. Intensive studies are in progress to link the mechanical loss of the bulk samples with the purity, surface preparation or the crystal orientation of the sample. Due to the huge demand of high purity silicon wafers for the semiconductor industry silicon bulk samples are available in relative large pieces. The available sample diameter is dependent on the fabrication process. The two main growing processes for single crystal silicon used in semiconductor industry are the Czochralski (CZ) and the Float Zone (FZ) method. CZ grown silicon is grown from a silicon melt in a silica crucible. It results in relative large samples with a reasonable purity. The most dominant impurities in undoped CZ grown silicon are carbon (typically 10^{18} cm^{-3}) and oxygen (typically up to 10^{19} cm^{-3}). In contrast, FZ silicon contains these impurities typically with much smaller concentrations (up to 10^3 times smaller). Single or poly-crystalline silicon is remelt by means of inductive heating in vacuum or under an inert atmosphere during the FZ process. Impurities dissolve better in the melt than in the solid part. The re-crystallised material has therefore a higher purity than the initial one. By slowly sweeping the melt from one end to the other it is possible to purify in steps. The mechanism of inductive heating

Parameter	T (K)	Fused Silica Value	Fused Silica Ref.	Sapphire Value	Sapphire Ref.	Silicon Value	Silicon Ref.
heat capacity (J/kg K)	10 K	6.3	[329]	0.085	[503]	0.276	[504]
	20 K	25.2	[329]	0.72	[503]	3.41	[504]
	30 K	54.6	[329]	2.6	[503]	18.55	[504]
	300 K	738	[329]	781	[503]	713	[504]
thermal conductivity (W/m K)	10 K	0.098	[316]	2900	[316]	2110	[315]
	20 K	0.13	[316]	15700	[316]	4940	[315]
	30 K	0.18	[316]	20700	[316]	4810	[315]
	300 K	1.5	[316]	46	[316]	148	[315]
thermal expansion coefficient (1/K)	10 K	-2.2×10^{-7}	[331]	1.0×10^{-9}	[503]	8.8×10^{-10}	[504]
	20 K	-5.8×10^{-7}	[331]	4.0×10^{-9}	[503]	-2.5×10^{-9}	[504]
	30 K	-8.0×10^{-7}	[331]	1.6×10^{-8}	[503]	-5.3×10^{-8}	[504]
	300 K	5.0×10^{-10}	[331]	5.6×10^{-6}	[503]	2.7×10^{-6}	[504]
mechanical loss	10 K	7.9×10^{-4}	[490]	5×10^{-9}	[494]	1×10^{-9}	[332]
	20 K	1.0×10^{-3}	[490]	5.6×10^{-9}	[494]	4×10^{-9}	[335]
	30 K	1.0×10^{-3}	[490]	1.4×10^{-8}	[494]	5×10^{-9}	[332]
	300 K	4×10^{-10}	[341]	3.8×10^{-9}	[333]	1×10^{-8}	[335]
dn/dT (1/K)	10 K	–	–	$< 9 \times 10^{-8}$	[505]	$< 1 \times 10^{-6}$	–
	20 K	–	–	$< 9 \times 10^{-8}$	[505]	1×10^{-6}	–
	30 K	1×10^{-6}	[506]	$< 9 \times 10^{-8}$	[505]	3.3×10^{-6}	[502]
	300 K	8×10^{-6}	[507]	1.3×10^{-5}	[508]	1.9×10^{-4}	[502]

Table 17: Temperature dependent thermal parameters for fused silica, sapphire and silicon bulk material used for thermal noise estimates at selected temperatures. dn/dT is given at 1064 nm for Fused Silica and Sapphire and at 1550 nm for Silicon.

sets limits to the currently available setups and leads to smaller currently available samples[9]. Well established polishing methods exist for silicon due to the wafer fabrication. Micro roughnesses and flatnesses needed for optical applications can be achieved. Additionally, silicon provides the possibility of jointing pieces by means of bonding techniques (see also section 4.6). Two possible techniques under discussion are anodic bonding and the well establish hydroxide catalysis bonding [320, 321] currently in use in 1st and 2nd generation detectors. Using silicon as a test mass material demands a change in operational wavelength. Silicon is not transparent at 1064 nm (optical absorption: approximately 10^{-1} at 1064 nm [500]). Silicon has a smaller optical absorption at longer wavelengths. Erbium-fibre lasers provide a reliable light source in the IR spectrum. At 1550 nm silicon is transparent and can be used as an standard optical material in reflection and transmission applications. Optical absorption measurements based on the creation of electron-hole-pairs suggests a minimum absorption of 3.2×10^{-2} at 1450 nm at room temperature [501]. However, a detailed analysis of absorption processes and the total optical absorption of silicon at 1550 nm and low temperatures does not exist so far. A similar lack of parameters exists for other optical properties like the refraction index n or the thermo-refractive coefficient dn/dT [502]. Currently, several institutions worldwide investigate these optical properties. Several institutions involved in this design study play a key role in this research.

A detailed description of the mechanical and thermal properties of Fused Silica, Sapphire and Silicon can be found in appendix 5.16.2 and appendix 5.16.3. Selected literature values at 10, 20, 30 and 300 K have been summarized in table 17 and 18. These values have been used for all thermal noise estimates presented within this document.

[9] There is still no technical limit reached for the float zone process of silicon. The maximum diameter currently available is set by the demands of the semiconductor market.

Parameter	Fused Silica		Sapphire		Silicon	
	Value	Ref.	Value	Ref.	Value	Ref.
density ρ (kg/m^3)	2202	[507]	3980	[507]	2330	[507]
Youngs modulus Y (GPa)	72	[507]	400	[507]	188	[507]
Poisson ratio ν	0.17	[507]	0.24	[499]	0.22	[507]
refractive index	1.45	[507]	1.75	[507]	3.453	[507]

Table 18: Parameters of bulk materials that are assumed to be temperature independent for the thermal noise calculations. The refractive index of Fused Silica and Sapphire is given at 1064 nm whereas this parameter is listed at 1550 nm for Silicon.

X	SiO_2	Al_2O_3	$Ti:Ta_2O_5$	Ta_2O_5	TiO_2	Nb_2O_5
Loss angle	0.5×10^{-4}	2.4×10^{-4}	2×10^{-4}	3.8×10^{-4}	6.3×10^{-3}	6.7×10^{-4}
Density ($kg\,m^{-3}$)	2200	3700	6425	6850	4230	4590
Thermal conductivity ($Wm^{-1}K^{-1}$)	0.5	3.3	0.6	0.6	0.45	1
Specific heat ($JK^{-1}kg^{-1}$)	746	310	269	306	130	590
Thermal expansion coefficient (K^{-1})	0.51×10^{-6}	8.4×10^{-6}	3.6×10^{-6}	3.6×10^{-6}	5×10^{-5}	5.8×10^{-6}
Thermo-optic coefficient (K^{-1})	8×10^{-6}	1.3×10^{-5}	14×10^{-6}	2.3×10^{-6}	-1.8×10^{-4}	1.43×10^{-5}
Young modulus (GPa)	60	210	140	140	290	60
Poisson's ratio	0.17	0.22	0.23	0.23	0.28	0.2
Refractive index	1.45	1.63	2.06	2.03	2.3	2.21

Table 19: List of the optical and mechanical values of different coating material at 300 K.

5.9.2 Coating material selection

J. Franc

Fabrication of 3rd generation of GWD has specific constraints on noise level. Several studies have already demonstrated that coating is the most important noise source in the frequency range of interest. To avoid that coating materials generate a noise level larger than the expected sensitivity, very high quality coating are needed. First, the absorption have to be less than 5 ppm and the loss angle of the material have to be as low as possible. To produce coating with such quality, an IBS coater is needed. Driven by the research performed for 1st and 2nd generation of GWD, a state of the art deposition technique exists that provide high performances coatings [?]. The concept of high reflective mirrors fabrication is based on the quarter-wavelength layer system composed from two materials, one with high refractive index and one with a low refractive index. At first, the work considered SiO_2 as the low refractive index material (n=1.45) and Ta_2O_5 as the high refractive index material (n=2.03). These two material were the oxide layers having the best optical and mechanical properties. In the past, this multilayer system has offered the best mirror quality for VIRGO interferometer but was improved in the future for the Advanced detector. The measurements made on the Ta_2O_5/SiO_2 coatings have shown that the lossier material is the Ta_2O_5. The improvement has been focused on this latter. Several doped material were tested to improve the mechanical losses of Ta_2O_5. By doping Ta_2O_5 with Ti and with an optimization of the deposition process, it is possible to decrease the losses of high refractive index material from 3.8×10^{-4} to 2×10^{-4}. To date, other materials were considered for doping the Ta_2O_5 layers. New materials should be also considered to replace the Ta_2O_5 layers with another high refractive index material. In this context, a table with the parameters values needed for thermal noise calculation for different coating materials is presented [491]:

I. Martin

Extensive studies of the temperature dependence of the mechanical loss of tantala (Ta_2O_5) have been undertaken and the effects of post-deposition heat-treatment and of doping with titania (TiO_2) have been investigated [342–344]. In general the loss increases at low temperature, with three loss peaks observed to occur at different heat-treatment temperatures. Tantala heat-treated at 300°C and 400°C exhibited a loss peak at approximately 35 K. A larger and narrower loss peak was observed at 20 K in tantala coatings heat-treated at 600°C. There is some evidence that the 35 K peak may also be present in tantala heat-treated at 600°C, underlying the peak at 20 K. It is known that ion-beam sputtered tantala crystallises at when heated above approximately 650°C. A large and very broad loss peak has been observed in tantala heat-treated at 800°C. While of interest for studies of the loss mechanisms in tantala, crystallised tantala is not suitable for use in an HR coating due to its poor optical properties.

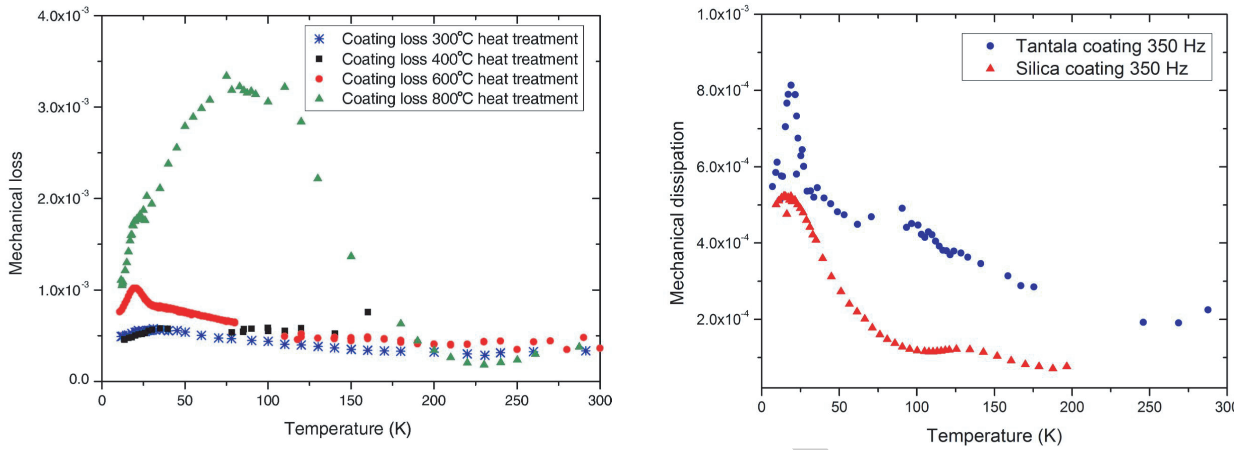

(a) (b)

Figure 198: (a) - Measured values of the coating loss of tantala annealed at different temperatures. (b) - Comparison of 600°C heat treated tantala and silica coatings at low temperatures and 350 Hz.

Further work may be required to establish the optimum heat-treatment temperature for a silica/tantala multilayer coating for use at cryogenic temperature. High heat-treatment temperatures are generally desirable for optimal optical properties. Furthermore, studies of the mechanical loss of ion-beam sputtered silica coatings have shown a systematic reduction in the loss at room temperature with increasing heat-treatment temperatures. Thus carrying out heat-treatment at the maximum temperature which can be achieved without inducing crystallisation in the tantala layers may be desirable. However, as shown in Figure 198(a), tantala has a significantly lower loss at temperatures below 100 K when heat-treated at lower temperatures (300 or 400°C) than when heat-treated at 600°C. While the loss of the tantala layers dominate the loss of a multilayer silica/tantala coating at room temperature, the loss of ion-beam sputtered silica has a similar magnitude as the loss of tantala at temperatures below 50 K. Thus further studies of the effect of heat-treatment on the temperature dependence of the mechanical loss of ion-beam sputtered silica are also required to allow the optimal heat-treatment temperature to be chosen. In addition, measurements of the temperature dependence of the optical properties of the coating may be required.

A comprehensive summary of R&D activites needed for understanding and characterising the coating properties can be found in section 5.15.2.

5.9.3 Thermal noise estimates for reflective components

Author: R. Nawrodt

Thermal noise of a fully reflective mirror comprises of thermal noise arising from the bulk material and the coating. The bulk material thermal noise itself consists of Brownian thermal noise and thermo-elastic noise. Brownian noise represents the thermal fluctuations ('Brownian motion') of the atoms within the bulk material and is dependent on the sample temperature T and the mechanical loss of the bulk material ϕ [509, 510]:

$$S_{\mathrm{x}}^{\mathrm{bulk}} = 2k_{\mathrm{B}}T\frac{1-\nu}{\pi^{3/2}fYw}\phi \tag{177}$$

with the Boltzmann constant k_{B}, the frequency f, the beam radius w, the substrate Poisson ratio ν and Youngs modulus Y. It is obvious that the Brownian thermal noise is only dependent on mechanical properties of the material.

The thermo-elastic noise of the bulk material is created by statistical temperature fluctuations. By means of the coefficient of thermal expansion α these fluctuations are translated into displacement noise. The thermo-elastic spectral noise density is given by [511]:

$$S_{\mathrm{TE}}^{\mathrm{bulk}} = \frac{4k_{\mathrm{B}}T^2\alpha^2(1+\nu)^2\kappa}{\sqrt{\pi^5}\rho^2C^2f^2w^3} \tag{178}$$

with the coefficient of thermal expansion α, the thermal conductivity κ, the heat capacity C nd the mass density ρ. This equation is valid if the thermal diffusion lengths

$$l_{\mathrm{th}} = \sqrt{\frac{a^2}{f}} \tag{179}$$

of the material is smaller than the beam diameter. The parameter $a^2 = \kappa/(\rho C)$. This assumption is called the adiabatic case. During one period of oscillation all temperature fluctuations that are present at the observation volume stay inside this volume. If the thermal diffusion lengths gets larger (e.g. by means of high thermal conductivity or low frequencies) the thermo-elastic effect gets weaker. Especially, for low temperature applications this non-adiabatic correction becomes important and reduces the contribution of thermo-elastic noise further. This correction has been taken into account for all calculations presented in this document. Details of the calculation can be found in [512, 513].

Figure 199 compares the Brownian and thermo-elastic noise of one single mirror made of fused silica, sapphire or silicon at 10 and 300 K. The parameters used for the calculation are listed in table 17 and 18.

At room temperature fused silica provides the lowest level of thermal noise due to its low mechanical loss and small coefficient of thermal expansion (see figure 199(a)). All crystalline materials show a high coefficient of thermal expansion and thus a large thermo-elastic noise. Therefore, crystalline materials need to be avoided at room temperature detectors in order to achieve the minimum thermal noise level of a mirror substrate.

In contrast, at low temperatures fused silica has a large mechanical loss reaching values of 10^{-3} around 10 K. Crystalline materials behave differently resulting in a low mechanical loss of better 10^{-8} at low temperatures (see tab. 17). Additionally, the coefficient of thermal expansion is very small at low temperatures. This reduces dramatically the thermo-elastic noise contribution compared to room temperature operation (see figure 199(b)). Thus, using cryogenic temperatures and crystalline materials will result in a low total bulk thermal noise.

Figure 200 compares the total bulk thermal-noise consisting of thermo-elastic and Brownian thermal noise for sapphire and silicon at selected temperatures. Due to the small mechanical loss and coefficient of thermal expansion a low thermal noise level is achieved. At 20 K both materials show a comparable thermal noise level. At higher temperatures thermo-elastic noise becomes dominant. Here, sapphire has a slightly lower level of thermo-elastic noise due to the combination of its thermal properties (mainly the high thermal conductivity). At 10 K silicon has a slightly lower total thermal noise as a sapphire mirror substrate.

All calculations so far are based on semi-infinite mirror substrates. This assumption is true for a first comparison of the materials and in cases where the beam radius compared to the mirror radius is small. However, for an application in gravitational wave detectors it is preferable to increase the beam diameter to the maximum possible size that is in agreement with the optical clipping losses. The corrections for finite size test masses has been made by different authors for the different noise contributions. The calculations are quite long and thus only the results are shown here. The detailed discussion can be found in the literature [514, 515].

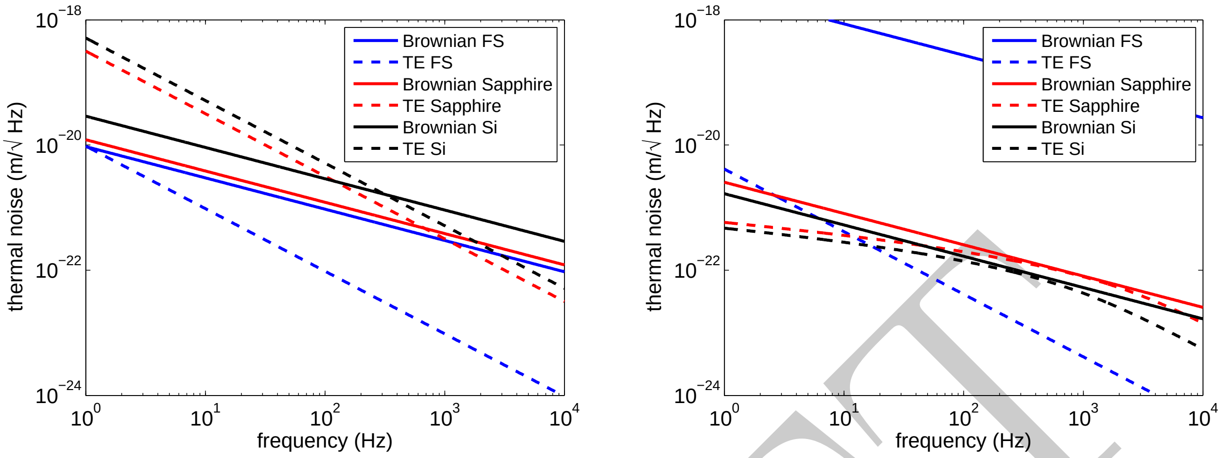

(a) (b)

Figure 199: Comparison of the Brownian and thermo-elastic noise for fused silica, sapphire and silicon at 300 K (a) and 10 K (b) (TE - thermo-elastic noise, FS - fused silica). At room temperature the crystalline substrate materials show a large thermo-elastic noise. In contrast, at cryogenic temperatures fused silica has a large Brownian thermal noise due to its large mechanical loss.

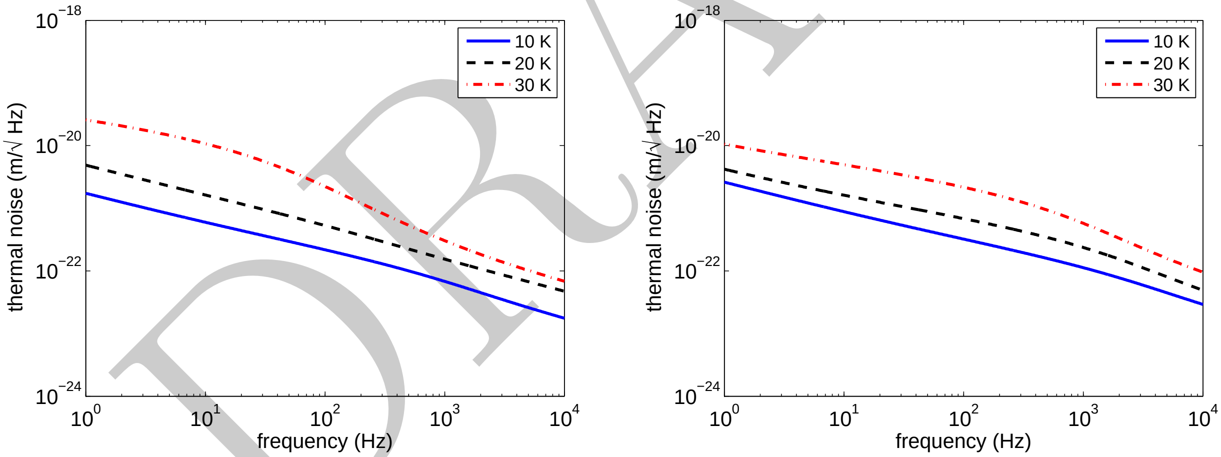

(a) (b)

Figure 200: Comparison of the total bulk thermal noise of a mirror substrate made of silicon (a) and sapphire (b) at different temperatures. The parameters used for this calculation are summarised in table 17 and 18.

Figure 201 gives the dependence of the substrate thermal noise. It is obvious that for reasonable thicknesses the substrate the correction is small. Only for very thin substrates a strong deviation from the simplified infinite half space model appears. At larger thicknesses the finite sample correction leads to a small decrease in thermal noise (approx. 5...10% for bulk Brownian and less than 1% for bulk thermo-elastic noise).

Optical components being used in GW detectors consist of a bulk material and a coating. The coating usually comprises of several alternating dielectric layers formed by high and low refractive index materials. Typically, these layers are formed by amorphous tantala and silica layers with an optical thickness of $\lambda/4$. The circulating laser beam of the interferometer interacts mainly with the coating (point of first contact between light and

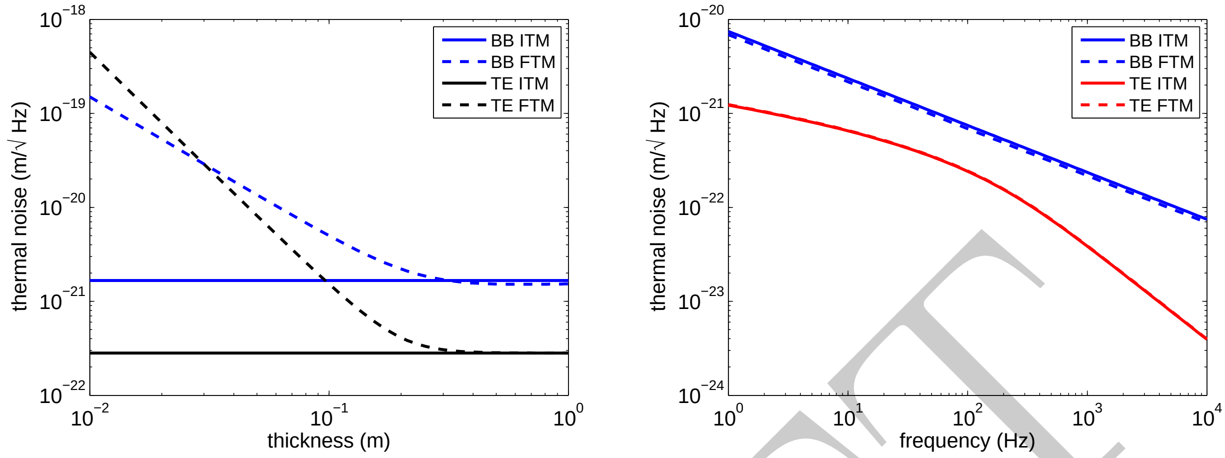

(a) (b)

Figure 201: Finite size test mass mirror thermal noise. (a) - Dependence of the mirror Brownian and thermo-elastic thermal noise of the thickness of the substrate (silicon, 10 K, diameter: 0.5 m, frequency 10 Hz). (b) - Effect of the finite size correction for a typical ET end mirror geometry (silicon, 10 K). BB - bulk Brownian, TE - thermo-elastic, ITM - inner test mass, ETM - end test mass.

matters). Thus, it can be expected that the optical coating contribute strongly to the total thermal noise of a mirror.

Similar to the thermal noise of the bulk materials coatings show Brownian thermal noise. It is again dependent on the temperature T and the effective mechanical loss ϕ_{eff} of the coating [509, 510]:

$$S_{\mathrm{x}}^{\mathrm{coating}} = 2k_{\mathrm{B}}T\frac{1-\nu}{\pi^{3/2}fYw}\phi_{\mathrm{eff}} \tag{180}$$

with the Boltzmann constant k_{B}, the frequency f, the beam radius w, the Poisson ratio ν and the Young's modulus Y of the substrate bulk material. The effective mechanical loss contains all coating relevant parameters and is given by:

$$\phi_{\mathrm{eff}} = \frac{t}{\sqrt{\pi}w}\left(\frac{Y}{Y_{\perp}}\phi_{\perp} + \frac{Y_{||}}{Y}\phi_{||}\right). \tag{181}$$

This description of the effective mechanical loss assumes small Poisson ratios of the coating materials which is usually fulfilled. t is the total thickness of the coating layer. The Young's moduli Y_i, the thicknesses t_i and the mechanical losses ϕ_i are combined as follows (i=1,2 to indicate the different coating layer properties):

$$Y_{\perp} = \frac{t_1+t_2}{\frac{t_1}{Y_1}+\frac{t_2}{Y_2}}, \tag{182}$$

$$Y_{||} = \frac{Y_1t_1+Y_2t_2}{t_1+t_2}, \tag{183}$$

$$\phi_{\perp} = \frac{Y_{\perp}}{t_1+t_2}\left(\frac{t_1}{Y_1}\phi_1+\frac{t_2}{Y_2}\phi_2\right) \tag{184}$$

$$\phi_{||} = \frac{Y_1t_1\phi_1+Y_2t_2\phi_2}{Y_{||}\left(t_1+t_2\right)} \tag{185}$$

Light penetrates the first dielectric layers of a high-reflective mirror and thus interacts not only with the front surface. Here, a fluctuating local temperature causes a change in the thickness of the layer by means of the coefficient of thermal expansion α and additionally a change of the refractive index n of the materials. In total, these two effects sum up and change the optical path of the light being reflected. This statistical process combining effects of thermo-elastic (due to α) and thermo-refractive (due to the change of n) is called thermo-optical noise. Depending on the sign of α and dn/dT these two effects can result in a smaller noise than the two terms predict separately.

Thermo-optical noise can be calculated following [?]:

$$S_{\mathrm{TO}}^{\mathrm{coating}} = ... \tag{186}$$

with ... Will be included after the Amsterdam meeting for completeness. Level of noise is more than an order of magnitude smaller than other noise sources -> not important for the design. Responsible: R. Nawrodt

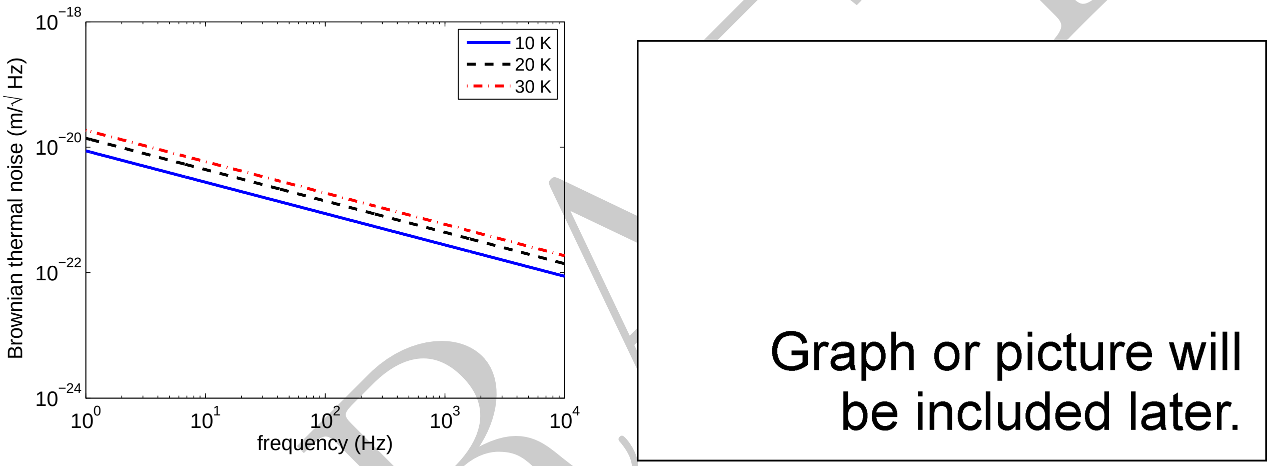

(a) (b)

Figure 202: (a) – Comparison of coating Brownian noise at different temperatures. (b) – Comparison of coating thermo-optical and Brownian noise at room temperature.

Figure 202 compares the Brownian and thermo-optical noise levels of different coatings at low temperatures and room temperature. Parameters are used from tables 16, 17, 18 and 19. A direct comparison reveals that the thermo-optical noise is much smaller than the coating Brownian noise. The level of coating Brownian noise is additionally larger than the total noise level of the bulk material presented in figure 200. Thus, coating Brownian noise is the most important type of thermal noise of a high reflective mirror and great care must be taken in choosing the optimum operational temperature and to choose the appropriate material combination. Details of the ongoing and future research are given in section 5.15.

5.9.4 Thermal noise estimates for transmittive components

J. Franc

The total thermal noise of a transmittive component considers the noise contribution described in the previous subsection and additionally the thermo-refractive noise that occurs from statistical fluctuations of the refractive index n due to its temperature dependence dn/dT. A temperature fluctuation produces a small change of n which leads to phase changes detected by the interferometer.

The thermo-refractive noise has been calculated by equations given by Braginsky [516] in addition with correction terms developed by Benthem and Levin [517].

Taking into account the configuration of Einstein telescope given in figure **??** and table **??** results in the following equation for the thermo-refractive noise in an interferometer with arm cavities of a finesse F:

Crosscheck by Janyce - break up equation into two lines if needed

Equation excluded - did not compile after changes. Please check.

$$\sqrt{S_h(f,T)} = 2\sqrt{2}\frac{1}{L}\frac{\lambda}{8F} \tag{187}$$

$$\sqrt{(kl\beta)^2 \frac{4kbT^2\kappa}{(C\rho)^2 l}\left(1+\frac{(kn)^2 w^2}{\left(1+\left(2kn\sqrt{\frac{\kappa}{C\rho\omega}}\right)^4\right)}\right)\int_0^\infty \frac{k_i dki}{2\pi}\exp\left(\frac{-Rb^2k_i^2}{2}\right)\frac{k_i^2}{\omega^2+a^4k^4}}, \tag{188}$$

with : l is the thickness of the input mirror, β the thermo-optic coefficient of the substrate material, T is the temperature, k_B the Boltzmanns constant, κ the thermal conductivity, C the specific heat, ρ the density of the substrate material, R_b the size of the laser beam which one?, L the arm length of the interferometer and the refractive index n of the substrate material. Details of this equation can be found in [518].

At 300 K, silica substrate provide the lowest Thermorefractive noise (see figure 203. Substrate materials with low thermo-optic coefficient show a low thermo-refractive noise. For information, for silica, sapphire and silicon, it is respectively 8×10^{-6}, 1.3×10^{-5} and 5.15×10^{-5}.

Then, the thermo-refractive noise is compared for silicon and sapphire as the most promising test mass materials at cryogenic temperatures. The substrate thermo-refractive noise is largely dependent on the thermo-optic coefficient. This values has been measured for sapphire at low temperatures and reaches $9 \times 10^{-8}\,1/K$ at around 20 K [?]. For silicon the parameter is not very well known. The currently only literature source reports values of n and dn/dT down to 30 K [502]. However, the values reported for dn/dT do not agree with the slope of the $n(T)$ curve. Thus, the knowledge of the parameter is strongly limited. A detailed discussion what can be estimated at temperatures below 30 K can be found in [?]. At temperatures around 20 K a value of $1 \times 10^{-6}\,1/K$ can be assumed as an upper limit of dn/dt based on the experimental values given in [502]. At even lower temperatures it is reasonable to assume a further decrease of the value due to thermodynamical assumptions: At 0 K all temperature dependent properties have to become constant - thus the temperature derivative has to vanish.

Figure 204(a) shows the thermo-refractive noise of silicon and sapphire at 10 K based on equation (**??**) given above. The dn/dT for silicon is assumed as $1 \times 10^{-6}\,1/K$ and the dn/dT for sapphire is $9 \times 10^{-8}\,1/K$

The sapphire shows a very small thermo-refractive noise. Although it is higher, the thermorefractive noise of silicon substrate is also very low and should not affect the total thermal noise of the system. The operational frequency of the LF detector is between 1 and 250 Hz. Above this frequency the HF detector takes over and limits the sensitivity of the Einstein Telescope. These estimates are based on reasonable upper limit extrapolation values for dn/dT. It is expected that an experimental values for the thermo-refractive coefficient of silicon is even lower than given here.

Figure 204(b) shows the evolution of the thermo-refractive noise for different temperatures (10 K, 20 K, 30 K). It shows that the thermo-refractive noise decreases with the temperature. Thus, operating at the highest possible temperature that allows a low thermal noise operation is preferred. This leads to an optimization process that is described in section 5.9.5.

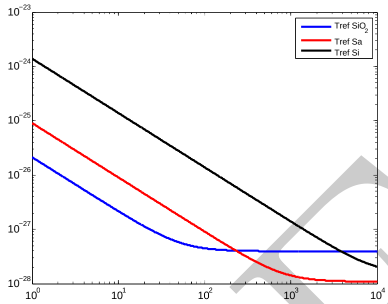

(a)

Figure 203: Substrate Thermorefractive noises for silica, sapphire and silicon at room temperature

5.9.5 LF interferometer large mirror definition

Author(s): J. Franc

Recently, a new estimation of ET detector has been provided (referred to ET-D sensitivity ([**?**]). This new sensitivity assumes a reduced radius beam size of 9 cm, corresponding to an effective test mass diameter of 45 cm, but at the same time keep the overall test mass weight at about 200 kg ([**?**]). This mass leads to a thickness for a future silicon test mass of 50 cm approximately. The thickness drops to more or less 30 cm for Sapphire due to the higher material density. In the case of substrate thermo-refractive noise is dependent on the thickness of the mirror. The thickness of the future test mass will be confirm subsequently. The following simulation are therefore given for information only and are open to improvement in the next months.

Figure 205 shows that Silicon and Sapphire Thermorefractive noises are below the ET sensitivity target. Therefore, we can foresee that these dimensions are potential and promising. To be more precise, the plot of all the thermal noises have been performed for Silicon and Sapphire (Figure206).

For silicon mirror, thermal noises are dominated by coating brownian noise and substrate thermo-refractive. Nevertheless, Coating Brownian noise is, in reality, higher than all other noises considered but still below ET sensitivity target. For sapphire substrate, coating brownian noise is also the highest thermal noise. Therefore, a cooled silicon (or sapphire) mirror provides a low enough thermo-refractive noise in the frequency band covered

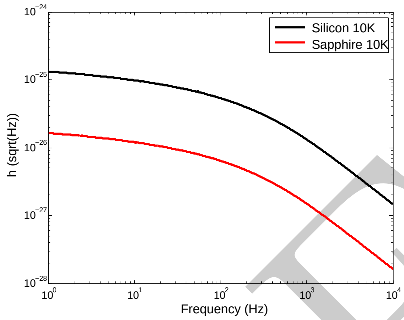

(a)

Figure 204: (a) - Substrate thermo-refractive noise of silicon and sapphire at 10 K (beam size: 9.6 cm). (b) - Substrate thermo-refractive noise of silicon at 10 K, 20 K, 30 K (dn/dT unchanged:1×10^{-6} $1/K$.

Figure 205: Substrate thermorefractive noise of Silicon (w : 9 cm, thickness 50 cm) and Sapphire (w : 9 cm, thickness 30 cm) substrate compared to ET-D sensitivity target

by the LF detector and HF detector.

The figure 207 compares the total thermal noises of reflective silicon mirror at four different temperatures : 10 K, 20 K, 30 K and 40 K. At 10 K and 20K, Silicon remains a good candidate because its total thermal noise is below the ET sensitivity target. From 30 K, Silicon is unsuitable owing to the substrate thermoelastic noise that increases at low frequency and goes above the ET sensitivity.

In conclusion, both materials - sapphire and silicon - provide low thermo-refractive noise levels that are compatible with the requirements for the Einstein Telescope. An exact estimate of the thermo-refractive noise level of silicon will not be possible until the thermo-refractive coefficient is measured for different types of silicon. It can be expected that this parameter strongly depends on the level of doping. Several institutions are currently working on experiments to extend the existing parameters to temperatures below 30 K.

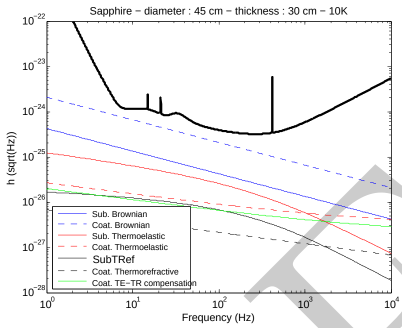

(a)

Figure 206: (a) - Thermal noises contribution for a silicon mirror (w=9cm, thickness : 50 cm, T:10 K). (b) - Thermal noises contribution for a sapphire mirror (w=9cm, thickness : 30 cm, T:10 K).

Figure 207: Total thermal noise of a silicon substrate at different low temperatures : 10 K, 20 K, 30 K and 40 K

Author(s): R. Nawrodt

Based on the calculations presented in section 5.9.3 and 5.9.4 it is possible to give an overall estimate of the expected thermal noise from the optical components of the ET LF detector. The total estimate is based on the simplified sketch of the ET-LF detector in figure 196. The input coupler of the cavity as well as the end test mass are cooled to cryogenic temperatures around 10 K. The beam splitter is operated at room temperature.

In order to achieve a good thermal noise performance of the optical components a large beam radius w as large as 90 mm is needed. This requires the use of large diameter bulk samples to avoid large clipping losses. This requirement lead to a typical substrate diameter of 50 cm. In addition the suppression of radiation pressure noise requires large masses - for the ET-D design a mass of 211 kg is needed. In combination with the maximum available diameter of a potential silicon test mass material this leads to a required minimum thickness of 46 cm for the optical components involved in the arm cavities (end test mass and input coupler). A further increase of the thickness will reduce radiation pressure noise further - however, it will increase the thermo-refractive noise of the input test mass.

The option to use sapphire as a test mass material seems to get limited strongly be the availability of the materials. So far, it is not expected that by the time ET will be built Sapphire test masses with a required diameter of 50 cm are available on the market. Thus, all estimated in this section are based on the choice of silicon as a test mass material - although sapphire will total satisfy all noise demands if operated at the same temperature and if it is available in the same geometry.

Figure 208(a) shows the total thermal noise of an end test mass cavity mirror for ET. The calculations are based on the properties presented in tables 16, 17, 18 and 19. A silicon test mass with a diameter of 50 cm and a thickness of 46 cm was assumed to be operated at 10 K. The ETM uses 18 $\lambda/4$-doublets of a tantala/silica layers and the ITM 9 $\lambda/4$-doublets of a tantala/silica to form the cavity. While the laser beam reads out the surfaces of the cavity mirrors

$$N = 2/\pi F \tag{189}$$

times (F - finesse of the cavity) it only senses the thermo-refractive noise of the ITM twice (input and output of the cavity). This reduction factor is included for the ITM and the thermo-refractive noise recalculated as an effective displacement noise for comparison.

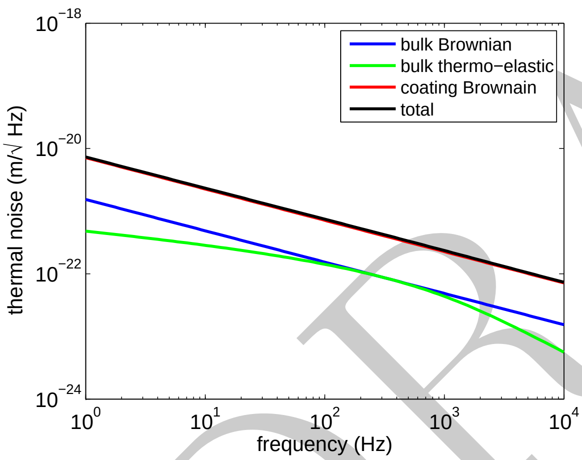

(a)

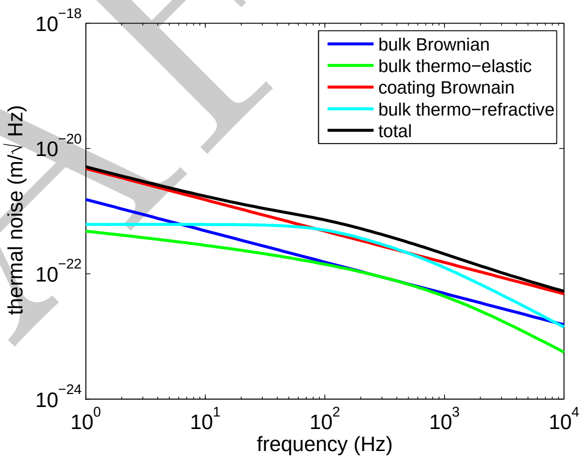

(b)

Figure 208: Total thermal noise of an end test mass (a) and an input test mass (b) of the arm cavity of ET-LF. Both substrates are assumed to be made of silicon with a diameter of 50 cm and a thickness of 46 cm. The operational temperature is 10 K. The ETM is equipped with 18 $\lambda/4$-doublets of a tantala/silica HR stack while the ITM is coated with 9 $\lambda/4$-doublets to achieve a transmission of about 7000 ppm.

For both - the ETM and the ITM - the coating Brownian noise dominates over all frequencies. For the input test mass the required 46 cm thickness leads already to significant contributions from the thermo-refractive noise. The uncorrelated sum of the different noise contributions in the ETM and the ITM can be used as a good estimate for the total thermal noise contribution of one arm cavity.

An additional noise source in the interferometer is given by the beam-splitter. Due to the fact that this element is situated outside the arm cavities its thermal noise contribution to the overall thermal noise of the detector is again reduced by the factor given in eq. (189). Thus, cooling might not be needed for this component. The beam splitter is assumed to be made of fused silica an operated at room temperature. The different thermal noise contributions based on the equations given in the previous sections are summarized in figure 209(a). The beam splitter is assumed to be coated with 3 $\lambda/4$-doublets of tantala/silica as an upper limit calculation. The thickness of the beam splitter is assumed to be about 30 cm while the diameter is kept around 50 cm for the initial estimates.

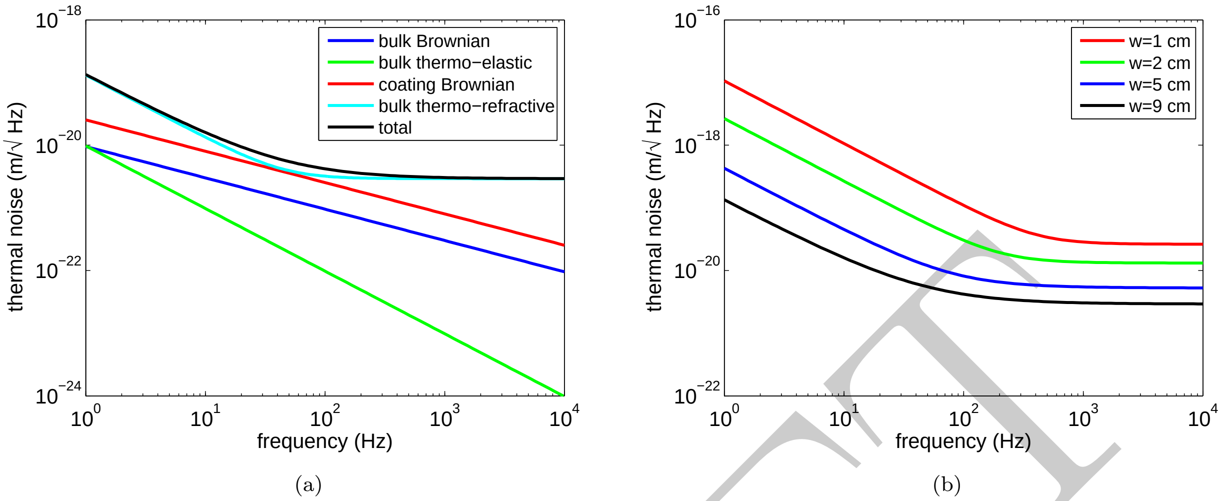

Figure 209: (a) - Summary of the different thermal noise sources in a potential ET-LF beam splitter made of fused silica and operated at room temperature. (b) - Evolution of the total thermal noise of the beam splitter with different beam radii at the beam splitter.

The thermo-refractive contribution from the beam-splitter is based on the calculation by Benthem and Levin for GEO600 [517]. Thermo-refractive noise is the most dominating noise source of the beam splitter due to the very low mechanical loss of fused silica at room temperature and the small number of coating layers. If the beam radius of the laser beam at the beam splitter is further reduced thermo-refractive noise increases as shown in fig. 209(b). This reduction of the beam radius might be beneficial to reduce the necessary size of the beam splitter. Due to the fact that the beam splitter is operated under an angle the necessary size is increased compared to an end mirror. These mirrors are currently already designed to be at or close to the edge of what is and will be available by the time ET will be built. Thus, a reduction of the dimensions of the beam splitter is needed.

Combining all noise contributions from the two arm cavities and the beam splitter (incoherent sum) leads to the estimate of the total thermal noise contribution for ET-LF which is given in figure 210 for different beam radii at the beam splitter.

It is obvious that the main thermal noise contribution comes from the arm cavities. Even if the beam radius at the beam splitter is chosen to be as small as 1 cm the noise contribution from the beam splitter is smaller than the contribution from the arm cavities. This relaxes the demands for the size of the beam splitter.

A small section about the final definition of the geometry of the optical components will be included here once the numbers are verified. (After Amsterdam meeting. Nawrodt responsible).

5.9.6 HF interferometer large mirror definition

Author(s): J. Franc

Fused Silica is the material of choice for the high frequency detector operating at room temperature. This material has already proven its reliability in GW detectors currently under operation (e.g. LIGO, VIRO, GEO600) due to its excellent optical properties. Fused Silica is one of the commonly used materials in optics and has been improved during many decades. Appropriate polishing methods exist to obtain a very high surface quality. Fused Silica has remarkable properties at room temperature: low mechanical loss (see section 5.16.2)

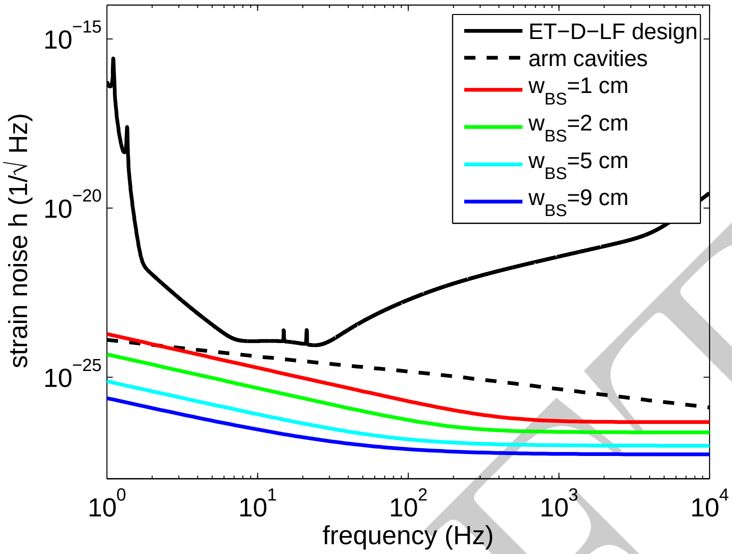

Figure 210: Total thermal noise arising from the optical components of ET-LF for different beam radii at the beam splitter.

which leads to a small substrate Brownian noise and an exceptional low coefficient of thermal expansion (see section 5.16.3) which results in a small thermo-elastic noise.

Parameter	ET-HF
temperature	290 K
arm length	10 km
mirror material	Fused Silica
mirror diameter	62 cm
mirror thickness	30 cm
mirror mass	200 kg
laser wavelength	1064 nm
beam shape	HG_{00}
beam radius	12 cm
coating high index	$Ti : Ta_2O_5$
coating low index	SiO_2

Table 20: Summary of the parameters used for the thermal noise estimate of the HF interferometer.

The assumed parameters for the HF interferometer are listed in Table 20. The mirror geometry was chosen that the mass reaches 200 kg (to suppress radiation pressure noise) and that the mirror has 1 ppm diffraction loss [380]. In order to compare the behaviour of different substrate materials the thermal noise of a high reflectivity mirror was calculated using the same 'standard' coating and different substrate materials. The 'standard' coating is a multilayer (HL)17HLL coating made of $Ti : Ta_2O_5$ and SiO_2 quarter wavelength layers. On a fused silica substrate this coating corresponds to a transmission of 6 ppm. The lowest mechanical losses have been considered for the coating materials (see section 5.16.2). The result of this comparison is shown in Figure 211. The graph compiles different noise sources in the substrate material as well as the coating.

At 300 K, silicon is unsuitable due to its large mechanical loss angle . The total thermal noise for silicon is limited by two substrates thermal noises : substrate brownian noise at high frequency and substrate thermo-elastic noise at low frequency. Sapphire must be also turned down due to its large thermoelastic noise at low

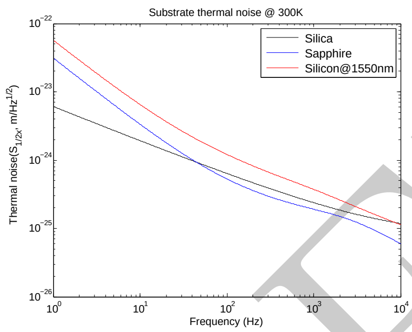

Figure 211: Total thermal noise of 3 different substrates at 300K: Silica, Sapphire and Silicon @ 1550 nm.

frequency. Therefore, the most adapted substrate at room temperature is fused silica. In this case, coating limits the sensitivity of the future detectors only through the Brownian motion. The fused silica thermal noises does not play a role in the sensitivity limitation that is why this substrate has been chosen for a GWD working at 300 K [491].

Mirror coating *Author(s): J. Franc*
As explained above, the total thermal noise of the test masses is a combination of coating Brownian, substrate Brownian, substrate thermo-eleastic, substrate thermo-refractive noise and thermo-optic noise. Taken into account this five noises, the coating Brownian noise is the most important one and can limit sensitivity target. A state-of-the-art of different coating material have been realized in order to compare different combination of multilayer stacks. Figure 212 shows the total thermal noise for different coatings on a silica substrate at room temperature. The calculations are based on the currently best available data of the materials (19). Each coating correspond to a transmission of 6 ppm on a fused silica mirror. Therefore, all multilayer are different according to materials taken into account. We need (HL)17HLL for coating made of $Ti : Ta_2O_5$ and SiO_2 quarter wavelength layers,(HL)13HLL for coating made of TiO_2 and SiO_2, (HL)13HLL for coating made of TiO_2 and SiO_2(HL)13HLL for coating made of Nb_2O_5 and SiO_2, (HL)13HLL for coating made of TiO_2 and SiO_2(HL)16HLL for coating made of ZrO_2 and SiO_2, (HL)24HLL for coating made of $Ti : Ta_2O_5$ and Al_2O_3 and(HL)22HLL for coating made of ZrO_2 and Al_2O_3. According to refractive index value of material the number of layer can double.

There is a clear advantage for the $SiO_2 - Ti : Ta_2O_5$ coating. The results obtained for $SiO_2 - Nb_2O_5$ and

$SiO_2 - ZrO_2$ are encouraging as well. However, including the optical absorption of the coatings even stronger supports the use of the standard coating. So far, there is no better coating to be used at room temperature than the $Ti : Ta_2O_5 - SiO_2$. Therefore, according to the results demonstrated in this section, the figure 213 show the different thermal noises contribution for this kind of mirror.

In conclusion, we have evaluated the total mirror thermal noise at room temperatures by implementing a model that includes Brownian noise, thermo elastic and thermo refractive noise. The different simulations presented and calculated with the parameters listed above allows understanding that silica is the good test mass material for the High frequency detector of the 3rd generation of GWD. The optimized mirror for the HF interferometer is, at present, a silica test mass with a diameter of 62 cm and a thickness of 30 cm. The best coating remains a multilayer system made of seventeen doublets of $Ti : Ta_2O_5$ and SiO_2.

5.9.7 Mirror surface defects

Mirror surface defects are investigated in order to understand their effects on cavity resonance and losses, and to define requirements for surface polishing. For convenience, the mirror surface deviations from the perfect surface can be classified in two categories, depending on their spatial frequencies. Defects in the high frequency range (above a few hundred m^{-1}) will scatter light outside the cavity and thus generate cavity losses and scattering noise. Defects in the spatial low frequency range (between 1 and 100 m^{-1}) may induce resonance of unwanted modes in the cavity, and thus degrade the mode purity inside the cavity.

The ET arm cavities were simulated by FFT propagation using the simulation software *SIESTA* [519]. Artificial mirror maps were applied to both mirrors of the cavity. The artificial maps were randomly generated in order to reproduce a defect distribution similar to that found in actual VIRGO and LIGO mirrors [520–522].

Table 21 shows the cavity gain and round-trip losses for the fundamental mode resonating in the cavity (wavelength of 1064 or 1550 nm), with varying RMS flatness of the surface defects. The defects distribution considered here goes as f^{-2}, where f is the spatial frequency. It has been shown in [522] that such a distribution, with a RMS of 1.0 nm, overestimates the low-frequency defects with respect to what has already been obtained for the Advanced LIGO mirrors. Therefore the surfaces obtained by current polishing techniques seem already good enough to obtain reasonably small round-trip losses for the fundamental mode. Using a wavelength of 1550 nm is particularly favourable from this point of view (smaller losses).

The situation for LG_{33} is more delicate. It has been shown [522] that LG_{33} is significantly more sensitive than the fundamental mode to surface defects in the low spatial frequency range. Essentially, since a cavity tuned for LG_{33} is degenerate for all modes of order 9, the low-frequency defects may induce the coupling between the injected LG_{33} and the other modes of the same order. Polishing tecniques such as corrective coating or ion beam polishing are able to reduce the amount of defects in the low-frequency region, approximately below 100 m^{-1} (1 cm^{-1}). Ion beam polishing has currently been used for Advanced LIGO, whereas corrective coating is under evaluation for Advanced VIRGO. Preliminary results indicate that a further improvement is required for LG_{33} with respect to the state of the art of such techniques. More work is planned to verify the agreement of FFT simulations with experiments on LG_{33} (see section 5.15.1).

In addition to the above work, the coupling between higher-order modes due to mirror surface defects was investigated using a frequency domain simulation tool, *Finesse* [483]. In this work, similarly to the simulation mentioned above, a Fabry-Perot cavity with imperfect mirrors was simulated. Real surface maps of VIRGO mirrors were reconstructed by fitting with Zernike polynomials, and an artificial map was built by a sum of Zernike polynomials. A LG_{33} beam was injected into a cavity where a surface map was applied on one of the two cavity mirrors. The light field inside the cavity was analyzed and found not only the couplings between the same order, but also the frequency split of the resonant frequency which will result in quasi-degenerate modes.

The next step is to expand the optical configuration to a realistic topology such as an RSE interferometer in order to obtain practical requirements for the mirror surface. Also, the effects of advanced polishing techniques such as corrective coating or ion beam polishing need to be better understood.

RMS flatness	LG_{00} 1064 nm		LG_{00} 1550 nm	
	cavity gain	r.t. losses [ppm]	cavity gain	r.t. losses [ppm]
0 nm	567.4	2	567.4	3
0.5 nm	564.5 ± 0.9	20 ± 6	566.7 ± 0.3	7 ± 2
1.0 nm	555.9 ± 3.7	73 ± 24	564.4 ± 0.9	21 ± 6

Table 21: Cavity gain and round-trip losses for the arm cavities, computed from FFT simulations, as a function of surface defects RMS. The fundamental LG_{00} mode is considered, for the wavelengths 1064 and 1550 nm. Data are expressed as mean ± standard deviation on an ensemble of 10 different cavities. For each cavity, random surface maps with a given RMS amount of defects are applied to both mirrors. The random surface maps are generated from a f^{-2} spectral distribution.

Reminder during writing

- coating TN as serious noise candidate
- description of all dependencies from equations (links to ET notes), optimisation plots
- possible coating materials for cryogenic operation (tantala, silica, hafnia, etc. - link to appendix with parameters)
- discussion of properties, links into (near) future R&D (links to Sec. 5.15)
- definition of coatings (number of layers, optimisation due to reflectivity, absorption and TN), include options (layer thickness) and give estimates on the influence
- ...
- silicon as test mass material → limitations (TR noise, size, absorption), sapphire option
- LF interferometer at low temperatures - thermal properties and parameters at low temperatures (link to appendix)
- definition of geometry, availability (several size options for comparison)
- temperature stabilisation (cooling) - limits in laser power due to absorption (links to suspension and cooling definition)
- ...

5.10 Injection system

Author(s): ***S. Hild***, *A. Thuering*

5.10.1 Pre-stabilized laser

At the development time of second generation GWDs, neodymium doped yttrium aluminum garnet (Nd:YAG) was the best choice as the gain material for 100 W class lasers. However, in the last years, particularly thin disc lasers based on ytterbium doped crystals have been undergoing a rapid development. While the pure power scaling of these systems into the multi-kW range was mainly driven either by material processing or defense applications [523, 524] which do neither require single-frequency nor fundamental mode output, good progress has also been achieved in the power scaling of high beam quality laser systems. In particular, near fundamental mode operation with more than 200 W of output power and up to 98 W of single-frequency output power has been demonstrated [525]. Further possible advantages are that the 940 nm pump diodes used for e.g. Yb:YAG have potentially longer lifetimes than their 808 nm Nd:YAG counterparts and that the lower quantum defect of

Yb:YAG causes less thermal effects. However, its main disadvantage is that Yb:YAG is a quasi-3-level system and thus more sensitive to increased temperatures within the gain medium.

Different design concepts are proposed to produce lasers with power levels of several 100 W and to amplify these systems into the kW region. The main concerns are the thermal management in the gain material and to reduce beam aberrations. In particular, Nd:YAG suffers from a significantly higher quantum defect compared to Yb:YAG making the thermal management even more important. One way to reduce the thermal effects is to use a zig-zag beam path to average over the thermal gradient in the laser crystal. Edge-pumped slab geometries can be combined with conduction-cooling techniques which avoid vibrations introduced by cooling fluids in conventional layouts. However, one of the main challenges in using slabs is to avoid parasitic oscillations within the high gain regions.

Problems caused by depolarization and by defocusing can be addressed in different ways. In principle, an efficient birefringence compensation can be implemented [526]. However, better than compensating effects is to reduce these. For this, there are in principle two different options. Firstly, [527] and [528] have shown that the amount of depolarization depends on the Nd:YAG crystal orientation. Therefore, crystal orientations other than the standard [111]-cut could be an option to reduce the depolarization intrinsically. [529] suggested the use of [110]-cut crystals in combination with small beam size in the high pumping regime to reduce depolarization. In recent experiments [530], the [100]-, [110]- and [111]-crystal orientations were compared in a single pass configuration in the pump power regime relevant for 2nd generation GWD. Although these results are very promising in terms of intrinsic reduction of depolarization effects, they also show that the non-symmetrical shape of the thermal lens in unconventionally cut crystals might limit the achievable beam quality in laser oscillators.

The second option is to reduce the thermal gradients which cause the stress-induced birefringence effects. By the use of multi-segmented laser rods, the maximum peak temperature of an end-pumped laser rod or slab can be reduced as shown in the work by [531, 532]. To decrease the overall heat load in a Nd:YAG laser media the pump wavelength can be changed from 807 nm to 885 nm which reduces the quantum defect and therefore the overall heat load by more than 30% (see e.g. [460, 533]). Core doped rods can be used (see e.g. [534]) to achieve an easier and more stable fundamental mode operation. These rods are comparable to a double clad fiber as described by [535] where only the inner core of the rod is doped and the outer core is used as a waveguide for the pump light. As the gain is only present in the doped inner core of the rod, this concept is similar to mode selective pumping, but has the advantage that no high brightness pump source is required.

Optical fiber amplifiers have a high potential to offer single-frequency output at higher efficiencies and at lower cost than solid-state amplifiers at similar power levels (see for example the overview paper by [536]). Until several years ago diode-pumped fiber amplifiers were limited to power levels of several Watts due to the unavailability of high brightness pump diodes and due to nonlinear effects in the fiber such as stimulated Raman scattering and stimulated Brillouin scattering (SBS). The invention of large mode-area (LMA) fibers and of photonic crystal fibers (PCF) has enabled output powers of single-mode fiber lasers to exceed 1 kW while retaining excellent efficiencies (see for example [537]). The large effective core diameter of these fibers decreases the average intensity of the light at the laser wavelength in the fiber and thereby increases the threshold of nonlinear processes. The large inner cladding of the double-clad LMA fibers allows high power multi-mode pumps to be coupled into the fiber. Bending losses can be used to ensure that the output remains single-mode, despite the large diameter of the core. The limiting factor for narrow-linewidth high-power fiber lasers for the use in GWDs is the onset of SBS.

A state-of-the art single-frequency fiber amplifier system with 150 W of output power with a good output beam profile (92% in TEM_{00}) is described in [538]. The optical-to-optical efficiency of this system with respect to incident pump power is 78% for a 195 W pump source. A good polarization ratio of about 100/1 was achieved. Recently, the output power of single-frequency, PCF-based, ytterbium-doped fiber amplifiers has been scaled to more than 400 W of output power [539].

A different approach to realize LMA fibers with excellent output beam quality and simultaneously larger mode areas are multifilament-core (MFC) fibers with core regions consisting of many small doped filaments. In contrast to conventional multi-core design, the multifilament core fibers aim for strong coupling between smaller filaments resulting in the propagation of only one supermode by adequately choosing diameter and spacing of the filaments. In the last years, MFC fibers with active and also with passive filaments were demonstrated, which enabled transversely single-mode output with nearly Gaussian-shaped intensity mode profile [540, 541]. The main advantage of this new fiber type is the low effective core numerical aperture which can be achieved without the need of flattening the refractive index profile as it is crucial for PCFs. Important properties of the MFC fibers, e.g. the low bending losses, can be explained using an equivalent step index based on the theory of the fundamental space filling mode [542]. Recently, it has been demonstrated that a TEM_{00} mode content of more than 95% can be achieved with such an actively doped fiber [543].

Novel ideas to increase the SBS threshold are under investigation. A promising concept is to shift the Brillouin frequency along the fiber to lower the effective Brillouin gain for each frequency component. This could be achieved by temperature or strain gradients, or by varying doping concentrations along the fiber. In addition to the reduction of nonlinear scattering effect, the reliability and noise performance of high power fiber lasers need to be further analyzed and possibly improved to meet the requirements of third generation gravitational wave detectors. Especially thermal effects and contamination at the air-glass interface have to be considered. The main problem is the large light intensity at these interfaces which could be reduced by undoped beam expansion section at the fiber ends or by all-fiber solutions for the pump-light coupling. One big advantage of fiber lasers is that they are compact and simple compared to the complex solid-state laser systems. Furthermore, modern splice techniques allow one to produce an all-fiber system including the master oscillator, the high power stage and possibly even a mode-cleaning fiber if required.

Erbium-doped fiber lasers emit around 1.56 μm where the absorption in silicon is small compared to the initially used silica at 1 μm wavelength. For an efficient design with low nonlinear effects in single frequency operation, the erbium-doped fiber should have high pump absorption and should be as short as possible. Unfortunately, the pump absorption cross sections of erbium are about a factor of 10 lower than those of ytterbium. In addition, quenching effects also limit the sensible doping concentrations to about a factor of 10 below that of ytterbium. This combined factors result in an about two orders of magnitude lower pump absorption of erbium doped fibers, if similar fiber geometries as used with ytterbium doped fibers are assumed. In order to avoid excessive fiber lengths, which is necessary to circumvent the onset of SBS, either the single-core to pump-core ratio has to be adapted or the amplifier has even to be pumped into the single-mode signal core. For this reasons, pump sources with very brightness or even single-mode beam quality are needed. This becomes even more obvious if the typically achieved optical-to-optical efficiencies of about 25%-30% (50% for 1480 nm pumping) are compared with the typical value of $> 70\%$ for ytterbium. Recently, a single-mode output power at 1480 nm was demonstrated with a Raman fiber laser [544] which can be used as a pump source for single-mode Er based systems. However, commercially available single-mode Raman fiber laser modules are currently limited to an output power of 10–20 W.

In order to overcome these limitations, Yb codoping of the Er-doped fiber and pumping at 980 nm can be used. This allows high pump absorption but also implicates a second gain band at the Yb wavelength around 1 μm. This second gain bands limits the achievable output power due to the onset of massive amplified spontaneous emission (ASE) which finally leads to pulsing instabilities of the amplifier system. The highest single-frequency output power of 151 W achieved with this concept was accompanied by more than 70 W of ASE at 1 μm [545]. Nevertheless, in recent experiments a new scheme was demonstrated by which the 1 μm oscillation in an Er-Yb codoped fiber amplifier could be effectively suppressed [546].

Concerning the direct generation or the amplification of spatial beam profiles other than the fundamental (fiber) mode, only very limited experimental results have been published. A good overview is given in the review article by [547]. For the generation of the higher order mode, the laser light is first coupled into the fundamental LP_{01} mode of a single-mode fiber. Then, an in-fiber long-period Bragg grating converts the LP_{01} into the desired LP_{0m} mode. This process can be very efficient with peak efficiencies of more then 99%. The usage of higher order modes in the optical fibers has several advantages compared to the fundamental mode. Firstly, the effective mode area is significantly enlarged increasing the threshold for SBS. Furthermore, the higher order modes are less sensitive to mode distortions due to fiber bending or refractive index profile imperfections due to the fiber fabrication process. Recently, fiber amplifiers have been demonstrated employing this technique for the first time in an active fiber with several Watts of output power [548, 549]. However, the used higher order LP_{0m} modes all have a central high intensity peak in common which is undesirable for the use in GWD

[550]. Thus, some research both on the generation of axisymmetric fiber modes with an intensity minimum in the center as well as on the amplification of these modes will have to be carried out. Most probably, this will also involve some special design of active fibers in which the active dopant distribution favors the amplification of the mode of interest.

As many different applications drive the laser development worldwide, many laser concepts at different wavelength and power levels are already available and advances in several fields are to be expected. Even though the large variety of optical layout and topology options for GWDs require a similarly large range of different laser parameters, we expect that at least one, if not more laser designs will allow one to build a laser source with the required power, wavelength and spatial profile.

5.10.2 Injection optics

Overview and General requirements

The Input Optics system (IO) of ET takes care of the optics downstream of the high power laser (1064nm) and low power one (1550nm). The whole system must deliver a beam with the required power, geometrical shape, frequency and angular stability at the Interferometer input. The general requirements for ET-LF and ET-HF IO system are listed in Table 22.

Requirement	**Value at 1064 nm**	**Value at 1550 nm**
Laser power available at the ITF input	$500W$	$3W$
Intensity noise	TBD	TBD
Beam jitter noise (misalignment mode amplitude)	TBD	TBD
IMC cavities throughput	>80% on LG_{33}	>80% on LG_{00}
IO overall throughput	>50% on LG_{33}	>50% on LG_{00}

Table 22: Requirements for the ET Input Optics (IO) system

An Electro-Optic Modulation (EOM) system should provide the needed RF phase or amplitude modulations (to sense longitudinal and angular degrees of freedom). Two in-vacuum suspended input mode cleaners (IMC) in series will be used to geometrically clean the beam and reduce its amplitude and lateral fluctuation. The resonant IMC could also serve in the loop of laser frequency stabilization. After the IMC an intensity stabilization section will provide the signal for stabilizing the laser RIN and reach the requirements. An in-vacuum Faraday isolator will prevent interaction of the ITF (interferometer) reflected light with the IMC and laser system. Finally, a mode matching telescope will give to the beam the correct dimension for matching it onto the interferometer. It is planned to use super-polished optics for ET-HF and ET-LF in order to lower as much as possible diffused light noise that could become a limiting noise. Moreover the beam pointing noise created in components in free-space propagation (mirrors, lenses, EOM, FI, etc. . .) can be dominated by acoustic, seismic and thermal noise. A particular care should be given to isolate the optics from seismic noise and as often as possible install all the sensors used in the control loops on suspended benches in the vacuum vessel of ET.

Input Mode Cleaner (IMC)

The laser light must be frequency and spatially stabilized before it can be used in the interferometer. The input mode cleaner (IMC) provides active frequency stabilization through feedback to the laser, passive frequency noise suppression above its cavity pole frequency, and passive spatial stabilization at all frequencies. The input mode cleaner also reduces higher order modal content of the laser light, suppressing beam jitter by a factor depending of the cavity Finesse.

The baseline configuration of the IMC for ET-HF is to use two 20 meter long IMC cavities placed in series (as done in GEO interferometer). Due to the high laser power that should be stored in the IMC cavity, radiation pressure effect and absorption in IMC cavity input and output mirrors should be the main limiting effects with such a high power. The radiation pressure effect will depend on the cavity finesse chosen. In Advanced Virgo, with about 60 kW power stored in this cavity it has been shown that the radiation pressure effect on angular degrees of freedom is manageable by using at least 3 kg mirror [551]. This means that this effect could be overcome by increasing the IMC mirrors weight or reducing the Finesse if possible. For the lock acquisition of the cavity it is likely that we need to lock the cavity at a lower power and go to full power once the cavity is locked [551]. Radiation pressure noise (linked to power fluctuation in the cavity) could also be responsible for frequency noise since it can affect the length of the IMC cavity and the angular control of the IMC end mirror if the beam is not well centered on this mirror. In linear regime, it has been shown that radiation pressure noise was not an issue for Initial Virgo sensitivity [552] and Advanced Virgo [553]. Specifications on this noise will have to be given for ET. Concerning input and output mirrors absorption, in order to avoid beam distortion induced by photothermal effect a low absorption fused silica with good homogeneity should be chosen as mirror substrate and coating absorption lower than 1 ppm is mandatory [554]. In order to cope with higher order Laguerre-Gauss modes, the resonant mode cleaner should be made with an even number of mirrors as explained in [555][556]. Cavity parameters (Finesse, Round-trip losses and cavity pole) will have to be defined according to the beam jitter, amplitude and frequency noise requirements at the interferometer input.

Due to the fact that a lot of things have been developed in the 1550 nm wavelength range for telecommunications, we should try to use as much as possible already existing components for the IMC of the ET-LF interferometers. For ET-LF, we have 2 possibilities to make a spatial filtering of the laser beam:

- use a resonant mode-cleaner as done in ET-HF
- use an optical fibre.

Some R&D activity is needed on this subject to see if the optical fibre is able to fulfill ET requirements. In any case, a resonant cavity will probably be needed at least to stabilize the laser frequency. The baseline solution remains to use two 20 meter long triangular cavity in series where we have more experience and now that this kind of suspended cavity should fulfill our requirements. As for ET-HF, IMC parameters should be defined according to beam stability, laser frequency and amplitude stability required at the interferometer input port.

Faraday isolator

Light back reflected by the interferometer should be picked up before being coupled back in the IMC cavities. The solution adopted in first and second generations of Gravitational wave detectors is to install a Faraday isolator in vacuum on the beam path between the interferometer and the Input mode cleaner cavity.

Faraday isolator for ET-HF: Faraday isolator design has evolved to cope with the increase of power between first and second generation detectors. An R&D program put in place at the European Gravitational Observatory has developed in collaboration with the Institute of Applied Physics (Nyzhni Novgorod Russia) a Faraday isolator with reinforced magnetic field and using thermal depolarization compensation technique [557]. This isolator uses Terbium Gallium Garnett (TGG)as magneto-optic material and the design has been optimized for thermal depolarization, thermal lensing and Verdet constant change compensation [558]. This device is able to achieve very good isolation performances (>38dB) in vacuum from low power up to 250W laser power [559]. We could use this experience and the same kind of design and scale it up to get the expected performances of the Faraday isolator in the 1kW power range. For ET-HF we could expect that the in-vacuum Faraday isolator should have the following characteristics:

- withstand high average power (1kW) on long periods;
- an optical isolation higher than 30 dB at full power;
- residual thermal lensing higher than 100 m;
- provide good transmission (at least 95%)

Faraday isolator for ET-LF: In the telecom wavelength range, TGG cannot be used due to its higher absorption at 1550nm. Fortunately, in the field of telecommunications a lot of possible materials to be used in Faraday isolator are available [560]. In any case, as for the high power Faraday isolator needed for ET-HF, the development of vacuum compatible Faraday isolator for 1550 nm wavelength requires to build up a test facility and collaborative work with laboratories or companies having experience with free space Faraday isolator adapted to telecom wavelength. The relatively low power used in the configuration will probably simplify the design of such an isolator with respect to the high power compatible one.

RF-Electro optical modulation system

In ET, RF modulation of the laser beam will be used in the control of the interferometer, both for longitudinal and angular controls.

RF modulation system for ET-HF: The main difference between the Electro Optical Modulation (EOM) system to be used in ET-HF respect to first and second generation detectors is the laser power that the EOM system will have to withstand (up to 1 kW for ET-HF). Thermal effects become more significant [561] and the choice of the appropriate material (electro-optic (EO) crystal) becomes crucial to limit as much as possible the consequence of these thermal effects on EOM properties. Indeed, it is important to select the right material not only to limit wavefront aberrations but also because it is a proof of local heating of the material. This heating can induce slow variation of the modulation index and disturb the ITF control. Requirements in ET for the electro optical modulation system (oscillator phase noise, modulation index and modulation index noise, . . .) will have to be defined. Many of these parameters will affect the driving electronics and signal generator choice.

RF modulation system for ET-LF: The experience of telecommunication field should be used extensively in the RF-modulation system of ET-LF. it is likely that integrated fibered optical components will be used to modulate the laser light.

Other high power compatible components

The selection and development of high power compatible components suitable for ET-HF is essential. Experience acquired during AdV Highpower input optics R&D program should be a good starting point in the selection of waveplates, polarizers and for the design of High power low diffusing beam dumps [558, 559].

R&D work needed for ET

Laser and Injection optics of ET can benefit of the many years of R&D already performed by LIGO and EGO for respectively aLigo and Advanced Virgo projects in investigating high power compliant components such as electro-optical modulators, Faraday isolator.
For ET, it is necessary to fund two R&D programs one focussed on ET-HF components that have to be compliant with high power laser and LG33 mode. The second one should concern ET-LF and the development and selection of IO components (Faraday isolator, EOM, Mirrors, waveplates and polarizers). Laser beam cleaning through a fiber has also to be studied for this configuration. Collaboration with experienced people (labs or companies) is essential in the success of these two R&D programs.

5.11 Detection system

Author(s): ***S. Hild***, *A. Thuering*

5.11.1 Readout options for the gravitational wave signal

Figure 214 shows simplified schematics of three different readout methods applied to a basic Michelson interferometer. Usually Michelson interferometers used for gravitational wave detection are operated at a dark fringe[10]. The differential arm-length is controlled to give destructive interference at the output port: ideally no carrier light (f_c, red solid line) reaches the photo detector. The interaction of a gravitational wave with the Michelson interferometer can be considered as shortening of one interferometer arm, whilst the perpendicular one is elongated. This change of the differential arm length causes phase modulation sidebands, i.e. gravitational wave

[10]Operating at the dark fringe has the advantage of providing good suppression of common mode noise and allows to make use of power recycling.

signal sidebands (blue dashed line). In contrast to the carrier light the gravitational wave signal sidebands interfere constructively at the beam splitter, exit the interferometer at its output port and finally reach the photo detector. The absolute frequency of the gravitational signal sidebands given is by $f_{\rm sig} = f_{\rm c} \pm f_{\rm gw}$, where $f_{\rm gw}$ is the frequency of the gravitational wave (usually in the audio-band) and $f_{\rm c}$ the frequency of the main laser light (carrier). Since $f_{\rm sig}$ is a few hundred Terahertz, the photo diode cannot directly detect the gravitational wave signal, unless the presence of an optical local oscillator is provided. Heterodyne, homodyne and DC-readout use different concepts to ensure the presence of a low-noise optical local oscillator at the output port photo diode.

In the heterodyne schemes, commonly used by the first generation gravitational wave detectors, radio frequency (RF) sidebands ($f_{\rm het}$, green dotted lines) are modulated onto the light at the input of the Michelson interferometer (Schnupp modulation [562]). Introducing a macroscopic arm length difference of several centimeter (so-called Schnupp asymmetry) allows the modulation sidebands to be transferred through the interferometer to the output port, where they serve as optical local oscillator for the gravitational wave signal. The photo-current produced by the beat between the different optical field components (optical demodulation) contains a radio frequency component at $f_{\rm het} \pm f_{\rm gw}$. In a second demodulation process the photo-current is then electronically demodulated at $f_{\rm het}$ (using a mixer) in order to finally derive a signal stream at $f_{\rm gw}$.

In the homodyne readout scheme (center plot of Figure 214) a small fraction of the carrier light is split off in front of the interferometer and guided directly to the output photo detector without passing through the interferometer. The big advantage of this form of homodyne readout is that a phase shifter, placed in the local oscillator path, allows an easy change of the optical demodulation phase, i.e. the readout quadrature, without any hardware changes. On the other hand homodyne readout has the disadvantage that the length and the alignment of the local-oscillator path needs to be highly stable. In practice this usually implies that the local-oscillator path length as well as its alignment need to be actively stabilized by a low-noise control system, and all components of the local-oscillator path must be seismically isolated inside a vacuum system. Due to these demanding noise and hardware requirements, so far there have been no serious plans to change the readout scheme of the currently operating gravitational wave detectors from heterodyne to homodyne readout.

DC-readout is a special case of homodyne readout which is much easier to combine with the existing elements of currently used gravitational wave detectors. In a DC-readout scheme the operating point of the Michelson interferometer is slightly shifted off the dark fringe, by introducing a so-called *dark-fringe offset*, thus a certain amount of carrier light leaves the interferometer at the output port and can serve as local oscillator. Compared with the previously described homodyne readout, DC-readout has the advantage that no additional local oscillator path outside the main interferometer is required. On the other hand, DC-readout offers no easy way to vary the phase of the optical demodulation.

DC-readout was already used in the first 'Michelson' interferometer ever by Michelson and Morley in 1887 [563]. It is probably the simplest way to read out a Michelson interferometer, but was considered to be unsuitable for the first generation of gravitational wave detectors due to the strong coupling of laser power noise. However, increased stability of the laser power inside future instruments gives hope for a renaissance of DC-readout for gravitational wave detectors, which was first proposed by Fritschel 2000 [564]. A demonstration of a DC-readout in a suspended prototype interferometer (without signal recycling) has recently been performed [565].

The next section briefly summarises the general advantages and disadvantages of DC-readout compared with heterodyne readout, especially taking into account the implications for an interferometer with tuned or detuned signal recycling [566].

5.11.2 Motivation for DC-readout

DC-readout has many advantages over the commonly used heterodyne readout:

1. When going from the currently-used heterodyne readout scheme to a DC-read scheme, the ratio of signal to shot noise will increase [567]. This is due to the fact that in the homodyne detection the shot noise contribution from frequencies twice the heterodyne frequency does not exist.

2. A reduced number of beating light fields at the detection port potentially reduces and simplifies the couplings of technical noise [566]. Especially the coupling of amplitude and phase noise of the heterodyne modulation is strongly reduced in a DC-readout scheme. In addition the frequency noise coupling to the gravitational wave channel is also expected to be reduced in DC-readout.
3. A simpler calibration procedure can be applied, because the GW-signal is present in a single data-stream even for detuned signal-recycling (and not spread over the two heterodyne quadratures as described in [568]).
4. As the main photo diode(s) and electronics for the detection do not need to be capable of handling RF signals, they can be simplified.
5. Large-area photo diodes[11] may be used. These should offer reduced coupling of beam-pointing noise, due to decreased beam clipping and decreased influence of photo diode inhomogeneity (by averaging over a larger area).
6. As in the homodyne readout the local oscillator and the GW-signal pass the same optical system an optimal spatial overlap is guaranteed. (Due to thermal distortion current GW detectors employing arm cavities encountered the problem of imperfect spatial overlap of the carrier light (GW signal) and the heterodyne sidebands (local oscillator) [569])
7. Finally, the realization of a squeezed light enhanced interferometer is simpler using DC-readout rather than heterodyne readout. DC-readout requires squeezed light to be present only at frequencies in the GW signal bandwidth compared to heterodyne readout which requires squeezed light around twice the heterodyne frequency as well [570]. [12]

This long list of advantages has to be compared with the drawbacks of DC-readout. Even though power fluctuations of the carrier light (i.e. the local oscillator) are strongly filtered by the cavity poles of the power recycling cavity and the high-finesse arm cavities, the major disadvantage of DC-readout is an increased coupling of laser power noise. In addition there is the potential problem that the response from DC-readout is not completely linear, due to the operating point sitting on the near-quadratic slope close to the dark fringe. However, this should not be a significant problem as long as the mean deviation from the differential arm length operation point is not too large.

5.11.3 Output mode cleaner

5.12 Main control and alignment strategies

Author(s): C. Graef, M. Mantovani, S. Hild

As a matter of fact, in interferometric GW detectors – the highly complex optical instruments they have grown – it is a crucial requirement for the multitude of their degrees-of-freedom (DOF) that they are held tightly at predefined operating points, to allow for full internal power build up, to enable active null operation, etc. Provided this, the instrument can unfold its full potential for ultra high sensitivity measurements. To fulfill this requirement for stable lengths and frequencies, electronic feedback control has proven as an essential tool, making a deterministic and reliable operation of a GW detector possible.

The task of controlling an interferometer can further be sub-divided in the control of longitudinal DOF and alignment control. In the following three subsections we will focus on aspects of controlling the longitudinal degrees of freedom, i.e. only variations along the axis of the optical mode in the interferometer will be considered. Alignment control will be treated in Section 5.12.4.

[11] RF photo diodes are required to have a low electrical capacitance.

[12] A squeezed light source working only in the GW signal bandwidth would result in the DC-readout case in a sensitivity enhancement limited by the squeezing strength generated, whereas the same source would act in a heterodyne-readout based interferometer as if 50% of the squeezing was reduced due to losses. Hence, a sensitivity improvement by a factor of 6 dB in the DC-readout case would result in the heterodyne case in an improvement factor of only 2 dB.

5.12.1 Fundamentals of length sensing and control

A succesful length sensing and control system for an interferometric GW detector has to satisfy three basic requirements: First, starting from a random initial state it must bring the instrument to a predefined operating point ("lock acquisition"). Second, it must prevent disturbances of any kind from causing deviations of the instrument from its operating point by an amount larger than specified. Finally, it must provide a low-noise electronic signal which contains the GW signal. In this discussion we will focus on the first two aspects.

A crucial element of a succesful longitudinal control scheme is the extraction of a complete set of signals which reflect the dynamical state of the longitudinal degrees-of-freedom and which, in particular, are a measure for the deviation of each of the interferometric degrees-of-freedom from its desired operating point. Generally, this is achieved by employing variants of the fundamental Pound-Drever-Hall technique [571]. The Pound-Drever-Hall scheme builds on imprinting radio-frequency (RF) phase modulation sidebands on the carrier beam prior to its injection into the optical cavity to be controlled. Cavity length fluctuations are efficiently converted to carrier phase shifts, which occurs near resonance as a linear effect. The RF sidebands in contrast do not experience a phase shift, as their frequencies are generally chosen off-resonant in the cavity. Pure phase modulation is thus partially converted to amplitude modulation. Heterodyne readout of the reflected beam provides a signal which is a direct measure for the cavity's deviation from resonance and which can further serve as an error signal for electronic feed back controls.

Ideally, a sensing system would provide a number of independent outputs, one for each DOF in the detector. However, in practice error signals obtained from an interferometer by means of heterodyne detection show more or less strong coupling. This is acceptable as long as these signals are at least linearly independent, due to the fact that this class of signals can be electronically post-processed, i.e. linearly transformed, resulting in separated signals. The underlying transforms can easily be implemented in the form of matrices in digital data processing systems. However, care must be taken to provide rubustness of the transformations under parameter changes of the optical plant and the sensing electronics. This is why in practice optically separated signals are usually preferred over signals obtained via electronic separation. Further potential disadvantages of electronically separated signals are a reduced signal-to-noise ratio and more complex dynamics during lock acquisition [572]. Generally, providing too few modulation frequencies or extraction ports complicates the task of finding a set of independent length signals and, in the worst case, leaves the optical system underconstrained due to a lack of information about its internal state.

A valuable form of description for the design of a sensing scheme is the *sensing matrix*. The sensing matrix describes the relation between the interferometer's degrees-of-freedom and the signal extraction ports. In the ideal case this matrix would be diagonal which would read as all sensing signals being fully decoupled. Likewise, the control problem would decouple to a single-input single-output problem for each degree-of-freedom in the interferometer. Contrasting this, the signal mixing of length error signals one encounters in practice would yield non-vanishing off-diagonal elements in the sensing matrix. This is tolerable, as long as the off-diagonal elements are smaller in magnitude than the diagonal ones as in this case a technique referred to as *gain hierarchy* can be applied to solve the control problem. This technique is based on suppressing a large signal that appears in more than one port by closing a control loop around the DOF that causes it. A small signal, previously covered by the large one, can in this way be dissected from the signal mixture and serve as an error signal for another, by then uncontrolled, degree-of-freedom.

The classical approach of implementing servo controllors by means of analog electronics is driven from predominance more and more by digital control systems. At the expense of their higher cost and obvious bandwidth limitation, digital systems provide a high precision and low noise environment allowing for rapid design and easy duplication of solutions. Massively multiple-input multiple-output systems become feasible and instrument automation can be easily implemented. Unlike analog electronics digital servo systems exhibit a high immunity to environmental parameter changes which makes them predestinated for applications which require long-term stable operation. Despite all these obvious advantages, it is fair to say that digital system complexity, in practice, rivals analog controls.

5.12.2 Longitudinal sensing and control in Advanced generation detectors

With increasing complexity and a growing number of degrees-of-freedom in the instruments comes the need for highly sophisticated length sensing and control schemes, which are substantial to setting the detector into operation. The interferometric topology that will be adopted by the Einstein Telescope is the cavity-enhanced dual recycling Michelson interferometer, which is also the underlying topology of the Advanced GW observatories currently under construction. In this section a review of central aspects of the sensing and control concepts of a typical Advanced generation GW observatory is given, focussing on Advanced LIGO [393] as an example. The optical setup is schematically depicted in Fig. 215.

For Advanced LIGO different modes of operation are foreseen, each of them involving e.g. different input laser power levels, signal recycling tunings, homodyne detection phases, etc., to yield optimum signal-to-noise ratio, depending on the cosmological source under investigation [573]. The main differential control requirement for Advanced LIGO is 10^{-15} m rms, yielding a shot noise limited sensitivity of $4 \times 10^{-21}\,\mathrm{m}/\sqrt{\mathrm{Hz}}$.

At the detector's operating point the carrier laser light is resonant in the power recycling cavity (PRC) and in the arm cavities. The signal recycling cavity (SRC) is tuned to carrier resonance only if the detector is operated in tuned mode. Two pairs of phase modulation sidebands, locked by a PLL, are imprinted on the input laser, forming the basis of the sensing scheme. The frequencies were chosen to be $f_1 = 9\,\mathrm{MHz}$ and $f_2 = 45\,\mathrm{MHz}$, both nearly anti-resonating in the arms to reduce arm-cavity induced phase shifts.[13] Both pairs of modulation sidebands are resonant in the power recycling cavity. The signal recycling cavity, however, is arranged to be nearly resonant for the f_2 sidebands while the f_1 sidebands do not resonate.

A typical property of the recycling cavities is their potential to cause mixing of modulation sidebands which immediately leads to coupled error signals. To prevent this effect from rendering the control scheme more complicated than necessary it is crucial to arrange for a configuration that reduces this mixing to the largest possible extent.

The Schnupp asymmetry – a macroscopic offset in the arm lengths of the central Michelson – is set to 5 cm to provide nearly critical coupling of the f_2 sidebands in the dual recycling cavity, with the implication of simultaneous resonance of the power recycling and the signal recycling cavities for this sideband frequency. By choosing an appropriate value for the Schnupp asymmetry one can arrange for a large modulation sideband power ratio in the SRC, providing improved signal separation. In this case the resulting power ratio is of the order of 10^3, in favor of the f_2 sidebands.

A variety of ports in the interferometer are read out to obtain a complete set of control signals for all longitudinal degrees-of-freedom. Besides the asymmetric port (AS), signals are extracted from the symmetric port (REFL) and from pick-off ports from within the power recycling cavity (POP) and a in reflection of one of the arm cavities (POX). These beams are directed to photodetectors and the resulting signals are in turn demodulated at f_1, f_2, $f_2 - f_1$ or $f_1 + f_2$, at appropriately set demodulation phases. Demodulation at the sum or difference frequency of two modulation sidebands, i.e. at their beat frequency, is a key concept in modern interferometric control system design and is often referred to as *double demodulation*.

The signal obtained in the symmetric port, after demodulation at the lower sideband frequency f_1 is used for common mode arm cavity (CARM) control. Consequently, the differential arm cavity mode control signal is obtained in the asymmetric port from the AS DC photodetector. For the DC readout scheme of the asymmetric port, which also contains the GW signal, a differential arm length (DARM) offset of the order of 10^{-11} m will be applied, yielding a DC power level in the asymmetric port of the order of 0.1 W of carrier light. The intra-cavity POP port yields signals for the PRC and the Michelson degrees-of-freedom, after demodulation at f_1 and f_2, respectively.

For controlling the signal recycling cavity, the optimum signal extraction port as well as the demodulation frequency depends on the mode of operation, i.e. the tuning of the SR cavity. Whereas for zero detuning an appropriate error signal can be extracted in the symmetric port in reflection of the interferometer or at the arm cavity pick off port, for detuned operation analyses have shown that double demodulation of the asymmetric

[13] This turns out to have a positive effect on the shot noise sensitivity of the Michelson (MICH) degree-of-freedom.

port signal yields better error signals. Thus, if it is desired to continuously tune the SR from tuned mode to a detuned science mode, at a detuning of about 5 deg it is necessary to switch between error signals for the control of the signal recycling cavity.

The underlying sensing matrix shows well-separated error signals for the arm cavities' degrees-of-freedom. The power recycling cavity is sufficiently decoupled from the other degrees-of-freedom but shows strong coupling to the ports where the Michelson and signal recycling cavity error signals are obtained. The most worrisome degrees-of-fredom are the Michelson phase and the signal recycling cavity which exhibit comparably large amount of cross-coupling. However, control of the interferometer can be gained i.e. with a gain hierarchical approach in conjuction with the arm length stabilization system (ALS) which is discussed in Sec. 5.12.3.

The control signals derived from the error signals are applied to the end mirrors in the case of the DARM degree-of-freedom, to the beamsplitter for Michelson phase feedback and to the recycling mirrors for SR and PR length stabilization. However, the common mode arm cavity length control loop is the most elaborate one. The CARM error signal is fed back to the main laser via multiply cascaded frequency loops, providing the final level of frequency correction. The required unity gain frequencies of the servo controllers are of the order of tens of Hz for PRC, SRC and MICH, hundreds of Hz for DARM and tens of kHz for the CARM degree-of-freedom.

With the exception of the arm cavity common mode controller all servo loops are realized using digital controls. The more demanding (in terms of bandwidth) CARM servo will be implemented in analog electronics. The digital feedback loops are implemented in a custom-made real-time control system with typical sampling rates of up to 65536 samples per second at up to 18 bit resolution. Digital control systems have proven to be a powerful solution with high flexibility. Complex filter structures, e.g. with blending of sensors and signals, can be conveniently realized and changed on-the-fly with little effort.

Similar to the initial LIGO control scheme, correction paths are included in the Advanced LIGO scheme. Correction signals are filtered copies of sensing noise limited MICH and SRCL control signals. To cancel the effects of known couplings, correction signals are fed from SRCL to DARM and from MICH to DARM at a precision of 1%. An additional correction path will feed signals from PRCL to DARM, at a lower precision of 10%.

5.12.3 Detector lock acquisition

Lock acquisition is the process of bringing an interferometer from its uncontrolled, initial state to a controlled state in which the instrument is fully operable. As in a GW detector lock acquisition has a direct impact on its duty cycle, this subject demands attention as early as the design phase of the instrument. Contrasting the case of a servo loop operating near resonance, where the error signal for an optical cavity shows a linear response to length changes, during lock acquisition one has to generally deal with highly nonlinear signals. Servo loops are usually optimized for control on resonance, resulting in a poor performance during acquisiton. The determining quantity in lock acquisition of an optical cavity system are the mirrors' relative velocities. Further, the *threshold velocity* is usually referred to as a measure which quantifies the performance of an acquisition scheme. By definition the threshold velocity is the maximal relative velocity of two cavity mirrors below which lock acquisition is successful. The threshold velocity strongly depends on the bandwidth of the underlying control loop. Only if the servo response time is suffiently short to follow the transient error signal it is capable of "capturing" an optic. As the probability for all DOF being simultaneously at their operating points is very small, a sequential approach must be taken, bringing the DOF to the locked state one after another.

The simplistic approach to lock acquisition, e.g. practiced in the early detector prototypes, is to wait for the instrument's DOF, driven by random ground motion, to move close to their operating points and then swiftly engage the control loops. As with this method lock acquisition of an interferometric GW detector would be a pure matter of coincidence more deliberate approaches were strongly desired. For initial LIGO an acquisition algorithm was developed which is based on a real-time estimate of the time-evolving sensing matrix, derived from measurable signals during lock acquisition [574]. With the implementation of this scheme on the LIGO digital control and data system lock of the detector was on average acquired on timescales of $\sim 1\,\mathrm{min}$. The Virgo approach to lock acquisition was to effectively decouple the instrument's DOF which is achieved by a deliberate misalignment of optics. This technique is often referred to as *variable finesse locking* [575]. Lock was usually acquired within a few minutes.

The Advanced LIGO quadruple suspension provides isolation to the test masses with respect to ground motion at frequencies above 10 Hz. Even though the active internal seismic isolation (ISI) platforms provide additional low frequency isolation, low frequency disturbances are expected to cause significant test mass displacement of the order of $10^{-7}\mathrm{m}/\sqrt{\mathrm{Hz}}$ at 0.5 Hz. This is due to the fact that at the suspension system's resonance frequency or at lower frequency perturbations are not well attenuated and couple into the test masses' positions as displacement noise. Besides this, the test masses will have electrostatic actuators instead of coil-magnet actuators which were used in initial LIGO. Electrostatic actuators deliver lower actuation noise, at the expense of significantly lower actuation force they can exert on the test masses. The Advanced LIGO electostatic actuators are expected to saturate at forces of $\sim 200\,\mu$N [576]. This severely complicates the process of lock acquisition.

In order to ease the difficulties of lock acquisition in the Advanced detector generation, auxiliary laser based schemes will be employed to complement the well-established techniques. This discussion focusses on the Advanced LIGO ALS (arm length stabilization) system [577]. For Advanced Virgo it is anticipated to employ a similar scheme. Other systems to aid lock acquisition, that were considered for use in Advanced LIGO, such as the suspension point interferometer or digital interferometry are described in [578]. The underlying idea of ALS is to provide for more deterministic lock acquisition by locking the arm cavities independently of the remaining degrees-of-freedom. The ALS system builds on frequency doubled laser beams launched into the arm cavities through the end test masses for pre-stabilization of the interferometer arms, independent of the science laser circulating in the interferometer. By applying additional coatings on the arm cavity mirrors the properties of the arm cavities, as seen from the ALS, can be shaped in accordance to the pre-stabilizations scheme's requirements. The choice of reflectivities for the input mirror and the end mirror results in an overcoupled cavity for the auxiliary laser, seen from the end mirror. The Finesse of the arm cavities for the 532 nm ALS beams is ~ 100. A simplified schematic of the ALS principle setup is depicted in Fig. 216.

The initial step in the acquisition process is to hold the arm cavities on anti-resonance for the main science laser. In the next step the recycling cavities are brought to the locked state, before the ALS brings the arm cavities onto resonance with the main laser and hands over the control authority to the global interferometer sensing and control scheme. For effectiveness, the ALS must reduce the residual arm cavity length fluctuations to a displacement of no more than one cavity line width, which is approx. 1.3 nm in the case of the Advanced LIGO arm cavities. Estimations have shown that with ALS engaged a level of displacement fluctuations of 0.115 nm rms can be reached.

Technically, once the arm cavities are locked with the 532 nm beams, a heterodyne measurement is performed on the ALS beam transmitted by the x-arm cavity and a frequency doubled sample of the main laser beam. A second one is performed between the x-arm and the y-arm transmitted beams. These measurements yield common and differential mode error signals which are in turn fed back to the corresponding actuators. By introducing a tunable offset into the heterodyne locking loop, the arm cavities can thus be adjusted to arbitrary tunings.

For a smooth transition from ALS arm cavity control to global control a robust phase-locked loop (PLL) is crucial, to provide a well-defined phase relationship between auxiliary lasers and the main science laser. Once the PLL is closed, the auxiliary lasers are locked to the arm cavities using PDH reflection locking. The resulting control signal acts on a voltage-controlled oscillator (VCO) which supplies the electronic local oscillator for the PLL. In this way the offset frequency of the auxiliary laser with respect to the reference is tuned. An analog servo is foreseen for this loop and is expected to have a bandwidth of a few kHz.

To provide a stable frequency standard for the auxiliary laser PLL, a technique based on the LISA (Laser Interferometer Space Antenna) back-link measurement is employed. Mullavey et al. [579] have experimentally demonstrated a scheme based on counter propagating two laser beams through an optical fiber and subsequent measurements of each of the outputs with LISA-style phasemeters. By subsequent combination of the output signals an error signal can be obtained which can be utilized to eliminate fiber induced phase noise. Their setup consisted of 4.6 km single mode optical fiber and two Nd:YAG lasers – operated in a master-slave configuration. To circumvent nonlinear forms of noise such as stimulated Brillouin scattering, the transmitted laser power was reduced to $\sim 50\,\mu$W. In the underlying bench top experiment a relative frequency noise of $0.5\,\text{mHz}/\sqrt{\text{Hz}}$ was reached for Fourier frequencies between 5 Hz and 20 Hz which is well below the Advanced LIGO requirements, with a margin of more than an order of magnitude.

5.12.4 Angular control - Automatic Alignment control system

The angular control system has to be implemented in order to reduce the mirror misalignments in the frequency region in which the seismic attenuation system does not fulfill the alignment requirements, i.e. below the mechanical resonances, to reduce the fluctuations of the mirror angular positions with respect to the beam, to maintain the overall alignment of the optical elements, ensuring long data taking periods, and to reduce the noise at the dark fringe port. The mirror angular positions in data taking mode can not be locally controlled because the long term drifts of the local references spoil the overall alignment. After the lock has been acquired the angular control has to be switched to a global control system, the *Automatic Alignment*, which uses error signals coming from the interferometer itself with a modulation-demodulation technique based on differential wave front sensing. The control scheme chosen for the second and third generation of gravitational wave interferometer is a Ward-like scheme where the sideband modulation frequencies are chosen to do not have any any sideband and higher order modes resonating in the cavities [580].

The main differences between the third generation and the first generation of gravitational wave detectors, which are already commissioned, are: the presence Stable Recycling Cavities; the higher circulating power; and the presence of the Signal Recycling cavity. These modifications produce an improvement in the interferometer stability and sensitivity but an increase of complexity for the development of the Automatic Alignment control system.

Stable Recycling cavities issue

The stable recycling cavities reduce the higher order modes content to be less affected by the point of view of thermal effects. This behavior influences the Automatic Alignment control system since the amplitude of the alignment error signals is proportional to the amount of the $\text{TEM}_{01/10}$ modes. For example in the case the recycling cavity with a Gouy phase of 15 deg the TEM_{01} mode is attenuated by a factor of about 6 while for 25 deg the attenuation factor is about 9. For this reason the choice of the recycling cavity Gouy phases has to be done taking into account both the stability requirements and the amount of first order higher order modes to ensure the angular controllability of the system.

High circulating power issue

In an high power interferometer the *radiation pressure* plays an important role. The light beam acts on the mirror such as an optical spring with strength increasing with the power. The higher effect would be in the long arm Fabry-Perot cavities, since there the higher amount of light power is stored , but the effect has to be also evaluated on the central interferometer mirrors.

The circulating power inside the arm interacts with the suspended mirrors via radiation pressure. The two cavity mirrors become coupled and their angular motion must be described in terms of two linear combinations [581]. When the circulating power becomes large enough one of the angular mode can become dynamically unstable.

As derived in [581], the interaction of beam and mirror can be written in term of the stiffness matrix:

$$\mathbf{k} = \frac{2PL}{c(1-g_1 g_2)} \begin{bmatrix} -g_2 & 1 \\ 1 & -g_1 \end{bmatrix} \tag{190}$$

where $g_i = 1 - L/R_i$ are the G-factors of the two mirrors. The eigenvectors and eigenvalues of the stiffness matrix determines the physical angular degrees of freedom and the corresponding stiffness applied to the mechanical system.

The normal stable situation corresponds to a positive stiffness of the system, given by the contribution of the mechanical stiffness of the mirror suspension and the extra-stiffness due to the radiation pressure, which gives a resonance made of a pair of complex poles with negative real part and quite large quality factor. The case of negative stiffness instead leads to an unstable system described with two real poles, one with positive and one with negative real part, with very close absolute frequency. The radiation pressure effects have then to be taken into account in the design of the control system.

Moreover the presence of the Signal Recycling mirror increases the number of degrees of freedom to control with respect the first generation of gravitational wave interferometers.

The design of the Automatic Alignment control system will be challenging because of the above mentioned issues and of the control accuracy and noise requirements to reach the ET sensitivity. From the other hand all these effects and problematics will be studied for the commissioning of the second generation interferometers, as Advanced Virgo and Advanced LIGO, gaining experience to deal with all these difficulties.

5.13 Thermal effects and their compensation

Author(s): V. Fafone, A. Rocchi

5.14 Rough cost evaluation

Author(s): ***A. Freise and H. Lueck***

The maximum size for Suprasil 3001 is the advanced LIGO size of 40kg. The heavier substrates for ET can only be made either of Suprasil 3002 which has inhomogeneities in the direction of the beam or from fused pieces of thinner Suprasil 3001. The price quoted by Heraeus for a substrate of 600mm in diameter and 400mm in thickness made of composite Suprasil 3001 is 700000 Euro.

At present Silicon is only available in Chzochalski grown crystals to a size of up to ??? 450mm, the maximum resistance available for this type is ??? In Floating zone crystals the maximum size at present is 200mm. The interest of the semiconductor industry in ultra-pure crystals is very limited and will most likely not drive the development of bigger size single crystals.

Costs of silicon are comparable to the one of ultra-pure fused silica.

The cumulative costs can be obtained from table ...

5.15 Technologies to be developed/RND

Author(s): ***K. Kokeyama****, S. Hild, A. Thuering, J. Franc, R. Nawrodt*

5.15.1 Thermal noise reduction due to the LG modes

Author(s): K. Kokeyama

Since ET HF interferometer targets the gravitational waves at lower frequencies where the mirror thermal noise dominates (30 - 300 Hz) the sensitivity, the thermal noise should be removed. Higher-order Laguerre-Gauss (LG) mode beams have been proposed and investigated for the reduction of mirror the thermal noise for the ET HF interferometer [379, 380]. LG modes are solutions of the paraxial wave equation in cylindrical coordinates, in a similar way to the Hermite Gaussian modes which are the solutions in Cartesian coordinates. They have radial power distributions as shown in Fig. 217 which are more uniform than those of the conventional fundamental mode (LG_{00} or TEM_{00} mode). Therefore, higher-order LG mode beams allow to reduce the thermal noise without introducing higher clipping-losses. Although flat-top and conical beams have been proposed for future gravitational-wave detectors, higher-order LG mode beams have the strong advantage that they have the spherical wave fronts, and so should be compatible with conventional optics such as spherical mirrors and lenses. On the other hand, flat-top and conical beams require non-spherical complex mirrors. Such mirrors were tested and found not to satisfactory for the requirement of angular alignment issues [582] and they are difficult to manufacture with the current technology.

Previous investigations have shown that the LG_{33} beam can realize a factor of seven smaller power spectral density of displacement equivalent coating Brownian thermal noise in comparison to the fundamental LG_{00} mode [486]. In addition, higher-order LG beam are fully compatible with the conventional length and angular sensing signals. This fact indicates that changing over from the fundamental mode to the higher-order LG mode should not require any new control strategy. Ref. [486] analyzed the control signals using numerical simulation tools and found that the performance of the LG_{33} beam in tilt-to-longitudinal phase coupling, generation of angular control signals, and the corresponding control matrices, was equivalent to or better than that of the LG_{00} beam.

LG mode technology for gravitational wave detectors is currently in a transition phase from the theoretical and simulation investigation to the experimental investigation phase. The first table-top experiment has been demonstrated the generation of a LG_{33} beam and the mode cleaner cavity performance with the generated LG_{33} beam [583]. The LG_{33} beam was generated by converting the LG_{00} beam to LG_{33} beam using a computer-controlled liquid-crystal-on-silicon spatial-light modulator (SLM). The PDH error signal was properly obtained with LG_{33} beam, and successfully used to control the longitudinal degree of freedom of the mode-cleaner cavity. The mode purity of the generated LG_{33} beam was increased from 66% to 99% upon transmission through the linear mode cleaner, demonstrating that very high-purity LG_{33} mode light sources can be produced in this way. Further experimental investigations, such as diffractive optical elements instead of SLM for the higher generation efficiency, are underway in order to determine the suitability of the technique for the ET HF interferometer.

One must note a practical problem which is the mode degeneration of higher-order beams. Several modes of (l, p) exists being the same order, $2|l| + p$, and they have identical Gaussian beam parameters, such as radius of curvature and Gouy phase. Therefore these modes can all resonate in the same mode-cleaner cavity, and not be rejected or cleaned away. They may contaminate the purity of the desired mode and may require a higher quality of a mirror surface deviation. It does not happen for the fundamental mode, since there is only one mode the in zeroth order.

5.15.2 Coating research

Author(s): I. Martin, R. Nawrodt

While silica:Ti-doped tantala coatings have thus-far proven to have the best combination of mechanical loss and optical properties at room temperature, the dissipation peaks in these materials at temperatures below 35 K are likely to reduce the improvement in coating thermal noise obtained from low temperature operation. Research into possible alternative coating materials is therefore ongoing. Hafnia (HfO_2) may be of particular interest as an alternative high index material as initial measurements have shown a significantly lower mechanical loss than tantala at temperatures below 150 K [? ?], although these coatings were found to have high optical absorption due to partial crystallisation. Crystallisation can be prevented by doping hafnia with silica, and there is evidence that this doping does not significantly affect the loss at room temperature. Further studies of the effects of heat-treatment and doping on the mechanical loss and optical properties of hafnia coatings are planned to assess the suitability of this material as a replacement of tantala.

Amorphous silicon can be used as the high-index component of a reflective coating suitable for use at 1550 nm. Experiments have shown that amorphous silicon coatings deposited by e-beam evaporation can have losses in the order of 10^{-5}, and that the low-temperature loss can be reduced by more than an order of magnitude by hydrogenation [?]. Additionally, the high refractive index of silicon reduces the number of layers needed for the same reflectivity. In order to achieve the same reflectivity in like a tantala-silica coating of 18 $\lambda/4$ doublets there are only 6 doublets of silicon-silica needed. Thus, the amount of coating material can be strongly reduced. Thus silicon may be a promising coating material for further investigation, potentially allowing for significant reductions in coating thermal noise. However, additional research is required. There are indications that the silicon-silica interface is chemically not stable. Oxygen starts diffusing from the silica into the silicon forming a silicon mono-oxide boundary layer. This layer might change the optical properties (reflectivity, scattering) of a potential HR stack made from these materials. Thus, a detailed investigation of optical properties of silicon-based optical coatings is required preferably at the desired operational temperature of the ET LF detector at around 10 K.

Recent results have strongly indicated that the mechanical loss of coating materials may be strongly related to the local atomic structure. Various techniques are being used to study the structural properties of amorphous coating materials. One technique using electron diffraction Reduced Density Function (RDF) analysis and amorphous modelling allows models of the atomic structure to be obtained from experimental data [**?**]. Initial results for tantala coatings indicate increased ordering of the tantala structure as the heat-treatment temperature rises, and it seems likely that these changes may be responsible for the loss peaks observed to occur at higher heat-treatment temperatures. This work is ongoing, with the aim of developing a full understanding of the relationship between the coating atomic structure and the mechanical loss. A better understanding of the mechanical loss processes will influence the final coating choice (exact doping concentration, post-deposition treatment, annealing, etc.).

5.15.3 Waveguide grating mirrors

Author(s): D. Friedrich

Test mass mirrors used in gravitational wave detectors are subject to several sources of thermal noise. A dominant contribution is given by Brownian thermal noise caused by mechanical loss of the high reflective multilayer coatings. These conventionally are made of up to 20 double layer of tantala (Ta_2O_5) and silica (SiO_2) each having a quarter wavelength optical thickness. Hence, concepts for a reduction of the mechanical lossy materials or for coating free mirrors are investigated to provide alternative mirror architectures in order to improve a detector sensitivity in its mid frequency band. For this purpose broadband waveguide grating (WG) structures have been proposed [584], which are based on resonant excitation of light fields in a nanostructured surface that theoretically allow for a perfect reflectivity under normal incidence without implementing multilayer stacks.

The basic principle of WGs is shown in Fig.218 using a ray picture [585].

WGs are basically constructed of a substrate with low index of refraction n_{L} and a nanostructered layer having a higher index of refraction n_{H}. The grating can be designed that only specular reflection and three transmitted orders exist. The first order beams in the nanostructured layer are totally reflected at the substrate and partially coupled out at the surface. By adjusting the grating dimensions (optical properties) the outcoupled light fields can be forced to interfere constructively giving a perfect reflectivity. For dielectric materials Rigorous-Coupled-Wave Analysis (RCWA) [586] is a numerical method to investigate the optical properties of WGs depending on their material and geometrical parameters and was used to optimize waveguide gratings in terms of parameter tolerant designs.

It was found that even a zero waveguide layer thickness (only ridges on top of a substrate) can show high reflectivity [584], which has experimentally been demonstrated using tantala ridges on a silica substrate for the prominent wavelength of 1064 nm [587]. The fabricated waveguide grating (see Fig. 218) was incoporated as a coupling mirror into a linear Fabry-Perot cavity together with a conventional high-reflectivity mirror. From the measured finesse of ≈ 660 the reflectivity of the waveguide grating was determined to be (99.08 ± 0.05) %.

Recent theoretical work [587] has shown that also monolithic waveguide grating structures are feasible by directly etching a T-shaped structure into a substrate (see Fig.218). Here, the lower grating is chosen to have a small enough fill factor (ratio of groove width to grating period) to act as an effective medium, namely having a lower index of refraction than the material used. This structure has been fabricated based on a silicon substrate aiming at a high reflectivity for a laser wavelength of 1550 nm. Therefor two etching steps were applied. In a first step the upper grating was defined via anisotropic etching and then protected on its sidewalls. Afterwards an isotropic etching was used to realize the low fill factor grating beneath. The reflectivity was determined in a table-top cavity setup to be $(99.79 \pm 0.01)\,\%$ [588] in full agreement with numerical simulations (RCWA) [586].

While the thermal noise models for conventional multilayer coatings and material parameters are well studied, the thermal noise performance of nanostructured surfaces is still to be investigated. It was experimentally shown that a nanostructured surface does not affect the mechanical quality of a substrate significantly [589]. However, the mechanical loss and other material parameters such as thermal conductivity of a nanostructure need to be further investigated in order to estimate the actual level of thermal noise. Also a direct measurement of thermal noise of a WG compared to a multilayer coating is of great interest.

Further, the fabrication process needs to be improved to meet the requirements for test masses used in gravitational wave detectors. Besides the optical quality in terms of high reflectivity and homogeneity over the grating area, techniques have to be developed to handle actual substrate dimensions. One approach being investigated is the bonding of a thin nanostructered waver on a thick substrate.

5.15.4 Speedmeter topology

Author(s): ***K. Kokeyama*** *and H. Mueller-Ebhardt*

As was reviewed in Section 5.4, speed meters are considered as the ET interferometer due to the strong advantage to surpass the quantum noise limit broadly in the low frequency region. However, few practical experience of speed meter technology has been accumulated, in contrast to well-studied Michelson-interferometer (MI) -type position-meter with currently operated gravitational-wave detectors. Practical speed meter characterization such as quantum noise surpass-ability and a capability to optical losses have to be examined in order to select the ET topology.

Speed-meters are realized by either MI-type or Sagnac-interferometer (SI) -type topology, and only few part of them is experimentally demonstrated:

Michelson-interferometer type A typical configuration of a MI type speed meter [411, 412] is depicted in the left panel in Fig 219. The configuration employs an RSE interferometer with the sloshing cavity at the anti-symmetric port. The south port of the RSE part is kept to be the dark fringe (destructive interference between the north and east arms). When the end mirror of one cavity moves, some light goes through to the south port, and enter into the sloshing cavity. The light comes back from the sloshing cavity and enter the RSE part from the south port. This field is 180 degrees different in phase and cancel the position information leaving only the phase shift proportional to the relative velocity of test masses. The sloshing cavity adds more complexity such as the length and alignment degrees of freedom to be controlled, compered with an RSE topology whose technology is mature and already being installed in, e.g., Advanced LIGO, therefore, it is necessary to examine the practical capability of ET.

Sagnac-interferometer type The SI-type speed meter [366] is depicted in the right panel in Fig 219. A SI is an more straightforward way to realize a speed meter than the MI-type. A basic SI is a ring interferometer (see, the middle panel in Fig. 173 in Section 5.4) and it is a speed meter by itself. The laser light is split into to paths by a beam splitter, then one of the two light fields propagates the ring path in the clockwise whereas the other in counter-clockwise. These two fields interfere at the same beam splitter. The two fields experience the same path but at the different timing depending on the path differences. Therefore the interference intensity depends only on the time depending part of the test masses. For an ET topology, a zero-area SI in which the area enclosed by the two counter-propagating beams is zero, will be preferable because it is insensitive to the interferometer rotation.

Before one realized that the speed meter is free from the quantum back-action noise, Sagnac interferometer has investigated as a candidate topology for the ground based gravitational-wave detectors. The shot-noise-limited phase sensitivities were demonstrated by [369] and [**?**] at high or low frequency region, respectively.

The squeezed-vacuum will be necessary to be injected from the dark port to enhance the ability for surpassing the SQL in the broadband frequency region. This technique has been already demonstrated experimentally for a zero-area Sagnac interferometer by a table-top experiment [416]. The non-classical sensitivity improvement of up to 8.2 dB with a simple zero-area Sagnac interferometer was experimentally verified.

5.16 Appendix

5.16.1 Optics properties data base

refractive index at 1064 nm, 1550 nm, dn/dT (T), absorption, etc.

The following two subsections might move directly into 5.9. Otherwise overview here and values at selected temperatures in main part of the section.

5.16.2 Mechanical properties of optical materials

Authors: R. Nawrodt, J. Franc, etc.

summary of mechanical data (TN relevant parameters) used for TN calculation parameters: Young's modulus, mechanical loss,...

bulk materials: fused silica, sapphire, *s*ilicon coatings: latest results on room temperature and cryogenic coating measurements (contrib. from *I. Martin*, ET note J. Franc et al. [491], R. Nawrodt et al. [513])

5.16.3 Thermal properties of optical materials

Authors: R. Nawrodt, J. Franc, etc.

summary of thermal properties used for the heat extraction estimates parameters: thermal conductivity, heat capacity, thermal expansion,...

Comparison of values and reasons for the selection of certain values at given temperatures (e.g. thermal conductivity [504])

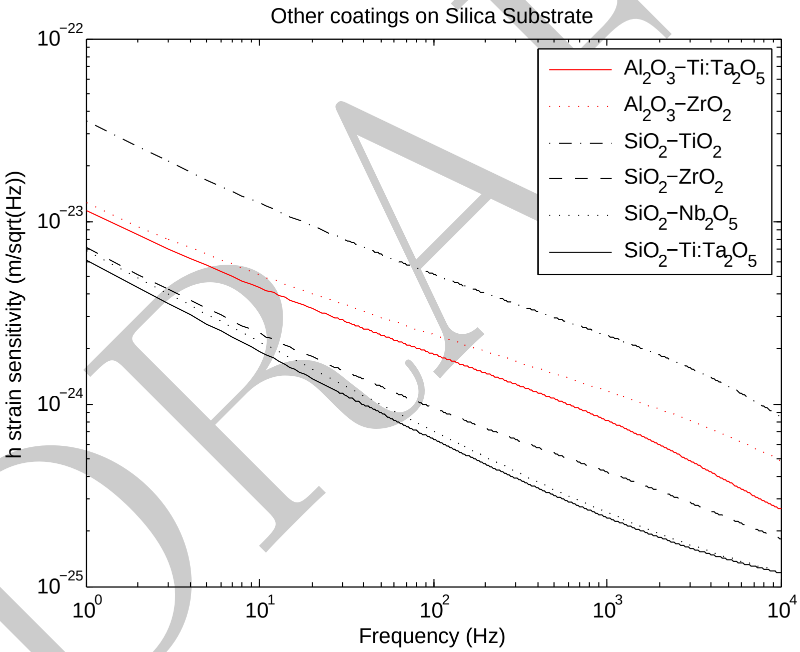

Figure 212: Comparison of the thermal noise of different coating materials on a fused silica substrate.

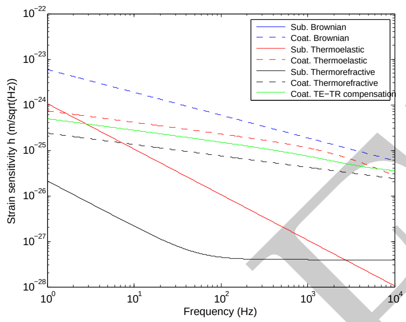

Figure 213: Contribution of the different thermal noises for a silica mirror.

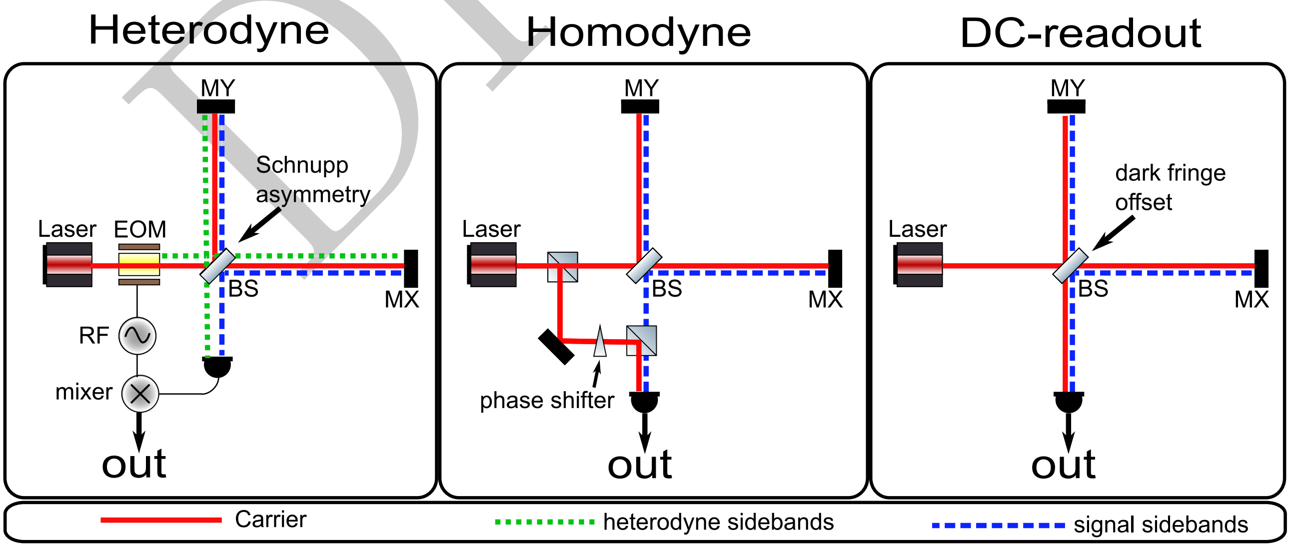

Figure 214: Illustration of three different readout methods of a Michelson interferometer: heterodyne, homodyne and DC-readout. A detailed explanation is given in the text.

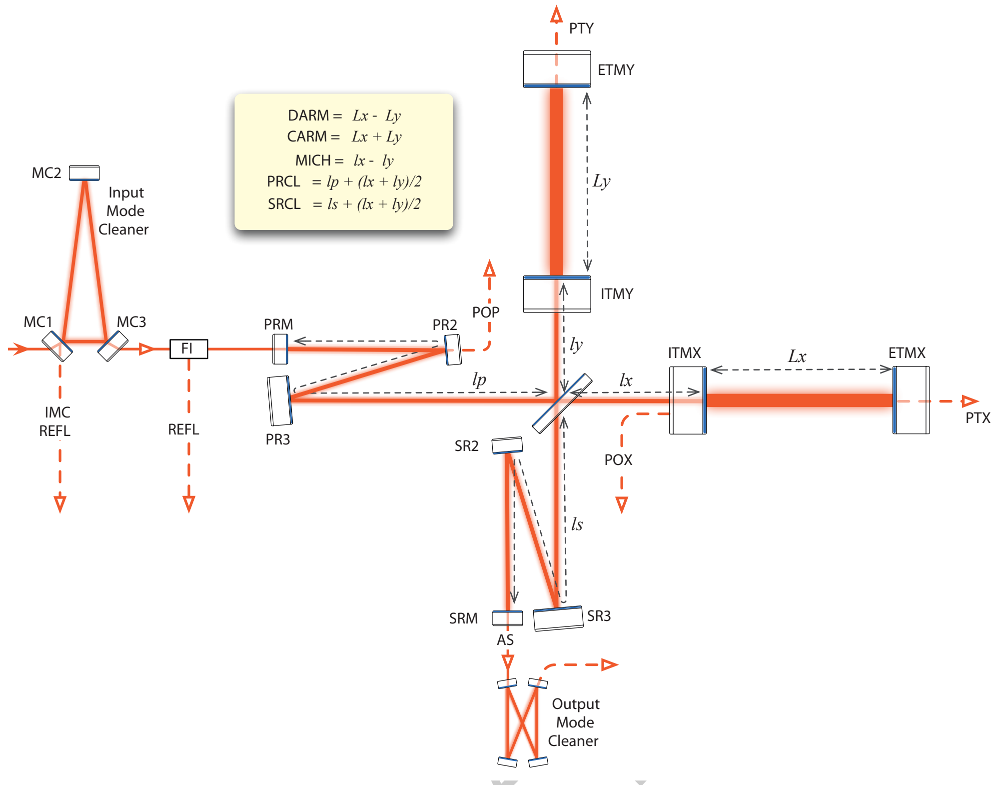

Figure 215: Schematic drawing of the Advanced LIGO optical layout, degrees-of-freedom and sensing ports [573]. Error signals for the control of the five longitudinal degrees-of-freedom are extracted from the four ports REFL, AS, POP and POX.

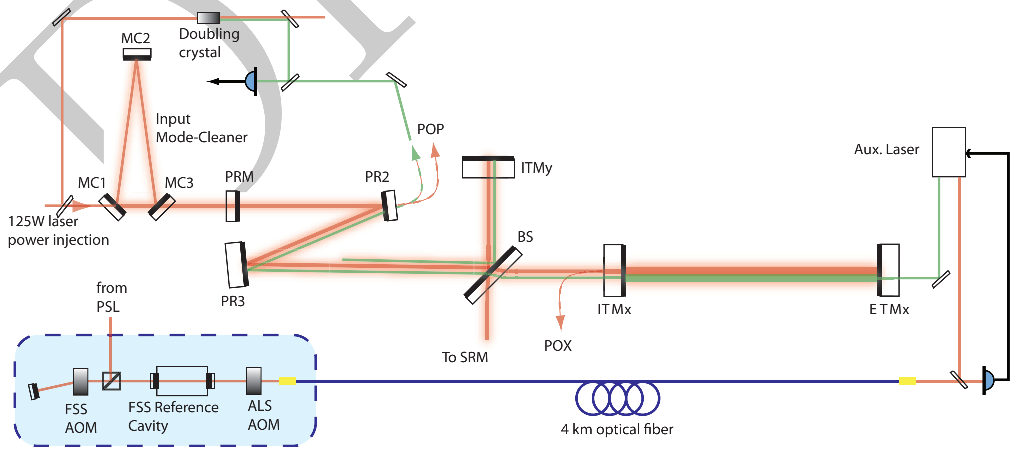

Figure 216: Schematic drawing of the Advanced LIGO arm length stabilization (ALS) subsystem [577]. The test mass motion is reduced prior to lock acquisition by a combined scheme of PDH reflection locking of an auxiliary laser to the arm cavities and hetorodyne detection of the transmitted beams. The optical fiber is necessary to provide an optical reference at the end stations, to lock the auxiliary lasers' phases to the science laser.

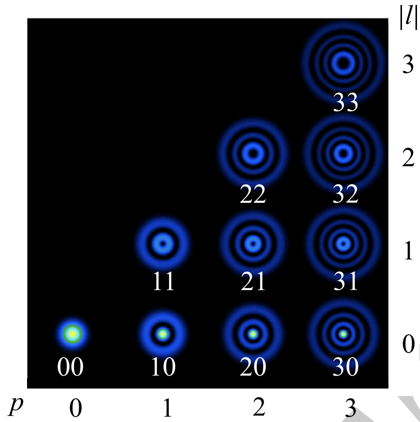

Figure 217: Power distributions of LG_{pl} mode. p is the radial mode index ($p \geq 0$), and l is the azimuthal mode index. The power distribution of LG_{00} mode is equivalent to that of the conventional HG_{00} mode.

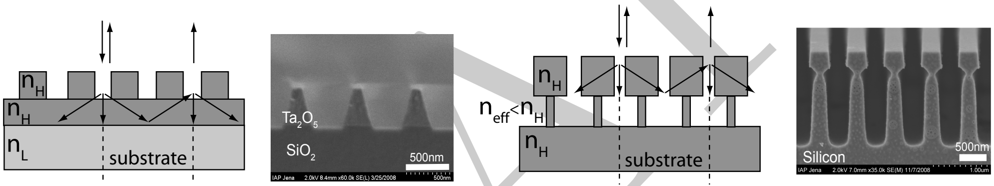

Figure 218: Single layer and monolithic waveguide grating architectures.

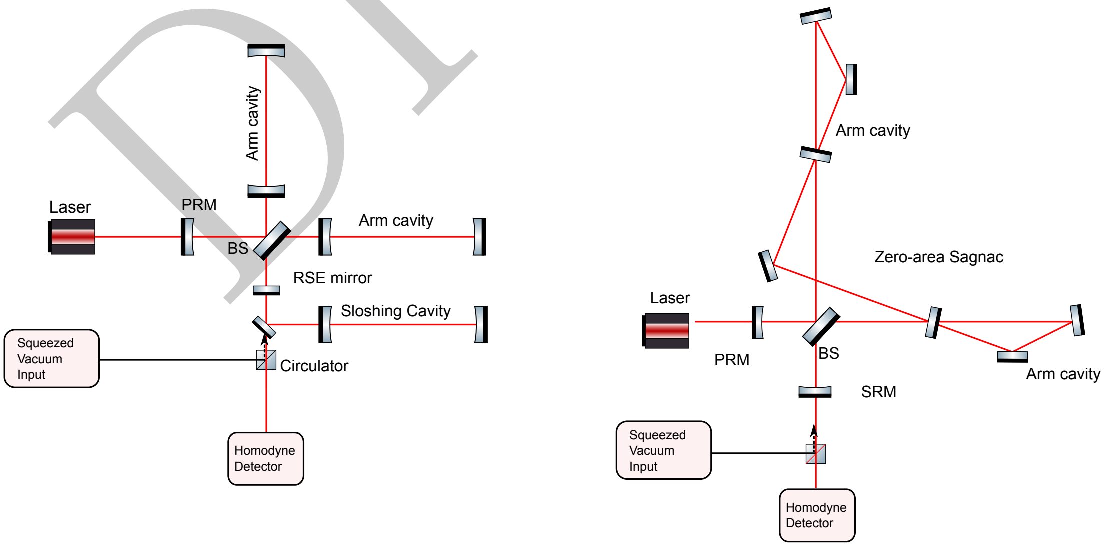

Figure 219: Left panel: An example configuration of a Michelson-interferometer-type speed meter. Right panel: An typical configuration of a Sagnac-interferometer-type speed meter with two ring cavities.

6 Overall budget and timeline considerations

The evolution toward the Einstein Telescope observatory has been, is and will be a long path. After a series of preliminary activities supported by the European Commission within the Framework Programme 6 (FP6), this conceptual design study is currently funded under FP7.

Although the efforts and the attention of the worldwide GW scientific community are currently focused on the realisation of the advanced detectors (Advanced LIGO, Advanced Virgo and LCGT), the activities devoted to the third generation must continue with increasing speed. In Fig. 220 the expected evolution of the GW detectors in the World is shown. The last line of the table shows the long path still in front of the European project ET. After the current conceptual design study phase, a preparatory phase is expected to be necessary to define the technological details, and the legal and organizational issues. The start of construction (2018–2019) is expected to occur after the first detection of GWs, which is reckoned to happen within at most one year after the advanced detectors will have reached their nominal sensitivity. The construction and commissioning phase is expected to be of about 6–7 years of intense activity, before collecting the first science data with the Einstein Telescope ET. In table 221 the cost summary and the time distribution of the expenditures are shown.

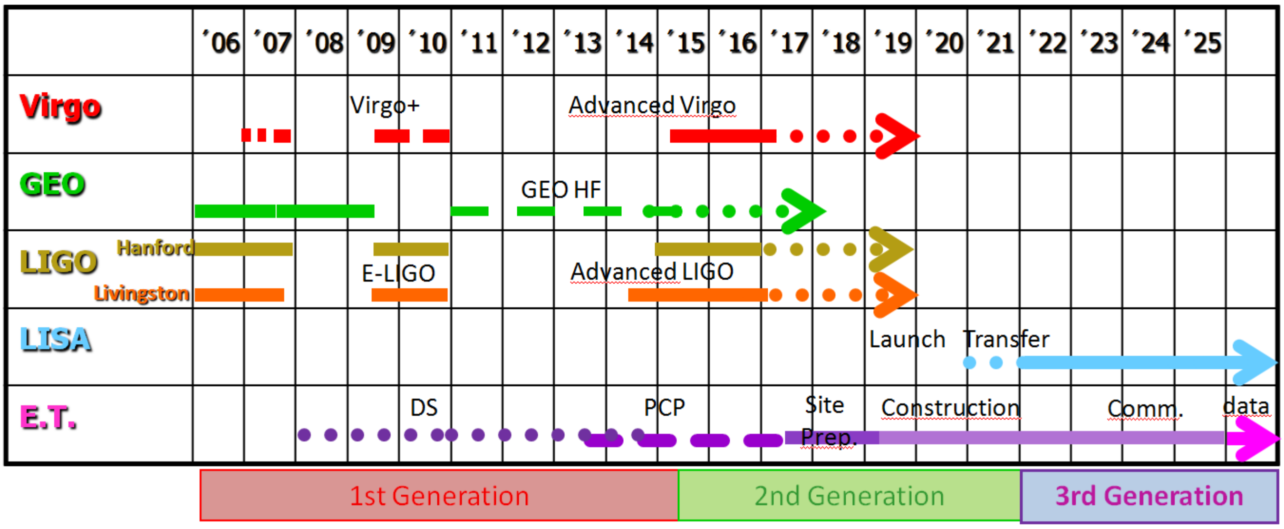

Figure 220: Roadmap for the evolution of some of the GW detectors in the World. In the last line the expected evolution of the third generation observatory ET (Einstein Telescope) is shown. After the current conceptual design phase (DS), and before the construction, a preparatory construction phase (PCP) is expected, where the detailed technical, legal and organization aspects of the project will be defined.In the evolution timeline of the Virgo and LIGO detectors are shown the (current) Virgo+ and E-LIGO phases, corresponding to a limited upgrade of the initial interferometers, with input laser power increased by about a factor 2 − 3 and other technical improvements preparatory of the "advanced" phase. The time evolution of the Japanese interferometers (TAMA, LCGT, DECIGO) and of the other projects like ACIGA in Australia are not plotted.

ET Costs Evaluation

Date: ________

Configuration: Xylophone configuration, 30 km arm total length, 100 m underground

Total Construction (M€)	???	Total R&D (M€)	???	Gran Total (M€)	???

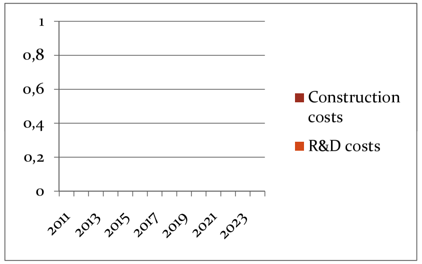

IDsystem	System	Configuration	Option	Subtotal (k€)	2011	2012	2013	2014	2015	2016	2017	2018	2019	2020	2021	2022	2023	2024	
1	Site	Xylophone - Triangular	=Common OR =LCGT	0						0	0	0	0	0	0	0	0	0	
2	Vacuum	Xylophone - Single detector	=Baseline	0						0	0	0	0	0	0	0	0	0	
3	Cryogenics	Xylophone - Single detector	ALL	0						0	0	0	0	0	0	0	0	0	
4	Suspensions	Xylophone - Single detector	ALL	0						0	0	0	0	0	0	0	0	0	
5	Optics	Xylophone - Single detector	ALL	0						0	0	0	0	0	0	0	0	0	
6	Computational	Xylophone - Triangular	ALL	0						0	0	0	0	0	0	0	0	0	
RD1	Site	Xylophone - Triangular	ALL	0	0	0	0	0	0	0	0	0	0						
RD2	Vacuum	Xylophone - Triangular	ALL	0	0	0	0	0	0	0	0	0	0						
RD3	Cryogenics	Xylophone - Triangular	ALL	0	0	0	0	0	0	0	0	0	0						
RD4	Suspensions	Xylophone - Triangular	ALL	0	0	0	0	0	0	0	0	0	0						
RD5	Optics	Xylophone - Triangular	ALL	0	0	0	0	0	0	0	0	0	0						
RD6	Computational	Xylophone - Triangular	ALL	0	0	0	0	0	0	0	0	0	0						
			R&D Totals	0	0	0	0	0	0	0	0	0	0	0	0	0	0	0	0
			Construction Totals	0	0	0	0	0	0	0	0	0	0	0	0	0	0	0	0
			Gran Totals	0	0	0	0	0	0	0	0	0	0	0	0	0	0	0	0

Figure 221: Cost summary and time distribution

Acknowledgements

The research leading to these results has received funding from the European Community's Seventh Framework Programme (FP7/2007-2013) under grant agreement n 211743.

References

References

[1] H. Grote for the LIGO Scientific Collaboration, "The status of GEO 600," *Classical and Quantum Gravity*, vol. 25, no. 11, p. 114043 (9pp), 2008. 7

[2] B. Abbott et al. (LIGO Scientific Collaboration), "LIGO: the Laser Interferometer Gravitational-Wave Observatory," *Reports on Progress in Physics*, vol. 72, no. 7, p. 076901, 2009. 7, 232

[3] K. Arai and the TAMA Collaboration, "Recent progress of TAMA300," *Journal of Physics: Conference Series*, vol. 120, no. 3, p. 032010, 2008. 7

[4] F. Acernese *et al.*, "Status of Virgo," *Classical and Quantum Gravity*, vol. 25, no. 11, p. 114045 (8pp), 2008. 7

[5] B. F. Schutz, "Determining the Hubble constant from gravitational wave observations," *Nature (London)*, vol. 323, p. 310, 1986. 15, 16, 38

[6] L. Blanchet, "Gravitational radiation from post-Newtonian sources and inspiralling compact binaries," *Living Rev. Relativity*, vol. 9, 2006. 16

[7] F. Pretorius, "Evolution of binary black hole spacetimes," *Phys. Rev. Lett.*, vol. 95, 2005. 16

[8] M. Campanelli, C. Lousto, P. Marronetti, and Y. Zlochower, "Accurate evolutions of orbiting black-hole binaries without excision," *Phys. Rev. Lett.*, vol. 96, 2006.

[9] J. Baker, J. Centrella, D.-I. Choi, M. Koppitz, and J. van Meter, "Gravitational wave extraction from an inspiraling configuration of merging black holes," *Phys. Rev. Lett.*, vol. 96, 2006. 16

[10] M. Hannam, "Status of black-hole-binary simulations for gravitational-wave detection," *arXiv:0901.2931 [gr-qc]*, 2009. 16

[11] V. Lipunov, K. Postnov, and M. Prokhorov *MNRAS*, vol. 288, p. 245, 1997. 18, 56

[12] K. Belczynski and T. Bulik *Astronomy and Astrophysics*, vol. 346, p. 91, 1999. 18, 56

[13] A. M. Hopkins and J. F. Beacom, "On the Normalization of the Cosmic Star Formation History," *Astrophys. J.*, vol. 651, pp. 142–154, Nov. 2006. 19, 53, 55

[14] M. Burgay, N. D'Amico, A. Possenti, R. Manchester, A. Lyne, B. Joshi, M. McLaughlin, M. Kramer, J. Sarkissian, F. Camilo, V. Kalogera, C. Kim, and D. Lorimer, "An increased estimate of the merger rate of double neutron stars from observations of a highly relativistic system," *Nature*, vol. 426, pp. 531–533, 2003. 19

[15] C. Kim, V. Kalogera, and D. R. Lorimer, "The Probability Distribution of Binary Pulsar Coalescence Rates. I. Double Neutron Star Systems in the Galactic Field," *Astrophys. J.*, vol. 584, pp. 985–995, Feb. 2003.

[16] C. Kim, V. Kalogera, and D. R. Lorimer, "Effect of PSR J0737-3039 on the DNS Merger Rate and Implications for GW Detection," in *A life with stars*, 2006. 19

[17] T. Regimbau and S. A. Hughes, "Gravitational-wave confusion background from cosmological compact binaries: Implications for future terrestrial detectors," *Phys. Rev. D*, vol. 79, pp. 062002–+, Mar. 2009. 19, 53, 66

[18] R. O'Shaughnessy, V. Kalogera, and K. Belcynski, "Binary compact object coalescence rates: The role of elliptical galaxies," *(arXiv:0908.3635)*, 2009. 19

[19] R. O'Shaughnessy, V. Kalogera, and C. Belczynski, "Short GRBs I: Predictions from population synthesis for a heterogeneous universe," *Astrophys. J.*, vol. 675, p. 566, March 2008. 19

[20] K. Belczynski, V. Kalogera, F. Rasio, R. Taam, A. Zezas, T. Maccarone, and N. Ivanova, "Compact Object Modeling with the StarTrack population synthesis code," *Astrophys.J. Suppl.*, vol. 174, pp. 223–260, Jan. 2008. 19

[21] K. Kulczycki, T. Bulik, K. Belczyński, and B. Rudak, "VIRGO sensitivity to binary coalescences and the Population III black hole binaries," *Astron. Astrophys.*, vol. 459, pp. 1001–1006, Dec. 2006.

[22] R. O'Shaughnessy, C. Kim, V. Kalogera, and K. Belczynski, "Constraining population synthesis models via observations of compact-object binaries and supernovae," *Astrophys. J.*, vol. 672, p. 479, Jan. 2008.

[23] K. Belczynski, R. E. Taam, V. Kalogera, F. A. Rasio, and T. Bulik, "On the rarity of double black hole binaries: Consequences for gravitational-wave detection," *Astrophys. J.*, vol. 662, p. 504, 2007. 19

[24] K. Belczynski, T. Bulik, C. L. Fryer, A. Ruiter, J. S. Vink, and J. R. Hurley, "On the maximum mass of stellar black holes," Apr. 2009. 20

[25] K. Belczynski, D. H. Hartmann, C. L. Fryer, D. E. Holz, and B. O'Shea, "On the origin of the highest redshift gamma-ray burst GRB 080913," Dec. 2008. 20

[26] R. O'Shaughnessy, R. Kopparapu, and K. Belczynski, "Impact of star formation inhomogeneities on merger rates and interpretation of ligo results," *submitted to Astrophys. J.*, 2008. 20

[27] T. Bulik, K. Belczynski, and A. Prestwich, "IC10 X-1: the immediate progenitor of a double black hole binary," 2008. 20

[28] R. O'Shaughnessy, R. O'Leary, and F. Rasio, "Dynamical Interactions and the Black Hole Merger Rate of the Universe," *Phys. Rev. D*, vol. 76, p. 061504, Oct. 2007. 20

[29] A. Sadowski, K. Belczynski, T. Bulik, N. Ivanova, F. Rasio, and R. O'Shaughnessy, "The Total Merger Rate of Compact Object Binaries in the Local Universe," *Astrophys. J.*, vol. 676, pp. 1162–1169, Apr. 2008.

[30] S. F. Portegies Zwart and S. L. McMillan, "Black hole mergers in the universe," *Astrophys. J.*, vol. 528, pp. L17–L20, 2000. 20

[31] G. Hinshaw *et al.*, "Five-Year Wilkinson Microwave Anisotropy Probe (WMAP) Observations:Data Processing, Sky Maps, & Basic Results," *Astrophys. J. Suppl.*, vol. 180, pp. 225–245, 2009. 20, 38

[32] L. Santamaria *et al.*, "Matching post-Newtonian and numerical relativity waveforms: systematic errors and a new phenomenological model for non-precessing black hole binaries," *Phys. Rev.*, vol. D82, p. 064016, 2010. 20

[33] M. C. Miller and E. J. M. Colbert, "Intermediate-Mass Black Holes," *International Journal of Modern Physics D*, vol. 13, pp. 1–64, Jan. 2004. 21

[34] M. C. Miller, "Intermediate-Mass Black Holes as LISA Sources," *ArXiv e-prints*, Dec. 2008. 0812.3028. 21

[35] S. A. Farrell, N. A. Webb, D. Barret, O. Godet, and J. M. Rodrigues, "An intermediate-mass black hole of over 500 solar masses in the galaxy ESO243-49," *Nature*, vol. 460, pp. 73–75, July 2009. 21

[36] I. Mandel, D. A. Brown, J. R. Gair, and M. C. Miller, "Rates and Characteristics of Intermediate Mass Ratio Inspirals Detectable by Advanced LIGO," *Astrophys. J.*, vol. 681, pp. 1431–1447, July 2008. 21, 39

[37] J. R. Gair, I. Mandel, M. C. Miller, and M. Volonteri, "Exploring intermediate and massive black-hole binaries with the Einstein Telescope," *ArXiv e-prints*, July 2009. 0907.5450. 21

[38] J. M. Fregeau, S. L. Larson, M. C. Miller, R. O'Shaughnessy, and F. A. Rasio, "Observing IMBH-IMBH Binary Coalescences via Gravitational Radiation," *Astrophysical Journal Letters*, vol. 646, pp. L135–L138, Aug. 2006. 21

[39] P. Amaro-Seoane, J. Gair, M. Freitag, M. Coleman, I. Mandel, C. Cutler, and S. Babak, "Intermediate and extreme mass-ratio inspirals – astrophysics, science applications and detection using LISA," *Class. Quant. Grav.*, vol. 24, pp. R113–R170, 2007. 21, 39

[40] P. Amaro-Seoane and L. Santamaria, "Detection of IMBHs with ground-based gravitational wave observatories: A biography of a binary of black holes, from birth to death," *Astrophys. J.*, vol. 722, pp. 1197–1206, 2010. 21

[41] P. Jaranowski, A. Krolak, and B. F. Schutz, "Data analysis of gravitational-wave signals from spinning neutron stars. I: The signal and its detection," *Phys. Rev.*, vol. D58, p. 063001, 1998. 22, 222

[42] B. Abbott et al. (LIGO Scientific Collaboration), "Limits on gravitational wave emission from selected pulsars using LIGO data," *Phys. Rev. Lett.*, vol. 94, 2005. 22

[43] B. Abbott et al. (LIGO Scientific Collaboration), "Upper limits on gravitational wave emission from 78 radio pulsars," *Phys. Rev. D*, vol. 76, 2007.

[44] B. Abbott *et al.*, "Beating the spin-down limit on gravitational wave emission from the crab pulsar," *The Astrophysical Journal Letters*, vol. 683, no. 1, p. L45, 2008. 22

[45] B. Abbott et al. (LIGO Scientific Collaboration), "First all-sky upper limits from LIGO on the strength of periodic gravitational waves using the Hough transform," *Phys. Rev. D*, vol. 72, 2005. 23

[46] L. Bildsten, "Gravitational radiation and rotation of accreting neutron stars," *Astrophys. J. Lett.*, vol. 501, p. L89, 1998. 26, 52

[47] B. Allen and J. Romano, "Detecting a stochastic background of gravitational radiation: Signal processing strategies and sensitivities," *Phys. Rev. D*, vol. 59, 1999. 27, 31

[48] R. Schneider, V. Ferrari, S. Matarrese, and S. Portegies Zwart, "Gravitational waves from cosmological compact binaries," *Mon. Not. R. Astron. Soc.*, vol. 324, p. 797, 2001. 28

[49] T. Regimbau and J. A. de Freitas Pacheco, "Stochastic Background from Coalescences of Neutron Star-Neutron Star Binaries," *Astrophys. J.*, vol. 642, pp. 455–461, May 2006.

[50] T. Regimbau and B. Chauvineau, "A stochastic background from extra-galactic double neutron stars," *Classical and Quantum Gravity*, vol. 24, pp. 627–+, Oct. 2007.

[51] T. Regimbau and V. Mandic, "Astrophysical sources of a stochastic gravitational-wave background," *Classical and Quantum Gravity*, vol. 25, pp. 184018–+, Sept. 2008. 28

[52] T. Regimbau and J. A. de Freitas Pacheco, "Gravitation wave emission from radio pulsars revisited," *Astronomy and Astrophysics*, vol. 359, pp. 242–250, July 2000. 28

[53] C.-A. Faucher-Giguère and V. M. Kaspi, "Birth and Evolution of Isolated Radio Pulsars," *Astrophys. J.*, vol. 643, pp. 332–355, May 2006.

[54] R. Soria, R. Perna, D. Pooley, and L. Stella, "How rapidly do neutron stars spin at birth?," 2008. 28

[55] R. C. Duncan and C. Thompson, "Formation of very strongly magnetized neutron stars - implications for gamma-ray bursts," *Astrophys. J.*, vol. 392, p. L9, 1992. 28

[56] C. Thompson and R. C. Duncan, "Neutron star dynamos and the origins of pulsar magnetism," *Astrophys. J.*, vol. 408, p. 194, 1993. 28

[57] T. Regimbau and J. A. de Freitas Pacheco, "Gravitational wave background from magnetars," *Astron. Astrophys.*, vol. 447, pp. 1–7, Feb. 2006. 28

[58] D. Brown *Phys. Rev. D*, vol. 62, p. 084024, 2000. 28

[59] K. C. B. New, J. M. Centrella, and J. E. Tohline, "Gravitational waves from long-duration simulations of the dynamical bar instability," *Phys. Rev. D*, vol. 62, no. 064019, 2000.

[60] M. Shibata, W. Baumgarte, and S. Shapiro *Astrophys. J.*, vol. 542, p. 453, 2000.

[61] M. Saijo, M. Shibata, W. Baumgarte, and S. Shapiro *Astrophys. J.*, vol. 548, p. 919, 2001.

[62] L. Baiotti, R. D. Pietri, G. M. Manca, and L. Rezzolla, "Accurate simulations of the dynamical bar-mode instability in full general relativity," *Phys. Rev. D*, vol. 75, p. 044023, 2007. 28

[63] M. Shibata and Y. Sekiguchi, "Three-dimensional simulations of stellar core collapse in full general relativity: Nonaxisymmetric dynamical instabilities," *Phys. Rev. D*, vol. 71, p. 024014, 2005. 28, 29

[64] B. J. Owen, L. Lindblom, C. Cutler, B. F. Schutz, A. Vecchio, and N. Andersson, "Gravitational waves from hot young rapidly rotating neutron stars," *Phys. Rev. D*, vol. 58, 1998. 29, 44

[65] V. Ferrari, S. Matarrese, and R. Schneider, "Stochastic background of gravitational waves generated by a cosmological population of young, rapidly rotating neutron stars," *Mon. Not. Roy. Astron. Soc.*, vol. 303, p. 258, 1999. 29

[66] L. Lindblom, B. Owen, and S. Morsink, "Gravitational radiation instability in hot young neutron stars," *Phys. Rev. Lett.*, vol. 80, pp. 4843–4846, 1998. 29

[67] D. Lai and S. L. Shapiro, "Gravitational radiation from rapidly rotating nascent neutron stars," *Astrophys. J.*, vol. 442, p. 259, 1995. 29

[68] C. D. Ott, A. Burrows, L. Dessart, and E. Livne, "A New Mechanism for Gravitational-Wave Emission in Core-Collapse Supernovae," *Physical Review Letters*, vol. 96, p. 201102, May 2006. 30, 31

[69] Y.-I. Sekiguchi and M. Shibata, "Axisymmetric collapse simulations of rotating massive stellar cores in full general relativity: Numerical study for prompt black hole formation," *Phys. Rev. D*, vol. 71, pp. 084013–+, Apr. 2005. 30, 31

[70] V. Ferrari, S. Matarrese, and R. Schneider, "Gravitational wave background from a cosmological population of core-collapse supernovae," *Mon. Not. R. Astron. Soc.*, vol. 303, p. 247, 1999. 29

[71] R. F. Stark and T. Piran, "GRAVITATIONAL WAVE EMISSION FROM ROTATING GRAVITATIONAL COLLAPSE," *Phys. Rev. Lett.*, vol. 55, pp. 891–894, 1985. 29

[72] J. C. N. de Araujo, O. D. Miranda, and O. D. Aguiar, "Stochastic background of gravitational waves," *Phys. Rev.*, vol. D61, p. 124015, 2000. 29

[73] F. Echeverria, "Gravitational wave measurements of the mass and angular momentum of a black hole," *Phys. Rev.*, vol. D40, pp. 3194–3203, 1989. 29

[74] S. Marassi, R. Schneider, and V. Ferrari, "Gravitational wave backgrounds and the cosmic transition from Population III to Population II stars," *ArXiv e-prints*, June 2009. 29

[75] Y. Suwa, T. Takiwaki, K. Kotake, and K. Sato, "Gravitational Wave Background from Population III Stars," *Astrophys. J. Lett.*, vol. 665, pp. L43–L46, Aug. 2007. 29

[76] E. Müller, M. Rampp, R. Buras, H.-T. Janka, and D. H. Shoemaker, "Toward Gravitational Wave Signals from Realistic Core-Collapse Supernova Models," *Astrophys. J.*, vol. 603, pp. 221–230, Mar. 2004. 31

[77] H. A. Bethe, "Supernova mechanisms," *Rev. Mod. Phys.*, vol. 62, pp. 801–866, Oct 1990. 31, 50

[78] H.-T. Janka, K. Langanke, A. Marek, G. Martínez-Pinedo, and B. Müller *Phys. Rep.*, vol. 442, p. 38, 2007.

[79] C. D. Ott, "The gravitational wave signature of core-collapse supernovae," *Class. Quant. Grav.*, vol. 26, p. 063001, 2009. 31, 32, 46, 50, 51

[80] C. D. Ott *submitted to Class. Quant. Grav.*, 2009. 31, 50, 51

[81] S. Ando and J. F. Beacom, "Revealing the supernova gamma-ray burst connection with TeV neutrinos," *Phys. Rev. Lett.*, vol. 95, no. 6, p. 061103, 2005. 32

[82] "Einstein telescope home page." 31, 51

[83] C. Will, "Bounding the mass of the graviton using gravitional-wave observations of inspiralling compact binaries," *Phys. Rev. D*, vol. 57, p. 2061, 1998. 34

[84] K. G. Arun and C. M. Will, "Bounding the mass of the graviton with gravitational waves: Effect of higher harmonics in gravitational waveform templates," 2009. 34

[85] L. Blanchet, B. R. Iyer, C. M. Will, and A. G. Wiseman, "Gravitational wave forms from inspiralling compact binaries to second-post-Newtonian order," *Class. Quantum Grav.*, vol. 13, pp. 575–584, 1996. 34

[86] K. G. Arun, L. Blanchet, B. R. Iyer, and M. S. S. Qusailah, "The 2.5PN gravitational wave polarisations from inspiralling compact binaries in circular orbits," *Class. Quantum Grav.*, vol. 21, p. 3771, 2004. Erratum-ibid. **22**, 3115 (2005).

[87] L. Blanchet, G. Faye, B. R. Iyer, and S. Sinha, "The third post-Newtonian gravitational wave polarisations and associated spherical harmonic modes for inspiralling compact binaries in quasi-circular orbits," *Class. Quantum. Grav.*, vol. 25, p. 165003, 2008.

[88] C. Van Den Broeck and A. Sengupta, "Phenomenology of amplitude-corrected post-newtonian gravitational waveforms for compact binary inspiral. i. signal-to-noise ratios," *Class. Quantum Grav.*, vol. 24, pp. 155–176, 2007. 34

[89] L. Blanchet, T. Damour, B. Iyer, C. Will, and A. Wiseman, "Gravitational-radiation damping of compact binary systems to second post-Newtonian order," *Phys. Rev. Lett.*, vol. 74, pp. 3515–3518, 1995. 34

[90] L. Blanchet, G. Faye, B. R. Iyer, and B. Joguet, "Gravitational-wave inspiral of compact binary systems to 7/2 post-Newtonian order," *Phys. Rev. D*, vol. 65, p. 061501(R), 2002. Erratum-ibid **71**, 129902(E) (2005).

[91] L. Blanchet, "Energy losses by gravitational radiation in inspiralling compact binaries to five halves post-Newtonian order," *Phys. Rev. D*, vol. 54, pp. 1417–1438, 1996. Erratum-ibid.**71**, 129904(E) (2005).

[92] L. Blanchet, T. Damour, G. Esposito-Farèse, and B. R. Iyer, "Gravitational radiation from inspiralling compact binaries completed at the third post-Newtonian order," *Phys. Rev. Lett.*, vol. 93, p. 091101, 2004.

[93] T. Damour, B. Iyer, and B. Sathyaprakash, "A comparison of search templates for gravitational waves from binary inspiral," *Phys. Rev. D*, vol. 63, 2001. Erratum-ibid. D**72** 029902 (2005).

[94] T. Damour, B. R. Iyer, and B. S. Sathyaprakash, "A comparison of search templates for gravitational waves from binary inspiral: 3.5-PN update," *Phys. Rev. D*, vol. 66, p. 027502, 2002. Erratum-ibid **66**, 027502 (2002). 34

[95] C. Cutler and E. Flanagan, "Gravitational waves from merging compact binaries: How accurately can one extract the binary's parameters from the inspiral wave form?," *Phys. Rev.*, vol. D49, pp. 2658–2697, 1994. 35

[96] E. Poisson and C. Will, "Gravitational waves from inspiraling compact binaries: Parameter estimation using second postNewtonian wave forms," *Phys. Rev. D*, vol. 52, pp. 848–855, 1995.

[97] K. Arun, B. Iyer, B. Sathyaprakash, and P. Sundararajan, "Parameter estimation of inspiralling compact binaries using 3.5 post-Newtonian gravitational wave phasing: The nonspinning case," *Phys. Rev. D*, vol. 71, 2005. 35

[98] M. Vallisneri, “Use and abuse of the fisher information matrix in the assessment of gravitational-wave parameter-estimation prospects,” *Phys. Rev. D*, vol. 77, 2008. 35

[99] C. Brans and R. H. Dicke, “Mach’s principle and a relativistic theory of gravitation,” *Phys. Rev.*, vol. 124, pp. 925–935, Nov 1961. 36

[100] B. Bertotti, L. Iess, and P. Tortora, “A test of general relativity using radio links with the Cassini spacecraft,” *Nature*, vol. 425, p. 374, 2003. 36

[101] C. M. Will, “Testing scalar - tensor gravity with gravitational wave observations of inspiraling compact binaries,” *Phys. Rev.*, vol. **D** 50, pp. 6058–6067, 1994. 36

[102] A. Królak, K. Kokkotas, and G. Schäfer, “Estimation of the post-Newtonian parameters in the gravitational-wave emission of a coalescing binary,” *Phys. Rev. D*, vol. 52, pp. 2089–2111, 1995. 36

[103] C. M. Will, *Theory and experiments in gravitational physics.* New York, USA: Cambridge University Press, 1981. 36

[104] P. D. Scharre and C. M. Will, “Testing scalar-tensor gravity using space gravitational- wave interferometers,” *Phys. Rev.* **D**, vol. 65, p. 042002, 2002. 37

[105] C. M. Will and N. Yunes, “Testing alternative theories of gravity using lisa,” *Class. Quantum Grav.*, vol. 21, p. 4367, 2004.

[106] E. Berti, A. Buonanno, and C. Will, “Estimating spinning binary parameters and testing alternative theories of gravity with lisa,” *Phys. Rev. D*, vol. 71, 2005. 37

[107] K. Arun, M. Iyer, Qusailah, and B. Sathyaprakash, “Testing post-newtonian theory with gravitational waves,” *Class. Quantum Grav.*, vol. 23, pp. L37–L43, 2006. 37

[108] K. Arun, B. Iyer, M. Qusailah, and B. Sathyaprakash, “Probing the non-linear structure of general relativity with black hole binaries,” *Phys. Rev. D*, vol. 74, p. 024006, 2007.

[109] C. Mishra, K. Arun, B. Iyer, and B. Sathyaprakash, “Parameterized tests of post-newtonian theory using advanced ligo and einstein telescope,” *Phys. Rev. D*, vol. 82, p. 064010, 2010. 37

[110] P. J. E. Peebles and B. Ratra *Rev. Mod. Phys.*, vol. 75, p. 559, 2005. 38

[111] B. Carter, “Axisymmetric black hole has only two degrees of freedom.,” *Phys. Rev. Lett.*, vol. 26, pp. 331–333, 1971. 39

[112] F. D. Ryan, “Gravitational waves from the inspiral of a compact object into a massive, axisymmetric body with arbitrary multipole moments,” *Phys. Rev. D*, vol. 52, pp. 5707–5718, Nov. 1995. 39

[113] D. A. Brown, J. Brink, H. Fang, J. R. Gair, C. Li, G. Lovelace, I. Mandel, and K. S. Thorne, “Prospects for Detection of Gravitational Waves from Intermediate-Mass-Ratio Inspirals,” *Phys. Rev. Lett.*, vol. 99, p. 201102, Nov. 2007. 39

[114] F. D. Ryan, “Spinning boson stars with large self-interaction,” *Phys. Rev. D*, vol. 55, pp. 6081–6091, May 1997. 39

[115] R. Penrose, “Gravitational Collapse: the Role of General Relativity,” *Nuovo Cimento Rivista Serie*, vol. 1, p. 252, 1969. 39

[116] M. Kesden, J. Gair, and M. Kamionkowski, “Gravitational-wave signature of an inspiral into a supermassive horizonless object,” *Phys. Rev. D*, vol. 71, p. 044015, Feb. 2005. 40

[117] J. M. Lattimer and M. Prakash, “Neutron star observations: Prognosis for equation of state constraints,” *J. Phys. Rep.*, vol. 442, pp. 109–165, Apr. 2007. 41

[118] T. Klähn *et al.*, “Constraints on the high-density nuclear equation of state from the p henomenology of compact stars and heavy-ion collisions,” *Phys. Rev. C*, vol. 74, p. 035802, Sept. 2006.

[119] D. Page and S. Reddy, "Dense Matter in Compact Stars: Theoretical Developments and Observational Constraints," *Ann. Rev. Nucl. Part. Sci.*, vol. 56, pp. 327–374, Nov. 2006. 41

[120] H. Dimmelmeier, C. Ott, H.-T. Janka, A. Marek, and E. Müller, "Generic gravitational wave signals from the collapse of rotating stellar cores," *Phys. Rev. Lett.*, vol. 98, 2007. 41

[121] A. Marek, H.-T. Janka, and E. Müller, "Equation-of-state dependent features in shock-oscillation modulated neutrino and gravitational-wave signals from supernovae," *AAP*, vol. 496, pp. 475–494, Mar. 2009. 41

[122] B. J. Owen *Phys. Rev. Lett.*, vol. 95, p. 211101, 2005. 41, 49

[123] A. Watts, B. Krishnan, L. Bildsten, and B. Schutz, "Detecting gravitational wave emission from the known accreting neutron stars." 2008. 41

[124] X. Zhuge, J. M. Centrella, and S. L. W. McMillan, "Gravitational radiation from the coalescence of binary neutron stars: Effects due to the equation of state, spin, and mass ratio," *Phys. Rev. D*, vol. 54, pp. 7261–7277, Dec 1996. 41

[125] F. A. Rasio and S. L. Shapiro, "Coalescing binary neutron stars," *Class. Quantum Grav.*, vol. 16, p. R1, 1999.

[126] É. É. Flanagan and T. Hinderer, "Constraining neutron-star tidal Love numbers with gravitational-wave detectors," *Phys. Rev. D*, vol. 77, p. 021502, Jan. 2008. 43

[127] J. S. Read, B. D. Lackey, B. J. Owen, and J. L. Friedman, "Constraints on a phenomenologically parameterized neutron- star equation of state," 2008. 43

[128] J. S. Read *et al.*, "Measuring the neutron star equation of state with gravitational wave observations," 2009. 41, 43

[129] M. Bejger, D. Gondek-Rosińska, E. Gourgoulhon, P. Haensel, K. Taniguchi, and J. L. Zdunik, "Impact of the nuclear equation of state on the last orbits of binary neutron stars," *Astron. Astrophys.*, vol. 431, pp. 297–306, 2005. 41

[130] M. Shibata, K. Taniguchi, and K. Uryū, "Merger of binary neutron stars with realistic equations of state in full general relativity," *Phys. Rev. D*, vol. 71, p. 084021, 2005.

[131] M. Shibata, "Constraining nuclear equations of state using gravitational waves from hypermassive neutron stars," *Phys. Rev. Lett.*, vol. 94, p. 201101, May 2005. 43

[132] R. Oechslin and H. T. Janka, "Torus formation in neutron star mergers and well-localized short gamma-ray burst," *Mon. Not. R. Astron. Soc.*, vol. 368, p. 1489, 2006.

[133] R. Oechslin and H. T. Janka, "Gravitational waves from relativistic neutron-star mergers with mycrophysical equations of state," *Phys. Rev. Lett.*, vol. 99, p. 121102, 2007.

[134] T. Yamamoto, M. Shibata, and K. Taniguchi, "Simulating coalescing compact binaries by a new code SACRA," *Phys. Rev. D*, vol. 78, pp. 064054–1–38, June 2008.

[135] L. Baiotti, B. Giacomazzo, and L. Rezzolla, "Accurate evolutions of inspiralling neutron-star binaries: prompt and delayed collapse to black hole," *Phys. Rev. D*, vol. 78, p. 084033, Apr. 2008. 41, 43

[136] L. Baiotti, B. Giacomazzo, and L. Rezzolla, "Accurate evolutions of inspiralling neutron-star binaries: assessment of the truncation error," *Class. Quantum Grav., in press, arXiv:0901.4955*, 2009. 41, 43

[137] J. A. Faber, T. W. Baumgarte, S. L. Shapiro, K. Taniguchi, and F. A. Rasio, "The Dynamical evolution of black hole-neutron star binaries in General Relativity: Simulations of tidal disruption," *Phys. Rev. D*, vol. 73, p. 024012, 2006. astro-ph/0511366. 41

[138] M. Shibata and K. Taniguchi, "Merger of black hole and neutron star in general relativity: Tidal disruption, torus mass, and gravitational waves," *Phys. Rev. D*, vol. 77, p. 084015, Apr. 2008.

[139] M. Shibata, K. Kyutoku, T. Yamamoto, and K. Taniguchi, "Gravitational waves from black hole-neutron star binaries I: Classification of waveforms," *Phys. Rev.*, vol. D79, p. 044030, 2009. 41

[140] B. Giacomazzo, L. Rezzolla, and L. Baiotti, "The influence of magnetic fields on the gravitational-wave emission from binary neutron stars," *arXiv:0901.2722*, vol. , 2009. 43

[141] N. Andersson, "A new class of unstable modes of rotating relativistic stars," *Astrophysical Journal*, vol. 502, pp. 708–713, 1998. 44

[142] P. Sá and B. Tome' *Phys. Rev. D*, vol. 74, p. 044011, 2006. 44

[143] P. Sá *Astrophys Space Sci.*, vol. 308, pp. 557–561, 2007. 44, 45, 46

[144] L. Baiotti, R. De Pietri, G. Manca, and L. Rezzolla *Phys. Rev. D*, vol. 75, p. 044023, 2007. 46

[145] C. Kouveliotou, C. A. Meegan, G. J. Fishman, N. P. Bhat, M. S. Briggs, T. M. Koshut, W. S. Paciesas, and G. N. Pendleton, "Identification of two classes of gamma-ray bursts," *Astrophys. J. Lett.*, vol. 413, pp. L101–L104, Aug. 1993. 46

[146] C. Conselice *et al. Astrophys. J.*, vol. 633, p. 29, 2005. 46

[147] T. J. Galama *et al. Nature*, vol. 395, p. 670, 1998. 46

[148] S. R. Kulkarni *et al. Nature*, vol. 395, p. 663, 1998.

[149] J. Hjorth *et al. Nature*, vol. 423, p. 847, 2003.

[150] S. Campana *et al. Nature*, vol. 442, 2006. 46

[151] S. E. Woosley *Astrophys. J.*, vol. 405, p. 273, 1993. 46

[152] K. Iwamoto *et al. Nature*, vol. 395, p. 672, 1998. 46

[153] J. S. Bloom and J. X. Prochaska, "Constraints on the Diverse Progenitors of GRBs from the Large-Scale Environments," *AIP Conf. Proc.*, vol. 836, pp. 473–482, 2006. 46

[154] J. S. Bloom *et al. Astrophys. J.*, vol. 654, 2007. 46

[155] E. Nakar, A. Gal-Yam, T. Piran, and D. B. Fox, "The Distances of Short-Hard Gamma-Ray Bursts and the Soft Gamma-Ray Repeater Connection," *Astrophys. J.*, vol. 640, pp. 849–853, Apr. 2006. 46, 59

[156] R. Chapman, R. S. Priddey, and N. R. Tanvir, "Short gamma-ray bursts from SGR giant flares and neutron star mergers: two populations are better than one," *Mon. Not. R. Astron. Soc.*, p. 430, Apr. 2009. 46, 49

[157] B. Abbott et al. (LIGO Scientific Collaboration) and K. Hurley, "Implications for the Origin of GRB 070201 from LIGO Observations," *Astrophys. J.*, vol. 681, pp. 1419–1430, 2008. 46, 47, 49

[158] J. Abadie *et al.*, "Search for gravitational-wave inspiral signals associated with short gamma-ray bursts during ligo's fifth and virgo's first science run," *The Astrophysical Journal*, vol. 715, no. 2, p. 1453, 2010. 47

[159] M. H. van Putten *et al. Phys. Rev. D*, vol. 69, p. 044007, 2004. 47

[160] K. Hurley *et al.*, "An exceptionally bright flare from SGR 1806-20 and the origins of short-duration γ-ray bursts," *Nature*, vol. 434, pp. 1098–1103, Apr. 2005. 49

[161] N. R. Tanvir, R. Chapman, A. J. Levan, and R. S. Priddey, "An origin in the local Universe for some short γ-ray bursts," *Nature*, vol. 438, pp. 991–993, Dec. 2005. 49

[162] A. J. Levan, N. R. Tanvir, P. Jakobsson, R. Chapman, J. Hjorth, R. S. Priddey, J. P. U. Fynbo, K. Hurley, B. L. Jensen, R. Johnson, J. Gorosabel, A. J. Castro-Tirado, M. Jarvis, D. Watson, and K. Wiersema, "On the nature of the short-duration GRB 050906," *Mon. Not. R. Astron. Soc.*, vol. 384, pp. 541–547, Feb. 2008. 49

[163] D. Frederiks, R. Aptekar, T. Cline, J. Goldsten, S. Golenetskii, K. Hurley, V. Ilinskii, A. von Kienlin, E. Mazets, and V. Palshin, "GRB 051103 and GRB 070201 as Giant Flares from SGRs in Nearby Galaxies," in *American Institute of Physics Conference Series* (M. Galassi, D. Palmer, and E. Fenimore, eds.), vol. 1000 of *American Institute of Physics Conference Series*, pp. 271–275, May 2008. 49

[164] E. O. Ofek *et al.*, "GRB 070201: A Possible Soft Gamma-Ray Repeater in M31," *Astrophys. J.*, vol. 681, pp. 1464–1469, July 2008. 49

[165] J. A. de Freitas Pacheco *Astronomy and Astrophysics*, vol. 336, p. 397, 1998. 49

[166] R. Price and K. S. Thorne, "Non-Radial Pulsation of General-Relativistic Stellar Models. II. Properties of the Gravitational Waves," *Astrophys. J.*, vol. 155, p. 163, Jan. 1969. 49

[167] N. Andersson and K. Kokkotas, "Towards gravitational wave asteroseismology," *Mon. Not. R. Astron. Soc.*, vol. 299, pp. 1059–1068, 1998. 49

[168] O. Benhar, "Neutron star matter equation of state and gravitational wave emission," *Mod. Phys. Lett. A*, vol. 20, pp. 2335–2349, 2005. 49

[169] K. Ioka *Mon. Not. R. Astron. Soc.*, vol. 327, p. 639, 2001. 49

[170] K. Nagamine, J. Ostriker, M. Fukugita, and R. Cen, "The history of cosmological star formation: Three independent approaches and a critical test using the extragalactic background," *Astrophys. J.*, vol. 653, pp. 881–893, 2006. 53, 55

[171] M. Fardal, N. Katz, D. Weinberg, and R. Davé, "On the evolutionary history of stars and their fossil mass and light," *MNRAS*, vol. 379, pp. 985–1002, 2007. 53, 55

[172] S. Wilkins, N. Trentham, and A. Hopkins *MNRAS*, vol. 385, p. 687, 2008. 53, 55

[173] A. Sesana, M. Volonteri, and F. Haardt, "The imprint of massive black hole formation models on the LISA data stream," *Mon. Not. R. Astron. Soc.*, vol. 377, pp. 1711–1716, June 2007. 57

[174] P. Madau and M. J. Rees, "Massive Black Holes as Population III Remnants," *Astrophys. J. Lett.*, vol. 551, pp. L27–L30, Apr. 2001. 57

[175] S. M. Koushiappas, J. S. Bullock, and A. Dekel, "Massive black hole seeds from low angular momentum material," *Mon. Not. R. Astron. Soc.*, vol. 354, pp. 292–304, Oct. 2004. 57

[176] M. C. Begelman, M. Volonteri, and M. J. Rees, "Formation of supermassive black holes by direct collapse in pre-galactic haloes," *Mon. Not. R. Astron. Soc.*, vol. 370, pp. 289–298, July 2006. 57

[177] P. Bender et al. (LISA Study Team), "LISA. Laser Interferometer Space Antenna for the detection and observation of gravitational waves. An international project in the field of Fundamental Physics in Space. Pre-Phase A report. Second Edition," tech. rep., Max-Planck-Institut für Quantenoptik, Garching, 1998. 57

[178] M. Volonteri, F. Haardt, and P. Madau, "The Assembly and Merging History of Supermassive Black Holes in Hierarchical Models of Galaxy Formation," *Astrophys. J.*, vol. 582, pp. 559–573, Jan. 2003. 57

[179] M. Volonteri, R. Salvaterra, and F. Haardt, "Constraints on the accretion history of massive black holes from faint X-ray counts," *Mon. Not. R. Astron. Soc.*, vol. 373, pp. 121–127, Nov. 2006. 57

[180] A. Sesana, J. Gair, I. Mandel, and A. Vecchio, "Observing Gravitational Waves from the First Generation of Black Holes," *Astrophys. J. Lett.*, vol. 698, pp. L129–L132, June 2009. 57

[181] K. Levenberg, "A method for the solution of certain non-linear problems in least squares," *The Quarterly of Applied Mathematics*, vol. 2, pp. 164–168, 1944. 60

[182] D. Marquardt, "An algorithm for least-squares estimation of nonlinear parameters," *SIAM Journal on Applied Mathematics*, vol. 11, pp. 431–441, 1963. 60

[183] S. Nissanke, D. Holz, S. Hughes, N. Dalal, and J. Sievers, "Exploring short gamma-ray bursts as gravitational wave standard sirens," *Astrophys. J.*, vol. 725, pp. 496–514, 2010. 60

[184] W. Zhao, C. Van Den Broeck, D. Baskaran, and T. Li, "Determination of dark energy by the einstein telescope: Comparing with cmb, bao and snia observations." http://arxiv.org/abs/1009.0206. 61, 62

[185] B. Allen, "The stochastic gravity-wave background: Sources and detection," in *Relativistic Gravitation and Gravitational Radiation* (J.-A. Marck and J.-P. Lasota, eds.), Cambridge Contemporary Astrophysics, pp. 373–418, 1997. 62

[186] D. H. Lyth, "What would we learn by detecting a gravitational wave signal in the cosmic microwave background anisotropy?," *Phys. Rev. Lett.*, vol. 78, pp. 1861–1863, 1997. 63

[187] M. S. Turner, "Detectability of inflation-produced gravitational waves," *Phys. Rev.*, vol. D55, pp. 435–439, 1997. 63

[188] S. Kuroyanagi, T. Chiba, and N. Sugiyama, "Imprint of inflation dynamics on the spectrum of the primordial gravitational wave background," *Phys. Rev.*, vol. D79, p. 103501, 2009. 63

[189] L. Grishchuk, "The implications of the microwave background anisotropies for laser-interferometer-tested gravitational waves," *Class. Quantum Grav.*, vol. 14, pp. 1445–1454, 1997. 63

[190] L. A. Boyle and A. Buonanno, "Relating gravitational wave constraints from primordial nucleosynthesis, pulsar timing, laser interferometers, and the CMB: implications for the early universe," *Phys. Rev.*, vol. D78, p. 043531, 2008. 63

[191] L. A. Boyle, P. J. Steinhardt, and N. Turok, "The cosmic gravitational wave background in a cyclic universe," *Phys. Rev.*, vol. D69, p. 127302, 2004. 63

[192] C. Cartier, E. J. Copeland, and M. Gasperini, "Gravitational waves in non-singular string cosmologies," *Nucl. Phys.*, vol. B607, pp. 406–428, 2001. 63

[193] M. B. Hindmarsh and T. W. B. Kibble, "Cosmic strings," *Rept. Prog. Phys.*, vol. 58, pp. 477–562, 1995. 63

[194] G. R. Dvali and S. H. Tye, "Brane inflation," *Phys. Lett.*, vol. B450, pp. 72–82, 1999. 63

[195] S. Sarangi and S. H. Tye, "Cosmic string production towards the end of brane inflation," *Phys. Lett.*, vol. B536, pp. 185–192, 2002. 63

[196] L. Pogosian, S. H. Tye, I. Wasserman, and M. Wyman, "Observational constraints on cosmic string production during brane inflation," *Phys. Rev.*, vol. D68, p. 023506, 2003. 64

[197] R. A. Battye, B. Garbrecht, and A. Moss, "Constraints on supersymmetric models of hybrid inflation," *JCAP*, vol. 0609, p. 007, 2006.

[198] N. Bevis, M. Hindmarsh, M. Kunz, and J. Urrestilla, "Fitting CMB data with cosmic strings and inflation," *Phys. Rev. Lett.*, vol. 100, p. 021301, 2008. 64

[199] C. J. Hogan, "Gravitational waves from light cosmic strings: Backgrounds and bursts with large loops," *Phys. Rev.*, vol. D74, p. 043526, 2006. 64

[200] T. Damour and A. Vilenkin, "Gravitational radiation from cosmic (super)strings: Bursts, stochastic background, and observational windows," *Phys. Rev. D*, vol. 71, 2005. 64

[201] X. Siemens, V. Mandic, and J. Creighton, "Gravitational wave stochastic background from cosmic (super)strings," *Phys. Rev. Lett.*, vol. 98, p. 111101, 2007. 64

[202] C. Caprini, R. Durrer, T. Konstandin, and G. Servant, "General Properties of the Gravitational Wave Spectrum from Phase Transitions," 2009. 65

[203] C. Grojean and G. Servant, "Gravitational Waves from Phase Transitions at the Electroweak Scale and Beyond," *Phys. Rev.*, vol. D75, p. 043507, 2007. 65

[204] A. Kosowsky, A. Mack, and T. Kahniashvili, "Gravitational radiation from cosmological turbulence," *Phys. Rev.*, vol. D66, p. 024030, 2002. 65

[205] M. Kamionkowski, A. Kosowsky, and M. S. Turner, "Gravitational radiation from first order phase transitions," *Phys. Rev.*, vol. D49, pp. 2837–2851, 1994. 65

[206] T. Kahniashvili, A. Kosowsky, G. Gogoberidze, and Y. Maravin, "Detectability of Gravitational Waves from Phase Transitions," *Phys. Rev.*, vol. D78, p. 043003, 2008. 65

[207] L. Randall and G. Servant, "Gravitational waves from warped spacetime," *J. High Energy Phys.*, vol. 2007, no. 05, 2007. 65

[208] N. J. Craig, "Gravitational Waves from Supersymmetry Breaking," 2009. 65

[209] R. Easther and E. A. Lim, "Stochastic gravitational wave production after inflation," *JCAP*, vol. 0604, p. 010, 2006. 65

[210] J.-F. Dufaux, A. Bergman, G. N. Felder, L. Kofman, and J.-P. Uzan, "Theory and Numerics of Gravitational Waves from Preheating after Inflation," *Phys. Rev.*, vol. D76, p. 123517, 2007. 65

[211] J. Garcia-Bellido, D. G. Figueroa, and A. Sastre, "A gravitational wave background from reheating after hybrid inflation," *Phys. Rev.*, vol. D77, p. 043517, 2008. 65

[212] J.-F. Dufaux, G. N. Felder, L. Kofman, and O. Navros, "Gravity Waves from Tachyonic Preheating after Hybrid Inflation," *JCAP*, vol. 0903, p. 001, 2009. 65

[213] J.-F. Dufaux, "Gravity Waves from the Non-Perturbative Decay of SUSY Flat Directions," 2009. 66

[214] S. Babak *et al.*, "The Mock LISA Data Challenges: from Challenge 1B to Challenge 3," *Classical and Quantum Gravity*, vol. 25, pp. 184026–+, Sept. 2008. 67

[215] C. Cutler and J. Harms, "Big Bang Observer and the neutron-star-binary subtraction problem," *Phys. Rev. D*, vol. 73, pp. 042001–+, Feb. 2006. 67

[216] "Moore's law."

[217] J. Richards, "Will computers reach top speed by 2020." http://technology.timesonline.co.uk/tol/news/tech_and_web/article2489053.ece.

[218] E. S. Hans Meuer, Jack Dongarra and H. Simon, "Top500 supercomputer sites." http://www.top500.org/. 69

[219] J. J. Dongarra, P. Luszczek, and A. Petitet, "The LINPACK Benchmark: past, present and future," *Concurrency and Computation: Practice and Experience*, vol. 15, no. 9, pp. 803–820, 2003. 69

[220] "Amd white paper: Amd fusion family of apus," 2010. 71

[221] J. C. A. D. N. V. W. L. D. K. P. D. Nadathur Satish, Changkyu Kim, "Fast sort on cpus, gpus and intel mic architectures." Technical Report, Intel Labs, 2010. 71

[222] "Silicon technology." 71

[223] "The scc platform overview," 2010. 71

[224] ""single-chip cloud computer" an experimental many-core processor from intel labs." Symposium in Santa Clara, 2010. 71

[225] "Tilera website." http://www.tilera.com.

[226] N. J. D. K. A. K. P. P. S. S. I. V. A. Azimi, M.; Cherukuri, "Integration challenges and tradeoffs for tera-scale architectures." Intel Technology Journal http://www.intel.com/technology/itj/2007/v11i3/1-integration/1-abstract.htm, 2007. 71

[227] L. L. D.Cipullo, L.Bosi.

[228] L. L. L.Fontana, L.Bosi.

[229] S. Pat Gelsinger and co-GM of Intel's Digital Enterprise Group (DEG). http://java.sys-con.com/node/557154.

[230] B. S. Sathyaprakash, B. Schutz, and C. V. D. Broeck, "Cosmography with the einstein telescope," *arXiv:0906.4151v1 [astro-ph.CO]*, June 2009. 75

[231] K. Arun, A. Buonanno, G. Faye, and E. Ochsner, "Higher-order spin effects in the amplitude and phase of gravitational waveforms emitted by inspiraling compact binaries: Ready-to-use gravitational waveforms," *Phys. Rev. D*, vol. 79, 2009. 75

[232] B. Owen, "Search templates for gravitational waves from inspiralling binaries: Choise of template spacing," *Phys. Rev. D*, vol. 53, pp. 6749–6761, 1996. 75

[233] S. Babak, R. Balasubramanian, D. Churches, T. Cokelaer, and B. S. Sathyaprakash, "A template bank to search for gravitational waves from inspiralling compact binaries ı: physical models," *Class. Quant. Grav*, vol. 23, 2006. 75

[234] A. Petiteau, Y. Shang, S. Babak, and F. Feroz, "The search for spinning black hole binaries in mock lisa data using a genetic algorithm," *Phys. Rev. D*, vol. 81, 2010. 76

[235] L. S. Collaboration, "Searching for a stochastic background of gravitational waves with ligo," 2006. 76, 77

[236] L. S. Collaboration and the Virgo Collaboration, "An upper limit on the stochastic gravitational-wave background of cosmological origin," 2009.

[237] B. Abbott et al. (LIGO Scientific Collaboration), "Upper limit map of a background of gravitational waves," 2007. 76

[238] "Fftw home page."

[239] E. Thrane, S. Ballmer, J. D. Romano, S. Mitra, D. Talukder, S. Bose, and V. Mandic, "Probing the anisotropies of a stochastic gravitational-wave background using a network of ground-based laser interferometers," 2009. 78

[240] S. Klimenko, G. Vedovato, M. Drago, G. Mazzolo, G. Mitselmakher, C. Pankow, G. Prodi, V. Re, F. Salemi, and I. Yakushin, "Localization of gravitational wave sources with networks of advanced detectors," 2011. 82

[241] M. H. van Putten, N. Kanda, H. Tagoshi, D. Tatsumi, F. Masa-Katsu, and M. D. Valle, "Prospects for true calorimetry on kerr black holes in core-collapse supernovae and mergers," 2011. 82

[242] J. Peterson, "Observations and modeling of seismic background noise." Open-File report 93-322, 1993. 85

[243] P.-Y. Bard *et al.*, "Sesame: Site effects assessment using ambient excitations.," tech. rep., 2003. Final report WP08. 85

[244] B. Gutenberg, "Microseisms," *Advances in Geophysics*, vol. 5, pp. 53–92, 1958.

[245] M. Asten, "Arrays estimators and the use of microseisms for reconnaissance of sedimentary basins," *Bulletin of the Seismological Society of America*, vol. 68, pp. 1623 – 1636, 2002.

[246] L. Peck, "Overview of seismic noise and its relevance to personnel detections." ERDC/CRREL TR-08-5, US Army Corps of Engineers, April 2008. Engineer Research and Development Center. 85

[247] J. Peterson, "Preliminary observations of noise spectra at the SRO and ASRO stations.." Open-File report 80-992, 1980. 85

[248] S. Hild, S. Chelkowski, and A. Freise, "Pushing towards the ET sensitivity using 'conventional' technology," *arXiv:0810.0604v2 [gr-qc]*, 2008. 86, 264

[249] R. Schofield, M. Ito, E. Mauceli, H. Radkins, C. Gray, G. Moreno, and G. Gonzalez., "Source and propagation of the predominant 1-50 hz seismic signal from off-site at ligo-hanford," LIGO Scientific Collaboration Meeting, LIGO Hanford Observatory, Hanford, Washington, 15-17 August 2000., 2000. 88

[250] D. Coward, D. Blair, R. Burman, , and C. Zhao., "Vehicle-induced seismic effects at a gravitational wave observatory," *Review of Scientific Instruments*, vol. 74, pp. 4846 – 4854, 2003. 88

[251] C. Young, "A comparison of the high-frequency (>1Hz) surface and subsurface noise environment at three sites in the United States," *Bull. of the Seism. Soc. of America*, vol. 86, pp. 1516–1528, 1996. 88, 90

[252] 89

[253] 90

[254] M. Withers *et al.*, "High-frequency analysis of seismic background noise as a function of wind speed and shallow depth," *Bulletin of the Seismological Society of America*, vol. 86, pp. 1507 – 1515, 1996. 90

[255] M. Beker, G. Cella, R. DeSalvo, M. Doets, H. Grote, J. Harms, E. Hennes, V. Mandic, D. Rabeling, J. van den Brand, and C. van Leeuwen, "Improving the sensitivity of future gw observatories in the 1ï¿½10ï¿½hz band: Newtonian and seismic noise," *General Relativity and Gravitation*, pp. 1–34, 2010. 10.1007/s10714-010-1011-7. 92, 114

[256] P. R. Saulson, "Terrestrial gravitational noise on a gravitational wave antenna," *Phys. Rev. D*, vol. 30, pp. 732–736, Aug 1984. 93, 97

[257] M. Beccaria *et al.*, "Relevance of Newtonian seismic noise for the VIRGO interferometer sensitivity," *Classical and Quantum Gravity*, vol. 15, pp. 3339–3362, 1998.

[258] S. A. Hughes and K. S. Thorne, "Seismic gravity-gradient noise in interferometric gravitational-wave detectors," *Phys. Rev. D*, vol. 58, p. 122002, Nov 1998. 93, 95, 97

[259] "Comsol multiphysics version 3.5a," 2009. 94

[260] M. Schevenels, *The impact of uncertain dynamic soil characteristics on the prediction of ground vibrations.* PhD thesis, Katholieke Universiteit Leuven, 2007. 94

[261] J. Achenbach, *Wave Propagation in Elastic Solids*, pp. 187–194. Amsterdam: North-Holland, 1973. 94

[262] W. Hassan and P. B. Nagy *J. Acoust. Soc. Am.*, vol. 104, p. 3107, 1998. 95

[263] R. Woods, "Screening the surface waves in soils," *Proceedings of ASCE*, vol. 94, pp. 951–979. 95

[264] D.-S. Kim and J.-S. Lee, "Propagation and attenuation characteristics of various ground vibrations," *Soil Dyn. and Earthq. Eng.*, vol. 19, pp. 115–126, 2000. 95

[265] A. Caticha and R. Preuss, "Maximum entropy and bayesian data analysis: entropic priors," *Phys. Rev. E*, vol. 70, p. 046127. 98

[266] K. S. Thorne and C. J. Winstein, "Human gravity-gradient noise in interferometric gravitational-wave detectors," *Phys. Rev. D*, vol. 60, p. 082001, Sep 1999. 104

[267] E. Marchetti and M. Mazzoni, "Evidence of oceanic microseism as a source of low frequency seismic signal recorded at Virgo," 2004. 109

[268] 115, 116

[269] J.-Y. Vinet, V. Brisson, S. Braccini, I. Ferrante, L. Pinard, F. Bondu, and E. Tourniï¿½, "Scattered light noise in gravitational interferometric detectors: A statistical approach," *Phys.Rev.*, vol. D 56, p. 6085, 1997. 128

[270] J.-Y. Vinet, V. Brisson, and S. Braccini, "Scattered light noise in gravitational wave interferometric detectors: Coherent effects," *Phys.Rev.*, vol. D 54, p. 1276, 1996. 128

[271] C. Ho, R. Powell, and P. Liley, "Thermal conductivity of the elements," *J. Phys. Chem. Ref. Data*, vol. 1, p. 279, 1972. 136

[272] J. R. Howell and R. Siegel, *Thermal Radiation Heat Transfer*. Taylor and Francis-Hemisphere, Washington, 3rd ed., 1992. 138, 141

[273] J. Howell, "A catalog of radiation heat transfer configuration factors, 3rd edition." http://www.engr.uky.edu/rtl/Catalog/. 138, 139

[274] J. R. Howell and R. Siegel, *Thermal Radiation Heat Transfer*. Taylor and Francis-Hemisphere, Washington, 4th ed., 2001. 139

[275] A. J. Buschman and C. M. Pittman, "Configuration factors for exchange of radiant energy between axisymmetrical sections of cylinders, cones, and hemispheres and their bases," Tech. Rep. D-944, NASA, 1961. 139

[276] E. M. Sparrow and S. L. Lin, "Radiation heat transfer at a surface having both specular and diffuse reflectance components," *Int. J. Heat Mass Transfer*, vol. 8, pp. 769–779, 1965. 141

[277] D. S. Tsai and W. Strieder, "Radiation across and down a cylindrical pore having both specular and diffuse reflectance components," *Ind. Eng. Chem. Fundam*, vol. 25, no. 2, pp. 244–249, 1986. 141

[278] T. T. et. al, "Conduction effect of thermal radiation in a metal shield pipe in a cryostat for a cryogenic interferometric gravitational wave detector." arXiv:0711.0839v1, 2007. 142

[279] T. T. et al., "Reduction of heat load of LCGT cryostat," *Journal of Physics: Conference Series*, vol. 122, p. 012009, 2008. 7th Edoardo Amaldi Conference on Gravitational Waves, Sydney, Australia, July 2007. 142

[280] D. Mosher and S. J. Stephanakis, "X-ray "light pipes"," *Applied Physics Letters*, vol. 29, no. 2, pp. 105–107, 1976. 142

[281] K. KURODA *et al.*, "Large-scale cryogenic gravitational wave telescope," *International Journal of Modern Physics D*, vol. 8, pp. 557–579, Oct 1999. 144

[282] T. Tomaru *et al.*, "Vibration analysis of cryocoolers," *Cryogenics*, vol. 44, pp. 309–317, 2004. 144

[283] S. Caparrelli, E. Majorana, V. Moscatelli, E. Pascucci, M. Perciballi, P. Puppo, P. Rapagnani, and F. Ricci, "Vibration-free cryostat for low-noise applications of a pulse tube cryocooler," *Review of Scientific Instruments*, vol. 77, Sept. 2006. 144

[284] S. Riabzev, A. Veprik, H. Vilenchik, and N. Pundak, "Vibration generation in a pulse tube refrigerator," *Cryogenics*, vol. 49, no. 1, 2009. 146

[285] T. Suzuki, T. Tomaru, T. Haruyama, N. Sato, A. Yamamoto, T. Shintomi, Y. Ikushima, and R. Li, "Pulse tube cryocooler with self-cancellation of cold stage vibration," 2006. 146, 150

[286] K. S. H. Blessing, Ph. Lebrun, "Very low-loss liquid helium trans- fer with long fexible cryogenic lines," cern lep-ma/89-38, CERN, 1989. 148

[287] P. Astone *et al.*, "Noise behaviour of the explorer gravitational wave antenna during the transition to the superfluid phase," *Cryogenics*, vol. 32, pp. 668–670, 1992. 149

[288] T. Koettig, F. Richter, R. Nawrodt, A. Zimmer, C. Schwarz, D. Heinert, M. Thürk, and P. Seidel, "Application of novel regenerator material within a coaxial two-stage pulse tube refrigerator," in *Advances in Cryogenic Engineering: Transactions of the Cryogenic Engineering Conference - CEC* (Boulder, ed.), vol. 53 of *AIP Conference Proceedings, Vol. 985 (2008) 235-242.*, AIP, 2008. 150

[289] N. Jiang, U. Lindemann, F. Giebeler, and G. Thummes, "A 3he pulse tube cooler operating down to 1.27 k," *Cryogenics*, vol. 44, pp. 809 –816, 2004. 150

[290] T. V. Collaboration, "Advanced virgo baseline design, virgo technical report, vir-0027a-09." 2009. 168, 231

[291] M. Punturo, "The virgo sensitivity curve," *Virgo Technical Report*, vol. VIR-NOT-PER-1390-51, 2004. 169

[292] F. Acernese *et al.*, "Properties of seismic noise at the virgo site," *Classical and Quantum Gravity*, vol. 21, no. 5, p. S433, 2004. 168

[293] M. Ohashi *et al.*, "Laser interferometer in the kamioka mine," *Proceedings of the 28th International Cosmic Ray Conference, Tsukuba, Japan, Universal Academy Press*, 2003, July 31-August 7. 168

[294] M. G. Beker *et al.*, "Selection criteria for et candidate sites (einstein telescope working group 1 report)," *ET Scientific Note*, vol. ET-030-09, 2009. 168

[295] T. V. Collaboration, "Virgo final design," *E.T.S.*, vol. E.T.S, Pisa, Italy, 1995. 171

[296] G. Losurdo *et al.*, "An inverted pendulum preisolator stage for the virgo suspension system," *Review of Scientific Instruments*, vol. 70, no. 5, pp. 2507–2515, 1999. 173

[297] G. Losurdo *et al.*, "Inertial control of the mirror suspensions of the virgo interferometer for gravitational wave detection," *Review of Scientific Instruments*, vol. 72, no. 9, pp. 3653–3661, 2001. 173

[298] M. Beccaria *et al.*, "Extending the virgo gravitational wave detection band down to a few hz: metal blade springs and magnetic antisprings," *Nuclear Instruments and Methods in Physics Research Section A: Accelerators, Spectrometers, Detectors and Associated Equipment*, vol. 394, no. 3, pp. 397 – 408, 1997. 173, 175

[299] M. Beccaria *et al.*, "The creep problem in the virgo suspensions: a possible solution using maraging steel," *Nuclear Instruments and Methods in Physics Research Section A: Accelerators, Spectrometers, Detectors and Associated Equipment*, vol. 404, no. 2-3, pp. 455 – 469, 1998. 174

[300] S. Braccini *et al.*, "The maraging-steel blades of the virgo super attenuator," *Measurement Science and Technology*, vol. 11, no. 5, p. 467, 2000. 174

[301] A. Delapierre and F. Frasconi, "Stress distribution on the suspension wires of the virgo superattenuator." 1997. 174

[302] S. Braccini *et al.*, "An improvement in the virgo super attenuator for interferometric detection of gravitational waves: The use of a magnetic antispring," *Review of Scientific Instruments*, vol. 64, no. 2, pp. 310–313, 1993. 175

[303] G. Ballardin *et al.*, "Measurement of the transfer function of the steering filter of the virgo super attenuator suspension," *Review of Scientific Instruments*, vol. 72, no. 9, pp. 3635–3642, 2001. 175, 177

[304] F. Acernese *et al.*, "Measurements of superattenuator seismic isolation by virgo interferometer," *Astroparticle Physics*, vol. 33, no. 3, pp. 182 – 189, 2010. 176, 177

[305] S. Braccini on behalf of the ET-WG2, "Einstein telescope - seismic isolation design study." Talk at the WP2-WP3 joint meeting (Jena), March 2010. 177, 182

[306] W. H. P. and, *Numerical Recipes in C.* Cambridge University Press, 2008 (Second Edition). 177

[307] F. Marchesoni, "Self-organized criticality and dislocation damping," *Journal of Alloys and Compounds*, vol. 211-212, pp. 124 – 127, 1994. 10th International Conference on Internal Friction and Ultrasonic Attenuation in Solids. 179

[308] R. Poggiani, "Materials and components of possible interest for cryogenic operation of einstein telescope," *Einstein Telescope Note*, vol. ET-026-9, 2009. 184, 185

[309] R. Poggiani, "Cryogenic properties of steels," *Einstein Telescope Note*, vol. ET-102A-10, 2010. 186

[310] M. V. Plissi, K. A. Strain, C. I. Torrie, N. A. Robertson, S. Killbourn, S. Rowan, S. M. Twyford, H. Ward, K. D. Skeldon, and J. Hough, "Aspects of the suspension system for GEO 600," *Review of Scientific Instruments*, vol. 69, no. 8, pp. 3055–3061, 1998. 190, 269

[311] B. Willke, P. Aufmuth, C. Aulbert, S. Babak, R. Balasubramanian, B. W. Barr, S. Berukoff, S. Bose, G. Cagnoli, M. M. Casey, D. Churches, D. Clubley, C. N. Colacino, D. R. M. Crooks, C. Cutler, K. Danzmann, R. Davies, R. Dupuis, E. Elliffe, C. Fallnich, A. Freise, S. Gossler, A. Grant, H. Grote, G. Heinzel, A. Heptonstall, M. Heurs, M. Hewitson, J. Hough, O. Jennrich, K. Kawabe, K. Kötter, V. Leonhardt, H. Lück, M. Malec, P. W. McNamara, S. A. McIntosh, K. Mossavi, S. Mohanty, S. Mukherjee, S. Nagano, G. P. Newton, B. J. Owen, D. Palmer, M. A. Papa, M. V. Plissi, V. Quetschke, D. I. Robertson, N. A. Robertson, S. Rowan, A. Rüdiger, B. S. Sathyaprakash, R. Schilling, B. F. Schutz, R. Senior, A. M. Sintes, K. D. Skeldon, P. Sneddon, F. Stief, K. A. Strain, I. Taylor, C. I. Torrie, A. Vecchio, H. Ward, U. Weiland, H. Welling, P. Williams, W. Winkler, G. Woan, and I. Zawischa, "The geo 600 gravitational wave detector," *Classical and Quantum Gravity*, vol. 19, no. 7, p. 1377, 2002. 190, 269

[312] G. M. Harry and the LIGO Scientific Collaboration, "Advanced LIGO: the next generation of gravitational wave detectors," *Classical and Quantum Gravity*, vol. 27, no. 8, p. 084006, 2010. 190, 239, 269

[313] N. A. Robertson, G. Cagnoli, D. R. M. Crooks, E. Elliffe, J. E. Faller, P. Fritschel, S. G. ler, A. Grant, A. Heptonstall, J. Hough, H. Lück, R. Mittleman, M. Perreur-Lloyd, M. V. Plissi, S. Rowan, D. H. Shoemaker, P. H. Sneddon, K. A. Strain, C. I. Torrie, H. Ward, and P. Willems, "Quadruple suspension design for Advanced LIGO," *Classical and Quantum Gravity*, vol. 19, no. 15, p. 4043, 2002.

[314] A. Cumming, A. Heptonstall, R. Kumar, W. Cunningham, C. Torrie, M. Barton, K. A. Strain, J. Hough, and S. Rowan, "Finite element modelling of the mechanical loss of silica suspension fibres for advanced gravitational wave detectors," *Classical and Quantum Gravity*, vol. 26, no. 21, p. 215012, 2009. 190, 269

[315] Y. S. Touloukian and C. Y. Ho, "Thermophysical Properties of Matter," in *Vol. 1 - Thermal Conductivity - Metallic Elements and Alloys*, Plenum, 1970. 190, 192, 271

[316] Y. S. Touloukian and C. Y. Ho, "Thermophysical Properties of Matter," in *Vol. 2 - Conductivity - Nonmetallic Solids*, Plenum, 1970. 190, 271

[317] T. Uchiyama, T. Tomaru, D. Tatsumi, S. Miyoki, M. Ohashi, K. Kuroda, T. Suzuki, A. Yamamoto, and T. Shintomi, "Mechanical quality factor of a sapphire fiber at cryogenic temperatures," *Physics Letters A*, vol. 273, no. 5-6, pp. 310 – 315, 2000. 191

[318] T. Tomaru, T. Suzuki, T. Uchiyama, A. Yamamoto, T. Shintomi, C. T. Taylor, K. Yamamoto, S. Miyoki, M. Ohashi, and K. Kuroda, "Maximum heat transfer along a sapphire suspension fiber for a cryogenic interferometric gravitational wave detector," *Physics Letters A*, vol. 301, no. 3-4, pp. 215 – 219, 2002.

[319] T. Suzuki, T. Tomaru, T. Haruyama, T. Shintomi, T. Uchinyama, S. Miyoki, M. Ohashi, and K. Kuroda, "Thermal Conductance through Sapphire-Sapphire Bonding," in *International Cosmic Ray Conference*, vol. 5 of *International Cosmic Ray Conference*, pp. 3131–+, July 2003. 191

[320] A. Dari, F. Travasso, H. Vocca, and L. Gammaitoni, "Breaking strength tests on silicon and sapphire bondings for gravitational wave detectors," *Classical and Quantum Gravity*, vol. 27, no. 4, p. 045010, 2010. 191, 270, 271

[321] A. A. van Veggel, J. Scott, D. A. Skinner, B. Bezensek, W. Cunningham, J. Hough, I. Martin, P. Murray, S. Reid, and S. Rowan, "Strength testing and sem imaging of hydroxide-catalysis bonds between silicon," *Classical and Quantum Gravity*, vol. 26, no. 17, p. 175007, 2009. 191, 214, 271

[322] M. Alshourbagy *et al.*, "First characterization of silicon crystalline fibers produced with the μ-pulling technique for future gravitational wave detectors," *Rev. Sci. Instrum.*, vol. 77, p. 044502, Apr 2006. 191, 193, 212

[323] S. Reid, G. Cagnoli, D. Crooks, J. Hough, P. Murray, S. Rowan, M. Fejer, R. Route, and S. Zappe, "Mechanical dissipation in silicon flexures," *Physics Letters A*, vol. 351, no. 4-5, pp. 205 – 211, 2006. 191, 193, 194

[324] J. Callaway, "Model for lattice thermal conductivity at low temperatures," *Phys. Rev.*, vol. 113, pp. 1046–1051, Feb 1959. 191

[325] J. Callaway and H. C. von Baeyer, "Effect of point imperfections on lattice thermal conductivity," *Phys. Rev.*, vol. 120, pp. 1149–1154, Nov 1960. 191

[326] T. Ruf, R. W. Henn, M. Asen-Palmer, E. Gmelin, M. Cardona, H. J. Pohl, G. G. Devyatych, and P. G. Sennikov, "Thermal conductivity of isotopically enriched silicon," *Solid State Communications*, vol. 115, no. 5, pp. 243 – 247, 2000. 192

[327] D. T. Morelli, J. P. Heremans, and G. A. Slack, "Estimation of the isotope effect on the lattice thermal conductivity of group iv and group iii-v semiconductors," *Phys. Rev. B*, vol. 66, p. 195304, Nov 2002. 191

[328] Y. S. Touloukian and C. Y. Ho, "Thermophysical Properties of Matter," in *Vol. 4 - Specific Heat - Metallic Elements and Alloys*, Plenum, 1970. 192

[329] Y. S. Touloukian and C. Y. Ho, "Thermophysical Properties of Matter," in *Vol. 5 - Specific Heat - Nonmetallic Solids*, Plenum, 1970. 192, 271

[330] Y. S. Touloukian and C. Y. Ho, "Thermophysical Properties of Matter," in *Vol. 12 - Thermal Expansion - Metallic Elements and Alloys*, Plenum, 1970. 192

[331] Y. S. Touloukian and C. Y. Ho, "Thermophysical Properties of Matter," in *Vol. 13 - Thermal Expansion - Nonmetallic Solids*, Plenum, 1970. 192, 271

[332] D. F. McGuigan, C. C. Lam, R. Q. Gram, A. W. Hoffman, D. H. Douglass, and H. W. Gutche, "Measurements of the mechanical Q of single-crystal silicon at low temperatures," *Journal of Low Temperature Physics*, vol. 30, pp. 621–629, 1978. 10.1007/BF00116202. 193, 270, 271

[333] S. Rowan, G. Cagnoli, P. Sneddon, J. Hough, R. Route, E. K. Gustafson, M. M. Fejer, and V. Mitrofanov, "Investigation of mechanical loss factors of some candidate materials for the test masses of gravitational wave detectors," *Physics Letters A*, vol. 265, no. 1-2, pp. 5 – 11, 2000. 271

[334] S. Rowan, R. L. Byer, M. M. Fejer, R. Route, G. Cagnoli, D. R. M. Crooks, J. Hough, P. H. Sneddon, and W. Winkler, "Test mass materials for a new generation of gravitational wave detectors," in *Proceedings of SPIE*, vol. 4856, 2003. 270

[335] R. Nawrodt, A. Zimmer, T. Koettig, C. Schwarz, D. Heinert, M. Hudl, R. Neubert, M. Thürk, S. Nietzsche, W. Vodel, P. Seidel, and A. Tünnermann, "High mechanical q-factor measurements on silicon bulk samples," *Journal of Physics: Conference Series*, vol. 122, no. 1, p. 012008, 2008. 271

[336] R. Nawrodt *et al.*, "Investigation of mechanical losses of thin silicon flexures at low temperatures," *arXiv:1003.2893v1*, 2010. 193

[337] S. Rowan, R. Hutchins, A. McLaren, N. A. Robertson, S. M. Twyford, and J. Hough, "The quality factor of natural fused quartz ribbons over a frequency range from 6 to 160 hz," *Physics Letters A*, vol. 227, no. 3-4, pp. 153 – 158, 1997. 193

[338] A. Heptonstall, G. Cagnoli, J. Hough, and S. Rowan, "Characterisation of mechanical loss in synthetic fused silica ribbons," *Physics Letters A*, vol. 354, no. 5-6, pp. 353 – 359, 2006.

[339] A. M. Gretarsson and G. M. Harry, "Dissipation of mechanical energy in fused silica fibers," *Review of Scientific Instruments*, vol. 70, no. 10, pp. 4081–4087, 1999.

[340] S. D. Penn, G. M. Harry, A. M. Gretarsson, S. E. Kittelberger, P. R. Saulson, J. J. Schiller, J. R. Smith, and S. O. Swords, "High quality factor measured in fused silica," *Review of Scientific Instruments*, vol. 72, no. 9, pp. 3670–3673, 2001.

[341] S. D. Penn, A. Ageev, D. Busby, G. M. Harry, A. M. Gretarsson, K. Numata, and P. Willems, "Frequency and surface dependence of the mechanical loss in fused silica," *Phys. Lett. A*, vol. 352, no. 1-2, pp. 3 – 6, 2006. 193, 269, 271

[342] I. Martin *et al.*, "Measurements of a low-temperature mechanical dissipation peak in a single layer of ta_2o_5 doped with tio_2.," *Classical and Quantum Gravity*, vol. 25, p. 055005, 2008. 194, 272

[343] I. W. Martin, E. Chalkley, R. Nawrodt, H. Armandula, R. Bassiri, C. Comtet, M. M. Fejer, A. Gretarsson, G. Harry, D. Heinert, J. Hough, I. MacLaren, C. Michel, J.-L. Montorio, N. Morgado, S. Penn, S. Reid, R. Route, S. Rowan, C. Schwarz, P. Seidel, W. Vodel, and A. L. Woodcraft, "Comparison of the temperature dependence of the mechanical dissipation in thin films of ta 2 o 5 and ta 2 o 5 doped with tio 2," *Classical and Quantum Gravity*, vol. 26, no. 15, p. 155012, 2009.

[344] I. W. Martin, R. Bassiri, R. Nawrodt, M. M. Fejer, A. Gretarsson, E. Gustafson, G. Harry, J. Hough, I. MacLaren, S. Penn, S. Reid, R. Route, S. Rowan, C. Schwarz, P. Seidel, J. Scott, and A. L. Woodcraft, "Effect of heat treatment on mechanical dissipation in ta2o5 coatings," *Classical and Quantum Gravity*, vol. 27, no. 22, p. 225020, 2010. 194, 272

[345] F. Piergiovanni, M. Punturo, and P.Puppo, "The thermal noise of the Virgo+ and Virgo Advanced Last Stage Suspension (The PPP effect)," tech. rep., 2009. 195, 196, 201

[346] P. Puppo, "A thermal noise model for a branched system of harmonic oscillators," *Journal of Physics: Conference Series*, vol. 228, no. 1, p. 012031, 2010. 195

[347] S. Amadori, E. Bonetti, L. Pasquini, P. Deodati, R. Donnini, R. Montanari, and C. Testani, "Low temperature anelasticity in ti6al4v alloy and ti6al4v-sicf composite," *Materials Science and Engineering: A*, vol. 521-522, pp. 340 – 342, 2009. 15th International Conference on Internal Friction and Mechanical Spectroscopy. 196

[348] A. Bernardini, E. Majorana, P. Puppo, P. Rapagnani, F. Ricci, and G. Testi, "Suspension last stages for the mirrors of the Virgo interferometric gravitational wave antennas," *Review of Scientific Instruments*, vol. 70, no. 8, pp. 3463–3472, 1999. 206

[349] P. Falferi, "http://www.magnetshop.com/." 206

[350] M. Hewitson, H. Grote, G. Heinzel, K. A. Strain, H. Ward, and U. Weiland, "Calibration of geo 600 for the s1 science run," *Class. Quantum Grav.*, vol. 20, pp. S885–S893, 2003. 210

[351] P. Amico, L. Bosi, L. Carbone, L. Gammaitoni, M. Punturo, F. Travasso, and H. Vocca, "Mechanical quality factor of mirror substrates for virgo," *Class. Quantum Grav.*, vol. 19, pp. 1663–1668, 2002. 210

[352] S. Grasso, C. Altucci, F. Barone, V. Ragozzino, S. Solimeno, T. Pham, J. Y. Vinet, and R. Abbate, "Electrostatic systems for fine control of mirror orientation in interferometric gw antennas," *Physics Letters A*, vol. 244, pp. 360–370, 1998. 210

[353] M. J. Mortonson, C. C. Vassiliou, D. J. Ottaway, D. H. Shoemaker, and G. M. Harrya, "Effects of electrical charging on the mechanical q of a fused silica disk," *Review of Scientifi Instruments*, vol. 74, pp. 4840–4845, 2003. 210

[354] M. Hewitson, K. Danzmann, H. Grote, S. Hild, J. Hough, H. Luck, S. Rowan, J. Smith, K. Strain, and B. Willke, "Charge measurement and mitigation for the main test masses of the geo 600 gravitational wave observatory," *Class. Quantum Grav.*, vol. 24, 2007. 210

[355] R. D. Rosa, F. Garufi, L. Milano, S. Mosca, and G. Persichetti, "Characterization of electrostatic actuators for suspended mirror control with modulated bias," *Jou. of Physics: Conf. Series*, vol. 228, p. 012018, 2010. 210, 211

[356] F. Acernese, F. Barone, A. Boiano, R. D. Rosa, F. Garufi, L. Milano, S. Mosca, A. Perreca, G. Persichetti, and R. Romano, "Application of a hybrid modular acquisition system to the control of a suspended interferometer with electrostatic actuators," *Jou. of Physics: Conf. Series*, vol. 122, p. 012011, 2008. 210

[357] C. Lam and D. Douglas, "Internal friction measurements in boron-doped single-crystal silicon," *Physics Letters*, vol. 85, pp. 41 – 42, 1981. 212

[358] D. F. McGuigan, C. Lam, R. Q. Gram, A. W. Hoffman, D. H. Douglas, and H. W. Gutche, "Measurements of the mechanical q of single-crystal silicon at low temperatures," *Journal of Low Temperature Physics*, vol. 30, p. 621, 1978. 212

[359] L. Lagonigro *et al.*, "Low loss silicon fibers for photonics applications," *Appl. Phys. Lett.*, 2010. 212

[360] A. Toncelli Private communication, 2010. 213

[361] J. Liu, L. Ju, and D. Blair, "Vibration isolation performance of an ultra-low frequency folded pendulum resonator," *Phys. Lett. A*, vol. 228, pp. 243–249, 1997. 216, 217

[362] A. Bertolini, R. DeSalvo, F. Fidecaro, M. Francesconi, S. Marka, V. Sannibale, D. Simonetti, A. Takamori, and H. Tariq, "Mechanical design of a single axis monolithic accelerometer for advanced seismic attenuation systems," *Nucl. Instr. and Meth.*, vol. 556, pp. 616–623, 2006. 216, 217

[363] F. Acernese, R. D. Rosa, G. Giordano, R. Romano, S. Vilasi, and F. Barone, "New tunable mechanical monolithic horizontal seismometer for low frequency seismic noise measurement," in *Sensors and Smart Structures Technologies for Civil, Mechanical, and Aerospace Systems* (P. of SPIE, ed.), vol. 7647, 2008. 216, 217

[364] F. Acernese, R. D. Rosa, G. Giordano, R. Romano, and F. Barone, "Mechanical monolithic horizontal sensor for low frequency seismic noise measurement," *Rev. Sci. Instrum.*, vol. 79, p. 074501, 2008. 216, 217

[365] A. Freise, S. Chelkowski, S. Hild, W. D. Pozzo, A. Perreca, and A. Vecchio, "Triple Michelson interferometer for a third-generation gravitational wave detector," *Classical and Quantum Gravity*, vol. 26, no. 8, p. 085012 (14pp), 2009. 222, 223, 224

[366] Y. Chen, "Sagnac interferometer as a speed-meter-type, quantum-nondemolition gravitational-wave detector," *Phys. Rev. D*, vol. 67, p. 122004, 2003. 223, 234, 264, 303

[367] S. L. Danilishin and F. Y. Khalili, "Practical design of the optical lever intracavity topology of gravitational-wave detectors," *Phys. Rev. D*, vol. 73, pp. 022002–+, Jan. 2006.

[368] Y. Chen, A. Pai, K. Somiya, S. Kawamura, S. Sato, K. Kokeyama, R. L. Ward, K. Goda, and E. E. Mikhailov, "Interferometers for displacement-noise-free gravitational-wave detection," *Physical Review Letters*, vol. 97, pp. 151103–+, Oct. 2006. 223

[369] K.-X. Sun, M. M. Fejer, E. Gustafson, and R. L. Byer, "Sagnac interferometer for gravitational-wave detection," *Phys. Rev. Lett.*, vol. 76, pp. 3053–3056, Apr 1996. 223, 234, 303

[370] J. Mizuno, A. R<FC>diger, R. Schilling, W. Winkler, and K. Danzmann, "Frequency response of michelson- and sagnac-based interferometers," *Optics Communications*, vol. 138, no. 4-6, pp. 383 – 393, 1997. 223

[371] W. Winkler, K. Maischberger, A. Ruediger, R. Schilling, L. Schnupp, D. Hoemaker, and D. Shoemaker, W. Winkler, K. Maischberger, A. Ruediger, R. Schilling, & L. Schnupp, eds., *Plans for a large gravitational wave antenna in Germany*, Aug. 1985. 223

[372] Y. Gürsel and M. Tinto, "Near optimal solution to the inverse problem for gravitational-wave bursts," *Phys. Rev. D*, vol. 40, pp. 3884–3938, 1989. 224

[373] S. Chelkowski, "A topology review: The sagnac effect." talk at Hannover ET-WP3 meeting 2009. 226

[374] V. B. Braginsky, "Classical and quantum restrictions on detection of weak distributions of a macroscopic oscillator," *Sov. Phys. JETP*, vol. 26, p. 831, 1968. 226

[375] V. B. Braginsky and F. Y. Khalili, *Quantum measurement*. Cambridge University Press, 1999. 226, 239

[376] S. Hild, S. Chelkowski, A. Freise, J. Franc, N. Morgado, R. Flaminio, and R. DeSalvo, "A xylophone configuration for a third-generation gravitational wave detector," *Classical and Quantum Gravity*, vol. 27, p. 015003 (8pp), 2010. 227, 231, 236

[377] V. B. Braginsky, M. L. Gorodetsky, F. Y. Khalili, A. B. Matsko, K. S. Thorne, and S. P. Vyatchanin, "Noise in gravitational-wave detectors and other classical-force measurements is not influenced by test-mass quantization," *Phys. Rev. D*, vol. 67, p. 082001, Apr 2003. 227

[378] H. J. Kimble, Y. Levin, A. B. Matsko, K. S. Thorne, and S. P. Vyatchanin, "Conversion of conventional gravitational-wave interferometers into quantum nondemolition interferometers by modifying their input and/or output optics," *Phys. Rev. D*, vol. 65, p. 022002, Dec 2001. 227, 235, 236

[379] B. Mours, E. Tournefier, and J.-Y. Vinet, "Thermal noise reduction in interferometric gravitational wave antennas: using high order TEM modes," *Classical and Quantum Gravity*, vol. 23, pp. 5777–5784, 2006. 228, 300

[380] J.-Y. Vinet, "Reducing thermal effects in mirros of advanced gravitational wave interferometric detectors," *Class. Quantum Grav.*, vol. 24, no. 15, pp. 3897 – 3910, 2007. 228, 284, 300

[381] M. Rakhmanov, "Response of test masses to gravitational waves in the local lorentz gauge," *Phys. Rev. D*, vol. 71, 2005. 228

[382] Y. Chen and S. Kawamura, "Displacement- and timing-noise free gravitational-wave detection," *Phys. Rev. Lett.*, vol. 96, 2006. 228

[383] Y. Chen *et al.*, "Interferometers for displacement-noise-free gravitational-wave detection," *Phys. Rev. Lett.*, vol. 97, 2006. 228

[384] K. Somiya *et al.*, "Utility investigation of artificial time delay in displacement-noise-free interferometers," *Phys. Rev. D*, vol. 76, 2007. 228

[385] S. Tarabrin and S. Vyatchanin, "Displacement-noise-free gravitational-wave detection with a single fabry-perot cavity: a toy model," *Phys. Lett. A*, vol. 372, 2008. 228

[386] A. Rakhubovsky and S. Vyatchanin, "Displacement-noise-free gravitational-wave detection with two fabry-perot cavities," *Phys. Lett. A*, vol. 373, 2008. 228

[387] S. Tarabrin and S. Vyatchanin, "Double michelson/fabry-perot interferometer for laser- and displacement-noise-free gravitational-wave detection." arXiv:0904.3296v1, 2009. 229

[388] S. Vyatchanin, "Displacement-noise-free resonant speed meter for gravitational-wave detection." arXiv:0808.3445v1, 2008. 229

[389] C. Hogan, "Holographic noise in interferometers." arXiv:0905.4803v8, 2009. 229

[390] C. Hogan and M. Jackson, "Holographic geometry and noise in matrix theory," *Phys. Rev. D*, vol. 79, 2009. 229

[391] C. Hogan *et al.*, "The fermilab holometer. a program to measure planck scale indeterminacy," 2009. 229

[392] S. Dimopoulos *et al.*, "Atomic gravitational wave interferometric sensor," *Phys. Rev. D*, vol. 78, 2008. 230

[393] Advanced LIGO Team, "Advanced LIGO Reference Design," tech. rep., 2006. 231, 233, 296

[394] H. Müller-Ebhardt, H. Rehbein, S. Hild, A. Freise, Y. Chen, R. Schnabel, K. Danzmann, and H. Lück, "Review of quantum non-demolition schemes for the einstein telescope." https://tds.ego-gw.it/itf/tds/file.php?callFile=ET-010-09.pdf, 2009. ET-010-09. 231, 233, 234, 236

[395] J. Harms, R. Schnabel, and K. Danzmann, "Finite mass beam splitter in high power interferometers," *Phys. Rev. D*, vol. 70, p. 102001, 2004. 232

[396] B. J. Meers, "Recycling in laser-interferometric gravitational-wave detectors," *Phys. Rev. D*, vol. 38, p. 2317, 1988. 232

[397] L. D. Fiore and the VIRGO collaboration, "The present status of the VIRGO Central Interferometer," *Class. Quant. Grav.*, vol. 19, p. 1421, 2002. 232

[398] M. Ando and the TAMA collaboration, "Stable operation of a 300-m laser interferometer with sufficient sensitivity to detect gravitational-wave events within our galaxy," *Phys. Rev. Lett.*, vol. 86, p. 3950, 2001. 232

[399] G. Heinzel, K. A. Strain, J. Mizuno, K. D. Skeldon, B. Willke, W. Winkler, R. Schilling, A. Ruediger, and K. Danzmann, "Experimental demonstration of a suspended dual recycling interferometer for gravitational wave detection," *Phys. Rev. Lett.*, vol. 81, p. 5493, 1998. 233

[400] A. Freise, G. Heinzel, K. A. Strain, J. Mizuno, K. D. Skeldon, H. Lück, B. Willke, R. Schilling, A. Rüdiger, W. Winkler, and K. Danzmann, "Demonstration of detuned dual recycling at the Garching 30 m laser interferometer," *Physics Letters A*, vol. 277, no. 3, pp. 135 – 142, 2000. 233

[401] K. Somiya, P. Beyersdorf, K. Arai, S. Sato, S. Kawamura, O. Miyakawa, F. Kawazoe, S. Sakata, A. Sekido, and N. Mio, "Development of a frequency-detuned interferometer as a prototype experiment for next-generation gravitational-wave detectors," *Appl. Opt.*, vol. 44, p. 3179, 2005. 233

[402] O. Miyakawa *et al.*, "Measurement of optical response of a detuned resonant sideband extraction gravitational wave detector," *Phys. Rev. D*, vol. 74, p. 022001, 2006. 233

[403] H. Grote, A. Freise, M. Malec, G. Heinzel, B. Willke, H. Lueck, K. A. Strain, J. Hough, and K. Danzmann, "Dual recycling for geo 600," *Class. Quantum Grav.*, vol. 21, p. S473, 2004. 233

[404] A. Buonanno and Y. Chen, "Quantum noise in second generation, signal-recycled laser interferometric gravitational-wave detectors," *Phys. Rev. D*, vol. 64, p. 042006, 2001. 233

[405] A. Buonanno and Y. Chen, "Signal recycled laser-interferometer gravitational-wave detectors as optical springs," *Phys. Rev. D*, vol. 65, p. 042001, 2002.

[406] A. Buonanno and Y. Chen, "Scaling law in signal recycled laser-interferometer gravitational-wave detectors," *Phys. Rev. D*, vol. 67, p. 062002, 2003.

[407] H. Rehbein, H. Müeller-Ebhardt, K. Somiya, S. L. Danilishin, R. Schnabel, K. Danzmann, and Y. Chen, "Double optical spring enhancement for gravitational wave detectors," *Phys. Rev. D*, vol. 78, p. 062003, 2008. 233

[408] T. Corbitt, Y. Chen, E. Innerhofer, H. Müller-Ebhardt, D. Ottaway, H. Rehbein, D. Sigg, S. Whitcomb, C. Wipf, and N. Mavalvala, "An all-optical trap for a gram-scale mirror," *Phys. Rev. Lett.*, vol. 98, p. 150802, Apr 2007. 233

[409] F. Y. Khalili and Y. Levin, "Speed meter as a quantum nondemolition measuring device for force," *Phys. Rev. D*, vol. 54, p. 4735, 1996. 233

[410] F. Y. Khalili, "The optical lever intracavity readout scheme for gravitational-wave antennae," *Phys. Lett. A*, vol. 298, p. 308, 2002. 233, 264

[411] P. Purdue, "Analysis of a quantum nondemolition speed-meter interferometer," *Phys. Rev. D*, vol. 66, p. 022001, 2002. 234, 303

[412] P. Purdue and Y. Chen, "Practical speed meter designs for quantum nondemolition gravitational-wave interferometers," *Phys. Rev. D*, vol. 66, p. 122004, 2002. 234, 236, 303

[413] K. McKenzie, "Private communication," 2008. 234

[414] S. L. Danilishin, "Sensitivity limitations in optical speed meter topology of gravitational-wave antennas," *Phys. Rev. D*, vol. 69, p. 102003, 2004. 234

[415] H. Müller-Ebhardt, *On quantum effects in the dynamics of macroscopic test masses.* PhD thesis, Leibniz Universität Hannover, 2009. 234

[416] T. Eberle, S. Steinlechner, J. Bauchrowitz, V. Haendchen, H. Vahlbruch, M. Mehmet, H. Müeller-Ebhardt, and R. Schnabel, "Quantum enhancement of the zero-area sagnac interferometer topology for gravitational wave detection," *Phys. Rev. Lett.*, 2010. 234, 236, 242, 304

[417] F. Khalili, S. Danilishin, H. Müeller-Ebhardt, H. Miao, Y. Chen, and C. Zhao, "Negative optical inertia for enhancing the sensitivity of future gravitational-wave detectors." http://arxiv.org/abs/1010.1124. 234

[418] V. B. Braginsky and F. Y. Khalili, "Nonlinear meter for the gravitational wave antenna," *Phys. Lett. A*, vol. 218, p. 167, 1996. 234

[419] V. B. Braginsky, M. L. Gorodetsky, and F. Y. Khalili, "Optical bars in gravitational wave antennas," *Phys. Lett. A*, vol. 232, p. 340, 1997.

[420] F. Y. Khalili, "Quantum speedmeter and laser interferometric gravitational-wave antennae." http://arxiv.org/abs/gr-qc/0211088v1, 2002. 235

[421] H. Rehbein, H. Müeller-Ebhardt, K. Somiya, C. Li, R. Schnabel, K. Danzmann, and Y. Chen, "Local readout enhancement for detuned signal-recycling interferometers," *Phys. Rev. D*, vol. 76, p. 062002, 2007. 234, 235

[422] C. M. Caves, "Quantum-mechanical noise in an interferometer," *Phys. Rev. D*, vol. 23, pp. 1693–1708, Apr 1981. 235, 237, 238, 239

[423] M. Xiao, L.-A. Wu, and H. J. Kimble, "Precision measurement beyond the shot-noise limit," *Phys. Rev. Lett.*, vol. 59, pp. 278–281, Jul 1987. 235, 239

[424] P. Grangier, R. E. Slusher, B. Yurke, and A. LaPorta, "Squeezed-light enhanced polarization interferometer," *Phys. Rev. Lett.*, vol. 59, pp. 2153–2156, Nov 1987. 239

[425] K. McKenzie, D. A. Shaddock, D. E. McClelland, B. C. Buchler, and P. K. Lam, "Experimental demonstration of a squeezing-enhanced power-recycled michelson interferometer for gravitational wave detection," *Phys. Rev. Lett.*, vol. 88, p. 231102, May 2002. 235, 242

[426] W. G. Unruh, *Quantum Optics, Experimental Gravitation and Measurement Theory*, ch. 6, p. 647. New York: Plenum, 1982. 235

[427] H. P. Yuen, "Contractive states and the standard quantum limit for monitoring free-mass positions," *Phys. Rev. Lett.*, vol. 51, pp. 719–722, Aug 1983. 235, 239

[428] A. F. Pace, M. J. Collett, and D. F. Walls, "Quantum limits in interferometric detection of gravitational radiation," *Phys. Rev. A*, vol. 47, pp. 3173–3189, Apr 1993.

[429] M. T. Jaekel and S. Reynaud, "Quantum limits in interferometric measurements," *Europhys. Lett.*, vol. 13, no. 4, pp. 301–306, 1990. 235, 239

[430] J. Harms, Y. I. Chen, S. Chelkowski, A. Franzen, H. Vahlbruch, K. Danzmann, and R. Schnabel, "Squeezed-input, optical-spring, signal-recycled gravitational-wave detectors," *Phys. Rev. D*, vol. 68, p. 042001, Aug 2003. 235, 242

[431] A. Buonanno and Y. Chen, "Improving the sensitivity to gravitational-wave sources by modifying the input-output optics of advanced interferometers," *Phys. Rev. D*, vol. 69, p. 102004, May 2004. 235, 236

[432] S. Chelkowski, H. Vahlbruch, B. Hage, A. Franzen, N. Lastzka, K. Danzmann, and R. Schnabel, "Experimental characterization of frequency-dependent squeezed light," *Phys. Rev. A*, vol. 71, no. 1, p. 013806, 2005. 235

[433] H. Vahlbruch, S. Chelkowski, B. Hage, A. Franzen, K. Danzmann, and R. Schnabel, "Demonstration of a squeezed-light-enhanced power- and signal-recycled michelson interferometer," *Phys. Rev. Lett.*, vol. 95, no. 21, p. 211102, 2005. 235, 242

[434] T. Corbitt, N. Mavalvala, and S. Whitcomb, "Optical cavities as amplitude filters for squeezed fields," *Phys. Rev. D*, vol. 70, p. 022002, Jul 2004. 235

[435] F. Y. Khalili, "Increasing future gravitational-wave detectors' sensitivity by means of amplitude filter cavities and quantum entanglement," *Phys. Rev. D*, vol. 77, p. 062003, Mar 2008. 235

[436] F. Y. Khalili, H. Miao, and Y. Chen, "Increasing the sensitivity of future gravitational-wave detectors with double squeezed-input," *Phys. Rev. D*, vol. 80, p. 042006, Aug 2009. 236, 246

[437] F. Y. Khalili, "Optimal configurations of filter cavity in future gravitational-wave detectors." http://arxiv.org/abs/1003.2859. 236

[438] S. P. Vyatchanin and A. B. Matsko *JETP*, vol. 77, p. 218, 1993. 236

[439] S. P. Vyatchanin and E. A. Zubova, "Quantum variation measurement of a force," *Physics Letters A*, vol. 201, no. 4, pp. 269 – 274, 1995. 236

[440] Y. Chen, S. L. Danilishin, F. Y. Khalili, and H. Müeller-Ebhardt, "Qnd measurements for future gravitational-wave detectors," *Gen. Relativ. Gravit.*, 2010. 236

[441] H. Vahlbruch, *Squeezed Light for Gravitational Wave Astronomy.* PhD thesis, Leibniz Universität Hannover, 2008. 238, 242

[442] H. P. Yuen, "Two-photon coherent states of the radiation field," *Phys. Rev. A*, vol. 13, pp. 2226–2243, Jun 1976. 237

[443] D. F. Walls, "Squeezed states of light," *Nature*, vol. 306, pp. 141–146, 1983. 237, 238

[444] G. Breitenbach, S. Schiller, and J. Mlynek, "Measurement of the quantum states of squeezed light," *Nature*, vol. 387, pp. 471–475, 1997.

[445] V. V. Dodonov, "'nonclassical' states in quantum optics: a 'squeezed' review of the first 75 years," *Journal of Optics B: Quantum Semiclass.*, vol. 4, pp. R1–R33, 2002. 237

[446] C. C. Gerry and P. L. Knight, *Introductory quantum optics.* Cambridge University Press, 2004. 237, 238, 240, 242

[447] J. DiGuglielmo, B. Hage, A. Franzen, J. Fiurášek, and R. Schnabel, "Experimental characterization of gaussian quantum-communication channels," *Phys. Rev. A*, vol. 76, p. 012323, Jul 2007. 238

[448] R. E. Slusher, L. W. Hollberg, B. Yurke, J. C. Mertz, and J. F. Valley, "Observation of squeezed states generated by four-wave mixing in an optical cavity," *Phys. Rev. Lett.*, vol. 55, pp. 2409–2412, Nov 1985. 238, 239, 241

[449] C. M. Caves, "Quantum-mechanical radiation-pressure fluctuations in an interferometer," *Phys. Rev. Lett.*, vol. 45, pp. 75–79, Jul 1980. 239

[450] K. S. Thorne, R. W. P. Drever, C. M. Caves, M. Zimmermann, and V. D. Sandberg, "Quantum nondemolition measurements of harmonic oscillators," *Phys. Rev. Lett.*, vol. 40, pp. 667–671, Mar 1978. 239

[451] V. B. Braginsky and F. Y. Khalili, "Quantum nondemolition measurements: the route from toys to tools," *Rev. Mod. Phys.*, vol. 68, pp. 1–11, Jan 1996. 239

[452] W. G. Unruh, *Quantum noise in the interferometer detector.* Plenum, 1983. 239

[453] C. M. Caves, "Defense of the standard quantum limit for free-mass position," *Phys. Rev. Lett.*, vol. 54, pp. 2465–2468, Jun 1985. 239

[454] D. Vitali, S. Gigan, A. Ferreira, H. R. Böhm, P. Tombesi, A. Guerreiro, V. Vedral, A. Zeilinger, and M. Aspelmeyer, "Optomechanical entanglement between a movable mirror and a cavity field," *Phys. Rev. Lett.*, vol. 98, p. 030405, Jan 2007. 239

[455] S. Pirandola, D. Vitali, P. Tombesi, and S. Lloyd, "Macroscopic entanglement by entanglement swapping," *Phys. Rev. Lett.*, vol. 97, p. 150403, Oct 2006. 239

[456] H. Müller-Ebhardt, H. Rehbein, R. Schnabel, and Y. Danzmann, K.and Chen, "Entanglement of macroscopic test masses and the standard quantum limit in laser interferometry," *Phys. Rev. Lett.*, vol. 100, p. 013601, Jan 2008. 239

[457] R. M. Shelby, M. D. Levenson, S. H. Perlmutter, R. G. DeVoe, and D. F. Walls, "Broad-band parametric deamplification of quantum noise in an optical fiber," *Phys. Rev. Lett.*, vol. 57, pp. 691–694, Aug 1986. 239, 241

[458] L.-A. Wu, H. J. Kimble, J. L. Hall, and H. Wu, "Generation of squeezed states by parametric down conversion," *Phys. Rev. Lett.*, vol. 57, pp. 2520–2523, Nov 1986. 239, 241

[459] H. Bachor and T. C. Ralph, *A Guide to Experiments in Quantum Optics*. Wiley-VCH, 2004. 239, 241

[460] M. Frede, R. Wilhelm, and D. Kracht, "250 W end-pumped Nd:YAG laser with direct pumping into the upper laser level," *Optics Letters*, vol. 31, pp. 3618–3619, 2006. 239, 288

[461] A. Furusawa, J. L. Sørensen, S. L. Braunstein, C. A. Fuchs, H. J. Kimble, and E. S. Polzik, "Unconditional Quantum Teleportation," *Science*, vol. 282, no. 5389, pp. 706–709, 1998. 239

[462] W. P. Bowen, N. Treps, B. C. Buchler, R. Schnabel, T. C. Ralph, H.-A. Bachor, T. Symul, and P. K. Lam, "Experimental investigation of continuous-variable quantum teleportation," *Phys. Rev. A*, vol. 67, p. 032302, Mar 2003.

[463] K. Schneider, M. Lang, J. Mlynek, and S. Schiller, "Generation of strongly squeezed continuous-wave light at 1064 nm," *Opt. Express*, vol. 2, no. 3, pp. 59–64, 1998.

[464] P. K. Lam, T. C. Ralph, B. C. Buchler, D. E. McClelland, H.-A. Bachor, and J. Gao, "Optimization and transfer of vacuum squeezing from an optical parametric oscillator," *Journal of Optics B: Quantum and Semiclassical Optics*, vol. 1, no. 4, p. 469, 1999. 239

[465] M. D. Reid and P. D. Drummond, "Correlations in nondegenerate parametric oscillation: Squeezing in the presence of phase diffusion," *Phys. Rev. A*, vol. 40, pp. 4493–4506, Oct 1989. 240

[466] H. Vahlbruch, A. Khalaidovski, N. Lastzka, C. Gräf, K. Danzmann, and R. Schnabel, "The geo 600 squeezed light source," *Classical and Quantum Gravity*, vol. 27, no. 8, p. 084027, 2010. 241, 242

[467] W. P. Bowen, R. Schnabel, N. Treps, H.-A. Bachor, and P. K. Lam, "Recovery of continuous wave squeezing at low frequencies," *Journal of Optics B: Quantum and Semiclassical Optics*, vol. 4, no. 6, p. 421, 2002. 241

[468] R. Schnabel, H. Vahlbruch, A. Franzen, S. Chelkowski, N. Grosse, H.-A. Bachor, W. Bowen, P. Lam, and K. Danzmann, "Squeezed light at sideband frequencies below 100 khz from a single opa," *Optics Communications*, vol. 240, no. 1-3, pp. 185 – 190, 2004. 241

[469] K. McKenzie, N. Grosse, W. P. Bowen, S. E. Whitcomb, M. B. Gray, D. E. McClelland, and P. K. Lam, "Squeezing in the audio gravitational-wave detection band," *Phys. Rev. Lett.*, vol. 93, p. 161105, Oct 2004. 241

[470] K. McKenzie, E. E. Mikhailov, K. Goda, P. K. Lam, N. Grosse, M. B. Gray, N. Mavalvala, and D. E. McClelland, "Quantum noise locking," *Journal of Optics B: Quantum and Semiclassical Optics*, vol. 7, no. 10, p. S421, 2005. 242

[471] H. Vahlbruch, S. Chelkowski, B. Hage, A. Franzen, K. Danzmann, and R. Schnabel, "Coherent control of vacuum squeezing in the gravitational-wave detection band," *Physical Review Letters*, vol. 97, no. 1, p. 011101, 2006. 242

[472] H. Vahlbruch, S. Chelkowski, K. Danzmann, and R. Schnabel, "Quantum engineering of squeezed states for quantum communication and metrology," *New Journal of Physics*, vol. 9, no. 10, p. 371, 2007. 242

[473] K. McKenzie, M. B. Gray, P. K. Lam, and D. E. McClelland, "Technical limitations to homodyne detection at audio frequencies," *Appl. Opt.*, vol. 46, no. 17, pp. 3389–3395, 2007. 242

[474] J. Gea-Banacloche and G. Leuchs, "Squeezed states for interferometric gravitational-wave detectors," *Journal of Modern Optics*, vol. 34, no. 6, pp. 798–811, 1987. 242

[475] K. Goda, O. Miyakawa, E. E. Mikhailov, S. Saraf, R. Adhikari, K. McKenzie, R. Ward, S. Vass, A. J. Weinstein, and N. Mavalvala, "A quantum-enhanced prototype gravitational-wave detector," *Nature Physics*, vol. 4, pp. 472–476, 2008. 242

[476] R. Schnabel, "Gravitational wave detectors: Squeezing up the sensitivity," *Nat Phys*, vol. 4, pp. 440–441, 2008. 242

[477] Y. Takeno, M. Yukawa, H. Yonezawa, and A. Furusawa, "Observation of -9 db quadrature squeezing with improvement of phasestability in homodyne measurement," *Opt. Express*, vol. 15, no. 7, pp. 4321–4327, 2007. 242

[478] H. Vahlbruch, M. Mehmet, S. Chelkowski, B. Hage, A. Franzen, N. Lastzka, S. G. ler, K. Danzmann, and R. Schnabel, "Observation of squeezed light with 10-db quantum-noise reduction," *Physical Review Letters*, vol. 100, no. 3, p. 033602, 2008.

[479] E. S. Polzik, "Quantum physics: The squeeze goes on," *Nature*, vol. 453, pp. 45–46, 2008. 242

[480] M. Mehmet, S. Steinlechner, T. Eberle, H. Vahlbruch, A. Thüring, K. Danzmann, and R. Schnabel, "Observation of cw squeezed light at 1550 nm," *Opt. Lett.*, vol. 34, no. 7, pp. 1060–1062, 2009. 242

[481] K. McKenzie, M. B. Gray, S. Gossler, P. K. Lam, and D. E. McClelland, "Squeezed state generation for interferometric gravitational-wave detection," *Classical and Quantum Gravity*, vol. 23, no. 8, p. S245, 2006. 242

[482] S. K. Ryutaro Takahashi, Koji Arai, "Direct measurement of the scattered light effect on the sensitivity in tama300," *Phys. Rev. D*, vol. 70, p. 062003, 2004. 256

[483] C. Bond, "Laguerre-gauss mode degeneracy in gravitational wave detectors." (Fourth Year Project Report, Internal document), 2010. 257, 286

[484] D. Shoemaker, "Future limits to sensitivity." G010026-00-G, 2001. 264

[485] G. Conforto and R. DeSalvo, "Proposal for lower frequency companions for the advanced ligo gravitational wave interferometric detectors," *Nuclear Instruments and Methods in Physics Research Section A: Accelerators, Spectrometers, Detectors and Associated Equipment*, vol. 518, no. 1-2, pp. 228 – 232, 2004. Frontier Detectors for Frontier Physics: Proceedin. 264

[486] S. Chelkowski, S. Hild, and A. Freise, "Prospects of higher-order laguerre-gauss modes in future gravitational wave detectors," *Phys. Rev. D*, vol. 79, p. 122002, Jun 2009. 266, 301

[487] E. Tournefier, "News from virgo : present statud and future upgrades." in2p3-00422110, version 1, October 2009. 269

[488] M. Lorenzini and the Virgo Collaboration, "The monolithic suspension for the Virgo interferometer," *Classical and Quantum Gravity*, vol. 27, no. 8, p. 084021, 2010. 269

[489] O. L. Anderson and H. E. Bömmel, "Ultrasonic absorption in fused silica at low temperatures and high frequencies," *Journal of the American Ceramic Society*, vol. 38, no. 4, pp. 125–131, 1955. 269

[490] C. Schwarz, R. Nawrodt, D. Heinert, M. Thuerk, R. Neubert, W. Vodel, A. Tünnermann, and P. Seidel, "Cryogenic setup for Q-factor measurements on bulk materials for future gravitational wave detectors," in *Proceedings of ICEC22-ICMC2008* (H.-M. Chang and other, eds.), The Korea Institute of Applied Superconductivity and Cryogenics, 2009. 269, 271

[491] J. Franc *et al.*, "Mirror thermal noise in laser interferometer gravitational wave detectors operating at room and cryogenic temperatures." ET document ET 09021, 2009. 270, 272, 285, 304

[492] T. Tomaru, T. Uchiyama, D. Tatsumi, S. Miyoki, M. Ohashi, K. Kuroda, T. Suzuki, A. Yamamoto, and T. Shintomi, "Cryogenic measurement of the optical absorption coefficient in sapphire crystals at 1.064?[mu]m for the large-scale cryogenic gravitational wave telescope," *Physics Letters A*, vol. 283, no. 1-2, pp. 80 – 84, 2001. 270

[493] C. T. Taylor, M. Notcutt, E. K. Wong, A. G. Mann, and D. G. Blair, "Measurement of the coefficient of thermal expansion of a cryogenic, all-sapphire, fabry-perot optical cavity," *Optics Communications*, vol. 131, no. 4-6, pp. 311 – 314, 1996. 270

[494] T. Uchiyama, T. Tomaru, M. E. Tobar, D. Tatsumi, S. Miyoki, M. Ohashi, K. Kuroda, T. Suzuki, N. Sato, T. Haruyama, A. Yamamoto, and T. Shintomi, "Mechanical quality factor of a cryogenic sapphire test mass for gravitational wave detectors," *Physics Letters A*, vol. 261, no. 1-2, pp. 5 – 11, 1999. 270, 271

[495] A. L. Alexandrovski, M. M. Fejer, and R. K. Route, "Effect of annealing on the light absorption in sapphire," in *Gravitational Waves - 3rd Edoardo Amaldi Conference*, 2000. 270

[496] L. collboration, "LCGT design document (ver. 3)," tech. rep., JGW-T0400030, 2009. 270

[497] M. Tokunari, T. Saito, S. Miyoki, M. Ohashi, and K. Kuroda, "Optical properties measurement of an Al2 O3 mirror substrate for the large-scale cryogenic gravitational wave telescope (LCGT)," *Class. Quantum Grav.*, vol. 27, p. 185015, 2010. 270

[498] M. Punturo *et al.*, "The third generation of gravitational wave observatories and their science reach," *Classical and Quantum Gravity*, vol. 27, no. 8, p. 084007, 2010. 270

[499] J. Software, "Material properties data base." 270, 272

[500] M. A. Green and M. J. Keevers, "Optical properties of intrinsic silicon at 300 k," *Progress in Photovoltaics: Research and Applications*, vol. 3, pp. 189–192, 1995. 271

[501] M. J. Keevers and M. A. Green, "Absorption edge of silicon from solar cell spectral response measurements," *Applied Physics*, vol. 66, 1995. 271

[502] B. J. Frey, D. B. Leviton, and T. J. Madison, "Temperature-dependent refractive index of silicon and germanium," in *Society of Photo-Optical Instrumentation Engineers (SPIE) Conference Series*, vol. 6273 of *Society of Photo-Optical Instrumentation Engineers (SPIE) Conference Series*, July 2006. 271, 278

[503] G. K. White and M. L. Minges, "Thermophysical properties of some key solids," *International Journal of Thermophysics*, vol. 15, pp. 1333–1343, 1994. 10.1007/BF01458841. 271

[504] R. Hull, *Properties of Crystalline Silicon.* The Institution of Engineering and Technology, 1999. 271, 304

[505] T. Tomaru *et al.*, "Thermal lensing in cryogenic sapphire substrates," *Classical and Quantum Gravity*, vol. 19, p. 2045, 2002. 271

[506] D. B. Leviton and B. J. Frey, "Temperature-dependent absolute refractive index measurements of synthetic fused silica," vol. 6273, p. 62732K, SPIE, 2006. 271

[507] A. A. A. Another, "Comingsoon," *A*, vol. 1, p. 1, 2000. 271, 272

[508] I. H. Malitson, "Refraction and Dispersion of Synthetic Sapphire," *J. Opt. Soc. Am.*, vol. 52, pp. 1377–1379, Dec 1962. 271

[509] G. M. Harry, A. M. Gretarsson, P. R. Saulson, S. E. Kittelberger, S. D. Penn, W. J. Startin, S. Rowan, M. M. Fejer, D. R. M. Crooks, G. Cagnoli, J. Hough, and N. Nakagawa, "Thermal noise in interferometric gravitational wave detectors due to dielectric optical coatings," *Classical and Quantum Gravity*, vol. 19, no. 5, p. 897, 2002. 273, 276

[510] G. M. Harry, H. Armandula, E. Black, D. R. M. Crooks, G. Cagnoli, J. Hough, P. Murray, S. Reid, S. Rowan, P. Sneddon, M. M. Fejer, R. Route, and S. D. Penn, "Thermal noise from optical coatings in gravitational wave detectors," *Appl. Opt.*, vol. 45, pp. 1569–1574, Mar 2006. 273, 276

[511] V. B. Braginsky, M. L. Gorodetsky, and S. P. Vyatchanin, "Thermodynamical fluctuations and photothermal shot noise in gravitational wave antennae," *Physics Letters A*, vol. 264, no. 1, pp. 1 – 10, 1999. 274

[512] M. Cerdonio, L. Conti, A. Heidmann, and M. Pinard, "Thermoelastic effects at low temperatures and quantum limits in displacement measurements," *Phys. Rev. D*, vol. 63, p. 082003, Mar 2001. 274

[513] R. Nawrodt *et al.*, "Mirror thermal noise calculation for ET." ET document ET 09027, 2009. 274, 304

[514] F. Bondu, P. Hello, and J.-Y. Vinet, "Thermal noise in mirrors of interferometric gravitational wave antennas," *Physics Letters A*, vol. 246, no. 3-4, pp. 227 – 236, 1998. 274

[515] Y. T. Liu and K. S. Thorne, "Thermoelastic noise and homogeneous thermal noise in finite sized gravitational-wave test masses," *Phys. Rev. D*, vol. 62, p. 122002, Nov 2000. 274

[516] V. B. Braginsky and S. V. Vyatchanin, "Corner reflectors and quantum non-demolition measurements in gravitational wave antennae," *Physics Letters A*, vol. 324, pp. 345–360, 2004. 278

[517] B. Benthem and Y. Levin, "Thermorefractive and thermomechanical noise in the beamsplitter of the GEO600 gravitational-wave interferometer," *Phys. Rev. D*, vol. 80, 2009. 278, 283

[518] J. Franc, J. Degallaix, and R. Flaminio, "Substrate thermo-refractive noise for future cryogenic gravitational wave detector." ET-00095A-10, 2010. 278

[519] B. Caron *et al.*, "SIESTA, a time domain, general purpose simulation program for the VIRGO experiment," *Astroparticle Physics*, vol. 10, pp. 369–386, 1999. 286

[520] M. Galimberti, "Requirements for et arm cavity mirrors." Talk at WP2-WP3 joint meeting, Jena, March 2010. 286

[521] M. Galimberti and R. Flaminio, "Surface specifications for ET mirrors: state of the art." ET-0133A-10, November 2010.

[522] M. Galimberti and R. Flaminio, "Mirror requirements for 3rd generation GW detectors." Talk at GWADW 2010, Kyoto, May 2010. 286

[523] J. Deile, R. Brockmann, and D. Havrilla, "Current status and most recent developments of industrial high power disk lasers," in *Conference on Lasers and Electro-Optics/International Quantum Electronics Conference*, p. CThA4, Optical Society of America, 2009. 287

[524] Y. Kalisky and O. Kalisky, "The status of high-power lasers and their applications in the battlefield," *Optical Engineering*, vol. 49, no. 9, p. 091003, 2010. 287

[525] A. Giesen and J. Speiser, "Fifteen years of work on thin-disk lasers: Results and scaling laws," *IEEE Journal of Selected Topics in Quantum Electronics*, vol. 13, no. 3, pp. 598–609, 2007. 287

[526] Q. Lü, N. Kugler, H. Weber, S. Dong, N. Müller, and U. Wittrock, "A novel approach for compensation of birefringence in cylindrical Nd:YAG rods," *Optical and Quantum Electronics*, vol. 28, pp. 59–69, 1996. 288

[527] W. Koechner and D. K. Rice, "Birefringence of YAG:Nd laser rods as a function of growth direction," *Journal of the Optical Society of America*, vol. 61, pp. 758–766, 1971. 288

[528] L. N. Soms, A. A. Tarasov, and V. V. Shashkin, "Problem of depolarization of linearly polarized light by a YAG: Nd^{3+} laser-active element under thermally induced birefringence conditions," *Soviet Journal of Quantum Electronics*, vol. 10, pp. 350–351, 1980. 288

[529] I. Shoji and T. Taira, "Intrinsic reduction of the depolarization loss in solid-state lasers by use of a (110)-cut $Y_3Al_5O_{12}$ crystal," *Applied Physics Letters*, vol. 80, pp. 3048–3050, 2002. 288

[530] O. Puncken, H. Tünnermann, J. J. Morehead, P. Weßels, M. Frede, J. Neumann, and D. Kracht, "Intrinsic reduction of the depolarization in Nd:YAG crystals," *Optics Express*, vol. 18, pp. 20461–20474, 2010. 288

[531] R. Wilhelm, D. Freiburg, M. Frede, D. Kracht, and C. Fallnich, "Design and comparison of composite rod crystals for power scaling of diode end-pumped Nd:YAG lasers," *Optics Express*, vol. 17, pp. 8229–8236, 2009. 288

[532] R. Wilhelm, M. Frede, and D. Kracht, "Power scaling of end-pumped solid-state rod lasers by longitudinal dopant concentration gradients," *IEEE Journal of Quantum Electronics*, vol. 44, pp. 232–244, 2008. 288

[533] R. Lavi and S. Jackel, "Thermally boosted pumping of neodymium lasers," *Applied Optics*, vol. 39, pp. 3093–3098, 2000. 288

[534] D. Kracht, D. Freiburg, R. Wilhelm, M. Frede, and C. Fallnich, "Core-doped ceramic Nd:YAG laser," *Optics Express*, vol. 14, pp. 2690–2694, 2006. 288

[535] S. Bedö, W. Lüthy, and H. P. Weber, "The effective absorption coefficient in double-clad fibres," *Optics Communications*, vol. 99, pp. 331–335, 1993. 288

[536] J. Limpert, F. Röser, S. Klingebiel, T. Schreiber, C. Wirth, T. Peschel, R. Eberhardt, and A. Tünnermann, "The rising power of fiber lasers and amplifiers," *IEEE J. of Selected Topics in Quantum Electronics*, vol. 13, pp. 537–545, 2007. 288

[537] Y. Jeong, J. K. Sahu, D. N. Payne, and J. Nilsson, "Ytterbium-doped large-core fibre laser with 1kW of continuous-wave output power," *Electronics Letters*, vol. 40, pp. 470–472, 2004. 288

[538] M. Hildebrandt, M. Frede, P. Kwee, B. Willke, and D. Kracht, "Single-frequency master-oscillator photonic crystal fiber amplifier with 148 W output power," *Optics Express*, vol. 14, pp. 11071–11076, 2006. 288

[539] C. Robin, I. Dajani, C. Vergien, C. Zeringue, and T. M. Shay, "Experimental and theoretical studies of single frequency PCF amplifier with output of 400 W," in *Fiber Lasers VII: Technology, Systems, and Applications* (K. Tankala, ed.), vol. 7580, p. 758011, SPIE, 2010. 288

[540] G. Canat, S. Jetschke, S. Unger, L. Lombard, P. Bourdon, J. Kirchhof, V. Jolivet, A. Dolfi, and O. Vasseur, "Multifilament-core fibers for high energy pulse amplification at 1.5 μm with excellent beam quality," *Optics Letters*, vol. 33, pp. 2701–2703, 2008. 289

[541] M. M. Vogel, M. Abdou-Ahmed, A. Voss, and T. Graf, "Very-large-mode-area, single-mode multicore fiber," *Optics Letters*, vol. 34, pp. 2876–2878, 2009. 289

[542] G. Canat, R. Spittel, S. Jetschke, L. Lombard, and P. Bourdon, "Analysis of the multifilament core fiber using the effective index theory," *Optics Express*, vol. 18, pp. 4644–4654, 2010. 289

[543] V. Kuhn, S. Unger, S. Jetschke, D. Kracht, J. Neumann, J. Kirchhof, and P. Wessels, "Experimental comparison of fundamental mode content in Er:Yb-codoped LMA fibers with multifilament- and pedestal-design cores," *Journal of Lightwave Technology*, vol. PP, no. 99, pp. 1–1, 2010. 289

[544] J. W. Nicholson, M. F. Yan, P. Wisk, J. Fleming, F. DiMarcello, E. Monberg, T. Taunay, C. Headley, and D. J. DiGiovanni, "Raman fiber laser with 81 W output power at 1480 nm," *Optics Letters*, vol. 35, pp. 3069–3071, 2010. 289

[545] Y. Jeong, J. K. Sahu, D. B. S. Soh, C. A. Codemard, and J. Nilsson, "High-power tunable single-frequency single-mode erbium:ytterbium codoped large-core fiber master-oscillator power amplifier source," *Optics Letters*, vol. 30, pp. 2997–2999, 2005. 289

[546] V. Kuhn, P. Wessels, J. Neumann, and D. Kracht, "Stabilization and power scaling of cladding pumped Er:Yb-codoped fiber amplifier via auxiliary signal at 1064 nm," *Optics Express*, vol. 17, pp. 18304–18311, 2009. 289

[547] S. Ramachandran, J. Fini, M. Mermelstein, J. Nicholson, S. Ghalmi, and M. Yan, "Ultra-large effective-area, higher-order mode fibers: a new strategy for high-power lasers," *Laser & Photonics Reviews*, vol. 2, pp. 429–448, 2008. 289

[548] J. W. Nicholson, A. M. DeSantolo, S. Ghalmi, J. M. Fini, J. Fleming, E. Monberg, F. DiMarcello, and S. Ramachandran, "Nanosecond pulse amplification in a higher-order-mode erbium-doped fiber amplifier," in *Conference on Lasers and Electro-Optics*, p. CPDB5, Optical Society of America, 2010. 289

[549] J. W. Nicholson *et al.*, "A higher-order-mode erbium-doped-fiber amplifier," *Opt. Express*, vol. 18, no. 17, pp. 17651–17657, 2010. 289

[550] J.-Y. Vinet, "On special optical modes and thermal issues in advanced gravitational wave interferometric detectors," *Living Reviews in Relativity*, vol. 12, no. 5, 2009. 290

[551] E. Genin, M. Mantovani, and P. Ruggi, "Advanced virgo inj: Radiation pressure effects in the advanced virgo imc longitudinal and angular directions," 2009. 291

[552] M. Punturo, "Radiation pressure effects on virgo mode cleaner," tech. rep., VIR-NOT-PER-1390-284, 2004. 291

[553] B. Canuel, R. Day, E. Genin, P. L. Penna, M. Mantovani, J. Marque, and F. Paoletti, "AdV INJ: Preliminary design study," tech. rep., VIR-0023A-09, 2009. 291

[554] E. Genin, J. Marque, B. Swinkels, and G. Vajente, "Virgo Input Mode Cleaner: Optical characterization," 2010. 291

[555] M. Barsuglia, "Some considerations about Laguerre-Gaussian modes for advanced Virgo," tech. rep., Presentation at AdV bi-weekly meeting July 1, 2008. 291

[556] S. Chelkowski, "Advanced virgo with higher order lg modes, implications for mirror radii of curvature," tech. rep., Presentation at Virgo week July 2008,VIR-0668A-08, 2008. 291

[557] E. Khazanov *et al.*, "Compensation of thermally induced modal distortions in faraday isolators," *IEEE Journal of Quantum Electronics*, vol. 40, p. 10, 2004. 291

[558] B. Canuel, R. Day, E. Genin, F. Nocera, and F. Paoletti, "High power input optics r+d : Final report," tech. rep., VIR-0296A-10, 2010. 291, 292

[559] E. Genin, "Advanced Virgo INJ: Faraday isolator, electro-optical modulator, high power beam dump and input mode-cleaner," 2010. 291, 292

[560] N. Mavalvala, D. McClelland, G. Mueller, D. Reitze, R. Schnabel, and B. Willke, "Lasers and optics: looking towards third generation gravitational wave detectors," *General Relativity and Gravitation*, vol. 2010. 291

[561] J. D. Mansell *et al. Appl.Opt*, vol. 40, pp. 366–374, 2001. 292

[562] L. Schnupp, "Presentation at european collaboration meeting on interferometric detection of gravitational waves." (Sorrent, Italy, Oct 1988), 1988. 293

[563] A. Michelson and E. Morley, "On the relative motion of the earth and the luminiferous ether," *Am. J.Sci. (3rd series)*, vol. 34, pp. 333–345, 1887. 293

[564] P. Fritschel, "talk at Technical Plenary Session of the LSC meeting 2003," 2003. 293

[565] R.L.Ward *et al.*, "dc readout experiment at the caltech 40m prototype interferometer," *Class. Quantum Grav.*, vol. 25, p. 114030, 2008. 293

[566] S. Hild, H. Grote, M. Hewitson, H. Lück, J. R. Smith, K. A. Strain, B. Willke, and K. Danzmann, "Demonstration and comparison of tuned and detuned signal recycling in a large-scale gravitational wave detector," *Classical and Quantum Gravity*, vol. 24, no. 6, pp. 1513–1523, 2007. 293, 294

[567] A. Buonanno, Y. Chen, and N. Mavalvala, "Quantum noise in laser-interferometer gravitational-wave detectors with a heterodyne readout scheme," *Phys. Rev. D*, vol. 67, p. 122005, Jun 2003. 293

[568] M. Hewitson *et al.*, "Optimal time-domain combination of the two calibrated output quadratures of GEO 600," *Classical and Quantum Gravity*, vol. 22, pp. 4253–4261, 2005. 294

[569] R.Lawrence *et al.*, "Adaptive thermal compensation of test masses in advanced ligo," *Class. Quantum Grav.*, vol. 19, p. 1803, 2002. 294

[570] V.Chickarmane *et al.*, "Squeezed light in a frontal-phase-modulated signal-recycled interferomete," *Phys. Rev. A*, vol. 57, pp. 3898–3912, 1998. 294

[571] R. W. P. Drever, J. L. Hall, F. V. Kowalski, J. Hough, and G. M. Ford, "Laser phase and frequency stabilization using an optical resonator," *Appl. Phys. B*, vol. 31, p. 97, 1983. 295

[572] S. Sato, S. Kawamura, K. Kokeyama, F. Kawazoe, and K. Somiya, "Diagonalization of the length sensing matrix of a dual recycled laser interferometer gravitational wave antenna," *Phys. Rev. D*, vol. 75, p. 082004, Apr 2007. 295

[573] R. Abbott *et al.*, "Advanced LIGO Length Sensing and Control Final Design," tech. rep., June 2010. 296, 307

[574] M. Evans *et al.*, "Lock acquisition of a gravitational-wave interferometer," *Optics Letters*, vol. 27, p. 598, 2002. 297

[575] F. Acernese *et al.*, "The variable finesse locking technique," *Classical and Quantum Gravity*, vol. 23, no. 8, p. S85, 2006. 298

[576] L. Barsotti and M. Evans, "Lock acquisition study for advanced LIGO," June 2010. 298

[577] M. Evans, P. Fritschel, D. McClelland, J. Miller, A. Mullavey, D. Shaddock, B. Slagmolen, and S. Waldman, "Advanced LIGO Arm Length Stabilization System Design," tech. rep., October 2010. 298, 307

[578] B. Slagmolen, G. de Vine, D. Rabeling, K. McKenzie, A. Mullavey, D. Shaddock, D. McClelland, M. Evans, and Y. Aso, "Advanced LIGO Arm Cavity Pre-Lock Acquisition System," tech. rep., July 2008. 298

[579] A. J. Mullavey, B. J. J. Slagmolen, D. A. Shaddock, and D. E. McClelland, "Stable transfer of an optical frequency standard via a 4.6 km optical fiber," *Optics Express*, vol. 18, pp. 5213–5220, 2010. 298

[580] E. Morrison *et al. Appl. Opt.*, vol. 33, p. 504, 1994. 299

[581] J. Sidles and D. Sigg, "Optical torques in suspended fabry-perot interferometers," *Phys. Lett. A*, vol. 354, pp. 167–172. 299

[582] P. Savov and S. Vyatchanin, "Estimate of tilt instability of mesa-beam and Gaussian-beam modes for advanced LIGO," *Phys. Rev. D*, vol. 74, p. 082002, 2006. 301

[583] P. Fulda, K. Kokeyama, S. Chelkowski, and A. Freise, "Experimental demonstration of higher-order Laguerre-Gauss mode interferometry," *Phys. Rev. D*, vol. 82, p. 012002, Jul 2010. 301

[584] A. Bunkowski, O. Burmeister, D. Friedrich, K. Danzmann, and R. Schnabel, "High reflectivity grating waveguide coatings for 1064 nm," *Classical and Quantum Gravity*, vol. 23, pp. 7297–7303, Dec. 2006. 302

[585] D. Rosenblatt, A. Sharon, and A. A. Friesem, "Resonant grating waveguide structures," *IEEE JOURNAL OF QUANTUM ELECTRONICS*, vol. 33, p. 11, 1997. 302

[586] M. G. Moharam and T. K. Gaylord, "Rigorous coupled-wave analysis of planar-grating diffraction," *J. Opt. Soc. Am*, vol. 71, pp. Issue. 7, 811–818, 1981. 302, 303

[587] F. Brückner, D. Friedrich, T. Clausnitzer, O. Burmeister, M. Britzger, E.-B. Kley, K. Danzmann, A. Tünnermann, and R. Schnabel, "Demonstration of a cavity coupler based on a resonant waveguide grating," *Opt. Express*, vol. 17, no. 1, pp. 163–169, 2009. 302

[588] F. Bruckner, D. Friedrich, T. Clausnitzer, M. Britzger, O. Burmeister, K. Danzmann, E.-B. Kley, A. Tunnermann, and R. Schnabel, "Realization of a monolithic high-reflectivity cavity mirror from a single silicon crystal," *Physical Review Letters*, vol. 104, p. 163903, 2010. 303

[589] R. Nawrodt *et al.*, "Mechanical Q-factor measurements on a test mass with a structured surface," *New Journal of Physics*, vol. 9, pp. 225–+, July 2007. 303